Mechanical Properties of Diamond Impregnated Cobalt Metal Matrix

James D. Dwan

Submitted in fulfilment of the requirements for the award of the degree of Doctor of Philosophy to the University of Dublin, Trinity College, 2011

Declaration

I declare that the present work has not been submitted as an exercise for a degree at any other university. This thesis consists entirely of my own work except where references indicate otherwise.

I agree that the library of the University of Dublin, Trinity College, Dublin may lend or copy this thesis upon request.

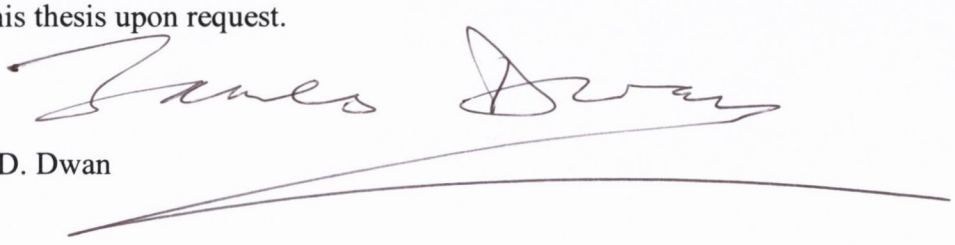

James D. Dwan

Acknowledgements

The author wishes to express his sincere gratitude and appreciation to the following people:

To my supervisor Professor David Taylor,

To my engineering colleagues at the Dept Mechanical Engineering, ITTDublin (Institute of Technology Tallaght) and technical staff in Dept. Mechanical & Manufacturing Engineering in Trinity College who encouraged and supported me in this work. Special thanks to Mr. David O'Mahony who as Technical Officer had the patience to try various means to grow fatigue cracks in very small specimens. Thanks must also be given to a number of my project students who helped me check various results,

To Element Six formerly De Beers Industrial Diamond Shannon, Co. Clare, Ireland, With special thanks to Mr. Colm De Barra and Mr. Brendan Kirwan,

To Boart Longyear, formerly Boart Technical Centre, Limerick, Co. Limerick, Ireland, for the use of their equipment with special thanks to Mr. Ken Kelly and Mr. Paul Wallek (now deceased),

To Eurotungstene in Grenoble, France for supplying the cobalt powder, with special thanks to M. Maxime Bonneau,

Finally, to my parents, especially my father (deceased) who I know would be very proud of me.

Summary

Diamond Impregnated Metal Matrix (DIMM) composite materials are a class of materials used in cutting and drilling of stone and construction materials. This thesis examined the effects of diamond size and diamond concentration on various mechanical properties of Diamond Impregnated Cobalt Metal Matrix (DICoMM). The mechanical properties investigated were: fracture toughness, fatigue crack propagation, transverse rupture strength, absorbed impact energy (absorbed energy), hardness and erosive wear behaviour. A range of diamond sizes and diamond concentrations were used in the investigation. Due to the Powder Metallurgy (PM) manufacturing process percent theoretical density is an important factor which strongly affects the mechanical properties of PM type materials. The effects of percent theoretical density on the different mechanical properties were also investigated.

The results reported and analysed show the various effects due to the addition of diamond to the cobalt metal matrix. From these results a number of predictive models were examined which yielded varying degrees of success. The Theory of Critical Distances (TCD) modelling was used to very good effect in predicting the transverse rupture strength of the DICoMM materials investigated in this thesis.

Also the TCD predicted transverse rupture strength was also shown to predict the experimentally determined Charpy impact energy (absorbed energy), for the different DICoMM metal matrix materials using the strain energy approach.

An empirical erosion wear model was proposed which was shown to reasonably predict the experimental wear results incorporating different pressures and angles of attack using eroding particles for DICoMM materials.

CONTENTS **PAGE NUMBER**

CHAPTER ONE: INTRODUCTION 1

1.1. Introduction 1

1.2. Background – Diamond Tools 1

1.3. Diamond Cutting Operation..... 3

1.4. Project Motivation..... 3

1.5. Objectives..... 5

1.6. Thesis Layout..... 6

CHAPTER TWO: LITERATURE REVIEW 8

2.1. Introduction..... 8

2.2. Diamond Impregnated Metal Matrices (DIMMs). 9

2.3. Metal Matrices..... 10

2.3.1. Cobalt Metal Matrix 11

2.4. Synthetic Diamonds..... 12

2.5. Diamond Impregnated Metal Matrix Tool Manufacture. 14

2.5.1. Diamond Concentration (DC) & the Diamond Tool. 15

2.5.1. Metal Powder & Diamond Grit Preparation... 17

2.5.2. Sintering Effects on Diamond..... 17

2.6. Mechanical Properties of PM, PMMC & DIMM Type Materials. 18

2.6.1. PM Materials & Sintered Density..... 18

2.6.2. Impact Properties & PM Materials..... 20

2.6.3. PM Materials - Impact Energy (Absorbed Energy) & Effects of Porosity ... 20

2.6.4. Fracture Toughness (FT) & PM Materials..... 21

2.7. Composite Materials - Particulate Metal Matrix Composites (PMMCs). 23

2.7.1. Mechanical Properties of PMMCs – An Overview. 24

2.7.2. Effects of Volume Fraction..... 25

2.7.3. Tensile Testing & PMMCs..... 25

2.7.4. Hardness Properties & PMMCs..... 25

2.7.5. Impact Properties & PMMCs..... 26

2.7.6. Transverse Rupture Strength (TRS) & PMMCs... 26

2.7.7. Fracture Toughness (FT) & PMMCs. 27

2.8. Mechanical Properties & Diamond Impregnated Metal Matrices (DIMMs). ...29

2.8.1. Tensile Testing & DIMMs..... 30

2.8.2. Impact Properties & DIMMs 30

2.8.3. Fracture Toughness (FT) & DIMMs. 31
2.8.4. Transverse Rupture Testing (TRS) & DIMMs. 31
2.8.5. Hardness & DIMMs..... 32
2.9. Role of Interparticle Spacing (IPS) 33
2.10. Wear & Diamond Impregnated Metal Matrices. 36
2.11. Predictive Models & Composite Models..... 41
2.12. Conclusions..... 44
CHAPTER THREE: EXPERIMENTAL PROCEDURES 47
3.1. Introduction. 47
3.2. Experimental Plan. 47
3.3. Test Specimen Designs. 48
3.3.1. Specimen Design Types. 48
3.4. Specimen Constituents or Materials. 50
3.5. Specimen Manufacture. 51
3.5.1. Specimen Mixing Calculations. 52
3.5.2. Mixing & Blending. 52
3.5.2.1. Mixing Speed & Time Test. 53
3.5.3. Hand-Loading of Diamond/Cobalt Material. 54
3.5.4. Hot Pressing (Pressure Sintering) 55
3.5.5. Specimen Hot Pressing Pressure Calculations. 59
3.5.6. Hot Pressing Temperature & Pressure Profiles. 60
3.5.7. Finishing Operations. 61
3.6. Hot Pressing Difficulties and Sources of Variation. 61
3.7. Specimen Compositions. 62
3.7.1. Cobalt Metal Matrix (CoMM) - Specimen Design Type 1. 62
3.7.2. Diamond Impregnated Cobalt Metal Matrix (DICoMM). 63
3.7.3. Charpy Impact Specimens – Specimen Design Type 2. 63
3.7.4. Bend Type Specimens - TRS - Specimen Design Type 2. 63
3.7.5. Bend Specimens – Fracture Toughness (FT) - Specimen Design Type 3. ... 64
3.8. Density Testing – DICoMM & CoMM Specimens. 65
3.9. Hardness Testing – DICoMM & CoMM Specimens. 66
3.10. Charpy Impact Testing. 68
3.10.1. Standard 50J Charpy Impact Testing – DICoMM Specimens. 68

3.10.2. Instrumented 300J Charpy Impact Testing – DICoMM & CoMM Specimens. 69
3.11. Bend-Transverse Rupture Strength (TRS). 70
3.11.1. TRS Three-Point Bend Testing - DIMM & CoMM Specimens. 71
3.11.2. TRS Four-Point Bend Testing - DIMM & CoMM Specimens. 73
3.12. TRS Elastic Moduli Property Determination - DIMM & CoMM Specimens. 73
3.13. Fracture Mechanics & Fracture Toughness. 73
3.13.1. Determination of Plane Strain Fracture Toughness (K_{1c}) & ASTM E-399-90. 74
3.13.2. Fracture Toughness Testing – PM & PMMC Type Materials. 77
3.13.3. Fracture Toughness Testing – DICoMM & CoMM Specimens. 77
3.13.4. Fatigue Precracking Procedure. 78
3.13.5. Fatigue Crack Length Measurement – Compliance Method. 79
3.13.6. Compliance Coefficients Determination Protocol. 83
3.13.7. Fracture Toughness Testing & DICoMMs – Precrack & FastTrack 2. 88
3.13.8. Fracture Toughness Testing & DICoMMs – No-Precrack & SERIES-IX. 89
3.14. Erosion Wear Test Procedure. 90
3.15. Determination of Experimental DC - Image Analysis – Scentis Software. 92

CHAPTER FOUR: RESULTS. 101
4.1. Introduction. 101
4.2. Compliance Coefficients Results. 101
4.3. Percent Theoretical Density (%TD) Test Results. 103
4.3.1. Fracture Toughness (FT) Specimen Test Results - %Theoretical Density. ... 103
4.3.2. TRS Specimen Test Results - %Theoretical Density. 106
4.3.3. Charpy Impact (CI) Specimen Test Results - %Theoretical Density 108
4.4. Hardness Test Results. 110
4.4.1. FT Specimen Test Results – Hardness. 110
4.4.2. TRS Specimen Test Results – Hardness. 113
4.4.3. Charpy Impact (CI) Specimen Test Results – Hardness. 115
4.5. Fracture Toughness (FT) Specimen Test Results - Fracture Toughness. 117
4.5.1. FT Specimen Test Results - ASTM E 399-90 Standard. 119
4.5.2. FT Specimen Test Results – Effect of Diamond Concentration. 122

4.5.3. FT Specimen Test Results – Effect of Diamond Size - US Mesh & Microns. 123
4.5.4. FT Specimen Test Results – Scentis & Diamond Concentration. 126
4.5.5. Fractography - Fracture Toughness Specimens. 127
4.6. Transverse Rupture Strength (TRS) Test Results... 130
4.6.1. TRS Specimen Test Results – Effect of Diamond Concentration (DC). 131
4.6.2. TRS Specimen Test Results – Effect of Diamond Size - US Mesh & Microns. 133
4.6.3. Fractography - TRS Specimens. 134
4.7. Elastic Modulus Determination. 136
4.8. Charpy Impact (CI) Specimen Test Results. 136
4.8.1. Impact Specimen Test Results – 300J Charpy Machine. 136
4.8.1.1. Impact Specimen Test Results – 300J Charpy – Effect of DC. 136
4.8.1.2. Impact Specimen Test Results – 300J Charpy – Effect of Mesh Size. 138
4.8.2. Impact Specimen Test Results – 50J & 300J Charpy Machines. 138
4.8.2.1. Impact Specimen Test Results – 50J & 300J Charpy – Effect of DC. 139
4.8.2.2. Impact Specimen Test Results –50J & 300J Charpy – Effect of Mesh Size. 140
4.9. Erosive Wear Test Results. 142
4.9.1. Erosive Wear Surface Photomacrographs. 146
4.10. Fractography of TRS, Impact & Fracture Toughness Specimens. 151

CHAPTER FIVE: DISCUSSION & ANALYSIS 156
5.1. Introduction. 156
5.2. Hardness & Percent Theoretical Density (%TD). 156
5.2.1. Fracture Toughness (FT) Specimens - Hardness & %Theoretical Density ... 157
5.2.2. Charpy Impact Specimens – Hardness & %Theoretical Density. 158
5. 2.3. TRS Specimens - Hardness & %Theoretical Density 158
5.2.4. Hardness Comparison of TRS, CI & FT. 159
5.3. Charpy Impact DICoMMs. 161
5.3.1. Charpy Impact Energy & %Theoretical Density 162
5.3.2. Charpy Impact Energy & Statistical Analysis – DC, US Mesh Size & 'Available-Energy'. 163
5.3.3. Charpy Impact Energy & Diamond Concentration (DC). 164
5.3.4. Charpy Impact Energy & Diamond Size (US Mesh Size). 166

5.3.5. Inter-Particle Spacing (IPS) & Charpy Impact Energy. 168
5.3.5.1. Charpy Impact Energy & IPS/MFP. 169
5.3.5.2. Charpy Impact Energy & IPS/NND. 172
5.4. Transverse Rupture Strength (TRS) – DICoMMs. 173
5.4.1. Transverse Rupture Strength (TRS) & %Theoretical Density. 173
5.4.2. Tensile Stressed Volume (TSV). 174
5.4.3. Inter-Particle Spacing (IPS) & TRS. 177
5.4.3.1. TRS & IPS/MFP. 177
5.4.3.2. TRS & IPS/NND. 180
5.4.4. TRS & Ductility – 'Displacement @ Break'. 180
5.5. Introduction Fracture Toughness Results Analysis. 182
5.5.1. Fracture Toughness Testing & %Theoretical Density. 182
5.5.2. FastTrack & SERIES-IX Method – K_{1C} Statistical Analysis. 187
5.5.3. Fracture Toughness & IPS (MFP & NND). 192
5.6. Modelling Strength and Fracture Properties in PMMCs. 196
5.6.1. Hahn-Rosenfield Fracture Toughness Model (Rice-Johnson Model). 196
5.6.2. Rabiei-Vendra-Kishi Fracture Toughness Model
– Modified Hahn-Rosenfield. 200
5.6.3. Lin & Queeney Fracture Toughness Model. 201
5.6.4. Kobayashi & Ohtani Fracture Toughness Model. 203
5.6.5. Jin & Batra Micromechanical Model. 204
5.7. Fracture Toughness & TRS Predictive Modelling. 205
5.7.1. Theory of Critical Distances & Fracture Toughness. 206
5.7.2. TCD & TRS Fracture Stress Analysis. 211
5.8. Charpy and TRS – Strain Energy Relationship. 215
5.9. Erosive Wear. 216
5.9.1. Erosion Wear Model - Modified Finnie Erosion Model. 218
5.9.2. Erosion Wear Patterns & Wear of Diamond Saw Blades. 223

CHAPTER SIX: CONCLUSIONS & RECOMMENDATIONS 225
6.1. Introduction. 225
6.2. Percent Theoretical Density (%TD). 225
6.3. Hardness. 225
6.4. Fatigue Crack Propagation. 226
6.5. Fracture Toughness. 226

6.6. Charpy Impact Energy 227
6.7. Transverse Rupture Strength (TRS). 228
6.8. Fracture Stress Predictive Model. 228
6.9. Erosive Wear. 229
6.10. Recommendations for Future Work. 229

REFERENCES 231

APPENDICES 249
APPENDIX 1. Cobalt Powder Couf. 249
APPENDIX 2 - Hot Press - Sintering Machine. 250
APPENDIX 3 - Specimen Type Hot Pressing Materials
Composition Spreadsheets – Charpy Impact, Tensile,
TRS & Fracture Toughness Specimens. 251
APPENDIX 4 - Alignment of Three-Pt Bend Fixture for Fracture
Toughness Testing. 256
APPENDIX 5 - Fracture Toughness Test Procedure. 257
APPENDIX 6 - Hardness & %Theoretical Density. 259
APPENDIX 7 - Charpy Impact IPS/MFP & IPS/NND. 260
APPENDIX 8 - Transverse Rupture Strength (TRS) IPS/MFP & IPS/NND. 265
APPENDIX 9 - Fracture Toughness IPS/MFP & IPS/NND. 271
APPENDIX 10 - Strain Energy TRS Predictions & Charpy Impact Energies. 276

LIST OF FIGURES AND TABLES **Page #**

Figure 1.1. Diamond Impregnated Metal Matrix (DIMM) 2
Figure 1.2. Diamond Tools in the Construction Industry Applications..... 2
Figure 1.3. Typical Diamond Metal Matrix Tools as used in Various Industries. 2
Figure 2.1. Diamond Impregnated Tools Process Flow Diagram 10
Figure 2.2. Diamond shapes can range from the well structured cubo-octahedral morphology, shown above to partially grown, irregular & fragmented crystals 12
Figure 2.3. Relationship between actual diamond size (μm) and US Mesh size. 13
Figure 2.4. Relationship between diamond sizes measured in US Mesh size to the actual number of diamond crystals or grits per carat (ct). 14
Figure 2.5. SDA Diamond Products (Saw Diamond Abrasive). 14
Figure 2.6. Number of diamond crystals for different diamond sizes (US Mesh Sizes) plotted against diamond concentration..... 16
Figure 2.7. Actual diamond size (microns) & number of diamond crystals for each diamond US Mesh size plotted against diamond concentration. 16
Figure 2.8. Diamond after Sintering at Various Temperatures. (a) Mild Attack, (b) Moderate Attack & (c) Severe Attack of the Diamond due to Matrix Metal. 18
Figure 2.9. Showing the effect of volume fraction with K_{1C} for a PPMC. 29
Figure 2.10. Interparticle Spacing (IPS) showing the two different interpretations, MFP & NND, also called MPS. 34
Figure 2.11. DIMM - Example of a Protruding Diamond in Metal Matrix. 37
Figure 2.12. Worn surface of saw blade after cutting, showing comet tail formation around diamond. 37
Figure 2.13. A worn surface of a diamond impregnated metal matrix segment showing diamonds in black and pull-outs where diamonds have been plucked prematurely. 38
Figure 2.14. Schematic Diagram of Erosive Wear. 40
Figure 2.15. Worn surface of a DIMM segment showing wear tracks on the metal matrix 41
Figure 3.1. Specimen Design Type 1 – 100% Cobalt Metal Matrix (CoMM) [Charpy, Bend-TRS, Bend-Fracture Toughness & Tensile Specimens]. 49
Figure 3.2. Specimen Design Type 2 – 100% Diamond Impregnated Cobalt Metal Matrix (DICoMM). [Charpy, Bend-TRS & Tensile Specimens]. 49
Figure 3.3. Specimen Design Type 3 - Diamond Impregnated Cobalt with Backing Layer (DICoMM+BL). [Bend - Fracture Toughness Specimens]. 50
Figure 3.4. Photomacrograph - SDA 85+ Diamond Grit. 50
Figure 3.5. Couf Co powder, ungranulated version of the powder showing very fine grains... 51
Figure 3.6. Turbula Type Mixer- 'Figure-of Eight' type mixing motion. 53
Figure 3.7. Soxhlet Filter Sleeve used to remove the dissolved wax from the Cobalt powder...54

Figure 3.8. Mould assembly including brass filling funnel, plastic cup, spatula, boron nitride spray & torque wrench. 55
Figure 3.9. Aluminium bolster with the graphite/insulation mould system. The bolster/mould is positioned on top of the aluminium filling grate. 56
Figure 3.10. Hot Press front view showing the mould assembly sitting on bottom graphite electrode. The water cooling pipes (black) can be seen with the electrical control panel on the right hand-side. 57
Figure 3.11. Showing close-up of the mould assembly on the lower graphite electrode with the thermocouple positioned in the aluminium bolster. 57
Figure 3.12. Shows the top graphite electrode in position with the Red colour indicating that current is passing through the mould system. 58
Figure 3.13. Hot pressing split-type mould for manufacture of tensile specimens. 59
Figure 3.14. Showing a hot pressed tensile specimen; the rough surface shows the diamond crystals protruding on the specimen surface. 59
Figure 3.15. Hot Pressing Cycle (Time, Temperature & Pressure Profile). 60
Figure 3.16. Belt grinder used to remove any remaining flashing following hot pressing..... 61
Figure 3.17. Ohaus Fine Balance (accuracy to 0.1mg). Used for density measurement Using Archimedes method. Shown in picture beaker with immersion apparatus for weighing in water. 65
Figure 3.18. Showing Indentec Rockwell hardness test machine. 67
Figure 3.19. Damage to the ball indenter as used in Rockwell HRB hardness testing due to the presence of diamond in DICoMM. 67
Figure 3.20. Zwick bench mounted Charpy impact tester, 50J machine. 68
Figure 3.21. Instron Instrumented Charpy Machine PW30 pendulum. 69
Figure 3.22. Instron 8516 Servohydraulic Universal Testing Machine. 72
Figure 3.23. Three-Point Bend Fixture Mark I showing TRS specimen & LVDT Extensometer. A safety cage also allowed the recovery of broken specimens. 72
Figure 3.24. Basic outline of a SENB type specimen sitting on rollers..... 76
Figure 3.25. Surface grinding (electroplated diamond wheel) operation used to ensure correct dimensions regarding the height (W) for the fracture toughness specimens..... 78
Figure 3.26. Mark II 3-point bend fixture with edm'ed recesses. A DICoMM specimen with CMOD gauge attached by integral knife edges can also be seen in the figure... 79
Figure 3.27. Transposition of Compliance, 'a/W' ratio and U called a transfer function. 81
Figure 3.28. Specimen arrangement with the 3-point bend fixture Mark I, with a brass SENB10 specimen in place for compliance coefficients determination. 84
Figure 3.29. Schematic representation of fatigue crack growth, showing fatigue crack growth da/dN plotted against stress intensity factor range, ΔK, log/log scales. 84

Figure 3.30. Normalised Compliance / a/W Relationship Determination Flow Diagram..... 86
Figure 3.31. Optical Profile Projector (OPP) showing the fracture surface of a wrought brass SENB10 specimen used in Compliance Coefficient Determination. 87
Figure 3.32. Brass SENB specimens with different fatigue cracks grown used for compliance coefficients determination. 87
Figure 3.33. SENB specimen on Mark II 3-point bend fixture with attached CMOD ready for testing. 88
Figure 3.34. Photomacrograph showing edm crack starter notch, fatigue precrack and finally the darker grey fast fracture surface following fracture toughness test of a DICoMM specimen. 89
Figure 3.35. Showing a typical DICoMM specimen which was fracture toughness tested with just the edm starter crack notch (a_0) using SERIES IX software. 90
Figure 3.36. 'Clarke' Siphons Hand Cabinet – modified for Erosion Wear Testing..... 91
Figure 3.37. Typical DIMM Specimen placed on stereo zoom microscope for image capture. 92
Figure 3.38. Image Capture of the typical specimen, Example Run 86/3..... 93
Figure 3.39. Imported specimen image in Scentis Program, Run 73/2 20/25, DC40..... 93
Figure 3.40. Percent Area Application launched in Scentis Program. 94
Figure 3.41. AOI Selection shown within the green border outline in figure. 94
Figure 3.42. Defining Number of Phases within the green bordered AOI. 95
Figure 3.43. Defining Phase 1 within the green bordered AOI. 95
Figure 3.44. Assigning Individual Colour to Phase 1 within the green bordered AOI. 96
Figure 3.45. Defining Cobalt Metallic surface within the green bordered AOI. 96
Figure 3.46. Assigning individual colour to Phase 2 within the green bordered AOI. 97
Figure 3.47. Defining Diamond Blooming within the green bordered AOI. 97
Figure 3.48. Phase 1, 2, and 3, defined within the green bordered AOI. 98
Figure 3.49. Selecting Measure Icon. 98
Figure 3.50. Output Table of Phase percentages. 99
Figure 3.51. Output Window in the Scentis Software. 99
Figure 3.52. Selection of the Entire Specimen Surface (AOI) TRS Run#179/2, 45/50, DC30. 100
Figure 3.53. Output Window for TRS Specimen Run#179/2. 100
Figure 4.1. Percentage difference between actual crack length & crack length determined using ASTM and new SENB10 Compliance Coefficients. 102
Figure 4.2. Percentage difference between actual crack length and crack length determined using ASTM and new SENB 5 Compliance Coefficients. 103
Figure 4.3. Fracture Toughness Specimen Results: Figure shows the Average %TD achieved for CoMM & DICoMMs for each DC. The average values recorded on the graph are the overall average obtained for each DC. CoMM is included for comparison purposes. ...104

Figure 4.4. Fracture Toughness Specimen Results: Figure shows %TD for each specimen achieved for CoMM and DICoMMs for each US Mesh size used plotted against DC. 105
Figure 4.5. Fracture Toughness Specimen Results: Figure shows the Standard Deviation for %TD achieved for CoMM and DICoMMs for each DC used. 105
Figure 4.6. TRS Specimen Results: Figure shows the Average %TD achieved for CoMM and DICoMMs for each DC. The average values recorded on the graph are the overall average obtained for each DC. CoMM is included for comparison purposes. 106
Figure 4.7. TRS Specimen Results: Figure shows the %TD for each specimen achieved for CoMM & DICoMMs for each US Mesh size used plotted against DC. 107
Figure 4.8. TRS Specimen Results: Figure shows the Standard Deviation for %TD achieved for CoMM and DICoMMs for each DC used. The results indicate that increasing diamond causes an increase in scatter in %TD. 107
Figure 4.9. Charpy Impact Specimen Results: Figure shows the Average %TD achieved for CoMM and DICoMMs for each DC. The average values recorded on the graph are the overall average obtained for each DC. CoMM is included for comparison purposes 108
Figure 4.10. Charpy Impact Specimen Results: Figure shows the %TD for each specimen achieved for CoMM and DICoMMs for each US Mesh size plotted against DC. 109
Figure 4.11. Charpy Impact Specimen Results: Figure shows the Standard Deviation for %TD achieved for CoMM and DICoMMs for each DC used. 110
Figure 4.12. Fracture Toughness Specimen Results: Figure shows the average Rockwell HRB hardness for all US Mesh sizes averaged for each DC, included is CoMM for comparison purposes. 111
Figure 4.13. Fracture Toughness Specimen Results: Rockwell HRB hardness plotted against DC with CoMM included. The hardness results are the average values found for each individual specimen for the different US Mesh sizes and DCs used. 112
Figure 4.14. Fracture Toughness Specimen Results: Figure shows Rockwell HRB hardness plotted against diamond size (US Mesh size). Average hardness results for each US Mesh size & DC30 & DC40. DC30 R = 0.68 and DC40 R = 0.83. 112
Figure 4.15. TRS Specimen Results: Figure shows the average Rockwell HRB hardness values for all US Mesh sizes averaged for each DC, included is CoMM for comparison purposes..... 113
Figure 4.16. TRS Specimen Results: Rockwell HRB hardness plotted against DC with CoMM included. The hardness results are the average values found for each individual specimen for the different US Mesh sizes and DCs used. 114
Figure 4.17. TRS Specimen Results: Shows Rockwell HRB hardness plotted against diamond size (US Mesh size). The hardness results are the average results for each US Mesh size and DC10 & DC40. 114

Figure 4.18. Charpy Impact Specimen Results: Figure shows Rockwell HRB hardness values for all US Mesh sizes averaged for each DC plotted against DC, included is CoMM for comparison purposes. 115
Figure 4.19. Charpy Impact Specimen Results: Figure shows the range of Rockwell HRB hardness plotted against DC with CoMM included. The hardness results are the average of three values for each individual specimen for the different US Mesh sizes and DCs used. 116
Figure 4.20. Charpy Impact Specimen Results: Figure shows Rockwell HRB hardness plotted against diamond size (US Mesh size), showing as diamond size gets finer an increasing trend in hardness occurs. Also, increasing DC causes a decrease in hardness. 116
Figure 4.21. Fracture Toughness Specimen Results: Plane Strain fracture toughness K_{1C} results for FastTrack and SERIES-IX. The results are individual results for each US Mesh size and DC..... 119
Figure 4.22. Fracture Toughness Specimen Results: Fracture toughness K_{1C} and K_Q results for FastTrack. The results are individual results for each US Mesh size and DC. 120
Figure 4.23. Fracture Toughness Specimen Results: Fracture toughness K_{1C} and K_Q results for SERIES-IX. The results are individual results for each US Mesh size and DC. 121
Figure 4.24. Fracture Toughness Specimen Results: Fracture toughness K_{1C} results for both FastTrack and SERIES-IX combined. The results are individual results for each US Mesh size and DC. 122
Figure 4.25. Fracture Toughness Specimen Results: Standard Deviation for the plane strain fracture toughness (K_{1C}) results for both FastTrack and SERIES-IX combined. The result for each diamond concentration is the standard deviation of the K_{1C} values making up each diamond concentration. 123
Figure 4.26. Fracture Toughness Specimen Results: Plane strain fracture toughness (K_{1C}) results for DC20 and DC30 FT specimens tested using FastTrack or SERIES-IX, showing the effect of increasing K_{1C} with decreasing diamond size is still showing significance at different diamond concentrations. 124
Figure 4.27. Fracture Toughness Specimen Results: Standard Deviation for each US Mesh size using all the K_{1C} results for both FastTrack and SERIES-IX combined. The result for each diamond size (US Mesh) is the Standard Deviation of the K_{1C} values of the different diamond concentrations for that size. 124
Figure 4.28. Fracture Toughness Specimen Results: Figure shows fracture toughness (K_{1C}) (FastTrack & SERIES-IX) averaged over all DCs for each diamond size plotted against US Mesh size. Correlation coefficient R = 0.84. 125
Figure 4.29. Fracture Toughness Specimen Results: Figure shows fracture toughness (K_{1C}) (FastTrack & SERIES-IX) averaged over all DCs for each diamond size plotted against diamond size in microns. 126

Figure 4.30. Fracture Toughness Specimen Results: Figure shows the plain strain fracture toughness (K_{1C}) (FastTrack & SERIES-IX) individual results plotted against diamond concentration. The diamond concentration used is both nominal and experimentally determined using SCENTIS image analysis software. 127
Figure 4.31. FastTrack Fracture Toughness fracture surface of specimen 40/45 DC10 showing diamonds present in the fast fracture failure surface, but with a diamond present at the interface between the fatigue crack and fast fracture. Run 19/5, mag. x 10. 128
Figure 4.32. FastTrack Fracture Toughness specimen showing fracture surface of specimen 30/35 DC10 showing two diamond clusters present on the fast fracture failure surface. Run 20/6, mag. x 10. 128
Figure 4.33. FastTrack Fracture Toughness specimen showing fracture surface of specimen 30/35 DC30 showing diamonds present along the fatigue/fast fracture interface. Run 96/3, mag. x 10. 129
Figure 4.34. FastTrack Fracture Toughness specimen showing fracture surface of specimen 50/60 DC30 showing diamonds present along the fatigue/fast fracture interface. Run 98/1, mag. x 10. 129
Figure 4.35. FastTrack Fracture Toughness specimen which failed to grow a fatigue crack but subsequently fracture toughness tested. The fast fracture surface of the 60/70 DC25 specimen shows diamonds present along the fracture surface. Run 78/1, mag. x 10. 130
Figure 4.36. TRS Specimen Results: Figure shows the individual specimen TRS results for CoMMs (50mm Span) & DICoMMs (40 & 50mm spans) plotted against DC. The results are for each specimen for each US Mesh size and DC. CoMM specimen results shown in red. ...131
Figure 4.37. TRS Specimen Results: Average failure stress for each DC for specimens which were tested using 40mm and 50mm spans. CoMM average TRS result (50mm span) shown in red. 132
Figure 4.38. TRS Specimen Results: Figure shows the average failure stress for 60/70 US Mesh diamond DICoMM specimens showing that failure stress decreases as diamond concentration increases. CoMM average TRS result (50mm span) shown in red. 132
Figure 4.39. TRS Specimens: All DC10 and DC30 TRS specimens tested using both 40mm & 50mm spans, showing the effect of increasing failure stress with decreasing diamond size is still showing significance at different diamond concentrations. 133
Figure 4.40. TRS Specimen Results: Figure shows the Standard Deviation for Failure Stress achieved for CoMM and DICoMMs for each DC used. 134
Figure 4.41. TRS specimen showing fracture surface of specimen 30/35 DC40 showing diamonds present on the fracture surface. Run 134/1, mag. x 10. 135
Figure 4.42. TRS specimen showing fracture surface of specimen 25/30 DC40 showing large clustering of diamonds present on the fracture surface. Run 146/2, mag. x 10. 135

Figure 4.43. TRS specimen showing fracture surface of specimen 45/50 DC30 showing large clustering of diamonds present on the fracture surface. Run 179/2, mag. x 10. 135
Figure 4.44. Charpy Impact Specimen Results: Impact energy where a selected sample were tested using a 300J Instron Charpy pendulum machine. This figure is for individual results. .. 137
Figure 4.45. Charpy Impact Specimens Results: Average Impact energy for each DC for specimens which were tested using the instrumented 300J Instron machine. 137
Figure 4.46. Charpy Impact Specimens Results: DC1 impact specimens tested using 300J machine, showing increasing impact energy with finer sized diamond. 138
Figure 4.47. Charpy Impact Specimen Results: Impact energy for all the CI specimens (50J & 300J) plotted against diamond concentration. The figure is for individual results for each US Mesh size. The individual 100% Cobalt specimen values are also plotted in red. 139
Figure 4.48. Charpy Impact Specimens Results: Figure shows the averaged impact energies for all the CI specimens (50J & 300J) plotted against diamond concentration. The averaged 100% Cobalt is also plotted. 140
Figure 4.49. Charpy Impact Specimens Results: All DC10 and DC40 impact specimens tested using 50J or 300J machines, showing the effect of increasing impact energy with decreasing diamond size is still showing significance at different diamond concentrations. ... 141
Figure 4.50. Charpy Impact Specimen Results: Figure shows the Standard Deviation for Impact Energy achieved for CoMM and DICoMMs for each DC used. 141
Figure 4.51. Charpy Impact Specimen Results: Figure shows the Standard Deviation for Impact Energy achieved for DICoMMs for DC1, DC10 and DC20 used. 142
Figure 4.52. DC10 Total Mass Loss versus Time, 3bar/15°. 143
Figure 4.53. DC10 Total Mass Loss versus Time, 5bar/35°. 143
Figure 4.54. Total Mass Loss versus Time: DC10 & DC30, 30/35, 40/45 & 60/70 @ 3bar/15°. DC30 30/35 is missing due to experimental error. 144
Figure 4.55. DC30 Total Mass Loss versus Time: 30/35, 40/45 & 60/70 @ 6bar/45° 144
Figure 4.56. DC10 & DC30 Total Mass Loss versus Time: 30/35, 40/45 & 60/70 @ 6bar/45°. 145
Figure 4.57. DC10 & DC30 Total Mass Loss versus Time: 30/35, 40/45 & 60/70 @ 5Bar/35°..... 145
Figure 4.58. DC10 & DC30 Total Mass Loss versus Time: 30/35, 40/45 & 60/70 @ 4Bar/25°, DC30 30/35 is missing due to experimental error. 146
Figure 4.59. Worn surface of DICoMM test specimen due to erosion showing comet tail formation around diamonds on surface of specimen. 147
Figure 4.60. Worn surface of DICoMM test specimen due to erosion showing comet tail formation around diamonds on the surface of specimen. 147

Figure 4.61. Comet tail formation due to erosion wear of cobalt matrix around diamond. Note, erosive flow is from bottom to top of picture. Mag. x 150. 148
Figure 4.62. SEM Photomicrograph of a DC40 Charpy specimen eroded at a pressure/angle of 6bar/45^0. Mag. x 1.0k. 148
Figure 4.63. SEM Photomicrograph of a DC10 Charpy specimen eroded at a pressure/angle of 3bar/45^0 . Mag. x 1.0k. 149
Figure 4.64. SEM Photomicrograph of a DICoMM specimen eroded at a pressure/angle of 6bar/15^0. Mag x 1.0k. 149
Figure 4.65. SEM Photomicrograph of a DICoMM specimen eroded at a pressure/angle of 3bar/15^0. Mag. x 1.0k. 150
Figure 4.66. Showing eroded surface of DICoMM where a pull-out has been rounded off due to the eroding particles. 150
Figure 4.67. SEM photomicrograph (mag. x 5.0k) of a fracture toughness specimen Run 96/6 showing the fine ductile failure with the typical cup & cone failure pattern found in the fast fracture area. 151
Figure 4.68. SEM photomicrograph (mag. x 3.0k) of fracture toughness specimen Run96/6 showing a large pore in the Cobalt metal matrix. 152
Figure 4.69. Charpy Run 48/2, 800^{0}C, (mag. x 1.0k) showing ductile failure. 153
Figure 4.70. Charpy Run 48/2, 800^{0}C, (mag. x 1.0k) & inset @ mag. x 4.0k showing ductile failure..... 153
Figure 4.71. SEM EDX chemical analysis of white spot on diamond surface as seen in Figure 4.70. 154
Figure 4.72. Charpy Run 48/2, 800^{0}C, (mag. x 5.0k) & inset @ mag. x2.0k showing poorly sintered cobalt on surface of diamond giving rise to increased porosity in DICoMM material..154
Figure 5.1. Fracture Toughness Specimens: Figure shows the average Rockwell (HRB) hardness plotted for each US Mesh size plotted against %Theoretical Density, with 100% Cobalt in red. Correlation coefficient R = 0.32. 157
Figure 5.2. Charpy Impact Specimens: Figure shows the average Rockwell (HRB) hardness result for each US Mesh size plotted against %Theoretical Density. Also included is 100% Cobalt in this graph. R = 0.56..... 158
Figure 5.3. TRS Specimens: Figure shows the average Rockwell (HRB) hardness result for each US Mesh size plotted against %Theoretical Density. Also included is 100% Cobalt in this graph. R = 0.56. 159
Figure 5.4. FT, CI & TRS Specimen Results: Figure shows the average Rockwell (HRB) hardness result for the US Mesh sizes plotted against diamond concentration. Included is 100% Cobalt for comparison..... 160
Figure 5.5. Charpy Impact Specimen Results: Figure shows Rockwell hardness (HRB) plotted against % Theoretical Density (%TD) for DC 10 & 40. 161

Figure 5.6. Charpy Impact Specimens Results: Shows effect of %TD on the impact energy. Including CoMM in results in red. This figure is for individual results. R = 0.37. 162
Figure 5.7. Charpy Impact Specimens Results: Shows effect of %TD on the impact energy. This figure is for individual results. Correlation coefficients for the diamond concentrations as follows: DC1 R = 0.51, DC10 R =0.33 & DC30 R = 0.16. 163
Figure 5.8. Charpy Impact Specimen Results: Impact energy for all the CI specimens (50J & 300J) plotted against diamond concentration. The figure is for individual results for each US Mesh size. The individual 100% Cobalt specimen values are also plotted in red. Note: Same figure as Figure 4.47. 165
Figure 5.9. Charpy Impact Specimen Results: Figure shows the Standard Deviation for Impact Energy achieved for CoMM and DICoMMs for each DC used. 166
Figure 5.10. Charpy Impact Specimen Results: DC1 impact specimens tested using 50J & 300J machines, showing increasing impact energy with finer sized diamond. 166
Figure 5.11. Charpy Impact Specimen Results: DC1 and DC40 impact specimens tested using 50J & 300J machines, showing increasing impact energy with finer sized diamond..... 167
Figure 5.12. Charpy Impact Specimen Results: Standard Deviations for DC1, DC10 and DC40 Charpy impact specimens (50J & 300J) for each US Mesh size. R = 0.46. 168
Figure 5.13. Charpy Impact Specimen Results: Graph of Charpy plotted against IPS/MFP (mm). DC1 was not used because of its large value of IPS/MFP (mm). R = 0.63. 170
Figure 5.14. Charpy Impact Specimen Results: Graph of Charpy plotted against IPS/MFP (mm). DC1 was not used because of its large value of IPS/MFP (mm). R = 0.12. 171
Figure 5.15. Charpy Impact Specimen Results: Graph of Charpy plotted against IPS /MFP (mm) for DC10 & DC40. DC10, R = 0.67. DC40, R = 0.58. 172
Figure 5.16. TRS Specimens Results: Shows effect of %TD on TRS failure stress, included are the CoMM results in red. This figure is for individual specimen results. R = 0.29. 173
Figure 5.17. TRS Specimens Results: Shows effect of %TD on the TRS plotted for different diamond concentrations. Correlation coefficients for the different diamond concentrations are as follows: DC1 R = 0.54, DC20 R = 0.51 & DC30 R = 0.62. 174
Figure 5.18. TRS Specimen Results: Figure shows the individual failure stress achieved for CoMM and DIMMs for each DC tested using 40mm & 50mm spans. The results plotted here are for each individual specimen for each US Mesh size & DC. 175
Figure 5.19. TRS Specimen Results: Figure shows the individual TRS failure stress plotted against TSV, for 40mm and 50mm spans. 176
Figure 5.20. TRS Specimen Results: Figure shows TRS plotted against TSV for DC1 & DC30 for 40mm and 50mm spans. Correlation coefficients for DC1 (40mm) R = 0.69, DC30 (40mm). R = 0.64, DC1 (50mm) R = 0.57 & DC30 (50mm) R = 0.39. 177
Figure 5.21. TRS Specimen Results: Graph of TRS plotted against IPS/MFP. DC1 was included in this graph using IPS/MFP. R = 0.21. 178

Figure 5.22. TRS Specimen Results: Graph of TRS plotted against IPS/MFP. DC1 was not used because of its large IPS/MFP. N = 156, R = 0.27. 179
Figure 5.23 TRS Specimen Results: Graph of TRS plotted against IPS/MFP for diamond concentrations, DC10 and DC30. DC10 R = 0.45 & DC30 R = 0.51. 180
Figure 5.24. TRS Specimen Results: Graph of 'Displacement @ Break' plotted against diamond size. The trendline showing a decreasing displacement with increasing diamond size, DC1, DC20 and DC30. R values for DC1 = 0.41, DC20 = 0.40 & DC30 = 0.48. 181
Figure 5.25. TRS Specimen Results: Graph of 'Displacement @ Break' plotted against DC. The trendline showing a decreasing displacement with increasing DC, R = 0.40. 181
Figure 5.26 Fracture Toughness Specimens: Figure shows FastTrack combined K_{1C} & K_Q results plotted against %TD. Sample size: Total 122, (K_{1C} 51 & K_Q 70), R = 0.22. 183
Figure 5.27 Fracture Toughness Specimens: Figure shows SERIES-IX combined K_{1C} & K_Q results plotted against %TD. Sample size: Total 132, (K_{1C} 37 & K_Q 99), R = 0.64..... 183
Figure 5.28 Fracture Toughness Specimens: Figure shows FastTrack results for K_{1C} & K_Q plotted against %TD. Sample size: K_{1C} 51, R = 0.05 & K_Q 70, R = 0.38. 184
Figure 5.29 Fracture Toughness Specimens: Figure shows SERIES-IX results for K_{1C} & K_Q plotted against %TD. Sample size: K_{1C} 37, R = 0.46 & K_Q 99, R = 0.50. 185
Figure 5.30. Shows the effect of a yield strength increase on a valid K_{1C} result according to ASTM E 399 standard. 186
Figure 5.31 Fracture Toughness Specimens: Figure shows K_Q for FastTrack & SERIES-IX plotted against %TD. SERIES–IX R = 0.5 & FastTrack R = 0.57..... 187
Figure 5.32 Fracture Toughness Specimens: Figure shows K_{1C} for FastTrack & SERIES-IX plotted against %TD. Sample size: SERIES-IX 37 & FastTrack 51. 188
Figure 5.33 Fracture Toughness Specimens: Figure shows K_{1C} results for SERIES-IX versus Diamond Size (Microns) for DC20 & DC30. DC20 R = 0.96 & DC30 R = 0.39. 190
Figure 5.34 Fracture Toughness Specimens: Figure shows K_{1C} results for SERIES-IX versus Diamond Size PSD, for DC20 & DC30. DC20 R = 0.94 & DC30 R= 0.58. 191
Figure 5.35 Fracture Toughness Specimens: Figure shows K_{1C} results for FastTrack versus Diamond Size (Microns) for DC10, DC20 & DC40. DC10 R =0.49, DC20 R = 0.99 & DC40 R = 0.58..... 192
Figure 5.36 Fracture Toughness Specimens: K_{1C} for FastTrack & SERIES-IX combined plotted against IPS/MFP (mm). R = 0.04. 193
Figure 5.37. Fracture Toughness Specimens: K_{1C} for FastTrack & SERIES-IX combined plotted against 1/(IPS/MFP). DC1 was not used because of its large IPS/MFP. R = 0.38. 194
Figure 5.38. Fracture Toughness Specimens: K_{1C} for FastTrack & SERIES-IX combined plotted against Reciprocal of IPS/NND. DC1 was not used because of its large IPS/NND. R =0.46. 195

Figure 5.39. Fracture Toughness Specimens: K_{1C} for FastTrack & SERIES-IX combined plotted against IPS/NND for DC20 & DC30. DC20 R = 0.87 & DC30, R = 0.40. 196
Figure 5.40. Fracture Toughness Specimen Results: Shows experimental fracture toughness K_{1C} with results using Hahn-Rosenfield model. Pore size used instead of particle size. 199
Figure 5.41. Fracture Toughness Specimen Results: Shows experimental fracture toughness K_{1C} results using Hahn-Rosenfield model & Rabiei Vendra & Kishi Model, a modified form of Hahn-Rosenfield model. Pore size was used instead of particle size..... 201
Figure 5.42. Fracture Toughness Specimen Results: Shows experimental fracture toughness K_{1C} results with prediction model of Lin & Queeney & variations of model. 202
Figure 5.43. Fracture Toughness Specimen Results: Experimental and predicted results as determined using Kobyashi-Ohtani model. The results for both experimental and model are average results for each diamond size. 204
Figure 5.44. Fracture Toughness Specimen Results: Experimental and predicted results as determined using Jin-Batra Micromechanics model. The results for both experimental and model are average results for each diamond size. 205
Figure 5.45. Fracture Toughness Specimens: Fracture stress σ_f as a function of defect size, i.e. diamond size, in 100%Cobalt PM matrix; hot pressed at 800°C. Red values indicate range of pertinent diamond sizes as used in this project. 209
Figure 5.46. Fracture Toughness Specimens: Fracture stress σ_f as a function of defect size, i.e. diamond size, in 100% Cobalt PM matrix; hot pressed at 800°C. Yellow points indicate range of pertinent diamond sizes present as clusters. 210
Figure 5.47. Fracture Toughness Specimens: Fracture stress σ_f as a function of defect size, i.e. diamond size, in 100%cCbalt PM matrix; hot pressed at 800°C. Red indicates cluster size i.e. diamond size x2 & yellow indicates cluster size i.e. diamond size x3. 211
Figure 5.48. Predicted TRS fracture stress σ_f and experimental TRS failure stress plotted as a function of diamond size for DC1 & DC40 using 40mm span. 212
Figure 5.49. Predicted TRS fracture stress σ_f and experimental TRS failure stress plotted as a function of diamond size for DC1 & DC40 using 50mm span. The TRS prediction lines show upper & lower bound results for the two DCs. 213
Figure 5.50. Predicted TRS fracture stress σ_f and experimental TRS failure stress plotted as a function of diamond size for DC1 & DC40 for 40mm & 50mm spans combined. The TRS prediction lines show upper & lower bound results for the two DCs. 214
Figure 5.51. Predicted TRS fracture stress σ_f and experimental TRS failure stress plotted as a function of diamond size for DC1 & DC40 for 40mm & 50mm spans combined. The TRS prediction lines show upper & lower bound results for the two DCs. 214

Figure 5.52. Predicted Strain Energy using Predicted TRS fracture stress σ_f and experimental Charpy impact energy plotted as a function of diamond size (microns) for DC1, DC10 & DC40. The Strain Energy TRS prediction lines show upper & lower bound results. 216
Figure 5.53. Flow Model – Convergent-Divergent Nozzle for Compressible Flows. 218
Figure 5.54. Wear Erosion Results: Experimental & Theoretical Results for 40/45 DC10 & DC30 @ different Pressures & Angles. 221
Figure 5.55. Wear Erosion Results: Experimental & Theoretical Results for DC10 30/35 @ different Pressures & Angles. 222
Figure 5.56. Wear Erosion Results: Experimental & Theoretical Results for DC10 60/70 @ different Pressures & Angles. 222

LIST OF TABLES

Table 2.1 Table shows relationship between Diamond Concentration and Vol. %..... 15
Table 3.1. CoMM (Specimen Type & Design 1 with Hot Pressing Temps.)..... 62
Table 3.2. DICoMM Charpy Impact Specimen Compositions & Design Type 2 (800°C). 63
Table 3.3. DICoMM Bend - TRS Specimen Compositions & Design Type 2 (800°C)..... 64
Table 3.4. DICoMM Bend - FT Specimen Compositions & Design Type 3 (800°C). 64
Table 3.5 Dimensions of SENB Specimen showing the nominal dimensions in mm..... 75
Table 3.6. Jablonski et al. SENB Compliance Coefficients. 82
Table 3.7. ASTM E399-90 SENB Compliance Coefficients. 82
Table 3.8. The test procedure showing the DC and US Mesh size specimens with the Pressures and Angles. 92

Glossary/Nomenclature

AM – Area Method

ANSI - American National Standards Institute

AOI – Area-of-Interest

ASTM – American Society for Testing and Materials

Bar – Unit of Pressure, an Accept Unit of Pressure in SI System. 1bar = 100kPa

C_d – Coefficient of Discharge

CI - Charpy Impact

CMOD – Crack Mouth Opening Displacement (gauge)

Co - Cobalt

COD – Crack Opening Displacement (gauge)

CoMM – Cobalt Metal Matrix

CSA – Cross Sectional Area

Ct – Carat

CTOD – Crack Tip Opening Displacement

DC – Diamond Concentration

DI – Diamond Impregnated (tools)

DICoMM – Diamond Impregnated Cobalt Metal Matrix

DIMM – Diamond Impregnated Metal Matrix

d_p – Particle Diameter

D_p – Particle Diameter (Abrasive Particle Diameter)

ΔK_{th} – Threshold Stress Intensity

E – Young's Modulus

E_R – Erosion Rate

EDS – Energy Dispersive Spectrum

FCC – Face Centred Cubic

FEPA - Federation Europeene des Fabricants de Produits Abrasifs

FI - Friability Index

FT – Fracture Toughness

γ – Specific Heat for Air

HCP – Hexagonal Close Packed

HP – Hot Pressing

J - Joule

ICM – Imaginary Crack Method

IPS – Interparticle Spacing

K_{1C} – Plane Strain Fracture Toughness

L – Critical Distance (TCD)

LEFM - Linear Elastic Fracture Mechanics

LM – Line Method

LVDT – Linear Variable Displacement Transducer

MFP – Mean Free Path

MMC – Metal Matrix Composite

MPIF – Metals Powder Industries Federation

NND – Nearest Neighbour Distance

OPP – Optical Profile Projector

P_0 – Gas Pressure

PM – Powder Metallurgy

PM/TCD – Point Method/TCD

PMMC – Particulate Metal Matrix Composite

PSD – Particle Size Distribution

R – Correlation Coefficient

ρ - Density

r – Ratio between Pressure in Reservoir to Ambient Pressure

R^2 – Coefficient of Determination

ROM – Rule of Mixtures

ρ_p – Particle Density

ρ_{water} – Density of Water

SEM – Scanning Electron Microscopy

SENB - Single Edge Notched Bend

TCD – Theory of Critical Distances

TI - Toughness Index

TRS – Transverse Rupture Stress TSI - Thermal Strength Index

TSV – Tensile Stressed Volume

TTI - Thermal Toughness Index

U – Strain Energy

UTS – Ultimate Tensile Strength

V_g – Velocity of Gas

VM – Volume Method

V_p - Velocity of Particle

V_f – Volume Fraction

%TD – Percent Theoretical Density

CHAPTER ONE: INTRODUCTION

1.1. Introduction

This chapter, the Introduction, will firstly cover the material being investigated, Diamond Impregnated Metal Matrices (DIMMs) in an overview format, their uses and applications, and very briefly how they function in a typical application. The chapter will then explain the reasons for initiating the project and background for it based on information found in the literature. The objectives will be covered, giving the main experimental variables and properties being investigated. The chapter will then outline the different chapters in the thesis and what aspects they will deal with.

1.2. Background – Diamond Tools

Diamond has been used for centuries as an industrial tool. Wapler [1] describes early patents for different applications of diamond. The first efficient circular saw blade was perfected in France in 1885 [2] and used in practice in 1889 in Euville stone quarries [3]. In 1892 the first diamond tipped drill was used to drill gold bearing 'reefs' in South Africa [4]. Jennings and Wright [2] describe the workings of these early saws, and how this led to the development of matrices from metal powders. The technique of mixing diamonds in metal powders and sintering gives rise to the term 'diamond impregnated metal matrix (DIMM) and is where the term 'diamond impregnated' (DI) tool originates.

DIMMs or DI tools consist of randomly dispersed and randomly orientated diamond crystals in a matrix, which can be metal, vitreous or resin, depending on the type of cutting application, see Figure 1.1. In this project, a metal matrix is only considered.

It was not until the mid 19th century that today's methods of manufacture using the PM process and uses originated [1].

Regarding the diamond, the application dictates what type and size of diamond is used. Metal bonded diamond tools are used extensively for cutting, sawing, drilling, and surface grinding of stone, concrete, advanced ceramics and cemented carbides [5].

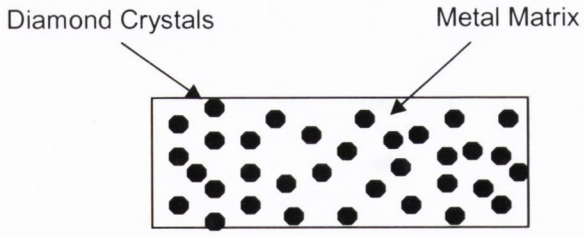

Figure 1.1. Diamond Impregnated Metal Matrix (DIMM).

For example, Figure 1.2 shows the different types of diamond impregnated metal bonded diamond tool applications as used in the construction industry. An up-to-date review of the role of diamond tools in the construction industry is given by [6].

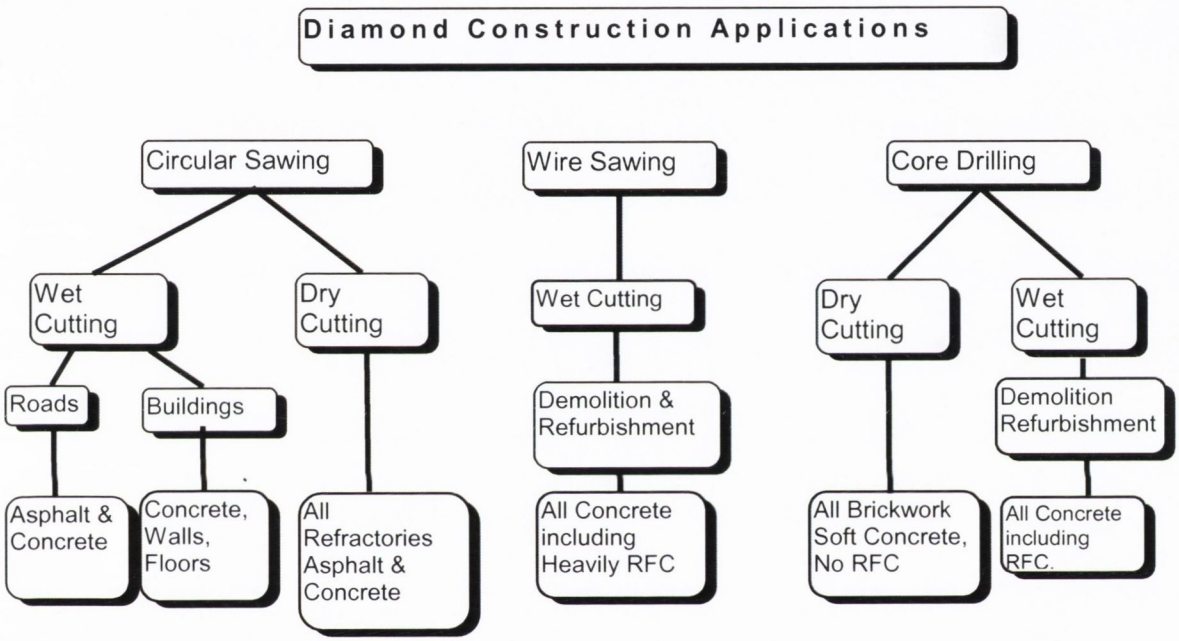

Figure 1.2. Diamond Tools in the Construction Industry Applications.

In Figure 1.3, different types of diamond impregnated metal matrix tools can be seen as used in the rock, stone and construction industries.

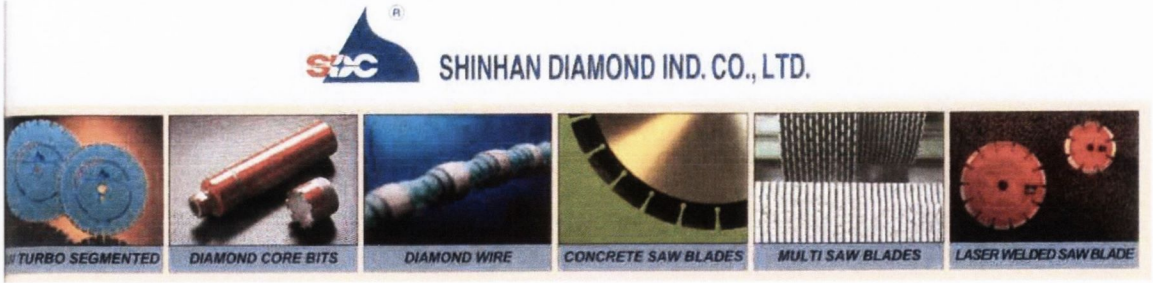

Figure 1.3. Typical Diamond Metal Matrix Tools as Used in Various Industries.

1.3. Diamond Cutting Operation

In a typical diamond impregnated (DI) tool, e.g. saw blade, diamond crystals are exposed and are proud on the cutting surface. It is these diamonds which are doing the cutting of the rock and producing rock cuttings or detrius. As the DI tool cuts, the matrix erodes away from these 'cutting' diamonds. This exposes the diamond and gives the crystals clearance for penetrating the hard rock material as well as allowing the cuttings to be flushed out. For their proper operation, the metal bond must wear away progressively so that new diamonds are exposed to continue the cutting action during the life of the diamond tool. The functions of the metal bond are two fold (a) to hold or support the diamond crystal rigidly and prevent it from sinking into the metal matrix and (b) to erode at a rate compatible with the diamond loss due to wear as it cuts the workpiece e.g. rock.

Designing a new diamond tool can be very expensive especially where full scale blade testing has to be carried out; a typical 600mm diameter blade contains 40 segments. Substantial cost savings can be made if this type of testing could be eliminated completely or greatly reduced by being able to match the mechanical properties of the DIMM with the properties of the material to be cut.

1.4. Project Motivation

This project examines the mechanical properties especially fracture properties of DIMMs which are used in a variety of industries, ranging from the construction to mining and stone industry. The main driver for the project was the extreme lack of design capability of a diamond tool for an application from a first principles aspect based on the mechanical properties of these DIMM materials. In the literature very scant information is available on the mechanical properties of DIMMs. The matching up of mechanical properties including wear properties of DIMMs with the resulting cutting performance in various applications is important when designing 'free-cutting' blades or 'hard' wear resistant blades. All this data is non-existent and at present blade design is based on limited scientific knowledge and hands-on experience.

Initially it was hope to investigate the relationship of mechanical properties to the wear behaviour of DIMMs in applications; however this proved very difficult for various reasons. In the general literature, a number of formulae relating mechnical properties to

wear resistance are presented including, e.g. fracture toughness [7, 8] and hardness [9]. With regard to erosion, there are again many formulae relating wear to mechanical properties [10].

The following references from the literature related to various mechanical properties are regarded as important for DIMM tools. Three main aspects are focussed on, diamond retention, properties of the metal matrix alone and DIMM as a composite. Most of the references focus on retention and the matrix. However, these opinions are just conjecture and have not been fully substantiated.

Konstanty [11] states that '*the knowledge of the actual interactions between the workpiece, the diamond and the matrix is poor, and there may be other factors affecting diamond retention which still remain unknown and are difficult to determine satisfactorily*'. During cutting the diamond-matrix interactions occur in a variety of forms depending on the size and shape of each individual diamond particle, its orientation and loading conditions, residual stresses in the matrix, diamond-matrix friction etc. Konstanty [11] comments that '*existing theoretical knowledge of diamond retention has evolved from simplistic models*', which is very true when one reads the various 'Thought Experimental Models' that have been developed about diamond retention presented in the literature.

The important mechanical properties of the matrix regarding diamond retention range from the modulus of resilience [12] yield strength, energy to yield, strain hardening coefficient [11], elastic deformation capability, its notch sensitivity (stress concentrations due to diamond crystals) [12] and finally high hot strength and toughness to overcome the heat generated with interrupted vibrations during cutting [13].

Also comparisons are made between what is considered to be more important regarding diamond retention capacity where ductility is more important than yield strength or hardness and resistance to abrasive wear is of secondary importance [11, 14]. However, regarding yield strength Konstanty states that a high yield strength which allows scope for large reversible elastic deformation can aid diamond retention because it prevents 'fall-out' [11, 14].

Regarding the matrix, transverse rupture strength (TRS), hardness and impact strength are deemed important [11, 15]. When considering DIMMs, residual stresses are built up around the diamonds in a metal matrix and consequently notch-sensitivity and ductility (impact damage) are also cited as important parameters [14].

Regarding DIMMs, fracture toughness properties are important [11, 16] with TRS being cited as a better indicator of tool life than matrix hardness [5]. Fatigue properties of DIMMs have also been mentioned to be an important property due to the complex alternating stresses on the diamonds as the tool cuts [11, 14].

Finally, Konstanty et al. state that the most important mechanical properties are workpiece dependent i.e. type of stone, which is very true. This is because the application workpiece has huge variability, e.g. with hard stones, ductility is a more important than hardness yield strength and resistance to abrasive wear. In soft abrasive stones, wear characteristics are important where ductility is of secondary importance [14]. Finally, materials with a high H/E (hardness/modulus of elasticity) have superior wear resistance [16].

So as can be seen from the above sources of what is considered to be important regarding DIMMs, there is no major consensus on what is really important. Also the concept that DIMMs are a composite material has not been accepted. The effects of the addition and amount of diamond on the mechanical properties of DIMMs and treated as a continuum is not yet considered. The above preamble sets the scene in outlining the objectives of the project.

1.5. Objectives

The objectives of the project are:

(a) Investigate the effect of diamond size and diamond concentration (DC) (vol. fraction) on the fracture properties, fracture toughness, hardness & impact energy (absorbed energy), of diamond impregnated cobalt matrix composite material,

(b) Investigate the effect of diamond size and diamond concentration (DC) (vol. fraction) on the TRS properties of diamond impregnated cobalt matrix composite material.

(c) Investigate the effect of diamond size and diamond concentration (DC) (vol. fraction) on the wear erosion properties of diamond impregnated cobalt matrix composite material.
(d) Compare the experimentally determined data with existing composite material models, fracture models and wear models, and discuss how the results are amenable to predictive analysis.

Initially, the project hoped to investigate if there was any correlation between the fracture properties of diamond-impregnated materials and their wear properties. However, due to the complexity and multi-disciplinary nature of such a project only a section could be investigated in this project.

For clarity, where impact energy or Charpy impact energy is mentioned in this work, it refers to the fracture energy absorbed by the specimen due to the impact event. It is the absorbed impact energy and is not the striker energy.

1.6. Thesis Layout

The intent of the layout of this thesis report is to lead the reader through the complexities of diamond impregnated metal matrix materials in as readable a format as possible.

In Chapter Two, Literature Review, will further outline DIMM materials, diamond types and aspects of diamond technology which are important to understanding the research carried out. DIMM manufacture, the metal matrices used especially cobalt and also the effects that processing has on the diamond crystals. As DIMM materials are manufactured by the PM process and also, the fact that DIMMs are similar to particulate metal matrix type composites (PMMCs). These materials, PM and PMMCs will be reviewed as a structure and material model in comparing DIMM mechanical properties with these existing materials where more research work has been carried out and is available in the literature. Both PM and PMMC materials will be reviewed in relation to their mechanical properties and the important factors which influence their mechanical properties. Regarding PM materials, how porosity level influences fracture toughness. Similarly PMMCs will be covered in relation to the effects that hard particulates have on the mechanical properties of these types of materials. Finally, the very little research work carried out on DIMMs and their metal matrices will be reviewed.

In Chapter Three, Experimental Procedures, the different material combinations of diamond size and concentration (vol. fraction) and metal matrix, the different temperatures tested will be covered, including tables for clarity. The DIMM manufacturing will be covered and aspects which were found to be difficult to produce a perfectly homogeneous material will be explained. The different tests which were then carried out will be covered and any experimental tests which are unusual will be explained in depth, e.g. instrumented charpy and fracture toughness testing.

In Chapter Four, Results, will be covered graphs and tables of the most important data will be delineated. Other experimental data will be referenced to the Appendices where appropriate. The main emphasis in recording the results will be to keep the chapter flowing and keep information clear and easy for understanding.

Chapter Five, Discussion & Analysis, the main analysis of the results and how they compare to that found in the Chapter Two. Also, predictive models as used in PM and PMMC type materials will be examined as to their applicability to the results and an analysis regarding cobalt based DIMMs.

Finally, Chapter Six, Conclusions & Recomendations, will cover the main results found in the project and what predictive models can be used.

CHAPTER TWO: LITERATURE REVIEW

2.1. Introduction

This literature review will cover a group of materials known as diamond impregnated metal matrices (DIMMs). It will review them from a number of different aspects because they strongly influence the mechanical behaviour of DIMMs. These aspects originate because of their method of manufacture and also their constituent parts which have very different mechanical and physical properties.

The review will briefly lead the reader through a course covering PM type materials and particulate composites especially Particulate Metal Matrix Composites (PMMCs). The justification for this is that DIMMs have similarities with PM type materials because they are processed by PM methods, regarding PMMCs their similarities encompass their typical make-up, hard brittle particulates impregnated in a soft metal matrix. The resulting mechanical properties due to PM processing and PMMCs are influenced by their structure and their manufacturing process. It is hoped that this will help the reader understand how DIMMs behave in comparison to PM and PMMC and build a structure in analysing DIMMs' mechanical properties.

As a quick overview, the author is considering DIMMs as a composite material. The reasons are simple. DIMMs are composed of two very different types of materials (diamond, a ceramic-like material & metal, the matrix) similar to Particulate Metal Matrix Composites (PMMCs) also known as Discontinuous Metal Matrix Composites (DMMCs). Also, since they are manufactured by the PM route, they behave and show the typical microstructures and mechanical properties of PM materials. Examining DIMMs from these two perspectives is important because they play roles in their resultant mechanical properties.

Diamond tool research is often carried out solely on the metal matrices because of the high cost of diamonds and the impression that the DIMM will behave similarly to the metal matrix. The assumption that the mechanical properties determined using just the metal matrices will be similar to DIMMs is incorrect, because the diamonds do influence the results appreciably as will be shown in the thesis. However, investigating the matrix

alone which is often found also in the literature [17] yields limited results because of the interaction of the diamond and matrix. So the investigation of the diamond/matrix material has to be carried out in order to move forward and add to the understanding of these materials and their interaction with the stone work piece.

This chapter will firstly give an overview of DIMMs, covering their uses and how they function in a typical application. It will then explain how diamond in these applications is manufactured so that the reader is fully aware of the difficulties of working with diamond grit types, diamond concentration (DC), diamond size measured using US Mesh Size (US-MS). It will briefly explain the cobalt powder used because readers are more aware of metal powders than diamond crystals. The review will then cover how the DIMMs are manufactured by the powder metallurgy (PM) process and how sintering influences and has the capability of degrading the diamond crystals.

2.2. Diamond Impregnated Metal Matrices (DIMMs)

As already mentioned above, DIMM based diamond tools are manufactured using the Powder Metallurgy (PM) process, and especially the PM process called Hot Pressing (HP). The PM process is chosen because it minimises the potential degradation of the diamonds which are susceptible to graphitisation at high temperatures, which is achieved by using a reduced sintering time. The PM process also allows different metal and alloy matrices to be tailored to suit the different workpiece conditions encountered. Finally, due to the extreme hardness of the diamond excessive wear on manufacturing tooling would result if other manufacturing processes were used. For more information regarding the PM process, the reader is referred to [18, 19, 20]. Even with the versatility of PM processing, there are a number of complexities associated with it. Regarding the metal powders the following play a major role: different types of powders, powder properties, particle size, particle size distribution, particle morphology, and surface condition. Regarding the PM process itself the following areas are very influential in the resulting PM component: powder mixing & blending, lubrication, cold pressing and sintering parameters. Finally the resulting microstructure which is produced strongly influences the mechanical properties of PM component. These same issues pertain to DIMMs type materials.

The typical PM manufacturing route used in DIMM production is (a) preparation of the metal powders and diamonds including mixing, blending and lubrication (b) cold pressing to the desired shape and (c) sintering of the diamond/metal green compact to produce the DIMM 'segment'. There are four methods of sintering the DIMM segment, (a) hot pressing, (b) free-sintering (c) infiltration and the less common method is (d) hipping. The process called hot-pressing (HP) is the mainstay for processing of DIMMs. The reader is referred to the paper by Dwan [21] for a comprehensive review of the manufacture of diamond tools and also to a recent book on the subject of powder metallurgy of diamond tools by Konstanty [12, 22, 23]. Typical process flow chart can be seen in Figure 2.1.

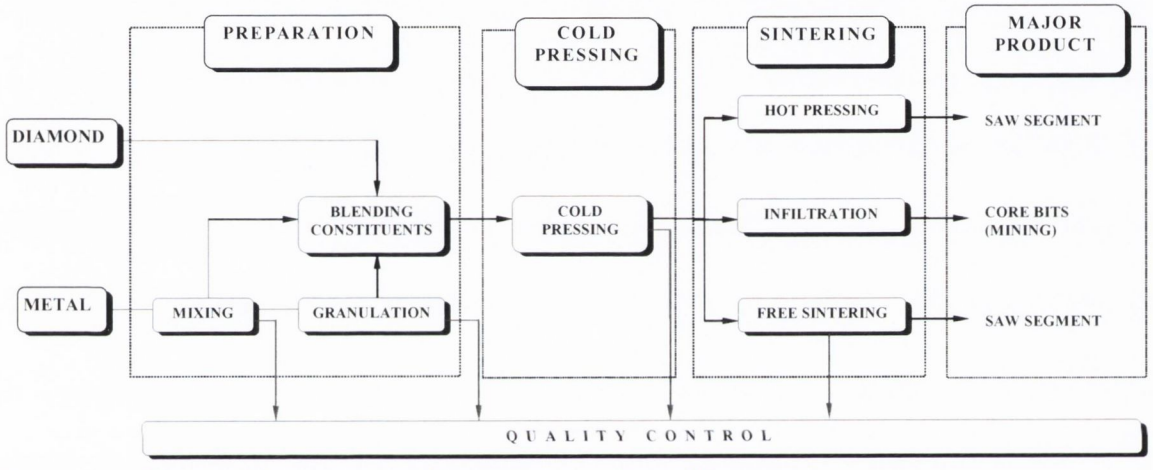

Figure 2.1. Diamond Impregnated Tools Process Flow Diagram.

2.3. Metal Matrices

Regarding the metal matrices used in DIMMs, Thakur [24] discusses in detail the different types of metal matrices used. The typical metals are cobalt, tungsten, iron and nickel and their alloys. Also, secondary hardening and abrasion resistant materials are used for increased matrix wear resistance in very abrasive rock conditions, e.g. tungsten carbide. The bonding mechanisms between the diamond and metal matrix are of two types, mechanical retention or chemical bonding (carbide formers or solid solution) or a combination of both [25]. Mechanical bonding is mainly due to residual thermal stresses due to the high sintering temperature [26]. Romanski et al. [27] try to quantify these residual stresses between the diamond and metal matrix.

2.3.1. Cobalt Metal Matrix

As cobalt is the metal matrix under investigation in this work, readers are referred to the excellent monograph by Konstanty [28] for a more detailed review of cobalt as a matrix used in diamond tools. Co and its alloys have a very wide range of applications, of which the diamond tool industry is one [29]. Because of its limited and workability, it is rarely used as a pure metal however, its use as a matrix in the diamond tool industry is an exception because of the versatility of Co and its alloys [12]. The unrivalled capacity of unalloyed Co to hold the diamonds tightly while the DIMM tool is cutting is due to a number of factors of which the following have been cited: (1) high yield strength, (2) toughness, (3) good ductility (4) hardness and (5) resistance to deformation at high rates of strain [11].

The type of bond which cobalt forms with diamond is not exactly clear, however some authors state a mechanical bond and others a chemical type bond with stable cobalt carbides [30]. Cobalt exhibits a diffusionless phase transformation at around 420°C where on cooling down from a high temperature, the more ductile FCC changes to a less ductile HCP phase. The FCC to HCP transformation causes a volume change of -0.3%. However the transformation is sluggish [31]. There are many factors which influence the FCC/HCP transformation [12, 23, 32, 33, 34]. The mechanical properties of DIMM tools are also influenced by the percentage of FCC or HCP [23, 32, 33].

The impurity oxygen, has a strong influence on the mechanical properties of cobalt [35] with oxygen level, oxide particle size [33, 36, 37] and oxide interparticle spacing (IPS) playing a role [38]. Romanski [39] studied the effect of oxygen and diamond content on the allotrophic phase transformation in hot pressed cobalt and found that oxide precipitates both present as intergranular and grain boundary, impede recrystallisation, grain growth and stabilise the metastable FCC phase at room temperature. When diamonds are present the effect is weaker. Also that diamonds present have an insignificant effect on recrystallisation and the grain growth process, and comments that at higher DCs e.g. 80, the higher metastable phase content is associated with residual stresses due to the ΔCTE diamond and cobalt [39].

2.4. Synthetic Diamonds

Originally, all diamond used in the manufacture of diamond tools was natural material until synthetic diamond became commercially available in the 1960s [2]. Now natural industrial diamond is used just for special applications e.g. tool dressers. Synthetic diamond is easier to manufacture with specific properties such as toughness and specific crystal shapes. Regarding diamond synthesis the reader is referred to the review by Dwan [40]. There are many types of diamond grit (crystals) available with different grit sizes, shapes and grades. The diamond morphology or shape ranges from cubes to cubo-octahedral to octahedral with the cubo-octahedral shapes being the best shapes for efficient cutting in a diamond tool, see Figure 2.2. A 'Morphology Index' is used for characterising diamond shapes in diamond products [41, 42].

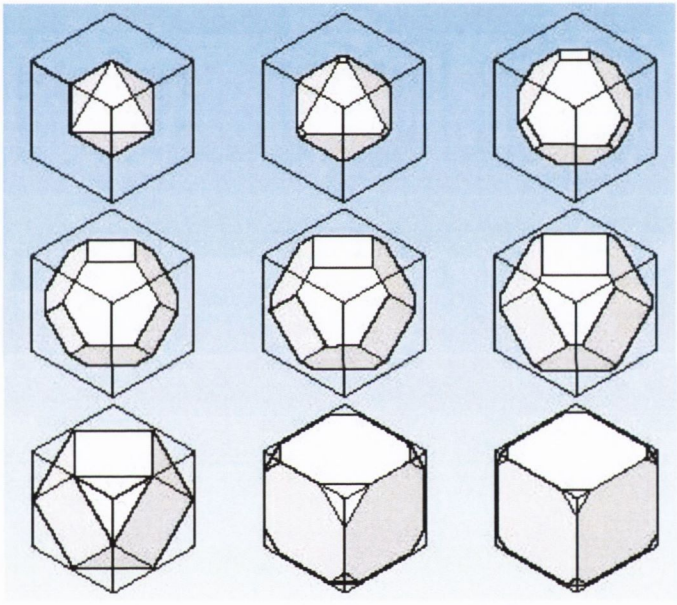

Figure 2.2. Diamond shapes can range from the well structured cubo-octahedral morphology, shown above to partially grown, irregular and fragmented crystals [43].

Due to the synthesis process, diamonds have metallic atoms dispersed as impurities, imparting magnetic properties however these metallic inclusions can cause graphitisation or cracking of the diamond and also influence toughness both at room temperature and high temperature when used in diamond tool manufacturing. Diamond properties e.g strength & toughness, including its shape and size are the key elements determining its end-use. Because diamond synthesis produces diamonds with different strengths and thermal properties post-processing is required. The post-pressing techniques employed are sieving (size), magnetic sorting (metallic inclusion content) and shaping (morphology).

Sieving also called sizing is carried following the strict American National Standards Institute (ANSI) [44] and Federation Europeene des Fabricants de Produits Abrasifs (FEPA) [45] industry standards. Instead of actual physical dimension, sieve sizes are used as a measure of diamond size. The US Standard fine series (1940) is often used as a standard, written down as US Mesh Size (US-MS). Regarding the size of diamond in a sample, different sieve sizes are used to measure the range of sizes. For example, a sample of diamond with a US Mesh Size of 20/25 will pass through the 20 US Mesh sieve but will be prevented by the next sieve, the 25 US Mesh sieve. The actual size of opening for the 20US Mesh sieve is 840μm and the 25 US Mesh is 710μm. The range of diamond sizes in this project will be from 20/25 to 80/100 US Mesh. The actual size of opening for the 80/100 US Mesh is 177/149μm.

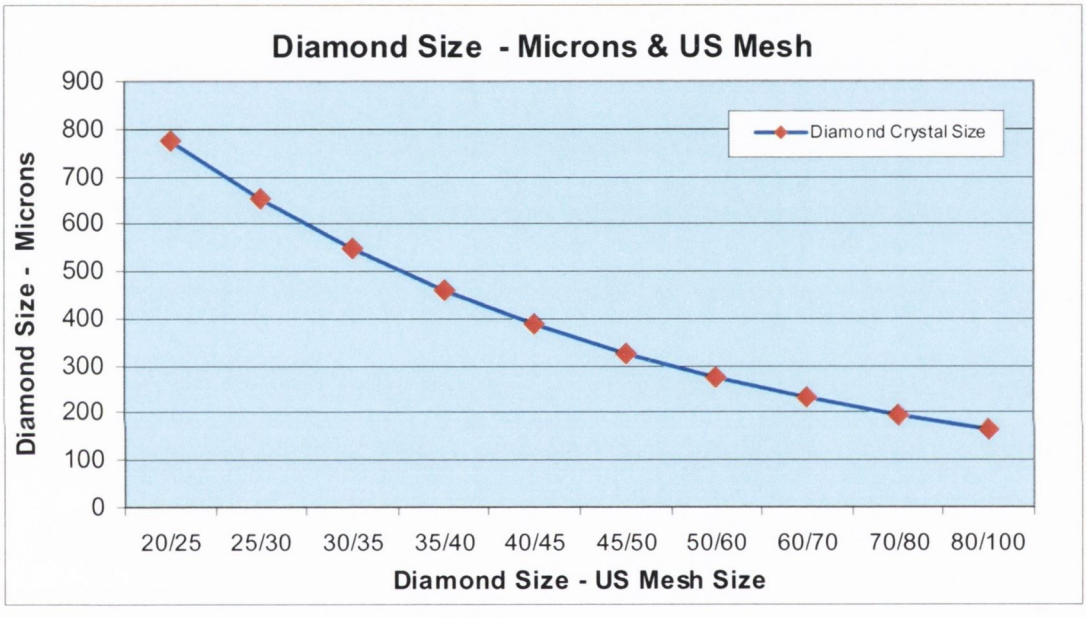

Figure 2.3. Relationship between actual diamond size (μm) and US Mesh Size.

Figure 2.3 shows the non-linear relationship between 'actual opening sieve size' (diamond size) and US Mesh sieve numbers. Figure 2.4 shows the number of diamond crystals per carat for each US Mesh sieve size, again a non-linear relationship.

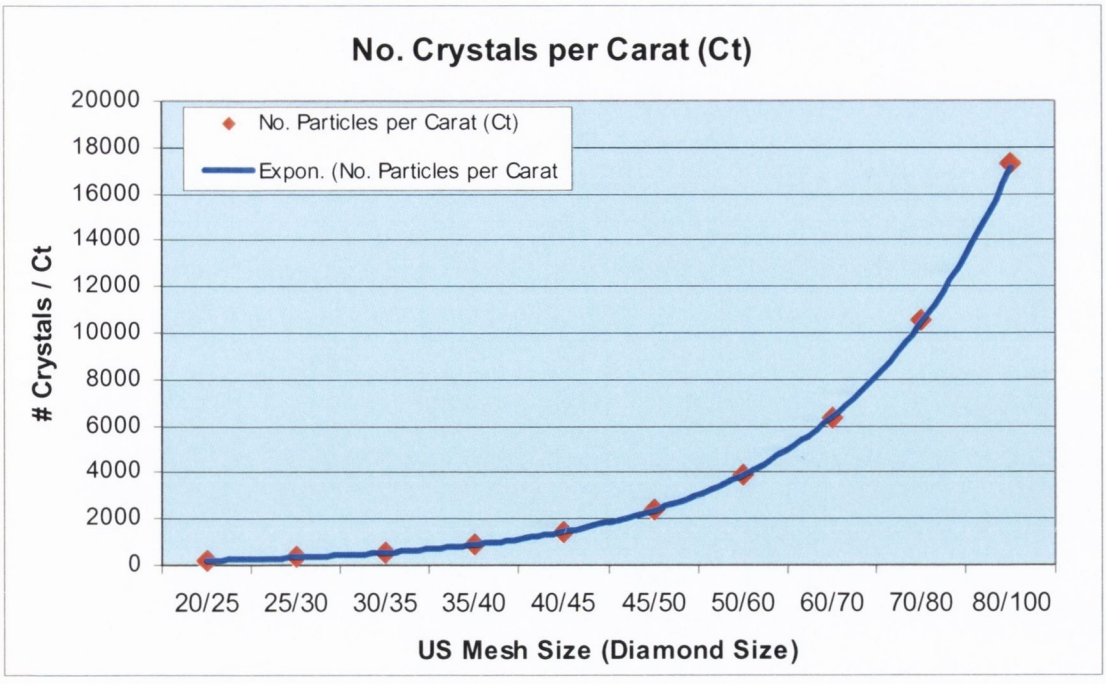

Figure 2.4. Relationship between diamond sizes measured in US Mesh Size to the actual number of diamond crystals or grits per carat (ct).

The mechanical properties of the diamond crystals are tested according to their toughness also called friability. Friability testing yields two measures of toughness; the toughness index (TI) or friability index (FI), and thermal toughness index (TTI) or thermal strength index (TSI).

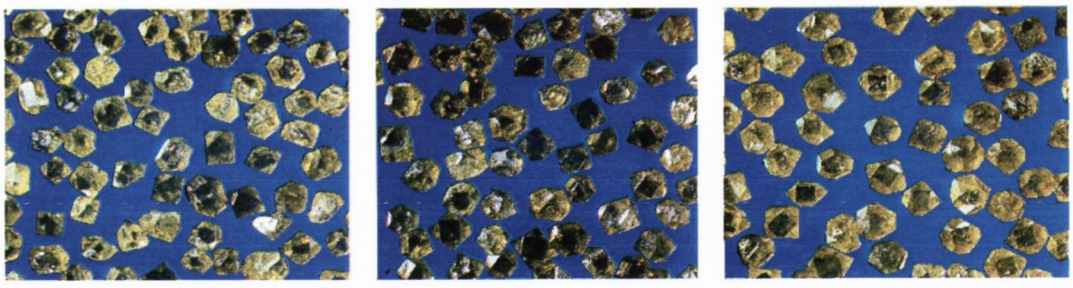

Figure 2.5. SDA Diamond Products (Saw Diamond Abrasive) [Courtsey of Element Six].

Typical commercial synthetic diamond grit products or grades as used in DIMMs are shown in Figure 2.5 showing the different diamond shapes with metallic inclusions as dark areas in the crystals. These metallic inclusions are the result of the growing process whereby metal became trapped in the crystal as it grew.

2.5. Diamond Impregnated Metal Matrix Tool Manufacture

As mentioned previously diamond tool research is often carried out solely on the the metal matrices because of the high cost of diamonds. But also there is an assumption that

the mechanical properties of metal matrices are similar to DIMMs. However this is not correct, because the diamonds do influence the results appreciably as will be seen in this work.

2.5.1. Diamond Concentration (DC) & the Diamond Tool

In the diamond tool industry, volume fraction (vol.%) is not used because it lacks sensitivity. A concept called Diamond Concentration (DC) which is directly related to volume fraction is used. A DC of 100 is equivalent to 25vol.%, and all other DC's work from there. In DIMM tools the DC's range from a minimum of 10 (2.5vol.%) up to 80 (20vol.%) which cover cutting tools like saw blades up to diamond core drills as used in exploration drilling. See Table 2.1 which shows the relationship between DC and vol.%. The DC (carats/cm^3), in conjunction with the diamond particle size, governs the number of cutting points per unit area, which is proportional to the DC and inversely proportional to the mean particle size.

DC	1	10	20	30	40	50	60	70	80	90	100
Vol%	0.25	2.5	5	7.5	10	12.5	15	17.5	20	22.5	25

Table 2.1. Table shows relationship between Diamond Concentration and Vol. %.

Figure 2.6 shows number of diamond particles present in a fracture zone for a 10mm x 5mm nominal fracture toughness specimen with a failure zone thickness of 0.25mm. There is a large difference in the number of diamonds with the coarser mesh sizes in comparison to the finer sizes. Also, from 40/45 onwards, the finer sizes show a large increase. The very fine US Mesh sizes are not plotted because the coarser US Mesh sizes would vanish off the x-axis.

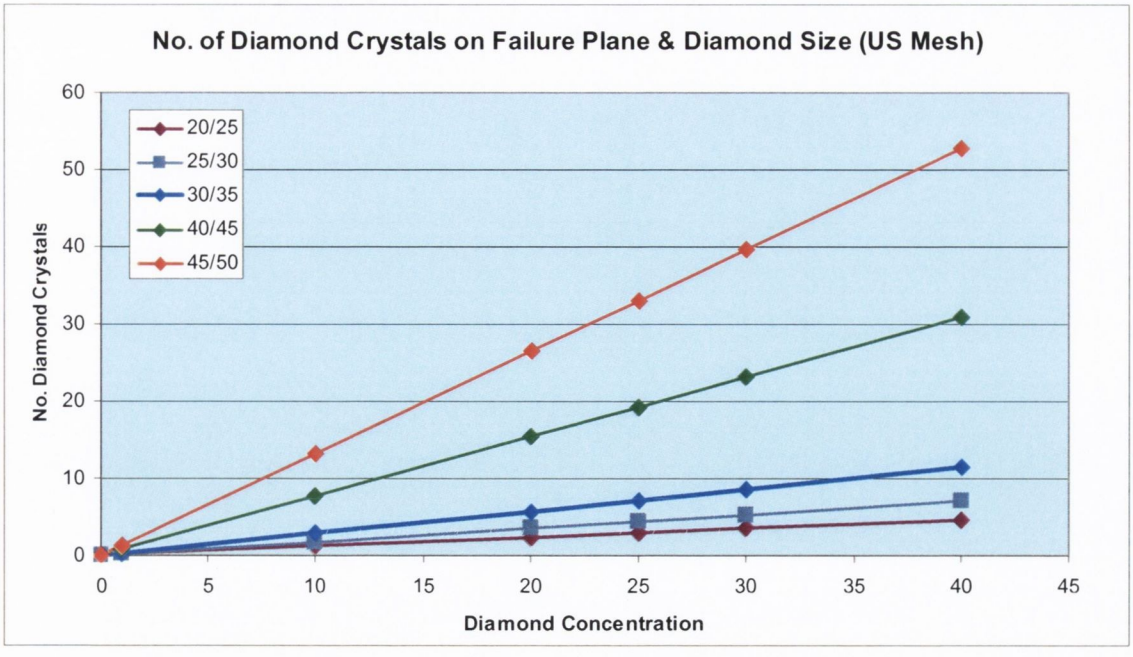

Figure 2.6. Number of diamond crystals for different diamond sizes (US Mesh Sizes) plotted against diamond concentration.

Figure 2.7 shows diamond size (microns) plotted against diamond size (US Mesh) with the histogram bars used to indicate the number of crystals for each Mesh Size for two different diamond concentrations, DC25 and DC40. The overall effect is that as diamond size decreases the number of diamond crystals increases exponentially.

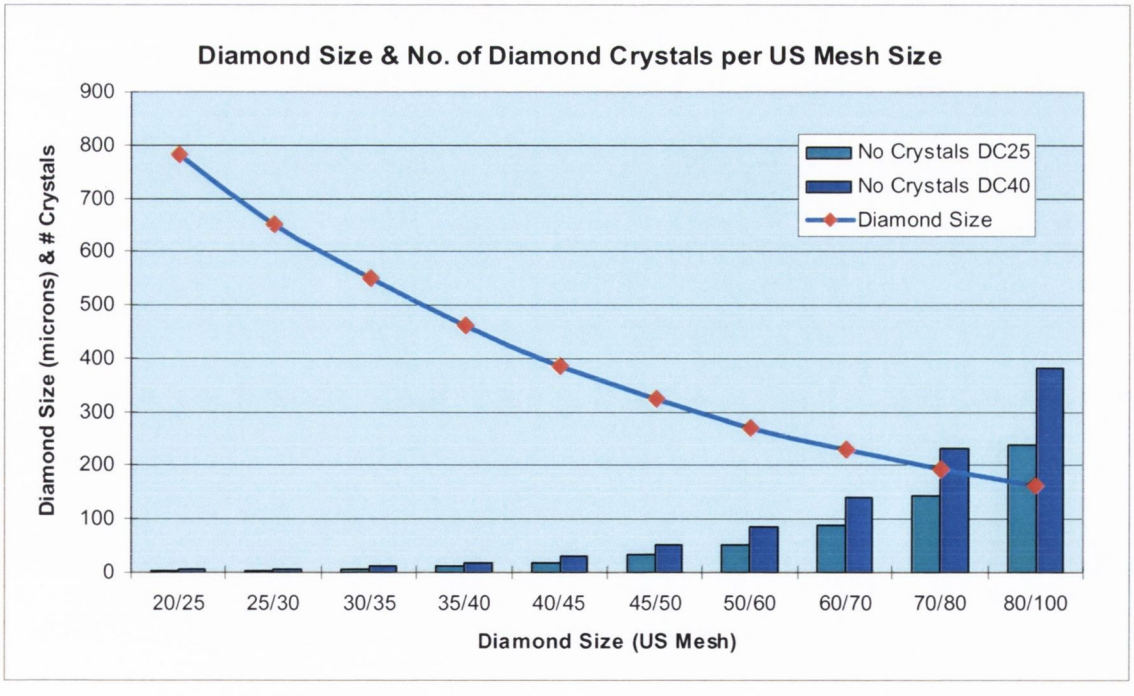

Figure 2.7. Actual diamond size (microns) & number of diamond crystals for each diamond US Mesh size plotted against diamond concentration.

2.5.1. Metal Powder & Diamond Grit Preparation

As in PM processing [46] the homogeneous mixing of the diamond and metal powder is one of the holy grails in the manufacture of DIMMs. A non-uniform distribution of both metal powder particles & diamond crystals will cause premature wear of the segment and so lead to poor cutting performance [47]. The whole area of blending/mixing regarding diamond impregnated metal matrices is very difficult with segregation (clustering & layering) the main problem regarding the mixing of diamonds with metal powders which is exacerbated by the large differences in density and size between metal powders and diamonds. Wetting of the diamond crystals with a solvent or oil is a common practise. However, smaller tool manufacturers just weigh out the diamond/metal powder segment weights and hand-load directly into the hot pressing moulds such as those used in this project. Hand-filled segments have been found to have a superior hardness and a lower standard deviation than cold-pressed segments [38]. Factors of importance in hot pressing are time, temperature, pressure, particle size and geometry and processing atmosphere [48]. In comparison to PM materials, DIMMs are found to have an increased level of porosity around the diamonds [49], this is similar to PMMCs [50]. In this project, no protective atmosphere was used. Following hot pressing, it is common in the industry to check for hardness and percent Theoretical Density (%TD) using Archimedes Principle to measure density [51].

2.5.2. Sintering Effects on Diamond

The graphitisation of diamond at normal temperatures and pressures proceeds negligibly slowly. However this changes at higher temperatures e.g. hot pressing temperatures. Synthetic diamonds begin to lose strength beyond 800°C and fairly rapidly at temperatures in excess of 1000°C especially when cobalt is the matrix [52]. Besides oxidation [53] a number of metal oxides react with diamond as well as the metallic inclusions in the diamond crystals causing degradation at elevated temperatures [54]. So during hot pressing the strength of the diamond changes and the amount of diamond degradation depends on the hot pressing temperature and chemical composition of the matrix [55]. The typical degradation which can occur in hot pressing can be seen Figure 2.8.

(a) (b) (c)

Figure 2.8. Diamond after Sintering at Various Temperatures. (a) Mild Attack, (b) Moderate Attack & (c) Severe Attack of the Diamond due to Matrix Metal [56].

2.6. Mechanical Properties of PM, PMMC & DIMM Type Materials

Most research work carried out to-date into the mechanical properties of diamond tools has concentrated on solely the metal matrices. The main research work has focussed on impact, TRS and hardness. However, little work has been actually conducted into the mechanical properties of DIMMs and only three papers exist of which this author is aware of on fracture toughness determination [5, 57, 58]. Because of the very little research work on DIMMs and its similarities with PM, PMMCs, this section will examine the mechanical properties of these types of material. Again only PM manufactured PMMCs will be considered.

2.6.1. PM Materials & Sintered Density

Up to the early 90's most of the PM research was devoted to determining mechanical properties such as strength [59], elastic modulus [60] and fatigue limit [61, 62, 63] and also the influence of porosity (percentage, pore size and shape) which is generally to decrease mechanical properties with increasing porosity [64, 65]. The mechanical and physical properties of PM materials depend strongly on the overall or final density also called sintered density [66] as well as their pore structure (both density and shape).

The density of PM parts is reported on a dry unimpregnated basis. Density may be calculated by any of several methods, a commonly used method is the Archimedes principle as per MPIF Standard 42 [67] which is also used for DIMMs. Density is mainly expressed as a relative density or %theoretical density (%TD) or %dense, which is defined as the ratio of a PM parts density to its theoretical density, its pore-free equivalent. In practice, PM parts which are above 90%TD are considered high density

[68] regarding DIMMs 95–97% dense is generally aimed for and achieved by hot pressing.

Mechanical properties of sintered metals are strongly related to the density of the material. Where the density is near theoretical density the mechanical properties can surpass those found in wrought materials because of a nearly full homogenous material in comparison to a wrought material with segregation.

Gegel et al. [69] found that with increasing density the fracture toughness, tensile strength, yield strength and notched impact energy increased linearly. However, Ganesan et al. show that for PM alloy steels the yield strength, fracture toughness as well as hardness are related to density by a power law [70]. Verdu et al. state that porosity affects static bulk properties (elastic modulii, tensile strength, fracture toughness), dynamic properties (impact & fatigue) decrease with increasing porosity, pore size and pore shape [64]. It is found that PM materials are quite markedly very notch sensitive due to the presence of pores [71]. When the volume fraction of pores is greater than about 10%, the pores are mostly interconnected. Properties are governed by the behaviour of interparticle necks and generally decay exponentially as porosity increases [72]. It is found that for fatigue and fracture toughness properties density is by far the most important influencing parameter [73] because of the introduction of an internal notch effect at pore edges, and so the mechanical response depends on the interaction between the stress multiaxiality induced by the geometry and the internal stress multiaxiality connected with pore morphology and distances between adjacent pores. Verdu et al state that PM materials failure is due to pore growth and coalescence, where controlling pore size, shape and amount will control microcrack initiation [64]. Porosity leads to a reduction in load bearing section which contributes to strength degradation in two ways, local stress concentrators and crack precursors. Deformation of porous materials takes place heterogeneously, localised in small regions in the vicinity of pores, and is always accompanied by cracks. A combination of small pores with rounded shape and large pore spacing has been reported to improve tensile and fatigue properties [74]. At densities of less than 90%TD, the impact energy has been regarded as a direct function of the yield strength where changes in the CSA of interparticle necks directly affect both strength and impact energies. At higher densities (ρ_r >0.9) this underlying relationship is compounded with bulk microstructural effects [75].

In PM parts, however, are the additional factors of density; metal powder particle size; pore size, pore shape and pore distribution; and extent of sintering, upon which the properties depend [68]. Because of this, mechanical property data are often given in graphs showing the relationship between the property and the density. Hardness as a material property in PM is very sensitive to variables such as material composition, %TD and sintering conditions [76].

2.6.2. Impact Properties & PM Materials

Many mechanical properties are strain rate sensitive and as a general rule materials become more brittle the faster the application of load. The term toughness is used as a measure of a material's sensitivity to strain rate. The three most common measures for toughness are: (a) area under the stress-strain curve as in a tensile test, (b) Charpy or Izod impact energy (absorbed energy) or impact strength and (c) fracture toughness, which can be static fracture toughness (K_{IC}) or dynamic fracture toughness (K_{Id}) [77]. Regarding PM materials, Charpy impact is commonly used to assess the toughness as per MPIF Standard 40 [75, 78. However, this method differs from the ASTM E23-88 [79] in that an un-notched specimen is used but other specimen dimensions remain similar because PM materials possess low impact tolerance [75, 78].

2.6.3. PM Materials - Impact Energy (Absorbed Energy) & Effects of Porosity

Test results [80] show that the most important factor affecting impact properties for any PM material, heat treated or not, is sintered density, with both elastic and plastic deformation behaviour strongly affected [81]. The development of plasticity depends on the amount, morphology and relative proportion of open and closed porosity [81]. Data shows that impact energy increases significantly at higher densities [68, 82]. However, even at high overall densities, poor dynamic properties are attributed to the presence of non-uniform concentrations of small & large pores [83]. Pores cause a reduction in load bearing cross section and increased stress concentration effects at pore edges [84].

Besides the inherently poor dynamic properties of PM materials, the total impact energy for fracture of un-notched PM metals has been found to be dependent on the 'available-energy' for impact of the machine, and where the 'available-energy' increases to approximately five times or more of the absorbed impact energy to fracture the specimen, the impact energy reaches a true minimum value [85]. MPIF Standard 40

states that the available energy must be 5 times the expected absorbed energy, similar to the ASTM E23 regarding impact testing [78]. Also cited that [86] the absorbed impact energy should be corrected to account for large changes in tup velocity. Shimansky found that impact energies for PM metals were independent of small changes in impact velocity [85]. When the available energy is close to the actual or true impact energy, the absorbed impact energy increases [87], as well as increased variability in results [85, 87]. However, to increase sensitivity and resolution of low impact strength metals, e.g. PM metals, smaller pendulum machines (<147J) are used [85] which was the reasons for using the 50J Zwick machine in this project.

2.6.4. Fracture Toughness (FT) & PM Materials

Up to the mid '90s, very few reports focused on the fracture toughness of P/M materials [88]. Some even incorrectly reported fracture toughness as the area under the TRS curve [89]. PM fracture toughness values are dependent on the type of powder [90], porosity level [91, 92] sintering atmosphere and sintering parameters [90, 93]. It has also been found for PM steel that as hardness increased fracture toughness decreased [94]. An increase in density makes a significant increase in fracture toughness but only a moderate increase in yield strength [88]. However it is also found that a lower density can show better fracture toughness than a higher density [95]. In contrast to wrought materials, it is found that the fracture toughness (K_{1C}) of PM materials increases in line with yield strength [88, 91, 96] which is achieved according to [97] by either reducing porosity [70] or by holding density constant and increasing the strengths of interparticle necks through alloying [97]. The presence of pores as measured by the level of porosity is the main cause of this increasing fracture toughness as seen in PM materials. Below very high densities, pore structure causes a lack of plane strain conditions where between the pores a three-dimensional state of stress cannot develop, resulting in the material between neighbouring pores to yield plastically and form a ductile failure on a microscopic scale, but show macroscopic failure and fulfil plane strain conditions. In PM steels, when there are large distances between pores in very high density material, the failure mode shifts from ductile neck failure to cleavage failure [70]. Most correlations between fracture toughness and impact strength were developed for mild steels and are very material and alloy sensitive [69].

Regarding the fracture toughness test procedure, normally fatigue precracking is the accepted method for introducing an atomically sharp crack, however it is stated that fatigue precracking is an unnecessary precursor to the fracture toughness testing of PM materials [95] and that a notch of root radius of less than 0.1mm, e.g. produced by a saw blade, is sufficient [98], Crane and Farrow [90] showed that the value of K_{IC} of both a radius cutter (0.13mm) and a fatigue precracked type notches are essentially no different for PM. Gegal et al. state that no difference is found between precracking by fatigue or edm'd slot (0.25mm notch width) or whether sample surface was ground or 'as-sintered'. [69]. Ganesan et al. comment that the pore sturucture causes the insensivity of fracture toughness to the sharpness of the precrack [70].

It is also stated that most of the PM data contains invalid results based on ASTM E-399 [99] because it is based on fully dense materials [88], where in PM materials, the plane strain requirement is violated in the sinter necks between the pores and ductile fracture occurs due to microvoid coalescence. The porosity & microstructure of PM alloys also make its fracture toughness very difficult to satisfy the validation criteria [91] especially the thickness and $P_{max}/P_Q<1.1$ criteria requirements for sintered PM alloys [91], with some authors suggesting that the thickness requirement could be relaxed [88]. However, Wang et al. [88] state that even after increasing specimen thickness, the P_{max}/P_Q criterion was still violated, due to the lack of crack tip plane strain constraint due to porosity, i.e. the crack tip triaxial stress state did not increase inspite of the increase of the specimen thickness. This lack of plane strain constraint caused the P_{max} to be significantly higher than P_Q so violating the $P_{max}/P_Q<1.1$ criterion. However, this did indicate though that the lack of constraint near the crack tip makes the PM material's critical fracture toughness have geometry independent characteristics because the fracture toughness value does not change much by increasing specimen thickness [88]. Also that Plane strain fracture toughness (K_{IC}) is more a function of density than yield strength [88] with an average increase of K_{IC} being about 50% from lowest to highest density for PM steels.

Finally, fracture toughness is normally conducted using a CMOD guage for measuring the displacement or opening of the crack mouth of the specimen as the test is proceeding. This displacement is used in plotting the load-displacement curve whereby the P_Q load is determined and subsequently used for calculating K_{IC}. Steigerwald [100] carried out fracture toughness testing using single edge notched bend (SENB) specimens

using the standard CMOD method but also measured the beam deflection using an LVDT and found that both methods for determing displacement were satisfactory. Measuring deflection makes fracture toughness testing easier.

2.7. Composite Materials - Particulate Metal Matrix Composites (PMMCs)

A metal matrix composite (MMC) material has two different phases, a ceramic reinforcement and a metal matrix. The reinforcement can be either continuous or discontinuous and where it is discontinuous it can be either present as whiskers or as particles also called particulates, giving the name Particulate Metal Matrix Composites (PMMCs). There are a number of reviews to which the reader is referred [101, 102, 103, 104, 105].

Because PMMCs closely resemble DIMM type materials in macrostructure will be used as a reference material in developing and understanding the mechanical properties obtained in this project. Particulates used in PMMCs can be regular or irregular in shape and can arranged in a random or with a preferred orientation. The PM process is a common method used for the fabrication of PMMCs and these will only be considered here [101, 106, 107, 108, 109]. Volume fractions can range from 5vol.% to 40vol.% and with sizes varying from 3 to 40 μm and some even up 250μm are used. The role of the reinforcement is generally to improve mechanical properties, by seeking to combine the high strength and stiffness of a ceramic with the toughness and damage tolerance provided by a softer metal matrix [110].

However in DIMMs, the role of the 'reinforcement' is completely the opposite. The role of the matrix is to support the diamond and wear at the optimum rate as the diamond cuts. In PMMCs, a major drawback is fracture that can occur under service loading conditions or during processing. Also, damage and cracks may occur in the particles and matrix and at the particle/matrix interface depending on the relative stiffness and strength of the two constituent materials and the interface strength. If the embedded particles are much stiffer and stronger than the matrix, which is the case of diamond in cobalt metal matrix, matrix cracking and particle/matrix interface debonding called dewetting become the major damage modes. If both constituent materials have material properties in the same order of magnitude, particle cracking can occur [111]. The composition and properties of the matrix affect the overall properties of PMMC both

directly, e.g. normal strengthening mechanisms, and indirectly, by chemical interactions at the reinforcement – matrix interface. The load acting on the matrix has to be transferred to the reinforcement via the interface [112]. Suffice to say that interfaces play an important role in determining the resultant composite properties, [113] e.g. strength and toughness [105]. A weak interface results in a low stiffness and strength but a high resistance to fracture, whereas a strong interface produces a high stiffness and strength but often a low resistance to fracture, i.e. brittle behaviour. Ibrahim et al. [101] review in detail the interaction of the matrix-ceramic interface of which the reader is referred.

2.7.1. Mechanical Properties of PMMCs – An Overview

The introduction of ceramic particulates can significantly improve the yield strength [114], UTS, stiffness [114, 115] dimensional stability and wear resistance [116], but generally lowers ductility and toughness [112]. However the properties that one achieves in PMMCs are influenced to a greater or lesser extent by the type of particulate, the volume fraction, the particle morphology, the particle size, particle size distribution (PSD) and interparticle spacing (IPS), particle/matrix interface condition, and finally the matrix [117]. Pillari et al found that increasing particulate size decreases toughness for a given volume fraction in Al based PMMCs [118].

However besides the previous mentioned list, similar to PM materials, porosity has a major affect on the mechanical properties in PM-type PMMCs where it has been found that increasing reinforcement leads to increasing porosity [119]. As already mentioned there is a strong similarity with DIMMs e.g. different diamond sizes, diamond concentrations, diamond grades and different metal matrices. In PM manufactured PMMCs similar problems to those experienced by DIMMs are encountered, e.g. heterogeneous dispersion of particles in the matrix, especially when there is a significant particle size disparity between the reinforcement and the matrix powder, different flow characteristics, particle shape (geometries) and finally different densities between particles and metal powders [120].

In PMMCs, any particle agglomeration deteriorates the mechanical properties, an effect which is often exacerbated by electrostatic charging during mixing [121]. The mixing process is the critical step towards a homogeneous distribution in PMMCs. Even though an increase in mechanical strength is found with a decrease in reinforcement size it leads

to a tendency for particle clustering [122]. This behaviour is opposite to that found in DIMMs. Overall, reported mechanical property data is very difficult to compare [123] with strength values showing wide variability [112].

2.7.2. Effects of Volume Fraction

Various strengthening models have been proposed to explain the strengthening mechanisms and predict the strength of PMMCs [124, 125, 126, 127, 128]. However, it has been shown that the addition of particulate reinforcement in a metallic matrix may not always increase its strength [119, 129, 130, 131, 132]. It was also found that [133] unless a critical volume fraction is reached, the load transfer between the matrix and the reinforcement will not be effective, e.g. critical volume was 11%SiC in a Al-Cu PMMC [134]. Qin et al. [134] proposed that in small volume fraction PMMCs, the particulates act as imperfections in the matrix causing high interfacial stress resulting in failure to occur at a lower stress than that of the unreinforced metal. This may be an issue for the diamond impregnated cobalt samples in this work because the max. vol. percent used is just 10 vol.%. Also, proportionately increasing the size of the inclusions and their spacing increases the stress concentration effect [135]. Finally Oliveira et al. [136] found that with increasing vol. fraction of particulates sinter density decreased linearly.

2.7.3. Tensile Testing & PMMCs

Published tensile strength data for PMMCs shows a lot of scatter [112]. Some data shows strength reaching a peak at a low wt.% e.g. 5.0 wt.%. [118]. The tensile ductility of PMMCs is far lower than that of the matrix alloys due to the addition of the reinforcements [117]. The ductility loss is not affected by the type or size of the particles but only by the volume fractions [137]. Serrations have been found on stress-strain curves of PMMCs which are caused by plastic instability, called the Portevin-Le Chatelier effect, due to the refinement of the matrix grain size, and reinforcement effects [138].

2.7.4. Hardness Properties & PMMCs

Regarding hardness it is found that the variation of hardness of PMMCs increases more or less linearly with increasing volume fraction of reinforcement [139, 140, 141]. It is also found that below 10.0 vol.% the addition of particulates significantly lowers the base-line hardness of the matrix [141] which is attributed to high levels of porosity.

2.7.5. Impact Properties & PMMCs

Only a limited amount of information is available on impact properties of PMMCs [142], with the Charpy test the most common method using notched or unnotched specimens [143]. As with PM materials, PMMCs perform at the bottom end of the normal toughness range when compared to high toughness materials [144, 145, 146]. Typical values are 25J for standard sized un-notched samples of SiC particulate reinforced aluminium metal matrix ($Al/20SiC_p$) [147]. Others show a substantial reduction of 4 to 5 times (27J to 6J) of that found for an unreinforced Al/SiC_p, with an addition of 20% volume fraction [148]. Strangely, Giridhar et al. [149] comment that impact energy values give a better indication of the fracture behaviour of PMMCs than fracture toughness values.

2.7.6. Transverse Rupture Strength (TRS) & PMMCs

Transverse rupture testing of PM as well as PMMCs is a very common test. Regarding hardmetals, it is used as a characteristic of resistance to fracture [150]. Various versions of it are used, e.g. 3-point and 4-point, and standards e.g. ASTM B528-76, different sample preparations are carried out including the grinding & polishing of the surfaces, different specimen dimensions, crosshead speeds and spans e.g. 16-40mm, are used, and so one must take care in using such values unless all test parameters are mentioned [50, 150, 151]. TRS of PM-type PMMCs depends on structure and composition but is also especially sensitive to the degree of porosity both micro and macropores which act as internal flaws. In TRS testing, maximum tensile stress is experienced on the outer fibres of the loaded beam and so any flaws present on this outer surface will be potential crack initiators. Also, depending whether it is three-point or four-point type test will influence the failure stress and the statistical probability of finding a critical flaw on the outer surface. So this high sensitivity to external flaws (stress concentrations) results in relatively high scatter of values. So for minimisation of scatter in results, sample preparation is paramount. However, in this project producing polished surfaces is not feasible due to the presence of diamond.

In PMMCs it is found that TRS is affected both by the size and type of the ceramic particles [50], some researchers found that the addition lowered TRS values [141], also that TRS increased with decreasing particle size and which also caused an increase in

variability in TRS data. There was also an increased scatter in the bending strength data [152].

2.7.7. Fracture Toughness (FT) & PMMCs

The primary disadvantage of PMMCs is their tendency to brittle behaviour, which manifests in a low fracture toughness [153]. Investigations of fracture toughness behaviour in PMMCs have concentrated on identifying the effects of reinforcement type, volume fraction, size, distribution and matrix strength/aging condition [102]. Numerous studies show that the addition of the ceramic reinforcement greatly lowers the fracture toughness in comparison to the metal matrix [112, 154, 155, 156]. The level of toughness reduction depends on a number of variables including particle size & shape [157], volume fraction [159], matrix composition [159,160], the test method used in determination [149], processing steps including quality control of material [161] and also interfacial bonding, inclusions and porosity [112].

Of these volume fraction is identified as the most consistently significant factor in reducing PMMC toughness levels, however, [102] direct correlations between toughness and reinforcement size are contradictory, e.g. Bolton et al. [162] found that ≤8% addition of different particulates had little effect on fracture toughness compared to the base-line value.

Duwel et al. [153] used three different ASTM fracture toughness test methods (ASTM E399, ASTM E1737 & ASTM E1290), and got three different results when investigating the effects of volume fraction. They found that with ASTM E399, there was a steep drop in fracture toughness at low volume fractions (<10vol.%). However, at vol. fractions of 25vol.%, all methods indicated the same fracture toughness values. Others found that K_{IC} is independent of particle size or of porosity levels [141]. The level of particle clustering has been cited as having a deleterious effect on fatigue and fracture toughness [163].

Zhao & Tuler [164] found that larger particles enhance fracture toughness of PMMCs, where different types and sizes of particles were used. They attributed it to the more severe strain localisation needed to fracture the larger particles and the larger plastic zone caused by the fractured particles. The effect of volume fraction on fracture toughness is weaker than particle size. The different particle-matrix interfaces and

different particle strengths do not seem to play an important role in the trend of fracture toughness particle size relationship. Lange [165] made similar observations that when particle size as measured by diameter d is greater than a critical diameter d_{cr}, an increase in volume fraction of particles decreased the fracture toughness of the PMMC, which he called the 'dilution effect' and seems to happen when the toughness of the reinforcement particles is considerably less than that of the matrix.

Pillai et al found that fracture toughness decreases with increasing interparticle spacing at a given vol. fraction [118]. Regarding particle size, the authors [118] found that as the particle size increased the toughness decreased for a given wt%. This they attributed to a decrease in void density that with a two-fold increase in particle diameter, the number of voids decreases by a factor of 8. And so, the chance of finding such voids near a crack tip (and so crack tip blunting) reduces.

Figure 2.9 shows an interesting graph reported by Kobyashi et al. [166] shows a fluctuating behaviour of fracture toughness results for a PMMC material when plotted against volume fraction, however the authors profer no explanation. However, if one examines the results in Figure 2.9, it can be seen that the error bars for the 100% matrix practically overlap the means and portions of the error bars of the results for the different volume fractions. An interesting point would to state that no real effect can be seen from the addition of reinforcement, except that they are acting as flaws and influence the fracture behaviour depending on their size and effects of clustering.

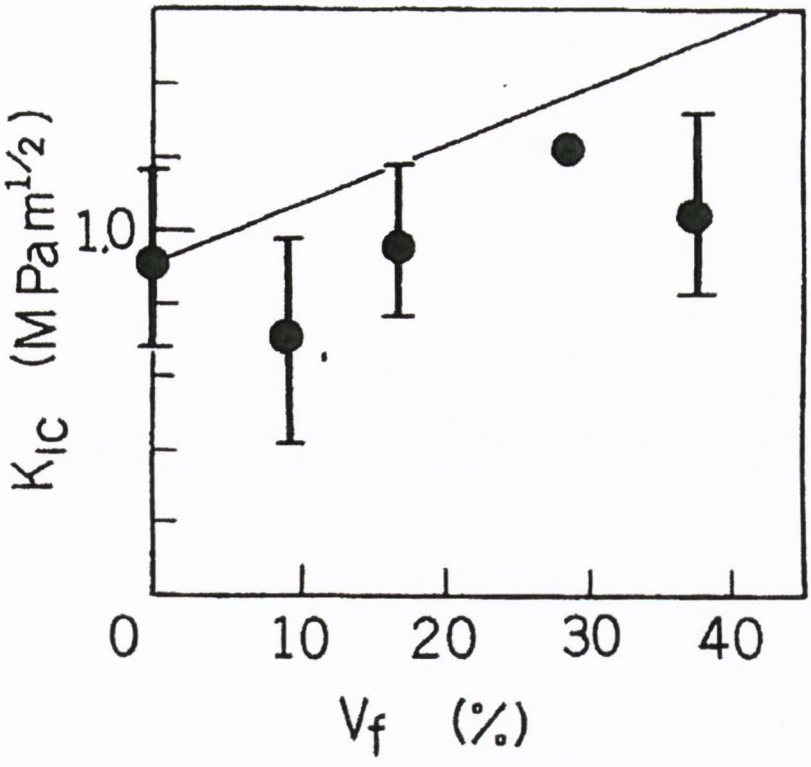

Figure 2.9. Showing the effect of volume fraction with K_{IC} for a PPMC [166].

This author feels that the trendline on the graph indicating increasing fracture toughness with increasing volume fraction is incorrect and misleading. Regarding actual fracture toughness testing, SENB type specimens of PMMCs have been used; however, they do not fully adhere to the ASTM E-399 standard [167]. Toughness has also been determined from the Breaking Energy (area under the load/displacement @break curve), with toughness obtained by dividing the Break Energy by the CSA of the test specimen, resulting in what is termed 'Work of Fracture' [168].

2.8. Mechanical Properties & Diamond Impregnated Metal Matrices (DIMMs)

It is only in the last few years that a serious attempt to gather together the mechanical properties of DIMMs metal matrices has been made. Two reviews appeared recently one focused totally on cobalt as the metal matrix [169], and the other on various types of metal matrices [170]. However, most of the mechnical properties mentioned deal solely with the metal matrices, as most of the literature covers also.

The following are types of defects which have been indicated as causing a decrease in the cutting efficiency of diamond tools due to their adverse affect on mechanical properties: powder contamination, inclusions, sintering process defects (entrapment of graphite, inadequate sintering) and microstructural defects caused by porosity level and

distribution, oxide level, hardness, diamond type and diamond metal bonding efficiency [171].

2.8.1. Tensile Testing & DIMMs

Regarding tensile testing of diamond tool matrices, not much work has been carried out [11, 172]. It has been all but abandoned because samples generally break in the grips, which this author has also found to occur. However, without tensile test data standard yield strength and other mechanical property data makes it difficult to carry out fatigue and fracture toughness tests.

2.8.2. Impact Properties & DIMMs

It is often stated that impact properties are very important properties of the matrix because the diamond experiences severe vibrational stresses or high frequency impact stresses as it cuts. However, it is also commented regularly that an increase in hardness or yield strength is usually accompanied by a loss in impact strength in the metal matrices used [11, 14].

After hardness testing, impact testing of metal matrices of DIMMs is the next most common test. Bonneau [15] mentions that the impact strength is an important property of the metal bond. He states that it is necessary to evaluate impact properties of the metal matrix in order to prevent catastrophic failure of the diamond tool due to severe sawing conditions. From practical experience it is considered that the safe working limit is an impact strength greater than $10J/cm^2$ [15]. Typical Charpy impact strengths for different DIMM matrices range from approximately $12J/cm^2$ to a high of $41J/cm^2$ [173]. Konstanty found that for 100% Co its impact was 4.6 J/cm^2 after hot pressing @ 850°C [11]. Impact strength of sintered Co is directly related to the % HCP Co phase in the compact and this is related to oxygen level [23, 32]. It is important to note too that the sintering temperature influences the impact strength achieved [173], as does the type of powder regarding size, e.g. fine or ultrafine [15]. Konstanty carried out impact tests using v-notched specimens on a range of different matrices based on hardness where results showed that higher hardnesses had higher impact strengths ranging from 4.8 to 6.3 J/cm^2, which for lower hardness test pieces the impact strengths were 1.4 J/cm^2, however the harder samples showed notch sensitivity [174]. However, this author has not found any references to impact work carried out on DIMM materials.

2.8.3. Fracture Toughness (FT) & DIMMs

Regarding DIMMS and fracture toughness testing, very little work has been actually conducted and only two papers exist of which the author is aware [57, 58]. However, their work was very limited and found that the addition of diamond reduced the fracture toughness of the matrix. Lin & Queeney [57] comment using knowledge found from PMMCs that,

"*Two changes in the fracture resistance of a matrix may be brought about by addition of a high modulus particulate. If the interface between the particulate and the matrix is weaker than the matrix alone, then the matrix will have its strength degraded. However, if the particulate is stiffer than the matrix, stresses and strain energy will be reduced locally for a given level of net section, the particulate will contribute to an increase in fracture resistance. Where the diamond matrix interface is very weak, the diamonds are basically free within the matrix and only able to transmit stresses due to their frictional contact*"

Lin and Queeney carried out fracture toughness tests on diamond impregnated hot pressed 60Cu/40Ni powders, with the two synthetic diamond sizes 80/100 (150-180 microns) and 20/30 (600-850microns) US mesh sizes, 25vol%, a diamond concentration of 100 which is very large [57]. The fracture toughness of a material with diamond particles and Cu-10%Ni was substantially enhanced when the diamond particles were coated with titanium [5]. Zeren et al. [171] make reference in their paper to types of defects found in DIMMs which decrease fracture toughness. However, no fracture toughness tests were carried out. Majstrenko [58] found that K_{IC} decreased with increasing diamond content, they tested SENB type specimens with 40/45 US Mesh size, however they provided no indication of the metal matrix used or hot pressing details. The DC was difficult to determine because a different measurement system was used unfamiliar to this author.

2.8.4. Transverse Rupture Testing (TRS) & DIMMs

The TRS test is one of the most common test methods for DIMMs to determine the toughness similar to other cutting tools [175] with three and four-point-bend tests used [176]. However, one of the major difficulties in comparing reported TRS results in the literature is the complete lack of test details. Typically, there is no indication of loading arrangement, whether it is a 3 or 4-point bend, span used and also specimen dimensions.

Typical TRS results for metal matrices used for DIMMs ranged from 490 – 735 MPa, again no span indicated [177].

Regarding cobalt matrices, Bonneau [15] determined using TRS 3-pt bend (again with no span indicated) that for a 100% cobalt matrix, HP @ 800°C, it had an elastic limit 925MPa with a deflection of 1.16mm. The type of cobalt used was the extra fine Couf powder by Eurotungstene. Borel [178] reported TRS strength of 1141 MPa for 100% Couf Co hot pressed at 780°C, again no test details were given. As with PMMCs, it is stated that the diamond crystals in DIMMs act as defects because of their size, form and area distribution worsened by clustering [179]. Regarding DIMMs and TRS strengths, it was found that for a Co-10Cu based matrix TRS was lowered by the addition of diamond (42/48US Mesh Size, DC60) from 780MPa to 660MPa (no test details being provided) [180]. Zeren et al. [171] showed that as time 'at-temperature' increased the TRS values of a copper based DIMM alloyed with 3%Sn, 30%Co and 10%Ni increased from 933 to 1200MPa, again no test details or diamond concentration or mesh size were given, or in fact any comments as to what effect increasing diamond size or concentration had on TRS values. Liao et al. [54] found that for a 100%Co matrix, 40/50US Mesh and a DC10, HP@830°C the TRS strength (3pt Bend), was 1120MPa at a 94%TD. Finally for a Fe-Cu matrix, 40/50 US Mesh, 0.74 cts/cc, free-sintering @860°C a TRS bend strength of 427MPa was found, (no test details provided) [181].

2.8.5. Hardness & DIMMs

Hardness is primarily used as a convenient quality check in the DIMM tool industry due to its ease of use and it is also utilised to indicate the diamond holding capacity of the matrix [11]. It has been cited that the addition of diamond increases the hardness of DIMMs [181]. Webb [49] found that the hardness of the diamond-free Couf cobalt matrix was the same as that of diamond containing segments (DC 1.5wt%) and that the presence of diamond retards densification by increasing macropores by a factor of 2 times. He also found that adding diamond weakens the TRS properties in tension, not by affecting density, but by adding weakly bonded surfaces [49]. This decrease in %TD is also found in PMMCs, where increasing volume fraction often increases agglomeration with resultant pores and lack of densification around the particles, which results in lack of increase in strength due to a decrease in %TD [182].

According to Hsieh et al. [5] cobalt as a matrix in DIMMs, does not possess a wide hardness range. The present author however has found that that it does depend on the type of cobalt used, hot pressing temperature and level of porosity. Liao et al. [54] found that for 100%Co with DC10, 40/50US Mesh, hot pressed @ 830°C with 6% porosity had a hardness of HRB94. Konstanty [11] found for a 100%Co with no diamond had a hardness of HRB106, hot pressed at 850°C. Regarding PMMCs, hardness found to increase with increasing volume fractioin of reinforcement [140].

2.9. Role of Interparticle Spacing (IPS)

It is well known that dispersed particles, whether present intentionally as second phase precipitates or present as inclusions, can have a considerable influence on the mechanical properties of metals e.g. strength, ductility [183], and toughness [184]. For example the relationship between interparticle spacing (IPS) and strength of a precipitate strengthened alloy is the well known Orowan Relationship. It is found that the magnitude of these effects depends on the size, shape and spacing of the particles. According to Corti et al. [185] these are rarely uniform throughout a specimen and so a measure of dispersion is required which can be determined by calculating a nominal value of interparticle spacing (IPS) or by actual measuring experimentally an ISP value.

However, throughout the literature various authors [184, 185] have many different ways of describing the distances between particles and with conflicting terminology. In this report, the author uses IPS as the global term for describing the distances between particles however measured. Very briefly, there are two main definitions of measuring IPS, the Mean Free Path (MFP) (λ), and Mean Particle Spacing (MPS)(Δ_s), which can also be termed Nearest Neighbour Distance (NND). This can be seen in Figure 2.10 which shows the main differences in MFP and NND/MPS.

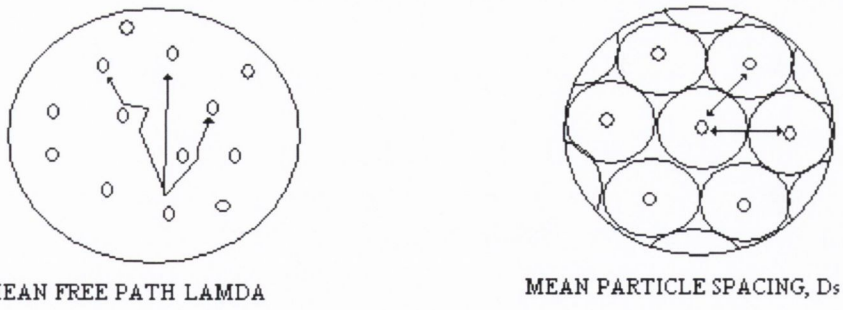

Figure 2.10. Interparticle Spacing (IPS) showing the two different interpretations, MFP & NND, also called MPS [184].

The MFP is the average distance or path taken from a specific particle to other particles in a microstructure. The number of particles used in calculating the MFP influences the result. However, the NND/MPS is taking a specific pattern or packing formation for the particles and calculating the distance from a specific particle to its nearest neighbour. A 2-D or 3-D analysis of NND/MPS can be calculated. Also, particles beyond nearest neighbour are not part of the calculation of NND/MPS which is different to MFP.

Dieter [186] states that the MFP (λ) is a critical parameter for measuring the dispersion of particles. A much quoted paper that of Gensamer et al. [187] found for steels that strength is proportional to the logarithm of the MFP (a semi-log relationship) of carbides present. Edelson et al. [184] state that the IPS measured as NND/MPS is the main variable whereby increasing the volume fraction and size of particles in a ductile matrix decreases ductility and toughness. In steels, NND/MPS of large carbides and inclusions influences toughness considerably [188], and in order to increase the K_{IC}, it is necessary to maintain as large as possible a NND/MPS. Which ever variable (NND/MPS or MFP) is the controlling factor is important and much debated in the literature [185].

In PM dispersion strengthened alloys, the yield stress varies with the reciprocal of the IPS, with yield stress increasing with increasing volume fraction and decreasing particle size, but particle clustering would limit this effect [189]. Similarly in PMMCs, MFP & NND/MPS was found to influence yield strength [123, 184], and matrix modulus and deformation characteristics, [190] as well as fracture toughness [191]. Similarly for coarse particles (200μm), yield stress was a function of MFP (particle size & volume fraction), which above a critical MFP it varied directly with the particle diameter [192]. Ductility was also found to be a function of volume-fraction and particle morphology

where block-like particle with sharp corners have a damaging effect which is found to lower ductility however is independent of particle size [192]. Regarding cobalt matrices as used in DIMM tools, Vedani et al. [38] stated that the MFP of oxides in the Co matrices influences its mechanical properties.

As already stated above, there are many ways of calculating IPS [186], and this leads to much confusion in the literature when only IPS is mentioned without explanation [185]. In addition, the MFP and NND/MPS can be calculated on the basis of any one of a number of different definitions and/or formulae, each of which leads to a different numerical value for a given system. Regarding the NND/MPS method, the interpretation depends on whether one takes it from particle to particle centres or edges, and also whether one considers it a random or uniform dispersion of particles. The general concept of MFP implies that its value should be independent of the direction of the line, or orientation of the plane section, on which it is measured, which is found in alloys with randomly distributed particles. As a point of clarity, MFP is also used in anisotropic materials where it is called Fabric Tensor [193]. The MFP is the distance from a reference particle to a second particle, averaged in all directions. However, if the distribution is geometrically uniform as distinct from random, it becomes a problem of linear, planar or even volumetric MFPs. Corti et al. [185] state that '*experimentally determined property values are presented solely in terms of their variation in the volume fraction of the dispersed phase, which if taken in isolation is merely a statement of the overall composition of the alloy*'.

Corti et al. [185] in their review cover the various methods of calculating MFP and MPS/NND. Typical formulae for relating MFP (λ) and NND/MPS (Δ_s) are as follows: Dieter [186] references Corti et al.'s [185] simple expression for the linear MFP (λ) which is:

$$\lambda = \frac{2}{3}\frac{d_p\left(1 - V_f\right)}{V_f} \qquad (2.1.)$$

where V_f the volume fraction of spherical particles of diameter, dp.[186] and for NND/MPS, a number of authors e.g. Ritter [123,194], Schwalbe [195] and Bhat [188] have used the formula by Edelson et al. [184], however Schwabe [195] and Bhat[188] seem to have incorrectly interpreted it.

Ritter et al. [123] [194] have used the following formula for MPS/NND, Δ_s:

$$\Delta_s = d_P\left(1 - V_f\right)\sqrt{\frac{2}{3V_f}} \tag{2.2.}$$

with V_f as volume fraction and particle diameter, d_p. On inspection of [184] one can appreciate the error or difficulty in interpretation of the text.

$$\Delta_s = \sqrt{\frac{2d_p^2}{3V_f}}\left(1 - V_f\right) \tag{2.3.}$$

Other methods for determining MPS/NND are available depending on whether one considers a plane where MPS/NND, Δ_2

$$\Delta_2 = 0.72 R_0 V_f^{-1/2} \tag{2.4.}$$

or volume dimension MPS/NND, Δ_3 as follows:

$$\Delta_3 = 0.89 R_0 V_f^{-1/3} \tag{2.5.}$$

where R_0 is particle radius, and V_f is volume fraction.

Interestingly, Δ_3 as in Equation 2.5 was the form of MPS/NND used in ductile fracture for the Rice & Johnson [218] fracture toughness model where fracture toughness is related to volume fraction, particle size and MPS/NND.

Regarding DIMMs, PMMCs and dispersion strengthened alloys, the main difference is that the particles used in PMMCs and dispersion strengthened alloys are generally much smaller than DIMMs with the consequence that the IPS (MFP or NND) is much larger than that found in PMMCs or dispersion strengthened alloys.

2.10. Wear & Diamond Impregnated Metal Matrices

The wear behaviour of the diamond tool determines its performance, including tool life and cutting rate. The wear process is complex and is affected by several factors. As the tool cuts, the matrix erodes away and gives the diamond crystals clearance for penetrating the rock material but also allows the cuttings to be flushed out [19]. Significant cutting efficiency and savings can be achieved by proper control of tool wear. Non-optimum wear can cause an increase or a decrease in the cutting rate of the

diamond blade. Analysis of diamond wear as it cuts reveals many types of wear of the diamond and the erosion of the bond material supporting the diamond. Where an increase in cutting energy occurs, this can cause major fracture of the cutting diamonds. Even with substantial attempts at understanding the wear of diamond tools, the different wear mechanisms operating in diamond tools are still not properly understood and more in-depth work is required.

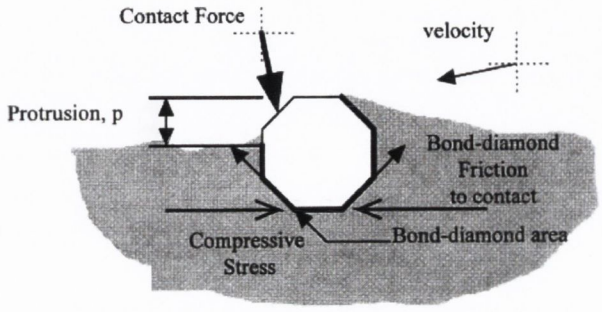

Figure 2.11. DIMM - Example of a Protruding Diamond in Metal Matrix [197].

Figure 2.11 shows a typical example of an exposed diamond crystal/grit embedded in the metal matrix on the surface of a segment of a diamond tool. Regarding the diamond crystal, wear occurs due to its contact and resulting large contact force with the workpiece. In addition to this, the metal matrix which supports the diamond is also slowly eroded [49].

The typical wear patterns on a diamond sawblade following cutting of a stone workpiece can be seen in Figure 2.12 showing the characteristic comet tail formation behind the diamond crystals as the blade cuts in the right-hand direction in the diagram.

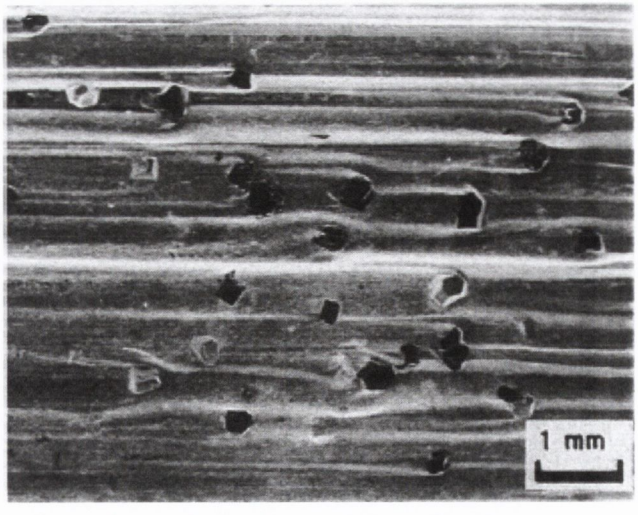

Figure 2.12. Worn surface of sawblade after cutting, showing comet tail formation around diamond [54].

A worn surface of a matrix of a diamond impregnated metal segment is shown in Figure 2.13. Interestingly in this figure a diamond has been pulled out prematurely giving a deep socket type hole on the worn working surface, rounding due to erosive wear can be seen around the edges of the socket. Even though the author [198] states that this occurs due to abrasive wear, this author believes that a large portion of it occurs due to erosive particles flushing past the pull-out socket which causes rounding of the socket edges but also deep into the socket wear can be found which would be very difficult for abrasive wear to produce.

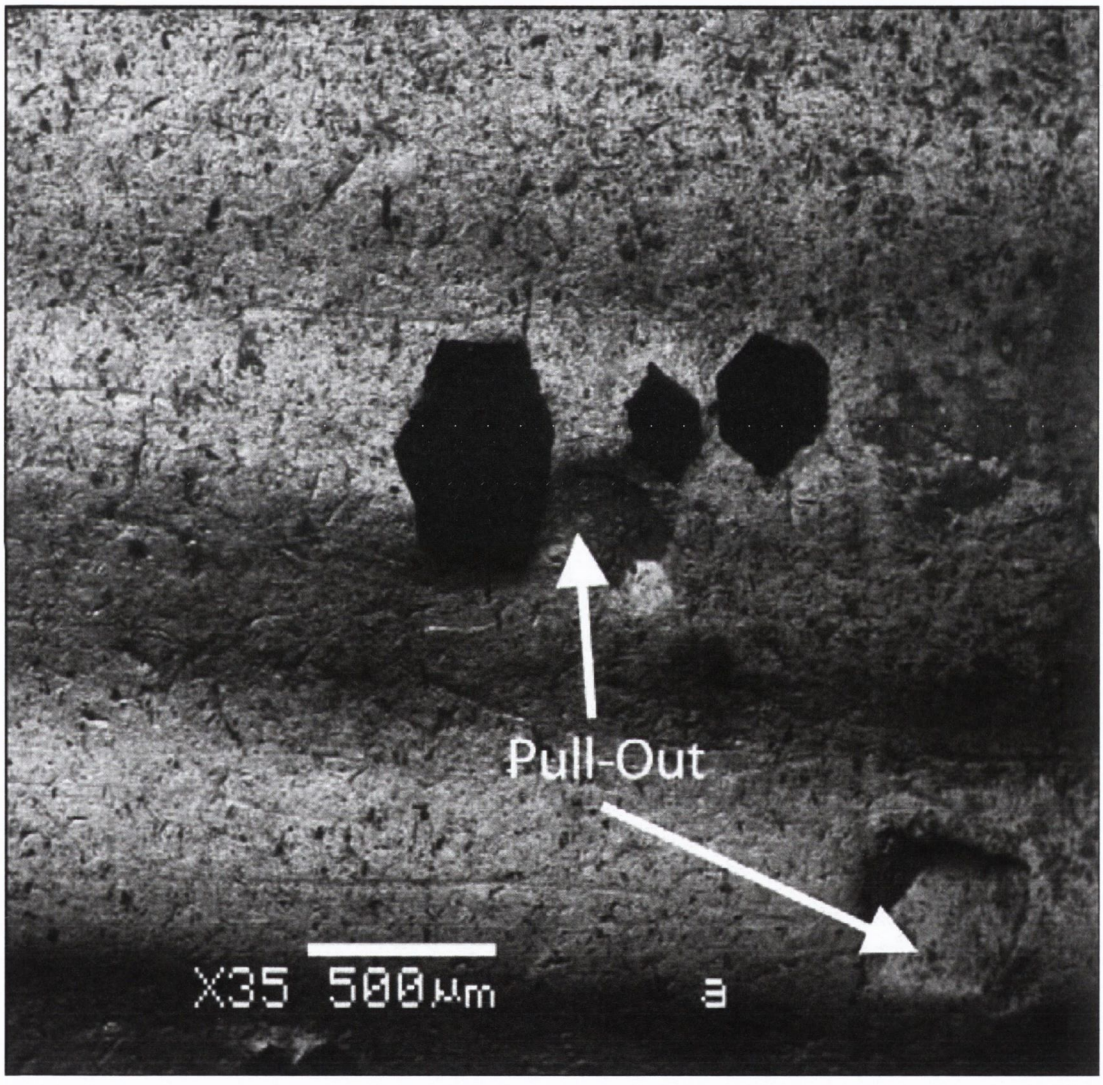

Figure 2.13. A worn surface of a diamond impregnated metal matrix segment showing diamonds in black and pull-outs where diamonds have been plucked prematurely [198].

To predict for example the cutting performance of a diamond saw blade, it is necessary to understand the mode of wear on each DIMM segment as the saw cuts. Equally important is to try to evaluate which mechanical properties influence the cutting operation and wear processes involved. The principal factors, which need to be

considered in predicting wear rates are (1) the composition and fabrication of the diamond tool, (2) the cutting parameters and (3) the characteristics of the workpiece material to be cut. The wear of diamond saw blades can take many forms, the most common mechanisms being abrasion and erosion. Impact loading and impact fatigue have also been cited as factors in accelerating the wear of saws [199]. Erosy et al. [198] have carried out a large body of work on circular diamond saw segment wear characteristics where they cited that main type of wear of the segments is by abrasion and erosion. Previous wear studies have mainly focused on cutting performance and wear behaviour of the diamond crystals but very little on the erosive wear of the matrix [49, 200, 201, 202, 203]. Konstanty et al. [204] have examined the 2-body and 3-body abrasive wear behaviour of diamond impregnated matrices regarding the effects of diamond grits from a laboratory perspective [204]. They found that coarser diamond grits protects the metal matrix against abrasion. Regarding the testing regime, the wear apparatus did not allow the formation of comet tails which are characteristic of segment wear in a saw blade.

Interestingly, Axén et al. [205] found that particle size and mean free path (MFP) influenced the erosive wear of PMMC materials [205, 206]. Hardness is often stated as an important factor in wear properties of metals however it is found that for composites erosive wear is not linearly related to hardness [207]. Regarding PMMCs and erosion, fracturing of the reinforcement is the most important factor and if this does not take place then a large increase in erosive wear resistance is found for PMMCs [206]. However, this is not an issue with DIMM materials for two reasons, firstly the large difference in hardness between diamond and rock cuttings, and secondly diamond size in DIMMs is much larger than the particulates used in PMMCs and also the volume fraction in DIMMs is much lower than that found in PMMCs.

The present investigation into this area should provide an understanding of the cutting process because the wear characteristics of the diamond and the metal matrix in stone cutting are substantially different and each has its own specific wear mechanisms.

Erosion is caused by a stream of abrasive particles blasting against a target, see Figure 2.14. The process is a combination of deformation, machining and cutting where small pieces of metal break away due to repeated stressing. Ductile materials will undergo

weight loss by a process of plastic deformation in which material is removed by a displacing or cutting action of the eroding particle. In brittle materials, on the other hand, material will be removed by the intersection of cracks which radiate out from the point of impact of the eroding particle.

In 1958 and 1960, Finnie published definitive papers which established the cornerstone for understanding the erosion of ductile metals by impingement of hard particles [208]. The important factors governing this form of erosion were identified as the particle velocity, angle of incidence 'θ' and flux. Ductile metals were generally observed to experience a maximum in erosion rate at angles of incidence between about 15° to 30°. Regarding diamond saw blades, the abrasive particles are provided by the rock flour (rock detrius) generated by the diamond as it cuts the rock, which then causes the erosion of the metal matrix holding the diamonds in place.

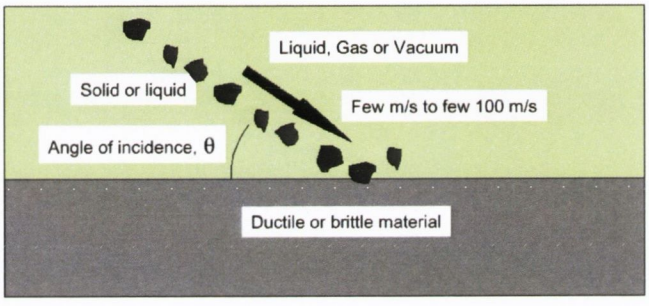

Figure 2.14. Schematic Diagram of Erosive Wear.

Erosion rate (E_r) described by Finnie [208] is quantified as the mass removed from the surface per unit mass of impinging particles. The velocity of the abrasive particles has a significant influence on erosion rate. The rate is also affected by the angle of incidence θ that the abrasive stream makes with the surface. Small angles of incidence are most effective with ductile materials and large angles ($<90^{\circ}$) with brittle materials.
For ductile materials, erosion can be predicted by using the following equation:

$$E_R = \frac{k\rho V^n}{H} \qquad (2.6.)$$

where E_R is erosion, and is dimensionless (mass of eroded material to mass of erodent), V is the velocity of the solid particles in the fluid stream; ρ and H are the density and hardness of the material respectively; the value of the index n is around 2 and k is a constant and is the ratio of the vertical force to the horizontal force of the particle [208].

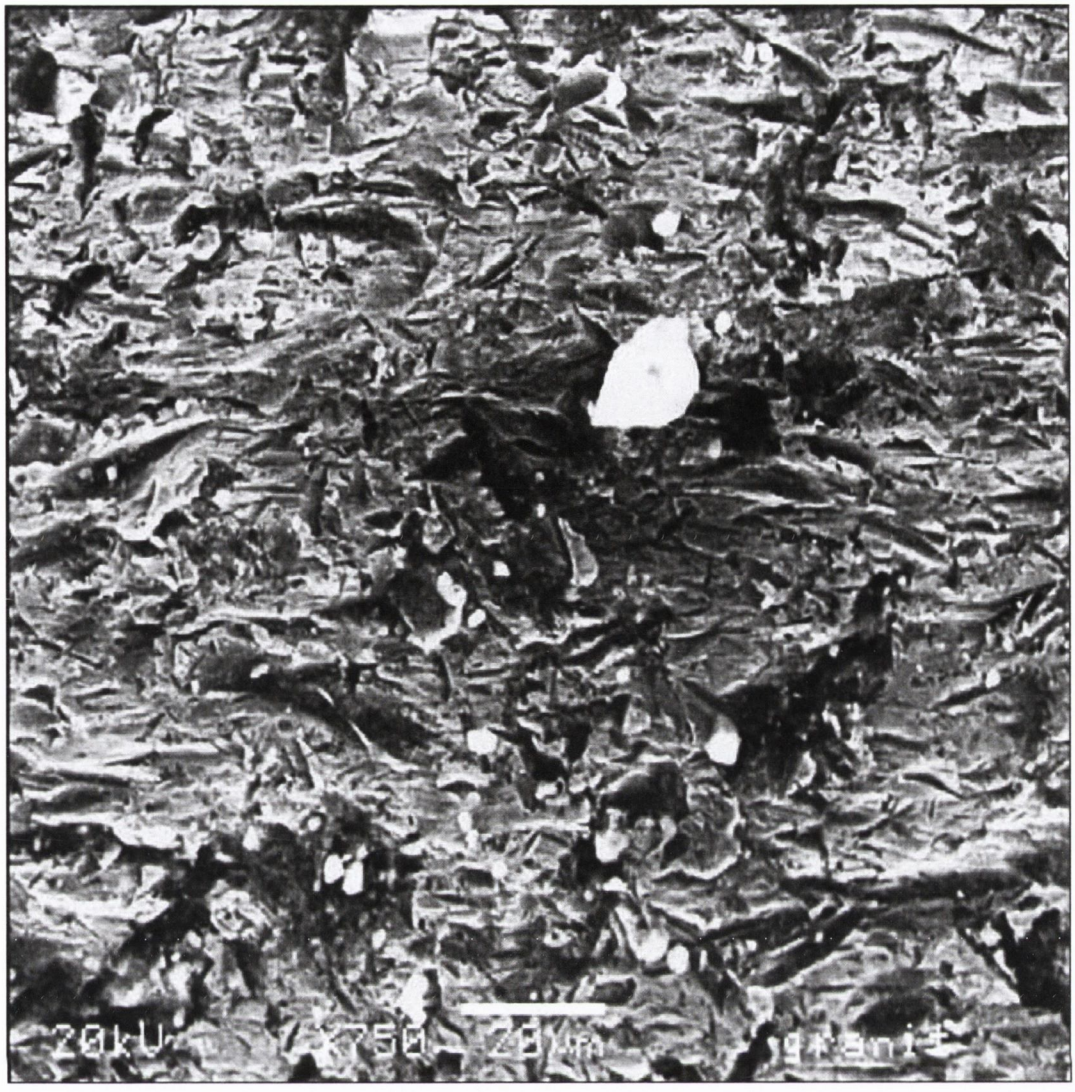

Figure 2.15. Worn surface of a DIMM segment showing wear tracks on the metal matrix [198].

In Figure 2.15, a worn surface of a DIMM segment can be seen. The author [198] comments that this is due to abrasive wear where the tracks seen on the surface have been caused by the segment being scratched by the workpiece. However, this author does not totally agree with this analysis of the wear patterns shown.

2.11. Predictive Models & Composite Models

An overview of various composite models used to predict different mechanical properties based on various composite constituent properties, e.g. volume fraction, is given. There are various references to the different mathematical models which try to describe the behaviour of composites with most of the work concentrating on composites which have a continuous reinforcement e.g. fibre reinforced, because of their ease of modelling. The reader is referred to the following references for more reviews on modelling of composites [100, 210]. Most of the models developed concentrate on

elastic moduli prediction [211]. Model predictions for strength are the most difficult and are still being developed since strength depends on a much more complex manner on the composite microstructure. There are many parameters which need to be considered including the effects of residual stresses, non-linear and temperature dependent work hardening of the matrix, interface strength and load transfer between reinforcement and matrix, statistical parameters associated with the intrinsic strength of the reinforcement and variations in microstructural parameters need to be considered [212].

The various approaches come under the general headings of dislocation type models, micromechanical models, phenomenological models, shear-lag models, Eshelby-type models and empirical treatments. Of all of the above different classes of modelling, numerous models have been developed and adapted from them because of their limitations. The dislocation type models can be further classified based on their contribution of Orowan strengthening, grain and substructure strengthening, quench hardening and work hardening [212].

Phenomenological modelling treats the material as a homogeneous material. In this type of modelling, fitting parameters can be used which can increase the predictive capabilities of the model. Another approach used is micromechanical modelling which takes a fundamental approach, where for example the PMMC, is treated as a composite made up of individual components, and relates the properties of the constituent matrix and reinforcement to that of the composite material. Micromechanical modelling is where the elastic constants and volume fraction are used in a bottom up approach in predicting the overall composite properties. There are two main streams of micromechanical modelling i.e. semi-empirical models and physical models. Examples of semi-empirical models are the Halpin-Tsai, Lewis & Neilsen and S-Mixing Rule. Examples of physical models are Rule of Mixtures (ROM) [213], Hashin-Shtrikman model, Composite Spheres (CS) model and the Generalized-Self-Consistent scheme (SCS). The simplest physical models are the Rule of Mixtures (ROM) of which there are two versions, approximately described as parallel (isostrain/Voigt/Maxwell) and series (isostress/Reuss). There are different mathematical forms from the simple to the more complex ROMs. They are used to calculate various composite material properties, elastic moduli, CTE [213], thermal conductivity [214] and density. Generally ROM is used for

composites which are reinforced with continuous reinforcement but these have been used successfully for PMMCs depending on property [213].

Limitations to the ROM approximation have resulted in correlations which take account, e.g. the non-isotropic properties of high aspect ratio reinforcements and the effects of thermal barriers at the interfaces. The Turner model considers the effects of isostatic stresses [213]. Another model developed by Kerner [103], is a more complicated model which takes into account the effects of shear stresses between matrix and isotropic, approximately spherical, reinforcements. The predictions of the Kerner model fall between those computed from the ROM and those computed using the Turner model [101]. Zhang et al. [213] found that predicted values according to the Kerner model were in good agreement, which they attributed to the fact that normal and shear stress were included in Kerner's model but ROM and Turner's model could not describe the complicated internal stress inside a composite.

Different authors have tried to account for strength, ductility and fracture toughness of PMMCs [210, 215]. There are two approaches for strength prediction in PMMCs, i.e. load transfer model and matrix strengthening model. Load transfer models are developed on the basis that hard & non-deformable particles in PMMCs may carry more loads than the relatively soft matrix. Models in this group are: Eshelby model, shear lag model and modified shear lag model. It is stated that the modified shear lag model of Nardonne & Prewo [210, 216] which was developed for platelet type PMMCs is the most successful [215]. The authors [215] examined experimental data (Fe-TiC PMMC) using the Nardonne & Prewo modified shear lag model found that it grossly overestimated the experimental data values, but also comment when models by Ashby & also Arsenault grossly underestimates the σ_{yc} values [215]. They comment that if the tensile transfer of load is ignored, then the modified shear-lag model is in complete agreement with the experimental data. Another strength model is Pukanszky Model which relates yield stress to filler concentration [215].

The modelling of fracture properties in PMMCs is difficult, with various models and types used. However the accuracy of the models to cover the range of properties is very wide indeed, e.g. an Al PMMC, the range had a magnitude of three times. Regarding brittle/brittle PMMCs, there are many models which have restricted ranges of

applicability or are contradicitory regarding volume fraction and particle size [217]. Regarding fracture toughness, simple models have been proposed to predict various strength responses of sintered metals containing porosity [91]. The only model found in the literature applied to DIMM materials was a basic one using 'true-area' fraction by Zin & Queeney [57].

The predictive model by Rice & Johnson [218] previously used for modeling the fracture toughness of dispersion reinforced alloys and have been used with some success with PMMCs [102, 219]. A number of models relating toughness to particle distribution have been developed for alloys which experience ductile failure [220]. Hahn & Rosenfield [221] have developed the Rice–Johnson model and failure criterion [218] for Al-based PMMCs with 'large' particles (10μm) with some success. Rabiei et al proposed a modified Hahn-Rosenfield model whereby they change the basic assumption using IPS/NND (λ) for coarse PMMCs with good success [220].

Others note that, some correlation with experimental data has been found [219, 222], various critical complicating micromechanical interactions have been identified, e.g. clustering/non homogeneous distribution of particles acting as preferential damage initiation sites, interfacial strengths also playing a role in decreasing fracture toughness. [219]. Kobyashi et al. [223] developed a model for predicting the plane strain fracture (K_{IC}) toughness of PMMC and found that the model gave an upper bound when compared to experimental results. A model by Jin & Batra where fracture toughness for a metal reinforced ceramic matrix type composite was determined [224].

Finally the modelling technique called The Theory of Critical Distances (TCD) is used for modelling fracture and failure strength of materials with flaws and notches very successfully. This will be used to analyse DIMM materials as presented in this thesis. For the interested reader they are referred to the excellent book by Taylor [225].

2.12. Conclusions

So in summary, a brief review of the class of materials called diamond impregnated metal matrices (DIMMs) was covered. The PM manufacturing processes used in the manufacture of these types of materials was given with special emphasis on hot pressing. The preparation of the metal matrix and diamond for the production of DIMM materials

was outlined with emphasis on the effects of the hot pressing process on diamond degradation. The different metal matrices used in DIMMs were briefly outlined but a more in-depth coverage of the metal matrix cobalt was reviewed.

Following this, the type of diamond used and the processes associated with the production and classification of suitable grades was explained. The concept of diamond size (Mesh Size) and the relationship between Mesh Size and actual diamond size was delieniated. Diamond concentration (DC) was explained which is important to the understanding of diamond tools.

As mentioned, because very little is known regarding the mechanical properties of DIMMs, a comparative study of PM and PMMCs materials has being undertaken in this review to try and understand the class of materials called DIMMs. Regarding PM and PMMC materials, the level of porosity is detrimental to their mechanical properties. This is expected to be similar for DIMM materials. Regarding impact testing of PM materials, a dependency on 'available-energy' is found, this will be investigated for DIMMs. Also, there are the difficulties of fracture toughness testing and the strict ASTM standard E399-90 requirements for a valid K_{1C} result. How DIMMs are affected with the strict ASTM requirements will be investigated.

Regarding PMMCs and the effects of volume fraction and particle size on their mechanical properties, similarily, the effects of DC and diamond size have on the mechanical properties will be interesting to explore. An important difference between PMMCs and DIMMs is particle size; in PMMCs reinforcement particles are much smaller in comparison to the diamonds used in DIMM materials. So how the larger diamond crystals influence the mechanical properties of DIMMs is important to investigate. Do the diamonds act as flaws or do they reinforce the metal matrix and increase its strength and toughness as measured by TRS, impact and fracture toughness.

Finally, predictive composite models of PMMC mechanical properties is found to depend on the specific mechanical properties in question; it is also very PMMC material specific. Some of these will be used to analyse the mechanical property results of the DIMM materials and investigate their predictive properties. Other predictive fracture

models will also be investigated and their effectiveness regarding DIMM materials will be tested and compared with experimental results.

Finally, wear of DIMM materials will be investigated, with special attention with erosive wear and the effects of DC and Mesh Size have on the erosion resistance of these materials. Again, a predictive model will be investigated and compared with experimental results. In addition the wear patterns on the eroded surfaces of the DIMM samples will be examined and compared with what is normally found for a DIMM working segment as used in a diamond tool.

CHAPTER THREE: EXPERIMENTAL PROCEDURES

3.1. Introduction

This chapter details the experimental methodology used in the project. Firstly, the experimental plan is outlined. The materials – diamond & cobalt metal powder; used in the project are described. This is then followed by an explanation of the specimen types, specimen designs and compositions. The different tests that were carried out are explained. The development of any test procedure will be outlined briefly or in detail where the author feels it necessary for the reader to aid understanding of a test, e.g. fracture toughness testing. The manufacturing route and the materials preparation is outlined in detail so that a good understanding of the difficulties of testing the diamond impregnated cobalt material can be appreciated.

3.2. Experimental Plan

From the outset, this project's aim was to investigate the effects of the addition of diamond, diamond size and diamond concentration on the mechanical properties of the cobalt metal matrix. The 100% cobalt metal matrix specimens were also tested and used as a datum for all the different types of tests. This part of the chapter outlines briefly the plan adopted in the project. An initial plan was devised using an experimental design approach using a 'partial-factorial' high and low factor levels experimentation. However it proved to be too difficult to implement due to equipment and time constraints. It was subsequently abandoned. This abandonment has not in any way taken from the project's findings. Overall, the types of specimens manufactured were Charpy Impact, Tensile, Bend -TRS, and Bend - Fracture Toughness. The broken Charpy Impact specimens were subsequently used for wear testing.

Manufacturing of the specimens was carried in Boart Longyear in Limerick, Ireland. A wide range of specimens were manufactured covering different diamond sizes, diamond concentrations, hot pressing temperatures and different specimen types. Besides the 100% cobalt specimens, the diamond impregnated cobalt specimens were hot pressed at 800°C. There were a number of reasons for this however the main reason was to minimize the degradation of the graphite moulds which occurs when using high hot pressing temperatures. This use of this lower hot pressing temperature of 800°C besides minimising the degradation of the graphite moulds minimised the degradation of the

diamond. The 100% cobalt specimens were hot pressed at 700°C, 750°C, 800°C, 900°C, 950°C and 1000°C.

The initial intention of the project was to investigate the wear and fracture toughness properties of diamond impregnated cobalt; however other mechanical properties had to be determined first before the determination of fracture toughness could proceed. These included the manufacture of tensile and bend-TRS type specimens so that yield strength, Young's modulus and Poisson's ratio could be determined. In addition to this, a requirement for an atomically sharp crack in the fracture toughness specimens for adherence to the ASTM standard E-399 proved problematic. Normally, a fatigue crack is an accepted method of achieving this. However, fatigue cracking of these DIMM samples proved a major challenge because of their size but also due to the presence of diamond. The compliance crack length method was used in measuring the growing fatigue crack. However, the determination of what are called compliance coefficients for these small samples led to a large amount of painstaking experimental work to achieve this. Another issue was that the investigation into wear proved to be very difficult and it was only towards the end of the project lifetime that actual success was achieved.

3.3. Test Specimen Designs

The mechanical properties investigated were as follows: impact, transverse rupture strength (TRS), hardness, tensile, elastic moduli, fracture toughness properties and wear. The types of specimens required to carry out these tests can be classified under three headings i.e. Fully-Impregnated, Partially-Impregnated or 100% Cobalt Metal Matrix. In total, four different types of specimens were manufactured. These were Charpy, Tensile, Bend (TRS), and Bend (Fracture Toughness) type specimens. However, the type of test being carried out dictated the specific design and configuration of the specimen and the required method of hot pressing.

3.3.1. Specimen Design Types

The three different types of specimen design can be seen in Figures 3.1, 3.2 and 3.3 below. The first configuration type (Specimen Design Type 1) is 100% cobalt metal matrix (CoMM).

(a) Specimen Design Type 1

This was manufactured with just 100% cobalt metal. It was hot pressed similar to all the other samples.

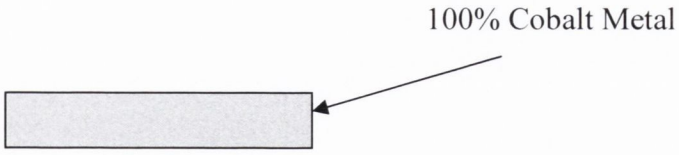

Figure 3.1. Specimen Design Type 1 – 100% Cobalt Metal Matrix (CoMM) [Charpy, Bend-TRS, Bend-Fracture Toughness & Tensile Specimens].

The next two design types (Specimen Design Type 2 & 3) are DICoMM. However there is one difference in that they differ depending whether they have what is termed in the diamond industry as a Backing Layer present or not.

(b) Specimen Design Type 2

Figure 3.2 shows Full-Impregnation, where the specimen has diamond impregnated metal matrix throughout the sample. The Charpy, Bend (TRS) and Tensile samples were manufactured like that in Figure 3.2 configuration. The specimen dimensions for Charpy were in accordance with MPIF Standard 40 [78].

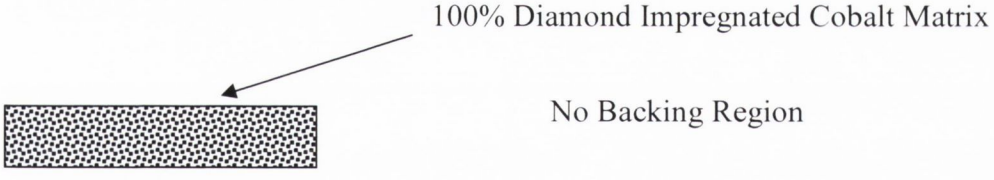

Figure 3.2. Specimen Design Type 2 – 100% Diamond Impregnated Cobalt Metal Matrix (DICoMM). [Charpy, Bend-TRS & Tensile Specimens].

(c) Specimen Design Type 3

Figure 3.3 shows a type of specimen design which has a Backing Layer, which is a diamond free layer. The presence of a Backing Layer is typical in the diamond tool industry because it is used for laser welding the diamond segments to the saw blade centre also called the core. This same approach was used in the manufacture of the Bend (Fracture Toughness) samples as shown in the Figure 3.3 configuration. In this project the Backing layer is required for EDM machining of a starter notch with integral knife edges to which a COD gauge is attached.

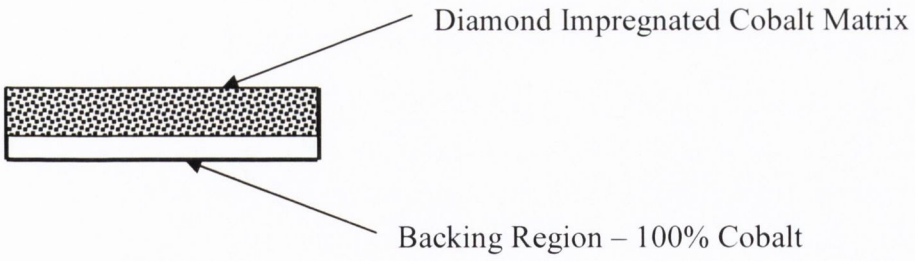

Figure 3.3. Specimen Design Type 3 - Diamond Impregnated Cobalt with Backing Layer (DICoMM+BL). [Bend - Fracture Toughness Specimens].

3.4. Specimen Constituents or Materials

The two materials used in the project were an industrial synthetic diamond grit and cobalt metal powder. The diamonds used were a standard diamond grit of medium grade called SDA 85+ manufactured by Element Six, Shannon Ireland. The diamond was from the saw grit family called SDA (Saw Diamond Abrasive). A photomacrograph can be seen in Figure 3.4 which shows the types of crystals which make up this high/medium grade diamond. The range of crystal morphology can be seen in the figure which makes up this grade of diamond. This grade of diamond is very commonly used in sawing applications, which was the reason for using it over using a superior grade diamond which would have very uniform diamond morphology.

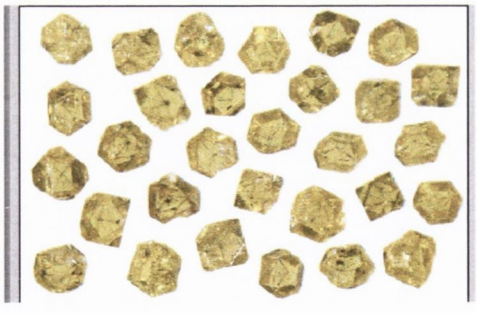

Figure 3.4. Photomacrograph - SDA 85+ Diamond Grit. [Courtsey of Element Six].

The diamond sizes were 20/25, 25/30, 30/35, 35/40, 40/45, 45/50, 50/60, 60/70, 70/80 and 80/100, all US Mesh sizes. The finest diamond grit, the 80/100 US Mesh size, was not SDA 85+ but an equivalent type with similar properties and crystal shape. For clarification the above Mesh sizes correspond to the following dimensions in microns: 20/25(840/710), 25/30(710/590), 30/35(590/500), 35/40(500/420), 40/45(420/350), 45/50(350/297), 50/60(297/250), 60/70(250/210), 70/80(210/177) and 80/100(177/149).

The cobalt used in the project was a standard cobalt powder used in the diamond tool industry manufactured by Eurotungstene in France. This cobalt powder is termed ultrafine grade cobalt, designated Couf. It is typical of the powder used for diamond tools. A SEM photomicrograph of the un-granulated version can be seen in Figure 3.5.

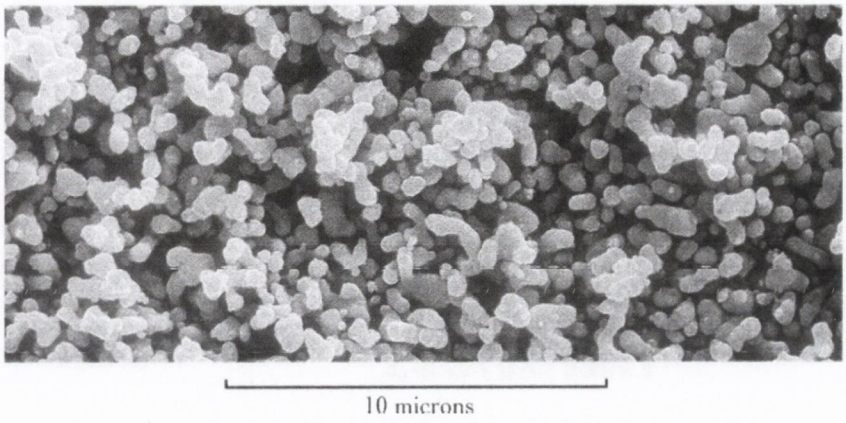

Figure 3.5. Couf Co powder, ungranulated version of the powder showing very fine grains. [Courtsey of Eurotungstene France].

The cobalt powder shown in Figure 3.5 is an un-granulated version of Couf cobalt powder. The Couf cobalt powder used in this project was a granulated version, with the granules ranging from 63-350μm in size. The Couf cobalt is produced by the conventional thermal reduction process. The granulated powder had 1.3wt% polyacrylate binder.

The stability of Eurotungstene cobalt powders during sintering (hot pressing) enable these powders to be sintered over a wide range of temperatures, ranging from 780° and 950°C, where no grain growth occurs and so the fine structure and resulting hardness are kept constant. The diamond/metal compositions of the specimens used in this project are given below.

For more information on Couf powder used in this project the reader is referred to Appendix 1, and also the following references [226].

3.5. Specimen Manufacture

All the specimens in the project were produced using the customary hot pressing PM route as used in the industry in manufacturing diamond impregnated metal matrices. In conventional standard PM parts processing hot pressing is not generally used. For a more detailed review of the manufacturing of diamond impregnated segments the reader is referred to Dwan [21]. Computer spreadsheets were used for calculating various inputs,

amounts of diamond and metal required for different specimen compositions and types. The various calculations in spreadsheet form can be found in the Appendix 3. Spreadsheets were also used to calculate the different theoretical densities for each specimen type which is used in calculating the %theoretical densities and the %porosities of the hot pressed specimens.

3.5.1. Specimen Mixing Calculations

Besides the use of spreadsheets in the calculation of specimen dimensions, matrix and segment densities for porosity calculations, the spreadsheets for each specimen type were also used for manufacturing process calculations. It is generally found in the diamond tool industry that the volume of the metal/diamond mixture should fill the mixing container to approximately 50% by volume in order to aid in producing a homogenous mix. In practise it was difficult to achieve this because of the different types and numbers of specimens being made. In order to guarantee enough diamond/cobalt powder was available for hot pressing of each combination, a contingency of 1% extra powder and diamond was made-up to cover loss, this extra powder was then used after filling of the graphite mould to make dummy samples. These dummy samples were used for test procedure development.

3.5.2. Mixing & Blending

In industry, good diamond distribution is very important for good tool operation in the field and all diamond tool manufacturers strive to achieve it. However, mixing and blending is a science in its own right and there is great difficulty in getting a good even distribution of diamond in metal powders for a number of reasons.

(1) Differences in the density of the diamond (3.52g/cc) versus the metal powders (8.85g/cc Co) greatly increases the chance of segregation,
(2) The large difference in size between the metal powder and diamond crystals. When large diamond is used, layering and clustering is common due to the finer metal powder flowing down between the coarser diamond crystals. The fine metal powder is typically 5μm to 0.5μm where the diamond size ranges from 150μm to 840μm. Even though granulated Couf was used in this project, when mixed with diamond the granules can be broken up into a fine powder. Another reason is electrostatic charge building up on the diamond due to mixing.

A mixing procedure sometimes used in the industry is to wet the diamond with liquid paraffin which helps coat it with the metal powder. The 'wetted' diamond grit and the cobalt powder are then placed in a container with springs, which aids the mixing process. The diamonds and the cobalt powder are then loaded in a 'Turbula' mixer for fifteen minutes at a medium speed (26rpm). The Turbula [227] type mixer, see Figure 3.6 is used extensively in the diamond industry. This mixer has a special mixing action called kinematic where it does a 'figure-of-eight' type motion which is supposed to give a good mixing to the diamond/metal blend. In the diamond tool industry the 'art of mixing' is very much a black one. Any added binding agents are burnt off during hot pressing at approximately 300 - 400°C.

Figure 3.6. Turbula Type Mixer – 'Figure-of-Eight' type mixing motion [227].

3.5.2.1. Mixing Speed & Time Test

As already stated above, mixing diamond and metal powder often results in poor distribution which increases the variability in test results. A series of mixing tests were carried out to try and obtain a procedure, which gave the best diamond distribution in the metal powder. Mixing speed was seen as an important variable. An optimum mixing speed would ensure a uniform diamond distribution in the metal powder. The aim was to ensure that after the mixing/blending of the diamond and metal powder in amounts for each hot pressing run, that each 'weigh-out' would contain approximately the same amount of diamonds. If this did not happen, variation would be introduced into each sample for the same composition, which would increase the variation in the sample population. Following discussions with Eurotungstene and Boart personnel, it was decided that it would be best to mix the powder with ethanol glycerine to soften the granules and so aid accretion of cobalt powder to the diamond surface. However the author found that it was very difficult to mix it properly and it was abandoned because the initial results obtained were very unsatisfactory.

Another approach was tried using another series of mixing tests with many different combinations of mixing speeds and times. From each mixing sample e.g. 100g of diamond & powder, sample 'weigh-outs' of 10g would be taken. The aim was to recover the diamonds from each sample 'weigh-out' and check for variation in the amount of diamond in each 'weight-out'. This procedure would be done for each combination of diamond size and diamond concentration. However difficulties in recovering the diamond occurred. Many different procedures were tried to recover the diamond but they were all found to be very difficult due to contamination of the diamond in the recovery process. The main contaminant was the wax that was used in the cobalt granulation process. It was found that it was extremely difficult to remove the wax from the metal powder in the recovery process. A common solvent aided technique called the Soxhelet technique was also attempted. Briefly the Soxhelet technique is where the mixture is passed through a filter sleeve as shown in Figure 3.7.

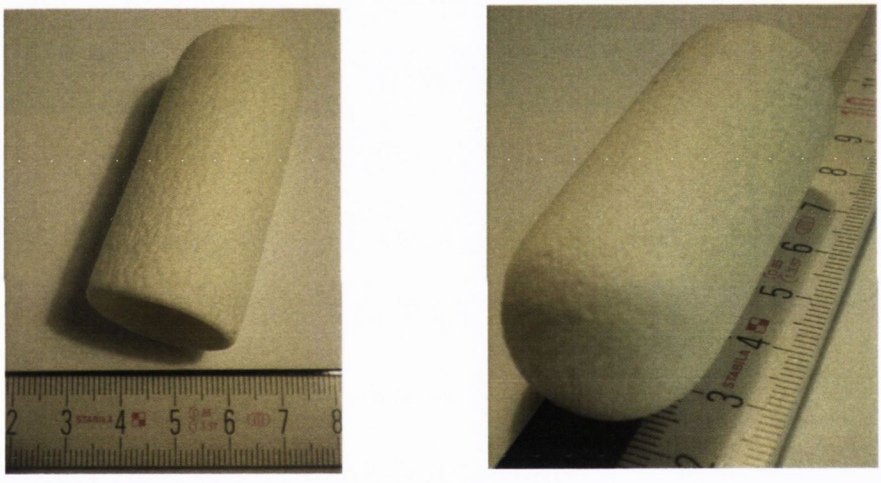

Figure 3.7. Soxhlet Filter Sleeve used to remove the dissolved wax from the Cobalt powder.

In this case the solvent with the wax dissolved would pass through leaving the fine cobalt powder and the diamonds in the sleeve. Following the filter process the diamond and powder could be separated. However the results with this technique proved to be very poor. Following the less than satisfactory results achieved in trying to develop an optimum mixing protocol, the decision was made to follow the normal mixing procedures as used in industry and accept the large variation that is very common in diamond impregnated metal matrix segments.

3.5.3. Hand-Loading of Diamond/Cobalt Material

As already stated diamond impregnated metal segments are usually cold pressed in practice because of the increased productivity in loading the hot pressing moulds.

However, cold pressing is not imperative to the manufacture of these segments. Hand-loading is often carried out by the smaller diamond tool manufacturers because of the cost of cold pressing machines. This hand-loading takes place where the diamond mixed with the metal powder is hand-loaded into the graphite moulds directly. In this project cold pressing was not carried out because of the difficulties of having to manufacture a die set and the time taken to cold press individual segments without the use of a dedicated cold pressing machine. Also using an Instron type of machine for cold pressing without pressing to a height or standard pressure would introduce density and work hardening variations in the metal powder. This would then lead to variations in the sintering behaviour of the powder. Due to the inherent variation in the final composite material, a proactive drive for limiting the introduction of variation was strived for but was very difficult to achieve.

3.5.4. Hot Pressing (Pressure Sintering)

Following the blending/mixing process, the next stage was the weighing out of correct weights of diamond/cobalt mixture for each specimen; these are called 'weigh-outs'.

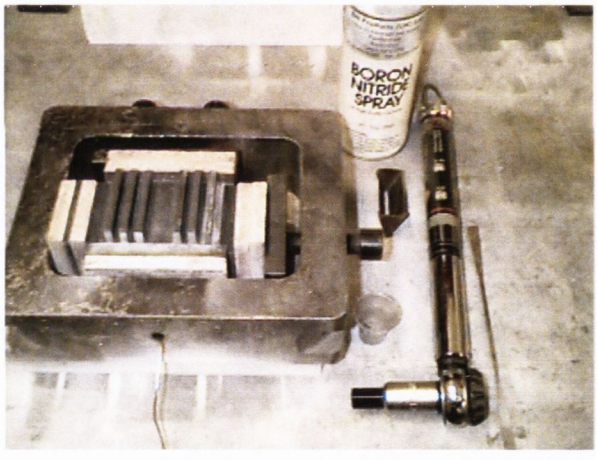

Figure 3.8. Mould assembly including brass filling funnel, plastic cup, spatula, boron nitride spray & torque wrench.

The correct 'weigh-out' for each specimen was put into a plastic cup type container. These were then transferred to the hot pressing mould and loaded into the graphite mould. The weighing out of the diamond/cobalt mixtures results in errors from segment to segment and also when hand-loading the diamond powder mixture into the graphite moulds. This was especially the case when filling the TRS and fracture toughness specimens because they were just 5 mm gaps between the graphite punches and spacers. Figure 3.8 shows the mould arrangement with Figures 3.9 & 3.10 showing how they are positioned in the hot-press. Figure 3.8 shows the mould assembly with the outer

aluminium bolster with the graphite punches, plates & insulation plates assembled. Also the brass filling funnel which was crafted to aid filling of the graphite mould spaces as well as the filling plastic cup used for weighing out the diamond/cobalt mixtures along with the spatula which was used for evening out the poured in mixture. In order to aid the preservation of the graphite a boron nitride powder coating was applied to graphite punches and plates for protection when hot pressing above 800°C. Graphite above these temperatures degrades very quickly especially at 1000°C. The boron nitride can be painted on or sprayed on as can be seen in the Figure 3.8. The torque wrench used for ensuring the correct amount of tightening can also be seen. Figure 3.8 shows the steel bolster where the graphite punches, end and front plates along with the insulation can be seen. The graphite punches can be seen proud of the rest of the graphite/insulation assembly.

In Figure 3.9 the bolster/mould system can be seen sitting on top of the aluminium filling grate which was manufactured to aid the hand-loading of the graphite mould. The filling grate allowed the bottom punches to remain proud which was imperative for equal pressing from the two directions. The torque wrench was used for ensuring that the correct tightening was applied. The torque was set to 30Nm to ensure that graphite punches were not broken due to excessive tightening or not enough. If tightened too loosely this would allow the powder go down between the punches which would result in poorly hot pressed samples or again punch breakage. Also if over-tightening occurred, the friction between the punches would be too great and the applied pressure would not be sufficient to apply the correct pressure to the powder mixture and very poor sintering would occur as a result.

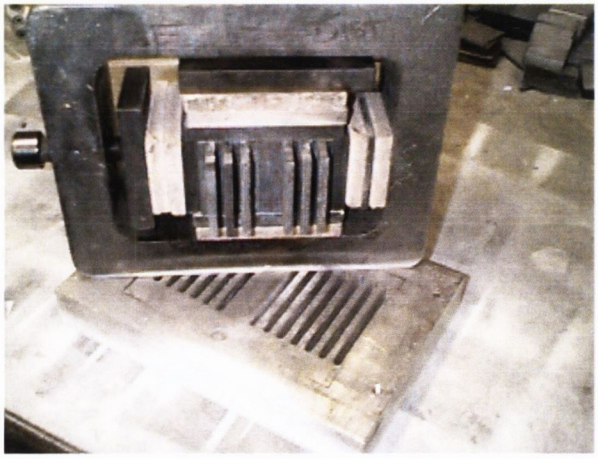

Figure 3.9. Aluminium bolster with the graphite/insulation mould system. The bolster/mould is positioned on top of the aluminium filling grate.

The hot press used was a Dr. Fritsch DSP 25 AT [228], see Figures 3.10 - 12. This is a standard small dedicated hot pressing machine as used in the diamond tool industry. The pressure and temperature profile and rates of increase were the same for all the specimen types. A 10MPa initial pressure and 35MPa final pressure were used for all.

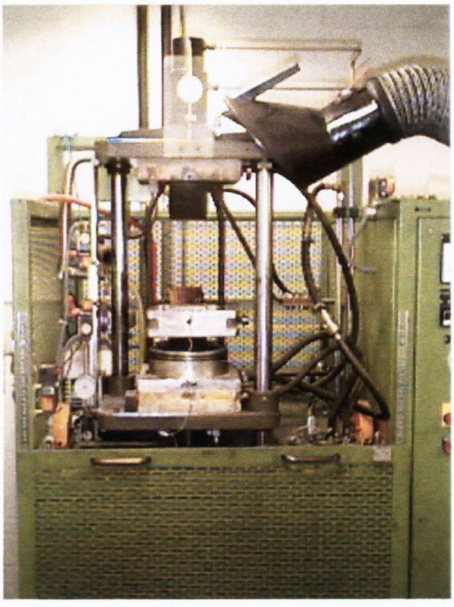

Figure 3.10. Hot Press front view showing the mould assembly sitting on bottom graphite electrode. The water cooling pipes (black) can be seen with the electrical control panel on the right hand-side.

Above one can see the pressing envelope of the Dr. Fritsch hot press with the steel bolster and mould materials located on the lower graphite electrode. The black pipes are the cooling water system. The steel rods are the platen guides which guide the bottom platen up for the mould system to engage with the top graphite electrode. Figures 3.10 & 3.11 show the mould assembly positioned on the bottom graphite electrode, with the thermocouple attached.

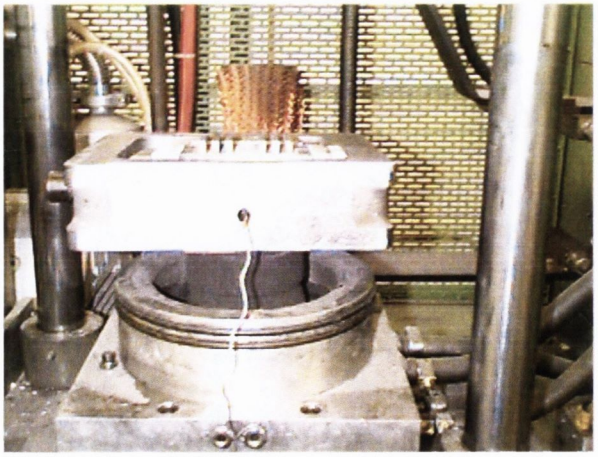

Figure 3.11. Showing close-up of the mould assembly on the lower graphite electrode with the thermocouple positioned in the aluminium bolster.

The thermocouple is pushed through a hole drilled in the steel bolster and then through the graphite end plate which is between two banks of diamond/cobalt powder segments to be hot pressed. It is important that the thermocouple is positioned between the two banks of segments to be hot pressed so that a reasonable measurement of the temperature is obtained.

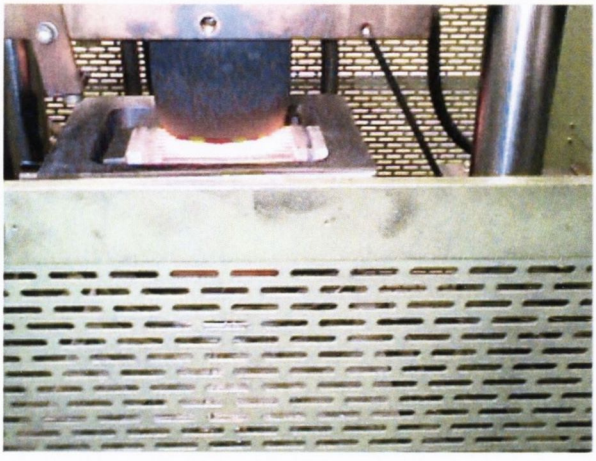

Figure 3.12. Shows the top graphite electrode in position with the red colour indicating that current is passing through the mould system.

Above in Figure 3.12 one can see the red glow of the mould system being heated by the passing of current through the graphite electrodes and punches and being heated up due to resistance heating.

A number of tensile test specimens were hot pressed. A special split mould was required which can be seen in Figure 3.13, where only one specimen at a time could be hot pressed. Hot pressing one specimen at a time proved difficult to locate the mould system in between the graphite electrodes of the machine which often resulted in misalignment. Added to this was the requirement to increase the pressing force to maintain electrical contact.

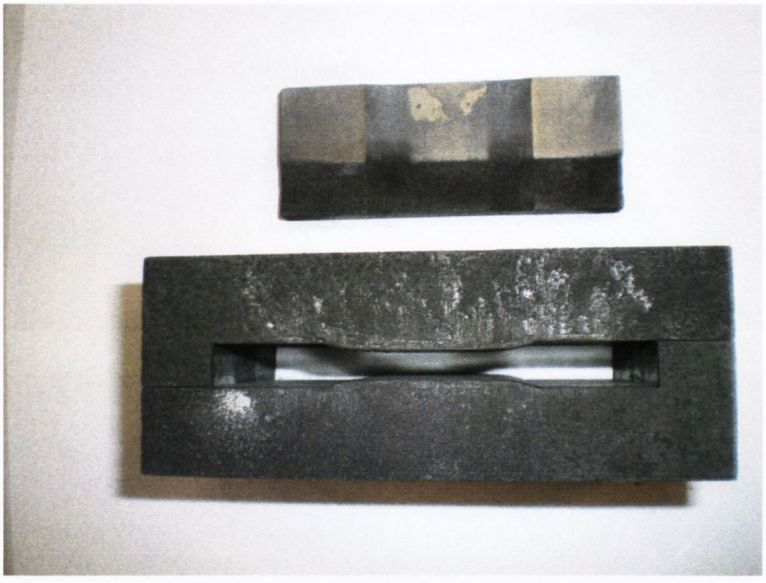

Figure 3.13. Hot pressing split-type mould for manufacture of tensile specimens.

A successfully hot pressed tensile specimen can be seen in Figure 3.14. The roughness of the surface is due to the diamond crystals protruding.

Figure 3.14. Showing a hot pressed tensile specimen; the rough surface shows the diamond crystals protruding on the specimen surface.

3.5.5. Specimen Hot Pressing Pressure Calculations

The hot pressing spreadsheets mentioned above were also used for calculating the pressure profile for the hot pressing operation. The calculated pressing forces depended on the number of specimens and the pressing area of each specimen. In the hot pressing process, the pressure profile has generally two to three stages – the last stage being the important sintering pressure or final pressure. The initial pressure is generally one third that of the final pressure. However, it is often found that in hot pressing a small number of specimens the contact area between the specimen graphite punches and the large graphite electrodes is too small which leads to the initial force applied being too low for proper electrical contact. In this situation, the initial contact pressure is increased just enough for electrical contact to be made. As can be concluded, this does add variability

to the hot pressing process, with a possible result that wax is not removed or burnt off correctly.

3.5.6. Hot Pressing Temperature & Pressure Profiles

The hot pressing time, temperature and pressure profile can be seen in Figure 3.15. The pressure profile on ramp-up and final pressure is also indicated. The initial pressure and slow heating ramp between 400°C and 600°C was used to allow the granulation binder to burn off. No protective atmosphere was used and temperature measurement was by thermocouple located in the centre of the graphite mould. Below is the hot-pressing profile as used in the manufacture of the specimens. The final temperature (Final Temp.) chosen depended on the test variable.

Hot-Pressing Profile

Temp. Range	**Heating Rate**	**Pressure**
RT. – 400°C	200°C/min	10 MPa Initial Pressure
400°C – 600 °C	50°C/min	10 MPa Initial Pressure
600°C – 800 °C	150°C/min	35 MPa Final Pressure
Final Temp e.g. 800°C	Heat-on	35 MPa Final Pressure
Cool-Down, 3 mins.	Heat-off	35 MPa Final Pressure

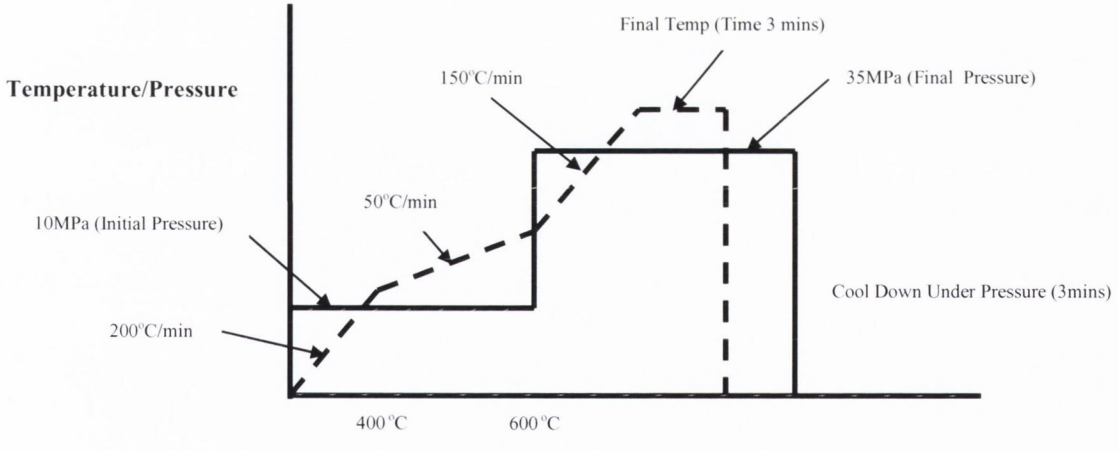

Figure 3.15. Hot Pressing Cycle (Time, Temperature & Pressure Profile)

Hot pressing spreadsheets as mentioned previously were used to calculate the pressing forces required to maintain the pressure profile described above. The forces used depend on the pressing area of each specimen but also on the number of specimens. This proved

problematic when hot pressing the tensile test pieces and only occasionally the TRS type specimens because the contact area was close to a minimum to maintain electrical contact. As can be seen in Figure 3.15 the pressure profile has generally two stages – the initial stage and the important sintering pressure or final stage pressure. The initial pressure is generally one third that of the final pressure.

3.5.7. Finishing Operations

The general finishing process is the grinding off of any flash or rough surfaces that occurred due to the hot pressing process. This grinding was carried out using a belt grinder Figure 3.16. Diamond crystals exposed on the surface and protruding can cause problems in cleaning up the edges and getting square and parallel faces. This caused problems later when testing. Akyüz et al. [37] have found in their work on PM cobalt, a porous layer with a thickness 10 - 260μm around each sample, which they indicated was due to interstitial carbon originating from the graphite punches, this has also been found by other authors. The authors machined this layer before calculating the density. However, in the present project this was not carried out because of the large number of specimens requiring machining with a diamond grinding wheel. The presence of diamond on the specimen surfaces would have made it extremely time consuming and expensive. The backing layer which was 100%Co of the fracture toughness specimens however were ground.

Figure 3.16. Belt grinder used to remove any remaining flashing following hot pressing.

Where other specimen preparation was carried out it will be explained when the need arises e.g. fracture toughness testing.

3.6. Hot Pressing Difficulties and Sources of Variation

There are many difficulties in hot pressing ranging from graphite degradation of the main electrode faces and also similar degradation of the graphite punches. Pressure transmission to the powder, correct temperature and its distribution throughout the mould were constant sources of variation. Regarding hand-filling of the powder, variation of powder initially in the mould can lead to variation in the final dimensions leading to

tapering. This can also be the result of the graphite punches shifting in the mould during hot pressing. An unusual situation arose when hot pressing the TRS specimens, where only 4 specimens were hot pressed at a time. If enough force was not applied to the graphite punches, electrical current would not pass even though when a larger number of segments were being hot pressed the 10MPa contact pressure would have been adequate. A close-fitting copper filling funnel was manufactured from sheet metal because loss of powder and diamond would result in hand-loading into the graphite moulds. In addition to the special filling-grates for hand-loading the powder in to the graphite moulds were machined from aluminium plate.

3.7. Specimen Compositions

The different specimen types and compositions hot pressed are laid out in Tables 3.1, 3.2, 3.3, 3.4, 3.5. The number inserted in the shaded box is the number of specimens for each combination of diamond size (US Mesh Size) and diamond concentration (DC). Where a number is absent indicates that no specimen for that combination was available for testing for a number of reasons e.g. graphite breakage, non-availability of hot press. Even though a DC of 1 does not make any sense from an industrial point of view, due to initial test results there was a large discontinuity between CoMM specimens and DICoMM specimens. Due to this, it was felt that DC1 DICoMM specimens may yield valuable information regarding the addition of diamond to a cobalt matrix.

3.7.1. Cobalt Metal Matrix (CoMM) - Specimen Design Type 1

Because very little test data was available in the literature, 100% cobalt (CoMM) specimens were hot pressed and used as reference data where appropriate. Table 3.1 shows the different types of test specimens made and hot pressing temperatures used. The number inserted in the shaded box is the number of samples hot pressed for each test type. Two tensile specimens were also hot pressed but this testing was discontinued as it proved of no value to continue.

Cobalt Metal Matrix (CoMM)	100% Cobalt Metal Matrix (CoMM)		
Design Type 1	Hot Pressing Temp. (°C) 800		
Specimen Type	Charpy	Bend (TRS)	Bend (Fracture Toughness)
No of Specimens	4	4	6

Table 3.1. CoMM (Specimen Type & Design 1 with Hot Pressing Temps.).

Other CoMM Charpy, TRS and FT specimens were hot pressed at 700°C, 750°C, 800°C, 850°C, 900°C, 950°C & 1000°C and tested accordingly. However, the reporting of these results is outside the scope of this project.

3.7.2 Diamond Impregnated Cobalt Metal Matrix (DICoMM)

The range of diamond sizes (US Mesh) and DCs was chosen to match as closely as possible as that used in the stone industry except for DC1 as already explained. The following tables show the compositions of the DICoMM specimen types with the number of repetitions hot pressed at different hot pressing temperatures. The number inserted in the shaded box is the number of specimens hot pressed for each combination of US Mesh size and DC.

3.7.3. Charpy Impact Specimens – Specimen Design Type 2

Nominal Dimensions: 10 x 10 x 55 mm – Fully Impregnation. Standard Pendulum Impact 50J and 300J. A number of the DICoMM and all of the CoMM specimens were tested using the Instrumented 300J Pendulum Charpy Impact machine. Table 3.2 shows the full range of diamond mesh sizes and DCs hot pressed. An exception was 25/30.

Specimen Type	Charpy Impact (CI) – Specimen Design Type 2									
Hot Pressing	HP Temp. 800°C									
Diamond Type	Diamond Size (US MESH Size) – SDA 85+									
Diamond Conc. (DC)	20/25	25/30	30/35	35/40	40/45	45/50	50/60	60/70	70/80	80/100
1	4	4	4	4	4	4	4	4	4	4
10	4		4	4	4	4	4	4	4	4
20	4		4	4	4	4	4	4	4	4
30	4		4	4	4	4	4	4	4	4
40	4		4	4	4	4	4	4	4	4

Table 3.2. DICoMM Charpy Impact Specimen Compositions & Design Type 2 (800°C).

3.7.4. Bend Type Specimens - TRS - Specimen Design Type 2

Nominal Dimensions: 10 x 5 x 55mm – Fully impregnated. 3-point & 4-point bend tests TRS. Table 3.3 shows the full range of diamond sizes (US Mesh) and DCs hot pressed.

Specimen Type	Bend - Transverse Rupture Strength (TRS) - Specimen Design Type 2									
Hot Pressing	HP Temp. 800°C									
Diamond Type	Diamond Size (US MESH Size) – SDA 85+									
Diamond Conc. (DC)	20/25	25/30	30/35	35/40	40/45	45/50	50/60	60/70	70/80	80/100
1	4	4	4	4	4	4	4	4	4	4
10	4	4	4	4	4	4	4	4	4	4
20	4	4	4	4	4	4	4	4	4	4
30	4	4	4	4	4	4	4	4	4	4
40	4	4	4	4	4	4	4	4	4	4

Table 3.3. DICoMM Bend - TRS Specimen Compositions & Design Type 2 (800°C).

Prior to 3-point and 4-point bend testing, the TRS specimens were used for Young's modulus and shear modulus determination, using natural frequency and ultrasonic methods. However, the reporting of these results is outside the scope of this project.

3.7.5. Bend Specimens – Fracture Toughness (FT) - Specimen Design Type 3

Nominal Dimensions: 10 x 5 x 55mm. (2mm backing layer - integral knife edges). Single Edged Notched Bend (SENB) Specimens. – Partial Impregnation. Table 3.4 shows the full range of diamond sizes (US Mesh) and DCs hot pressed.

Specimen Type	Bend - Fracture Toughness (FT) - Specimen Design Type 3									
Hot Pressing	HP Temp. 800°C									
Diamond Type	Diamond Size (US MESH Size) – SDA 85+									
Diamond Conc. DC)	20/25	25/30	30/35	35/40	40/45	45/50	50/60	60/70	70/80	80/100
1	6		6		6	6	6	6	6	6
10	6		6		6	6	6	6	6	6
20	6		6		6	6	6	6	6	6
25	6		6		6	6	6	6	6	6
30	6		6		6	6	6	6	6	6
40	6		6		6	6	6	6	6	6

Table 3.4. DICoMM Bend - FT Specimen Compositions & Design Type 3 (800°C).

3.8. Density Testing – DICoMM & CoMM Specimens

Density measurements were carried out on all specimens. From the experimentally determined density and the known theoretical density, the level of porosity can be calculated. As already stated in the Chapter Two, Literature Review, this is one variable which plays a dominant role in the resulting mechanical properties of PM and PMMC type materials.

There are many ways of measuring accurately the density of small samples [229] and for this project two different types of density measurement methods were carried out, the commonly used Archimedes principle method and a method called Picnometer.

The MPIF Standard 42 [230] details the method for applying Archimedes principle. The final or sintered densities of all the specimen types were tested using this method. An Ohaus fine balance with the Archimedes apparatus immersed in a water (soapy) filled beaker can be seen in Figure 3.17. An accuracy of 0.1mg is required to accurately determine the density of these specimen types.

Care must be exercised when weighing in water due to air bubbles that can attach themselves to porosity and surface imperfections present on the PM based materials as this can greatly influence results.

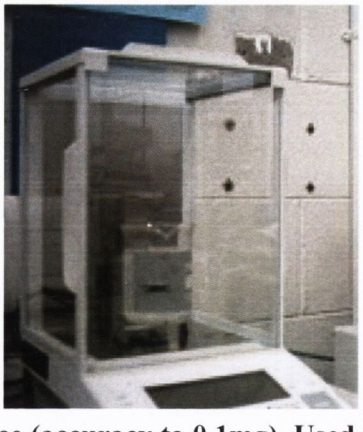

Figure 3.17. Ohaus Fine Balance (accuracy to 0.1mg). Used for density measurement using Archimedes method. Shown in picture beaker with immersion apparatus for weighing in water.

The formula for calculating the final or sintered density or just density for short can be seen below in Equation 3.1.

$$Final.Density = \left(\frac{M_{Air}}{M_{Air} - M_{Water}} \right) \rho_{Water} \tag{3.1}$$

where

M_{air} = mass of the object weighed in air,

M_{water} = mass of the object weighed in water,

ρ_{water} = density of water

The units for density as used in the diamond tools industries is generally g/cc.

Regarding the picnometer method, the technique entails placing the specimen in a closed chamber which is back filled with gas. The difference in volume from the fixed chamber volume to the back-filled volume gives the volume of the specimen. The density can then be calculated using the specimen weight and volume. The Picnometer method was used on some of the Charpy specimens. However it was found to be very slow and not practical because some of the specimens were too big for the chamber.

3.9. Hardness Testing – DICoMM & CoMM Specimens

The MPIF Standard 43 [231] which follows the ASTM Standard E18 details the method for carrying out hardness testing on PM materials and was used in this project for Rockwell hardness testing. However hardness testing of DIMMs materials is very difficult to carry out successfully due to the presence of diamond. The normal hardness testing carried out on DIMMs in the industry is Rockwell HRB. However, HRB is not the most appropriate when one considers that most readings are greater than 100 on the HRB scale. So for this project HRB and two other scales were used, HRA (diamond indenter, 60kg load) and HRG (1/16"steel ball, 150kg load). The HRA and HRG were used to try and achieve Rockwell hardness values that were within the recommended range within a given Rockwell scale of 10 to 100. An Indentec Rockwell hardness test machine was used as can be seen in Figure 3.18 below. The hardness value was measured in three places along each specimen, giving an average value for each specimen.

Figure 3.18. Showing Indentec Rockwell hardness test machine.

As already mentioned above, one of the issues with hardness testing of DICoMMs is the presence of diamond which has the potential of causing damage to the indenter, whether it is diamond or ball. Figure 3.19 shows the typical damage caused to a ball if it is not regularly checked which yields inaccurate hardness results. The damage seen in Figure 3.18 is excessive and is only shown as an example.

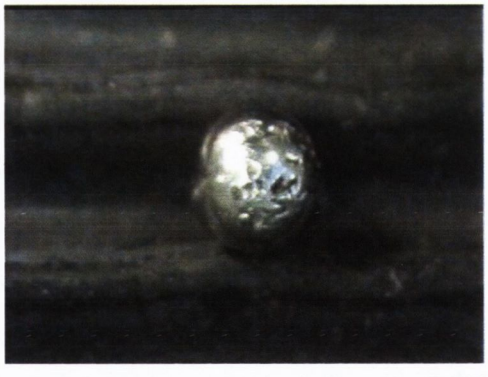

Figure 3.19. Damage to the ball indenter as used in Rockwell HRB hardness testing due to the presence of diamond in DICoMM.

The HRA and HRG were only used on some specimen types and had to be discontinued. Using HRA scale damage to the diamond indenter required it to be discontinued because of the risk of replacement costs. Regarding HRG, even though the initial results were satisfactory, damage to the ball was very frequent due to the higher load and so was discontinued.

In order to minimise damage when using the HRB scale, 1/16"carbide indenter was used because it has better damage resistance than a steel indenter. However, this did not totally remove the occurrence of ball fracture due to the diamond.

3.10. Charpy Impact Testing

As a measure of toughness impact testing using Charpy or Izod is the easiest, most commonly used [232, 233] and low cost technique but it is only semi-quantitative. The test methodology for wrought metals is well developed, with the ASTM-E23 [234] standard for Charpy impact testing of notched metallic bars being widely utilised however, is only relevant for relatively high toughness materials [235]. Regarding PM materials the same Charpy impact test is performed using an unnotched specimen according to the Metal Powders Industry Federation (MPIF) standard (MPIF 40) [78] which is comparable to the ASTM E23 [234]. Regarding this project, two types of Charpy impact machine were used; a standard bench-mounted 50J Charpy and an instrumented 300J Charpy, both pendulum type. The majority of the DICoMM specimens were tested using the standard Charpy impact machine. However all of the CoMM and some of the DICoMM specimens were tested using the instrumented Charpy impact machine which allows more data regarding the fracture process due to impact.

3.10.1. Standard 50J Charpy Impact Testing – DICoMM Specimens

The standard impact testing was carried out using a bench mounted Zwick 5113, type pendulum 50J digital read-out Charpy impact tester with a span of 40mm which can be seen in Figure3.20. The MPIF Standard 40 [78] was used as a guide. Un-notched Charpy specimens were hot pressed, with the following dimensions: 10mm x 10mm x 55mm. A minimum of three specimens (repetitions) were used for each DC and US Mesh size.

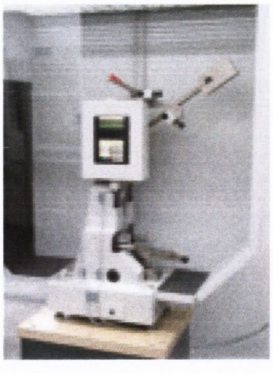

Figure 3.20. Zwick bench mounted Charpy impact tester, 50J machine.

The requirement for exact specimen dimensions i.e. 10mm x 10mm cross-sectional dimensions, with a tolerance of +/- 0.125mm was very difficult to adhere to due to the

hot pressing technique but more importantly the presence of diamonds which made it very difficult to remove flashing or grind down to exact size. An 'Air-swing' test was carried out to ensure that windage losses were at a minimum. Each specimen was struck perpendicular to the direction of pressing.

3.10.2. Instrumented 300J Charpy Impact Testing – DICoMM & CoMM Specimens

The instrumented Charpy impact test was used to determine the various energy contributions to the fracture process i.e. energy to yield, energy to max. load and energy to crack propagation [236]. However it was found when testing PM metals no differences exist when different impact velocities at fixed available energy levels were used [85].

The Instrumented 300J Charpy Impact testing was carried out at Instron's facility in High Wycombe, UK using a PW30 Charpy Pendulum Impact testing machine which can be seen in Figure 3.21. Tup energy of 300 joules with a velocity of 5.52m/s was used. Each specimen was struck perpendicular to the direction of pressing.

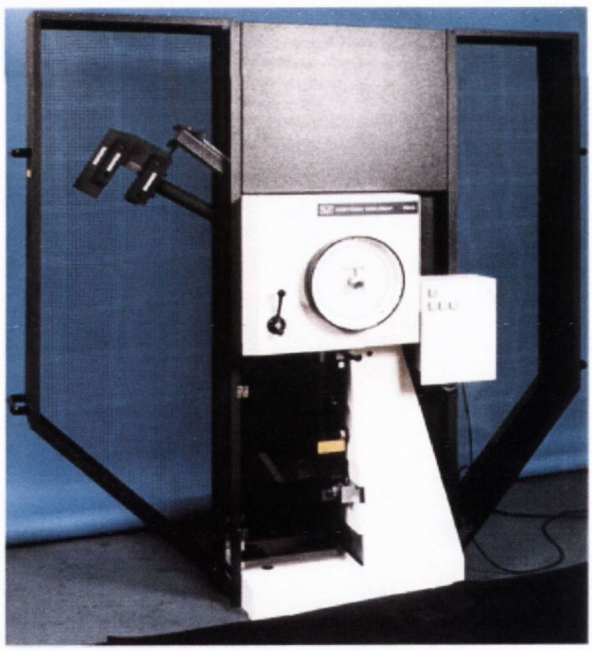

Figure 3.21. Instron Instrumented Charpy Machine PW30 pendulum.

All of the CoMM specimens were tested. However only a restricted number of the DICoMM specimens were tested using the instrumented Charpy. Only one specimen from each diamond US Mesh size and DC combination was tested. Instron was concerned that damage and excessive wear could result to the strain gauged anvil/striker

system due to the presence of diamond in the samples. The remainder of the DICoMM specimens were tested using the 50J Zwick bench mounted machine.

Other Charpy-type CoMM specimens had been hot pressed at 700^0C, 750^0C, 800^0C, 850^0C, 900^0C, 950^0C and 1000^0C were tested using the Instrumented 300J Charpy impact machine, where the different energy contributions to failure were recorded. However, the reporting of those results is outside the scope of this project.

3.11. Bend-Transverse Rupture Strength (TRS)

Transverse Rupture Strength (TRS) testing is a commonly used mechanical test using beam-type specimens, in three or four-point bending arrangement. The three point bend test is probably the most common for brittle and low ductile materials e.g. PM & PMMCs, or even green compacts to asses relative strength, with four point bend testing on the other hand more commonly used for assessing the strength of sintered ceramics. With these types of materials it is difficult to get meaningful results when using the standard tensile test and so TRS testing is carried out. The disadvantage with tensile testing is that the specimens break in the grips or fracture prematurely due to their inherent brittleness or more correctly low toughness. However, a major disadvantage of TRS testing is that an accurate value for Young's modulus and also yield strength is not achieved. With TRS testing one gets a flexural modulus and breaking stress at a specific span and bend arrangement. However, these mechanical properties cannot be used for satisfying the typical validating criteria required for fracture toughness testing or when using the compliance crack measurement technique in fatigue testing. Different specimen dimensions, test spans ranging from 28mm to 40mm, with varying crosshead speeds ranging from 0.1mm/min to 0.5mm/min are used. Even the type of bend test is all very important in comparing results but the recording of this is severely lacking in the literature [50, 167, 237].

The maximum load to break the specimen is quoted using many different terms including: 'flexural strength' (σ), 'bend strength' (σ_R), 'cross-breaking strength' or 'Modulus of Rupture' (MOR), or simply TRS. The MPIF Standard 41 [238] for TRS testing PM materials was consulted but was not adhered to because the test span and specimen specification related to a much smaller specimen than used in this project. The aim of this project was to use specimen dimensions similar to the size of segments used in typical diamond saw blades. Some researchers ensure that the shear stress effects are

reduced as low as possible by using a fully articulated 3PB fixture and that the thickness/span ratio gives a maximum shear stress of less than 1% of the max. tensile stress i.e. $\tau_{max} / \sigma_{max} = h/2L = 0.0063$ [239]. In this project the thickness/span ratio was 0.0063 for standard TRS, also a ratio of $b:h$ of 2:1 was used for TRS specimens which is considered to be optimum. In the MPIF Standard 41, the ratio was 0.125 which is the main reason that the standard was not adhered to. The ratio of the separation distance between the loading and support points (l) to depth (h) should at least be 4:1; the TRS specimens were 8:1. Rollers were 10mm diameter and free to rotate, which is considered ideal. Surface finish is most important because failure tends to occur from the surface, and particularly from the edges of the specimen. However, in this project it was very difficult to produce flat and even edges and a wide variation in results was expected which could not be overcome. The test results will generally depend on the size of the specimen being tested. Large specimens tested over wide spans will, on average, appear weaker than small ones tested over a narrow span. A number of factors can influence the TRS value being lower than expected because failure is expected to initiate from the surface, maximum stress e.g. failure from a defect within the test piece; away from the loading point in 3-pt bend.

At the time of four-point bend testing, there was no standard [240]. As TRS testing can be carried out using different methodologies e.g. 3-point-or 4-point bend, span length differences, it was decided to TRS test using both 3-point and 4-point bend set-ups in this project. Even though polishing and grinding is recommended for PM and PMMC materials, [151, 239], only flash removal was carried out in this project, the difficulties being previously explained.

3.11.1. TRS Three-Point Bend Testing - DIMM & CoMM Specimens

In carrying out the TRS testing, a new three-point bend fixture Mark I had to be designed and machined to be acceptable for testing small specimens; an external linear variable differential transducer (LVDT) was used to accurately measure the beam deflection, allowing the Flexural Modulus to be determined. The three-point bend fixture Mark I with the external LVDT in place can be seen in Figure 3.23. The three-point bend samples chosen by US Mesh size were 20/35, 30/45, 40/45, 50/60 & 70/80. All DCs with these US Mesh sizes were tested. As a variation, two different spans (40mm & 50mm) were used for the three-point bend testing. An Instron 8516

servohydraulic universal testing machine Figure 3.22, with interface software SERIES-IX [241] was used. A 10kN load cell with a strain rate of 0.5mm/min was used.

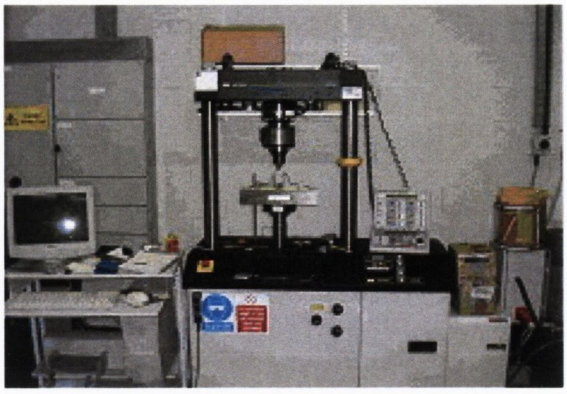

Figure 3.22. Instron 8516 Servohydraulic Universal Testing Machine.

The loading arrangement with external LVDT can be seen in Figure 3.23 with a specially designed safety rig and easy retrieval of broken specimen halves.

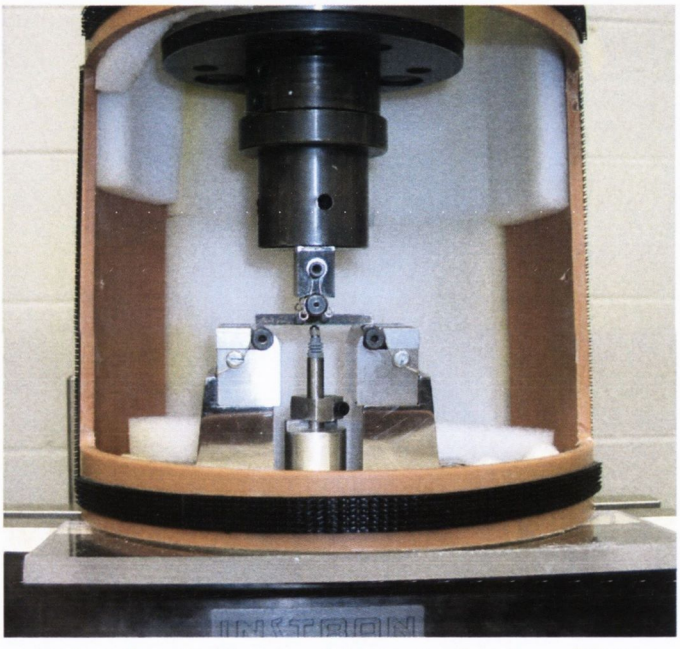

Figure 3.23. Three-Point Bend Fixture Mark I showing TRS specimen & LVDT extensometer. A safety cage also allowed the recovery of broken specimens.

Having measured the load to break the specimen, Modulus of Rupture (MOR) or simply TRS which is valid if no plasticity is detected in the bend test was calculated using the conventional formula, Equation 3.2, as found in the ASTM Standard B528-76:

$$TRS = \frac{3 \times P \times L}{2 \times t^2 \times w} \qquad (3.2.)$$

where P = break load (N), L = distance between the supporting rollers (mm),

t = thickness of the test specimen (Specimen Depth or Height) (mm),

w = width of the test specimen (mm).

3.11.2. TRS Four-Point Bend Testing - DIMM & CoMM Specimens

As already stated above, a plan to test a range of specimens with different US Mesh sizes (25/30, 35/40, 45/50, 60/70 & 80/100) and DCs using four-point bend was set-up. However, having carried out an initial number of tests, it was found that it was very difficult to get the upper rollers absolutely parallel with the lower fixed rollers. This resulted in specimens fracturing consistently at the upper left-hand roller. It was found that the left-hand roller was approximately 0.2mm lower than the corresponding right-hand one and so the increased the stress caused the specimen to fracture prematurely under this roller. Various methods were investigated e.g. shims but to no avail and it was decided to discontinue the four-point bend testing. So the vast majority of the hot pressed TRS specimens were tested using three point bend using either 40 or 50mm spans.

3.12. TRS Elastic Moduli Property Determination - DIMM & CoMM Specimens

Prior to carrying out TRS testing the specimens were firstly used for the determination of elastic moduli by using resonance where the natural frequency was measured. A number of samples were also tested using ultrasonics again for the determination of elastic moduli. However as already said previously, reporting these results is outside the scope of this project. Following the determination of elastic moduli, TRS testing was then carried out on the specimens.

3.13. Fracture Mechanics & Fracture Toughness

The whole area of fracture mechanics relates and allows the quantification of the relationships between material properties, stress level, the presence of crack producing flaws and crack propagation mechanisms. The following references are recommended for the reader for further background into fracture mechanics [242, 243, 244, 245, 246, 247, 248 & 249]. Briefly, in the '50s Irwin developed the Stress Intensity (K) approach to catastrophic failure, which states that fracture will occur when a critical stress distribution ahead of a crack tip is reached. This led to the development of Linear Elastic Fracture Mechanics (LEFM), which states that the form of the stress distribution around and close to the crack tip is always the same, and that the stress intensity factor, K, characterizes the intensity of the crack tip stress field. So the crack tip stresses can be described in terms of the remotely applied stress, the crack length and other geometrical features by the stress intensity factor, K. So when the remotely applied stress increases,

the value of stress intensity factor, K, also increases and reaches a critical value at which the crack becomes unstable. This critical value of stress intensity is called the materials Fracture Toughness (K_C) and it is a measure of the material's resistance to unstable cracking [250, 251]. Fracture toughness generally depends on geometric effects called constraint. As maximum constraint occurs under Plane Strain conditions, the fracture toughness varies with specimen thickness until the limiting conditions of maximum constraint are reached. So the measured value of fracture toughness under maximum constraint is called its Plane Strain Fracture Toughness or K_{IC} and under plane stress conditions it is just K_C. Plane Strain Fracture Toughness (K_{IC}) is the limiting value of K_C and is a material property.

A number of standard test methods for determining the critical stress intensity factors for metallic materials are readily available [252, 253, 254, 255, 256, 257, 258]. The ASTM E399-90 method as used in this project is for metals showing a very limited plastic zone with unstable crack growth [252].

3.13.1. Determination of Plane Strain Fracture Toughness (K_{IC}) & ASTM E-399-90

The ASTM E-399 standard will be briefly explained here. As the test procedure is complex, the reader is referred to the standard [252] or to a shortened version as pertaining to this project in Appendices 4 & 5 Fracture Toughness Test Procedure.

There are a number of aspects which are very important and must be followed strictly if one wants to successfully determine the Plane Strain Fracture Toughness (K_{IC}) of a material. These include specimen size and dimensions where a certain minimum value has been found [259] which ensure that plane strain conditions exist. This is achieved by having the specimen dimension B large (Figure 3.24) when compared to the plastic zone size, r_p, around the crack tip where any effect of the plastic zone on the stress intensity analysis can be neglected. Another factor is the correct determination of the fracture load (P_Q) which is used to calculate a preliminary value of fracture toughness called K_Q. Correctly determining P_Q is very important and a strict procedure has been laid down according to the ASTM E-399 standard using a 5% secant line to account for the plastic zone. To prevent the acceptance of a test record where excessive stable crack growth occurred, it is required that P_{max}/P_Q is less than 1.10. However, before K_Q can be considered as the material's Plane Strain fracture toughness (K_{IC}) other validity checks must be performed. For example, following fatigue precracking, the initial crack (a_i) tip

should be straight with a limited curvature and obliqueness, and also the plastic deformation at the crack tip should be limited ensuring that an atomically sharp crack existed. A very important check is to ensure that the specimen thickness B as can be seen in Figure 3.25, is sufficiently large in comparison with the plastic zone size to ensure plane strain testing conditions. ASTM standard requires the following relation to be satisfied.

$$a, B, \frac{W}{2} \geq 2.5\left[\frac{K_Q}{\sigma_{ys}}\right]^2 \qquad (3.3.)$$

where a = crack length,

B = specimen thickness,

W = specimen height or depth,

K_Q = the provisional fracture toughness,

σ_{ys} = the yield strength.

Following the validity checks, if K_Q meets these requirements then $K_Q = K_{IC}$, the Plane Strain Fracture Toughness. Where Plane Strain Fracture Toughness (K_{IC}) is deemed not to have been determined, a K_Q value is recorded; however, it is not an ASTM standard value.

There are four standard test specimen designs of which the Single Edge Notch Bend (SENB) is one that is used in this project as can be seen in Figure 3.24. The Table 3.5 shows the nominal dimensions for the SENB type specimen used.

Specimen Type	W	B	a_0	N	K	Span (4W)
SENB (SENB5)	10	5	2.0	1	10	40

Table 3.5. Dimensions of SENB Specimen showing the nominal dimensions in mm.

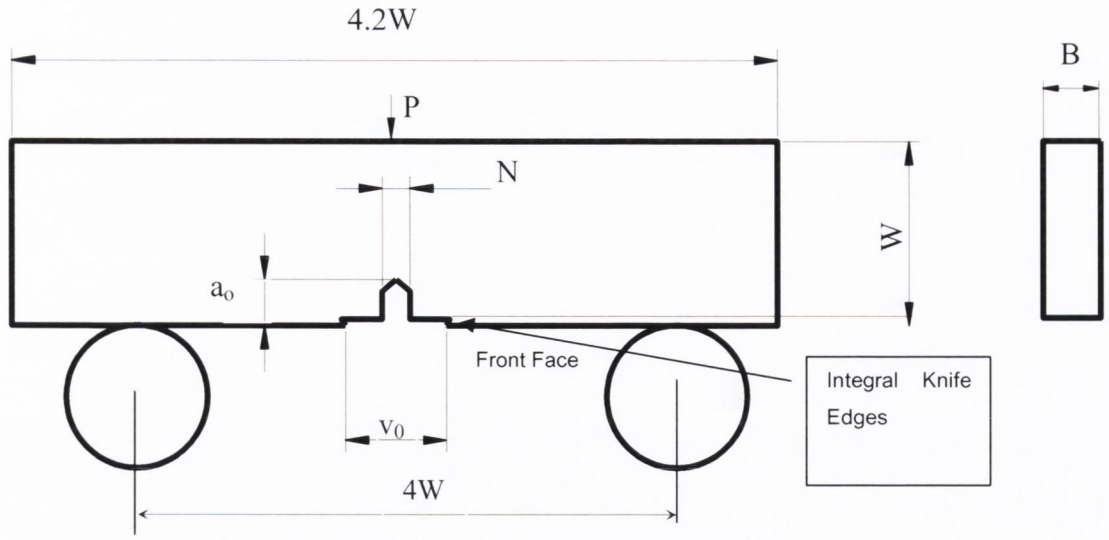

Figure 3.24. Basic outline of a SENB type specimen sitting on rollers.

Regarding the calculation of the initial value of Fracture Toughness (K_Q) from P_Q for the SENB specimen, Bakker used the 3-point bend stress intensity and compliance functions by Gross [260] and fit the K-values which are a function of the relative crack length, *a/w* using a polynomial proposed by Srawley [261, 262] which is now used in the ASTM Standard E399-90. This equation is as follows:

$$K = \frac{PS}{BW^{3/2}} f\left(a/W\right) \tag{3.4.}$$

where

$$f\left(a/W\right) = \frac{3\left(a/W\right)^{1/2}}{2\left(1+2a/W\right)\left(1-a/W\right)^{3/2}} \times \left[1.99 - \left(a/W\right)\left(1-a/W\right)\left(2.15 - 3.93\,a/W + 2.7\,a^2/W^2\right)\right] \tag{3.5.}$$

where P = fracture load (P_Q),

S = span, distance between the lower rollers, equal to $4W$,

B = specimen thickness,

W = specimen height or depth,

a = crack length.

Equation 3.4, is for the condition where $S/W = 4$.

Srawley's expression for the SENB type specimen covers the entire range of a/W, and is accurate to ±0.2% [260].

3.13.2. Fracture Toughness Testing – PM & PMMC Type Materials

Regarding fracture toughness testing of PM and PMMCs there are no proper standards available. It is stated that most PM data contains invalid results based on ASTM E399-90 [252] because it is based on fully dense materials [88] and that the porosity & microstructure of PM alloys make their fracture toughness very difficult to satisfy the validation criteria especially the specimen thickness and $P_{max}/P_Q<1.1$criterion, which pertains to limited plasticity requirements indicated by the amount of non-linearity which ASTM E399-90 implicitly assumes [91]. A major difficulty is the requirement for an atomically sharp crack which is normally carried out by fatigue precracking. Regarding PM and PMMCs, it is commented [98] that an atomically sharp crack is not necessary and also that results are no different whether a machined radius or fatigue precracked type notches are used [90] the ASTM E399-90 method is very sensitive to the level of obliqueness and curvature of the crack front, it has been found that for PMMCs the attainment of a sharp straight and perpendicular crack front is difficult [153].

3.13.3. Fracture Toughness Testing – DICoMM & CoMM Specimens

Following hot pressing the flashing on the fracture toughness specimens was cleaned off using a belt grinder. The specimens were then surface ground on the diamond impregnated side with an electroplated diamond wheel to ensure that the specimens were as close as possible to 10mm in height (W) as per the ASTM E399-90 standard. This also helped to reduce or minimise any errors when fatigue precracking due to the sensitivity of the compliance crack measurement method. The surface grinding procedure can be seen in Figure 3.25.

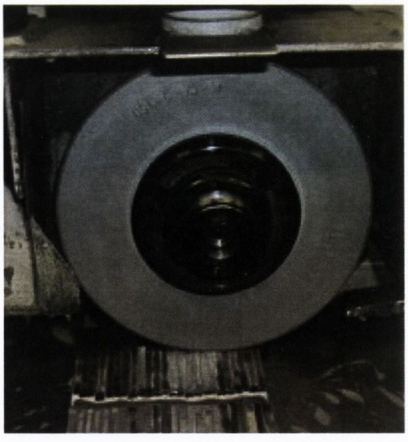

Figure 3.25. Surface grinding (electroplated diamond wheel) operation used to ensure correct dimensions regarding the height (W) for the fracture toughness specimens.

3.13.4. Fatigue Precracking Procedure

The ASTM E-399-90 [252] was followed as closely as possible but within reason due to the many material and specimen size limitations which were not apparent at the start of the fracture toughness investigation. Besides strain channel data acquisition faults, the need to design and build a crack mouth opening displacement gauge (CMOD) checking fixture, the purchase of a more sensitive load cell, with a 100kN to a 10, 5kN and a 1kN dynamic capability, fatigue precracking proved very difficult. A CMOD is a device for measuring the opening v_0 which is the distance between the integral knife edges where it is located as can be seen in Figure 3.24.

Firstly, the Mark I three-point bend fixture (Figure 3.23.) proved to be unsuitable because the CMOD gauge could not be accurately located consistently on the specimens. A new three-point bend fixture Mark II was designed and edm'ed from solid stock with integral bottom rollers with recesses to accommodate the CMOD gauge as can be seen in Figure 3.26. It also transpired that the standard CMOD gauge was not sensitive enough for fatigue crack length measurement on small specimens, so a new CMOD gauge with longer legs was purchased.

Regarding precracking, the ASTM standard [252] states that a fatigue crack initiates from the tip of a fatigue crack starter notch a_0 and grows a set distance into the specimen, whereby the condition $0.45 \leq a/W \leq 0.55$ is satisfied (Figure 3.24.). This new 'atomically sharp' crack called the precrack initiates fast fracture on fracture toughness testing. The crack length a_f is the length of the fatigue crack starter notch a_0 plus the precrack.

From the outset, fatigue crack length measurement proved the most difficult and challenging to achieve. Following this, it was found that some specimens fatigued whereas others just refused to grow any crack. This resulted in carrying out fracture toughness tests on both specimens which precracked successfully and others which did not grow any crack. These specimens had just an edm crack starter notch a_0 to initiate fast fracture, i.e. $a_f = a_0$. As mention above, it is cited that PM type materials do not require any precracking and so this could help investigate this claim [90, 98].

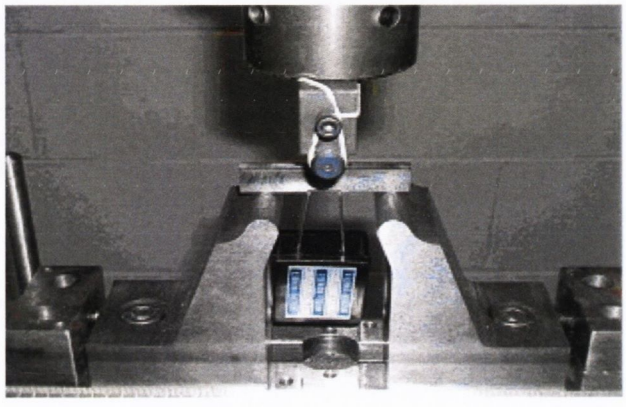

Figure 3.26. Mark II 3-point bend fixture with edm'ed recesses. A DICoMM specimen with CMOD gauge attached by integral knife edges can also be seen in the figure.

As already stated above, the precracking using fatigue proved the most difficult to measure accurately and necessitated the determination experimentally of what are called compliance coefficients which are used for crack length measurement. The next section 3.14.5 deals with the experimental determination of these coefficients.

3.13.5. Fatigue Crack Length Measurement – Compliance Method

Fatigue crack lengths can be measured directly or indirectly, the compliance method is an indirect technique. It has been proven to be an effective technique in a number of fracture specimens [263]. Compliance is the loss of stiffness of a component as a crack grows through it and measuring this loss of stiffness allows one to calculate crack length. An advantage of the compliance method is that it can be automated however using small specimens the compliance method posed a major challenge.

Compliance crack measurement uses strain gauges [264] of which the double cantilever crack tip gauge commonly called a COD gauge or more correctly a crack mouth opening displacement gauge (CMOD) is the most common [265]. A CMOD measures directly the crack mouth opening v_0 at the front-face, see Figure 3.24., and allows one to

calculate the compliance of the cracked specimen. A review of compliance values of different specimen types is given in [266]. There are two positions where one can measure compliance of specimens (a) load-line compliance and (b) crack-mouth or front-face compliance. For SENB type specimens, it is found that local deformations due to roller indentations cause uncertainties in load-line compliance that is avoided by using the front-face compliance [260]. Tada et al. used the results of Bakker [260] for the front-face compliance [267] to obtain the following fit for the compliance calculations of the SENB type specimen:

$$v_0 = \frac{4\sigma a}{E'} F_1(a/W) \tag{3.6.}$$

where,

v_0 = *crack..mouth..opening..displacement – CMOD..gauge*

$$F_1(a/W) = 0.76 - 2.28(a/W) + 3.87(a/W)^2 - 2.04(a/W)^3 + \frac{0.66}{(1-(a/W))^2} \tag{3.7.}$$

$$\sigma = \frac{6M}{BW^2} \tag{3.8.}$$

$$M = PS/4 \tag{3.9.}$$

where E = Young's modulus,

B = specimen thickness,

v_0 = crack mouth opening displacement, (CMOD)

P = load.

M = bending moment,

S = span.

Substituting Equations 3.7, 3.8, 3.9, into Equation 3.6, and simplifying the results, leads to Equation 3.10, which is a formula from which the normalised compliance can be determined:

$$\frac{E' v_0 B}{P} = 24\left[0.76(a/W) - 2.28(a/W)^2 + 3.87(a/W)^3 - 2.04(a/W)^4 + \frac{0.66(a/W)}{(1-(a/W))^2}\right]$$

for S/W = 4.0

(3.10.)

E' is Young's modulus adjusted for Plane Strain, $E(1-\nu)$.

The expression $E'v_0B/P$ is referred to as the normalised specimen compliance.

The above normalised specimen compliance $E'v_oB/P$ Equation 3.10 can only be used to calculate the normalised compliance from the normalised crack length a/W, however, in automated fatigue testing, compliance is measured directly rather than the crack length. So Jablonski et al. [263] transformed the normalised specimen compliance numerically to obtain a relationship giving crack length. Figure 3.27 shows graphically the transformation of compliance so that the ratio a/W can be found.

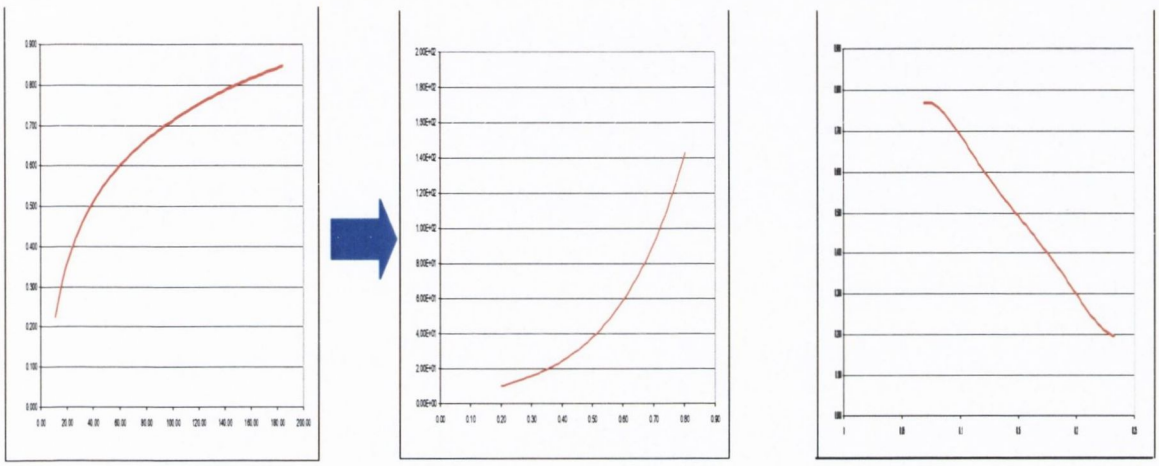

Compliance v a/W a/W v Compliance a/W v U

Figure 3. 27. Transposition of Compliance, 'a/W' ratio and U called a transfer function.

Saxena and Hudak [268] found a functional form to get a/W as a function of BEv_0/P for other specimens, e.g. CT. The transformation can be accomplished by defining a function, U_x which is a function of the normalised specimen compliance, as follows:

$$U_x = f(E'v_oB/P) \qquad (3.11.)$$

They then used the transfer function to fit a fifth order polynomial to obtain the best fit to satisfy the following expression:

$$a/W = C_0 + C_1U_x + C_2U_x^2 + C_3U_x^3 + C_4U_x^4 + C_5U_x^5 \qquad (3.12.)$$

In Equation 3.12, the coefficients are determined by a polynomial regression analysis [269]. Saxena and Hudak [270] found that the following function Equation 3.13 was the most appropriate

$$U_x = \frac{1}{\left(\frac{E'V_0B}{P}\right)^{1/2} + 1} \qquad (3.13.)$$

They obtained the best fit using this function for CT type specimen [269]. Jablonski et al. [263] used the same function for SENB and fitted the transfer function to a fifth polynomial to obtain the best fit expression as follows:

$$a/W = C_0 + C_1U_x + C_2U_x^2 + C_3U_x^3 + C_4U_x^4 + C_5U_x^5 \qquad (3.14.)$$

The coefficients in Table 3.6., were determined by Jablonski et al. [263] for the SENB specimen in three-point bending, with the measurement of the crack opening (v_o) at the front face.

C_0	C_1	C_2	C_3	C_4	C_5
0.994516	-3.6925	-1.70627	36.472	-106.443	125.51

Table 3.6. Jablonski et al. SENB Compliance Coefficients [263].

The ASTM E399-90 [252] standard gives a different set of coefficients, which are a truncated version of Anderson's [271] can be seen in Table 3.7.

C_0	C_1	C_2	C_3	C_4	C_5
0.9997	-3.95	2.982	-3.214	51.52	-113.0

Table 3.7. ASTM E399-90 SENB Compliance Coefficients [252].

Both sets of compliance coefficients, Jablonski et al. [263] and ASTM E399-90 have been proven to work. Instron with their FastTrack 1 da/dN software used Jablonski et al. [263] but changed in the upgrade FastTrack 2 Software suite, to the ASTM E399-90 [252] SENB compliance coefficients as the default. However, both were found not to work correctly leading to test failure due to compliance errors when using the small specimens in this project.

It is generally found that when the crack is short, with an a/W between 0.2 - 0.4 the compliance is less sensitive to changes in crack length than when the crack is longer, greater than an a/W of 0.5. The sensitivity of the compliance method is significantly improved for longer crack lengths because of the increased crack mouth opening and the resulting displacement gauge signal is larger. The sensitivity of this method is also a function of the location of the load line which is a reference point for crack extension

and the position of the displacement gauge as the location of the load line affects the crack mouth opening displacement. The farther away from the crack tip that the measurement can be made the more displacement occurs and the sensitivity of the method will be improved. This is the reason for having to change the CMOD in this project from a standard CMOD to a 'long-legged' CMOD gauge.

3.13.6. Compliance Coefficients Determination Protocol

As already stated above, whether using the ASTM E399-90 or the Jablonski et al. compliance coefficients large errors occurred in crack length measurement when precracking the DICoMM SENB specimens. These errors were large when using small starter crack lengths, i.e. a/W of 0.2. Errors of up 80% have been found when using either ASTM E399-90 or Jablonski coefficients for measuring crack growth when compared with actual crack lengths of DICoMM specimens. These errors were not as large when wrought SENB of same size as the DICoMM specimens were used. A protocol was developed whereby new compliance coefficients could be experimentally determined which would allow the accurate measurement of crack length is described as follows.

Two different sized SENB specimens were used, large (SENB10) and small (SENB5). The small SENB5 specimens were all nominally 10mm x 5mm x 55mm, which were similar to the project test specimens. The SENB10 specimens were 20mm x 10 mm x 84mm. Both specimens were made from wrought MS58 brass. All specimens had crack starter notches (a_0) edm'ed as per ASTM E399-90 standard (a/W =0.2). Figure 3.28 shows an SENB10 specimen with CMOD gauge attached in the Mark I type three-point bend fixture. This Mark I three-point bend fixture was not suitable for SENB5 specimens as already stated above and Mark II were used for these sized specimens.

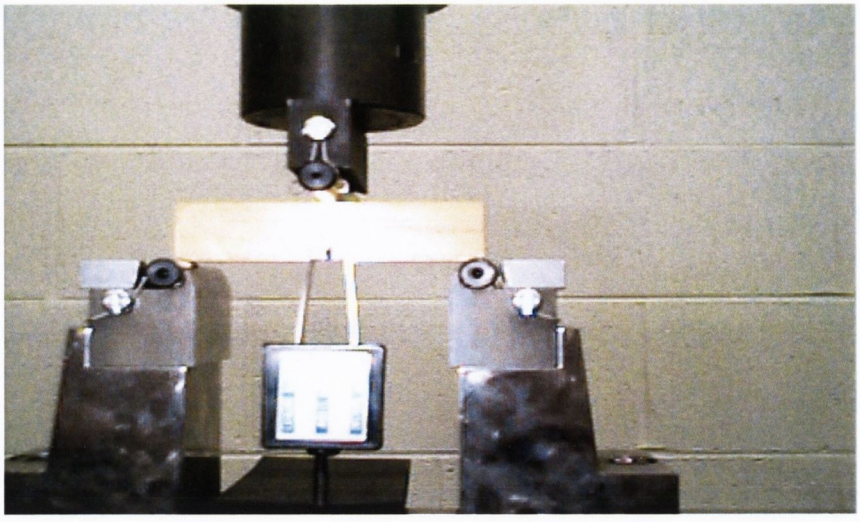

Figure 3.28. Specimen arrangement with the 3-point bend fixture Mark I, with a brass SENB10 specimen in place for compliance coeffficients determination.

A brief explanation of the well-known fatigue crack growth (da/dN) versus stress intensity (ΔK) graph which will help the reader understand the method will be given firstly. For more information on the da/dN fatigue graph the reader is referred to [244].

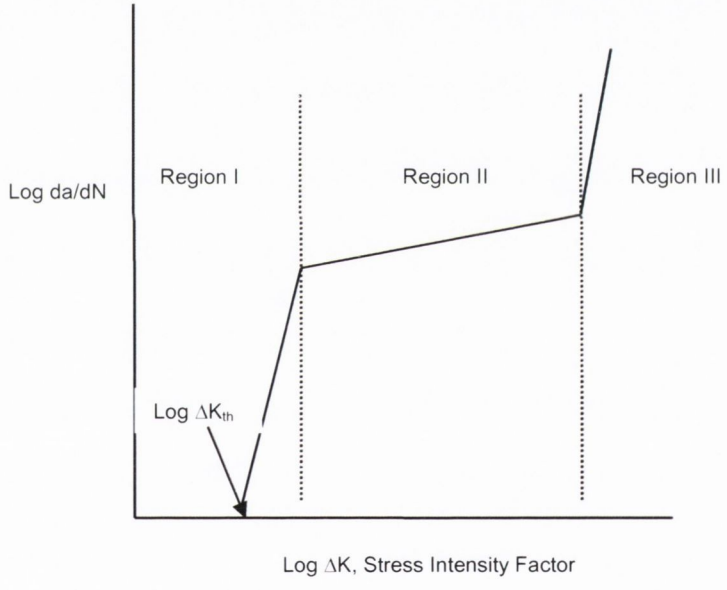

Figure 3.29. Schematic representation of fatigue crack growth, showing fatigue crack growth da/dN plotted against stress intensity factor range, ΔK, log/log scales.

From the da/dN graph in Figure 3.29 one can see three regions outlined on it. In Region I there is no crack growth or very slow crack growth with a da/dN of approximately 10^{-7} to 10^{-8} mm/cycle. Where the downwards sloping curve crosses the x-axis indicates the threshold stress intensity, ΔK_{th}. This is said to occur at 10^{-9} to 10^{-10} mm/cycle [273] and at this point the crack will not initiate. Region II or Crack Propagation stage is where the crack appears to propagate in a linear log-log relationship and this is where Paris' Crack

Growth Law applies [274]. Region III is where the crack propagates catastrophically to failure. Regions I & II are the areas which are used for compliance coefficients determination.

The experimental procedure for the determination of compliance coefficients was carried out in two stages, Stage I & II, as outlined in the flow diagram Figure 3.30. An Instron 8516 Servohydraulic Universal Testing machine as seen in Figure 3.22 with a 10kN dynamic load cell or dynacell was used. The fatigue testing was carried out at 20Hz with an R = 0.1. The machine was computer controlled using INSTRON proprietary fatigue software called FastTrack 2 Software Fatigue Crack Propagation da/dN [275] using the compliance method. Initially, ASTM E399-90 default compliance coefficients were used for the fatigue crack propagation for the SENB10 specimens. Raw data was logged at intervals of 0.001mm of crack growth. Stage I is conducted in Region II and is called precracking. This was carried out using a decreasing ΔK testing scenario because the value of ΔK_{th} for the SENB10 brass specimens was required for Stage II. As each test was run, it was monitored to ensure that the required crack length (a/W) was achieved for each specimen. A number of SENB10 specimens were precracked to different a/W values ranging from, 0.2 up to 0.8 a/W, in increments of 0.1. Note it is not important that the crack length according to the da/dN software is reading accurately, as the actual crack length will be physically measured.

Stage II was the determination of the normalised elastic compliance ($E'v_oB/P$) for each specimen with a different crack length (a/W). This was carried out under constant load control in Region I of the crack growth curve just below ΔK_{th} which ensured that a crack didn't grow. A fixed number of fatigue cycles (5000) were run with data logging every 100 cycles which allowed the normalised compliance ($E'v_oB/P$), to be accurately measured for each SENB10 specimen with a different a/W.

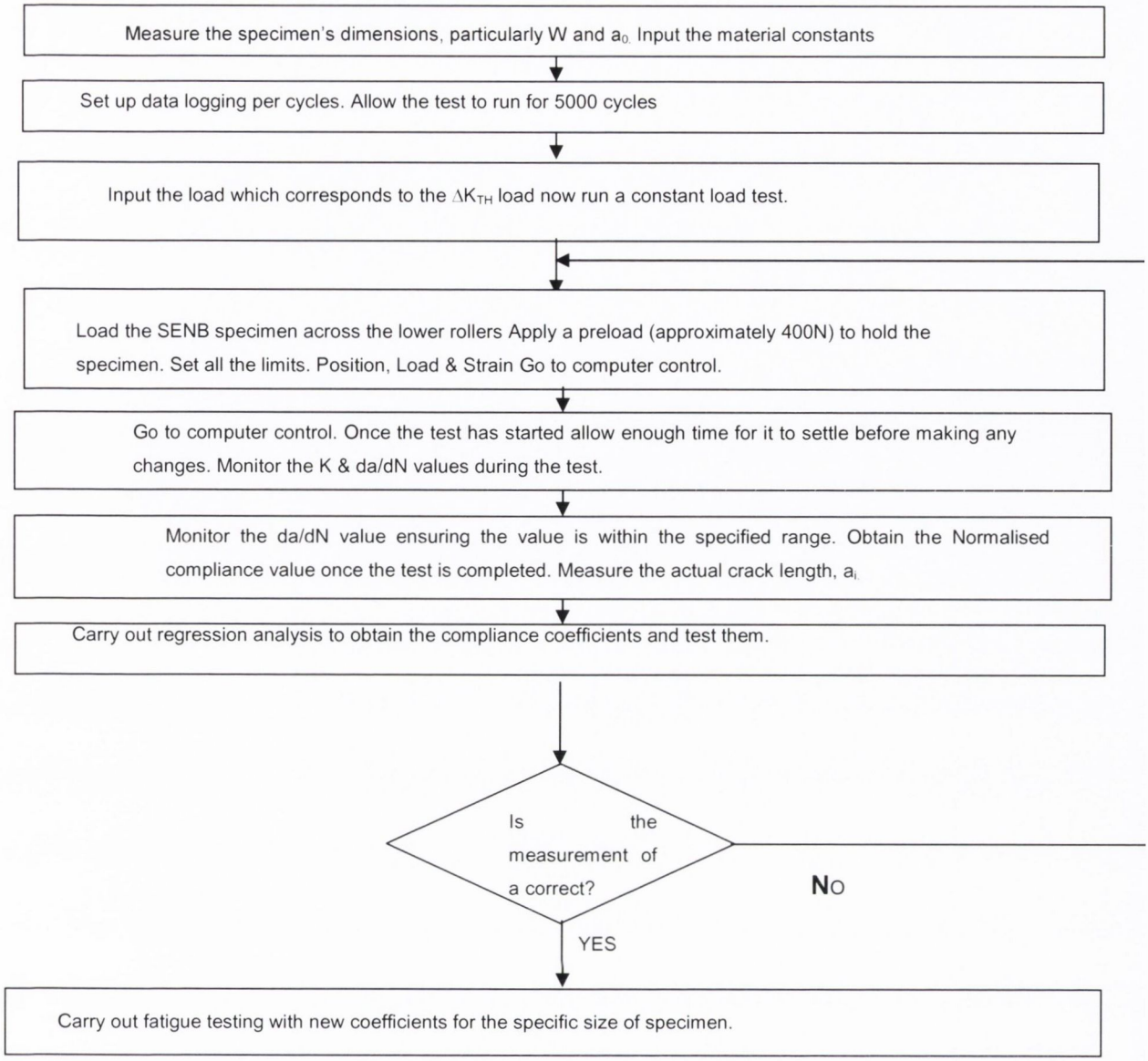

Figure 3.30. Normalised Compliance / a/W Relationship Determination Flow Diagram.

Following this each SENB10 specimen was broken and the fatigue crack was accurately measured using an Optical Profile Projector (OPP) as can be seen in Figure 3.31. The specimens were then measured according to ASTM E1820-99a. This involves measuring the crack length in 9 equally spaced divisions about the centre of the specimen. An average is then taken of these readings and added to the fatigue crack starter notch length (a_0).

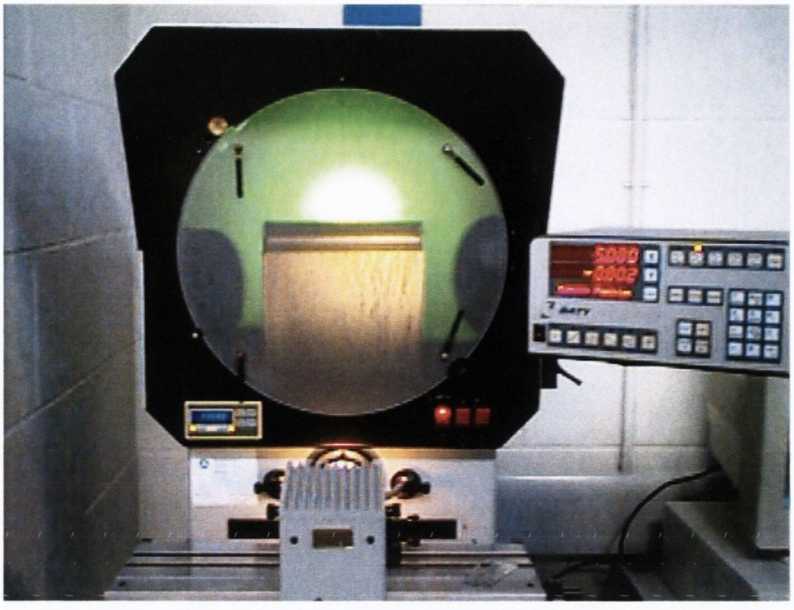

Figure 3.31. Optical Profile Projector (OPP) showing the fracture surface of a wrought brass SENB10 specimen used in Compliance Coefficient Determination.

The recorded normalised compliance values for the SENB10 specimens and the accurately measured normalised crack lengths a/W's are plotted. From which using regression analysis the compliance coefficients can be determined using a 5^{th} order polynomial as per the method developed by Jablonski et al. [263]. The SENB brass specimens showing the different fatigue cracks for compliance coefficient determination can be seen in Figure 3.32.

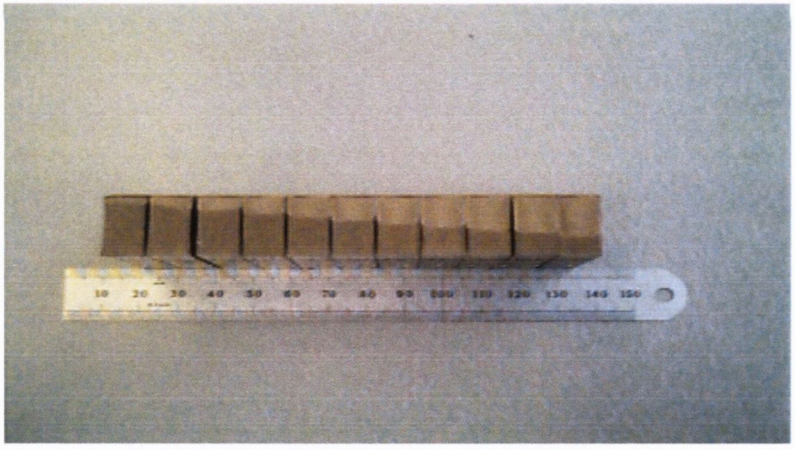

Figure 3.32. Brass SENB specimens with different fatigue cracks grown used for compliance coefficients determination.

The new SENB10 compliance coefficients were used by repeating the protocol using SENB5 sized specimens and again rerunning the protocol again for improved accuracy. This was repeated a number of times using SENB5 specimens until a satisfactory fatigue crack length could be reliably obtained. The final compliance coefficients were then used for normal precracking of the DICoMM specimens for subsequent fracture toughness testing. The new coefficients will be reported in the Chapter Three, Results.

3.13.7. Fracture Toughness Testing & DICoMMs – Precrack & FastTrack 2

As explained above, due to the large number of specimens the precracking by fatigue of all of them was going to take an inordinate amount of time. So the fracture toughness specimens were divided into two groups, one half of the SENB specimens were precracked by fatigue and the other half of SENB specimens were tested with just the edm starter crack notch present. The edm starter crack notch used for both test methods was nominally 2mm. The fatigue precracked set were tested using Instron FastTrack 2 Crack Propagation da/dN software and the other set using just the nominal edm starter crack notch were tested using Instron SERIES-IX software.

So one set of specimens were precracked using FastTrack 2 Software Fatigue Crack Propagation da/dN [275] to $0.45 \leq a/W \leq 0.55$ using a 10kN dynamic load cell and decreasing ΔK testing environment. This was then followed by setting the Instron servo-hydraulic universal test machine to automatically switch to FastTrack 2 Software Fracture Toughness [276] where the SENB specimens were broken under fracture toughness methodology as per the ASTM E399-90 standard (Figure 3.33.).

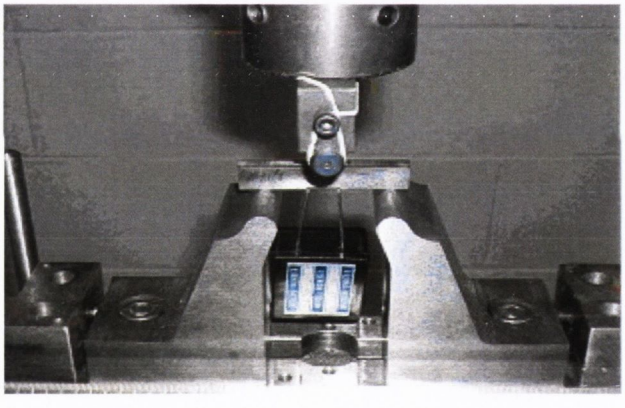

Figure 3.33. SENB specimen on Mark II 3-Pt bend fixture with attached CMOD ready for testing.

As can be seen in Figure 3.33, the CMOD gauge attached to the SENB specimens was used to measure the 'opening' or v. The displacement v value is plotted against the load to failure, so giving the characteristic Load-Displacement graph whereby the load P_Q, as well as the other ASTM fracture toughness test criteria is determined.

Figure 3.34 shows one of the SENB precracked specimens and subsequently fractured showing the edm fatigue crack starter notch a_0, the fatigue precrack followed by fast fracture. The precrack in Figure 3.34 was measured accurately according to the ASTM

E399-90 standard using Optical Profile Projector (OPP) as seen in Figure 3.31. The fatigue precrack crack lengths are measured differently using ASTM E399-90, where the crack is measured at the outer surfaces called surfaces 1 & 2, and then at 25%, 50% and 75%, where the 50% is at the centre of the specimen. An average is then taken of these readings which are added to the fatigue crack starter notch a_0 to give the final crack length a_f. This value is then used to calculate K_Q as previously mentioned using Equation 3.14.

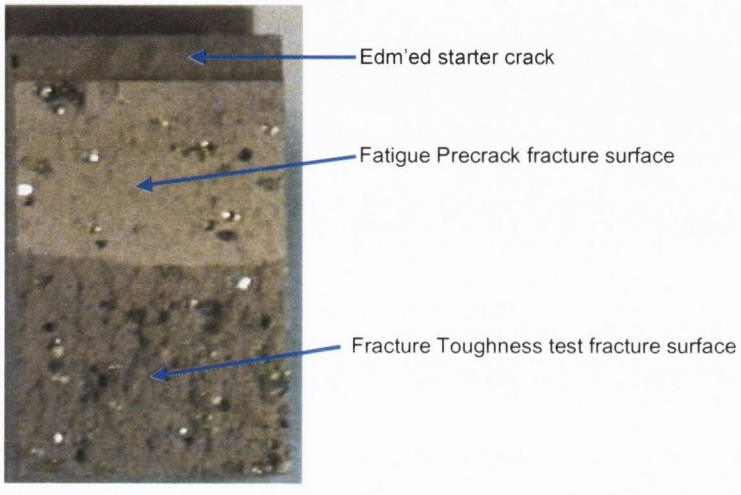

Figure 3.34. Photomacrograph showing edm crack starter notch, fatigue precrack and finally the darker grey fast fracture surface following fracture toughness test of a DICoMM specimen.

Following this, the necessary validity checks were performed automatically by the FastTrack 2 Fracture Toughness software [276], which then indicated if the specimen result was K_{IC} or just K_C.

Some specimens after a period of fatigue precracking failed to grow any crack, even the intervention of increasing the ΔK proved of no avail. These specimens were tested using the FastTrack 2 Fracture Toughness software [276] even though they had not got the required crack length. A fracture toughness value was calculated and recorded, but they automatically failed the validity checks.

3.13.8. Fracture Toughness Testing & DICoMMs – No-Precrack & SERIES-IX

The second half of the set of SENB DICoMM specimens which just had an edm starter crack notch (a_0) were tested in three-point bend using Instron SERIES-IX software. In this test configuration no CMOD gauge is used. As detailed in section 3.14.7 above, the output from the fracture toughness test is the 'Load-Displacement' curve and since the SERIES-IX specimens do not have a CMOD gauge cannot be attached a different

method is used to determine the 'Displacement'. The machine actuator measures the deflection Δ between the rollers which is taken as the 'Displacement' along with the measured load yields the 'Load-Displacement' curve. The fracture load P_Q is determined as normal, with a_0 as the crack length and with the other necessary specimen dimensions equations 3.14 and 3.15 were used to calculate a K_Q. Carrying out a fracture toughness test without a CMOD gauge has been investigated before by [100] and found to work satisfactorily. Following this the normal validity checks were performed by SERIES-IX software to determine if the resultant K_Q was a valid K_{IC} result if one ignores the incorrect a/W used. However, it is acknowledged that since precracking had not been carried out this part of the ASTM E399-90 standard was violated, however the results found were interesting.

Figure 3.35 shows a SENB DICoMM specimen with just an edm starter crack notch a_0. As a note, one can see that at times it was difficult to edm a starter crack notch a_0 due to the presence of diamond having been present in the backing layer.

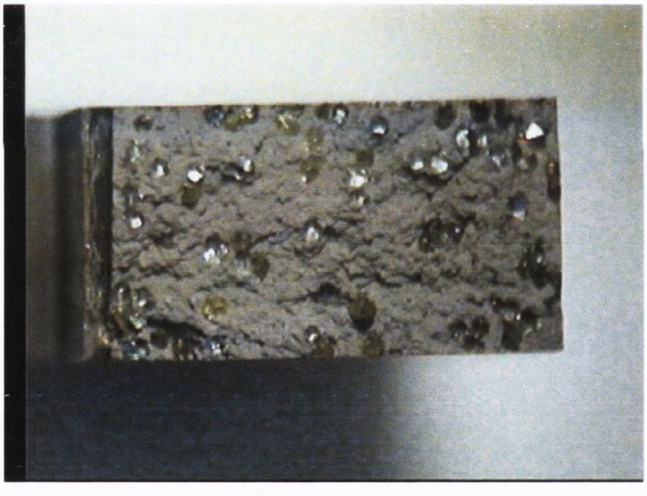

Figure 3.35. Showing a typical DICoMM specimen which was fracture toughness tested with just the edm starter crack notch (a_0) using SERIES-IX software.

It is important to note that other researchers have used this method in determining a fracture toughness result on PMMCs [167].

3.14. Erosion Wear Test Procedure

The aim of this investigation was to reproduce the typical wear experienced by a diamond impregnated metal matrix tool, e.g. a saw blade, when used in a 'dry-cutting' mode i.e. no water as coolant. A shot blasting method was used to try to mimic this

environment. The shot blasting cabinet used in this study was a Clarke Abrasive Shot blaster SB9006 (Figure 3.36). It works on the induction siphon method. The abrasive (aluminium oxide) is expelled under pressure from a nozzle that operates on the venturi principle. Compressed air is fed through a regulator into the nozzle and picks up the abrasive. The compressed air and abrasive mixture is then blasted onto the surface of the test piece. Both the pressure (bar) and the angle of incidence θ of the airflow can be adjusted.

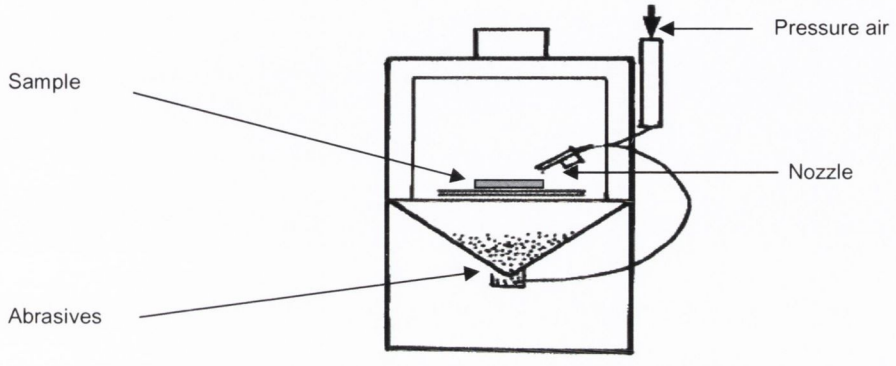

Figure 3. 36. 'Clarke' Siphons Hand Cabinet – modified for Erosion Wear Testing.

Previously tested Charpy DICoMM specimens were used for the erosion testing. The specimens had DCs of DC10 & DC30 with US Mesh sizes of 30/35, 40/45 & 60/70 for each DC and were hot pressed at 800°C. The abradant was an angular alumina 80-120μm with a mean of 100μm. Prior to the actual erosion testing an 'opening' stage was carried out. This prepared the surface of the sample and is similar to that normally carried out when a new diamond saw blade is 'opened' where 'ready-to-cut' diamonds are exposed. If this was not done inaccurate erosion data would have been obtained due to the excessive metal layer on the surface of the samples.

The erosion test variables used were pressure (bar) and angle of incidence θ (degrees). A combination of fixed pressures (P) and angles θ were used as follows: P3bar/15°, P4bar/25°, P5bar/35° and P6bar/45°. For each sample of diamond size and concentration a fixed pressure and angle combination was used. Each sample was subjected to an erosion test of 5 minutes duration, with each erosion test repeated on the same sample three times, giving a total test time of 15 minutes. For each combination of pressure and angle a new sample was used. This was to ensure that no previous erosion test conditions could interfere with the results of new test. As an example Table 3.8 shows the test layout for a 30/35 DC10. This was repeated for the other diamond sizes and concentrations, giving a total of 24 samples used.

Dia. Conc.	US Mesh Size	Sample Number	Pressure (Bar)	Angle (Deg.)
DC10	30/35	51/1	3	15
DC10	30/35	51/2	4	25
DC10	30/35	51/3	5	35
DC10	30/35	51/4	6	45

Table 3.8. The test procedure showing the DC and US Mesh size specimens with the Pressures and Angles.

After each erosion test, weight loss measurements were taken, as well as Vickers microhardness measurements. All diamond sizes and concentrations were tested with the same combination of pressures and angles as described above.

3.15. Determination of Experimental DC - Image Analysis – Scentis Software

Scentis [277] was the image analysis software used in the DC measurement of the FT and TRS specimens. Scentis was developed and trademarked by Mediacybernetics and supplied by Struers Ltd.

The first step in the analysis was the capturing of the fracture surface image using a Meiji stereo zoom microscope using a video link, as can be seen in Figure 3.37 Correct lighting was the most important issue so that a good image was obtained.

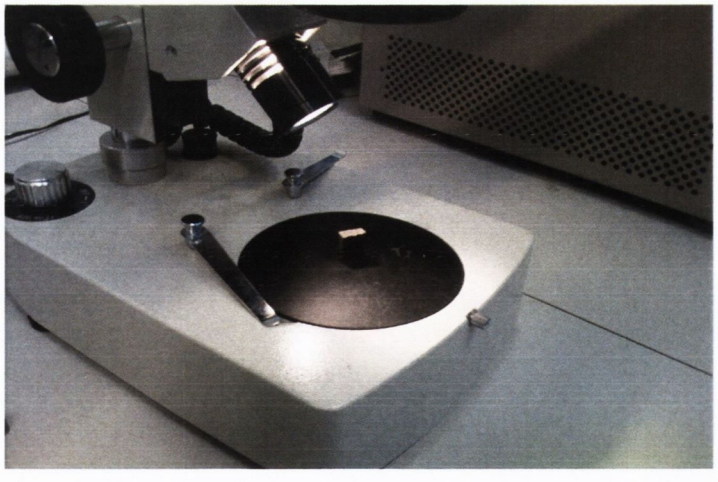

Figure 3.37. Typical DIMM Specimen placed on stereo zoom microscope for image capture.

The captured image was then downloaded into Scentis for processing and analysis which can be seen in Figure 3.38 below.

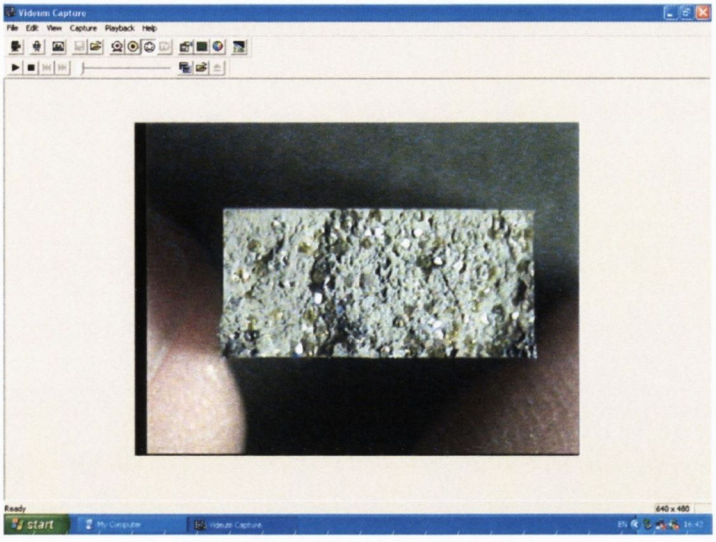

Figure 3.38. Image Capture of the typical specimen, Example Run 86/3.

The next step of the image analysis process involved importing each of the captured images into the Scentis image analysis software. The software was initialised and each individual specimen image was processed as can be seen in Figure 3.39 below.

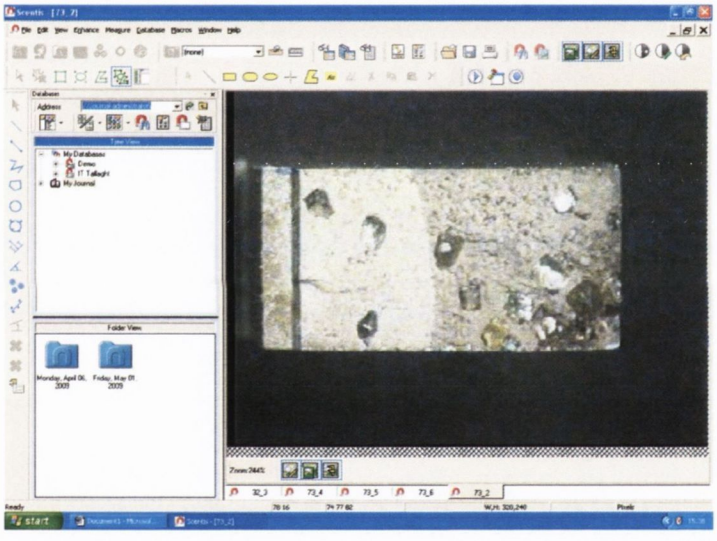

Figure 3.39. Imported Specimen Image in Scentis Program, Run 73/2, 20/25, DC40.

It can be seen from the image that this specific specimen has undergone a 2mm EDM (on backing layer), and was then pre-fatigued a further 3mm. In order to carry out a percent area measurement of the specimen, the "Percent Area" application was launched within the software. This can be seen in Figure 3.40 below.

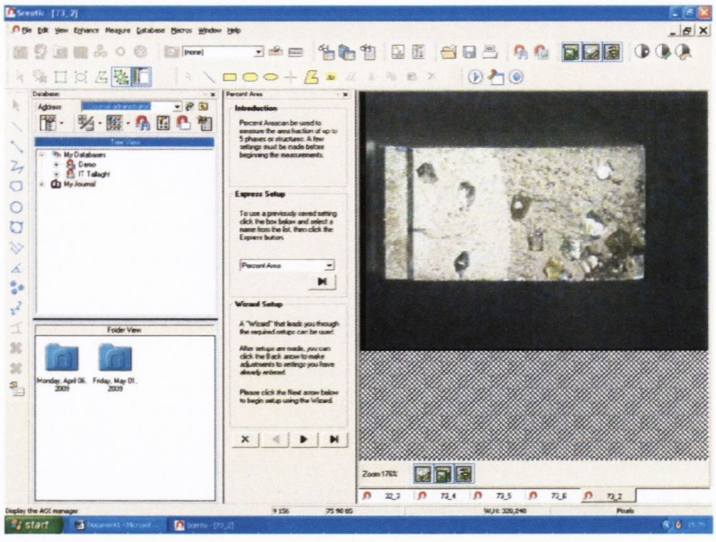

Figure 3.40. Percent Area Application launched in Scentis Program.

In order to carry out the measurement, the software requested that the author define the 'Area-of-Interest' (AOI). This was achieved by creating a boundary around the fracture surface, ensuring that as much of the fracture surface was selected as possible. Some of the specimens required a compromise of the fracture surface selection, as the fatigued crack did not grow at the same rate throughout the specimen. This can be seen in Figure 3.41.

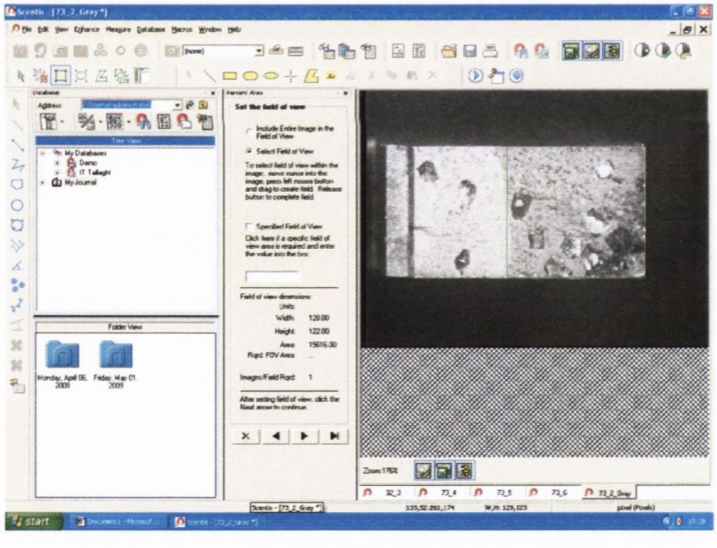

Figure 3.41. AOI Selection shown within the green border outline in figure.

The next step of the process required that the author define the number of phases present within the AOI. Every specimen contained 3 phases which were as follows:

Phase 1 – Diamonds (Dark) & Pullouts (Dark)

Phase 2 – Cobalt Metallic Surface (Light)

Phase 3 – Diamond Blooming (Light).

Diamond blooming is where the light shining on the diamond is totally reflected back which makes the diamond appear white as can be seen in Figure 3.41. The defining of the number of these phases can be seen in Figure 3.42.

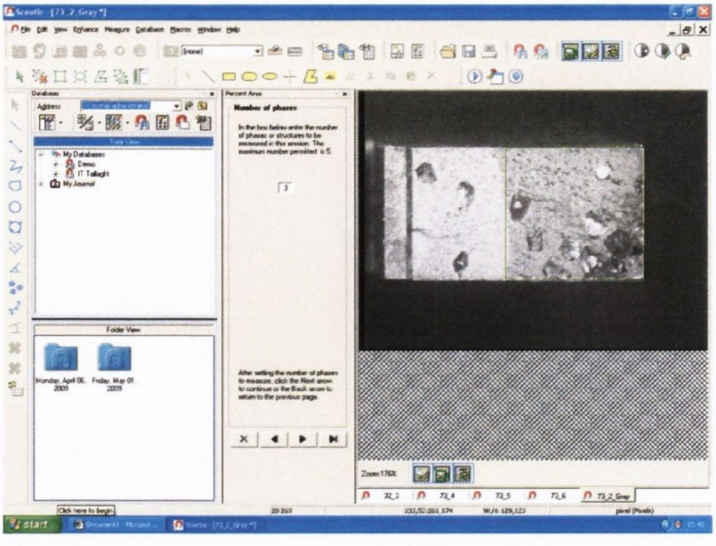

Figure 3.42. Defining Number of Phases within the green bordered AOI.

Each phase was then required to be defined in terms of the intensity of the light on the fracture surface. Firstly, Phase 1 was defined by the author as the darkest parts of the fracture surface. This was generally the dark diamonds, and the pullouts on the fracture surface. On some occasions, the metallic surface contained dark sections which were neither diamond nor pullout which needed to be filtered from the defining process. This can be seen in Figure 3.43 below.

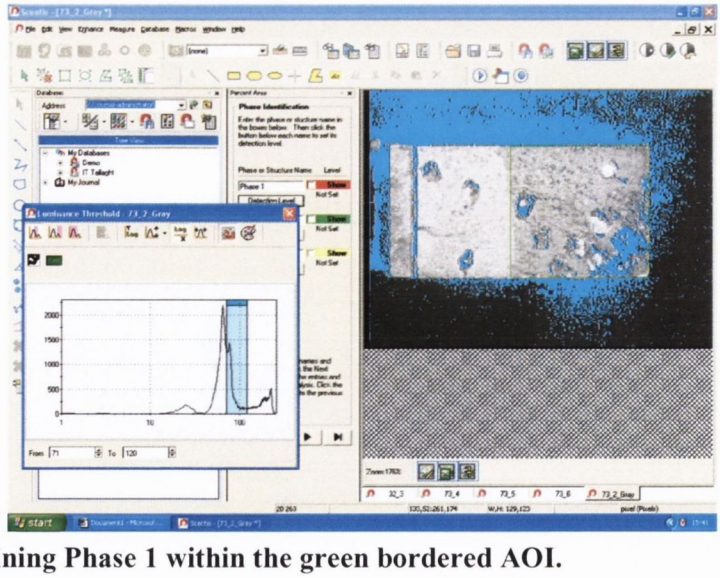

Figure 3.43. Defining Phase 1 within the green bordered AOI.

Once the phase was defined, the author could then choose a colour to represent the selection of that phase. This is highlighted by the "Red" colour Figure 3.44.

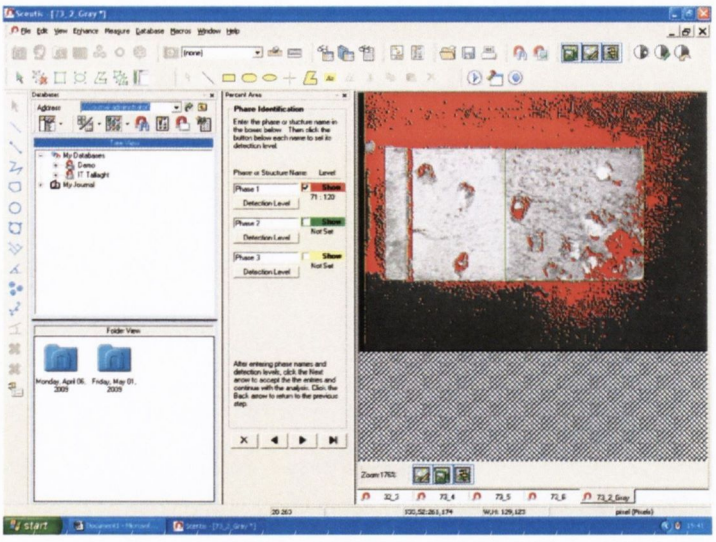

Figure 3.44. Assigning Individual Colour to Phase 1 within the green bordered AOI.

Phase 2 was defined as the cobalt metallic surface of the fracture surface. This was done by selecting the lighter portion of the surface, ensuring that the previously selected phase 1 was filtered out. Again, this phase was given an individual colour (Green) and can be seen in Figure 3.45 and Figure 3.46 below.

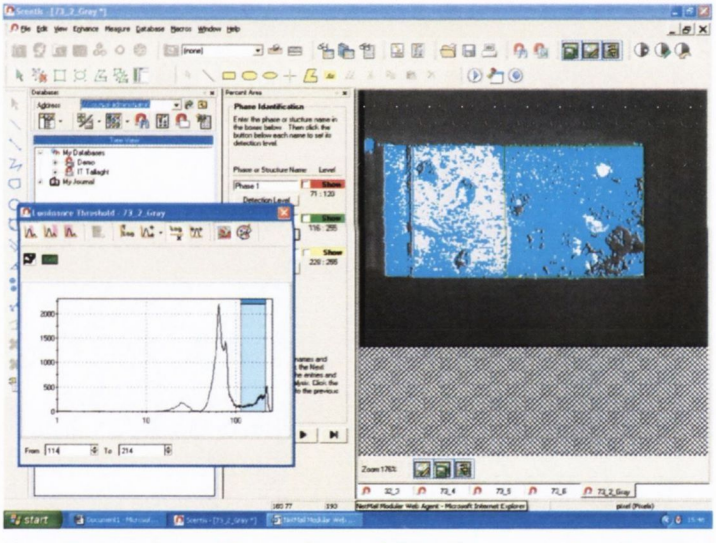

Figure 3.45. Defining Cobalt Metallic surface within the green bordered AOI.

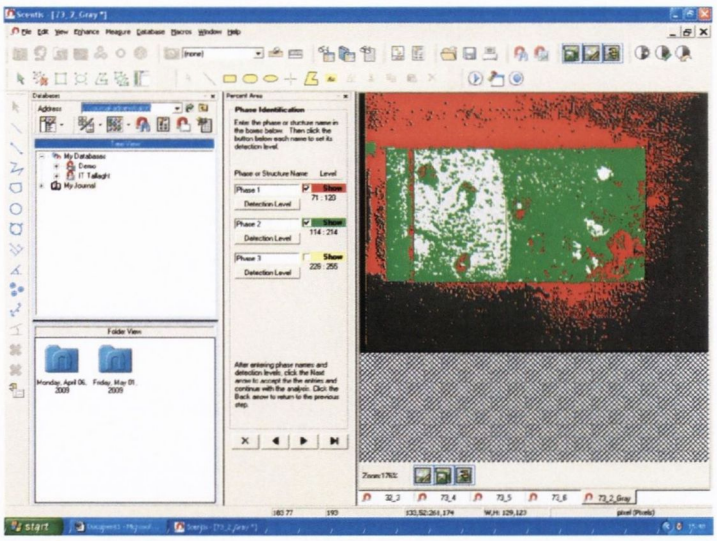

Figure 3.46. Assigning Individual Colour to Phase 2 within the green bordered AOI.

Finally, the third phase required definition and was carried out by selecting the brightest parts of the fracture surface. This was achieved by selecting the diamond blooming portions of the fracture surface, and filtering out the previously defined Phase 1 & 2.

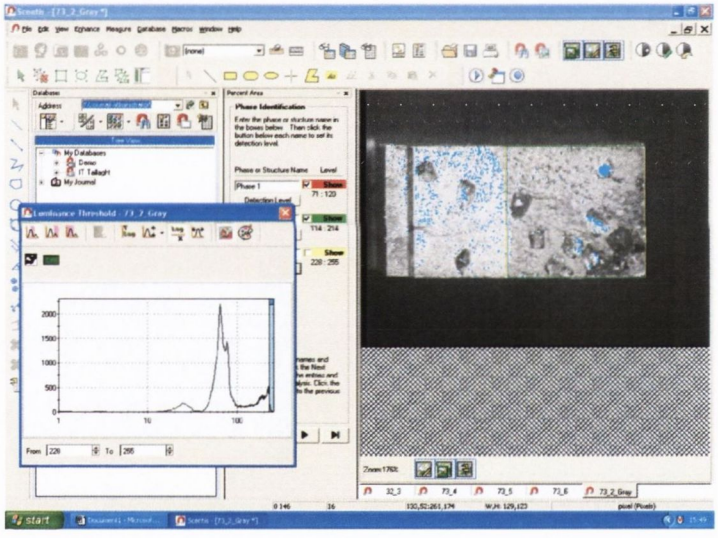

Figure 3.47. Defining Diamond Blooming within the green bordered AOI.

This phase was also assigned an individual colour (Yellow), at which point each phase could be observed within the AOI. This can be seen in Figure 3.48.

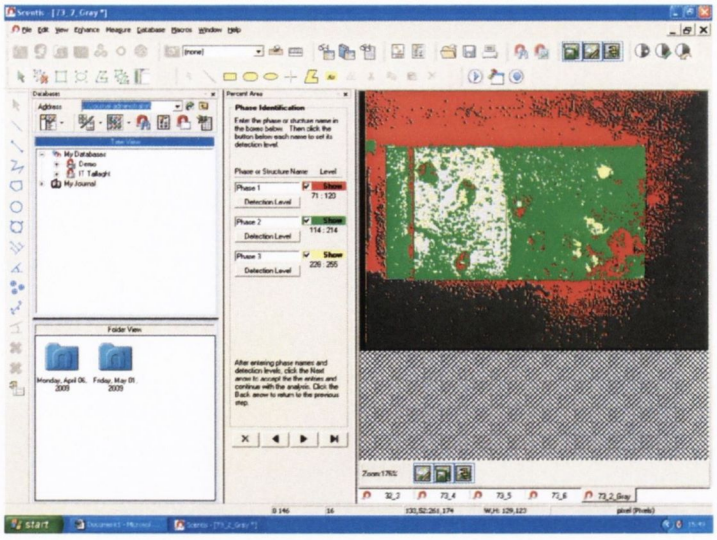

Figure 3.48. Phase 1, 2, and 3 defined within the green bordered AOI.

After each of the phases had been defined, the software was then ready to carry out the percentage measurement. This was simply done by selecting the "Measure" key, and can be seen in Figure 3.49 below.

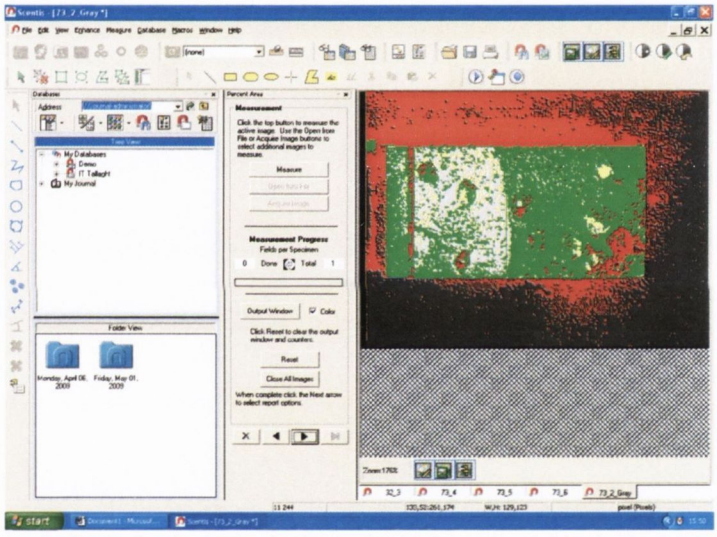

Figure 3.49. Selecting Measure Icon.

The calculation for the percent area measurement was carried out by the software in approximately 2 seconds. The software then produced an output window, highlighting the percentages of the area for each of the 3 phases as can be seen in Figure 3.50.

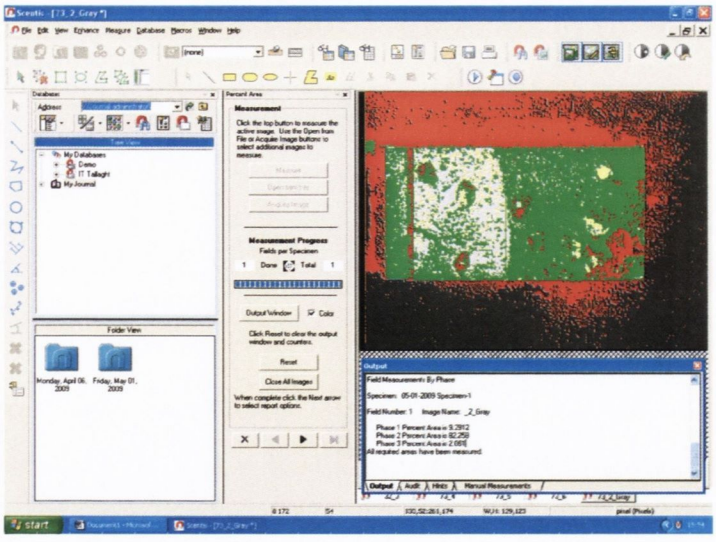

Figure 3.50. Output Table of Phase Percentages.

In the interest of clarity, Figure 3.51 below highlights the output window from the programme. This image shows each of the calculated phase percentages.

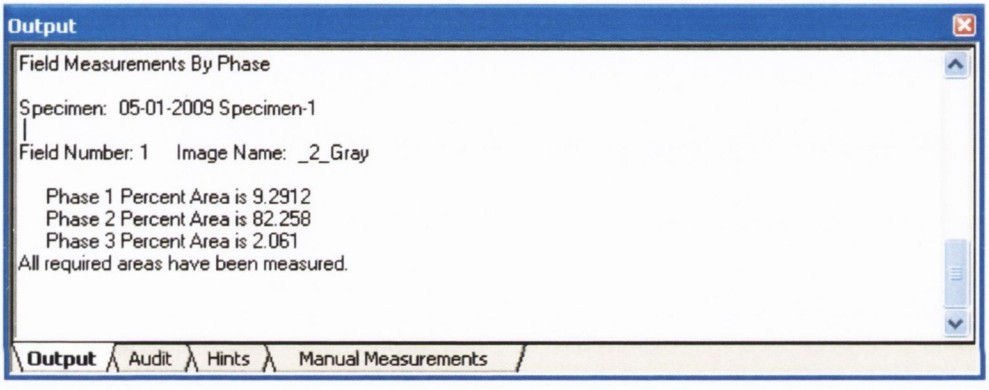

Figure 3.51. Output Window in the Scentis Software.

In relation to the DC, the phases of interest were Phase 1 & 3, which were then added to give the total percentage of diamond on the fracture surface. This total was found to be 11.35% for specimen 73_2. As the nominal value of the DC was 40 (10%), this indicates that the measurement was accurate.

Regarding the TRS specimens exactly the same procedure was carried out to determine the experimental DC.

Series-IX specimens, the entire cross section of the specimen was selected. The reason for this was because the TRS specimens did not have an EDM, or a backing layer. This can be seen in Figure 3.52.

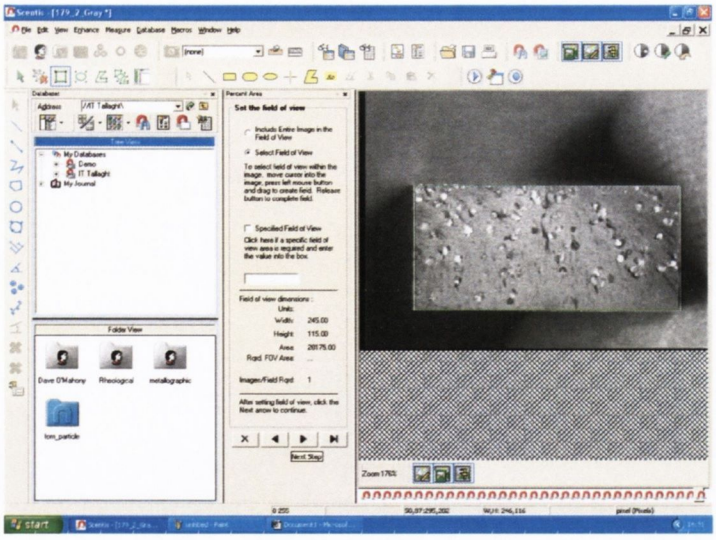

Figure 3.52. Selection of the Entire Specimen Surface (AOI), TRS Run#179/2, 45/50, DC30.

The 3 phases were again defined, and the measurement carried out. The TRS specimen in Figure 3.53 was Run#179/2, 45/50 US Mesh size with a nominal DC30 or 7.5%Vol%, however the experimentally determined indicates that it is 6.8Vol%. This can be seen in Figure 3.53 below by combining Phase 1 and Phase 3 in the analysis routine.

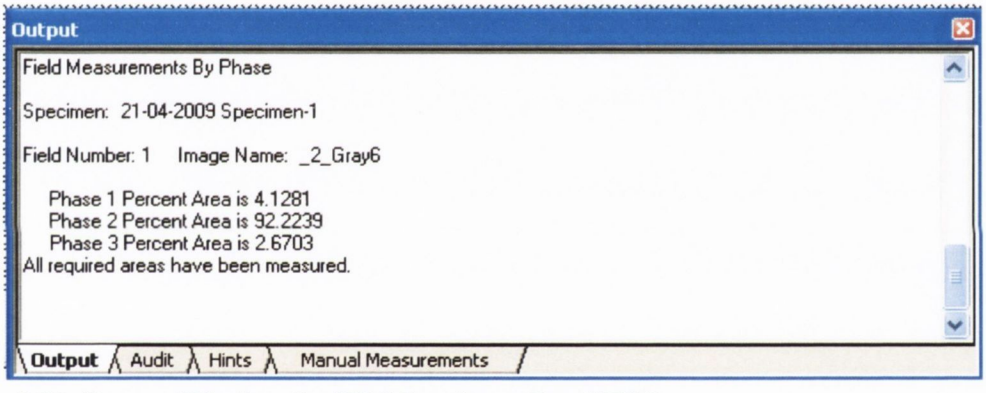

Figure 3.53. Output Window for TRS Specimen Run#179/2.

CHAPTER FOUR: RESULTS

4.1. Introduction

This chapter will outline the results obtained and will briefly explain any difficulties encountered. Due to the large number of variables and tests carried out the results reported in the chapter will in general be average results. However, where the author feels it more appropriate and for better clarity, individual results will be given. Other results will be given in Appendices where necessary. Preliminary test results dealing with the manufacture of the specimens will be also given.

The results reported in this chapter will cover firstly, the compliance coefficients determined for the fatigue precracking for the fracture toughness specimen preparations. Following this, the percent theoretical density (%TD) and hardness results for each type of specimen will be given. This is then followed by the main results for each specimen type e.g. Charpy. Fractographic results will be presented as each specimen type is dealt with where necessary. Erosion wear results will then follow including SEM fractographic evidence. Finally, any remaining fractographic SEM images for the different specimen types will be given which will aid understanding the results and following analysis.

Because of the large amounts of data to be reported, different types of graphical representations will be used to aid the reader grasp the results. Even though a DC1 does not make sense from an industrial point of view, it was felt by the author that the addition of a very small amount of diamond to the cobalt matrix might indicate the initial effect of the addition of diamond. The results indicate that it does add significantly to the understanding of the diamond impregnated cobalt metal matrix materials.

4.2. Compliance Coefficients Results

The compliance coefficients for the SENB10 brass specimens were determined using the standard ASTM E399 coefficients and the new coefficients can be seen in Table 4.1. As already said in Chapter 3, Experimental Procedures, Section 3.14.6, these SENB10 compliance coefficients were used to develop compliance coefficients for the smaller SENB5 brass specimens which were identical dimensionally to DICoMM specimens.

C0	C1	C2	C3	C4	C5
0.577	7.4842	-112.51	564.0	-1302.2	1112.6

Table 4.1. Compliance Coefficients determined using SENB10 brass specimens.

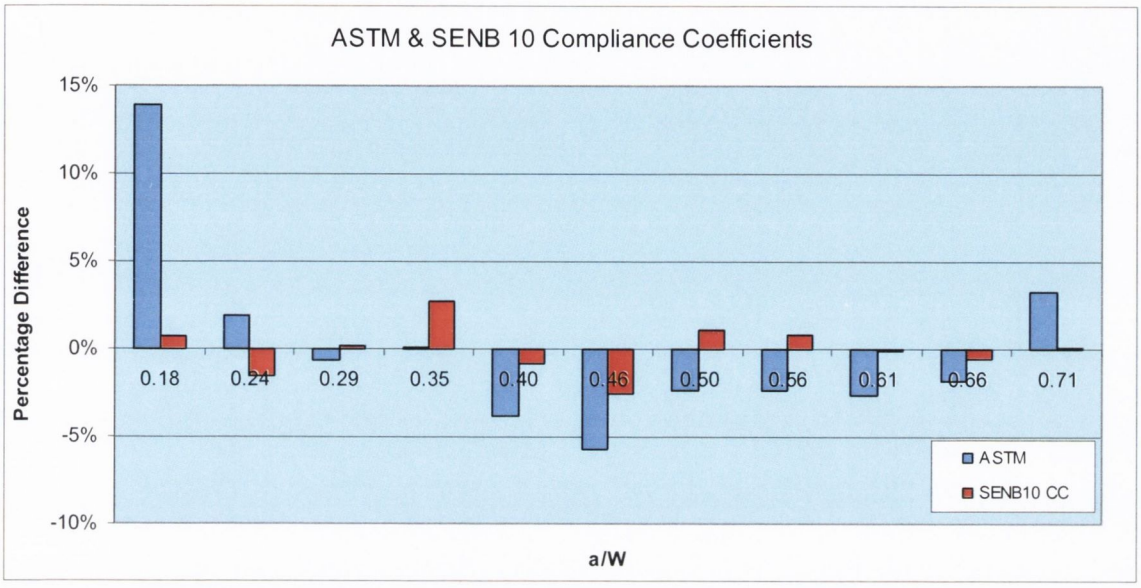

Figure 4.1. Percentage difference between actual crack length and crack length determined using ASTM and new SENB10 Compliance Coefficients.

Figure 4.1 shows the improved accuracy achieved using the new SENB10 compliance coefficients in comparison to the ASTM compliance coefficients where large percentage differences were found. The problematic area using the ASTM compliance coefficients was especially evident in the vary small starter crack notch length, with $a/W = 0.2$.

The compliance coefficients for the SENB5 brass specimens were determined and can be seen in Table 4.2. Again, these compliance coefficients were used to fine tune the results and develop a further set of compliance coefficients which could be used for fatigue precracking the FT DICoMM and CoMM specimens.

C0	C1	C2	C3	C4	C5
-0.9792	83.73	-1461.7	11791.0	-45794.0	68294.0

Table 4.2. Compliance Coefficients determined using SENB5 brass specimens.

The final set of compliance coefficients for use with the DICoMM and CoMM SENB5 specimens can be in Table 4.3. Again, these compliance coefficients were used to fine

tune the results and develop a further set of compliance coefficients which could be used for fatigue precracking the FT DICoMM and CoMM specimens.

C0	C1	C2	C3	C4	C5
-1.3541	86.67	-1301.9	9033.1	-30329.0	39552.0

Table 4.3. Compliance Coefficients determined using SENB5 brass specimens.

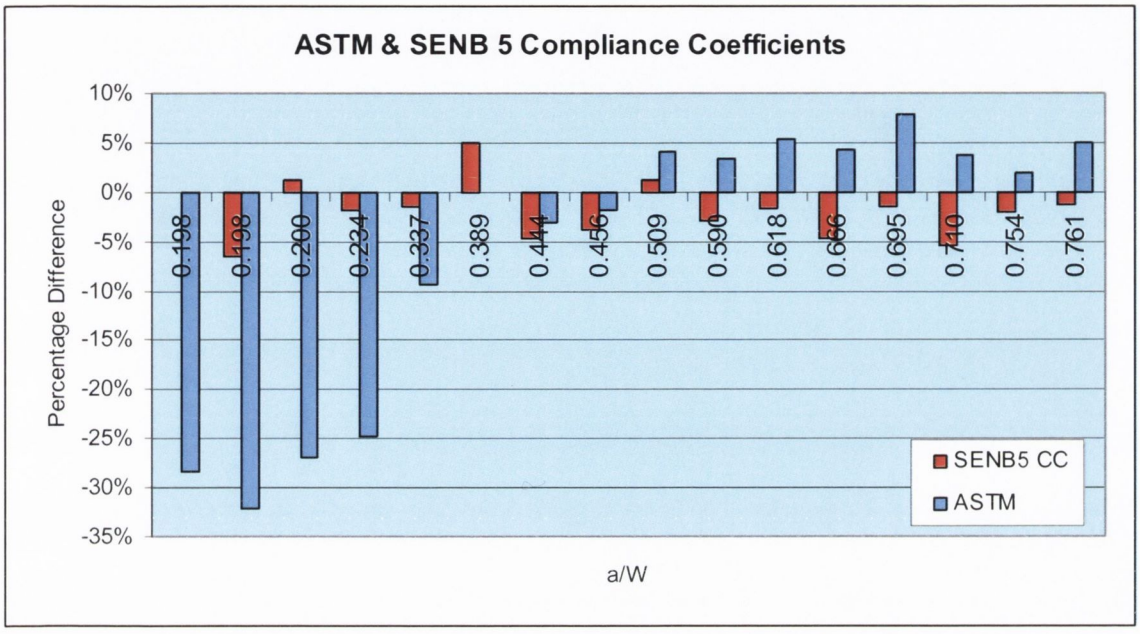

Figure 4.2. Percentage difference between actual crack length and crack length determined using ASTM and new SENB 5 Compliance Coefficients.

Figure 4.2 shows the improved accuracy achieved using the new SENB5 compliance coefficients in comparison to the ASTM compliance coefficients where very large percentage differences were found. Again, similar to SENB10 sized specimens, the problematic area using the ASTM compliance coefficients is especially evident in the vary small starter crack notch length, where $a/W = 0.2$.

4.3. Percent Theoretical Density (%TD) Test Results

In this section, the %TD achieved for each specimen type i.e. FT, TRS and Charpy, are reported. FT is covered firstly followed by TRS and Charpy. The results of the experimental data will be recorded using histograms and scatter plots.

4.3.1. Fracture Toughness (FT) Specimen Test Results - %Theoretical Density

Figure 4.3 shows the %TD as a histogram, showing the results achieved for CoMM (in Red) and the average results achieved for each DC. It is important to note that in each of

the average DC result are the different US Mesh sizes ranging from 20/25 up to 80/100 diamond mesh size. The average %TD for CoMM is 95.56% whereas the average for all the FT DICoMMs specimens is 94.81%.

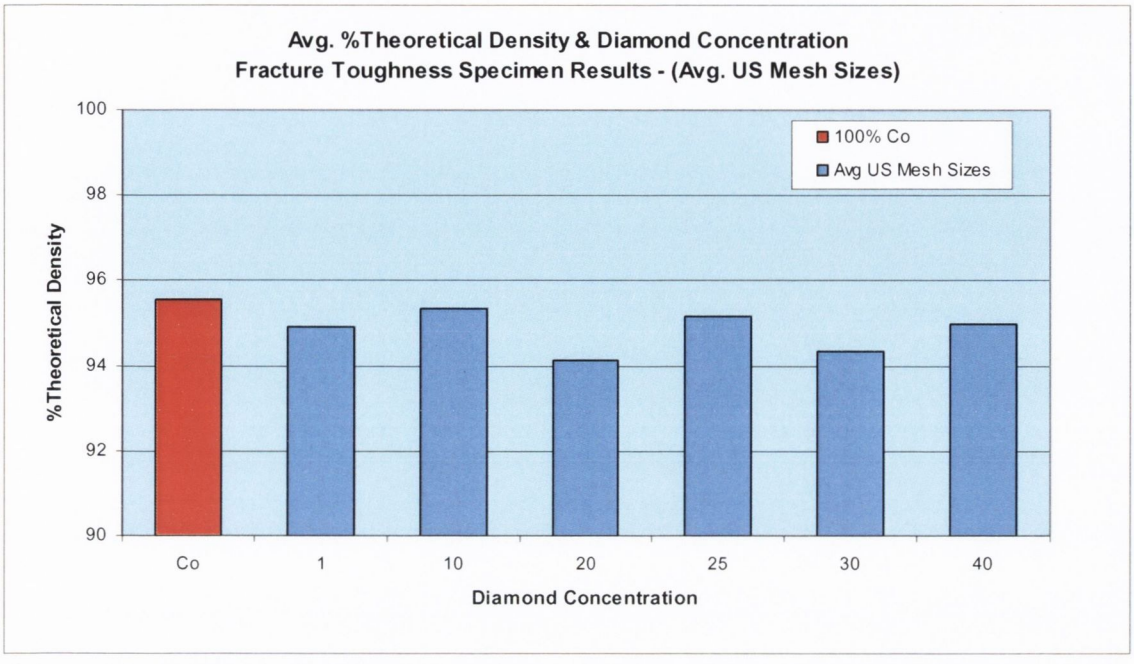

Figure 4.3. Fracture Toughness Specimen Results: Figure shows the Average %TD achieved for CoMM and DICoMMs for each DC. The average values recorded on the graph are the overall average obtained for each DC. CoMM is included for comparison purposes.

As can be seen in Figure 4.3, the addition of diamond to the cobalt matrix causes a small reduction in %TD. However, Figure 4.4 represents the %TD results for individual specimens for each US Mesh size plotted against DC shows that the increasing addition of diamond seems to increase the amount of scatter in %TD as can be seen as diamond concentration increases.

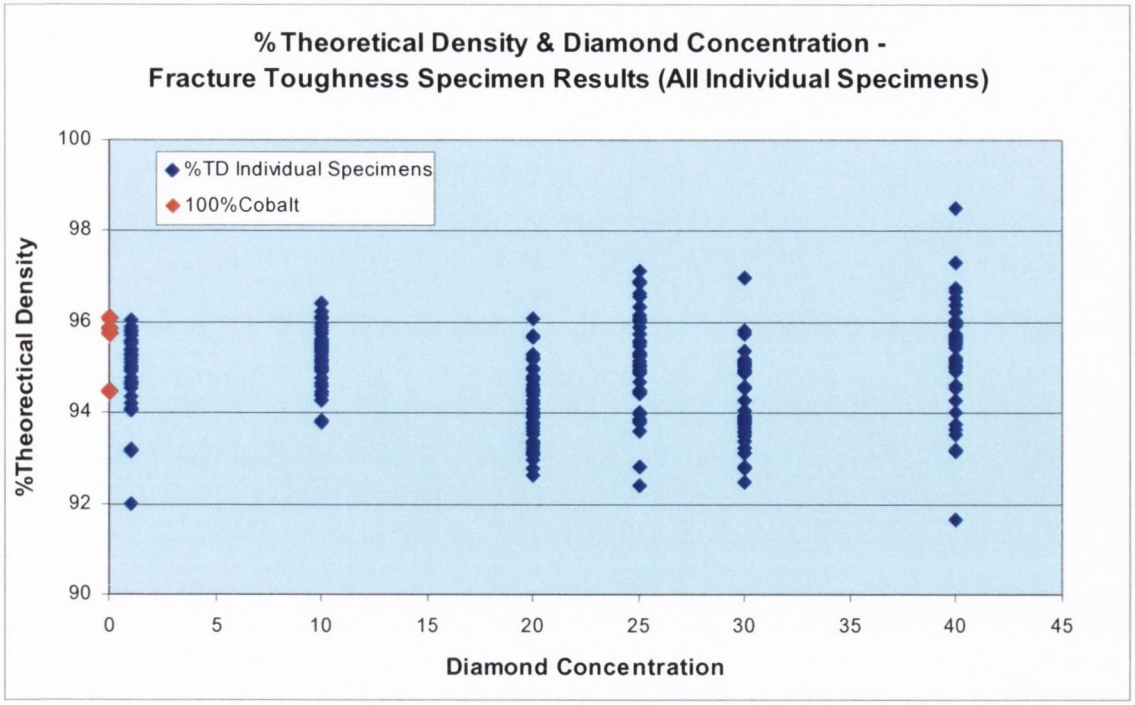

Figure 4.4. Fracture Toughness Specimen Results: Figure shows %TD for each specimen achieved for CoMM and DICoMMs for each US Mesh size used plotted against DC.

The amount of increasing scatter can be examined by plotting the standard deviation for each US Mesh size in each DC. This can be seen in Figure 4.5.

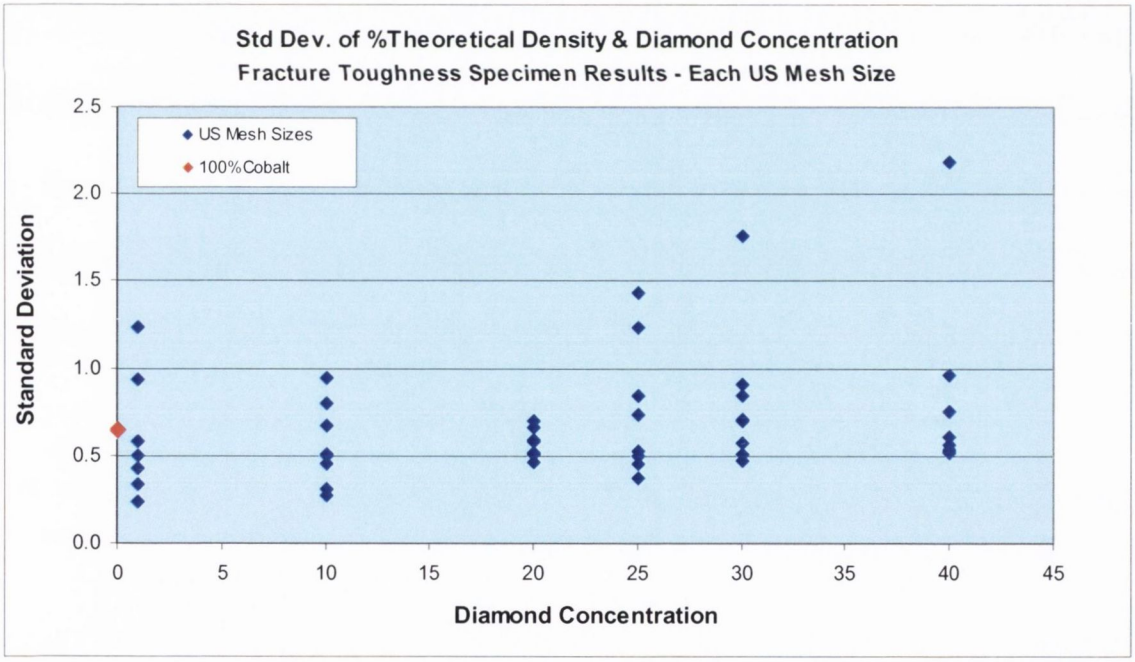

Figure 4.5. Fracture Toughness Specimen Results: Figure shows the Standard Deviation for %TD achieved for CoMM and DICoMMs for each DC used.

Standard Deviation of %TD for each US Mesh size plotted against DC does show an increasing standard deviation for increasing DC. Figure 4.5 clearly shows a steadily rising level of scatter with increasing DC.

4.3.2. TRS Specimen Test Results - %TD

Similar to the fracture toughness results Figure 4.6 shows for the TRS type specimens the average %TD value for each DC. Included is the %TD for CoMM in red in the graph. As can be seen in Figure 4.6, the addition of diamond does cause a reduction in %TD when added to the cobalt matrix however it is a bit more significant in comparison to the results found for the FT specimens when one considers the results shown in Figure 4.7. The average %TD for CoMM is 95.6% whereas the average for all TRS DICoMM specimens is 93.9%.

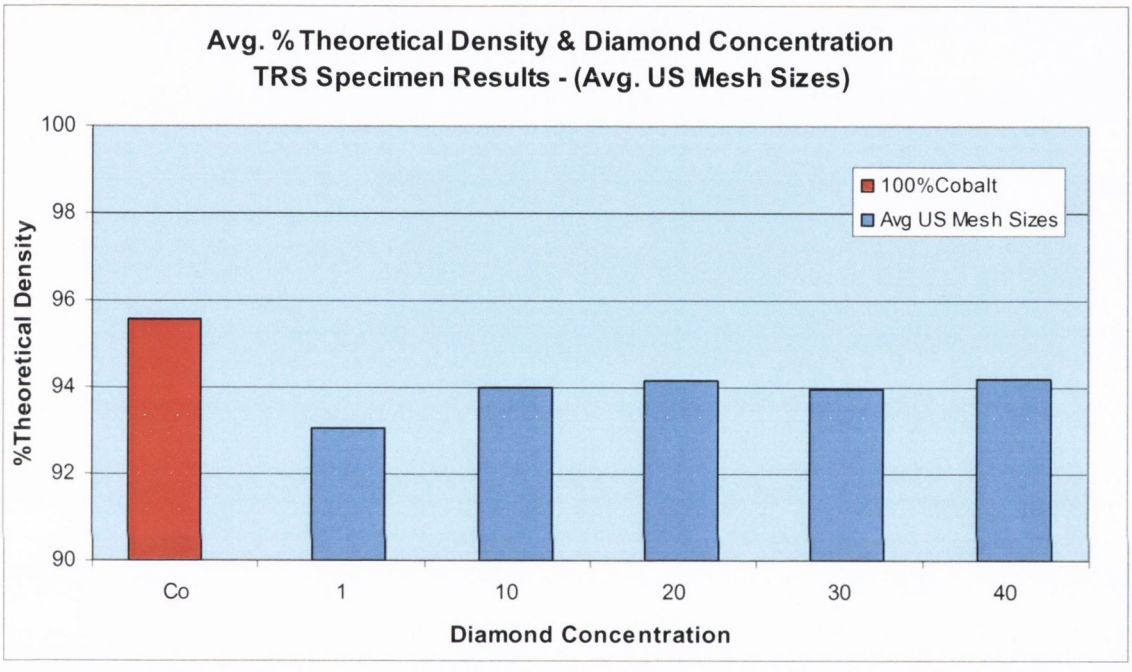

Figure 4.6.TRS Specimen Results: Figure shows the Average %TD achieved for CoMM and DICoMMs for each DC. The average values recorded on the graph are the overall average obtained for each DC. CoMM is included for comparison purposes.

Figure 4.7 represents the %TD results for each individual specimen for each US Mesh size plotted against DC. The graph shows the large spread found in %TD due to the addition of diamond to the cobalt matrix.

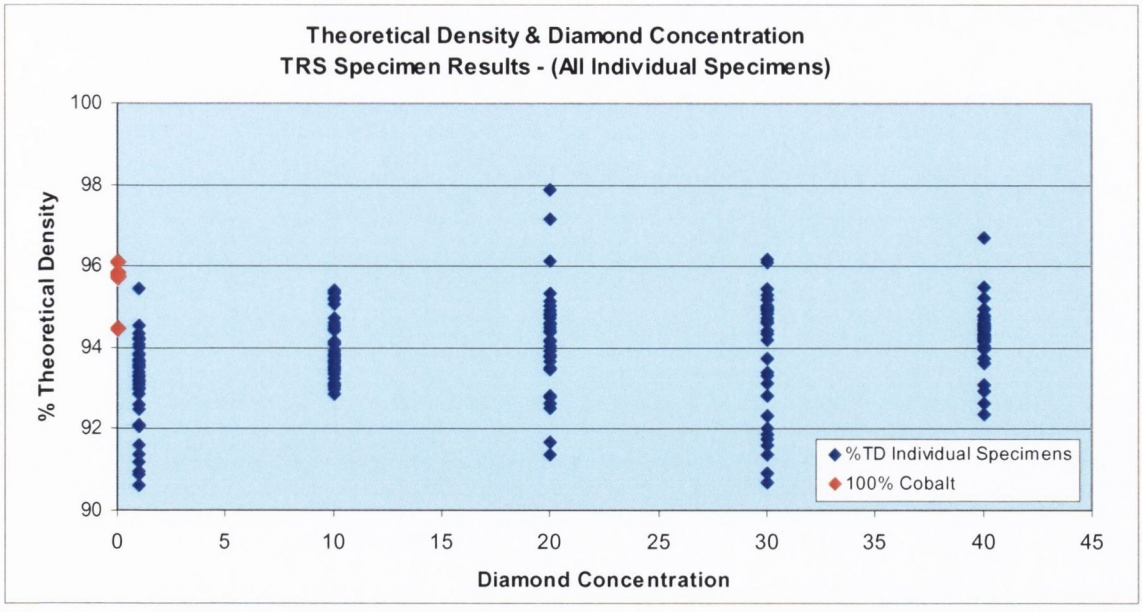

Figure 4.7. TRS Specimen Results: Figure shows %TD for each specimen achieved for CoMM and DICoMMs for each US Mesh size used plotted against DC.

The results are similar to Figure 4.6, except that the results plotted here are for each sample for each US Mesh size. The results are plotted for each DC. The graph shows the large spread found for each of the DCs. Another observation is that the increasing addition of diamond seems to increase the amount of scatter in %TD as can be seen as DC increases.

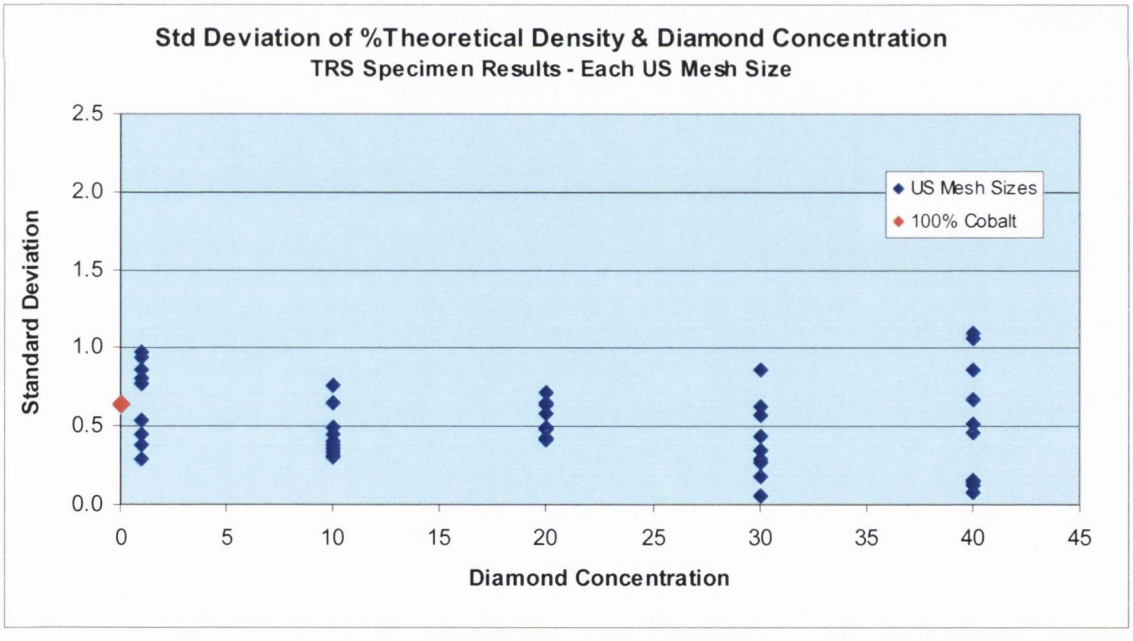

Figure 4.8. TRS Specimen Results: Figure shows the Standard Deviation for %TD achieved for CoMM and DICoMMs for each DC used. The results indicate that increasing diamond causes an increase in scatter in %TD.

Standard Deviation of %TD for each US Mesh size plotted against DC does show increasing scatter for increasing DC but it is not as pronounced as for the FT specimens as can be seen in Figure 4.8.

4.3.3. Charpy Impact (CI) Specimen Test Results - %Theoretical Density (%TD)

Again similar to FT and TRS Figure 4.9 shows for Charpy Impact specimens, the average %TD value for each DC. Included is the %TD for CoMM in red in the graph. As can be seen in Figure 4.9, the addition of diamond does seem to cause a reduction in %TD in comparison to 100%Co. The average %TD for CoMM is 95.38% whereas the average for all CI DICoMM specimens is 94.97%.

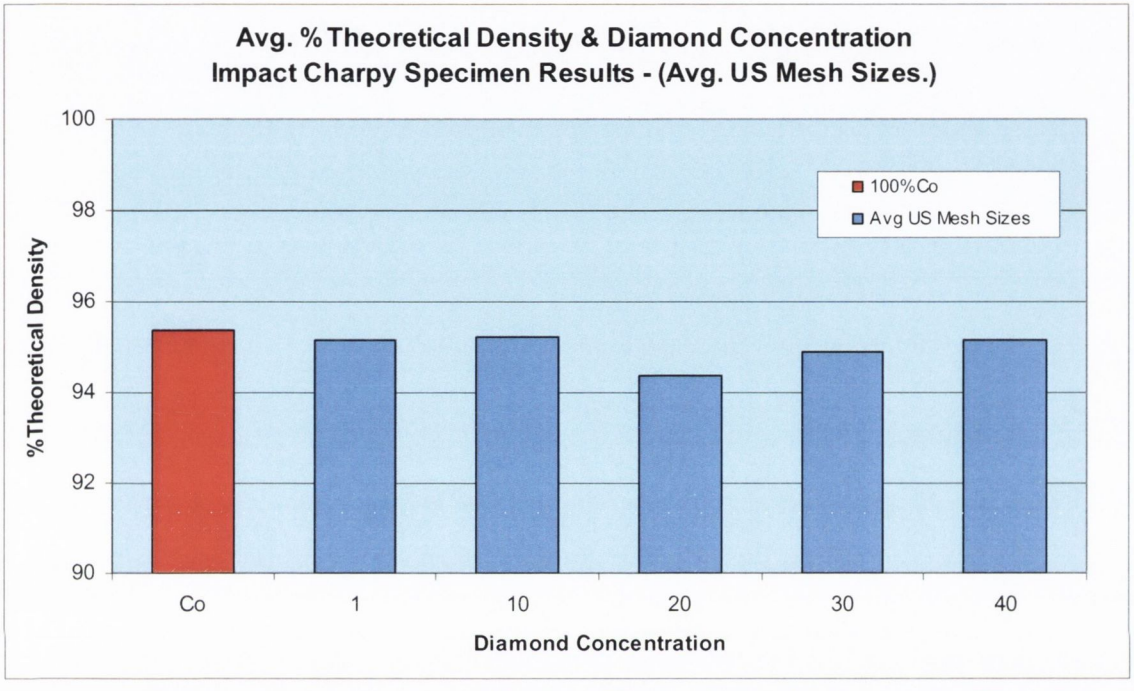

Figure 4.9. Charpy Impact Specimen Results: Figure shows the Average %TD achieved for CoMM and DICoMMs for each DC. The average values recorded on the graph are the overall average obtained for each DC. CoMM is included for comparison purposes.

In Figure 4.10, the %TD is plotted similar to Figure 4.9 except that each individual result for the different US Mesh sizes is plotted against DC. This shows the large scatter found in the different DCs and due to the addition of diamond which is similar to that found for fracture toughness and TRS specimens.

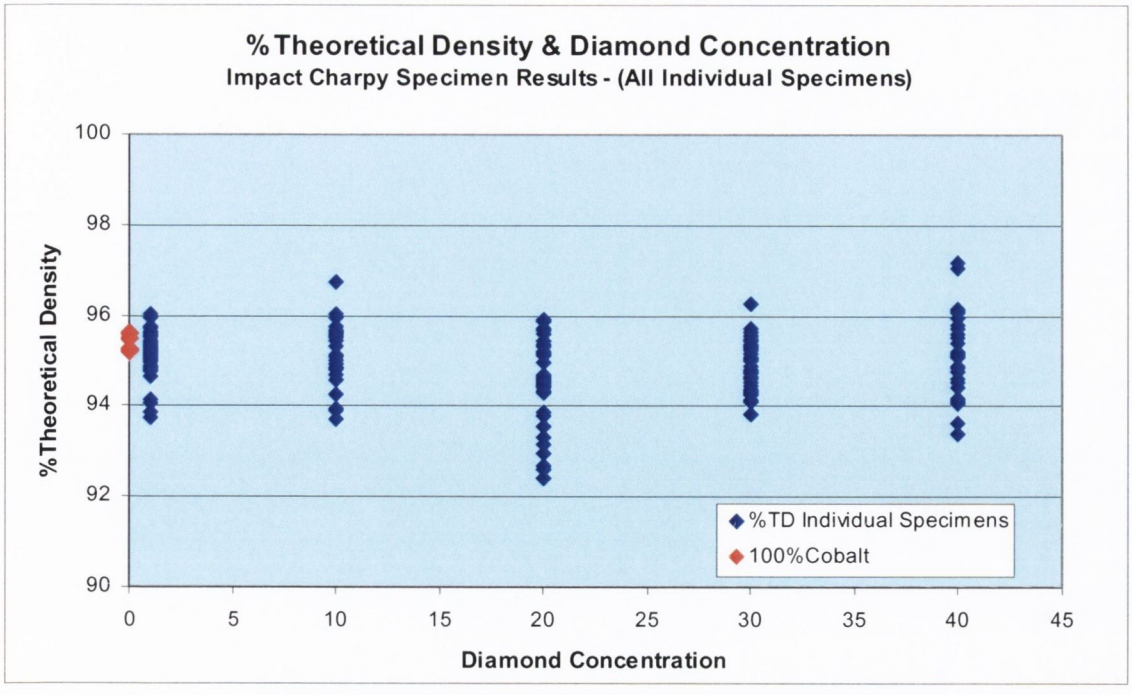

Figure 4.10. Charpy Impact Specimen Results: Figure shows the %TD for each specimen achieved for CoMM and DICoMMs for each US Mesh size used plotted against DC.

The results in Figure 4.10 are similar to those in Figure 4.9, except that the results plotted here are for each sample for each US Mesh size. The results are plotted for each DC. The graph shows the large spread found for each of the DCs. The data is for each individual sample obtained for each US Mesh size and DC. Again similar to FT and TRS specimen %TD results, it is evident that the addition of diamond seems to increase the amount of scatter in %TD. Standard deviation of %TD for each US Mesh size plotted against DC does show an increase in scatter with increasing diamond concentration as can be seen in Figure 4.11.

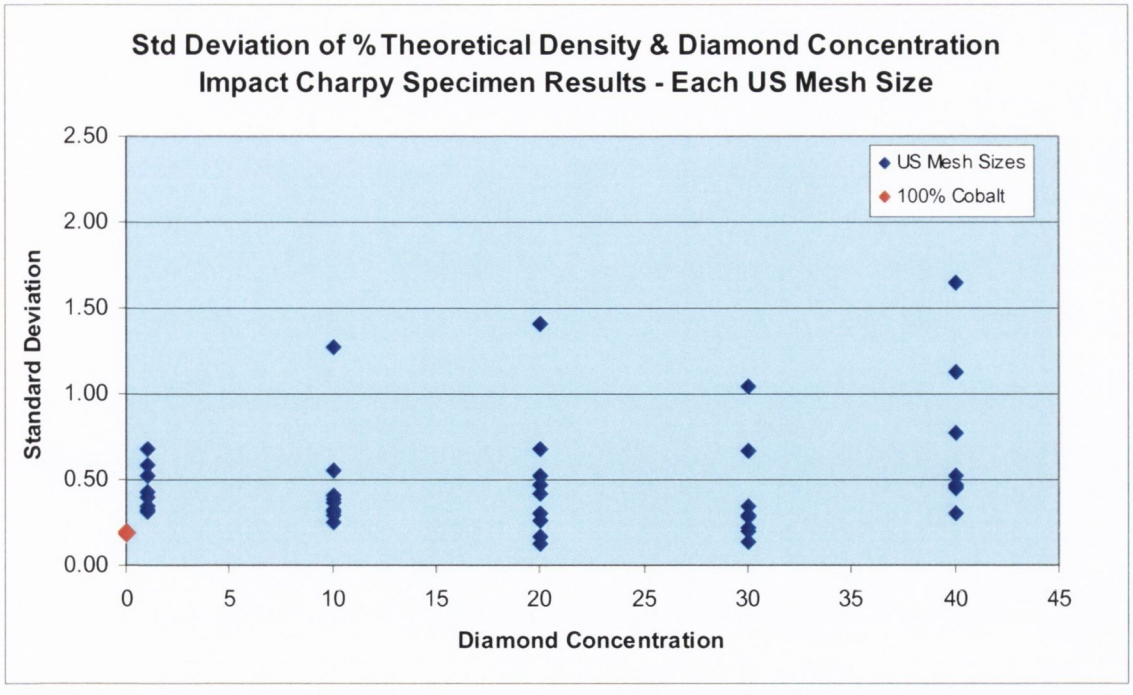

Figure 4.11. Charpy Impact Specimen Results: Figure shows the Standard Deviation for %TD achieved for CoMM and DICoMMs for each DC used.

4.4. Hardness Test Results

Again similar to %TD results reported in the previous section, a similar approach will be given here for the hardness results. This is to make it easier for the reader due to the large amounts of data to report. Also reporting each and every US Mesh size for each DC would make it very laborious as the data shows a large amount of variation with no real increase in understanding.

4.4.1. FT Specimen Test Results - Hardness

The histogram in Figure 4.12 shows the average Rockwell B hardness value for each DC, which incorporates the hardness values for all the US Mesh sizes for each DC. The remarkable result is that it is amazingly consistent over all the diamond sizes and DCs. Examining Figure 4.12, the average hardness for 100%Co is 103.7 HRB, whereas the average for the DICoMMs for the range of US Mesh sizes and DCs investigated in this project is 101.6HRB.

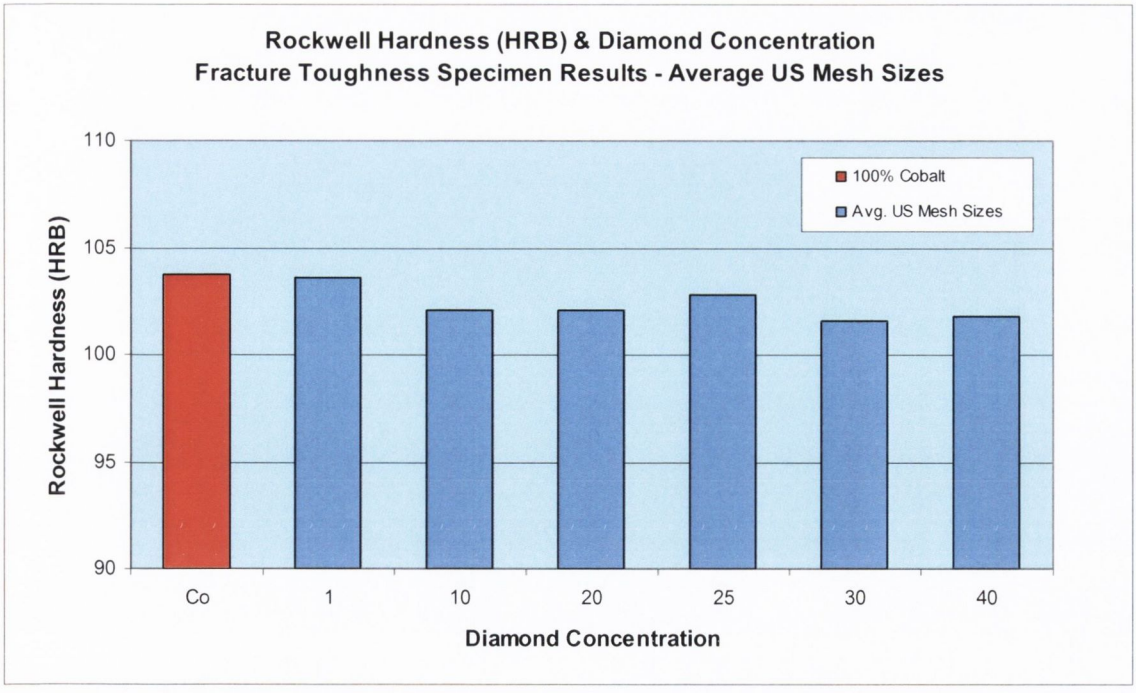

Figure 4.12. Fracture Toughness Specimen Results: Figure shows the average Rockwell HRB hardness values for all US Mesh sizes averaged for each DC, included is CoMM for comparison purposes.

Figure 4.12 shows a decreasing trend in hardness with increasing diamond concentration. When one examines the individual results for each US Mesh size and plotted against DC, one sees that hardness is 100 +/- 5 irrespective of DC as can be seen in Figure 4.13.

Figure 4.14 shows the Rockwell hardness results plotted against US Mesh size for the diamond concentration DC30 and DC40, showing that as diamond size (US Mesh size) decreases the hardness shows an increasing trend. The two trend lines drawn indicate correlation coefficients of $R = 0.68$ for DC30 and $R = 0.83$ for DC40, both being statistically significant, ($p<0.05$).

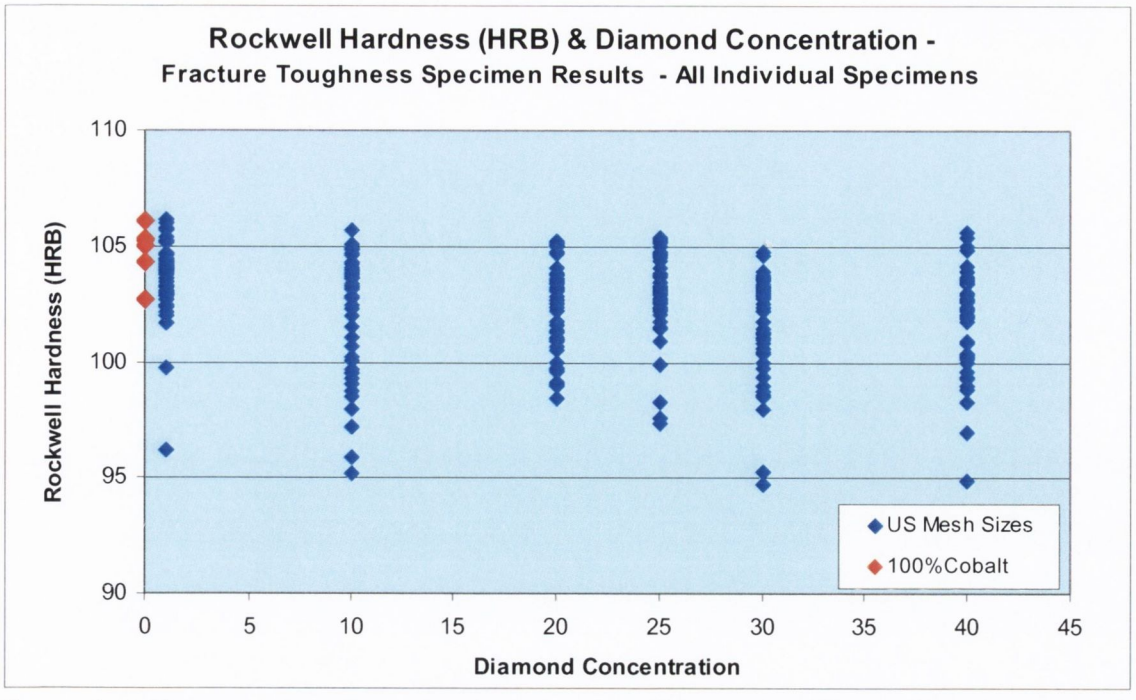

Figure 4.13. Fracture Toughness Specimen Results: Rockwell hardness plotted against DC with CoMM included. The hardness results are the average values found for each individual specimen for the different US Mesh sizes and DCs used.

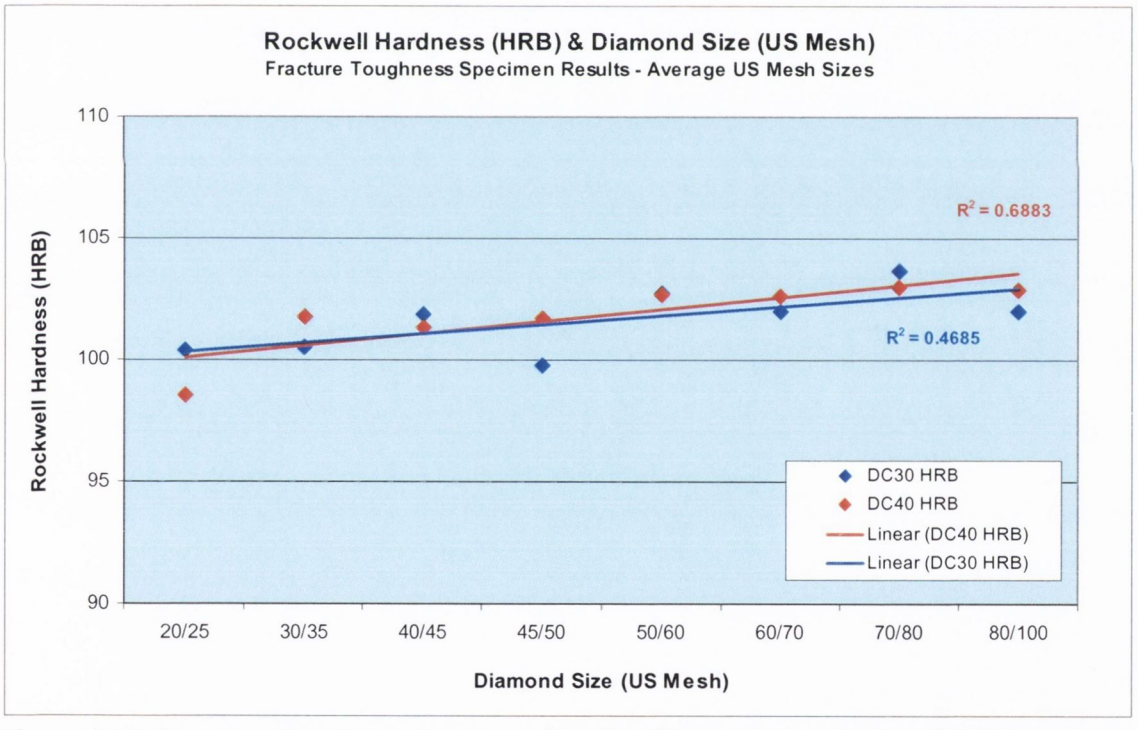

Figure 4.14. Fracture Toughness Specimen Results: Figure shows Rockwell HRB hardness plotted against diamond size (US Mesh size). Average hardness results for each US Mesh size and DC30 & DC40. DC30 R = 0.68 and DC40 R = 0.83.

4.4.2. TRS Specimen Test Results - Hardness

Again, very similar to FT hardness results, there is not a large difference with the addition of diamond with increasing DC. From the histogram a small downward trend is indicated with increasing diamond content as is evident in Figure 4.15.

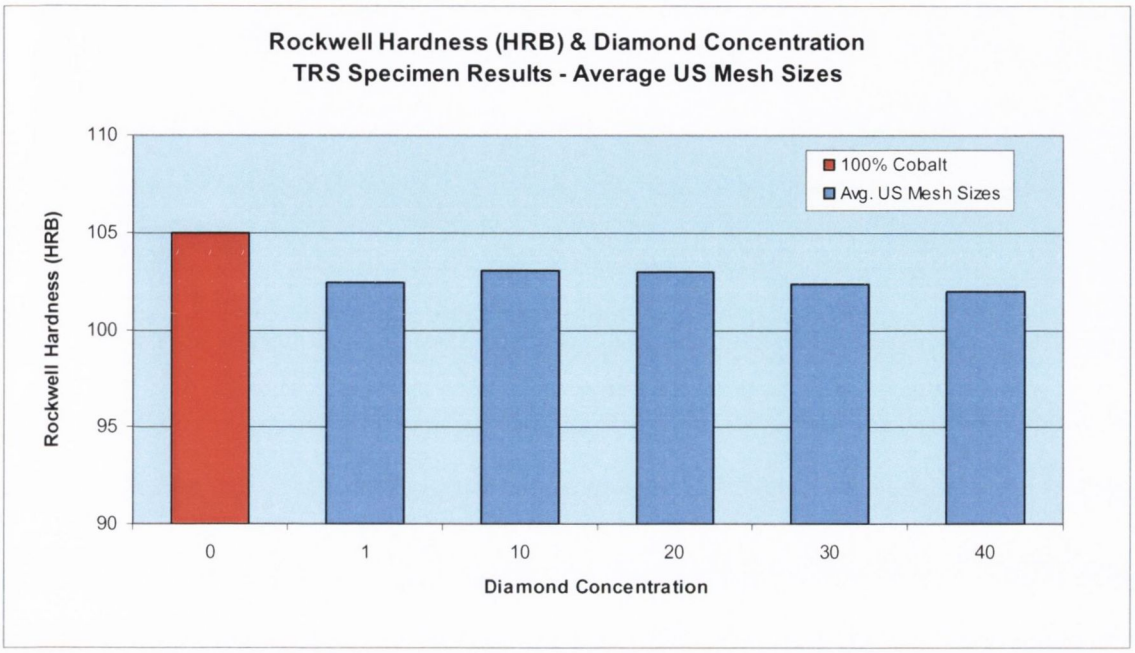

Figure 4.15. TRS Specimen Results: Figure shows the average Rockwell HRB hardness values for all US Mesh sizes averaged for each DC, included is CoMM for comparison purposes.

Examining Figure 4.15, the average HRB for 100%Co is 105.1 where the average for the DICoMM materials for the range of US Mesh sizes and DCs investigated in this project is 102.57HRB. Again the addition of diamond introduces a much wider range of scatter in comparison to that of the 100%cobalt matrix as can be seen in Figure 4.16.

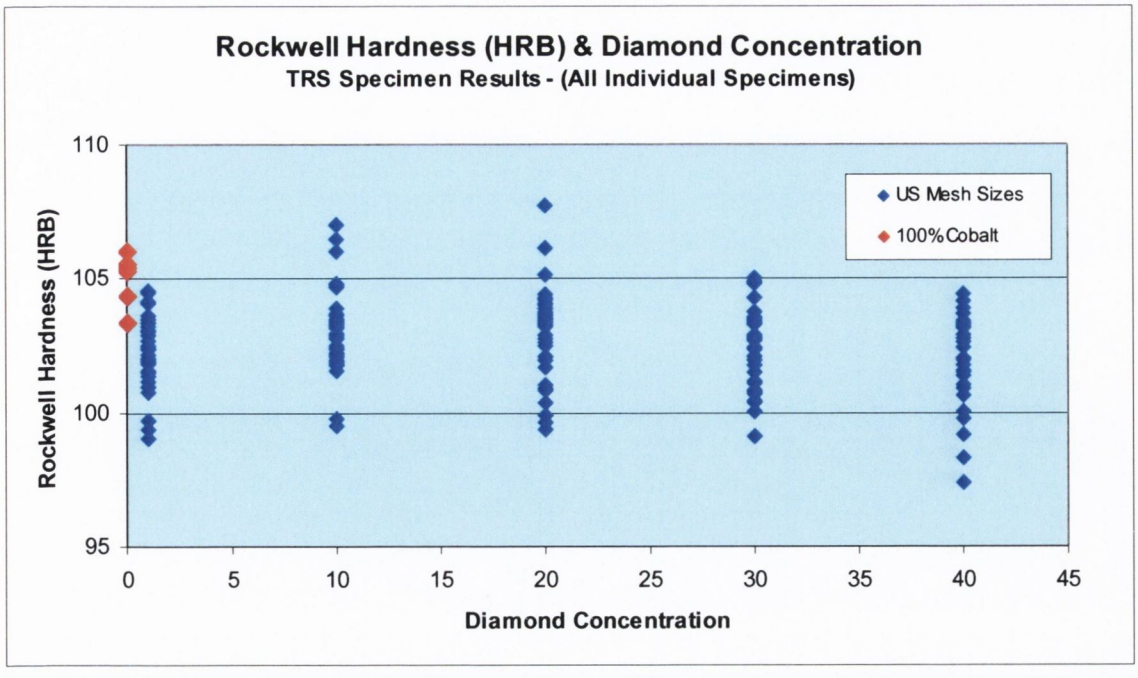

Figure 4.16. TRS Specimen Results: Rockwell HRB hardness plotted against DC with CoMM included. The hardness results are the average values found for each individual specimen for the different US Mesh sizes and DCs used.

Figure 4.17 shows hardness results plotted against US Mesh size for diamond concentrations DC10 and DC40, showing that as diamond size (US Mesh size) decreases the hardness shows a slightly increasing trend however the trend is not statistically significant for both diamond concentrations.

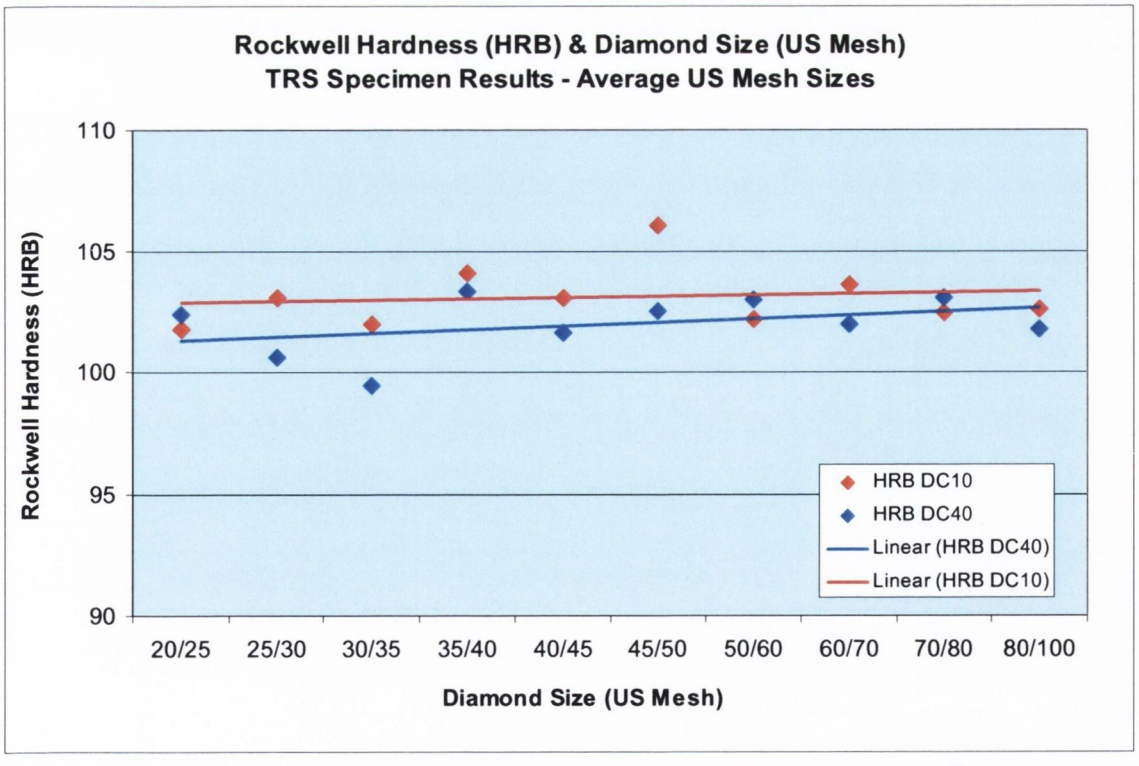

Figure 4.17. TRS Specimen Results: Shows Rockwell HRB hardness plotted against diamond size (US Mesh size). The hardness results are the average results for each US Mesh size and DC10 & DC40.

Increasing diamond concentration however does show a decreasing hardness level across the different diamond sizes (US Mesh size).

4.4.3. Charpy Impact (CI) Specimen Test Results - Hardness

Again, similar to FT hardness results, there is not a large difference with the addition of diamond with increasing diamond concentration. From the histogram shown in Figure 4.18 a downward trend is indicated with increasing diamond content. Examining Figure 4.18, the average hardness for 100%Co is 104.92HRB whereas the average for the DICoMM materials for the range of US Mesh sizes and DCs investigated in this project is 103.03HRB.

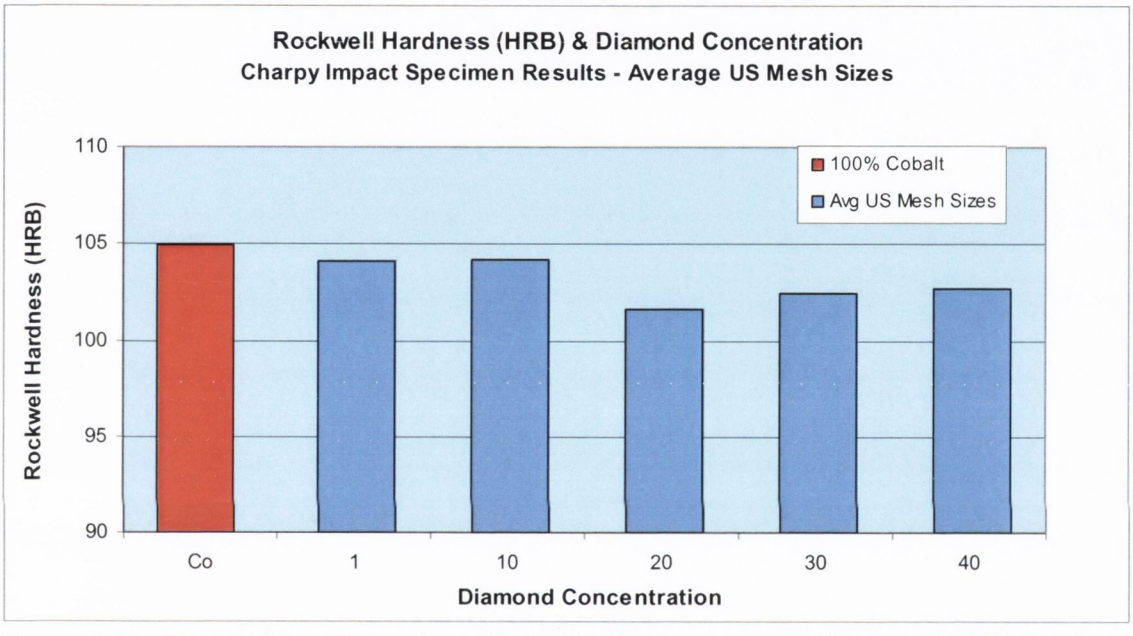

Figure 4.18. Charpy Impact Specimen Results: Figure shows the Rockwell HRB hardness values for all US Mesh sizes averaged for each DC plotted against DC, included is CoMM for comparison purposes.

Again the addition of diamond introduces a much wider range of scatter in comparison to that of the 100%Cobalt matrix as can be seen in Figure 4.19.

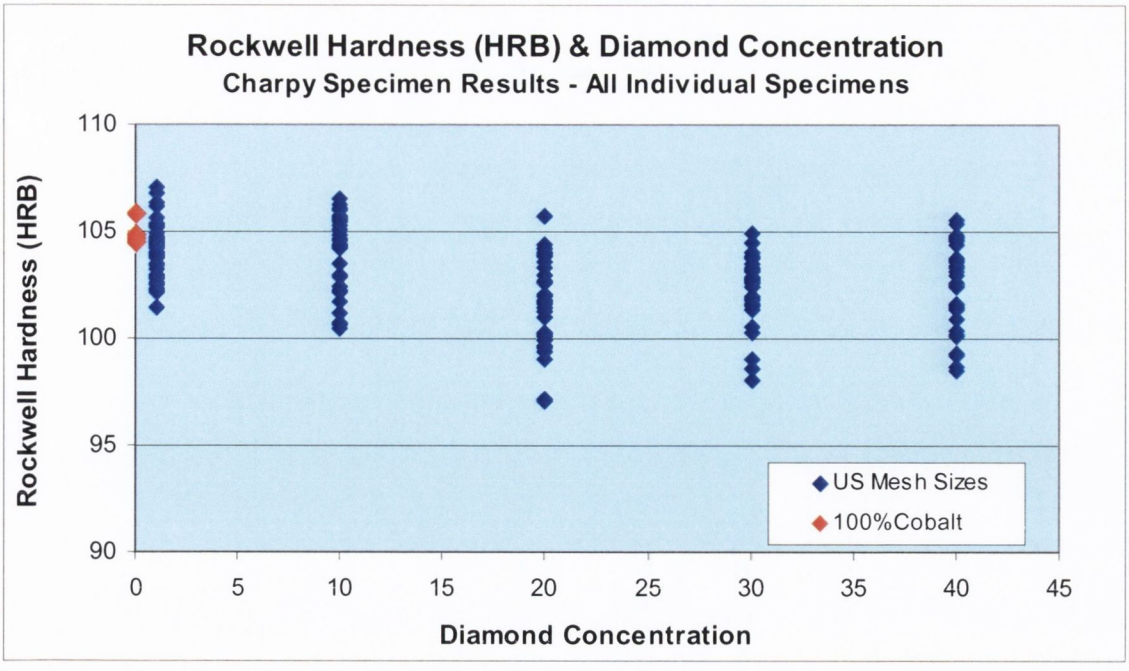

Figure 4.19. Charpy Impact Specimen Results: Figure shows the range of Rockwell HRB hardness plotted against DC with CoMM included. The hardness results are the average of three values for each individual specimen for the different US Mesh sizes and DCs used.

Similar to the TRS results, when hardness is plotted against US Mesh size for constant diamond concentration, an increasing trend in hardness is found for DC10 and DC40 as can be seen in Figure 4.20. Also that increasing diamond concentration leads to a decreasing hardness level across the different diamond sizes (US Mesh).

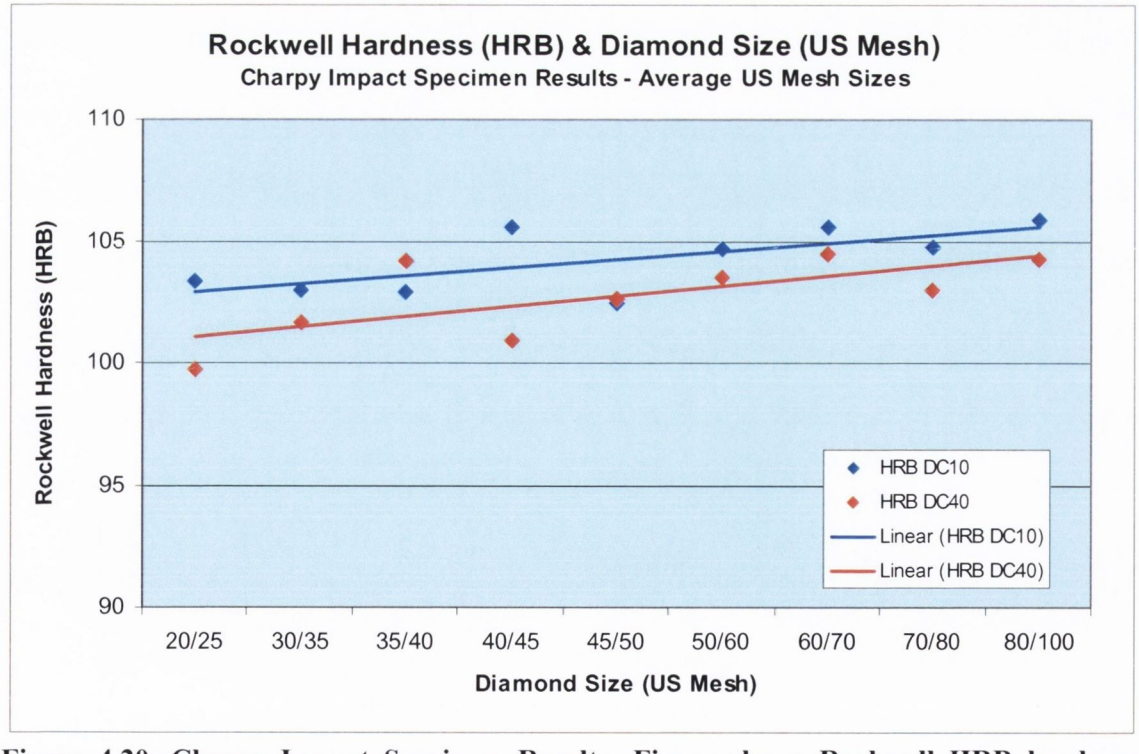

Figure 4.20. Charpy Impact Specimen Results: Figure shows Rockwell HRB hardness plotted against diamond size (US Mesh size), showing as diamond size gets finer an increasing trend in hardness occurs. Also, increasing DC causes a decrease in hardness.

4.5. Fracture Toughness (FT) Specimen Test Results - Fracture Toughness

Below are the results of the FT tests which have been carried out using two different software packages; FastTrack and SERIES-IX both proprietary to Instron, as described in Chapter 3, Experimental Procedures. The results have been determined according to the ASTM E-399-90 standard and have been adhered to as closely as possible. For clarity, FastTrack software is a suite of software packages, of which FastTrack Fatigue Crack Propagation da/dN and FastTrack Fracture Toughness have been used in this project. FastTrack Fracture Toughness is fully compliant with the ASTM E-399-90 standard requiring the pre-fatigue cracking information in calculating specimen fracture toughness and conforming to the various validity criteria as set out in the standard. Regarding SERIES-IX software however, testing using this package did not require any fatigue precrack information and so 2mm edm notched specimens could be tested directly to determine specimen fracture toughness.

There are a number of reasons for using both FastTrack FT and SERIES-IX software methods. On initial testing using FastTrack, the pre-fatiguing stage was found to take approximately 4-6 hours per specimen. Some specimens actually took days to grow a fatigue crack and sometimes fatigue cracks just did not grow. Also, prior to being able to grow fatigue cracks in these size specimens, the technique for growing fatigue cracks in such small specimens using the compliance method was challenging, as already outlined new compliance coefficients had to be determined for more accurate crack length measurement. So with a total of 288 specimens to test, it was decided to test half using the FastTrack software method and the other half of the specimens using the SERIES-IX software method where just the edm notch would be used. By using the SERIES-IX method it allowed the author to investigate the validity of the references [69, 95, 98, 90] in the literature where it was cited pre-fatiguing that was not necessary for PM type materials.

Three fracture toughness specimens per US Mesh size and DC combination were used for each test method. The SERIES-IX method was the easiest to carry out from a testing point of view in comparison to the FastTrack method which for various reasons outlined below was very problematic. Regarding the SERIES-IX method, the only crack present in the specimens was the nominal edm 2mm starter crack notch, giving an a/W of 0.2. This firstly invalidates the ASTM requirement for the atomically sharp crack with an

a/W inequality of $0.45 < a/W < 0.55$. SERIES-IX software method ignores this and when the other ASTM requirements and criteria were passed it deemed the result as Plane Strain Fracture Toughness value for the material. In this chapter, these are reported as K_{1C} -SERIES-IX or K_{1C} S-IX, or K_{1C} -NFCs (No Fail Codes). A total of 37 specimens were successfully determined as being valid Plane Strain Fracture Toughness K_{IC} values using the SERIES-IX method. The specimens which were deemed to have invalid K_{IC} results failed other aspects of the other ASTM E-399-90 criteria and are reported in this thesis as K_Q – SERIES-IX or K_Q -S-IX, a total sample size of 99 specimens.

As an atomically sharp crack is a requirement of ASTM standard, fatigue precracking was carried out using the FastTrack da/dN software to the correct a/W requirements of $0.45 \leq a/W \leq 0.55$. FastTrack da/dN is linked with FastTrack Fracture Toughness where the fatigue precracking data is transferred for the correct determination of fracture toughness. One of the requirements of ASTM E 399-90 is that the last 2.5% of the fatigue crack growth should be carried out at a low value of ΔK so that the plastic zone size is at a minimum. This ensures that crack blunting effects are minimised and that fast fracture occurs and that slow crack growth is not predominant at the start. This data can be automatically downloaded from da/dn to FastTrack. What will be apparent below is that not all the specimens in which pre-fatiguing was attempted were successful. This was not apparent until the fracture toughness testing was carried out using FastTrack.

The prefatigued specimens were then tested using FastTrack FT software and those that fulfilled all the necessary requirements of ASTM Standard E-399-90 are distinguished as Plane Strain Fracture Toughness, K_{IC}. A total of 51 were successful. However, not all the specimens fulfilled this requirement. Some in fact did not actually achieve to grow a fatigue crack. So, the a_f or final crack length would have remained the same length as the edm'ed crack starter notch length of a_o. Some of these specimens were fatigued for millions of cycles without actually growing a crack. These specimens and those that did grow a fatigue crack but failed one of the ASTM E-399-90 criteria are recorded as K_Q fracture toughness values, a total of 70 specimens. The Plane Strain Fracture Toughness, K_{IC} results are shown in Figure 4.21.

For some fracture toughness specimens no results were obtained for a number of reasons, e.g. specimen failed on set-up, 'bedding-in' or 'pre-loading' cycle test to non-compliance to the ASTM E-399-90 criteria.

4.5.1. FT Specimen Test Results - ASTM E-399-90 Standard

It the graph Figure 4.21, the plane strain fracture toughness K_{IC} as determined by FastTrack and SERIES-IX can be seen. The results are for individual specimens regarding each diamond US Mesh size and DC. Interestingly, the results using the two different methods are very comparable. Their average values and standard deviations are practically the same, K_{IC} (FastTrack) being 26.33 $MPam^{0.5}$, with 2.81std. dev. and SERIES-IX K_{IC} average value of 26.09$MPam^{0.5}$, and 2.97 std. dev. Just to recap, the FastTrack K_{IC} results were all precracked specimens to the correct dimension i.e. $0.45 < a/W < 0.55$, whereas the SERIES-IX K_{1C} results had not been fatigue precracked which resulted in an a/W of approximately 0.2 giving a a_f being ~2.00mm, the starter edm notch.

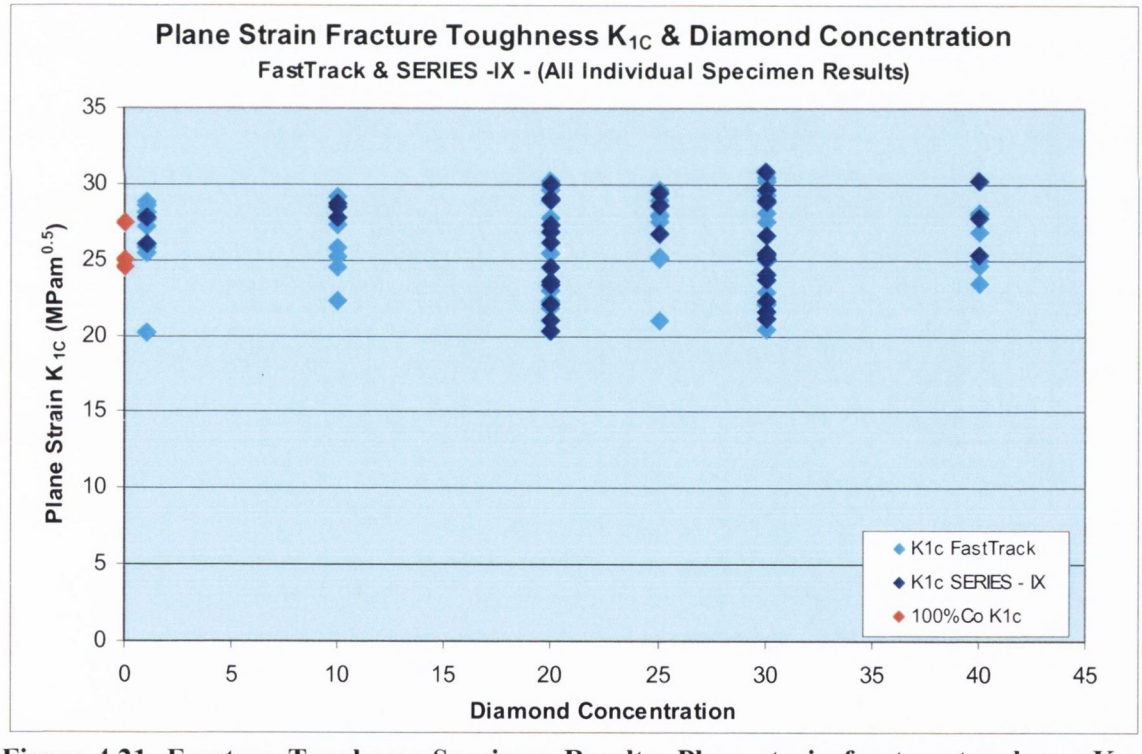

Figure 4.21. Fracture Toughness Specimen Results: Plane strain fracture toughness K_{1C} results for FastTrack and SERIES-IX. The results are individual results for each US Mesh size and DC.

The FastTrack and SERIES-IX plane strain fracture toughness K_{IC} results are very similar and do not vary with diamond concentration. Included in the figure are the plane

strain fracture toughness results for 100%Co. Interesting that all the results both for the cobalt matrix and the DICoMMs all lie within a band of approximately 20 to 30MPam$^{0.5}$.

Figure 4.22 shows the K_{IC} and K_Q fracture toughness results for FastTrack. In the graph one can see that K_Q fracture toughness values show a much large range of scatter in results in comparison to the plane strain fracture toughness K_{IC} results. As K_Q are an invalid fracture results according to the ASTM E-99-90 standard there are many reasons why they failed to fulfil the criteria, e.g. a/W incorrect, failed to grow a fatigue crack which resulted in the a criterion being violated, surface crack lengths incorrect were the main reasons.

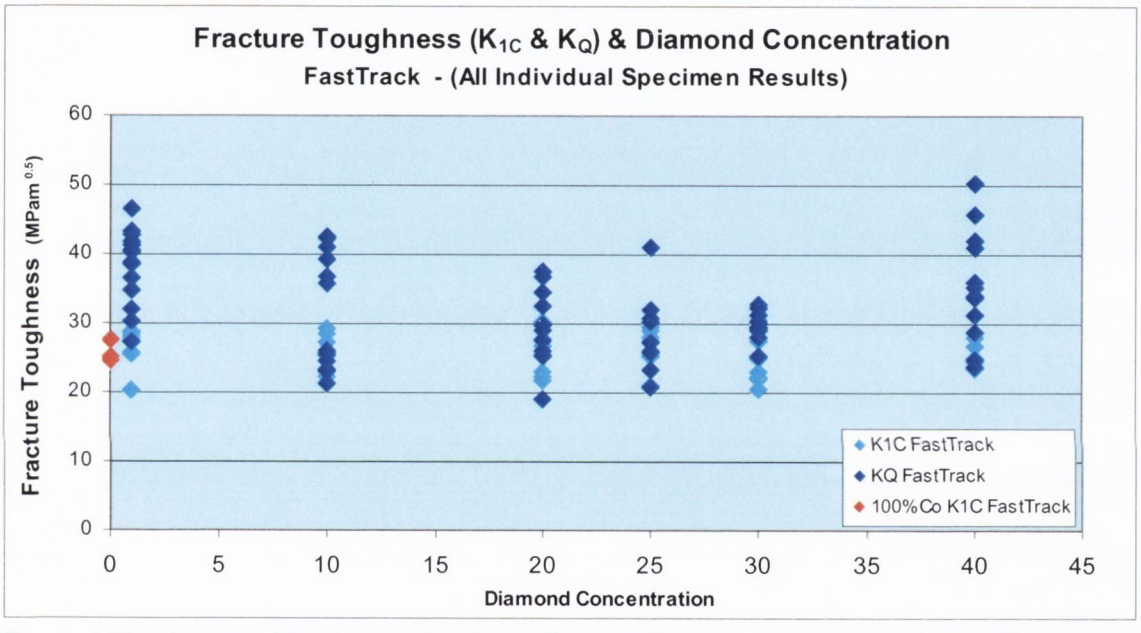

Figure 4.22. Fracture Toughness Specimen Results: Fracture toughness K_{1C} and K_Q results for FastTrack. The results are individual results for each US Mesh size and DC.

The results shown in Figure 4.22 are very similar to the pattern shown in Figure 2.9 in Chapter 2, Literature Review, as reported by Kobyashi et al. [166] without explanation.

Figure 4.23 shows the SERIES-IX K_{IC} and K_Q fracture toughness results. In the graph one can see that K_Q fracture toughness values show a much larger range of scatter in comparison to the plane strain fracture toughness K_{IC} results, similar to FastTrack results as seen in Figure 4.22. The majority of the SERIES-IX K_Q results failed because they did not fulfil the criteria $2.5(K_{IC}/\sigma_{Yld})^2$.

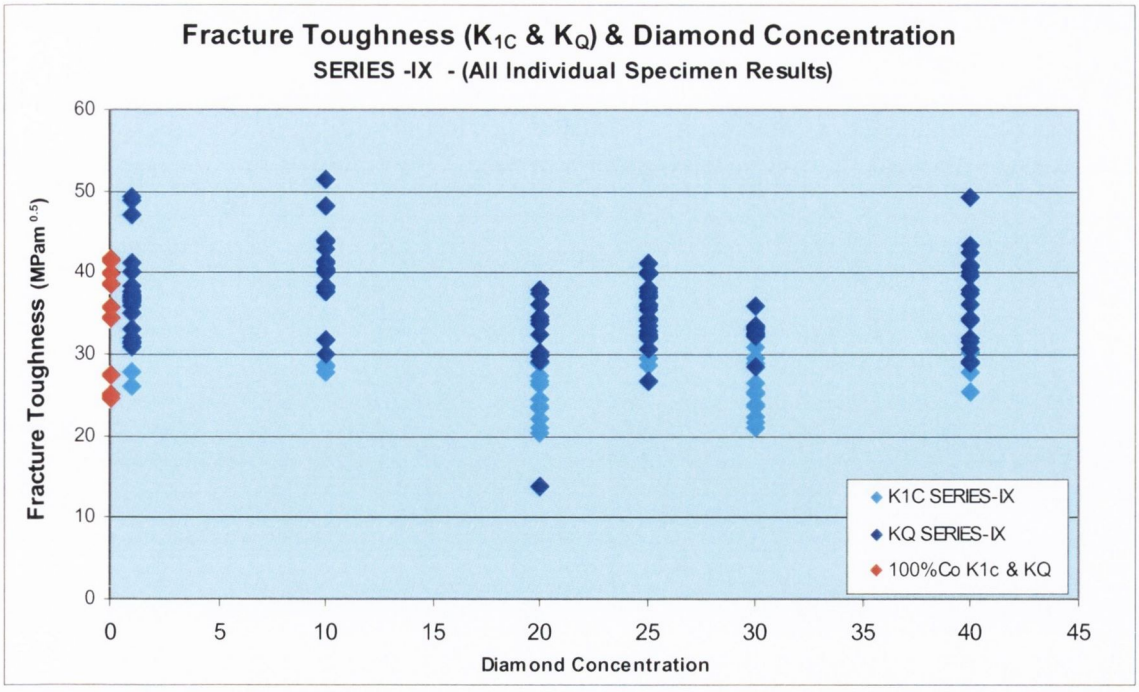

Figure 4.23. Fracture Toughness Specimen Results: Fracture toughness K_{1C} and K_Q results for SERIES-IX. The results are individual results for each US Mesh size and DC.

In summary then for FastTrack there were 51 valid K_{IC} specimen results and 70 K_Q specimen results. The average FastTrack K_{IC} result is 26.33 MPa.m$^{0.5}$, with a standard deviation of 2.81.

Regarding the 70 K_Q FastTrack specimens, a total of 37 failed to grow a fatigue precrack, and their average K_Q fracture toughness result is 36.58MPa.m$^{0.5}$. The overall FastTrack K_Q fracture toughness for the 70 specimens the average value is 32.7 MPa.m$^{0.5}$ and a std. dev. of 6.99.

Regarding SERIES-IX there were 37 valid K_{IC} and 99 K_Q specimen results. The average SERIES-IX K_{IC} result is 26.09MPa.m$^{0.5}$ with a standard deviation of 2.97. The average SERIES-IX K_Q result is 36.31 MPa.m$^{0.5}$ with a std. dev. of 5.58. This gives 42% valid plane strain fracture toughness results for FastTrack and only 27% valid for the SERIES-IX method.

Regarding 100%Cobalt or CoMM, the fracture toughness values for both K_{IC} and K_Q for 100%Co are included; the average plane strain fracture toughness for 100%Cobalt is 25.64MPam$^{0.5}$. Interestingly the K_Q values for 100%Co have a very similar range as the K_Q values for the DICoMM specimens.

4.5.2. FT Specimen Test Results – Effect of Diamond Concentration

When fracture toughness results are examined, it suggests that the effect of DC does not indicate any effect. This is opposite to what is generally found in the literature for PMMCs [164]. Figure 4.24 show the effect of diamond concentration on the K_{IC} fracture toughness results for both FastTrack and SERIES-IX methods combined as one data set, the results show no great effect. Again, the plane strain fracture toughness for 100%Co matrix is included as a datum for comparison. The average value for K_{IC} for 100%Co is 25.64MPam$^{0.5}$ and the average K_{IC} value for DICoMMs is 26.33MPam$^{0.5}$.

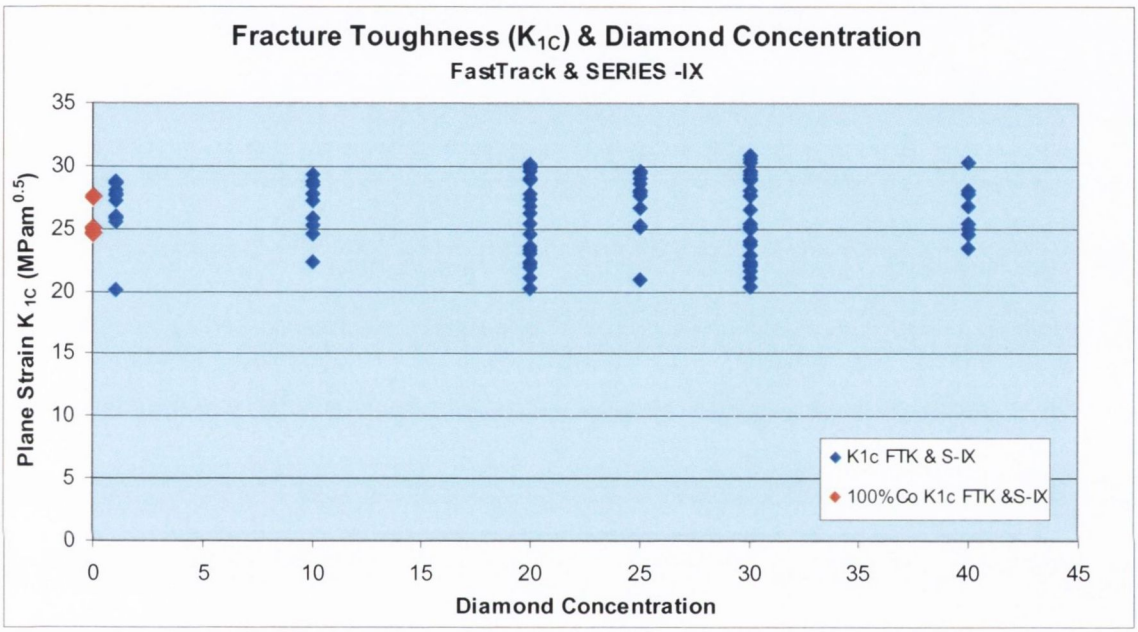

Figure 4.24. Fracture Toughness Specimen Results: Fracture toughness K_{1C} results for both FastTrack and SERIES-IX combined. The results are individual results for each US Mesh size and DC.

Figure 4.25, shows the standard deviation for the plane strain fracture toughness (K_{IC}) results for both FastTrack and SERIES-IX combined. The results show that the level of variability between the diamond concentrations is not significant and therefore no trend exists.

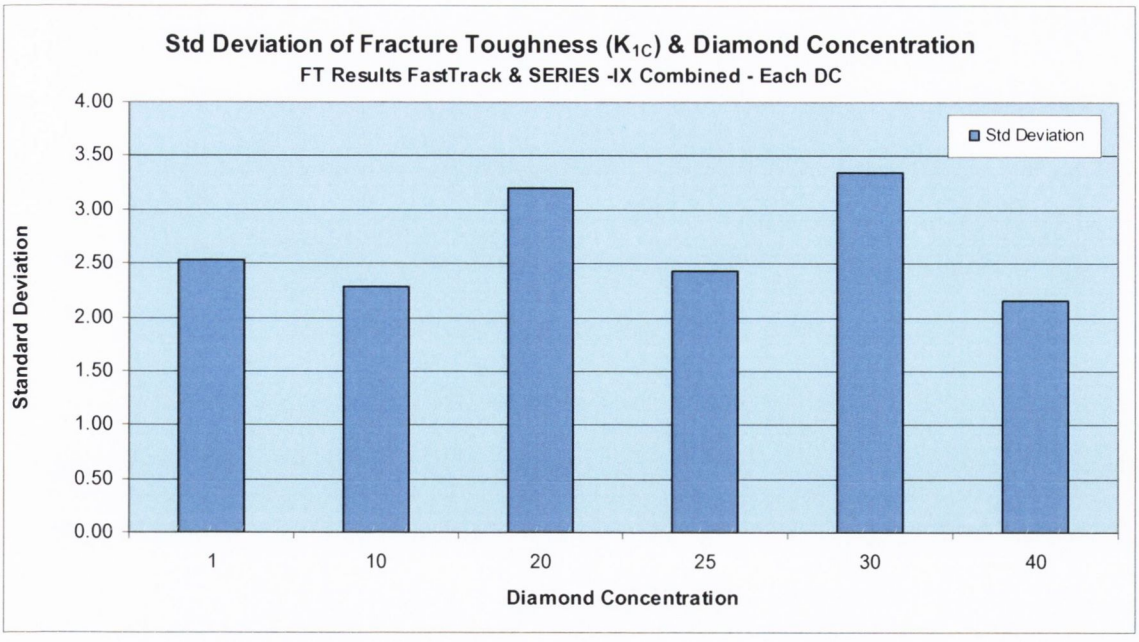

Figure 4.25. Fracture Toughness Specimen Results: Standard Deviation for the plane strain fracture toughness (K_{1C}) results for both FastTrack and SERIES-IX combined. The result for each diamond concentration is the standard deviation of the K_{1C} values making up each diamond concentration.

When the plane strain fracture toughness for each US Mesh size plotted against diamond concentration it was found again that the plane strain fracture toughness results do not change appreciably and changes are not consistent.

4.5.3. FT Specimen Test Results – Effect of Diamond Size - US Mesh & Microns

When plane strain fracture toughness K_{IC} (FastTrack & SERIES-IX) was plotted against US Mesh size at a constant diamond concentration a trend showing increasing plane strain fracture toughness with decreasing diamond size was found as can be seen in Figure 4.26. In this figure, DC20 and DC30 results are plotted with similar trends found for other diamond concentrations.

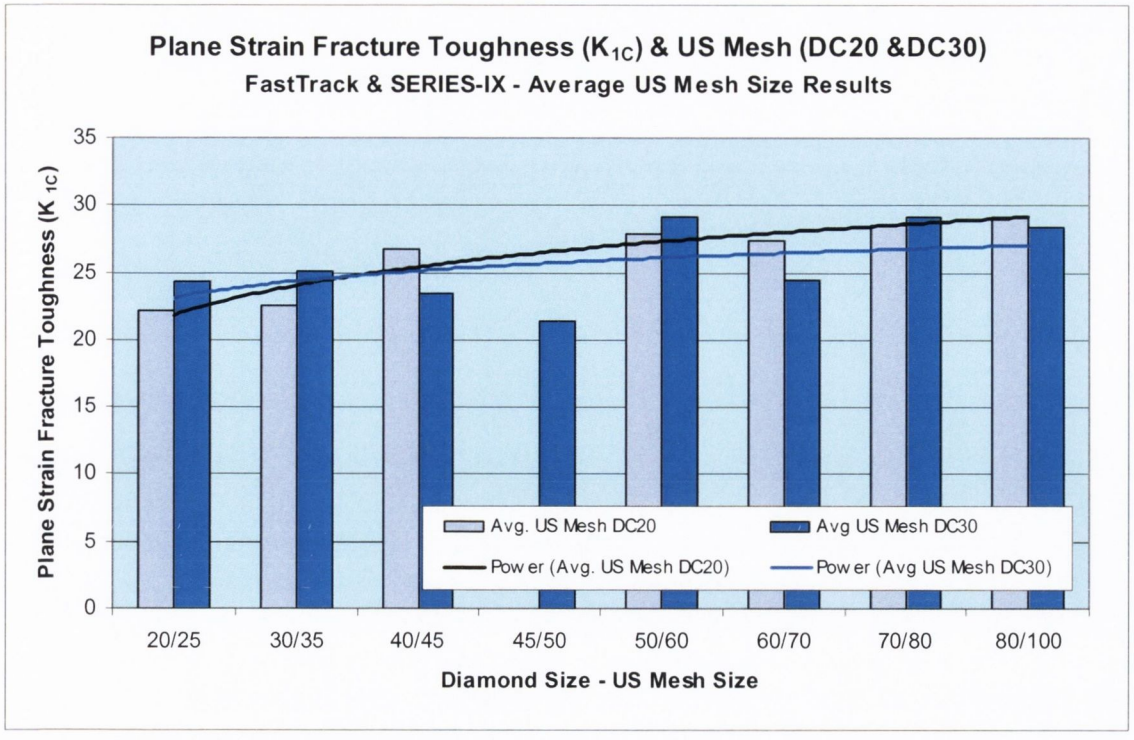

Figure 4.26. Fracture Toughness Specimen Results: Plane strain fracture toughness (K_{1C}) results for DC20 and DC30 FT specimens tested using FastTrack or SERIES-IX, showing the effect of increasing K_{1C} with decreasing diamond size is still showing significance at different diamond concentrations.

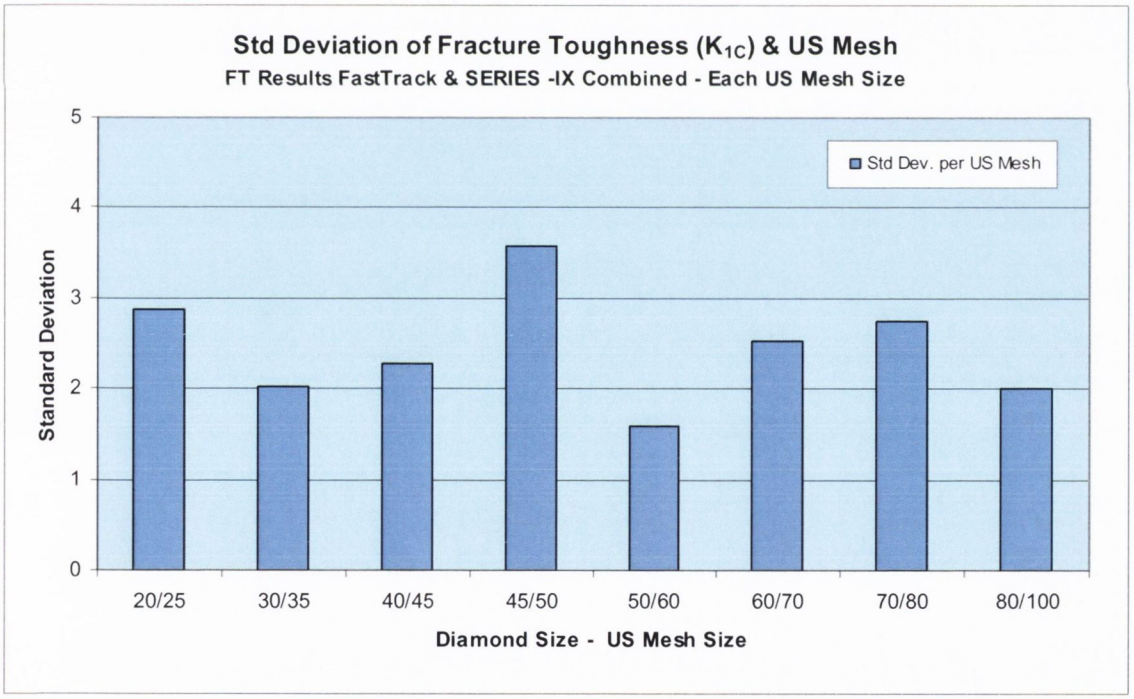

Figure 4.27. Fracture Toughness Specimen Results: Standard Deviation for each US Mesh size using all the K_{1C} results for both FastTrack and SERIES-IX combined. The result for each diamond size (US Mesh) is the Standard Deviation of the K_{1C} values of the different diamond concentrations for that size.

The variation in results between the different US Mesh sizes for the all K_{IC} results (FastTrack & SERIES-IX) is not very significant as can be seen in Figure 4.27. The standard deviation has been determined using the K_{IC} results for all the diamond concentrations for each diamond size.

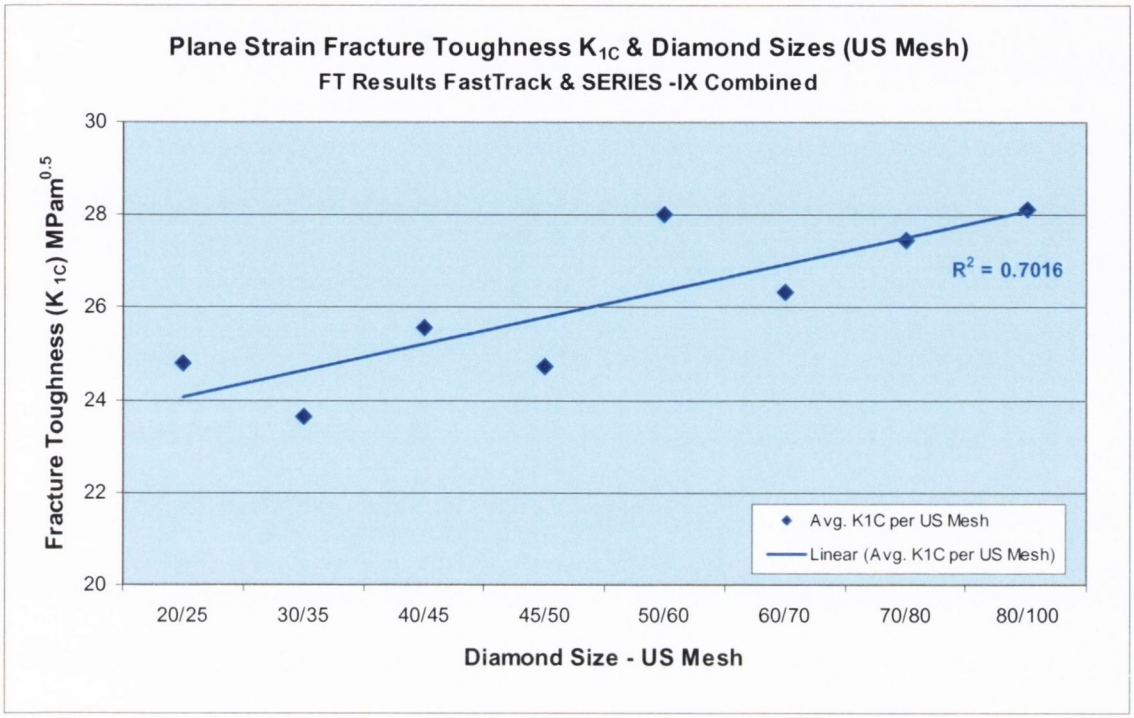

Figure 4.28. Fracture Toughness Specimen Results: Figure shows fracture toughness (K_{1C}) (FastTrack & SERIES-IX) averaged over all DCs for each diamond size plotted against US Mesh size. Correlation coefficient R = 0.84.

Figure 4.28 plots the plane strain fracture toughness (K_{IC}) for each US Mesh diamond size averaged over all the DCs. The figure shows clearly that with decreasing diamond size the plane strain fracture toughness increases. The linear trendline gives a correlation coefficient of 0.84 which is statistically significant even with a small sample size due to average results.

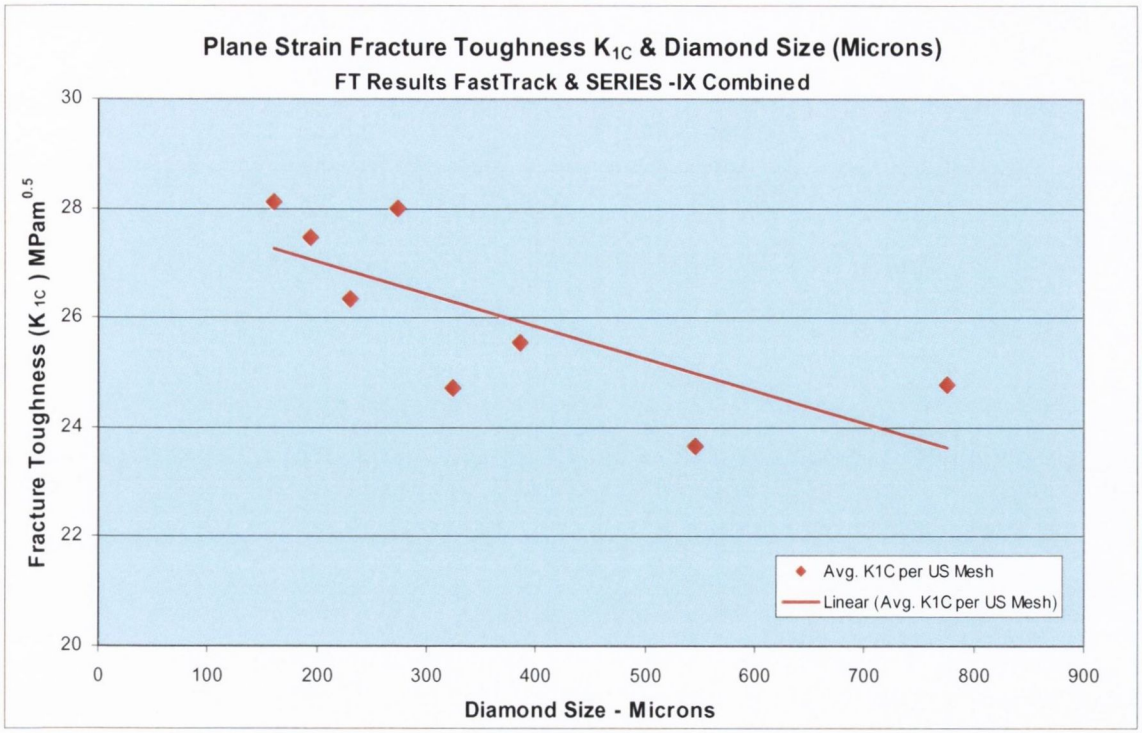

Figure 4.29. Fracture Toughness Specimen Results: Figure shows fracture toughness (K_{1C}) (FastTrack & SERIES-IX) averaged over all DCs for each diamond size plotted against diamond size in microns.

Figure 4.29 plots the value for plane strain fracture toughness (K_{IC}) for each US Mesh diamond size now measured in microns averaged over all the DCs. The figure shows clearly that with decreasing diamond size in actual linear dimension the plane strain fracture toughness increases.

4.5.4. FT Specimen Test Results – Scentis & Diamond Concentration

In Figure 4.30, the results for plain strain fracture toughness for both FastTrack and SERIES-IX determined results are plotted against the nominal diamond concentration and also the experimentally determined using the image analysis software SCENTIS. As can be seen in the figure the experimentally determined diamond concentration shows a spread of diamond concentration about the nominal value which was captured from the fracture surface of each specimen. Only the fast fracture surface was used in the measuring protocol.

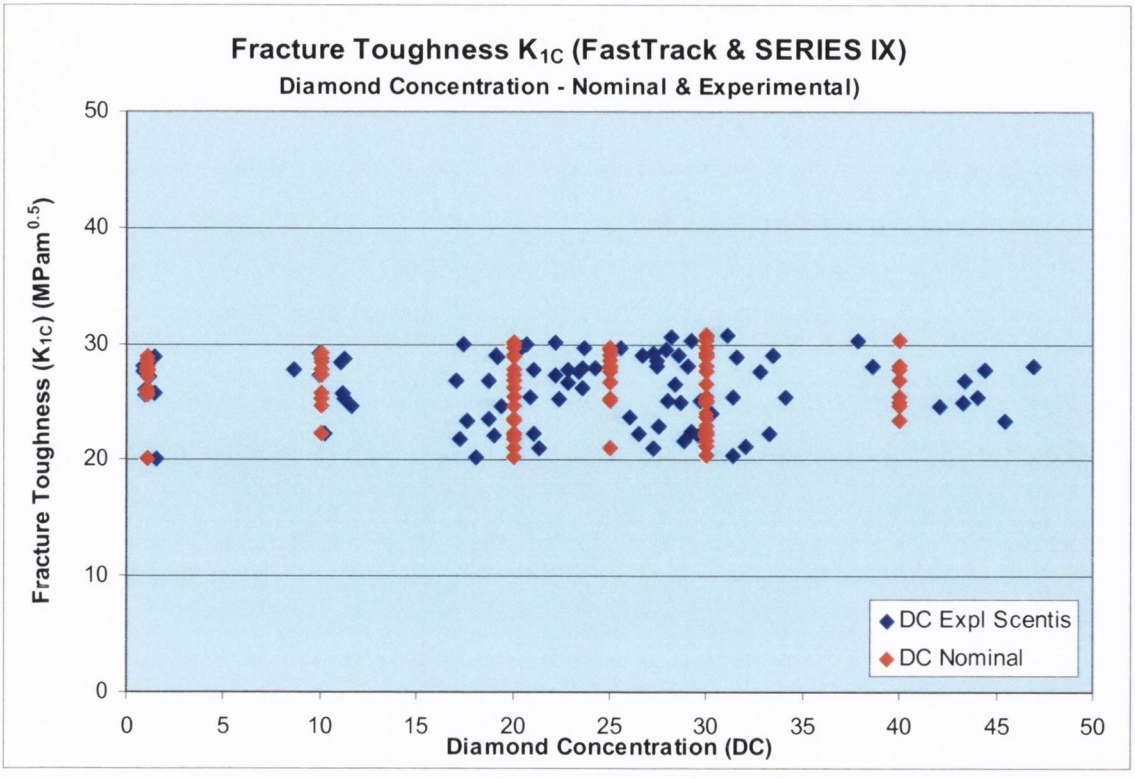

Figure 4.30. Fracture Toughness Specimen Results: Figure shows the plain strain fracture toughness (K_{1C}) (FastTrack & SERIES-IX) individual results plotted against diamond concentration. The diamond concentration used is both nominal and experimentally determined using SCENTIS image analysis software.

4.5.5. Fractography - Fracture Toughness Specimens

This section is going to show a range of different fracture surfaces that were produced during testing. Presented will be just a sample to indicate the typical variability found. Fracture surfaces that the author thinks will be interesting to the reader and that will also aid understanding the results and their analysis. Results clearly show that even with a fatigue precrack, the diamond influences the crack initiation process, possibly by increasing the crack size 'a_f' with the presence of a single diamond or diamond clustering at the crack tip.

Regarding FastTrack testing, Figure 4.31 shows a photomacrograph of DC10 40/45 with a diamond sitting at the fatigue crack tip fast fracture interface, which possibly aided the crack initiation of the 'fast-fracture' event in the fracture toughness testing.

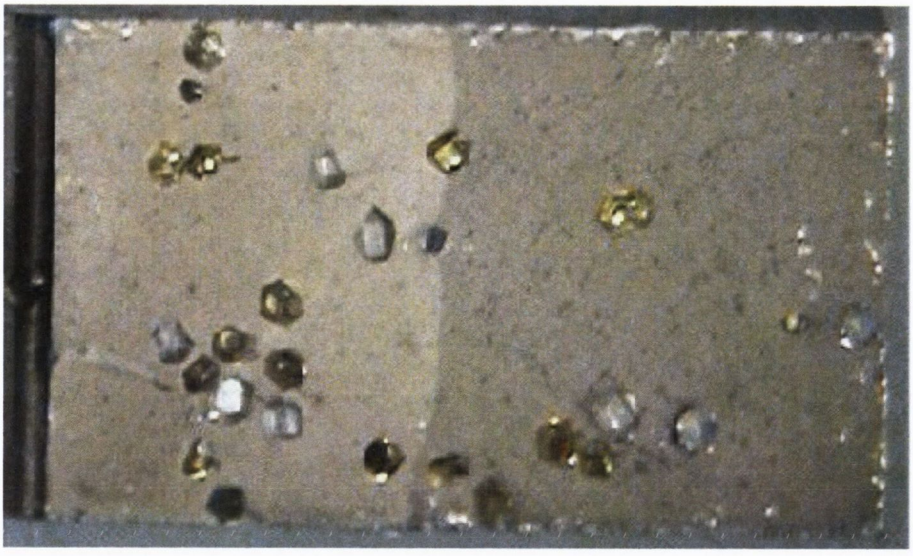

Figure 4.31. FastTrack Fracture Toughness fracture surface of specimen 40/45 DC10 showing diamonds present in the fast fracture failure surface, but with a diamond present at the interface between the fatigue crack and fast fracture. Run 19/5, mag. x 10.

Figure 4.32 shows typical clusters of diamonds that have been found on a number of fracture surfaces of fracture toughness specimens. This photomacrograph shows a FastTrack specimen of composition 30/35, DC10 showing a large cluster of coarse diamonds on the fast fracture failure surface. This specimen failed during 'bedding-in' and no fracture toughness result was determined. However what is interesting about this photomacrograph is that the fatigue crack front weaves to one side as it grew from left to right of the photomacrograph. If this fracture toughness test was tested successfully the weaving fatigue crack could possibly have invalidate the test because it could be outside the 10% allowance between shortest and longest in fatigue crack length measured from the starter crack notch on the left.

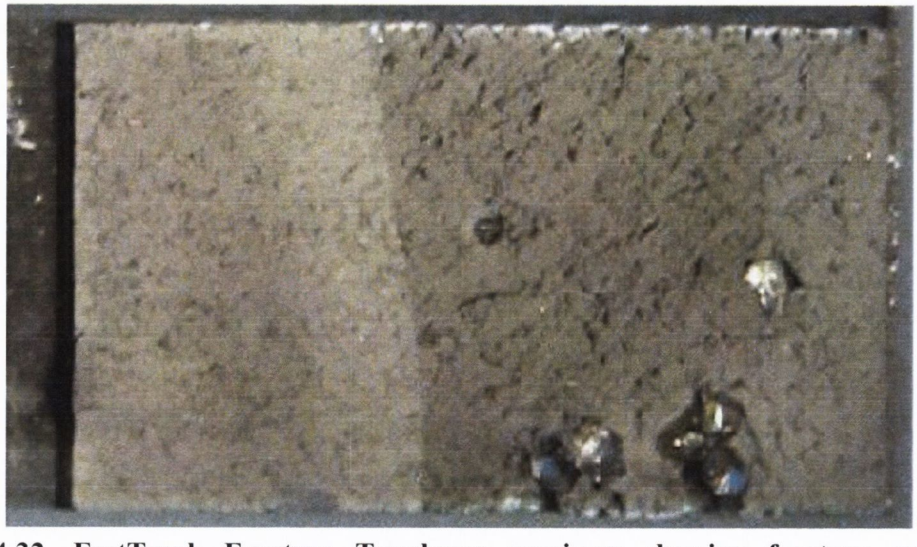

Figure 4.32. FastTrack Fracture Toughness specimen showing fracture surface of specimen 30/35 DC10 showing two diamond clusters present on the fast fracture failure surface. Run 20/6, mag. x 10.

Figure 4.33. FastTrack Fracture Toughness specimen showing fracture surface of specimen 30/35 DC30 showing diamonds present along the fatigue/fast fracture interface. Run 96/3, mag. x 10.

In Figure 4.33 large diamonds can be seen at the fatigue crack fast fracture interface which possibly could influence the crack initiation in the fracture toughness test.

Regarding the finer diamond sizes, one can see in Figure 4.34 the fracture surface of a FastTrack specimen of composition 50/60 DC30, where at the fatigue crack/fast fracture interface diamonds are present which possibly, influenced the crack initiation of the fast fracture event.

Figure 4.34. FastTrack Fracture Toughness specimen showing fracture surface of specimen 50/60 DC30 showing diamonds present along the fatigue/fast fracture interface. Run 98/1, mag. x 10.

Finally in Figure 4.35 a FastTrack specimen which failed to grow a fatigue crack can be seen. A fracture toughness test was carried out similar to that carried out using SERIES-IX method. The photomacrograph shows the complete fast fracture failure surface for a 60/70 DC25 specimen showing fine diamonds present throughout the fracture surface. There is actually a good distribution of diamond throughout the specimen, which is easier to accomplish than if for the same diamond concentration with coarser US Mesh diamond size. On the extreme left of the photomacrograph is the edm notch.

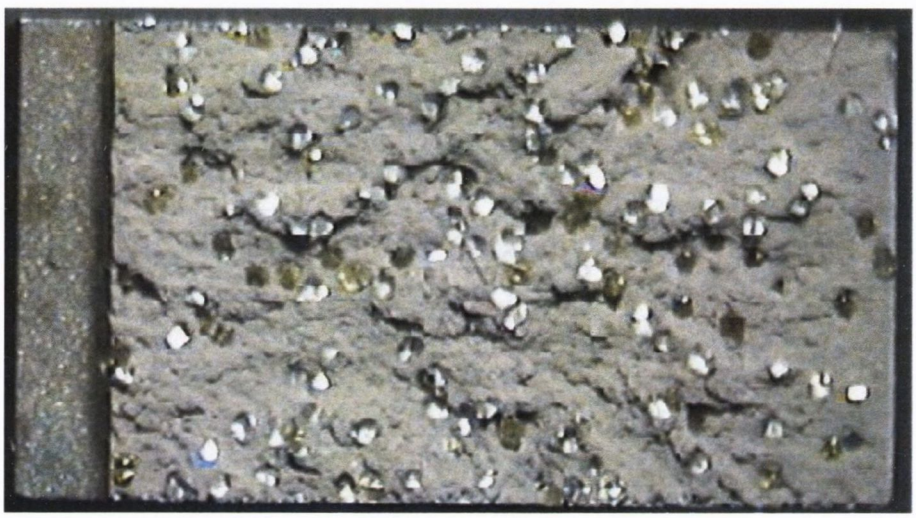

Figure 4.35. FastTrack Fracture Toughness specimen which failed to grow a fatigue crack but subsequently fracture toughness tested. The fast fracture surface of the 60/70 DC25 specimen shows diamonds present along the fracture surface. Run 78/1, mag. x 10.

4.6. Transverse Rupture Strength (TRS) Test Results

TRS results again are very similar to those found for fracture toughness. DICoMM materials show a large variability. A number of test variations were carried out which will be outlined here but also will be mentioned throughout the TRS section so that it will be clear for the reader. Firstly, TRS testing using both three-point and four-point test modes were used. However, the four-point test was discarded very quickly because the rollers were getting jammed due to the short specimen size but also premature fracture of the specimens occurred due roller alignment difficulties. So only a handful of specimens were tested using four-point bend and will not be reported here. A variation in the span (40 & 50mm) was also tried for the three-point bend test but only a relatively small number were tested. Some results were determined using an external LVDT while other results were determined using the machine actuator LVDT which is not as accurate. The reasons are that the stroke at times was limited using the external LVDT.

4.6.1. TRS Specimen Test Results – Effect of Diamond Concentration (DC)

In this section, the effects of diamond concentration on the TRS strengths of DICoMMs are reported. Included in the graphs are the TRS results for the 100%Co matrix for comparison, tested at both 40 and 50mm spans. Regarding the 100% Co matrix, only specimens tested using 50mm span are included here. No 100% Co specimens were tested at 40mm span because the hot pressing run was not consistent with the hot pressing procedure used for all the other specimens.

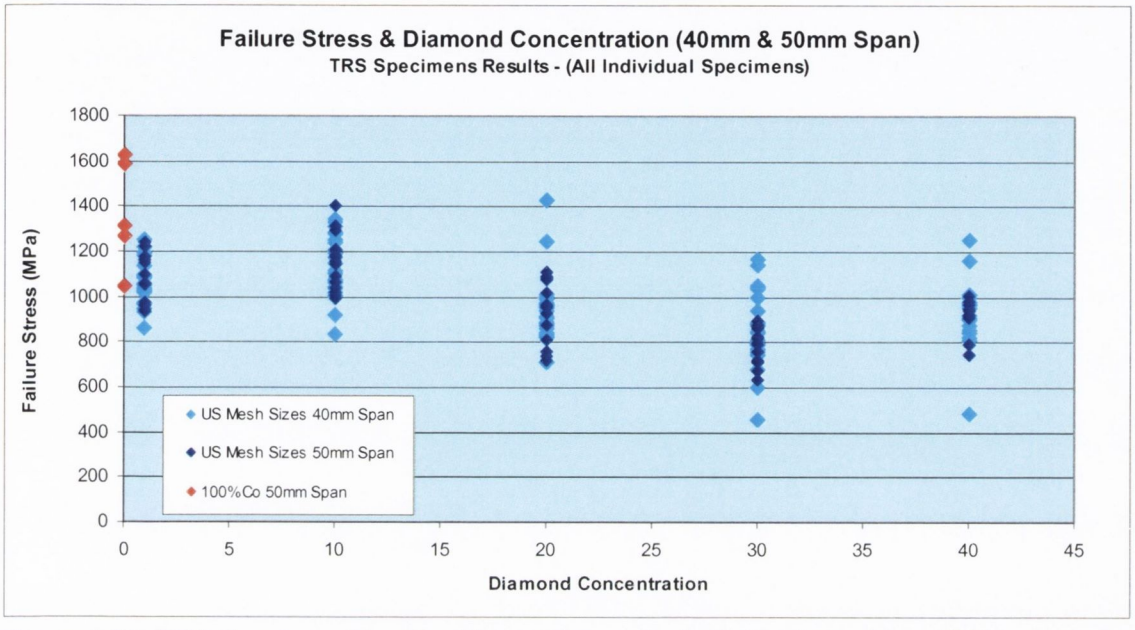

Figure 4.36. TRS Specimen Results: Figure shows the individual specimen TRS results for CoMMs (50mm Span) & DICoMMs (40 & 50mm spans) plotted against DC. The results are for each specimen for each US Mesh size and DC. CoMM specimen results shown in red.

Figure 4.36 shows the individual failure stress achieved for CoMM and DIMMs specimens for each DC. The failure stress results plotted show that DICoMMs tested using 50mm span (darker blue) do not show as much scatter as the DICoMM specimens tested using 40mm span (pale blue). However, the graphs do show the large spread found for each diamond concentration. The graph also shows the spread for the 100% cobalt specimens tested using 50mm span.

Averaging all the results for 100% cobalt and the DICoMM specimens for each diamond concentration the graph in Figure 4.37, clearly shows that with increasing diamond concentration, TRS failure stress decreases.

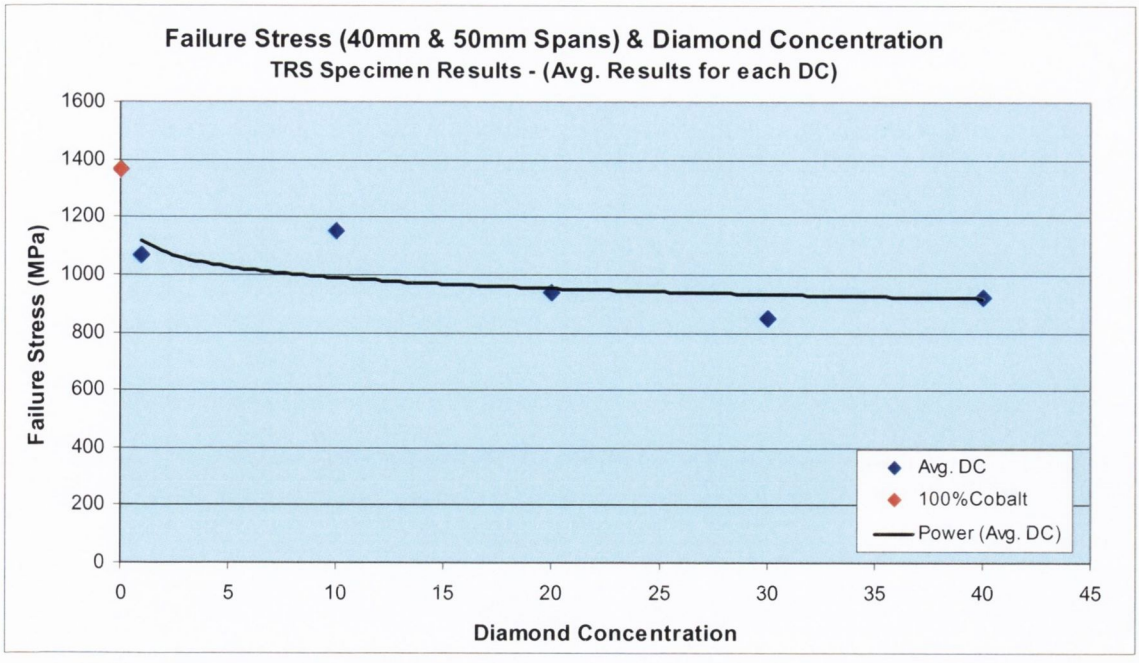

Figure 4.37. TRS Specimen Results: Average failure stress for each DC for specimens which were tested using 40mm and 50mm spans. CoMM average TRS result (50mm span) shown in red.

What is not evident in Figures 4.36 & 4.37 is how failure stress behaves with increasing diamond concentration for each US Mesh size. As an example, Figure 4.38 shows the average failure stress for 60/70 US Mesh diamond DICoMM specimens showing that as diamond concentration increases the failure stress decreases. This effect is found for all the other US Mesh sizes with some showing it clearly while others not as strongly.

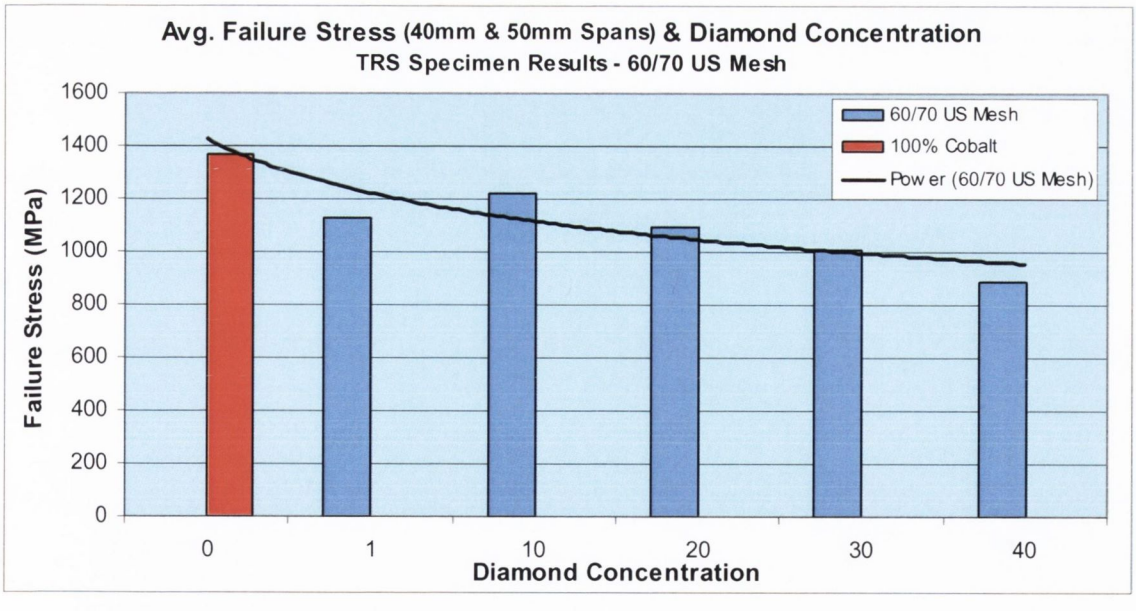

Figure 4.38. TRS Specimen Results: Figure shows the average failure stress for 60/70 US Mesh diamond DICoMM specimens showing that failure stress decreases as diamond concentration increases. CoMM average TRS result (50mm span) shown in red.

4.6.2. TRS Specimen Test Results – Effect of Diamond Size - US Mesh & Microns

Figure 4.39 shows clearly when diamond size decreases there is an increase in TRS failure stress. This effect is found for all DCs even though the effect is more pronounced in some in comparison to others the effect is still present. The effect is in keeping with that found in the literature. Another observation is that as diamond concentration increases there is a drop in TRS failure stress which was already pointed out previously.

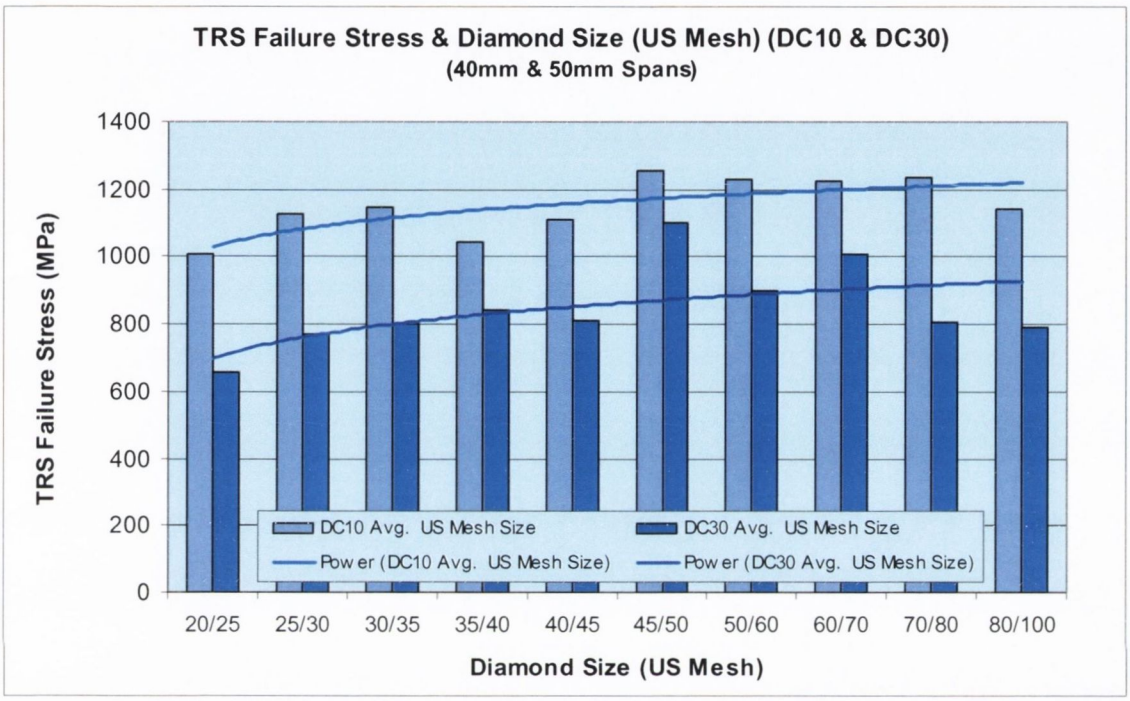

Figure 4.39. TRS Specimen Results: All DC10 and DC30 TRS specimens tested using both 40mm & 50mm spans, showing the effect of increasing failure stress with decreasing diamond size is still showing significance at different diamond concentrations.

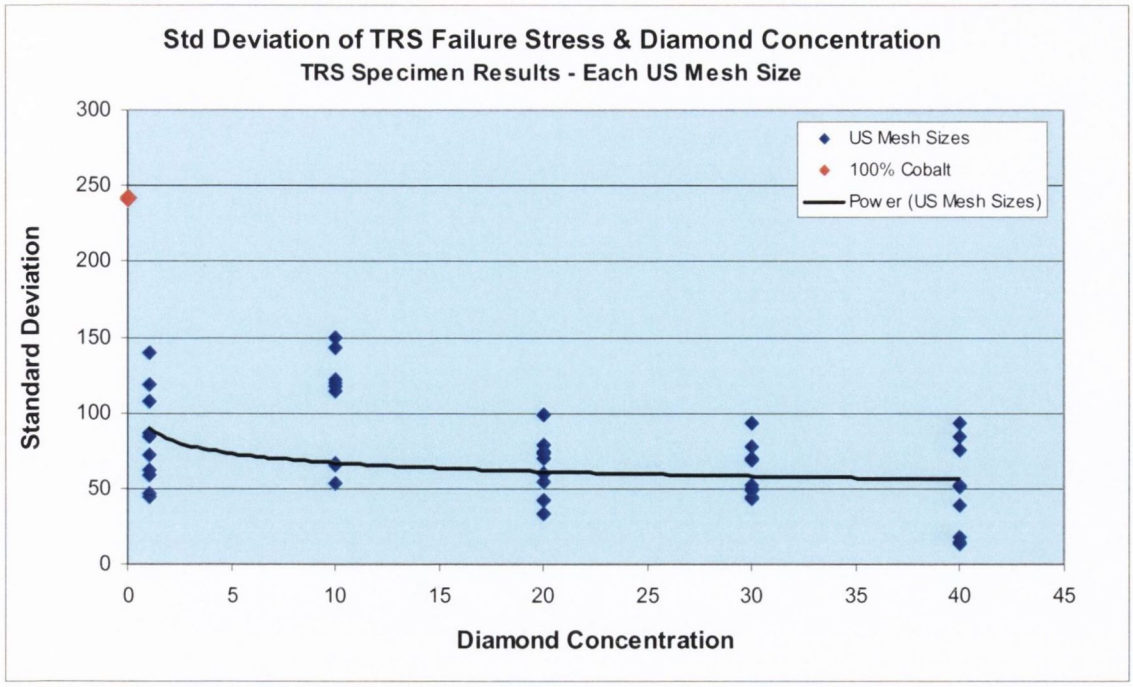

Figure 4.40. TRS Specimen Results: Figure shows the Standard Deviation for Failure Stress achieved for CoMM and DICoMMs for each DC used.

As can be seen in Figure 4.40, the standard deviation for each US Mesh size is plotted against DC. From the graph it can be seen that there is a decrease in the level of scatter with increasing DC. Within each DC, there is a slight increase in the range of scatter for DC1 and DC10 in comparison with the other DCs. Regarding the level of scatter with diamond size (US Mesh), in all DCs there is no significant increase or decrease in scatter as measured by standard deviation with diamond size discernable. Interestingly, the level of scatter for 100% cobalt is greater than any DC as seen in the figure; this value would reduce considerably if a single specimen TRS value was much lower than the other 100%Co specimen results.

4.6.3. Fractography - TRS Specimens

This section is going to show a range of photomacrographs of the fracture surfaces of the DICoMM materials found during the TRS testing. Presented will be just a sample to indicate the typical variability found. Fracture surfaces chosen are ones that the author thinks will be interesting to the reader and that will also aid understanding the analysis of the results to be presented later.

Figure 4.41 shows the fracture surface of a specimen which was hot pressed using a 30/35US Mesh size and a diamond concentration DC40. The diamond present can be seen as yellow/green in colour and also areas of showing a strong reflection are 'pull-

out's which are sockets where diamond has been pulled out of during the fracture process and would be present in the opposing fracture surface of the fractured specimen. Another interesting feature is the presence of clusters of diamonds which in high diamond concentrations and especially coarse sized US Mesh sizes are very common, however are detrimental to TRS fracture strength of the specimen.

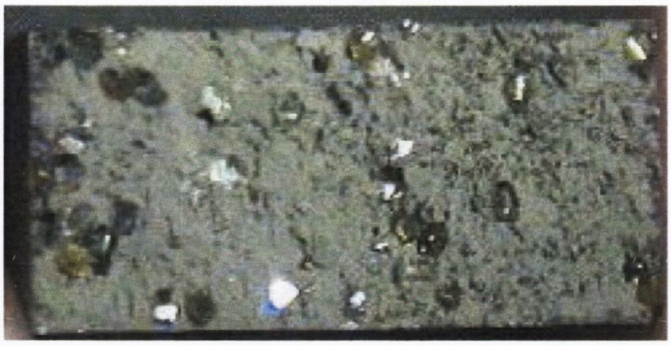

Figure 4.41. TRS specimen showing fracture surface of specimen 30/35 DC40 showing diamonds present on the fracture surface. Run 134/1, mag. x 10.

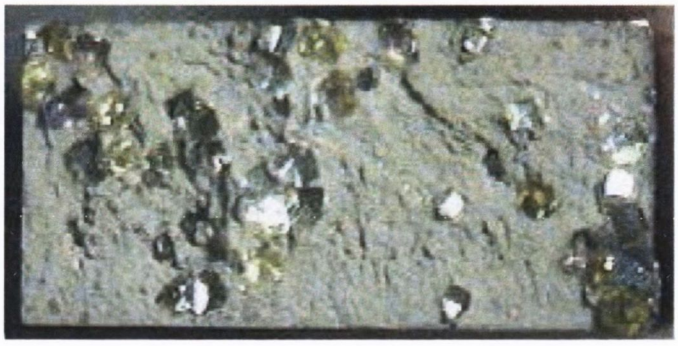

Figure 4.42. TRS specimen showing fracture surface of specimen 25/30 DC40 showing large clustering of diamonds present on the fracture surface. Run 146/2, mag. x 10.

Figure 4.42 shows a TRS fracture surface showing coarse diamonds of US Mesh size 25/30 and DC40, which have large areas of clustering present throughout the specimen. This clustering of diamond behaves as a great source of flaws to initiate fracture.

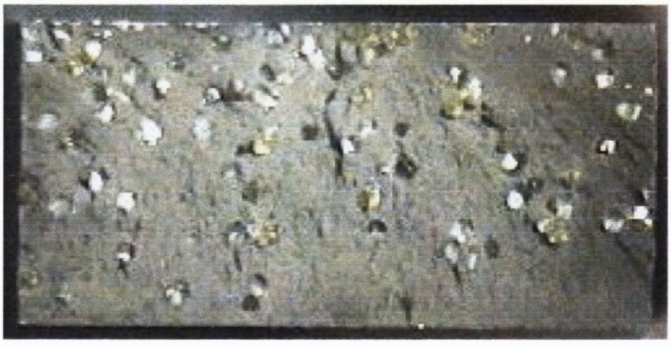

Figure4.43. TRS specimen showing fracture surface of specimen 45/50 DC30 showing large clustering of diamonds present on the fracture surface. Run 179/2, mag. x 10.

Figure 4.43 shows the fracture surface of the TRS specimen with 45/50 US Mesh diamond size and a diamond concentration of 30. It shows a good distribution of diamond throughout the fracture surface which would be expected because finer diamond generally gives better distribution than coarser diamond sizes.

4.7. Elastic Modulus Determination

The TRS specimens were used for Young's modulus and shear modulus determination, using natural frequency and ultrasonic methods. However, the reporting of these results is outside the scope of this project.

4.8. Charpy Impact (CI) Specimen Test Results

In this section, the different CI results are presented. For clarity, where impact energy or Charpy impact energy is mentioned in this work, it refers to the fracture energy absorbed by the specimen due to the impact event. It is the absorbed impact energy. As has already been described in Experimental Procedures, Chapter 3, there are different sets of CI results due to using a bench mounted 50J Zwick Charpy impact machine and a standard 300J instrumented Charpy impact machine. All of the CoMM samples were tested using the large 300J impact machine. The majority of the DICoMMs specimens were tested using the small 50J machine. Forty five (45) DICoMM specimens were tested using the Instron 300J Charpy machine and one hundred & seventy eight (178) were tested using the 50J Zwick machine.

4.8.1. Impact Specimen Test Results – 300J Charpy Machine

As already stated above only 45 DICoMM specimens were tested using the 300J machine and only 70/80 DC1 where three specimens were tested, the other DICoMMs had just one specimen per US Mesh size and DC tested. No specimens for 60/70 DC40 and 80/100 DC40 were tested using the 300J machine. All the CoMM specimens four (4) in total; were tested using the 300J machine.

4.8.1.1. Impact Specimen Test Results – 300J Charpy – Effect of DC

Figure 4.44 shows the individual impact energy results plotted against diamond concentration, included in the plot are the results for the 100% cobalt specimens. The trendline drawn is a power law showing as DC increases impact energy decreases, which is similar to trends found in the literature for PMMC materials.

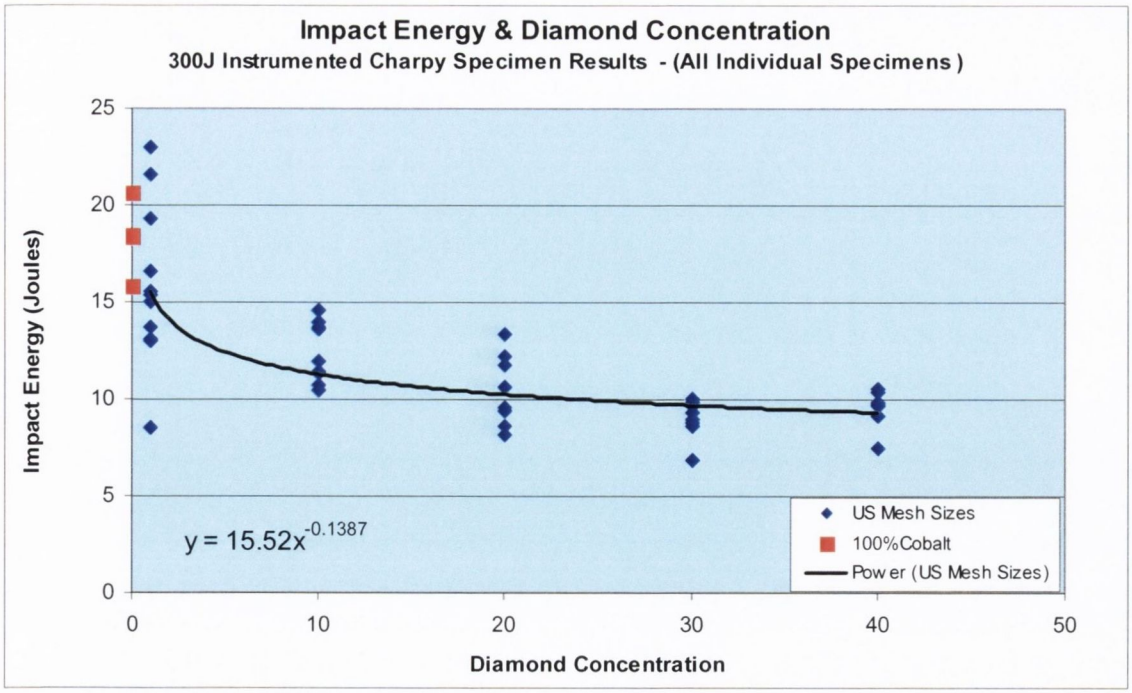

Figure 4.44. Charpy Impact Specimen Results: Impact energy where a selected sample were tested using a 300J Instron Charpy pendulum machine. This figure is for individual results.

In Figure 4.45, this graph represents those specimens which were tested using the Instron 300J Instrumented Charpy machine. Each result is the averaged value for each DC and clearly shows that with increasing DC, impact energy decreases. The next section will examine the effect of diamond size (US Mesh) on impact energy at a constant DC.

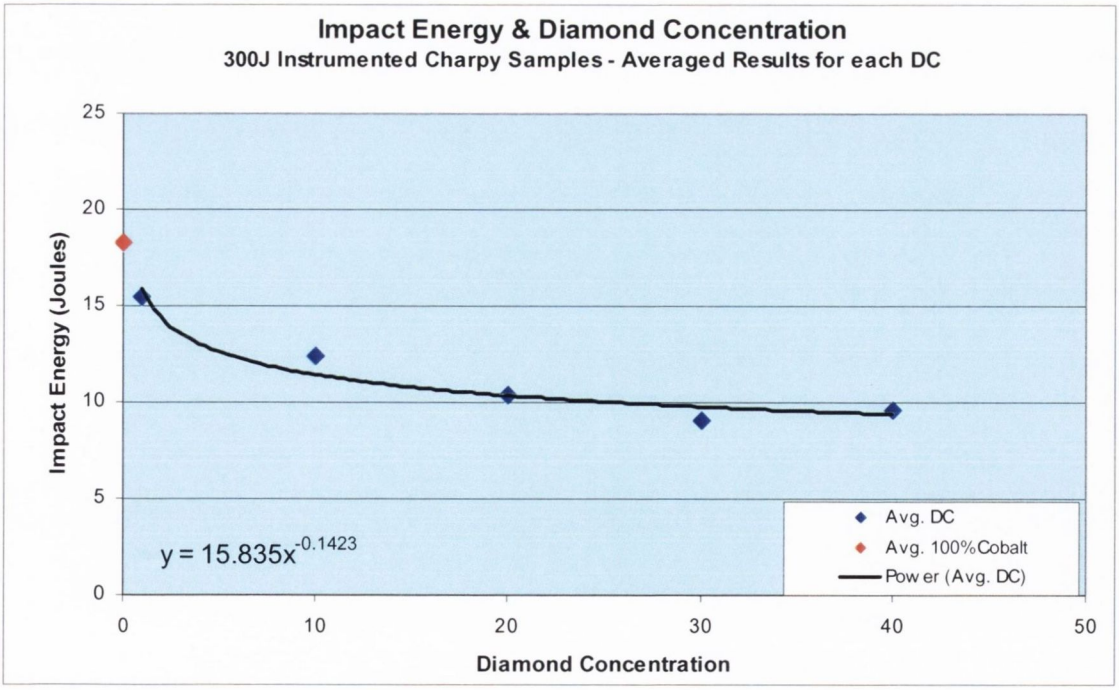

Figure 4.45. Charpy Impact Specimen Results: Average Impact energy for each DC for specimens which were tested using the instrumented 300J Instron machine.

4.8.1.2. Impact Specimen Test Results - 300J Charpy – Effect of Mesh Size

The impact energy plotted against diamond size (US Mesh) at a constant DC an interesting graph is produced. Figure 4.46 shows the results taken from Figure 4.44 for DC1 and show that as diamond size reduces or gets finer, the impact energy increases. Again, the results are for individual specimens even though the legend indicates average US Mesh size. For each US Mesh size only a single specimen was tested except for 70/80 size which is an average of 3 specimens.

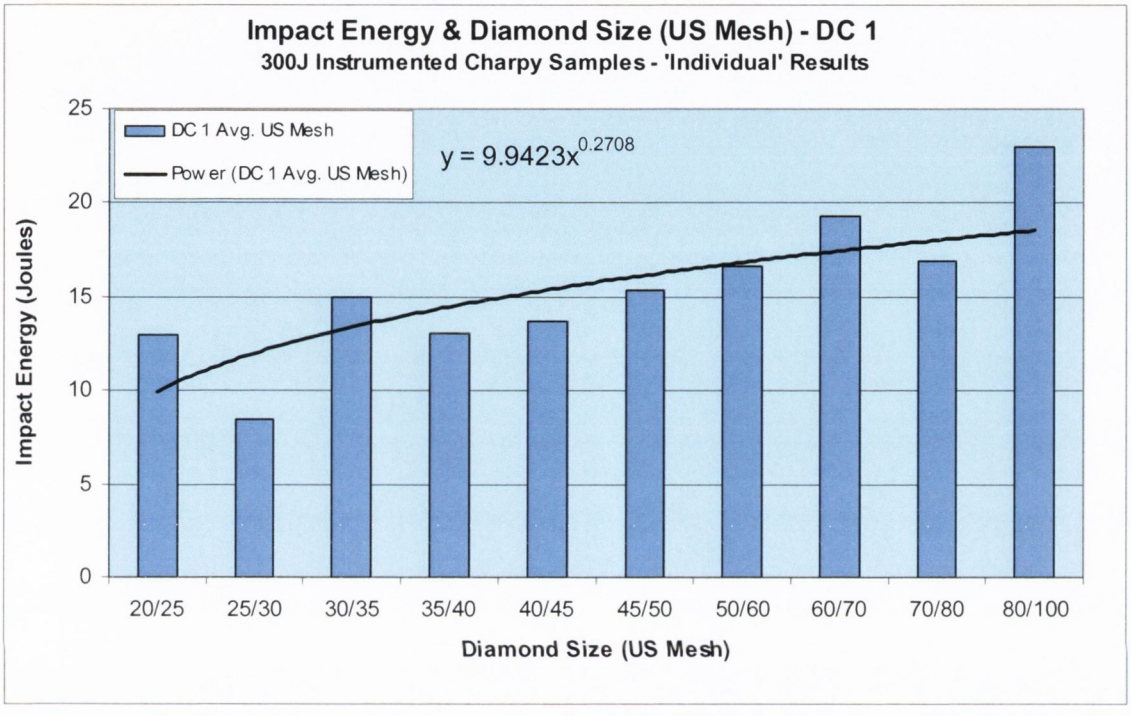

Figure 4.46. Charpy Impact Specimens Results: DC1 impact specimens tested using 300J machine, showing increasing impact energy with finer sized diamond.

When other DCs are plotted, the effect is not as significant as can be seen in Figure 4.46, however, most of these results are just for one specimen per US Mesh size and so the large variation found in these type of materials shows when single specimen results are plotted. In Section 4.8.2 the full set of CI results (50J & 300J) are used and the effect of decreasing diamond size and impact energy is more evident.

4.8.2. Impact Specimen Test Results – 50J & 300J Charpy Machines

In this section all of the CI results are reported, which includes the specimens tested using the 50J & 300J Charpy impact machines. The effects of diamond concentration and diamond size on the resulting impact energies for DICoMM materials and 100%cobalt are reported.

4.8.2.1. Impact Specimen Test Results – 50J & 300J Charpy – Effect of DC

Figure 4.47 shows the individual impact energy results plotted against diamond concentration, included in the plot are the results for the 100% cobalt specimens. The trendline drawn is a power law showing as DC increases impact energy decreases, which is similar to trends found in the literature for PMMC materials. The DC1 does show more scatter in impact values than the other DCs.

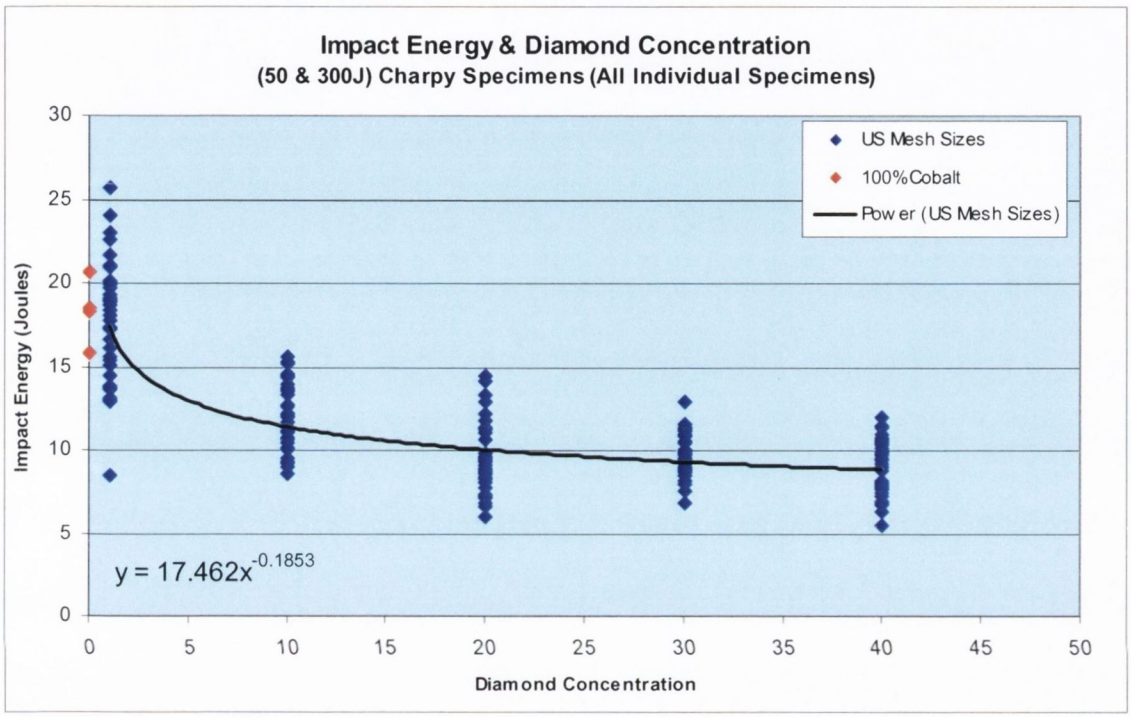

Figure 4.47. Charpy Impact Specimen Results: Impact energy for all the CI specimens (50J & 300J) plotted against diamond concentration. The figure is for individual results for each US Mesh size. The individual 100% Cobalt specimen values are also plotted in red.

In Figure 4.48, this graph represents all the CI specimens (50J & 300J) averaged for each DC and it clearly shows that with increasing DC impact energy decreases. This is in keeping with that found in the literature for PMMC materials.

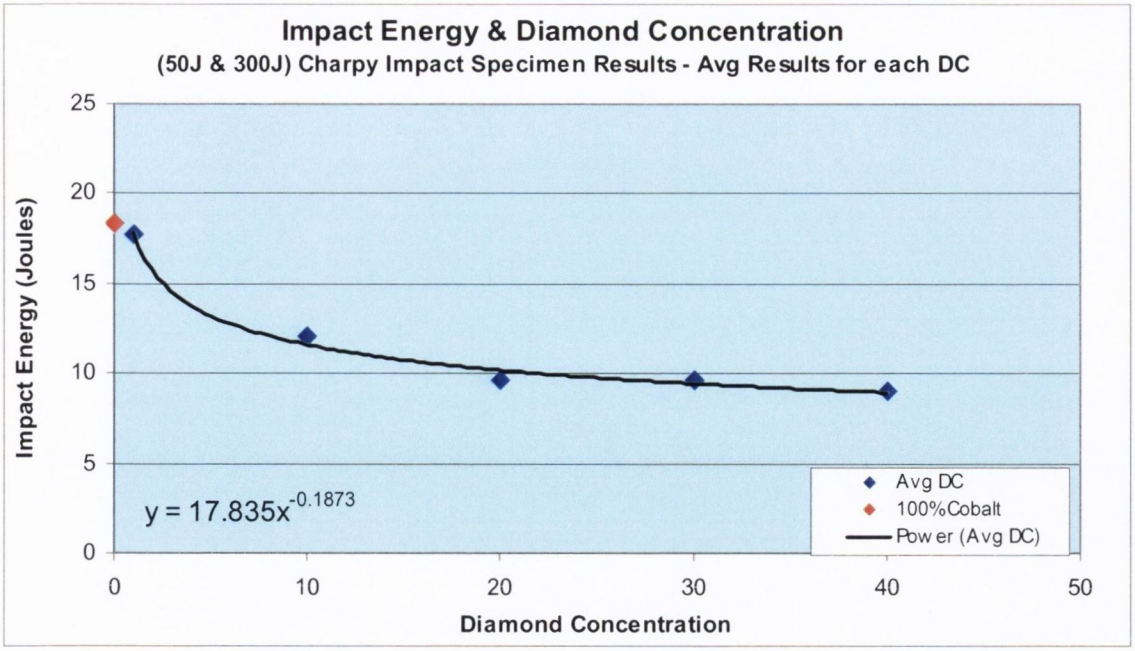

Figure 4.48. Charpy Impact Specimen Results: Figure shows the averaged impact energies for all the CI specimens (50J & 300J) plotted against diamond concentration. The averaged 100% Cobalt is also plotted.

4.8.2.2. Impact Specimen Test Results –50J & 300J Charpy – Effect of Mesh Size

In Figure 4.49 where all the impact specimens tested using either the 300J or 50J machines for DC10 and DC40 are plotted, shows that as diamond size gets finer an increase in impact energy is found, and this effect is shown to occur for the other diamond concentrations. There is a definite increase found for DC40, however the increase in DC10 is not as pronounced.

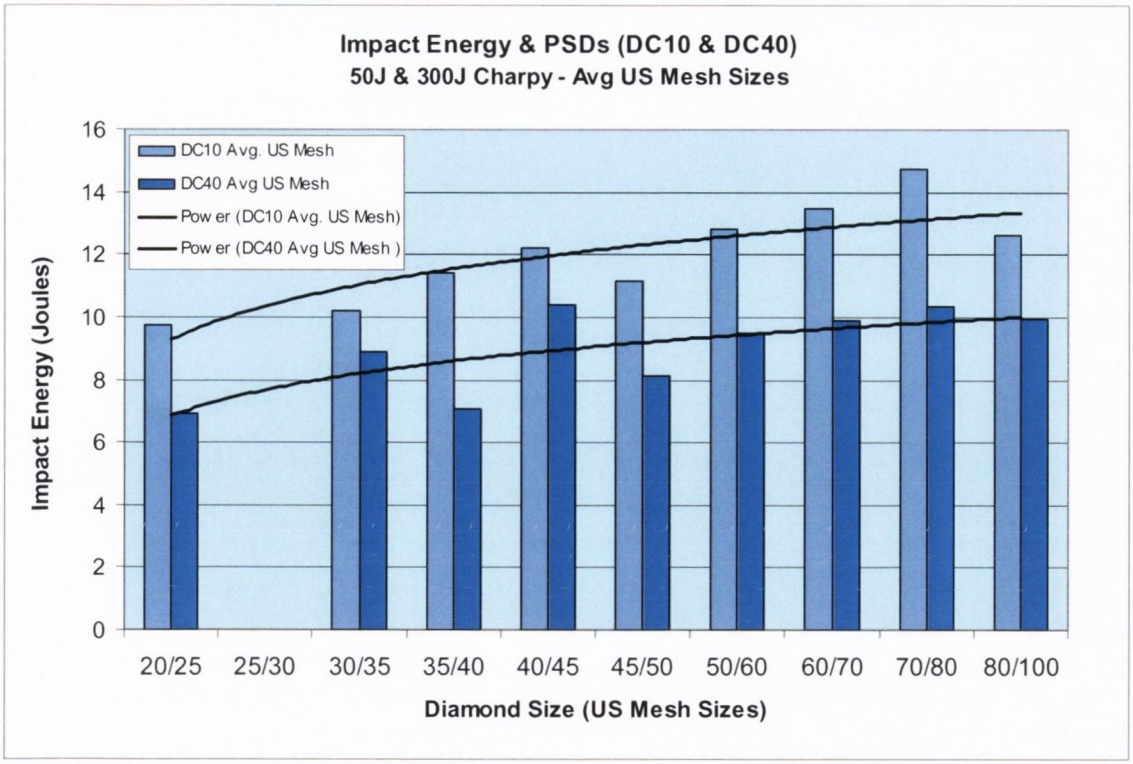

Figure 4.49. Charpy Impact Specimen Results: All DC10 and DC40 impact specimens tested using 50J or 300J machines, showing the effect of increasing impact energy with decreasing diamond size is still showing significance at different diamond concentrations.

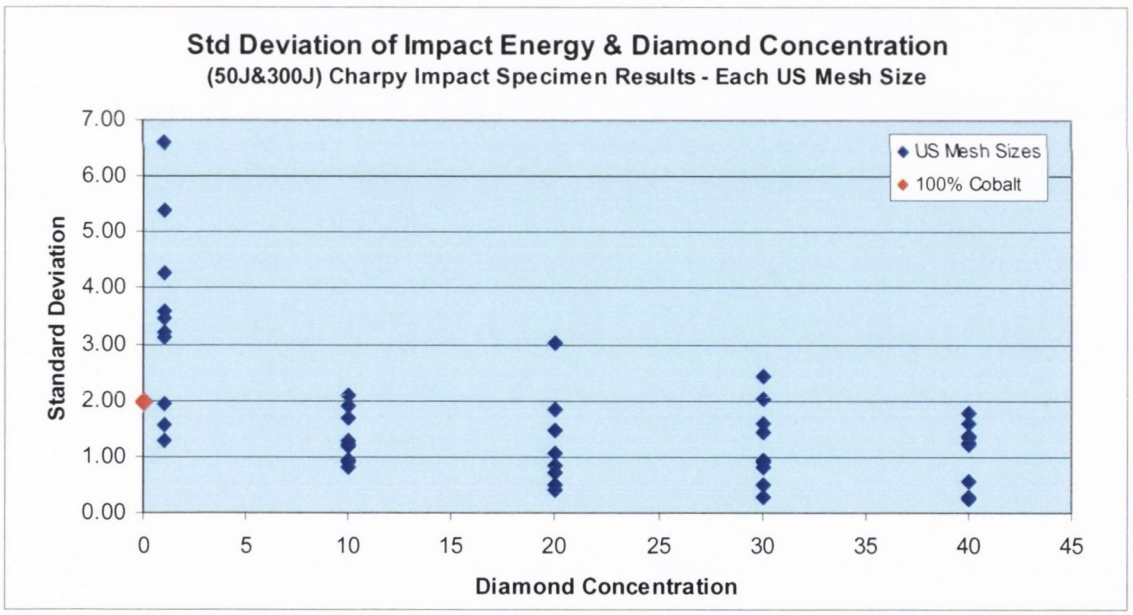

Figure 4.50. Charpy Impact Specimen Results: Figure shows the Standard Deviation for Impact Energy achieved for CoMM and DICoMMs for each DC used.

Variation in impact energy results due to diamond concentration can be seen by plotting a graph of standard deviation and diamond concentration as can be seen in Figure 4.50. In this graph it can be seen that for DC1 there is a large variability in impact energies for some of the US Mesh sizes only.

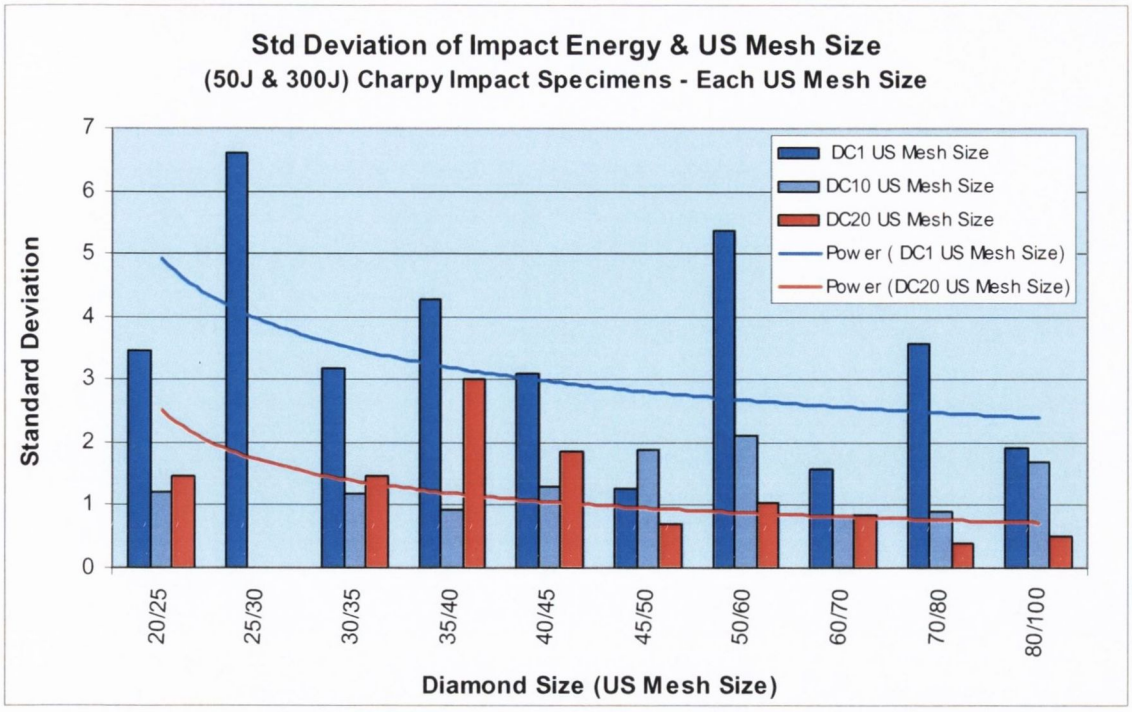

Figure 4.51. Charpy Impact Specimen Results: Figure shows the Standard Deviation for Impact Energy achieved for DICoMMs for DC1, DC10 and DC20 used.

Figure 4.51 shows the standard deviations plotted against a range of US Mesh sizes for a number of diamond concentrations, it can be seen that for DC1 and DC20 there is decreasing trend in standard deviation with decreasing diamond size, from 20/25 to 80/100. However, this is trend is not found for the other DCs e.g. DC10. However, if more specimens were tested the trend for decreasing variability with decreasing diamond size may be evident.

4.9. Erosive Wear Test Results

The results outlined show the effects of pressure, angle of incidence, US Mesh size and DC. The results clearly show that DC and US Mesh size affect the erosion resistance of DICoMM specimens. Also, pressure and angle of incidence have a significant effect on the erosion rates of all combinations of DICoMM samples.

The test results from DC10 specimens at a pressure of 3bar and angle of incidence of 15° plotted in Figure 4.52 show that the coarser diamond sizes, 30/35 and 40/45 have better erosion wear resistance.

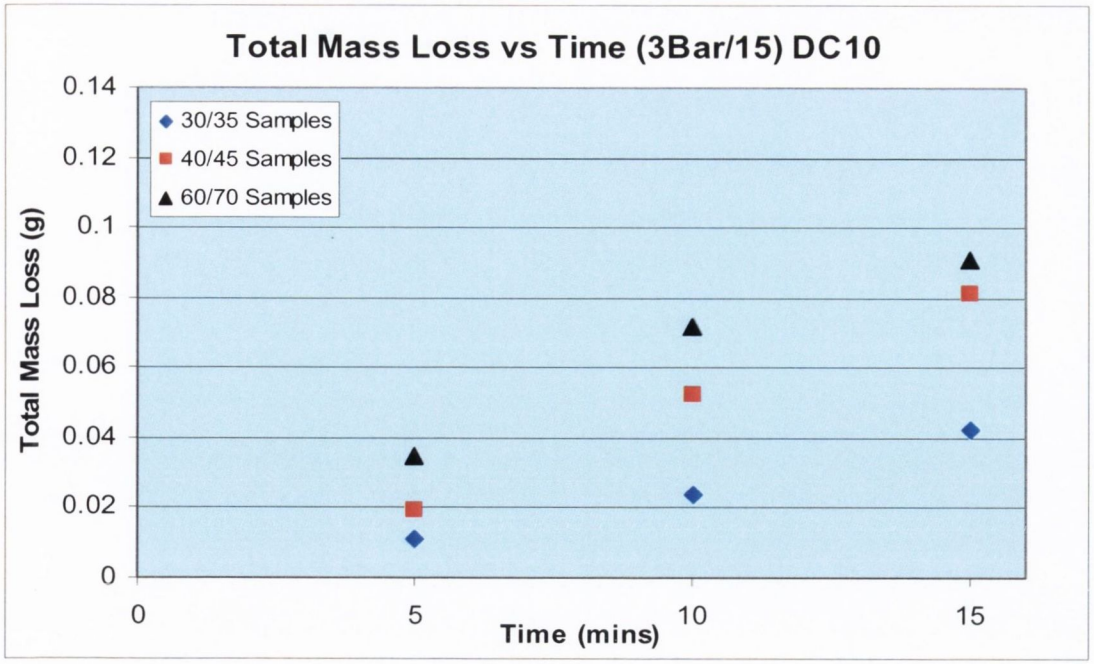

Figure 4.52. DC10 Total Mass Loss versus Time, 3bar/15°.

However in Figure 4.53, when the pressure/angle is increased to 5bar/35° the results are completely reversed, with the finer size showing better erosion resistance.

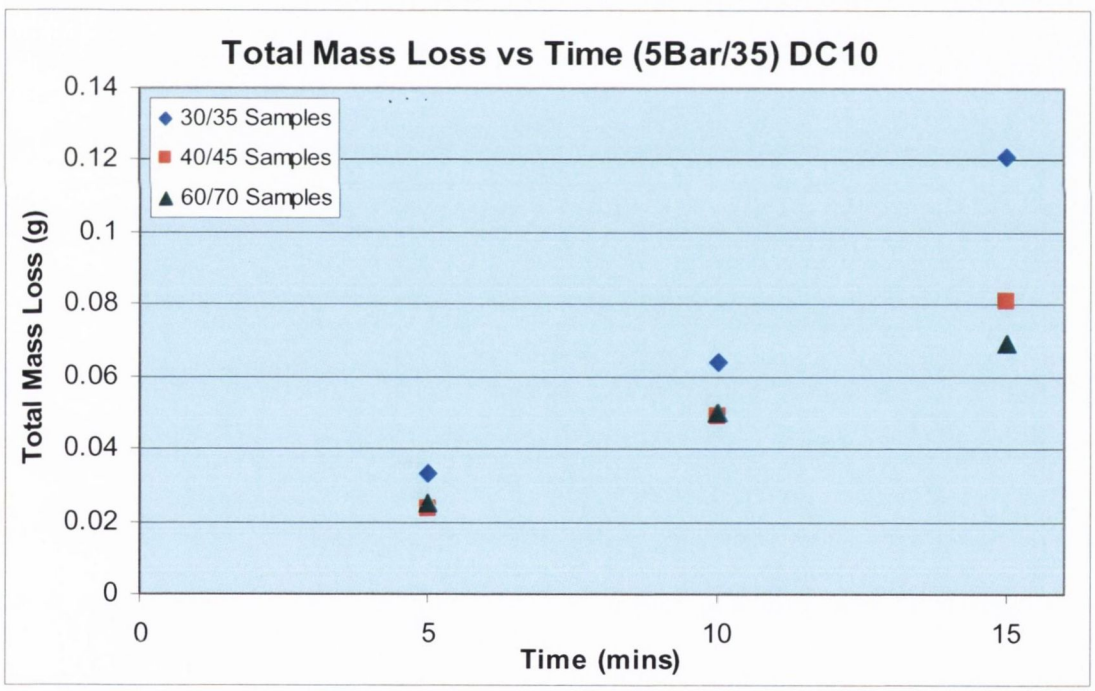

Figure 4.53. DC10 Total Mass Loss versus Time, 5bar/35°.

In Figure 4.54, using a pressure of 3bar at an angle of 15°, it shows that increasing diamond concentration from DC10 to DC30 increases its wear resistance. Also, for each DC, the finer diamond (60/70) shows less wear resistance than the coarser 40/45 size.

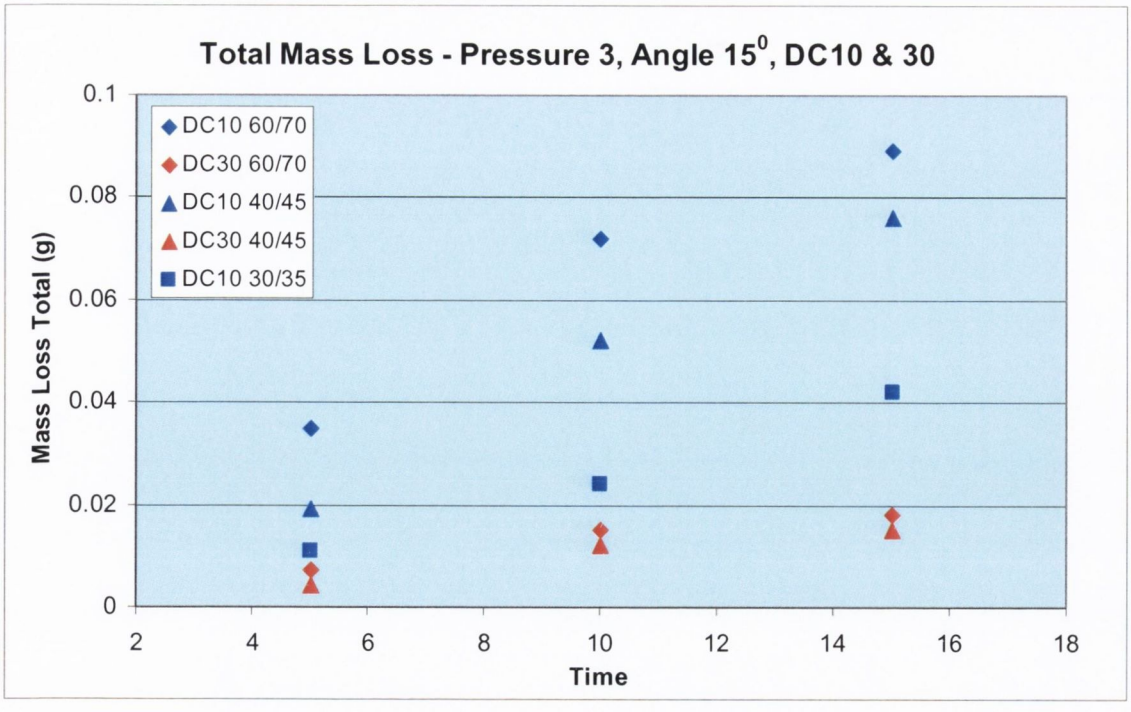

Figure 4.54. Total Mass Loss versus Time: DC10 & DC30, 30/35, 40/45 & 60/70 @ 3bar/15°. DC30 30/35 is missing due to experimental error.

However, when higher pressures (6bar) and steeper angles (45°) are used, the coarser diamond 30/35 sample shows the greatest erosive wear as can be seen in Figure 4.55.

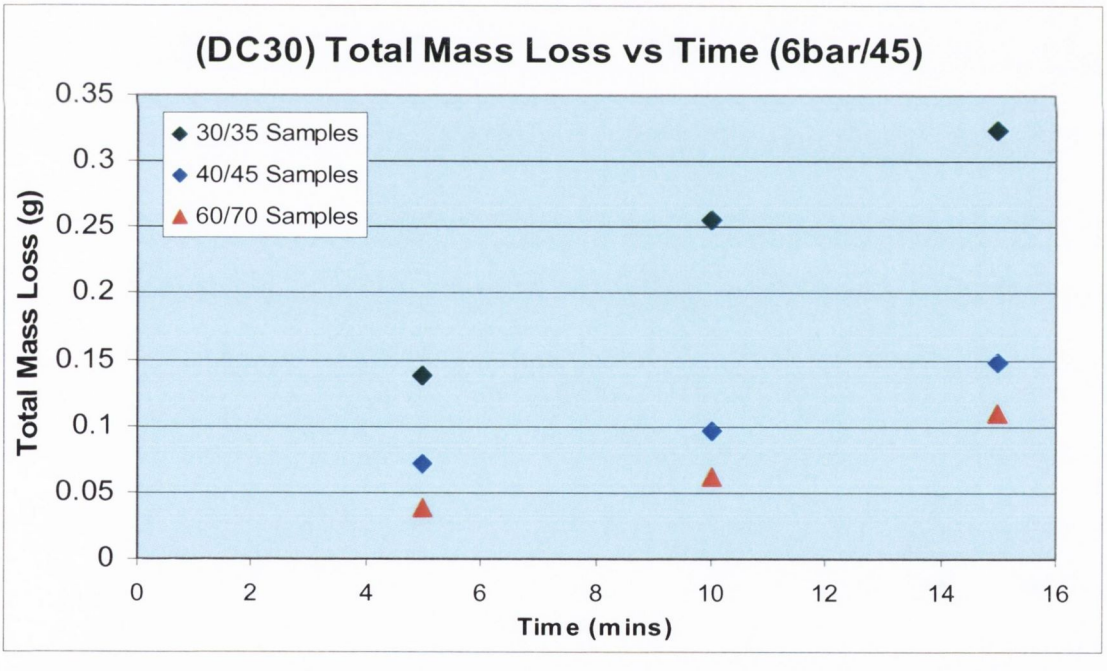

Figure 4.55. DC30 Total Mass Loss versus Time: 30/35, 40/45 & 60/70 @ 6bar/45°.

In Figure 4.56, it shows both diamond concentrations, DC10 & DC30 for the three US Mesh sizes. As already explained in Figure 4.55, at a high pressure and steep angle, coarser diamond shows higher erosive wear than finer diamond as can be seen with US Mesh size 60/70.

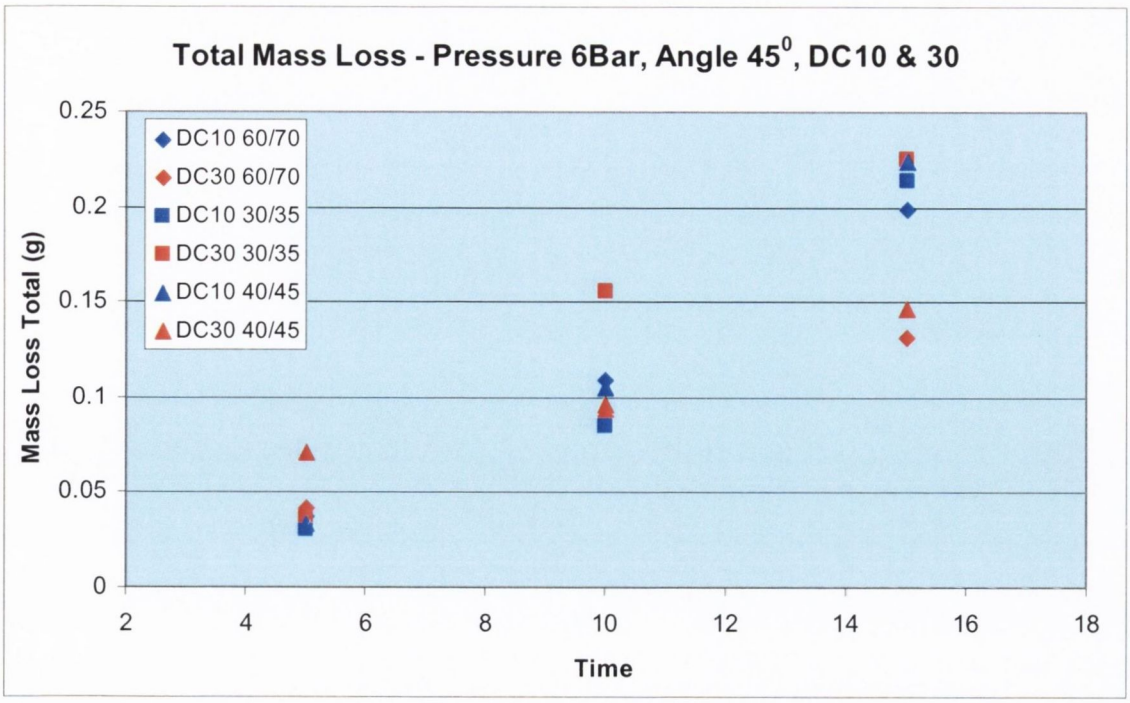

Figure 4.56. DC10 & DC30 Total Mass Loss versus Time: 30/35, 40/45 & 60/70 @ 6bar/45°.

As pressures and angles reduce erosive wear reduces for all diamond sizes and diamond concentrations. Also as said above, steep angles and high pressures the coarser diamond experiences more erosive wear, but as pressure and angles reduce there is a switch where finer diamond experiences more erosive wear than the coarser diamond as can be seen in Figures 4.57 and 4.58.

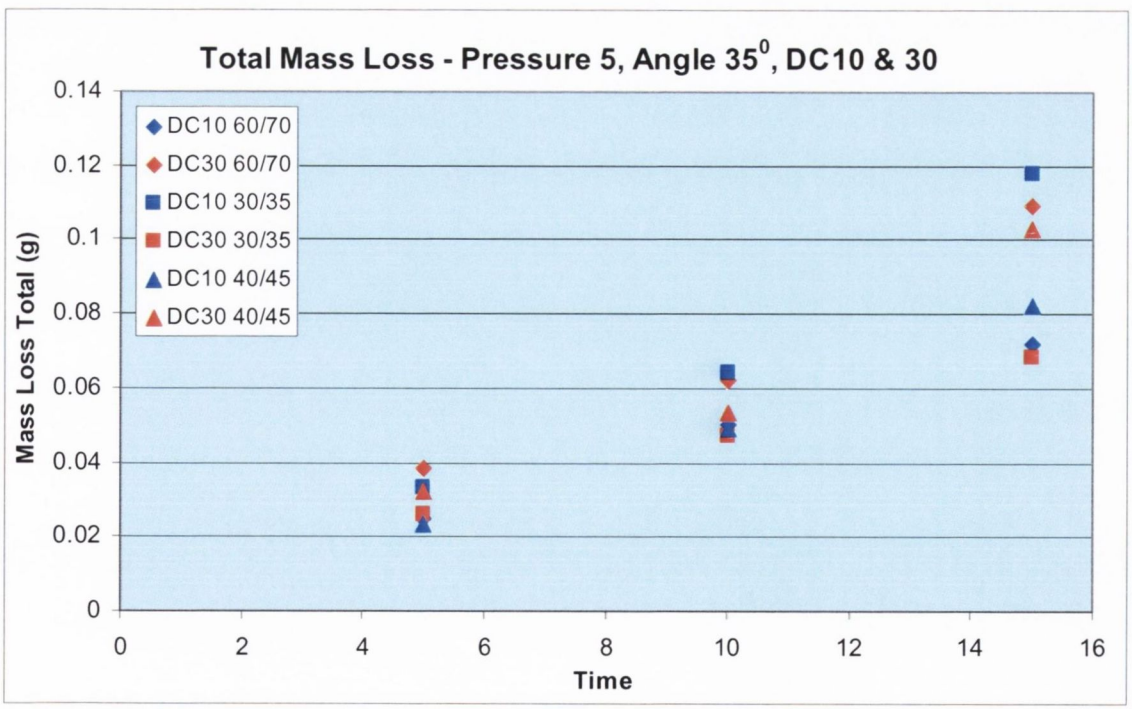

Figure 4.57. DC10 & DC30 Total Mass Loss versus Time: 30/35, 40/45 & 60/70 @ 5bar/35°.

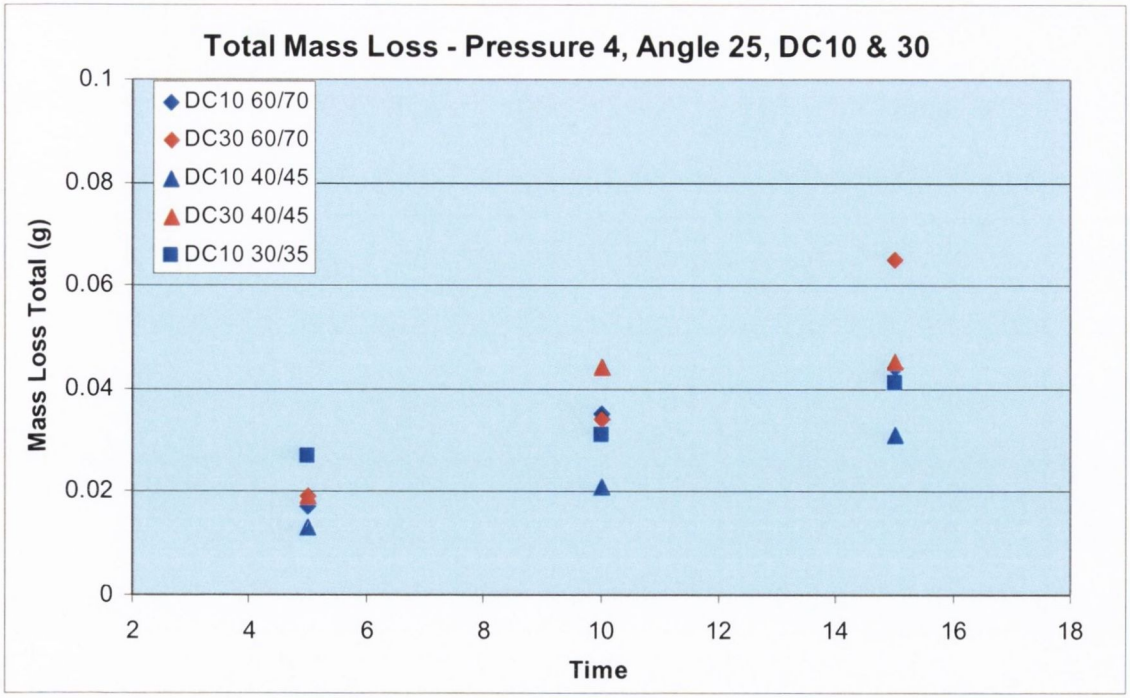

Figure 4.58. DC10 & DC30 Total Mass Loss versus Time: 30/35, 40/45 & 60/70 @ 4bar/25°. DC30 30/35 is missing due to experimental error.

4.9.1. Erosive Wear Surface Photomacrographs

Figures 4.59 and 4.60 show the typical erosion wear patterns found on the DICoMM specimens tested using the erosion apparatus as described in Chapter 3, Experimental Procedures. The wear patterns with the characteristic comet tails are typical of those found on diamond impregnated metal segments on saw blades as seen on the photomacrograph by Liao et al. [54] as seen in Chapter Two, Literature Review. The erodent passes from right to left of the photomacrograph in the figure. In Figure 4.59 shows a test specimen which had been eroded for an extended period of time of three hours, and the typical wear patterns can be seen, especially the comet tails which have formed around the diamond crystals.

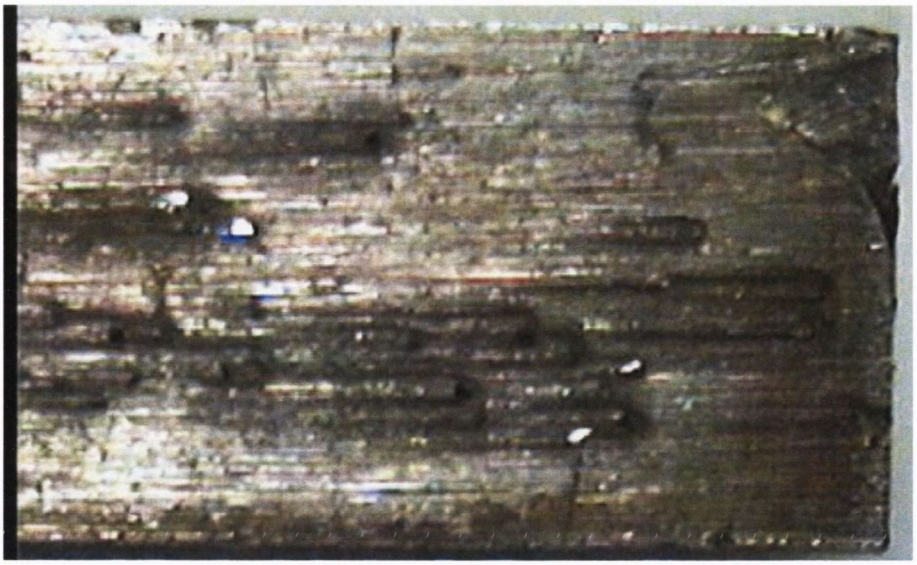

Figure 4.59. Worn surface of DICoMM test specimen due to erosion showing comet tail formation around diamonds on surface of specimen.

Figure 4.60 shows the same specimen seen in Figure 4.59 at a slightly higher magnification, 20x. The erosion of the metal around the diamond crystals can be seen clearly, with comet tail formation on the leeward side of each diamond crystal, typical of that found on a saw blade segment surface.

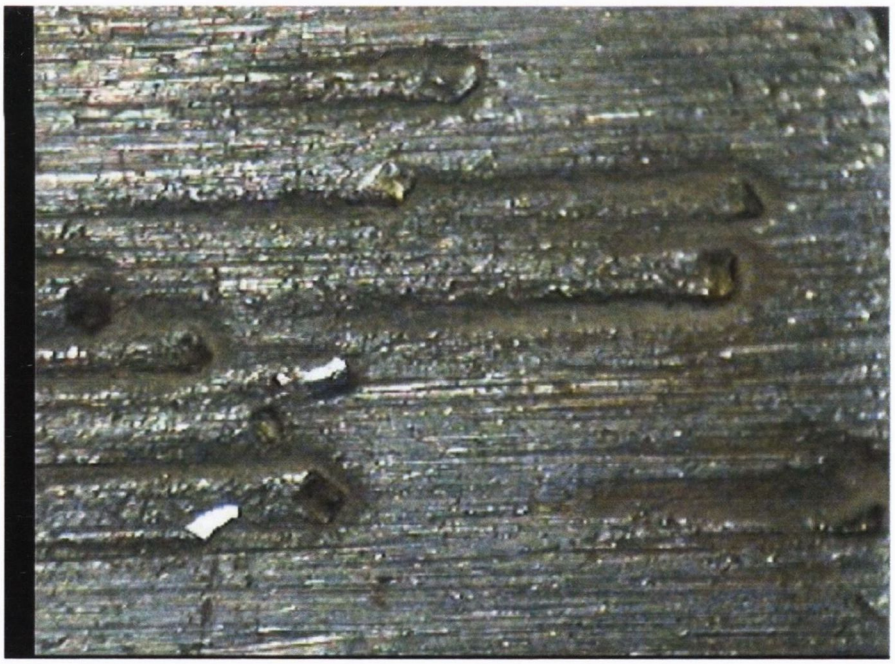

Figure 4.60. Worn surface of DICoMM test specimen due to erosion showing comet tail formation around diamonds on the surface of specimen.

Figure 4.61 shows a photomacrograph of a specimen magnified to x150, clearly showing the eroded metal surface and the two diamond crystals with a comet tail forming to the top of each. The eroding grit passes from the bottom on the SEM photomacrograph

image to the top of the photomacrograph. The erosion wear impacts can be seen clearly too on the metal surface.

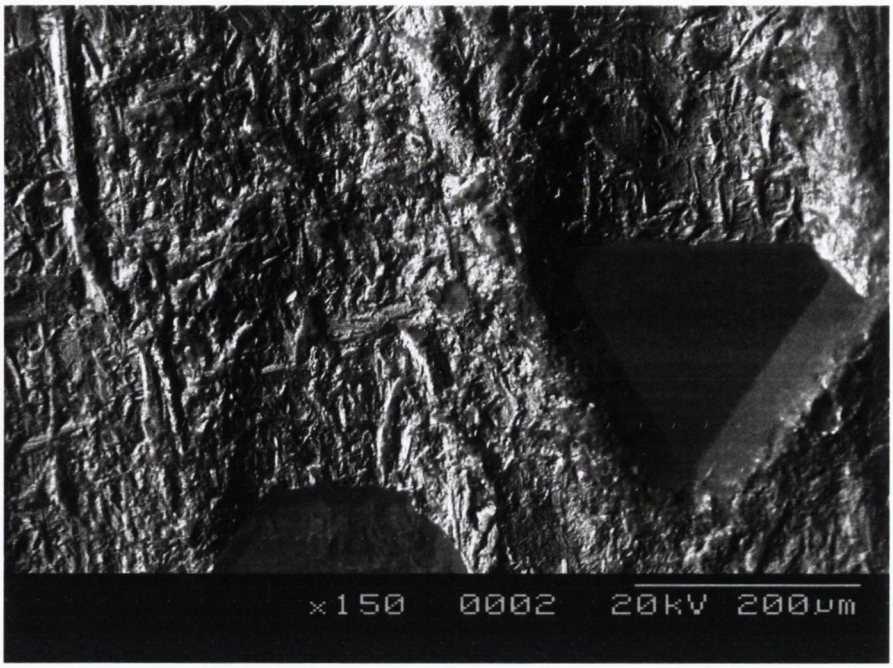

Figure 4.61. Comet tail formation due to erosion wear of cobalt matrix around diamond. Note: erosive flow is from bottom to top of picture. Mag. x 150.

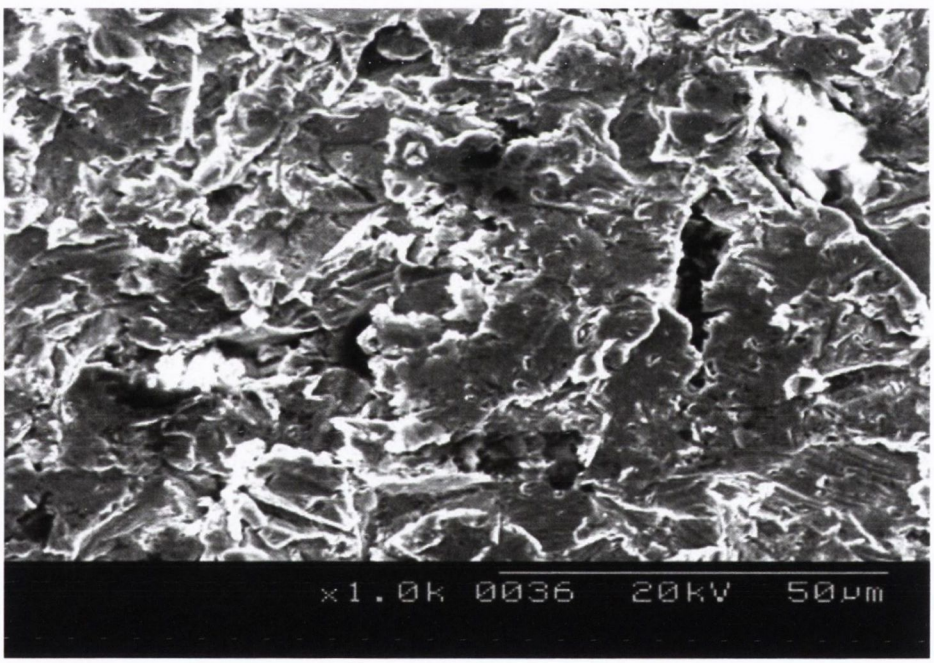

Figure 4.62.SEM Photomicrograph of a DC40 Charpy specimen eroded at a pressure/angle of 6bar/45^0. Mag. x 1.0k.

Figure 4.62 shows the cobalt metal surface with the characteristic plastic deformation of the metal surface due to the impacting alumina grits particles as it impacts the surface at a pressure of 6bar and impact angle of 45^0.

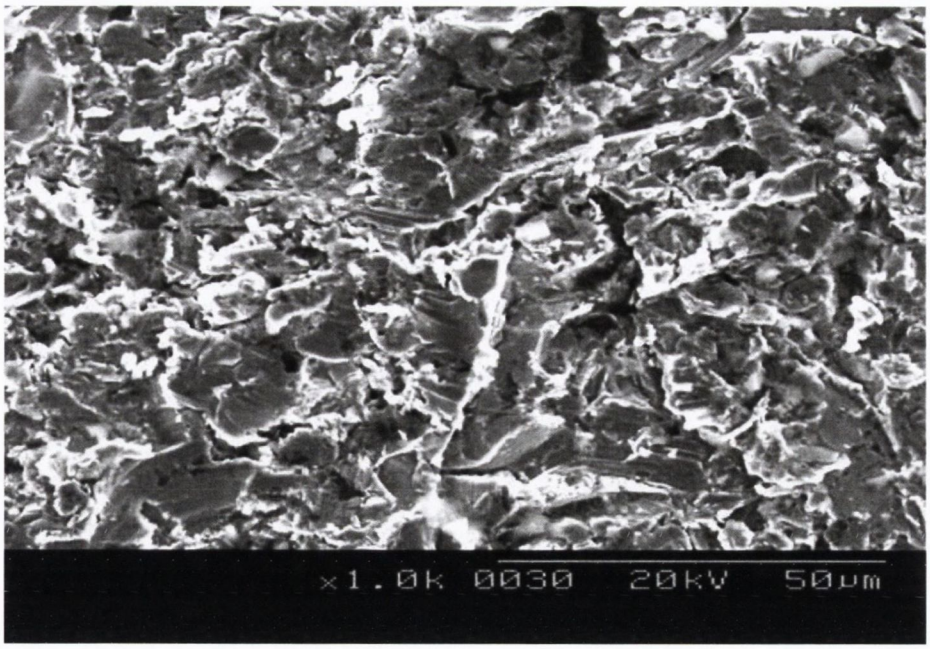

Figure 4.63. SEM Photomicrograph of a DC10 Charpy specimen eroded at a pressure/angle of 3bar/45^0. Mag. x 1.0k.

Figure 4.63 shows the cobalt metal surface with the characteristic plastic deformation of the metal surface due to the impacting alumina grits particles as it impacts the surface at a pressure of 3bar and impact angle of 45^0.

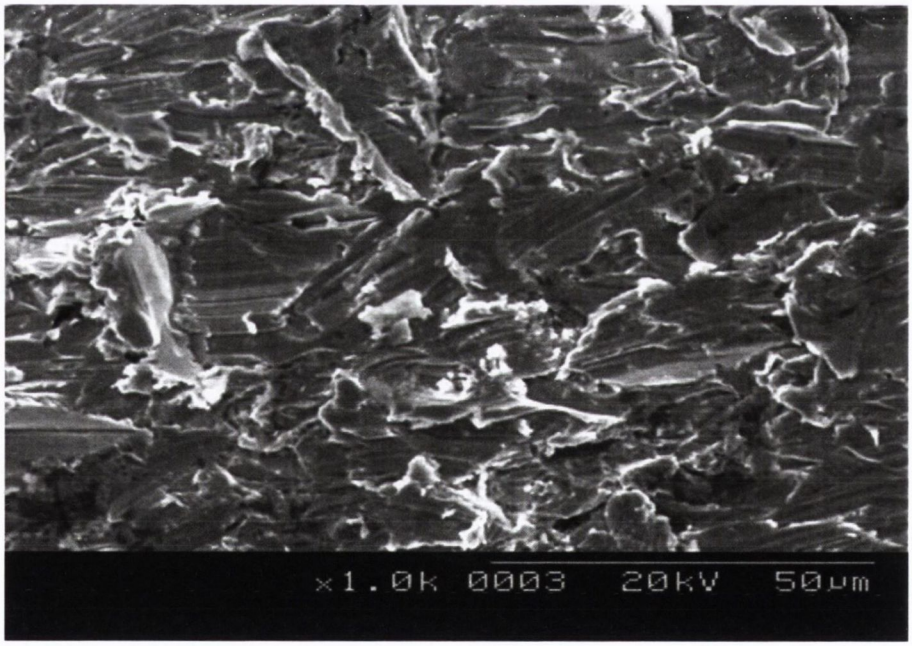

Figure 4.64. SEM Photomicrograph of a DICoMM specimen eroded at a pressure/angle of 6bar/15^0. Mag. x 1.0k.

Figure 4.64 shows the cobalt metal surface with the characteristic ploughing of the metal due to the impacting alumina grits particles as it impacts the surface at a pressure of 6bar and impact angle of 15^0.

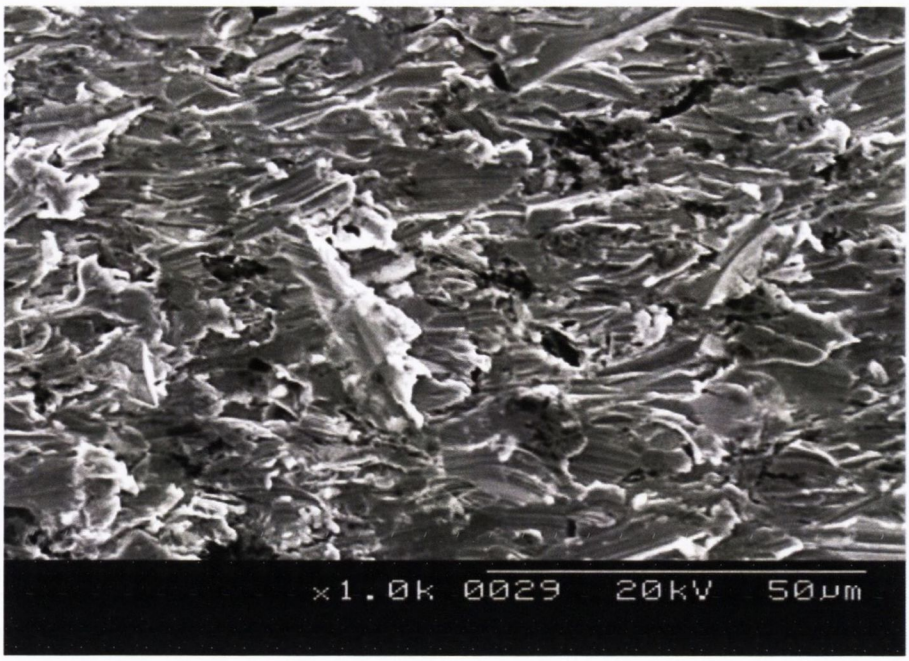

Figure 4.65. SEM Photomicrograph of a DICoMM specimen eroded at a pressure/angle of 3bar/15^0. Mag. x 1.0k.

Figure 4.65 shows the cobalt metal surface with the characteristic ploughing of the metal due to the impacting alumina grits particles as it impacts the surface at a pressure of 3bar and impact angle of 15^0.

Finally the erosive wear pattern around a diamond pull-out can be seen in Figure 4.66, where the conditions were very severe at a pressure of 6bar and at an angle of 45^0. Another feature of this photomacrograph is that comet tails are absent, which is found for the severe pressure and steep angle of erosive particle attack.

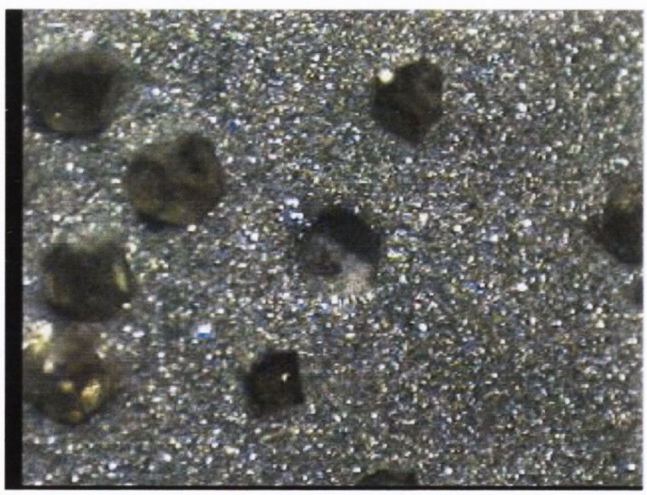

Figure 4.66. Showing eroded surface of DICoMM where a pull-out has been rounded off due to the eroding particles.

4.10. Fractography of TRS, Impact & Fracture Toughness Specimens

The following section reports the fractographic results of the various specimen types. Common to all the specimen types is the macro-brittle micro-ductile type fracture behaviour which is commonly found in PM materials [278]. Only a sample will be covered here because of the similarity between the different specimens.

The typical fracture surface found can be seen in Figure 4.67 which is from a fracture toughness sample in the fast fracture area shows the typical ductile failure with cup & cone dimple failure pattern.

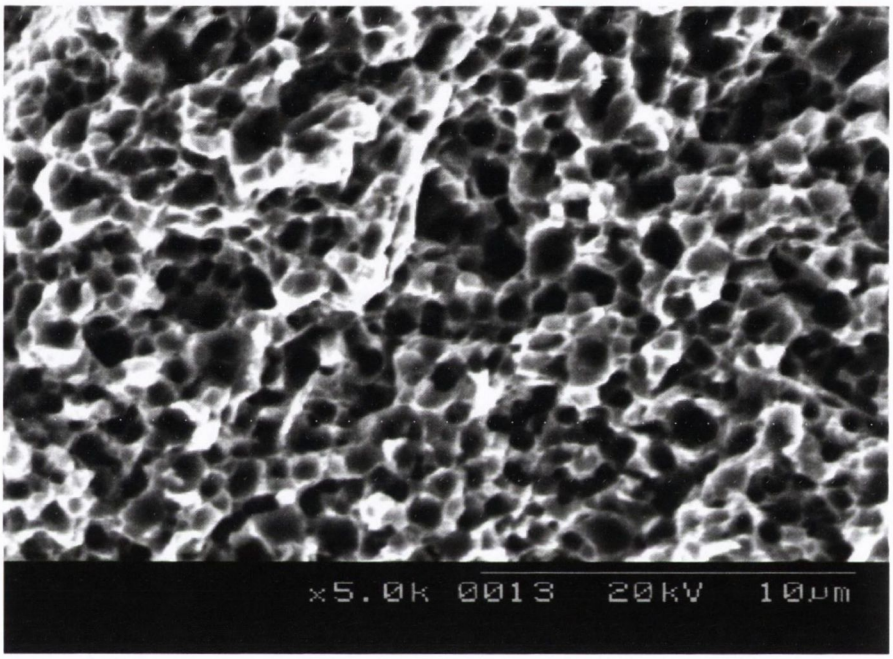

Figure 4.67. SEM photomicrograph (mag. x 5.0k) of a fracture toughness specimen Run 96/6 showing the fine ductile failure with the typical cup & cone failure pattern found in the fast fracture area.

The above photomicrograph Figure 4.67 of the FT specimen Run 96/#5 (mag x 5k) shows ductile fracture of a fracture toughness specimen. The cup & cone size is very fine, indicating a very limited ductile failure, practically being considered as ductile micro-volume conditions. The very limited ductile failure found can be considered to fulfil the ASTM E399-90 requirement for less than 5% plasticity required for plane strain conditions. Other authors have found for Al based PMMCs that greater then 5% plasticity level due to Al ability to plastically deform [153]. Cobalt which is HCP/FCC has less than 5 independently active slip systems, and so will quickly exhaust its ability to plastically deform and so fail with limited ductility. Also the allotropic transformation from FCC to HCP is strain sensitive and so will quickly transform to HCP and so reduce its deformation capability.

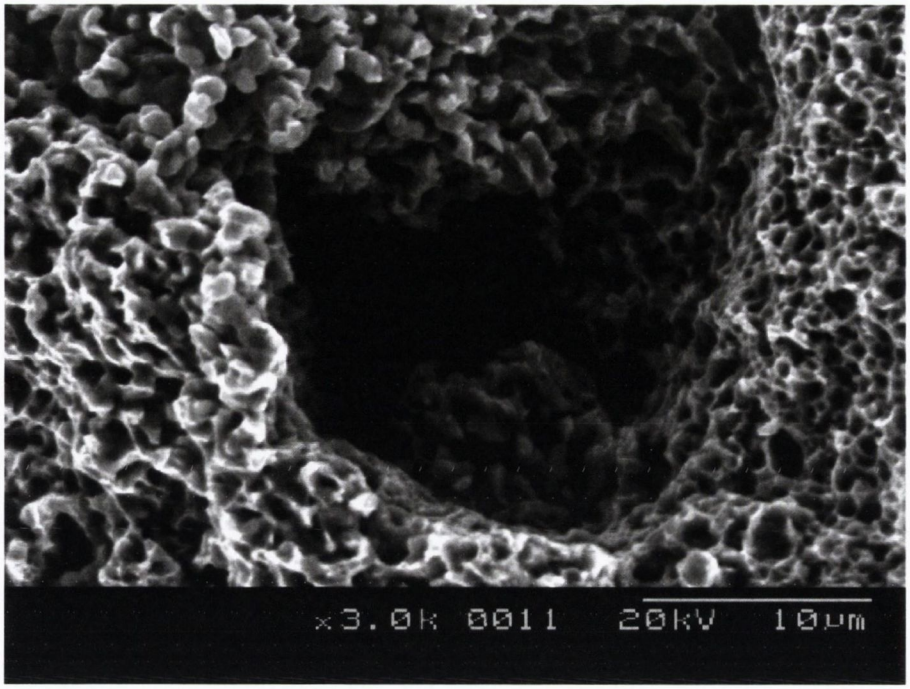

Figure 4.68. SEM photomicrograph (mag. x 3.0k) of fracture toughness specimen Run 96/6 showing a large pore in the Cobalt metal matrix.

The photomicrograph (Run 96/6) in Figure 4.68 shows an atypical large pore approximately 20µm in size. Finer pores also seen in Figure 4.67 are more typical are found evenly distributed throughout the different specimens, Charpy, TRS and FT and for both CoMM and DICoMM specimens. The photomicrograph in Figure 4.69 shows the typical ductile failure pattern for a Charpy specimen. Again the very fine ductile cup and cone type fracture surface can be seen.

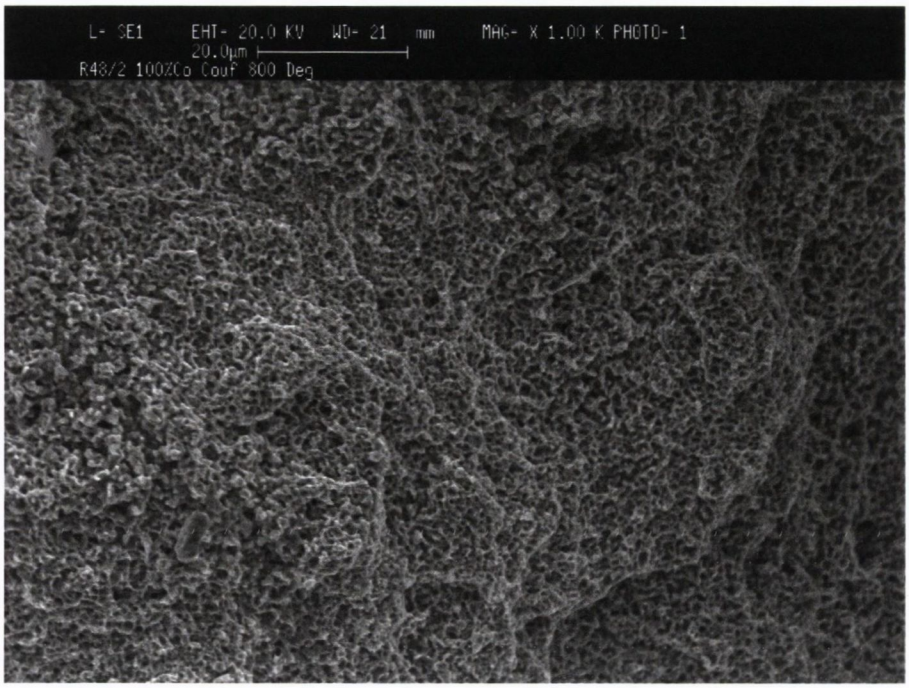

Figure 4.69. Charpy Run 48/2, 800°C, (mag. x 1.0k) showing ductile failure.

This image shows the interface between the cobalt metal matrix and diamond shown on the right of the image at a mag x 1.0k. The image shows also the ductile failure fracture surface of the cobalt matrix on the left. The debonding of the diamond from the metal matrix is often found on the fracture surfaces.

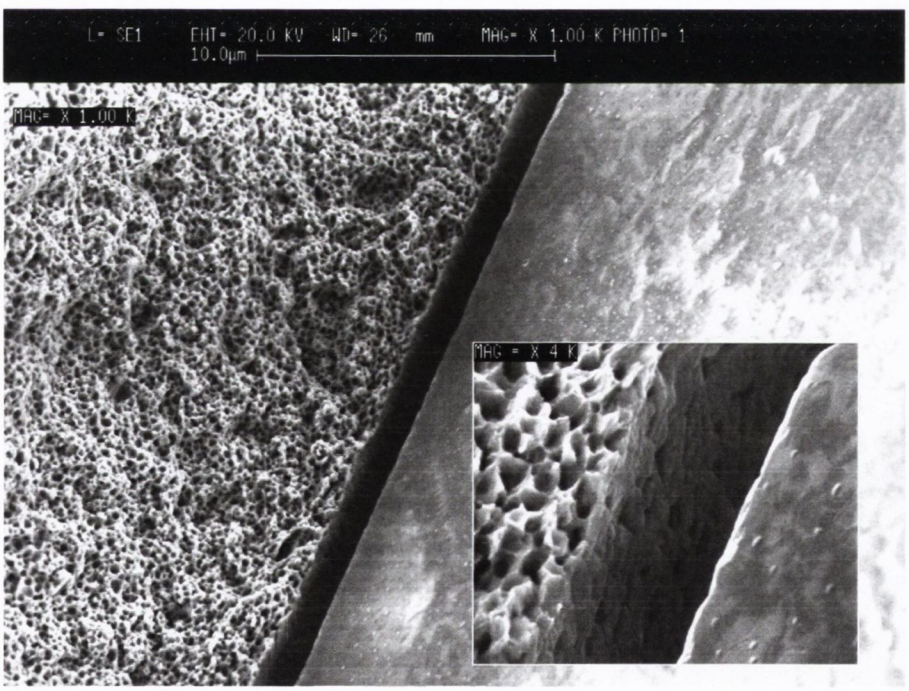

Figure 4.70. Charpy Run 48/2, 800°C, (mag. x 1.0k) & inset @ mag x 4.0k showing ductile failure.

This image shows the interface between the cobalt metal matrix and diamond shown on the right of the image at a mag x 1.0k. The image shows also the ductile failure fracture surface of the cobalt matrix on the left. The debonding of the diamond from the metal

matrix is often found on the fracture surfaces. Also shown in the inset part of the photomicrograph in Figure 4.70 is the very fine scale porosity at the diamond and metal interface. Regarding the inset photomicrograph at a mag. x 4.00K, shows more detail of the interface especially the very fine porosity. The white spots on the diamond surface were analysed using spot EDS and found to be cobalt carbides as seen in Figure 4.71 below.

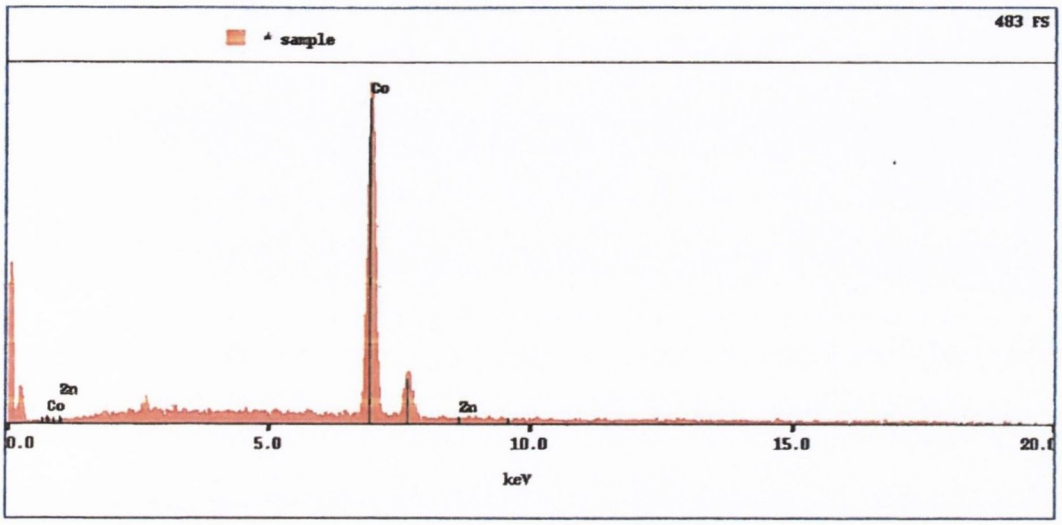

Figure 4.71. SEM EDX chemical analysis of white spot on diamond surface as seen in Figure 4.70.

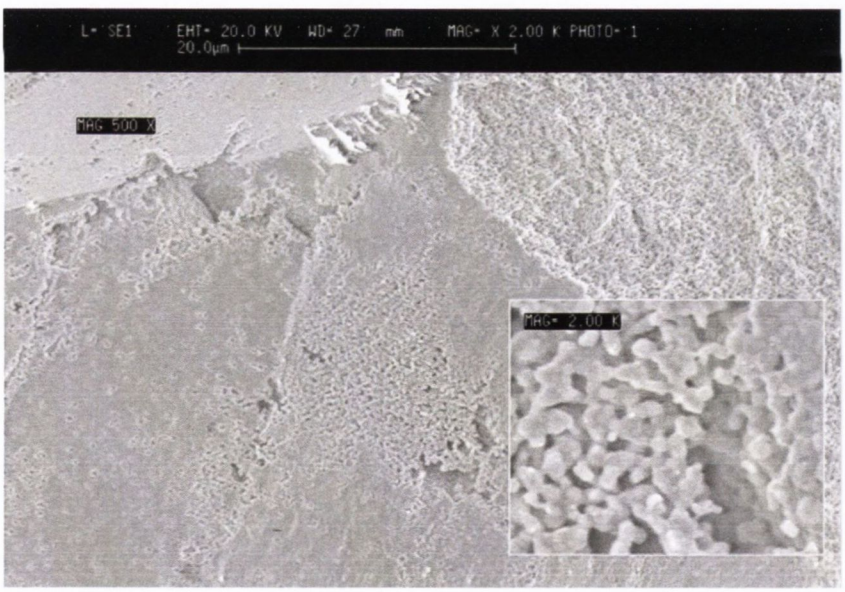

Figure 4.72. Charpy Run 48/2, 800°C, (mag. x 5.0k) & inset @ mag x 2.0k showing poorly sintered cobalt on surface of diamond giving rise to increased porosity in DICoMM material.

Figure 4.72 shows an SEM photomicrograph of a diamond surface with very fine filigree of cobalt sintered to the surface of the diamond, showing a very fine pattern of porosity, where some cobalt powder failed to sinter correctly at the diamond surface.

This fine porosity around the hard diamond increases the level of porosity in the DICoMM materials.

This has been cited in Chapter Two, Literature Review, where Webb [49] reported that it is more difficult to densify DIMMs and also for PMMCs where it is found that porosity levels are higher for PMMCs than the 100% metal matrix, and also that with increasing volume fraction leads to increasing porosity [119, 141, 279].

CHAPTER FIVE: DISCUSSION & ANALYSIS

5.1. Introduction

This chapter will cover all the different mechanical properties measured and investigated regarding how the presence of a large hard particulate in a metal matrix manufactured using an unusual powder metallurgy process called hot pressing. One important property which is crucial to PM materials is percent theoretical density (%TD). Percent theoretical density will be dealt with in concert with the other mechanical properties as they are being treated because it strongly influences their result throughout the chapter. Firstly hardness and the effects of diamond addition will be examined for the three different specimen types. The effects of percent theoretical density on this property will be also included. The reason for dealing with hardness first, is it's commonality with the different specimen types. This will be followed by Charpy impact followed by TRS where the fracture toughness will be analysed. Throughout the latter stages of the chapter predictive models that can be applied regarding the different mechanical properties in question will be used. Before starting, the author would like to reiterate that DICoMM materials as studied in this project show a large amount of scatter in experimental results and this should be kept in mind when reading the analysis of the results.

5.2. Hardness & Percent Theoretical Density (%TD)

As already stated above, this section is going analyse the very commonly measured mechanical property called hardness along with percent theoretical density as it pertains to it. The hardness results of the three specimen types investigated i.e. Charpy impact, TRS and fracture toughness, will be dealt with together where it helps to avoid tedium for the reader. Carrying out hardness testing on these types of materials proved very difficult for a number of reasons. One, was the presence of the hard reinforcement diamond, but also the fact that it been impregnated in a 'soft' matrix in relative terms which increases the difficulties of achieving a representative result. Factors that contribute to the difficulty are the presence of not only diamond, but also specimen composition varied due to diamond size and DC. Diamond damages the indenter and leads to a false hardness reading. As already mentioned in Chapter Three, Experimental Procedures, the HRB scale as used in the diamond tool industry is not the most appropriate because hardness numbers border on the upper scale and often exceed 100.

However, even though HRB has its limitations regarding scale its common use in the industry is more appropriate for its use in this project.

5.2.1. Fracture Toughness (FT) Specimens - Hardness & %Theoretical Density

Figure 5.1 shows for the frarture toughness specimens the average Rockwell hardness (HRB) plotted against percent theoretical density for each diamond size (US Mesh). The results plotted in Figure 5.1 are for all the fracture toughness specimens including K_{1C} and K_Q results. The points in red are the 100% cobalt HRB hardness results. As would be expected, increasing percent theoretical density one gets an increase hardness. This increase in hardness due to an increase in %TD is totally due to an increase in the Co matrix density, the reduction in porosity and has nothing to do with the presence of diamond. The data in the scatter plot is for all the different diamond sizes and diamond concentrations used in this project. The trendline drawn on the scatter plot gives a correlation coefficient, R a value equal to 0.32. So one can say that percent theoretical density and hardness have been found to be statistically significant, ($p<0.05$) [280]. The point in red is the average value for the 100%Co matrix. As can be seen, all the DICoMM materials have hardness values below the 100% matrix value.

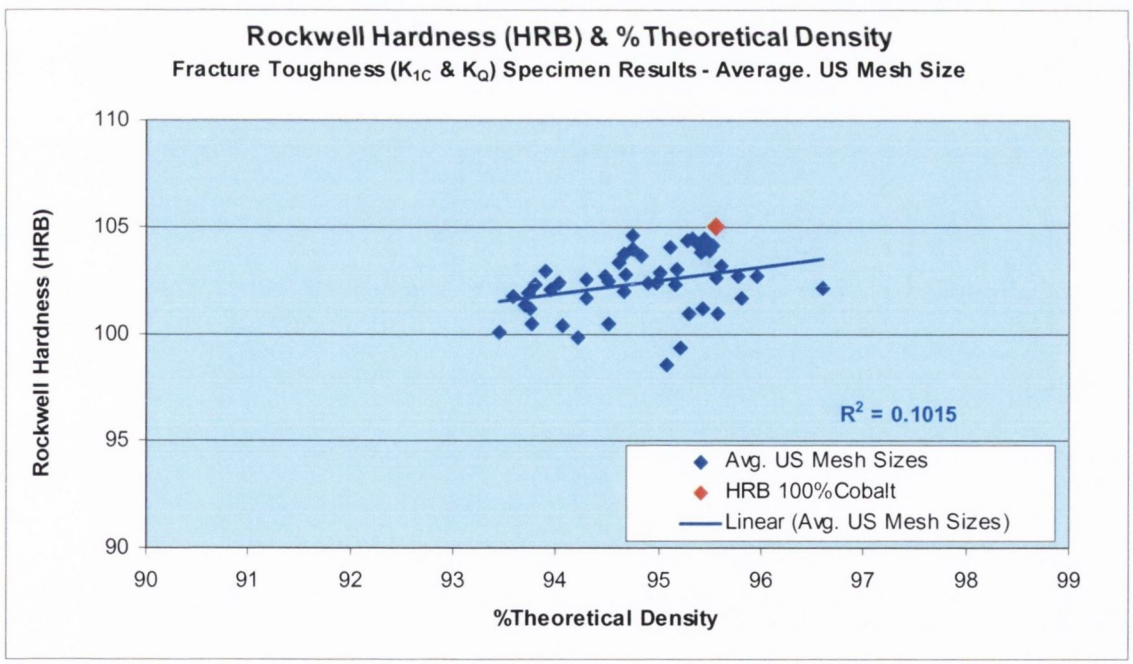

Figure 5.1. Fracture Toughness Specimen Results: figure shows the average Rockwell (HRB) hardness result for each US Mesh size plotted against %Theoretical Density, with 100% Cobalt in red. Correlation coefficient R = 0.32.

5.2.2. Charpy Impact Specimens– Hardness & %Theoretical Density

Similar to section 5.2.1, Figure 5.2 shows the variation of hardness with percent theoretical density (%TD) for Charpy impact specimens. Again, increasing percent theoretical density one gets an increase in HRB hardness. A trendline drawn on the scatter plot gives a correlation coefficient of R = 0.56, which indicates that %TD and hardness are statistically significant, ($p<0.05$) [280], again similar to those results for the fracture toughness. The point in red is the average value for the 100%Co matrix. As can be seen, most of the DICoMM materials have hardness values below the 100% matrix value.

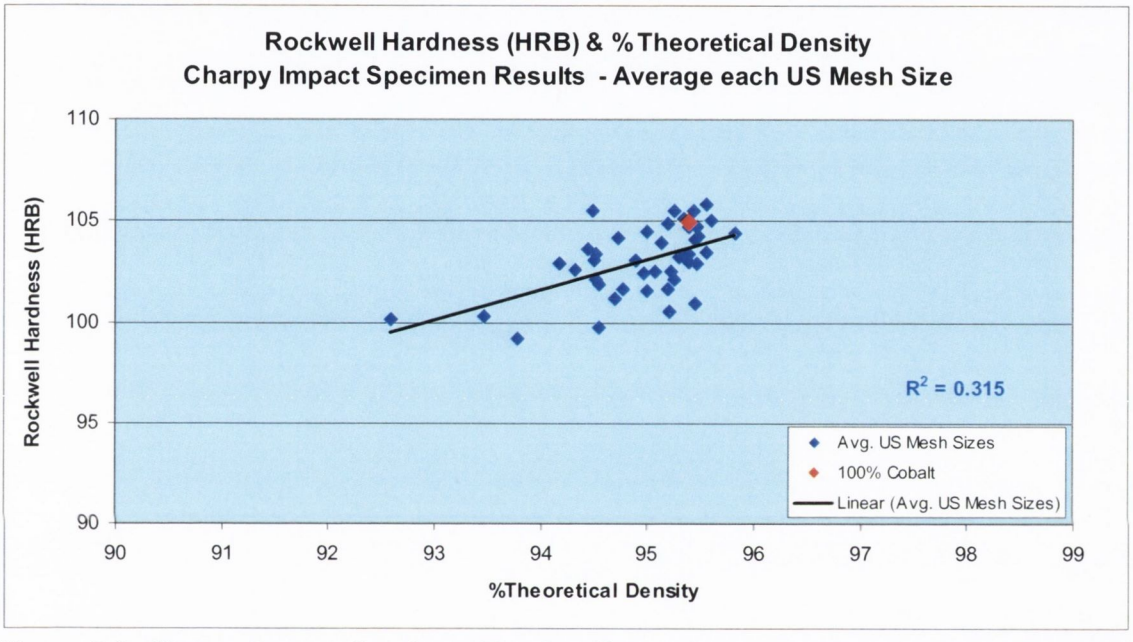

Figure 5.2. Charpy Impact Specimen Results: figure shows the average Rockwell (HRB) hardness result for each US Mesh size plotted against %Theoretical Density. Also included is 100% Cobalt in this graph. R = 0.56.

5. 2.3. TRS Specimens - Hardness & %Theoretical Density

Figure 5.3 shows the variation of hardness with %Theoretical Density for TRS specimens. Again, one gets an increase in hardness with an increase in percent theoretical density. The trendline drawn on the scatter plot gives a correlation coefficient of R = 0.56, again percent theoretical density and hardness have been found to be statistically significant, ($p<0.05$) [280]. The point in red is the average value for the 100%Co matrix. As can be seen, all the DICoMM materials have hardness values below the 100% cobalt matrix value bar one.

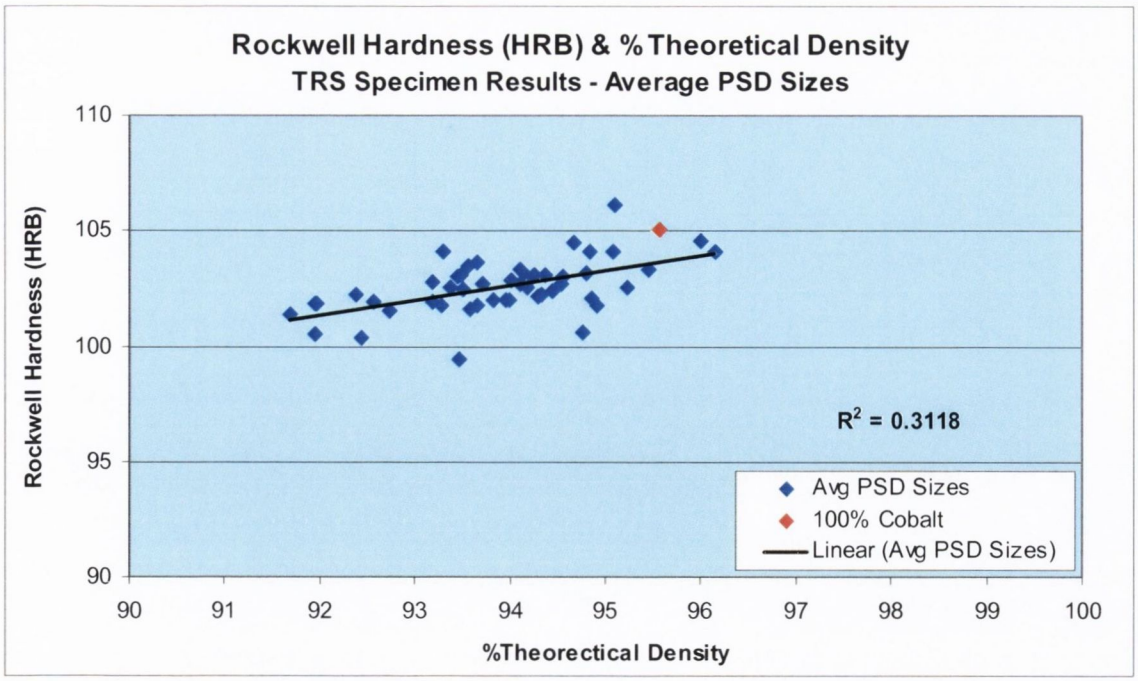

Figure 5.3. TRS Specimens Results: figure shows the average Rockwell (HRB) hardness result for each US Mesh size plotted against %Theoretical Density. Also included is 100% Cobalt in this graph. R = 0.56.

5.2.4. Hardness Comparison of TRS, CI & FT

The hardness results of the three different types of specimens are practically the same, with the average hardness results for the DICoMM TRS at 102.6HRB, CI at 103.1HRB and the FT at 102.2HRB.

With the addition of diamond to the cobalt matrix ones gets a decrease in overall hardness for all the specimen types bar a few results. This can be seen in Figure 5.4 where Rockwell hardness results for the different specimen types are plotted against diamond concentration.

Another general trend is that an increase in diamond concentration causes a decrease in hardness and within each diamond concentration decreasing diamond size yields an increasing hardness as seen in Chapter Four, Results, for example for the Charpy impact specimens in Figure 4.20.

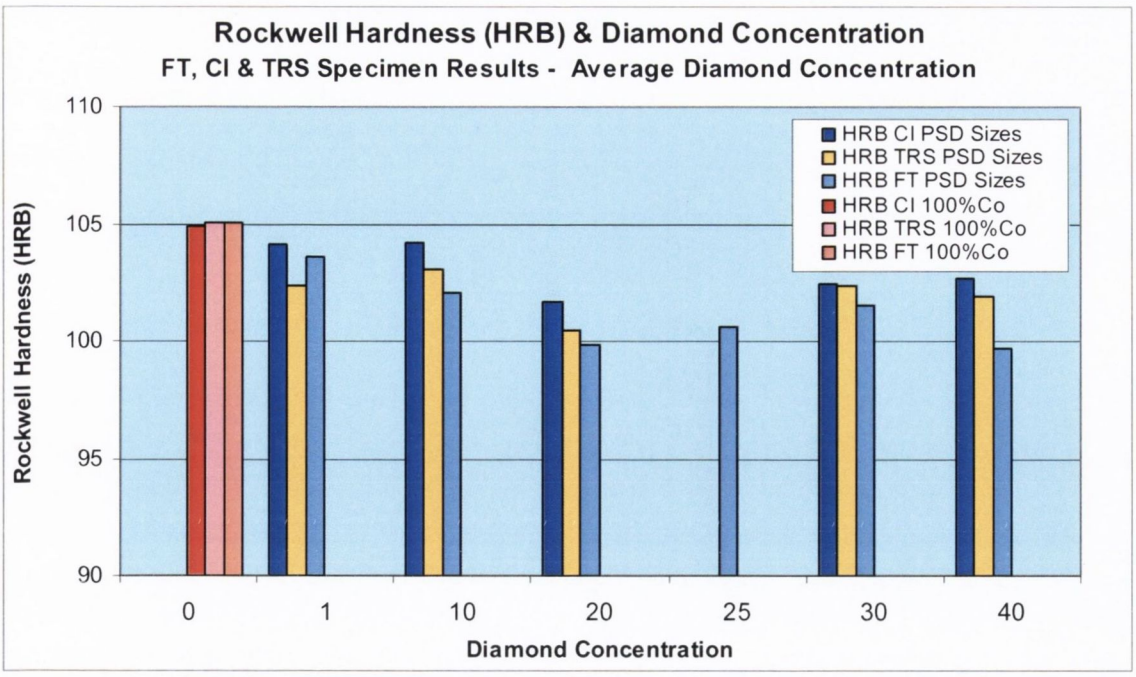

Figure 5.4. FT, CI & TRS Specimen Results: figure shows the average Rockwell (HRB) hardness result for the US Mesh sizes plotted against diamond concentration. Included is 100% Cobalt for comparison.

When hardness is plotted against percent theoretical density for individual diamond concentrations, increasing diamond concentration yields lower hardness but the graph also shows hardness's dependence on percent theoretical density as seen in Figure 5.5 for Charpy impact. Similar graphs for TRS and fracture toughness results can be seen in Appendix 6.

As reported in Chapter Four, Results, a fine porosity around the diamond crystals as seen in the SEM photomicrograph in Figure 4.66, will lower the hardness of DICoMM material, and with increasing diamond concentration an increased chance of the presence of porosity followed by lower hardness. This difficulty in densifying DIMM materials was found by [49] but also found for PMMCs where porosity levels are higher for PMMCs than the 100% metal matrix, and also that with increasing volume fraction leads to increasing porosity [119, 141, 279].

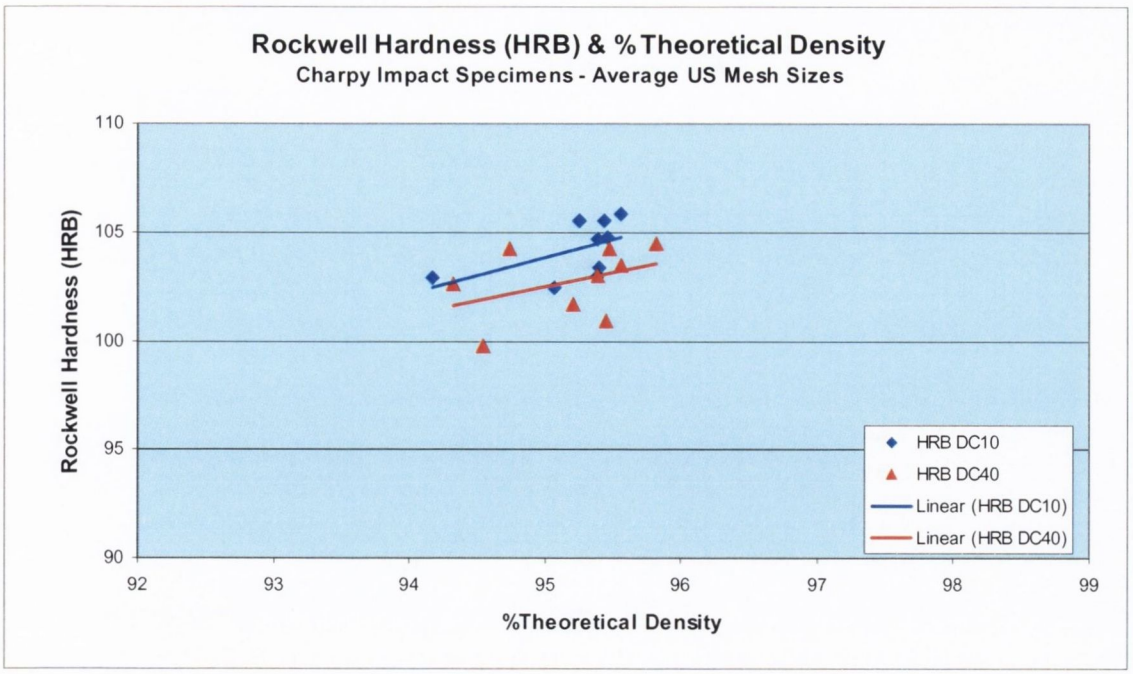

Figure 5.5. Charpy Impact Specimen Results: Figure shows Rockwell hardness (HRB) plotted against %Theoretical Density (%TD) for DC 10 & 40.

As reported in Chapter Four, Results, hardness results found for the different specimen types showed a large scatter. A possible reason for some of this behaviour is that in testing a diamond maybe present just below the surface where the indenter is placed giving an occasional higher hardness reading than would have been the case if no diamond had been present. Also the possibility arises if the diamond is not that well held due to a sightly higher porosity around the diamond in comparison to the bulk the diamond may be able to move and so lower the hardness result.

Regarding the modelling of hardness of DICoMM materials by using the concept of fractional area due to the diamond being present, no predictive capability was found to satisfactory for DICoMM materials as used in this project. Finally, the difference in the average hardness for the DICoMM materials is not very large overall, a difference of 5HRB when compared to 100% cobalt matrix.

5.3. Charpy Impact DICoMMS

In this section, Charpy impact energy results will be analysed. Firstly, the role of %TD will be examined and it's influence on impact energy, followed by diamond concentration and US Mesh size. This will then be followed by the influence of interparticle spacing (IPS).

5.3.1. Charpy Impact Energy & %Theoretical Density

The results here are for the effect of %TD on the impact energy of the samples. Included here are the results for all samples tested, instrumented Charpy and standard Charpy. It shows that as percent theoretical density increases impact energy also increases. Figure 5.6 shows the results for each individual samples, including those for 100%cobalt. It shows a large spread of results and also for a narrow range of %TD the resulting impact energy can be quite large.

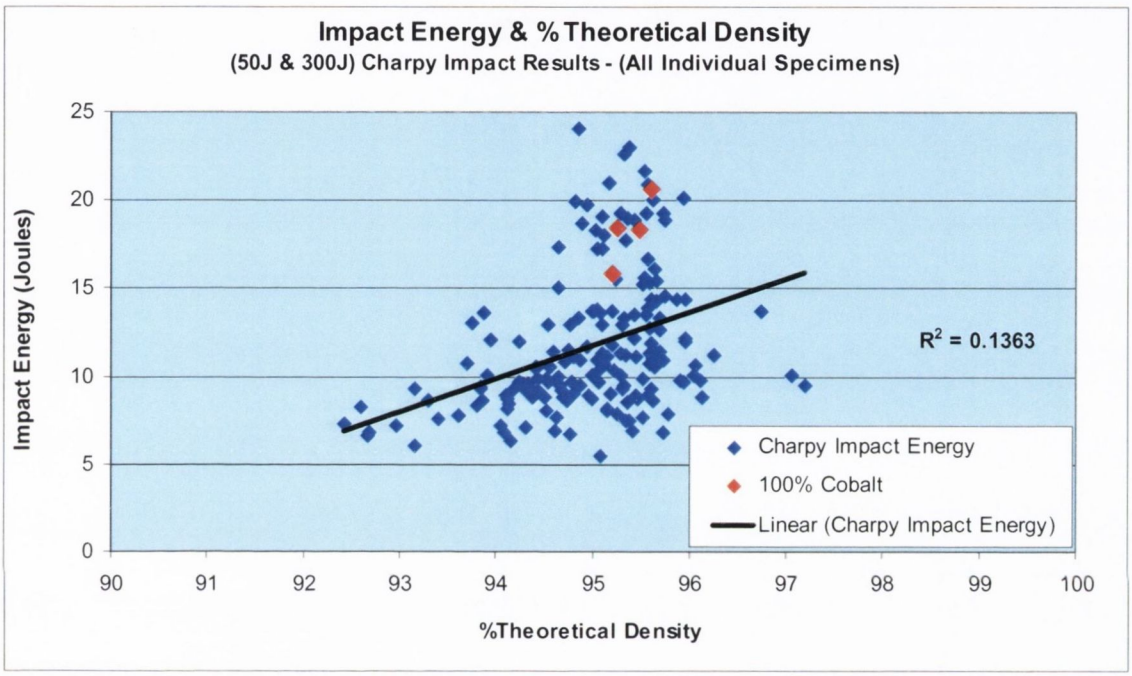

Figure 5.6. Charpy Impact Specimen Results: shows effect of %TD on the impact energy. Including CoMM in results in red. This figure is for individual results. R = 0.37.

In the Figure 5.6 the Charpy impact energy results for each individual specimen comprising US Mesh size and DC plotted against %Theoretical Density shows that for some specimens with low %TD have low impact energy. However for the higher %TD specimens, some have a higher impact energy due to increased %TD, which is indicated by the correlation coefficient, R = 0.37 between impact energy and percent theoretical density. But as can be seen from the graph, there are specimens which have high %TD but have much higher impact energies than what can be explained by %TD. So %TD is not the only factor influencing the impact energy of these materials. This is very evident especially at 'median' density levels where there is a large scatter in impact energy, which is strongly indicating another strong influencing factor, diamond size and diamond concentration being strong possible candidates. Another factor influencing

Charpy impact energies of DICoMMs is DC, which can be seen in Figure 5.7, which shows as DC increases impact energy decreases and also within each DC increasing %TD, an increasing in impact energy occurs. The reasons for the influence of DC will be analysed using the Theory of Critical Distances [225] later in the chapter in conjunction with fracture toughness and TRS failure stress.

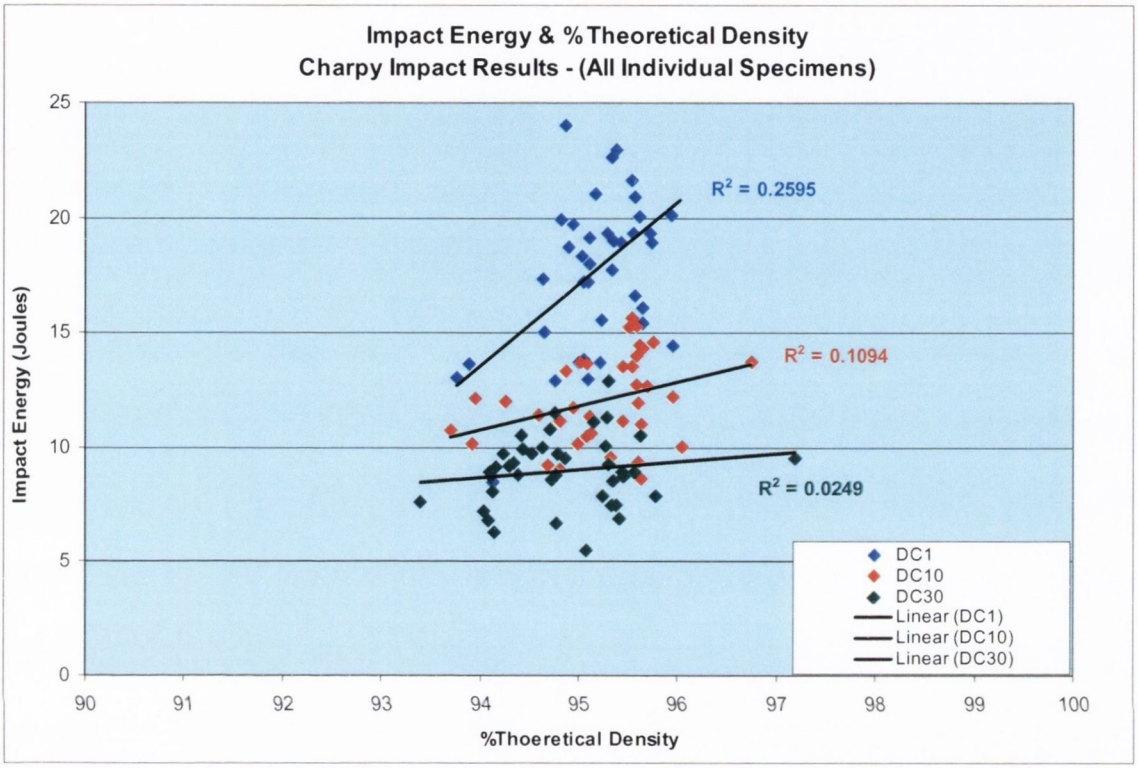

Figure 5.7. Charpy Impact Specimen Results: shows effect of %TD on the impact energy. This figure is for individual results. Correlation coefficients for the diamond concentrations as follows: DC1 R = 0.51, DC10 R =0.33 & DC30 R = 0.16.

5.3.2. Charpy Impact & Statistical Analysis – DC, US Mesh Size & 'Available-Energy'

A statistical analysis of the Charpy impact energy (Absorbed-Energy) results was undertaken using Mintab, a proprietary statistical software package. An Anova analysis using a General Linear Model was used to test for significance between the results to determine if US Mesh Size, DC and the level of 'Available-Energy' (300J & 50J machines) were important factors. The statistical results can be seen in Table 5.1. Table 5.2 is the result from a statistical test to check for the 'Power of the Test' and that the sample size was adequate.

Table 5.1 Impact Energy - 'Available-Energy' Anova Statistical Test - Minitab

General Linear Model: Strength versus US Mesh Size, DC, m/c

```
Factor   Type   Levels  Values
US Mesh  fixed      10  20/25, 25/30, 30/35, 35/40, 40/45, 45/50, 50/60, 60/70,
                        70/80, 80/100
DC       fixed       5  1, 10, 20, 30, 40
m/c      fixed       2  50, 300

Analysis of Variance for Strength, using Adjusted SS for Tests
Source    DF    Seq SS    Adj SS   Adj MS       F      P
US Mesh    9    218.61    152.97    17.00    4.04  0.000
DC         4   1808.61   1813.93   453.48  107.78  0.000
m/c        1      5.75      5.75     5.75    1.37  0.244
Error    166    698.46    698.46     4.21
Total    180   2731.42
S = 2.05124   R-Sq = 74.43%   R-Sq(adj) = 72.27%
```

The Power of the Test and sample size was then checked to ensure that the sample size was large enough and that the test was powerful enough from a statistical point of view. The results gave a value of 0.999 for power and sample size, which is excellent. This can be seen in Table 5.2 below.

Table 5.2 Power & Sample Size Test - Minitab

Power and Sample Size

```
2-Level Factorial Design
Alpha = 0.05     Assumed standard deviation = 2.05
Factors:    3    Base Design: 3, 8
Blocks:  none
Center                  Total
Points  Effect  Reps    Runs      Power
  0       2      20     160      0.999985
```

The results show that Diamond Concentration and US Mesh are very significant with a '*p*' value of 0.000 for both, indicating a very storng influence on the impact energy of DICoMM materials.

Regarding the importance of 'Available–Energy', a '*p*' value of 0.244 was determined which indicates that no significance exists between the two different machines, which is contrary to what was found by Shimansky [85] and also Turner [87]. The reader is referred to an excellent statistical primer by Reilly [281] for more on these typical statistical analysis treatments.

5.3.3. Charpy Impact Energy & Diamond Concentration (DC)

As mentioned above, %TD only tells part of the story, and from Figure 5.8 where impact energy is plotted against diamond concentration, it can be seen that with increasing

diamond concentration a decrease in impact energy occurs, indicating the importance of DC. The introduction of hard diamond particles into a ductile matrix would introduce stress concentration effects causing lower impact strength with increasing DC.

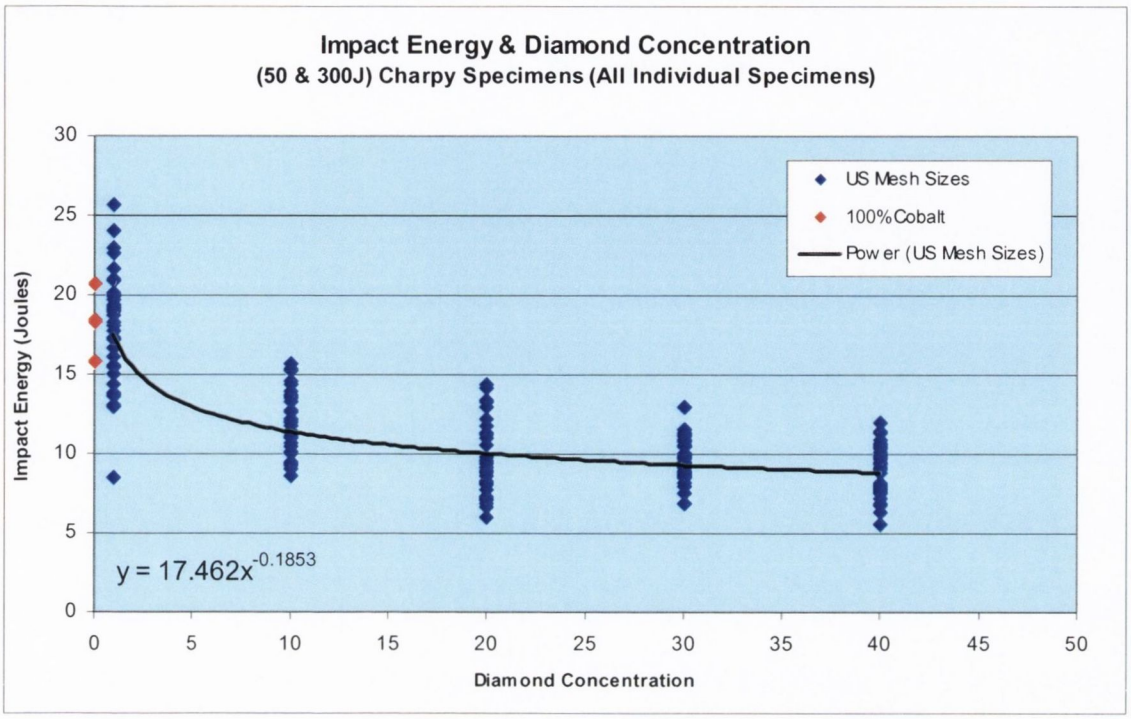

Figure 5.8. Charpy Impact Specimen Results: Impact energy for all the CI specimens (50J & 300J) plotted against diamond concentration. The figure is for individual results for each US Mesh size. The individual 100% Cobalt specimen values are also plotted in red. Note: Same figure as Figure 4.47.

From Figure 5.8 one can notice a large spread of impact energy results within each DC; this the author proposes is due to diamond size. This will be treated in the next section 5.3.4. When one plots the standard deviations of each US Mesh size within each DC, see Figure 5.9, in can be seen that DC1 shows a large range in standard deviations in comparison to the other DCs. This is due to some US Mesh Sizes having a wide range of impact energies. If one accepts that the presence of diamonds are acting as flaws in the cobalt matrix, in DC1 specimens the chance of finding a fatal flaw (diamond crystal) would be less, especially for the coarser sizes.

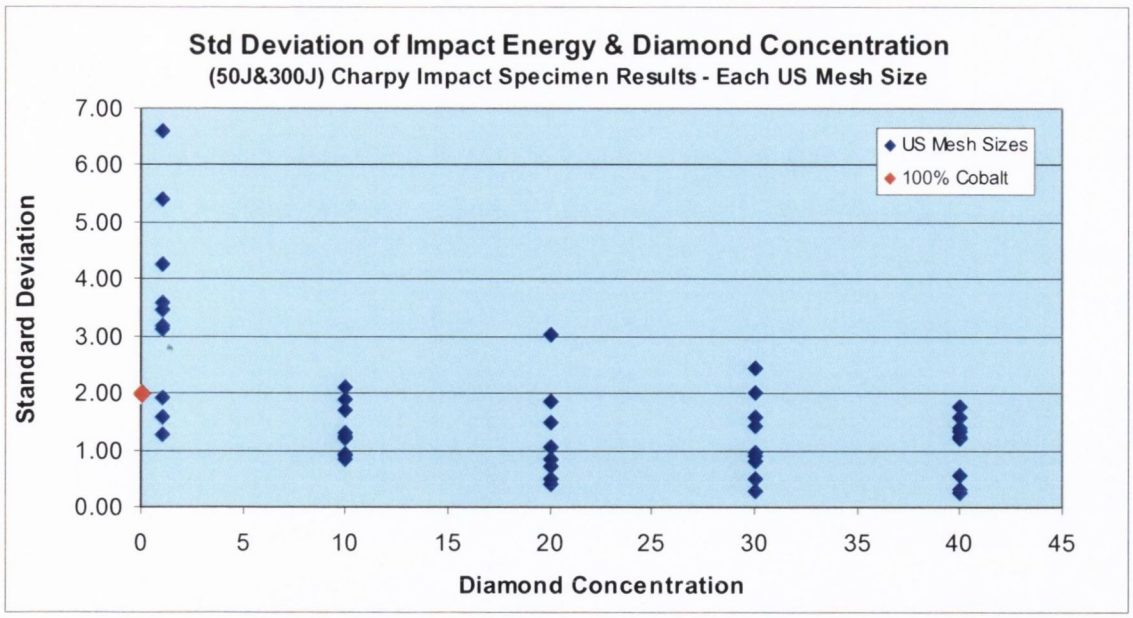

Figure 5.9. Charpy Impact Specimen Results: Figure shows the Standard Deviation for Impact Energy achieved for CoMM and DICoMMs for each DC used.

5.3.4. Charpy Impact Energy & Diamond Size (US Mesh Size)

Regarding Charpy impact energy and diamond size (US Mesh size), Figure 5.10 shows for DC 1 that with decreasing diamond size a steady increase in impact energy is found, which indicates flaw-size behaviour, with decreasing flaw size the energy to break increases, similar to 'work-of-fracture'.

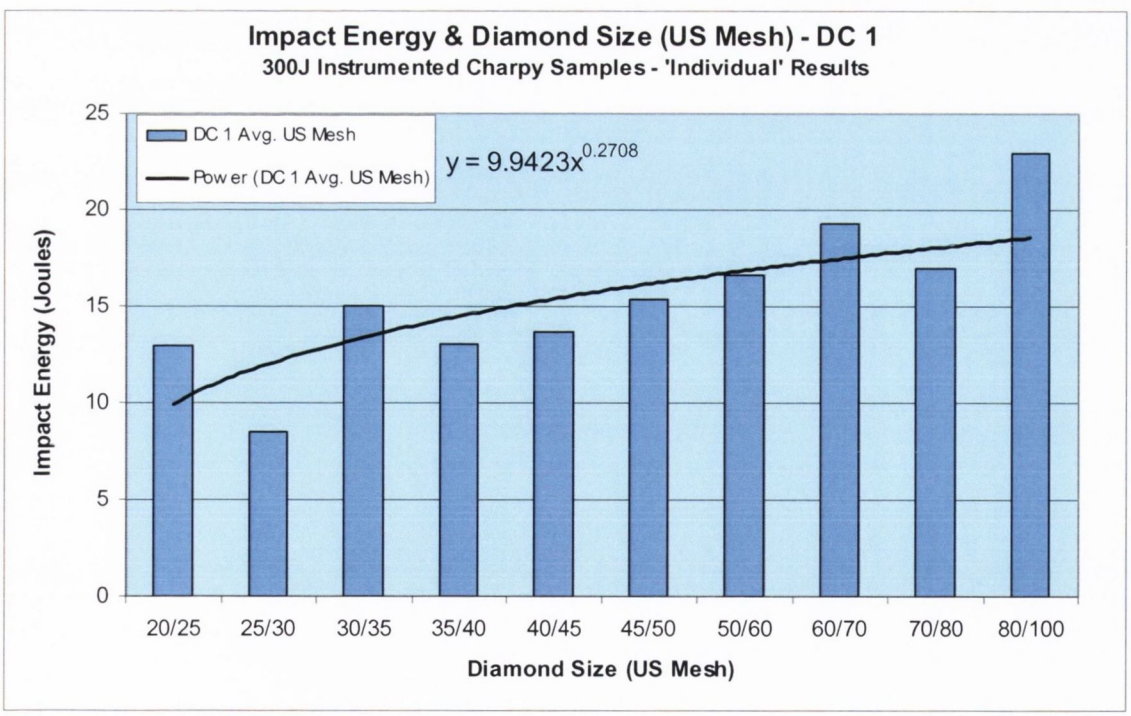

Figure 5.10. Charpy Impact Specimen Results: DC1 impact specimens tested using 50J & 300J machines, showing increasing impact energy with finer sized diamond.

When one plots impact energy plotted against US Mesh sizes for other diamond concentrations as can be seen in Figure 5.11 it can be seen that DC and US Mesh size are a very strong influencer. As diamond size gets finer, a higher impact energy is found, and when one increases DC, a lowering of impact energy results. Increasing DC increases the chance of finding a flaw in the tensile volume of the Charpy impact specimen on impact, so lowering the impact energy absorbed.

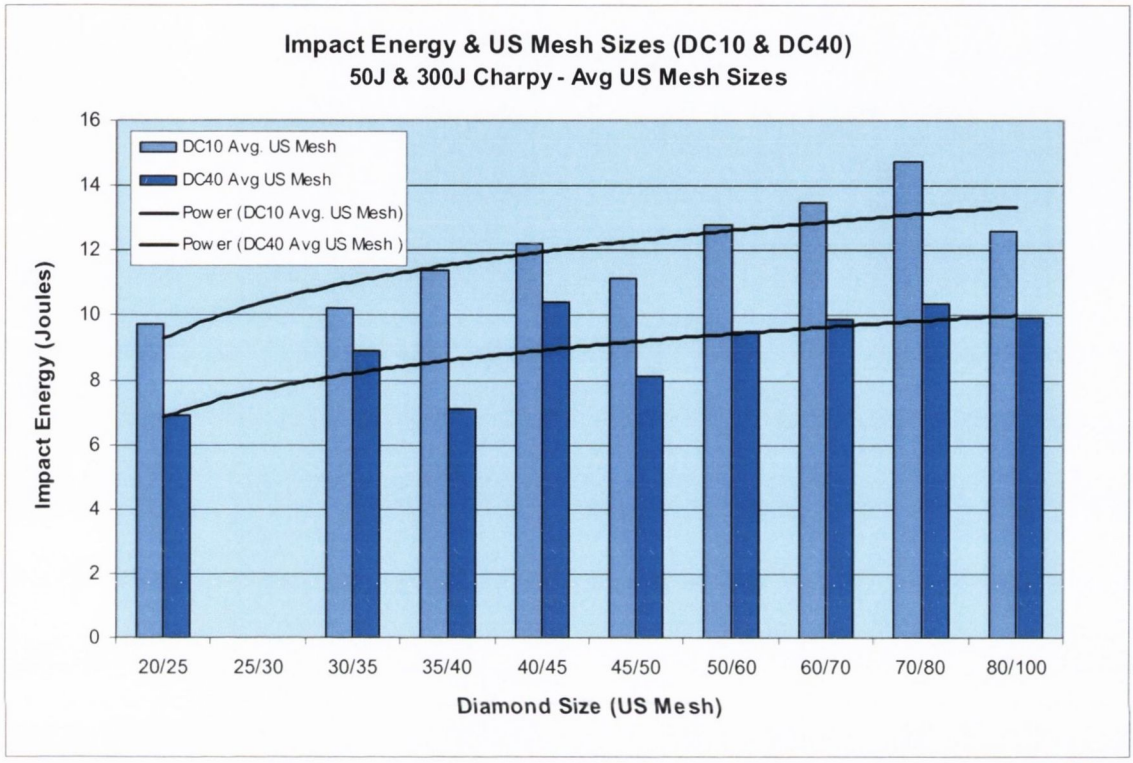

Figure 5.11. Charpy Impact Specimen Results: DC1 and DC40 impact specimens tested using 50J & 300J machines, showing increasing impact energy with finer sized diamond.

However, DC shows that it is an important influencer. Again this was to be expected, because the introduction of hard diamond particles into a ductile matrix would introduce stress concentration effects and so lower the impact strength of the metal matrix. This is largely due to the fact that the chance of finding a fatal flaw (diamond crystal) is less.

When the standard deviation for the Charpy impact energy results are plotted against US Mesh size as can be seen in Figure 5.12, for DC1, a large standard deviation is found in comparison to the other DC's e.g. DC10 & DC40. One can see from the graph that diamond size is important, as diamond size gets finer (80/100) the standard deviation reduces considerably for DC1. The DC1 trendline (red) gives a correlation coefficient of 0.46, which indicates that diamond size has a strong influence. Again, as already mentioned above, the diamond crystals are acting as flaws and for very low DC e.g.

DC1, the chance of finding a diamond is less for the coarser sizes so leading to the larger standard deviations.

The higher DCs show much smaller and consistent values of standard deviation right across all diamond sizes indicating that there is a far greater chance of finding a diamond or even a cluster of diamonds, to act as crack initiating flaws in the stressed volume when impacted by the hammer. The trendline drawn for DC40 for instance is flatlined.

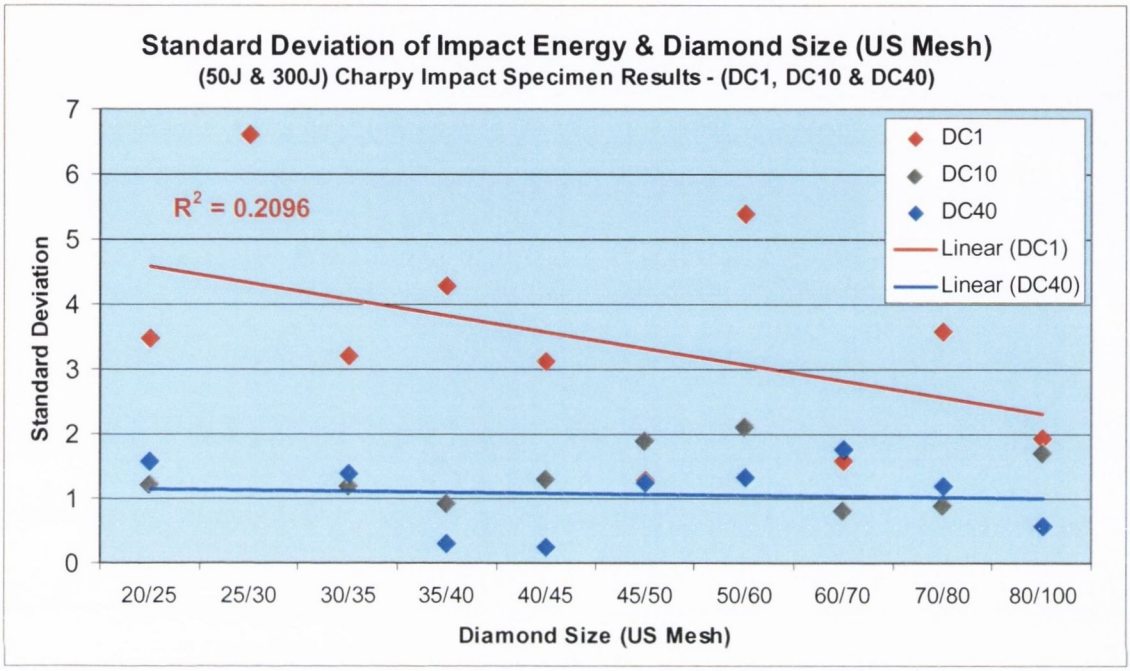

Figure 5.12. Charpy Impact Specimen Results: Standard Deviations for DC1, DC10 and DC40 Charpy impact specimens (50J & 300J) for each US Mesh size. R = 0.46.

So to recap, the presence of diamond crystals in the cobalt matrix are acting as flaws, whereby DC and US Mesh size are important factors in influencing the impact energy of DICoMM materials. Increasing diamond size and increasing DC reduces impact energy. At a very low diamond concentration e.g. DC1, the chance of finding a diamond is important, with coarser US Mesh sizes showing a large variation. For higher diamond concentrations, chances of finding a flaw increases substantially, also the chance of clustering also increases and so lowers impact energy and also standard deviation of results.

5.3.5. Inter-Particle Spacing (IPS) & Charpy Impact Energy

The role of interparticle spacing (IPS) as a measure of particle dispersion will be examined in relation to mechanical properties of DICoMM materials. In this section the effects of IPS on Charpy impact of DICoMM materials will be examined. IPS and TRS

and fracture toughness will be coverd later in this chapter. As already mentioned in the Chapter Two, Literature Review, second phase particles however present and their volume fraction play a major role in the mechanical properties of a material. The two main methods will be used, the Mean Free Path (MFP) (λ) and Nearest Neighbour Distance (NND) also called Mean Particle Spacing (MPS), (Δ_s). To avoid confusion the following designation will be used, IPS/MFP and IPS/NND will be used for MFP and NND respectively, because in the literature reference to IPS is used to refer to MFP or NND without any explanation.

5.3.5.1. Charpy Impact Energy & IPS/MFP

As can be seen in Figure 5.13 when the Charpy impact energy is plotted against IPS/MFP (λ) (mm) using the following equation,

$$\lambda = \frac{2}{3}\frac{d_p(1-V_f)}{V_f} \tag{5.1}$$

where

V_f = volume fraction of spherical particles and

d_p = particle diameter [185,186].

Specimen results for all diamond concentrations and US Mesh sizes are used in the graph in Figure 5.13. As can be seen, the inclusion of DC1 causes the other DC data to be compressed. The IPS/MFP determined for DC1 is very large in comparison to the other DCs. The graph also seems to show two different sets of data, one set for DC1 and the other the compressed data for the other DCs.

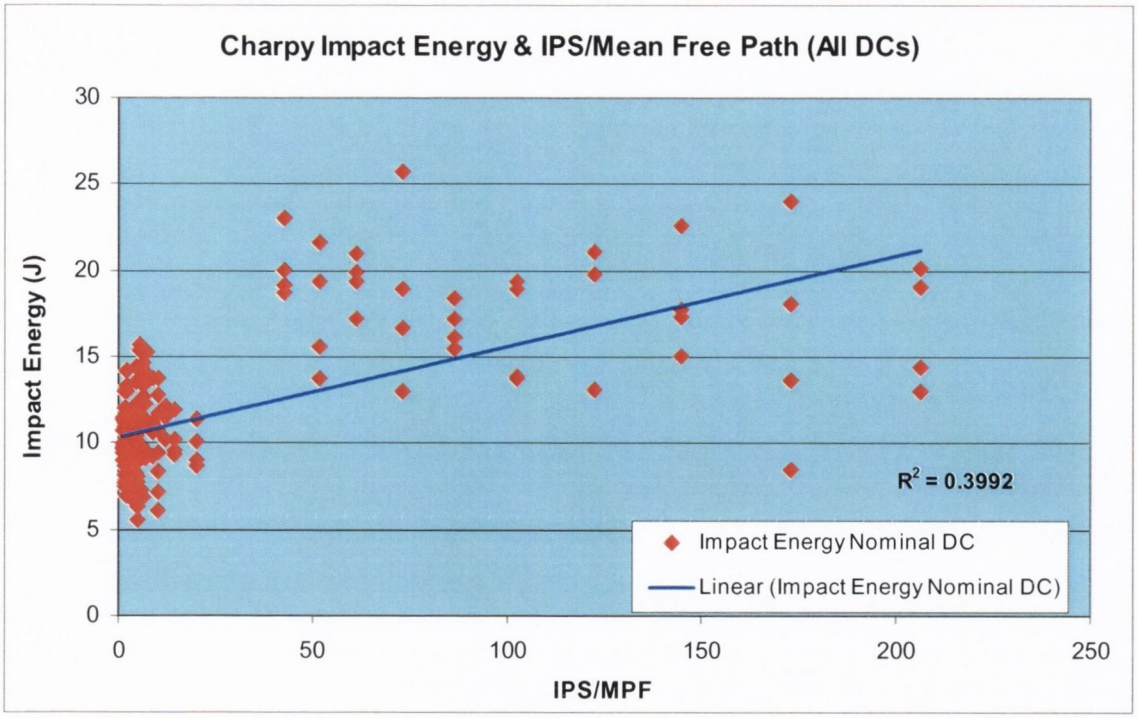

Figure 5.13. Charpy Impact Specimen Results: Graph of Charpy plotted against IPS/MFP (mm). DC1 was not used because of its large value of IPS/MFP (mm). R = 0.63.

So when replotted with DC1 excluded a better result is found in that the compressed data can be examined, as seen in Figure 5.14. The scatter graph in Figure 5.14 where IPS/MFP is plotted against impact energy is not very significant with a coefficient of determination R^2 states that only 1.5% of the variation in impact energy being explained by IPS/MFP. However, inspecting the graph it can be seen that there is a large range of impact energies for a short range of IPS/MFPs, which was found to hide interesting but not surprising results when the IPS/MFP against impact energy was plotted for each DC as can be seen in Figure 5.15.

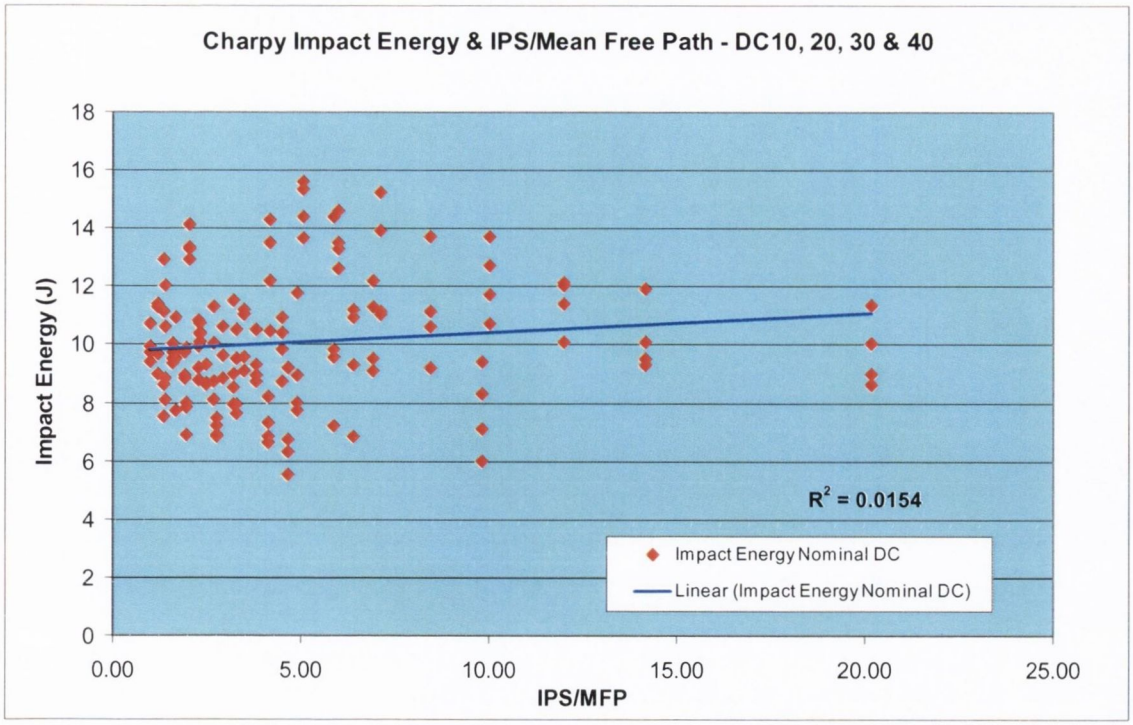

Figure 5.14. Charpy Impact Specimen Results: Graph of Charpy plotted against IPS/MFP (mm). DC1 was not used because of its large value of IPS/MFP (mm). R = 0.12.

Figure 5.15 clearly shows that US Mesh size is an important factor. This is not to say that DC is not important but the effect of DC and US Mesh size is hidden when plotted using IPS/MFP against the full set of data. The graphs in Figure 5.15 clearly show that diamond size and IPS/MFP are statistically significant, (p<0.05) [280] with correlation coefficients of 0.67 and 0.58 for DC10 and DC40 respectively. This is to be expected, because the introduction of hard diamond particles into a ductile matrix would introduce stress concentration effects and so lower the impact energy of the metal matrix. At a constant DC, the IPS/MFP increases with increasing size of diamond. It also shows that DC is an important influencer, which also shows that as DC increases it has a bigger effect with increasing diamond size.

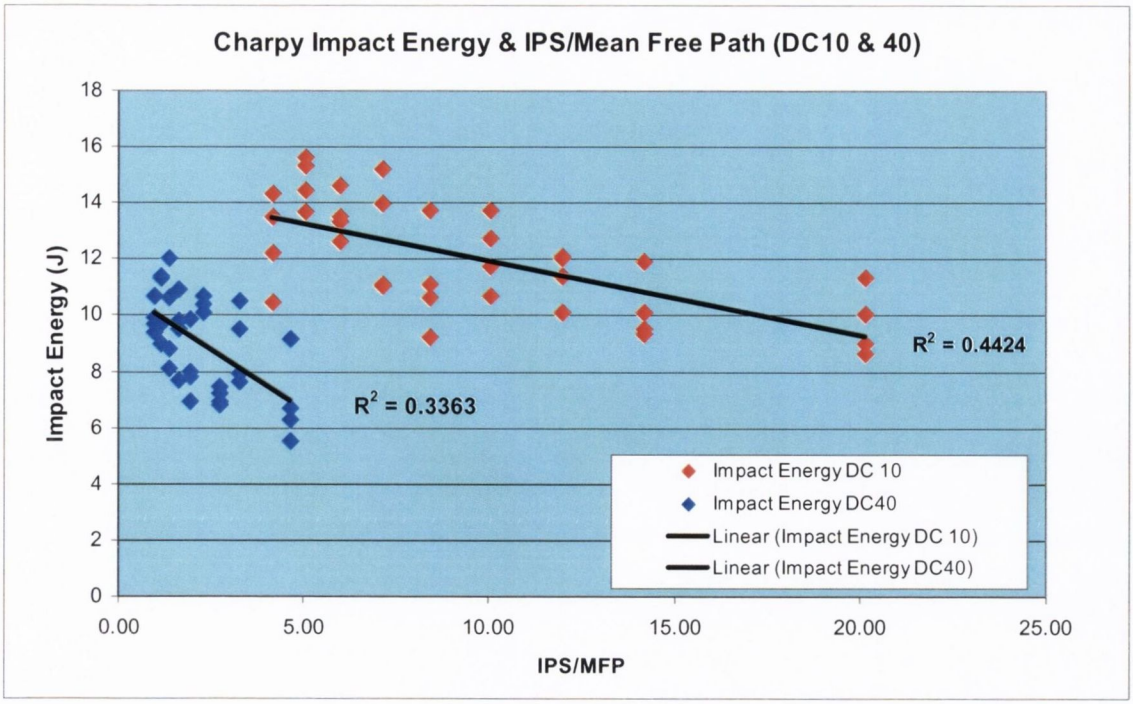

Figure 5.15. Charpy Impact Specimen Results: Graph of Charpy plotted against IPS/MFP (mm) for DC10 & DC40. DC10, R = 0.67. DC40, R = 0.58.

Even though coarser diamond does result in a larger IPS/MFP it clearly indicates that for each DC, the coarser US Mesh sizes have the lowest impact energy within each DC. It clearly indicates that diamond size is very important and that the diamond is present as a flaw and under impact causes crack iniatition.

When IPS/MFP is plotted as 1/(IPS/MFP) & $\sqrt{}$(IPS/MFP) against impact energy very similar results to the standard form are found which can be seen in Appendix 7. The graphs of IPS/MFP for the other DCs can be seen also in the Appendix 7.

5.3.5.2. Charpy Impact Energy & IPS/NND

When the Charpy impact energy of DICoMM materials is plotted against IPS/NND, 1/(IPS/NND) or $\sqrt{}$(IPS/NND) the results are very similar to IPS/MFP for DCs combined as well as for individual DCs and can be seen in Appendix 7. The results of IPS/MFP and IPS/NND are contrary to that found by Bhat et al. [188] who found that increasing particle size for a given volume fraction increases the IPS/NND which increases toughness.

In conclusion, when IPS/MFP is plotted against impact energy for a range of US Mesh sizes and DCs, it does not show any correlation with impact energy and this is similar for

IPS/NND. However when IPS/MFP and also IPS/NND is plotted against impact energy for a range of diamond sizes at a constant DC, both IPS/MFP and IPS/NND are significantly correlated with impact energy.

5.4. Transverse Rupture Strength (TRS) - DICoMMS

The TRS results for the various combinations of diamond size (US Mesh size) and diamond concentrations (DCs) will be examined in this section from various aspects, e.g. the role of percent density and TRS and at a later stage in the chapter the prediction and relationship of TRS and Charpy energy using strain energy approaches will be covered.

5.4.1. Transverse Rupture Strength (TRS) & %Theoretical Density

The results here are for the effect of %TD on the TRS or maximum stress at failure of the specimens. Included here are the results for TRS specimens tested using 40mm and 50mm spans. It shows clearly that, as density increases TRS stress also increases. Figure 5.16 shows the results for all specimens, including those for 100%cobalt. It shows a large spread of results both in TRS and %Theoretical Density with a correlation coefficient R equal to 0.29 which is not very significant and indicates that a large factor remains that is influencing the TRS mechanical properties of DICoMM materials.

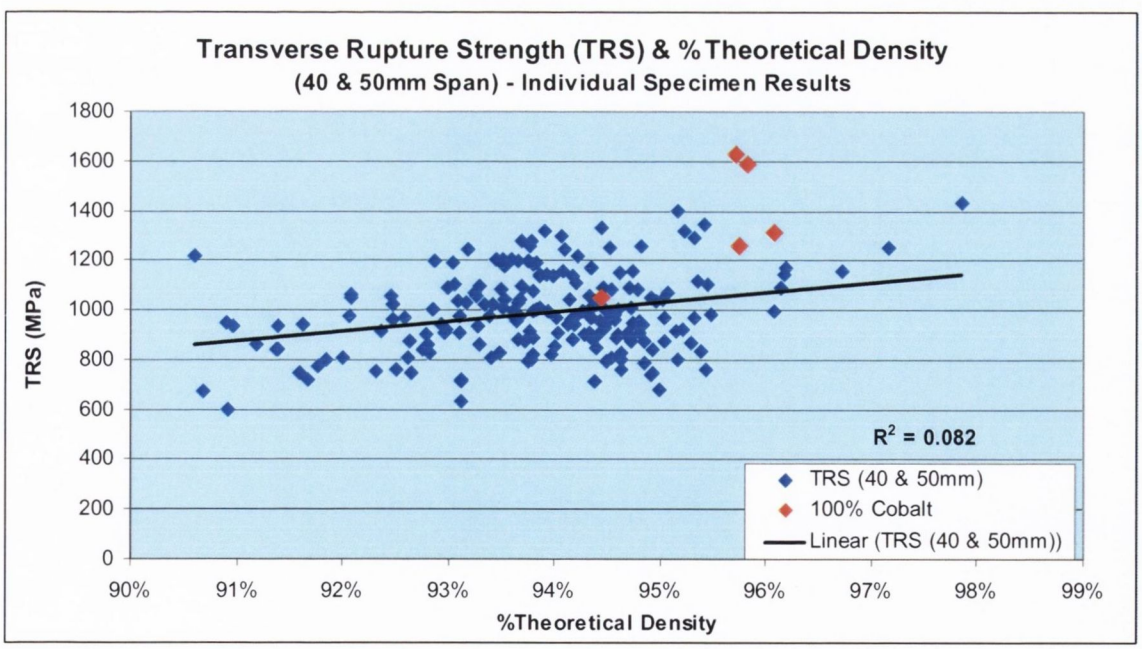

Figure 5.16. TRS Specimen Results: Shows effect of %TD on TRS failure stress, included are the CoMM results in red. This figure is for individual specimen results. R = 0.29.

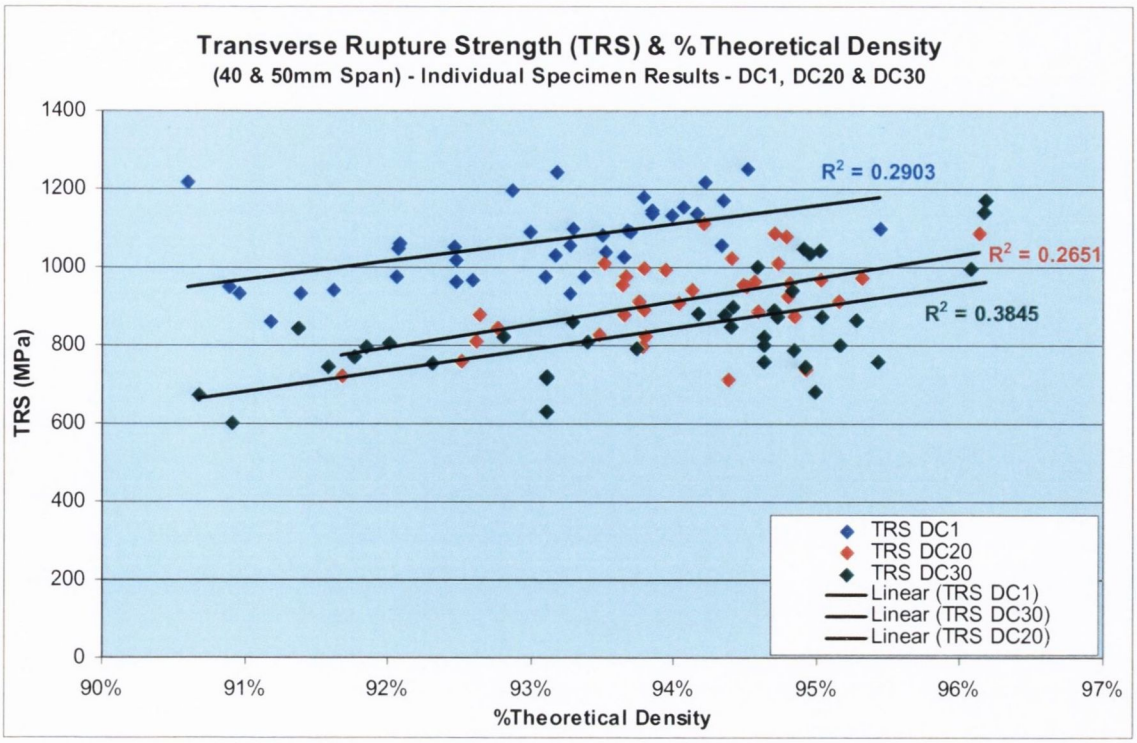

Figure 5.17. TRS Specimen Results: Shows effect of %TD on the TRS plotted for different diamond concentrations. Correlation coefficients for the different diamond concentrations are as follows: DC1 R = 0.54, DC20 R = 0.51 & DC30 R = 0.62.

Interesting to see in Figure 5.17 where %TD plotted against different diamond concentrations shows that for different diamond concentrations even with increasing TRS with increasing percent theoretical density, there is a shift downwards for increasing diamond concentration. The reason for this behaviour will become apparent later in the analysis.

5.4.2. Tensile Stressed Volume (TSV)

Flexural strength is an important mechanical property frequently used to test brittle materials e.g. ceramics, because of the difficulty in testing them using standard tensile testing. It is a bend test which combines tensile and compressive strengths. As previously mentioned in Chapter Two, Literature Review, interpretation of flexural test data caution is required because several test variables influence the results. These include: cross-sectional shape of specimen (round, square or rectangular), specimen dimensions (width to thickness ratio) and specimen surface roughness. Also the type of loading arrangement i.e. three-point or four-point, used is very important. All the above mentioned variables influence the stress-field generated within the specimen upon loading and so the resulting flexural strength obtained.

So the flexural strength of the material to be tested depends on the volume of the material under tension. As the failure process of all brittle materials shows instantaneous crack propagation with crack initiation being the critical step, a critical flaw size under tension must be present. So the greater the chance of finding one increases as the volume of material under tension increases. This implies that if the volume of material under the maximum tensile stress is smaller; the strength will increase as the probability of a larger flaw (e.g. diamond) under maximum tensile stress decreases. So decreasing dimensions or span will lead to higher flexural strengths. During three-point bend flexural testing, the volume of material below the neutral axis is under maximum tensile stress and this is where the failure will be initiated. Since the diamond particles are crack initiators in DICoMM materials, the crack iniation is the critical step in flexural testing. This means that material in the immediate vicinity of the lower surface would influence the failure initiation. So, the flexural strength is plotted as a function of tensile stress volume (*TSV*) which is calculated as follows:

$$TSV = W.\left(\frac{S}{T}\right)(T^2) \qquad (5.2)$$

where

W = width,

S = span

and T = thickness, the ratio S/T is know as the span-thickness ratio.

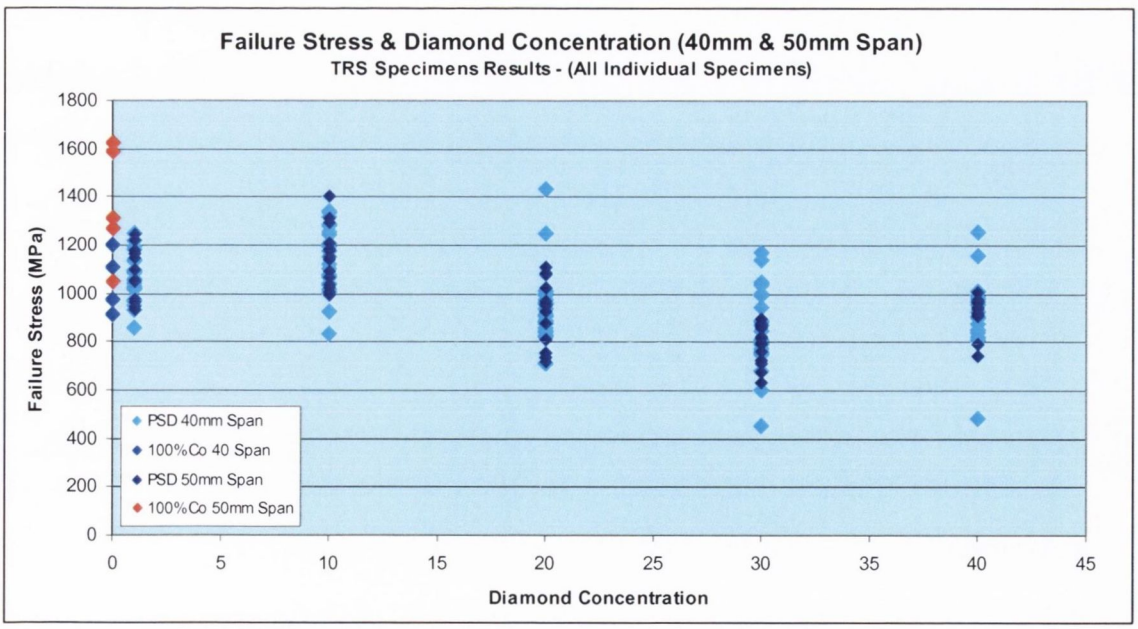

Figure 5.18. TRS Specimen Results: Figure shows the individual failure stress achieved for CoMM and DIMMs for each DC tested using 40mm & 50mm spans. The results plotted here are for each individual specimen for each US Mesh size & DC.

The graph in Figure 5.18 shows the large spread of individual results for each US Mesh size and diamond concentration. It shows TRS specimens tested using 40 mm span and 50mm spans, CoMM specimen results also shown. As can be seen in Figure 5.18, the results for the stress to failure for the 50mm span TRS specimens show a much narrow spread, which can be explained by the *TSV*, which is larger for the 50mm span specimens when one plots the stress to failure against the *TSV*. It shows the dependence of flexural strength on the tensile volume. The average *TSV* for 50mm span specimens is 2.64 cm^3 whereas the average *TSV* for the 40mm span specimens is 2.10cm^3.

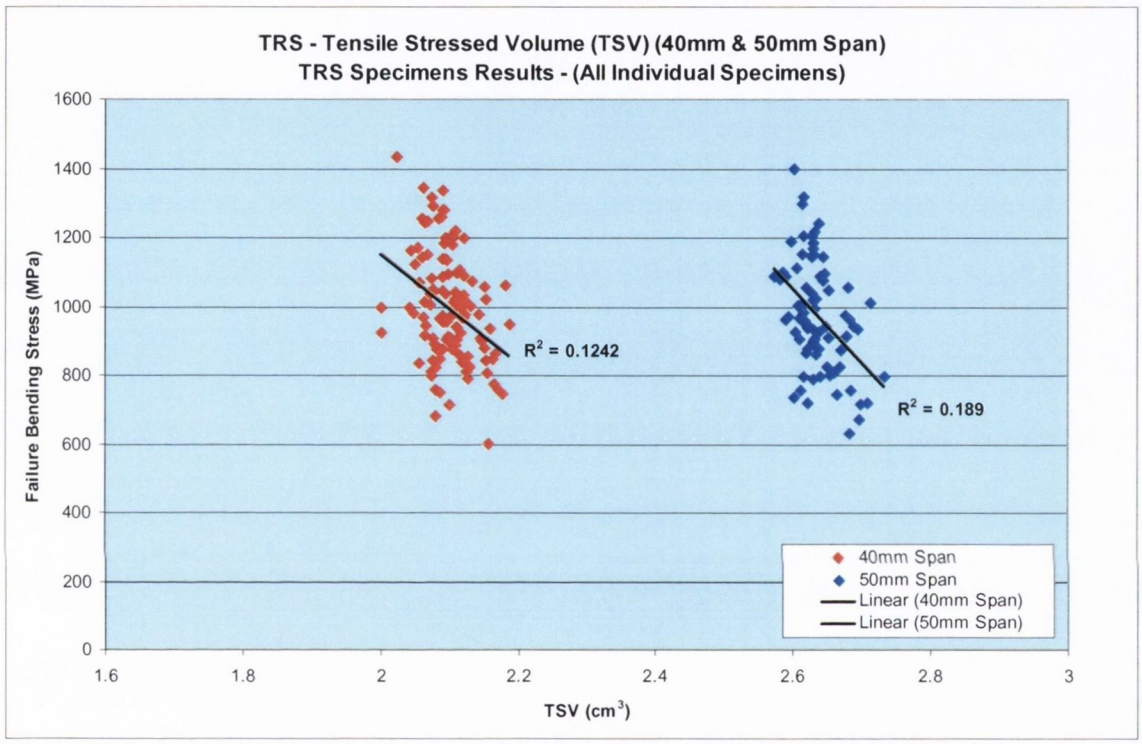

Figure 5.19. TRS Specimen Results: Figure shows the individual TRS failure stress plotted against TSV, for 40mm and 50mm spans.

The results plotted in Figure 5.19 show for the two different spans the TRS against the *TSV*. There is a trendlines drawn show as *TSV* increases the TRS decreases. However, when the data is plotted for individual diamond concentrations an interesting result appears as can be seen in Figure 5.20 below.

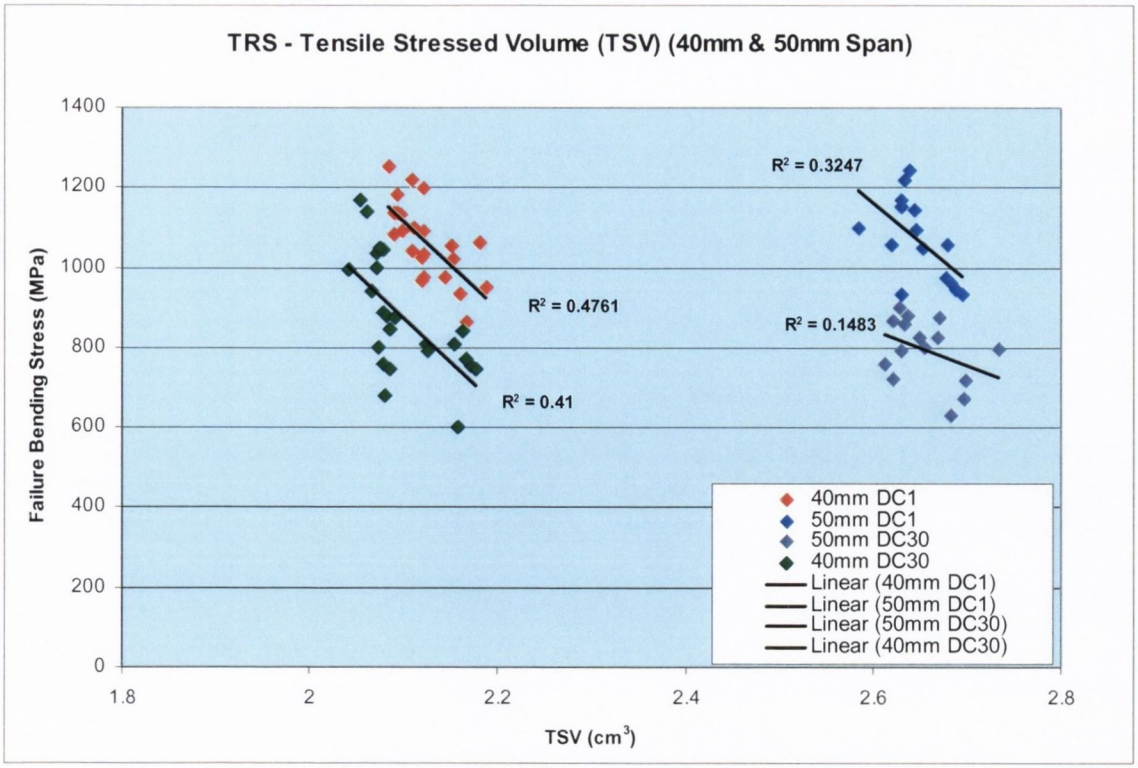

Figure 5.20. TRS Specimen Results: Figure shows TRS plotted against TSV for DC1 & DC30 for 40mm and 50mm spans. Correlation coefficients for DC1 (40mm) R = 0.69, DC30 (40mm) R = 0.64, DC1 (50mm) R = 0.57 & DC30 (50mm) R = 0.39.

When plotted for individual diamond concentrations for both spans, as can be seen in Figure 5.20 that as diamond concentration increases TRS decreases for given *TSV* values. This indicates that the diamond is behaving as a flaw and so a crack initiation mechanism, and with increasing diamond more opportunity is available for crack initiation and also clustering effects would be more prevalent. As already stated above, this will be treated in more detail later in this chapter.

5.4.3. Inter-Particle Spacing (IPS) & TRS

Similar to Charpy impact the relationship of IPS and TRS will be coverd here. The same formulae and designations for IPS/MFP and IPS/NND as that used for Charpy impact will be used.

5.4.3.1. TRS & IPS/MFP

Similar to Charpy impact, using Equation 5.1 for IPS/MFP and plotting TRS against IPS/MFP (λ) (mm) for the full range of DCs and US Mesh sizes the results can be seen in Figure 5.21. Again the inclusion of DC1 causes the other DC data to be compressed. The IPS/MFP determined for DC1 is very large in comparison to the other DCs. The

graph also seems to show two different sets of data, one set for DC1 and the other the compressed data for the other DCs.

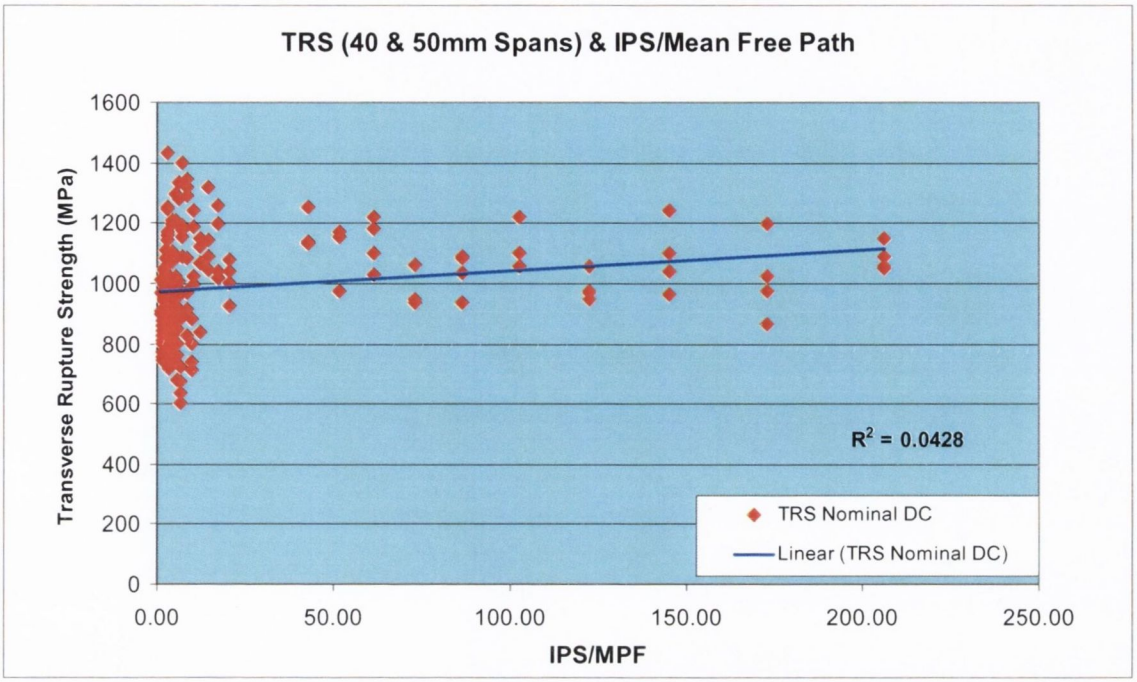

Figure 5.21. TRS Specimen Results: Graph of TRS plotted against IPS/MFP. DC1 was included in this graph using IPS/MFP. R = 0.21.

So with DC1 excluded a better result is found in that the compressed data can be examined more clearly in Figure 5.22. Contrary to that found for Charpy impact, TRS and IPS/MFP were found to be statistically significant, ($p<0.05$) [280], with a correlation coefficient R equal to 0.27, as seen in Figure 5.22. Similarly TRS and √IPS/NND and also Log (IPS/NND) were found to be statistically significant, ($p<0.05$) [280].

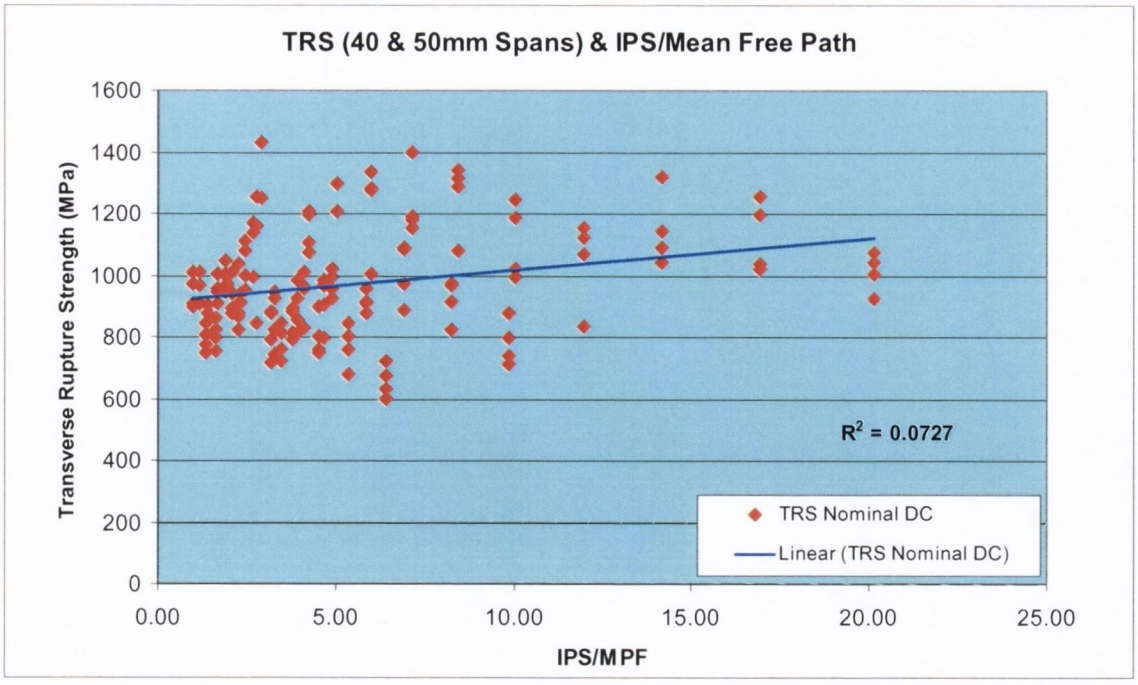

Figure 5.22. TRS Specimen Results: Graph of TRS plotted against IPS/MFP. DC1 was not used because of its large IPS/MFP. N = 156, R = 0.27.

When the IPS/MFPs for a range of diamond sizes for constant DC similar to Charpy impact it indicates that US Mesh size is an important factor. This is not to say that DC is not important but the effect of DC and US Mesh size is hidden when plotted using IPS/MFP against the full data set. The graphs in Figure 5.23 clearly show the strong influencer that diamond size is with correlation coefficients of 0.45 and 0.51 for DC10 and DC30 respectively.

Even though coarser diamond does result in a larger IPS/MFP it clearly indicates that for each DC, the coarser US Mesh sizes have the lowest TRS within each DC. It clearly indicates that diamond size is very important and that the diamond is present as a flaw and under stress causes crack iniatition. At a constant DC, the IPS/MFP increases with increasing diamond size but also as DC increases, it is similar to increasing flaw sizes through the formation of clusters and also the greater chance of finding a diamond 'flaw' in the stressed volume.

The graphs of 1/(IPS/MFP) & √(IPS/MFP) against TRS can be seen in the Appendix 8.

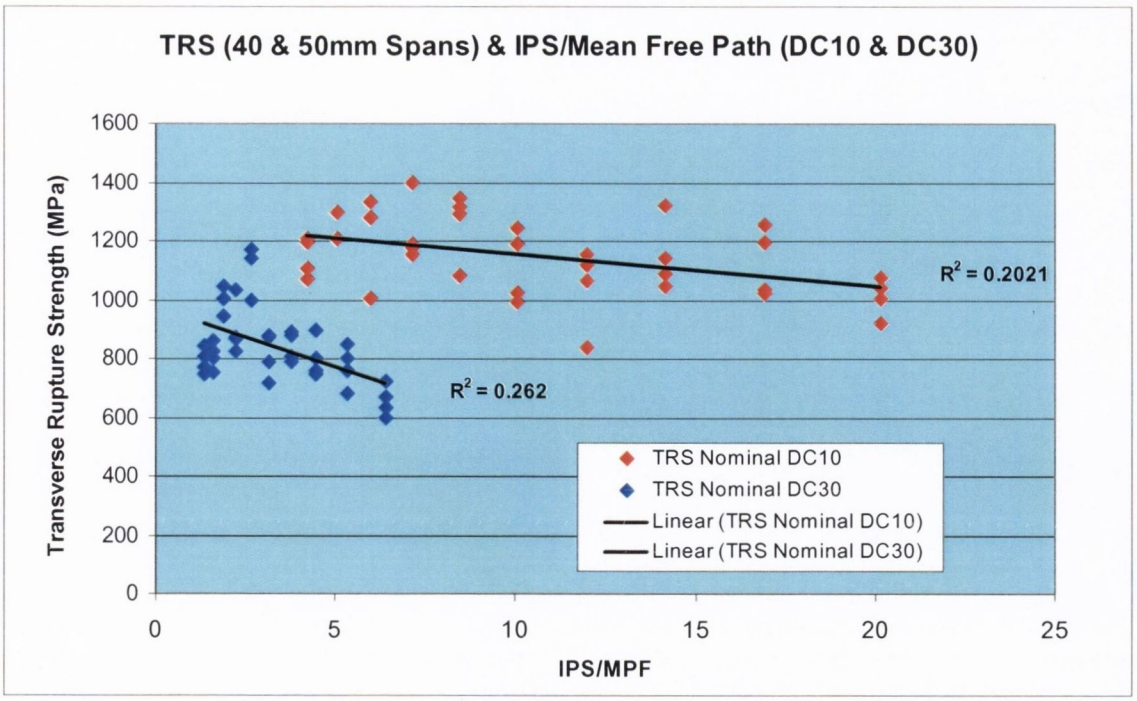

Figure 5.23. TRS Specimen Results: Graph of TRS plotted against IPS/MFP for diamond concentrations, DC10 and DC30. DC10 R = 0.45, & DC30 R = 0.51.

5.4.3.2. TRS & IPS/NND

When the TRS of DICoMM materials are plotted against IPS/NND using 'Edelson & Baldwin–Ritter', 'Edelson & Baldwin–Bhat' and also 1/(IPS/NND) or √(IPS/NND)) the results are not very conclusive. However when TRS and IPS/MFP's for a range of US Mesh sizes at constant DCs are plotted very similar results to those of Charpy impact are found. Graphs of the results can be seen in Appendix 8 for IPS/NND.

5.4.4. TRS & Ductility – 'Displacement @ Break'

The ductility of bend specimens can be measured as the 'Displacement-at-Break'. Hosking et al. have found that for PMMCs the ductility is a function of volume-fraction but is independent of particle size. Regarding DICoMM materials, it is found that diamond concentration and particle size strongly influence ductility as measured by 'Displacement-at-Break', as can be seen in Figures 5.24 and 5.25 below. The results are just for the TRS tests carried out on DICoMM specimens using 40mm span. For diamond size, results for different DCs are plotted against diamond size and show a reasonable correlation, with correlation coefficients for DC1 of $R = 0.41$, DC20 of $R = 0.40$ & DC30 of $R = 0.48$.

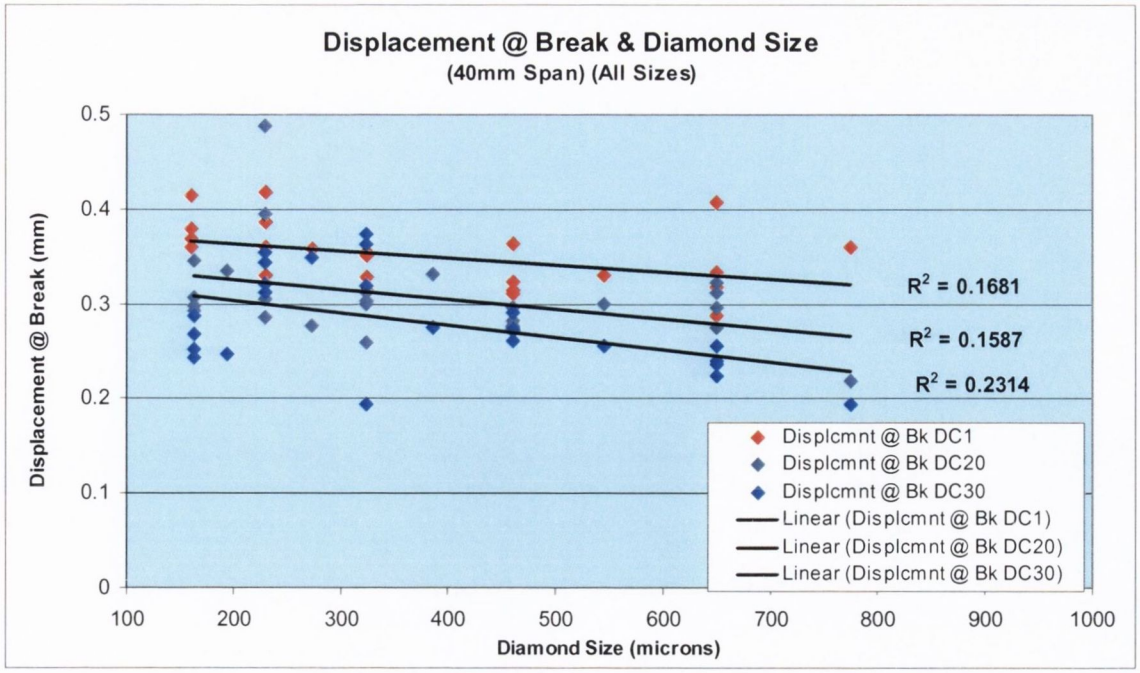

Figure 5.24. TRS Specimen Results: Graph of 'Displacement @ Break' plotted against diamond size. The trendline showing a decreasing displacement with increasing diamond size, DC1, DC20 and DC30. R values for DC1 = 0.41, DC20 = 0.40 & DC30 = 0.48.

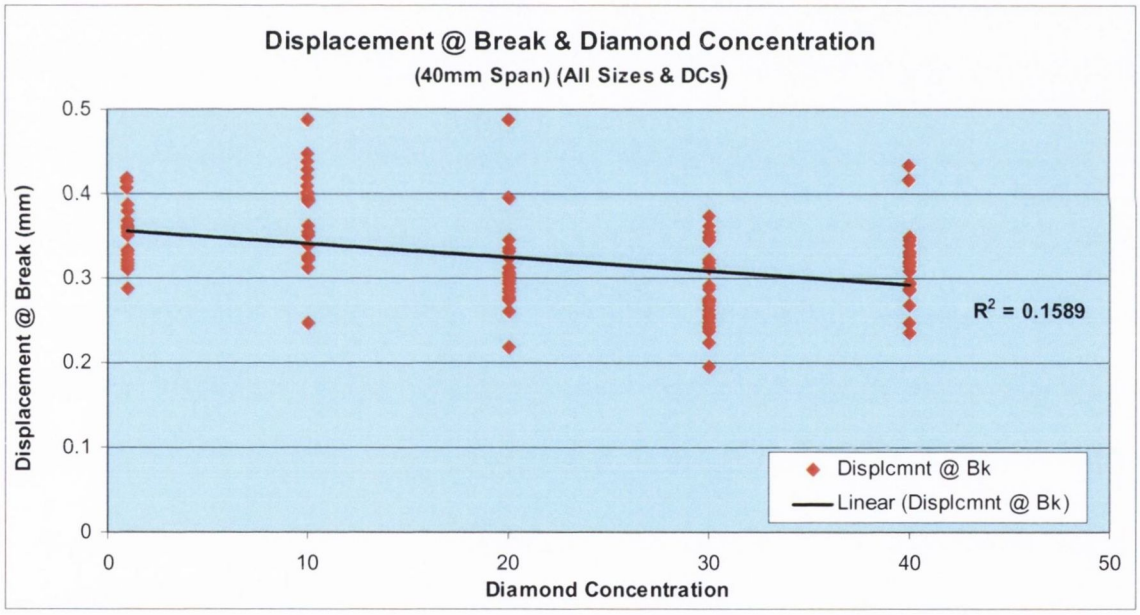

Figure 5.25. TRS Specimen Results: Graph of 'Displacement @ Break' plotted against DC. The trendline showing a decreasing displacement with increasing DC, R = 0.40.

In Figure 5.25 where 'Displacement-at-Break' is plotted against diamond concentration shows with increasing diamond concentration 'displacement-at-break' decreases with a correlation coefficient *R* equal to 0.40, in agreement with Hosking et al. [192]. Again from the previous results in this project it shows that addition of diamond introduces crack initiating flaws to the cobalt matrix, and with increasing DC and diamond size it increases the chance of finding a fatal flaw thus reducing DICoMM ductility.

Failure may occur from a defect within the test piece and not from the surface. The true fracture stress is then rather lower than that calculated. Failure may occur away from the loading point in three-point bending, or between the loading and support points in four-point bending. Again, the true fracture stress is lower than that calculated, but this error can be corrected if the position of the failure relative to the loading point is noted.

5.5. Introduction Fracture Toughness Results Analysis

As already covered in previous chapters, the fracture toughness properties of DICoMM materials were determined experimentally using two different methods i.e. FastTrack & SERIES-IX, which yielded two different sets of results: plane strain fracture toughness K_{IC} and a nominal result, K_Q. To recap, the FastTrack method conformed fully to the ASTM E-399-90 standard but the SERIES-IX method only partially conformed. These results will now be analysed from a number of aspects in this section. Firstly, the relationship between percent theoretical density and fracture toughness, K_{IC} and K_Q will be examined for both methods. This will be followed by comparing the FastTrack and SERIES-IX K_{1C} results to see if the stringent procedures are fully necessary. Following this will be the modelling and prediction of fracture toughness K_{IC}.

5.5.1. Fracture Toughness Testing & %Theoretical Density

The effect of increasing percent theoretical density on the fracture toughness (K_{IC} & K_Q) of DICoMM materials can be seen in Figure 5.26 for FastTrack and Figure 5.27 for SERIES-IX. Both indicate an increasing trend between percent theoretical density and overall fracture toughness. For both FastTrack and SERIES-IX the results are statistically significant, ($p<0.05$) [280]. In SERIES-IX, with a coefficient of determination $R^2 = 0.41$, indicates that 41% of fracture toughness can be accounted by percent theoretical density, which agrees with that found by other researchers for PM materials [69, 70, 91, 92, 282]. Interestingly for FastTrack only 5% can be accounted for by percent theoretical density.

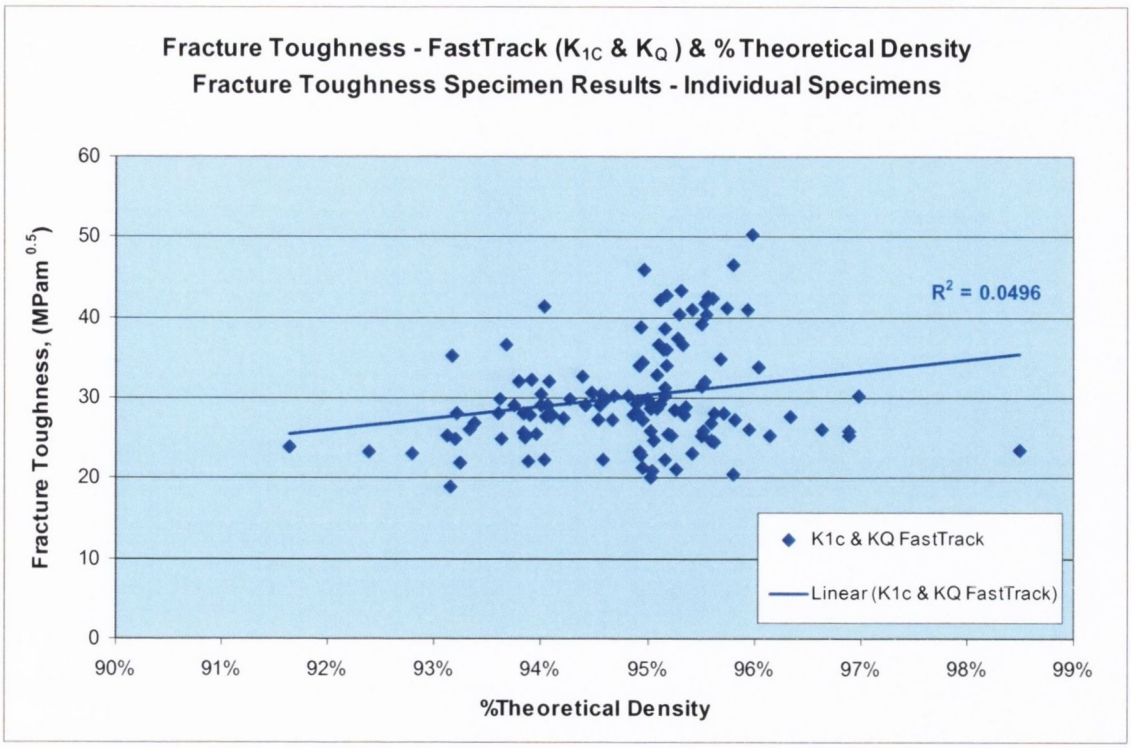

Figure 5.26. Fracture Toughness Specimen Results: Figure shows FastTrack combined K_{1C} & K_Q results plotted against %TD. Sample size: Total 122, (K_{1C} 51 & K_Q 70), R = 0.22.

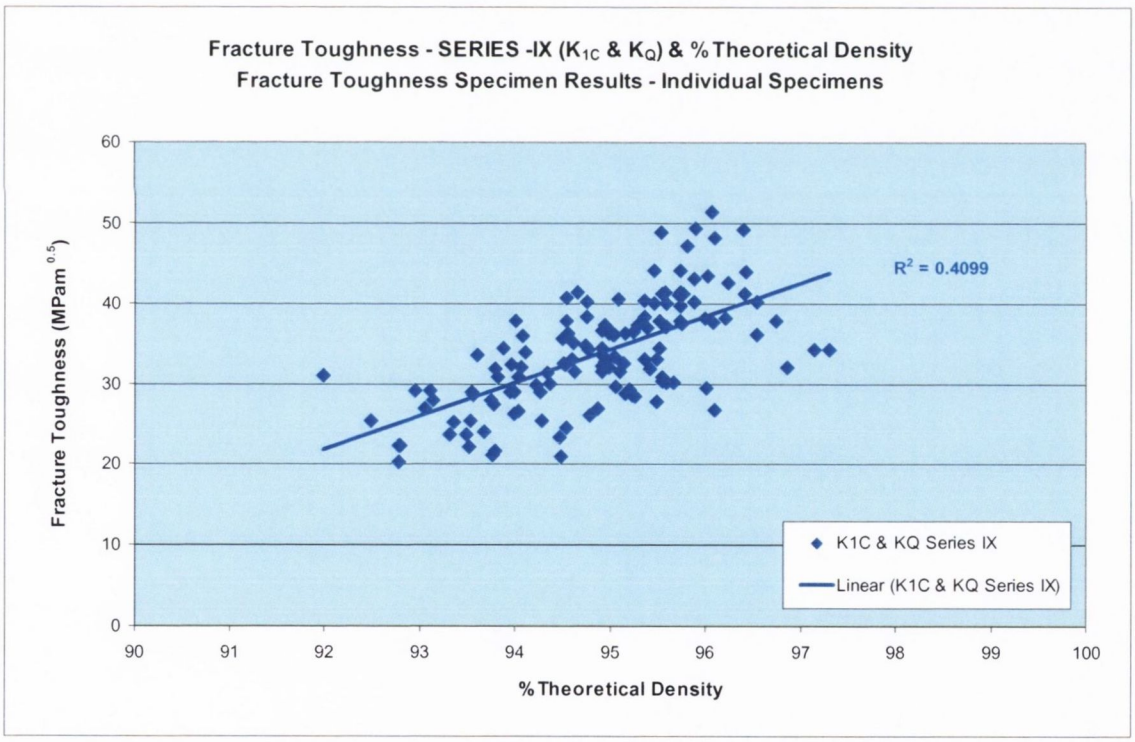

Figure 5.27. Fracture Toughness Specimen Results: Figure shows SERIES-IX combined K_{1C} & K_Q results plotted against %TD. Sample size: Total 132. (K_{1C} 37 & K_Q 99), R = 0.64.

When K_{IC} and K_Q are separated out and plotted against %TD for FastTrack and SERIES-IX, as can be seen in Figures 5.28 and 5.29 differences between the two methods does become apparent. For FastTrack, the K_Q and %TD were found to be statistically significant, (p<0.05) [280] with a correlation coefficient R of 0.38. It also shows that

14% of the variation in K_Q can be explained by %TD. However, K_{IC} FastTrack shows no statistical signficance with %TD, which the author proposes is the result of using a fatigue crack and also the presence of diamond.

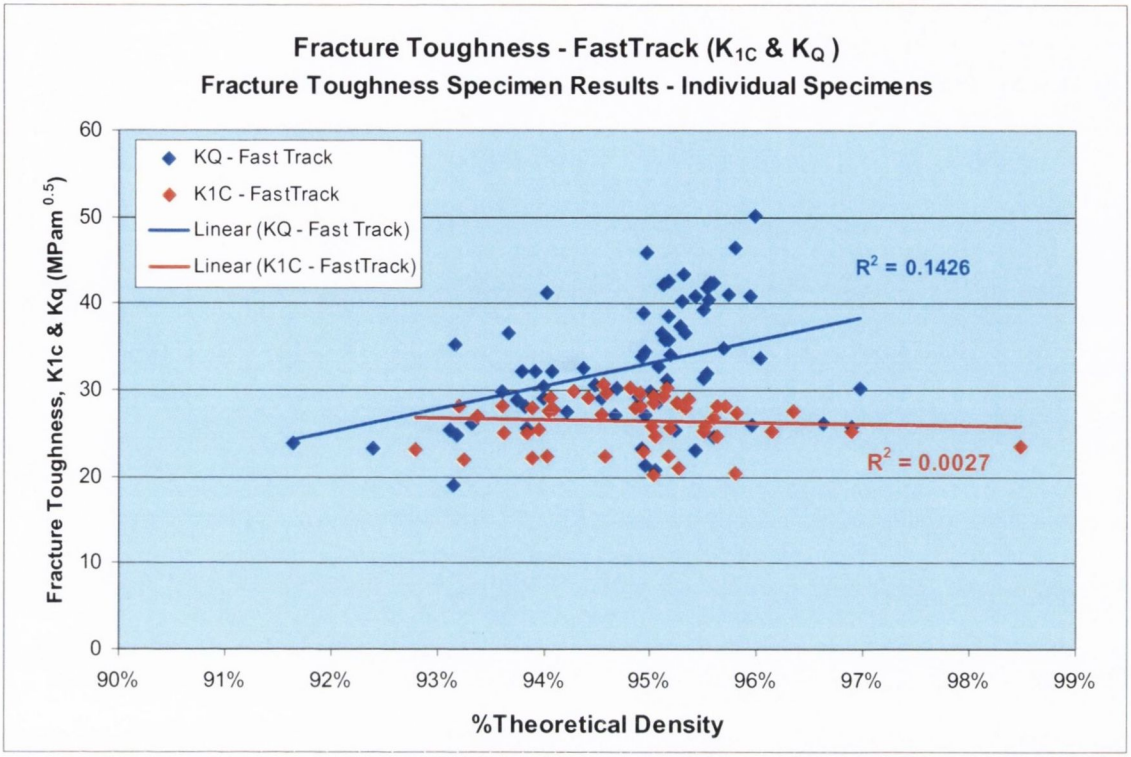

Figure 5.28. Fracture Toughness Specimen Results: Figure shows FastTrack results for K_{1C} & K_Q plotted against %TD. Sample size: K_{1C} 51, R = 0.05 & K_Q 70, R = 0.38.

Regarding SERIES-IX fracture toughness results both K_{IC} and K_Q with regard to percent theoretical density were found to be statistically significant, (p<0.05) [280], with correlation coefficients, R equal to 0.46 and 0.50 respectively. The differences found between K_{IC} FastTrack and K_{IC} SERIES–IX results will be treated in more detail later in this section.

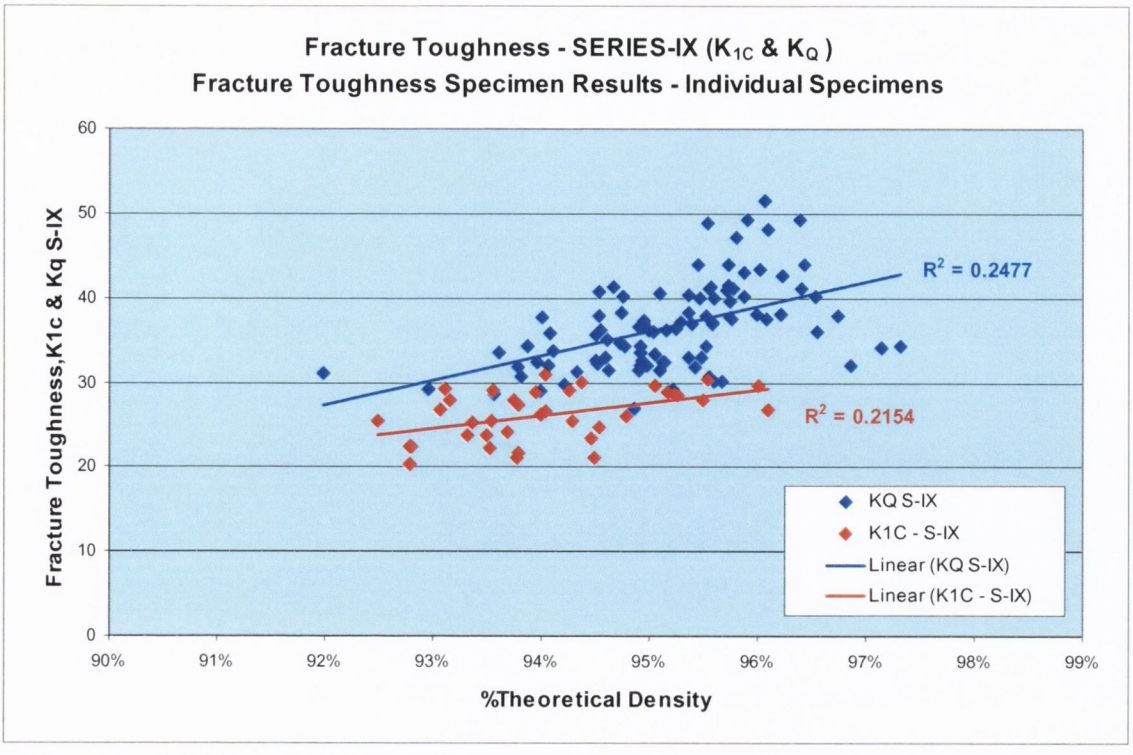

Figure 5.29. Fracture Toughness Specimen Results: Figure shows SERIES-IX results for K_{1C} & K_Q plotted against %TD. Sample size: K_{1C} 37, R = 0.46 & K_Q 99, R = 0.50.

As already mentioned in Chapter Four, Results, there are many reasons why specimens failed to qualify as valid plane strain fracture toughness K_{IC} values. Percent theoretical density does play a role in this because for PM materials an increase in %TD increases the yield strength which increases fracture toughness, Ganesan et al. [70] found that fracture toughness increases proportionally if the yield strength is varied with higher densities. However, when an increase in yield strength due to an increase in %TD cannot be accommodated in the ASTM E-399-90 validity criteria false positives could result.

The other two important factors that are particular to this project are the presence of a fatigue crack and an edm notch which influences the load P_Q to fracture the specimen. A fatigue crack has very different notch acuity than an edm crack. Also, for an edm notched specimen, a larger fracture surface is present than that for a fatigued specimen and so the P_Q to fracture will be increased resulting in a higher fracture toughness result which could possibly fail the 'a', 'B' $\geq 2.5(K_Q/\sigma_{ys})^2$ validity criteria, especially when a constant yield strength is used. For the FastTrack method the more stringent criteria can invalidate results which don't happen for SERIES-IX. Also, a fatigue precrack crack tip has a much lower value of notch acuity making it easier for crack initiation to occur leading to a lower P_Q value at higher %TD than for a similar SERIES-IX specimen with the same %TD. Regarding the K_{IC} SERIES-IX result notch acuity is much greater than

that of a fatigue crack, which with an increasing %TD will require a higher P_Q value to cause fast fracture, resulting in a higher fracture toughness value.

Figure 5.30 shows the effect of an increase in yield strength on the determination of a valid plane strain fracture toughness result according to the ASTM E-399-90 standard. Regarding this project where 680MPa has been used, an increase from 680MPa to 780MPa in yield strength would increase the validity range for a valid K_{IC} of 5MPam$^{0.5}$.

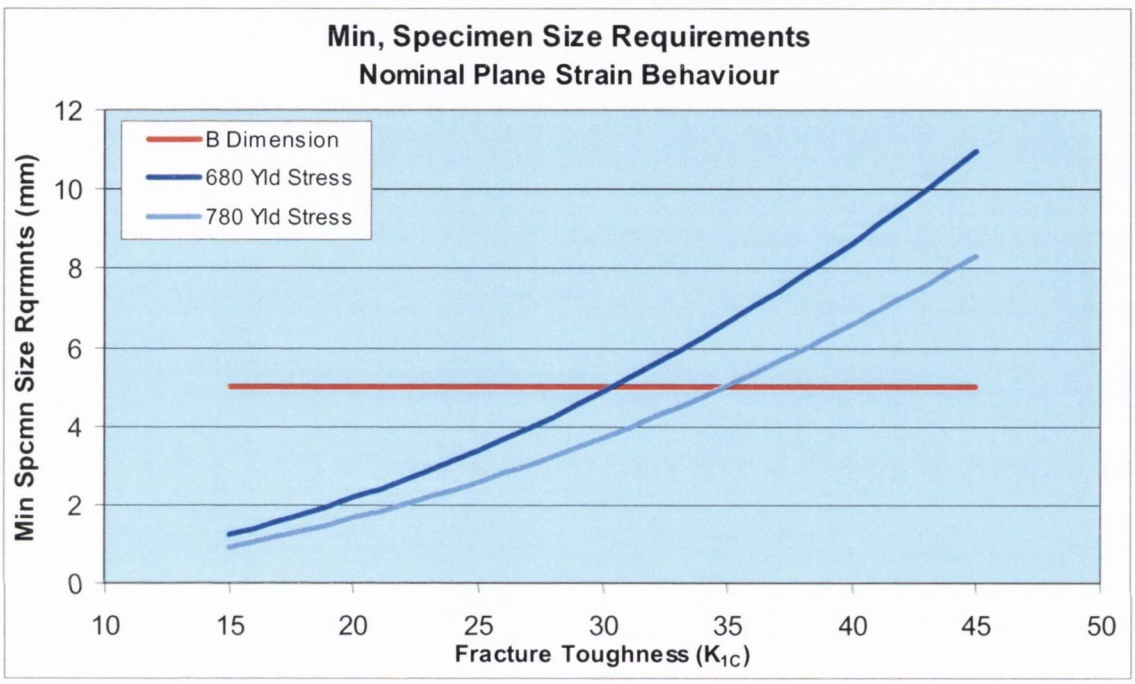

Figure 5.30. Shows the effect of a yield strength increase on a valid K_{1C} result according to ASTM E-399-90 standard.

The inequality $(K_{IC}/\sigma_{ys})^2$, developed by Brown & Srawley [260] found empirically that a valid plane-strain fracture toughness test is performed when the specimen thickness and crack length are both greater than a certain minimum value. From equations 5.3 & 5.4 below $(K_{IC}/\sigma_{ys})^2$ is related to the size of the plastic zone. For plane strain conditions the triaxial stress field suppresses the plastic zone size, the plane strain zone radius is smaller and has been estimated to be

$$r_y \approx \frac{1}{6\pi}\frac{K^2}{\sigma_{ys}^2} \quad \text{for plane strain conditions} \qquad (5.3)$$

$$r_y \approx \frac{1}{2\pi}\frac{K^2}{\sigma_{ys}^2} \quad \text{for plane stress conditions} \qquad (5.4)$$

A higher yield strength would maintain plane strain conditions in the specimen thickness.

Regarding the SERIES-IX and FastTrack in Figure 5.31 K_Q values are plotted against %TD, what is clearly evident is that higher density leads to higher fracture toughness. As said previously, a higher %TD in PM materials is found to lead to an increase in yield strength so a portion of these K_Q results could be considered as valid. The results are statistically significant for both SERIES-IX and FastTrack. The FastTrack results shown in Figure 5.31 are only for FastTrack specimens which failed to grow a fatigue crack so are similar to the SERIES-IX specimens with an edm starter crack of 2.0 mm.

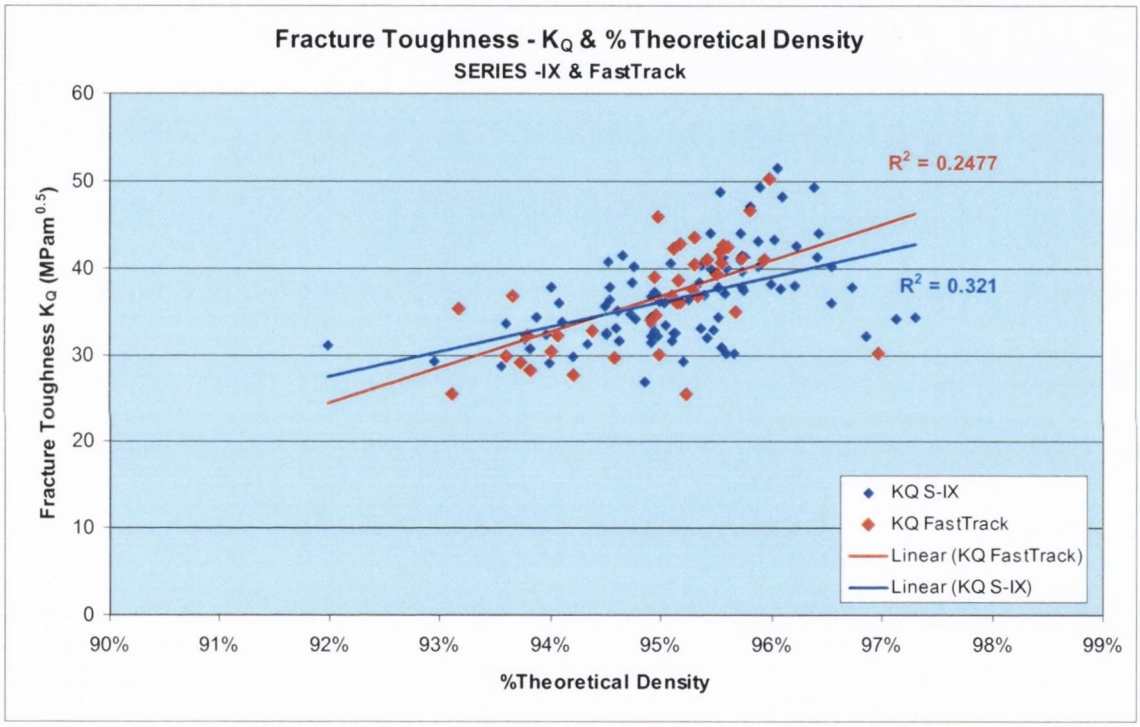

Figure 5.31. Fracture Toughness Specimen Results: Figure shows K_Q for FastTrack & SERIES-IX plotted against %TD. SERIES–IX R = 0.5 & FastTrack R = 0.57.

It must not be forgotten too that the presence of diamonds does confound the fracture toughness results, because as will be presented later in this chapter, the diamonds are acting as flaws which influence the fracture stress required for crack propagation and final failure.

5.5.2. FastTrack & SERIES-IX Method – K_{IC} Statistical Analysis

In Figure 5.32, the K_{IC} results for FastTrack and SERIES-IX are plotted against %TD, where it can be seen that using the different methods the results are very comparable.

The average value and standard deviation for K_{IC} (FastTrack) is 26.33 MPa.m$^{0.5}$, and 2.81std. dev. and SERIES-IX is 26.09MPa.m$^{0.5}$, and 2.97 std. dev. Standard deviations across all diamond concentrations are very similar and can be seen in Chapter Four, Results.

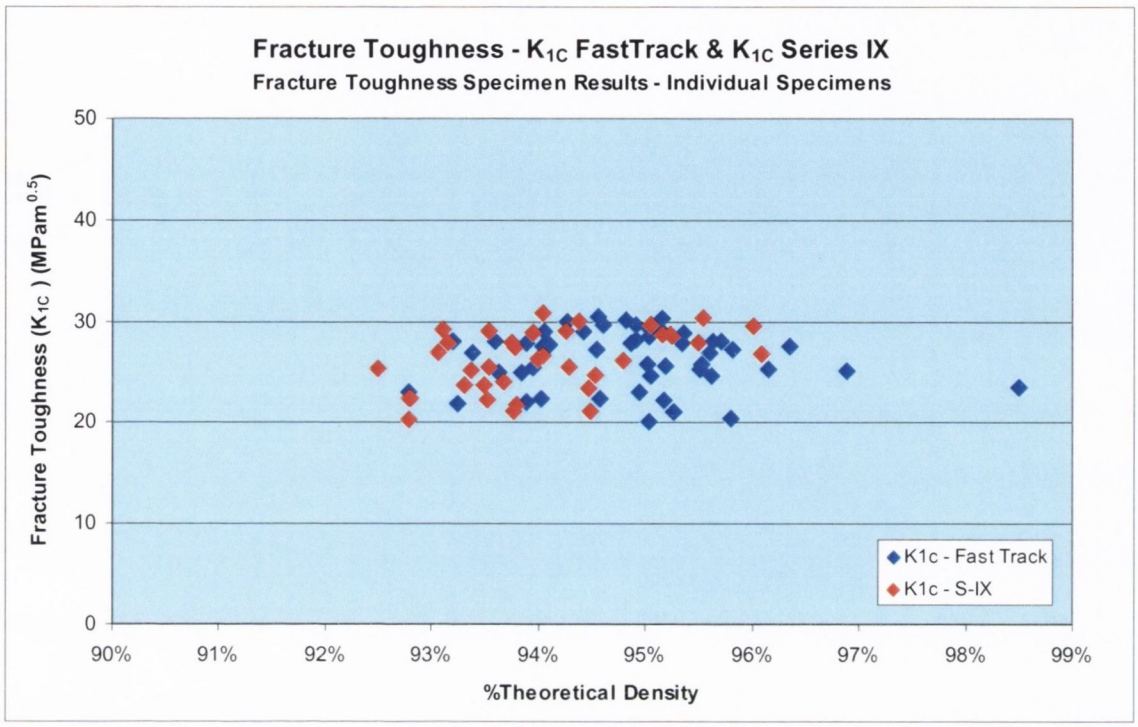

Figure 5.32. Fracture Toughness Specimen Results: Figure shows K_{1C} for FastTrack & SERIES-IX plotted against %TD. Sample size: SERIES-IX 37 & FastTrack 51.

FastTrack K_{IC} versus SERIES-IX K_{1C} same family, show, no need for atomically sharp crack and also that a/W doesn't matter. One of the important questions to be answered robustly is whether there is a need to use a full scale fracture toughness test procedure following strictly the ASTM E-399 or are the researchers who state that there is no need for an atomically sharp crack or even a correct a/W ratio in order to obtain a valid K_{IC} fracture toughness. This question was briefly answered when the data for K_{IC} plane strain fracture toughness determine using FastTrack was plotted against K_{IC} was determined using SERIES-IX, which showed no difference. Statistical analysis was carried out using Mintab statistics software. When the results of K_{IC} for the various DICoMM specimens using the FastTrack method are compared with the K_{IC} results using SERIES-IX, the statistics states that no difference remains, which is in agreement with the literature regarding PM materials. Also it shows that an atomically sharpy crack is not required, but also that the a/W requirement is also unnecessary [95]. This result was tested using Mintab, a statistical software package, where an Anova using a General

Linear Model was used to test for significance between the results determined using FastTrack method against the SERIES-IX method. A p value of 0.272 indicates no significance between the two methods for determining valid K_{IC} results. See in results displayed in Table 5.1 below,

Table 5.1 Minitab – General Linear Model

General Linear Model: K_{1C} versus DC, US Mesh Size, Method

```
Factor   Type   Levels  Values
DC       fixed       6  1, 10, 20, 25, 30, 40
US Mesh  fixed       8  20/25, 30/35, 40/45, 45/50, 50/60, 60/70, 70/80, 80/100
Method   fixed       2  FasTrck, Series IX


Analysis of Variance for K1c, using Adjusted SS for Tests
Source   DF   Seq SS   Adj SS  Adj MS     F      P
DC        5   26.455   28.064   5.613  0.89  0.495
US Mesh   7  212.248  219.915  31.416  4.96  0.000
Method    1    7.761    7.761   7.761  1.23  0.272
Error    74  468.796  468.796   6.335
Total    87  715.259

S = 2.51696   R-Sq = 34.46%   R-Sq(adj) = 22.94%
```

The null hypothesis asserts that US Mesh size has an affect but we cannot assert that DC and method (FastTrack & SERIES-IX) are having an affect. This lack of certainity is that sample size may not be large enough or that DC and method have no effect at all. This is statistically tested by checking the power of the test and sample size. An effect value or difference in K_{IC} of 2 was used as being of interest in determining the power and sample size. A value as low as 2 for K_{IC} was used because it increases the power of the test. A result of 0.9389 was determined which is statistically an excellent result. This can be seen in Table 5.2 below.

Table 5.2 Power and Sample Size - Minitab

Power and Sample Size

```
2-Level Factorial Design
Alpha = 0.05  Assumed standard deviation = 2.51696
Factors:    3   Base Design: 3, 8
Blocks:  none
Center                  Total
Points  Effect  Reps    Runs      Power
   0       2    10      80      0.938930
```

The reader is referred to the excellent statistical primer by Reilly for more on these typical statistical analysis treatments [281].

However, an important result indicates that for DIMM materials an EDM crack starter notch of 2mm into the backing layer is sufficient. It shows that an atomically sharp crack is not required, but the a/W $(0.45<a/W<0.55)$ requirement is also unnecessary. In addition to this the requirement for knife edges for CMOD gauge attachment is unnecessary as found by [100].

The other interesting result is that DC is not significant regarding plane strain fracture toughness, which had a p value of 0.495. But US Mesh diamond size is found to be very significant regarding influencing the plane strain fracture toughness of DICoMM materials.

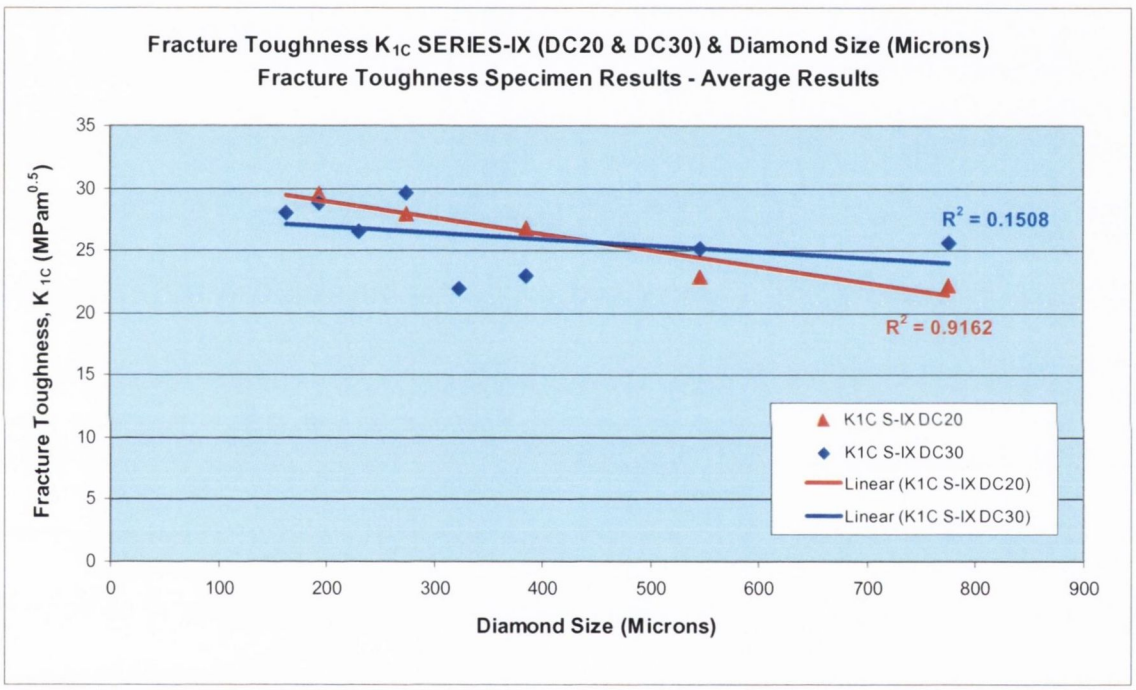

Figure 5.33. Fracture Toughness Specimen Results: Figure shows K_{1C} results for SERIES-IX versus Diamond Size (Microns) for DC20 & DC30. DC20 R = 0.96 & DC30 R = 0.39.

Figure 5.33 shows the effects of diamond size on the plane strain fracture toughness of DICoMMs for DC20 and DC30. The effect seen for DC20 is more pronounced showing a very high correlation coefficient in comparison to DC30. The author believes this is due to the fact that the results for DC30 are being interfered by clustering effects which is clouding the results. The results for DC20 show a very strong correlation with diamond size, with a correlation coefficient R equal to 0.96, and a reasonable R value for DC30 equal to 0.39 for DC30. Data for the other DCs is lacking because of very small numbers of valid K_{IC} data points for SERIES-IX. This effect of increasing particulate size decreasing toughness for a given volume fraction has been found for PMMCs by

Pillai et al. [118]. In Figure 5.34, the same data is plotted but using US Mesh size instead of diamond size measured in microns. The results for DC20 show a very strong correlation with diamond size, with an R value equal to 0.94, and a reasonable R value for DC30 equal to 0.58 for DC30. There is a definite trend of increasing diamond size and decreasing plane strain fracture toughness.

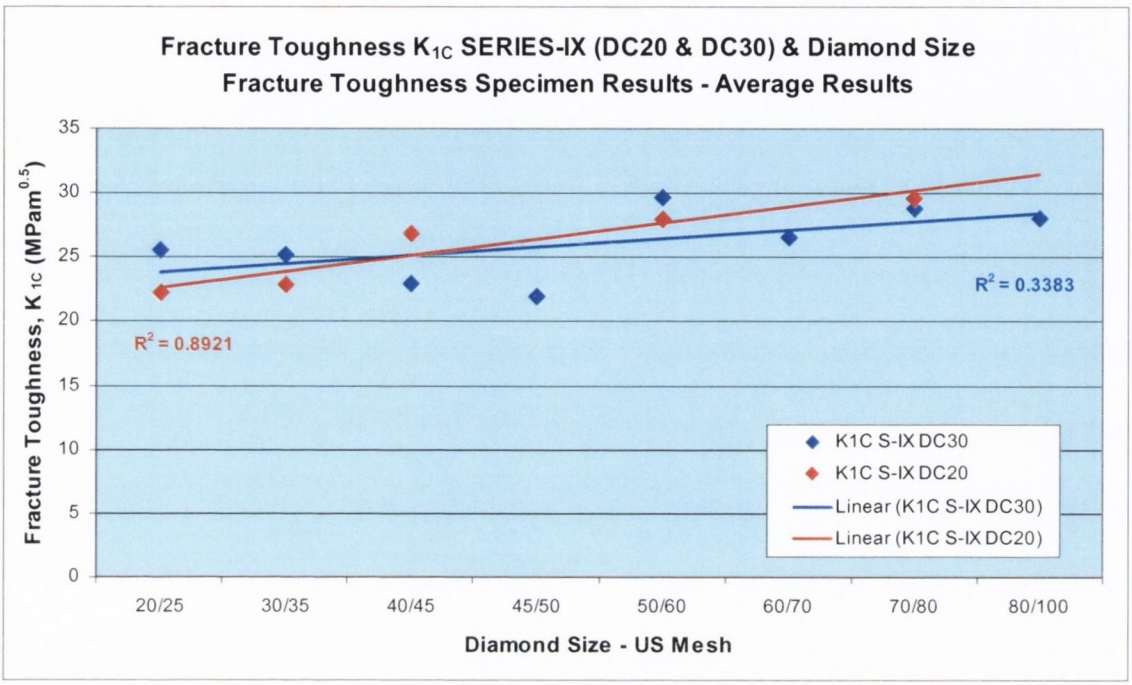

Figure 5.34. Fracture Toughness Specimen Results: Figure shows K_{1C} results for SERIES-IX versus Diamond Size (US Mesh), for DC20 & DC30. DC20 R = 0.94 & DC30 R = 0.58.

In Figure 5.35 K_{IC} FastTrack results are plotted against diamond size (microns) and shows for DC10, DC20 and DC40 strong correlation coefficients for decreasing fracture toughness with increasing diamond size. Results show that even with a fatigue precrack, diamond size influences the crack initiation process, possibly by increasing the crack size a_f with the presence of a single diamond or from diamond clustering at the crack tip as reported in Chapter Four, Results, section 4.10.

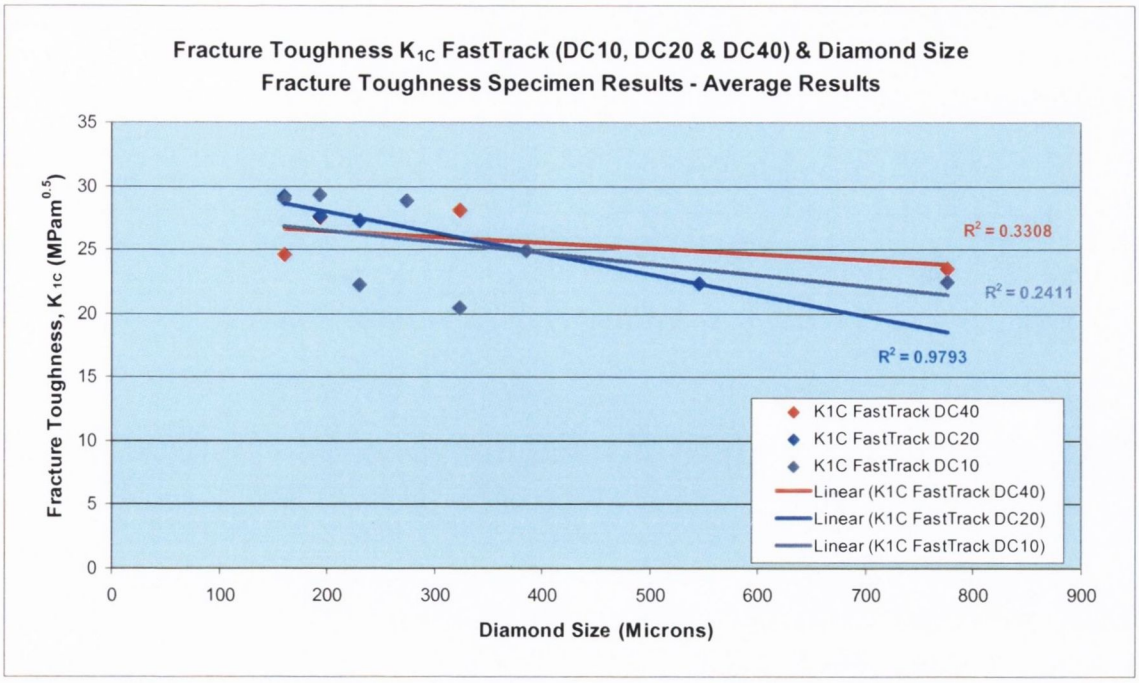

Figure 5.35. Fracture Toughness Specimen Results: Figure shows K_{1C} results for FastTrack versus Diamond Size (Microns) for DC10, DC20 & DC40. DC10 R =0.49, DC20 R = 0.99 & DC40 R = 0.58.

5.5.3. Fracture Toughness & IPS (MFP & NND)

As referred to in Chapter Two, Literature Review second phase particles however present and their volume fraction play a major role in mechanical properties including fracture toughness in PMMCs [191] with interparticle separation being an important factor [102]. So examination of IPS/MFP and IPS/NND is necessary to check if similar behaviour can be found for DICoMM materials. Before detailing IPS results, important to mention that besides nominal diamond concentration being used, experimentally determined diamond concentration is also included. As described in Chapter Three, Experimental Procedures the actual diamond concentration of the fracture surface was measured for each specimen using the image analysis software called Scentis. The plane strain fracture toughness results used here are the combined K_{1C} results for FastTrack & SERIES-IX.

Figure 5.36 shows the plane strain fracture toughness plotted against IPS/MFP (λ) (mm) using the following equation,

$$\lambda = \frac{2}{3}\frac{d_p(1-V_f)}{V_f} \qquad (5.5)$$

where V_f = volume fraction of spherical particles and d_p = particle diameter [186].

Specimen results for all diamond concentrations and US Mesh sizes are used in the graph in Figure 5.36. As can be seen, the inclusion of DC1 causes the other DC data to be compressed. The IPS/MFP determined for DC1 is very large in comparison to the other DCs.

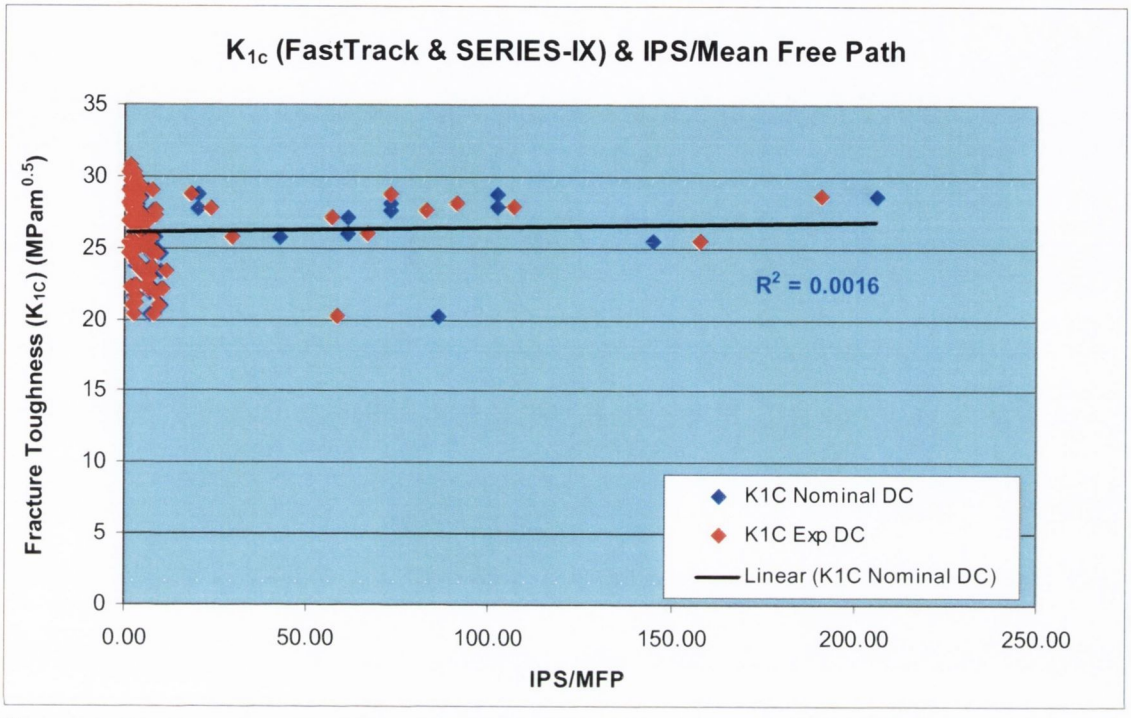

Figure 5.36. Fracture Toughness Specimen Results: K_{1C} for FastTrack & SERIES-IX combined plotted against IPS/MFP (mm). R = 0.04.

When DC1 is excluded a better result is found however when plotted as 1/(IPS/MFP) a better result is found relating IPS/MFP and K_{IC} which can be seen in in Figure 5.37. The data shows a reasonable correlation with an R value = 0.25. Plotting the experimentally determined diamond concentrations using Scentis does not really add anything to the results and using the nominal value for DC is acceptable. Examining this result indicates that an increasing 1/(IPS/MFP) one gets an increase in plane strain fracture toughness for diamond size and DC. However, DC has been shown not to be a factor using ANOVA statistical analysis in the previous section. So using 1/(IPS/MFP) alone would lead one to make an erronous assumption because IPS/MFP uses both diamond size and DC (as a volume fraction) in its calculation.

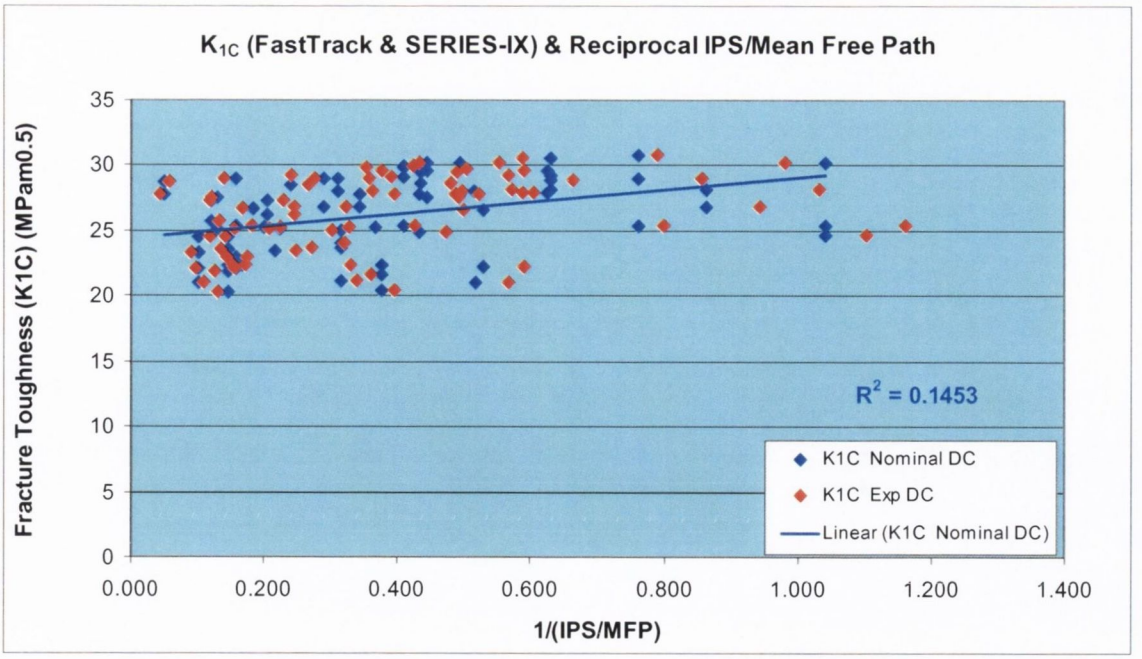

Figure 5.37. Fracture Toughness Specimen Results: K_{1C} for FastTrack & SERIES-IX combined plotted against of 1/(IPS/MFP). DC1 was not used because of its large IPS/MFP. R = 0.38.

IPS/MFP plotted against IPS/MFP, √(IPS/MFP) and Log IPS/MFP, as per Gensamer [187] against K_{IC}, reasonable correlations are found but the reciprocal of IPS/MFP gives the best result. The graphs of IPS/MFP & √(IPS/MFP) and Log IPS/MFP can be seen in the Appendix 9.

The formula used for IPS/Mean Particle Spacing also called IPS/NND (Δ_s) by Ritter [123, 194] based on Edelson & Baldwin [184] is as follows:

$$\Delta_s = d_P\left(1 - V_f\right)\sqrt{\frac{2}{3V_f}} \tag{5.6}$$

where

V_f = volume fraction of spherical particles and

d_p = particle diameter.

Again, similar to IPS/MFP, K_{IC} and the reciprocal of IPS/NND or 1/(IPS/NND) were found to be statistically significant, (p<0.05) [280], with a correlation coefficient R equal to 0.46, as seen in Figure 5.38.

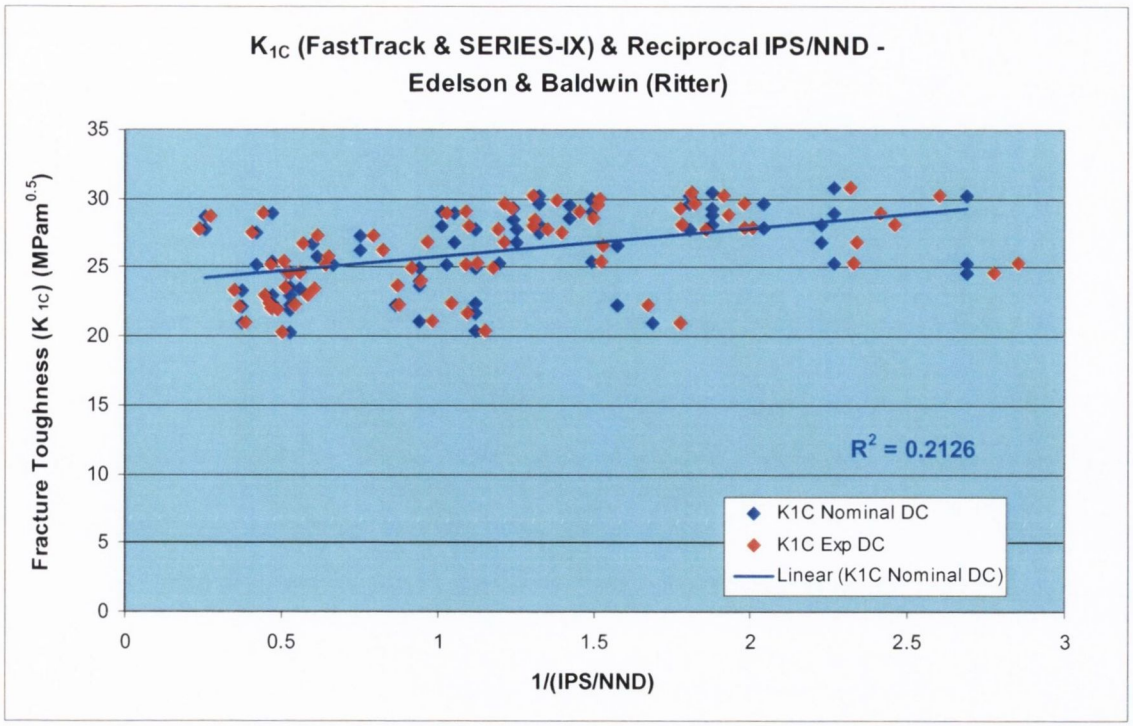

Figure 5.38. Fracture Toughness Specimen Results: K_{1C} for FastTrack & SERIES-IX combined plotted against Reciprocal of IPS/NND. DC1 was not used because of its large IPS/NND. R =0.46.

If one uses the Edelson & Baldwin – Bhat version of IPS/NND as referred to in the Chapter Two, Literature Review, only a marginally better correlation coefficient *R* equal to 0.47 is found [188]. These graphs can be seen in Appendix 9.

In Figure 5.39 where K_{IC} is plotted against IPS/NND for DC20 and DC30 shows as diamond size increases the value of K_{IC} decreases but still stays within the range of 20 to 30 approximately. Again this shows the influence of diamond size on crack initiation.

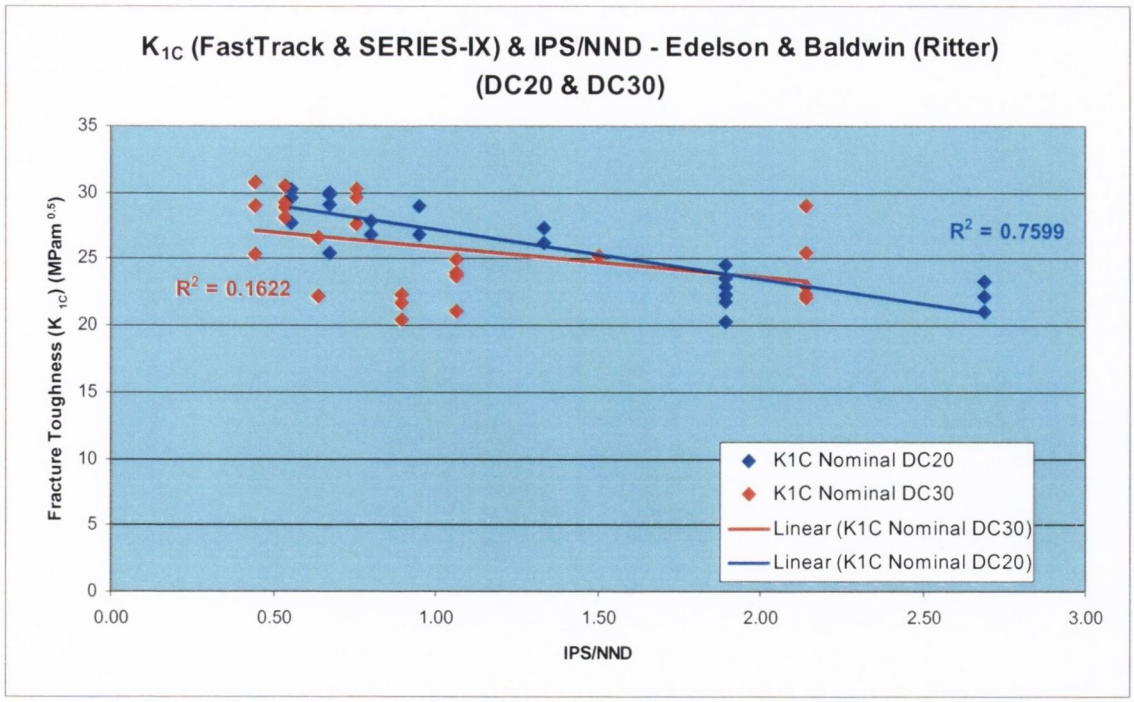

Figure 5.39. Fracture Toughness Specimen Results: K_{1C} for FastTrack & SERIES-IX combined plotted against IPS/NND for DC20 & DC30. DC20 R = 0.87 & DC30 R = 0.40.

Overall, the results of both IPS/MFP and IPS/NND are contrary to that of Bhat et al, [188] who found that increasing particle size for a given volume fraction increases the IPS/NND which increases toughness.

5.6. Modelling Strength and Fracture Properties in PMMCs

This next section will look at different models which are used in PM and PMMC materials. The modelling of strength and fracture properties in PMMCs is difficult, with many different models and types of models e.g. Ashby. However the accuracy of the models to cover the range of properties is very wide indeed, e.g. in an Al PMMC, the range had a magnitude of three times. Regarding brittle/brittle PMMCs, there are many models which have restricted ranges of applicability or are contradicitory regarding volume fraction and particle size [217]. A number of different models based on PM and PMMC models will be examined and their applicability to DICoMM materials will be examined. Some are micromechanical models while others are continuum type models.

5.6.1. Hahn-Rosenfield Fracture Toughness Model (Rice-Johnson Model)

The predictive model by Rice & Johnson [218] which was used for modeling the fracture toughness of dispersion reinforced alloys and have been used with some success with PMMCs [102, 219]. A number of models relating toughness to particle distribution have been developed for alloys which experience ductile failure [220]. The models are

basically where the process of nucleation of voids formed at or near the particle/matrix interface by decohesion or particle cracking, grow and finally coalesce. These models propose that the nucleated voids grow until they reach a critical size at which they coalesce through failure of the matrix ligaments. The Rice-Johnson model attempts to predict the true strain distribution ahead of a sharp crack and assumes that 'crack extension proceeds when the extent of the heavily deformed region is comparable to the width of the unbroken ligaments separating cracked particles' [221] giving the following formula:

$$\lambda_c \approx \delta^* \tag{5.7}$$

where λ_c, is the spacing of cracked particle approximates the ligament width, and δ^* approximates the extent of the heavily strain region, which corresponds to a predicted tensile strain of approximately 0.25 for small-scale yielding case. The model assumes that voids nucleate instantaneously and grow to coalescence.

Hahn & Rosenfield [221] have developed the Rice–Johnson model and failure criterion [218] for Al-based PMMCs with 'large' particles (10μm) with some success. Hahn & Rosenfield state that voids can be considered as 'inclusions' with no cracking resistance when it comes to dimple formation and that void nucleation occurs instantaneously and grows to coalescence. They assumed that crack extension would proceed when the crack tip opening displacement (CTOD) is comparable to the width of the ligament separating voids, i.e. δ^*, nucleated at the second phase particles. The CTOD is then used as a measure of fracture initiation toughness. For small yielding conditions, the CTOD, δ_{IC}, at fracture initiation is related to the plane strain fracture toughness by:

$$\delta_{IC} = \frac{K_{1C}^2}{2E\sigma_{ys}} \tag{5.8}$$

where σ_{ys} = yield strength, E = Young's modulus, and K_{IC} = plane strain fracture toughness.

Fracture initiation is assumed to occur when CTOD is equal to the spacing of void nucleating particles (λ), i.e. $\delta_{IC} = \lambda$, and so from Equation 5.8 the predicted plane strain fracture toughness is:

$$K_{1C} = \sqrt{2E\sigma_{ys}\lambda} \tag{5.9}$$

where λ = mean centre-to-centre particle spacing assuming a cubic array, given by

$$\lambda = \left(\frac{4\pi}{3V_f} \right)^{1/3} r \qquad (5.10)$$

where r = particle radius, (particles are taken as being spherical and uniformly distributed),

V_f = volume fraction.

Note, incorrectly notated as λ by both [220] and Downes [222] because it is intended to be IPS/NND and not IPS/MFP.

By substituting Equation 5.10 into Equation 5.9, one gets Equation 5.11. So this results in a model of fracture toughness as a function of particle size, spacing and volume fraction.

$$K_{1C} = \left[2\sigma_{ys} E \left(\pi/6 \right)^{1/3} d \right]^{1/2} V_f^{-1/6} \qquad (5.11)$$

where K_{IC} is the plane strain fracture toughness, where:

V_f = volume fraction of particulates (the void nucleating particle volume fraction).

d = particle diameter, (the void nucleating particle size),

σ_{ys} = yield strength

E = Modulus of Elasticity

A common criticism of the Hahn-Rosenfield model by a number of researchers [219,220], is that the above model indicates increasing yield strength gives an increase in fracture toughness, which is generally not the case; also K_{IC} being directly related to particle size and volume fraction, i.e. as particle size increases, fracture toughness increases, and as volume fraction increases fracture toughness decreases. Dependence of fracture toughness on particle size contradicted experimentally according to Legzdins [212] and Aikin [283]. Aspects that are missing are interfacial property relationship with fracture toughness, particle properties & matrix properties besides yield strength. [219].

Hahn et al. suggest that the reason for the anomaly is that void growth to coalescence is interrupted by the premature rupture of the material between the voids [221]. However,

this author would point out that for PM materials fracture toughness is found to increase with decreasing levels of porosity, which also leads to an increase in yield strength.

Applying the Hahn-Rosenfield model to DICoMM materials and taking the void nucleating particles as the diamonds with diamond concentration expressed as volume fraction proved to be totally unsatisfactory, and in fact gave results for fracture toughness two orders of magnitude greater than the experimentally determined K_{IC}. However, when the pore size of the cobalt matrix was used along with porosity expressed as a volume fraction a more representative result was found for the plane strain fracture toughness of DICoMM materials, as can be seen in Figure 5.40. As commented by another researcher [222] no nucleating particles could be found that could be taken to form the necessary voids. This author proposes that the presence of fine pores are providing the nucleating sites required. When the centre-to-centre distances of the ductile fracture dimples were taken as the pore spacings and used a more realistic value was found for the fracture toughness.

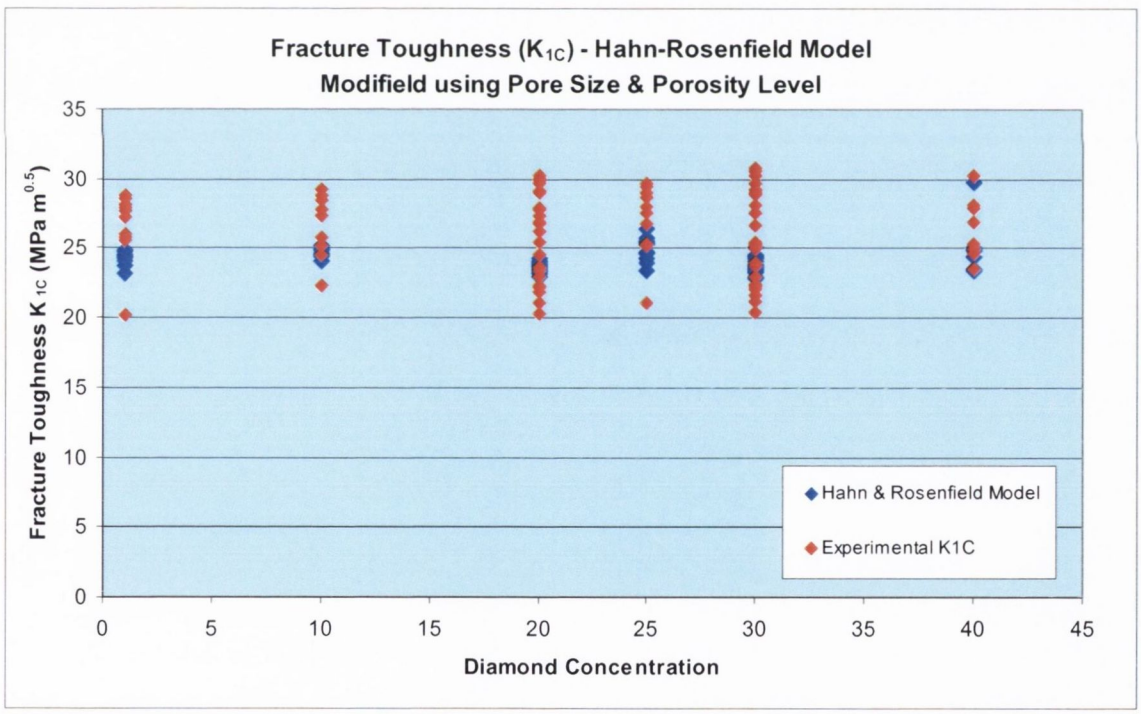

Figure 5.40. Fracture Toughness Specimen Results: Shows experimental fracture toughness K_{1C} with results using Hahn-Rosenfield model. Pore size used instead of particle size.

This finding is in keeping with Downes et al. [284] who describe in their findings that nucleation of matrix voids precedes particle fracture and that Hahn-Rosenfield model can be successfully applied and yielded similar results to experimentally determined

fracture toughness values. This author believes that this is what is happening with the DICoMM materials in this project, which will be shown in a later section to be actually the case.

Also, Rabiei et al. [220] indicate that the assumption of spherical shape for particles with uniform size and distribution in the model will result in a upper bound fracture toughness. Others note that, some correlation with experimental data has been found [222] various critical complicating micromechanical interactions have been identified, e.g. clustering/non homogeneous distribution of particles acting as preferential damage initiation sites, interfacial strengths also playing a role in decreasing fracture toughness [219].

5.6.2. Rabiei-Vendra-Kishi Fracture Toughness Model – Modified Hahn-Rosenfield

Rabiei et al. [220] proposed a modified Hahn-Rosenfield model whereby they change the basic assumption from the equality of CTOD with IPS/NND (λ) for coarse PMMCs, to the equality of CTOD with the centre-to-centre distance IPS/NND as used in the H-R model adjusted to the edge-to-edge IPS/NND. They do this not by using a standard IPS/NND equation but by subtracting the particle diameter (D) from the IPS/NND (λ) distance as used in the derivation of Equation 5.11. Following this they get Equation 5.12,

$$K_{1C} = \left[2D\sigma_{ys} E \left(\left(\pi / 6V_f \right)^{1/3} - 1 \right) \right]^{1/2} \qquad (5.12)$$

where V_f = volume fraction of particulates

D = particle diameter, (the void nucleating particle size),

σ_{ys} = yield strength

E = Modulus of Elasticity

Rabiei et al. [220] get a very good correlation using the Modified Hahn-Rosenfield model with their experimental results. Initially, using diamond size for D in both Hahn-Rosenfield model and the Modified Hahn-Rosenfield model, results were an order of magnitude greater than the experimentally determined plane strain fracture toughness results. However, when the cobalt metal pore size measured from SEM fractographs of

FT specimens and using porosity expressed as a volume fraction in both models more acceptable results were found. Figure 5.41 shows the experimental and predicted results. The average results for each DC are used for both the experimental and predicted results for clarity.

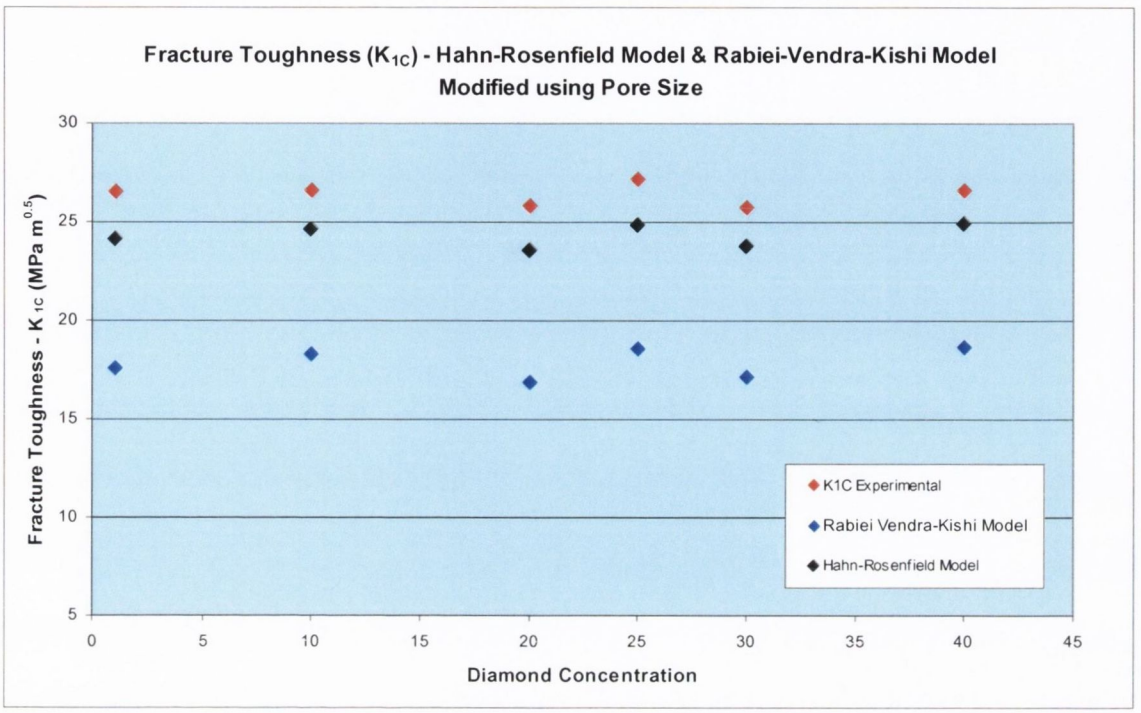

Figure 5.41. Fracture Toughness Specimen Results: Shows experimental fracture toughness K_{1C} results using Hahn-Rosenfield model & Rabiei Vendra & Kishi Model, a modified form of Hahn-Rosenfield model. Pore size used instead of particle size.

The prediction and experimental results are individual results for K_{1C} as determined by FastTrack and SERIES-IX.

5.6.3. Lin & Queeney Fracture Toughness Model

Regrading fracture toughness, simple models have been proposed to predict various strength responses of PM metals containing porosity [91. One such model used by Lin & Queeney [57] is as follows:

$$K_{1cp} = K_{1cFD} \cdot \chi \qquad (5.13)$$

where K_{1cp} = fracture toughness of PM,

K_{1cFD} = fracture toughness of full density PM,

χ = 'true-area' fraction of load bearing cross-section on the plane of fracture.

Lin et al. [57] used the diamond concentration expressed as a volume fraction as the 'true-area' fraction, which they assumed to be equivalent to the area fraction of pores on the fracture plane [91]. Zin et al found a 13% discrepancy between 100% matrix material and diamond impregnated samples.

Using the above model and using the diamond concentration as the 'true-area' fraction similar to Lin et al the results can be seen in Figure 5.42. Also plotted is using the diamond concentration and the porosity combined as the 'true-area' fraction. The average K_{IC} values for the different diamod concentrations are plotted. The two variations of Lin & Queeney models can be seen. One using diamond and porosity expressed as a volume fraction and the other variation using porosity only. The model using porosity only more closely follows the experimental results. The other two models are influenced by the diamond concentration because as DC increases the predicted K_{IC} decreases, even though the experimentally determined K_{IC} stays at a 'constant' value with increasing DC.

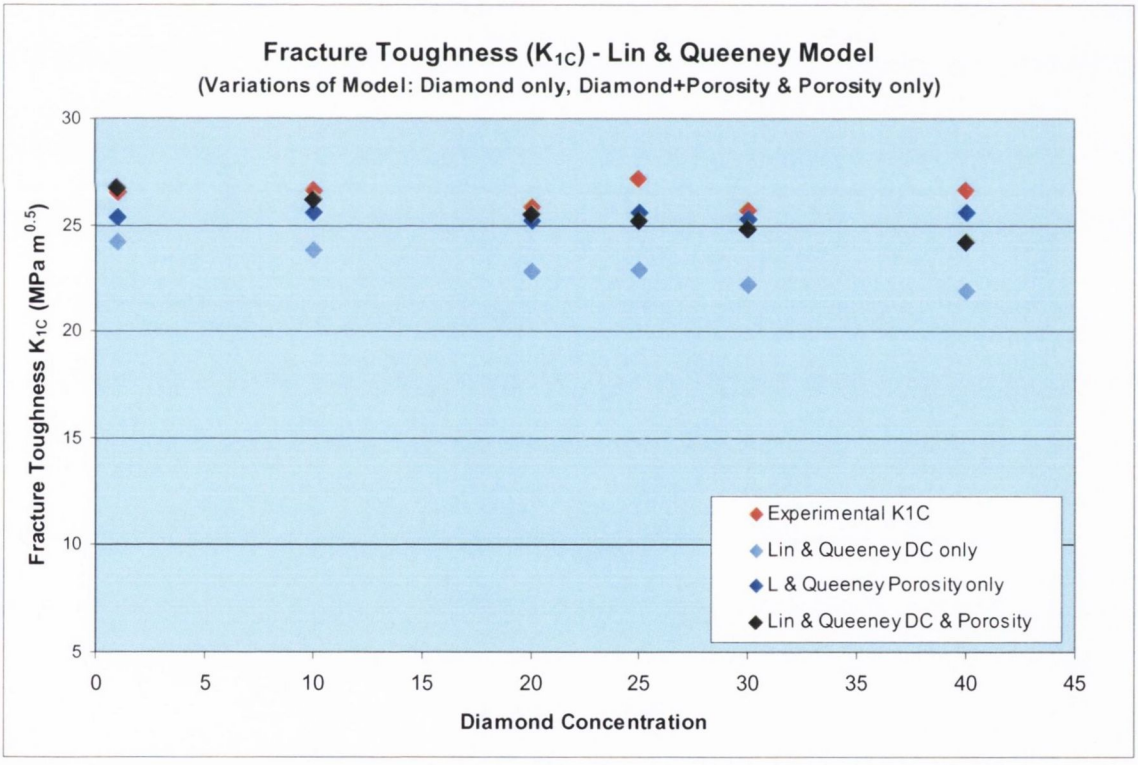

Figure 5.42. Fracture Toughness Specimen Results: Shows experimenatal fracture toughness K_{1C} results with prediction model of Lin & Queeney & variations of model.

Even though the diamonds are much stiffer than the metal matrix and so would be expected to increase the fracture resistance of the matrix, the diamond/matrix interface is weaker than the matrix and so the matrix will have its strength degraded, which is what

was found in this work. This will be examined further later in this chapter in more detail using the Theory of Critical Distances (TCD).

5.6.4. Kobayashi & Ohtani Fracture Toughness Model

Kobyshashi et al. [166] developed a model for predicting the static plane strain fracture (K_{IC}) toughness of particulate reinforced composite and found that the model gave an upper bound when compared to experimental results. From experimental evidence, Kobyashi et al describe the composite plane strain fracture toughness taking into account the composite constituent fracture toughnesses and volume fractions, as

$$K_{1C} = (K_M - K_P)\left(1 - V_f\right)^{1/2} + K_P \tag{5.14}$$

where

K_{IC} = composite fracture toughness,

K_M = matrix fracture toughness,

K_P = particulate fracture toughness,

and V_f = volume fraction of particulate.

Using the Kobyashi et al predictive model the results can be seen in Figure 5.43. Taking the plane strain fracture toughness of diamond as 5.6 $MPam^{0.5}$ [285] and the plane strain fracture toughness K_{IC} for CoMM as 25.64 $MPam^{0.5}$, as determined by experimentation in this project, the following result is found as can be seen in Figure 5.43.

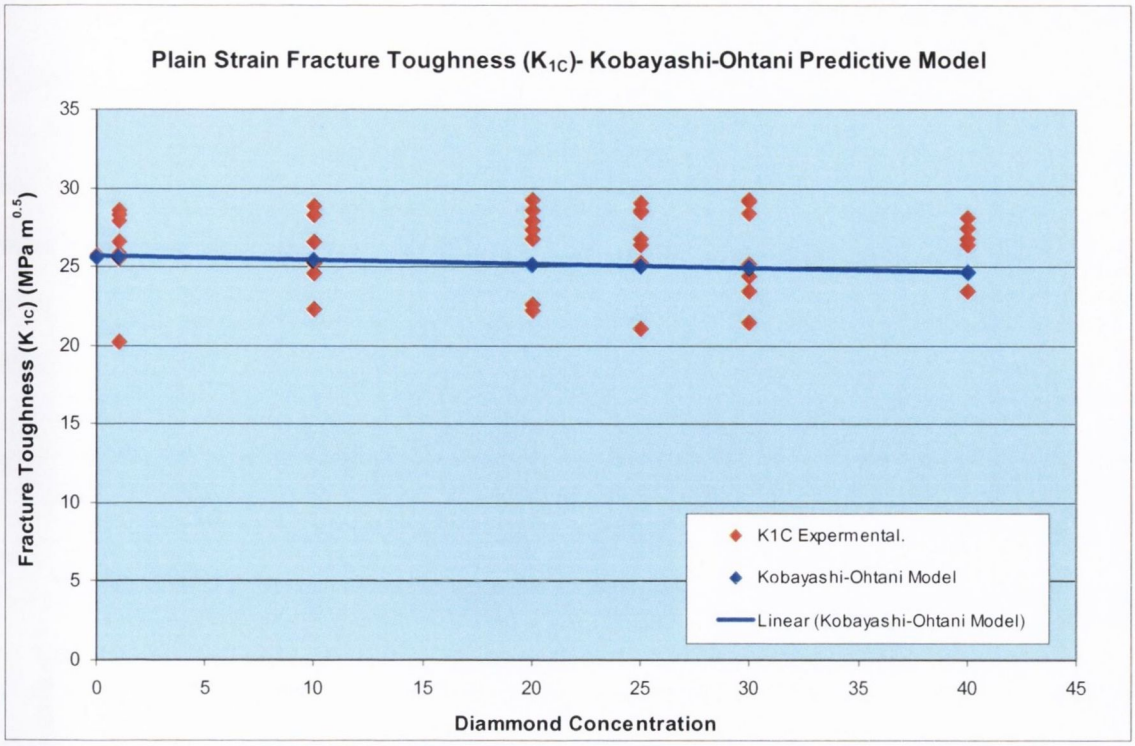

Figure 5.43. Fracture Toughness Specimen Results: Experimental and predicted results as determined using Kobyashi-Ohtani model. The results for both experimental and model are average results for each diamond size.

An issue with the Koyabashi-Ohtani model is that it does not take into account particulate size or porosity of the composite material and interfacial properties are also absent. However, even with these limitations the model does follow the experimental results found in this research work. However, any model to properly predict DICoMM materials must include diamond size because it has been shown to be a very important factor.

5.6.5. Jin & Batra Micromechanical Model

A model by Jin & Batra [224] where the fracture toughness for a metal reinforced ceramic matrix type composite was determined when applied to DICoMMs in this thesis yielded interesting results. The model is as follows:

$$K_c = \sqrt{\frac{E_m\left(1-\nu_p^2\right)\left(1-V_p\right)}{E_p\left(1-\nu_m^2\right)}}K_m \qquad (5.15)$$

where K_c = fracture toughness of composite,

E_m and E_p, Young's modulus of the matrix and particulate respectively,

ν_m and ν_p, Poisson's ratio of the matrix and particulate respectively,

V_p = volume fraction of particulate and K_m = matrix fracture toughness.

Again, this micromechanical model as seen in Figure 5.44 predicts the plane strain fracture toughness and is similar to that of Koyabashi & Ohtani model. However, it does not take into consideration particulate size or porosity of the composite material or interfacial properties. However, even with these limitations the model does follow the plain strain fracture toughness DICoMM experimental results. But as already stated above, any model for DICoMM materials must include diamond size.

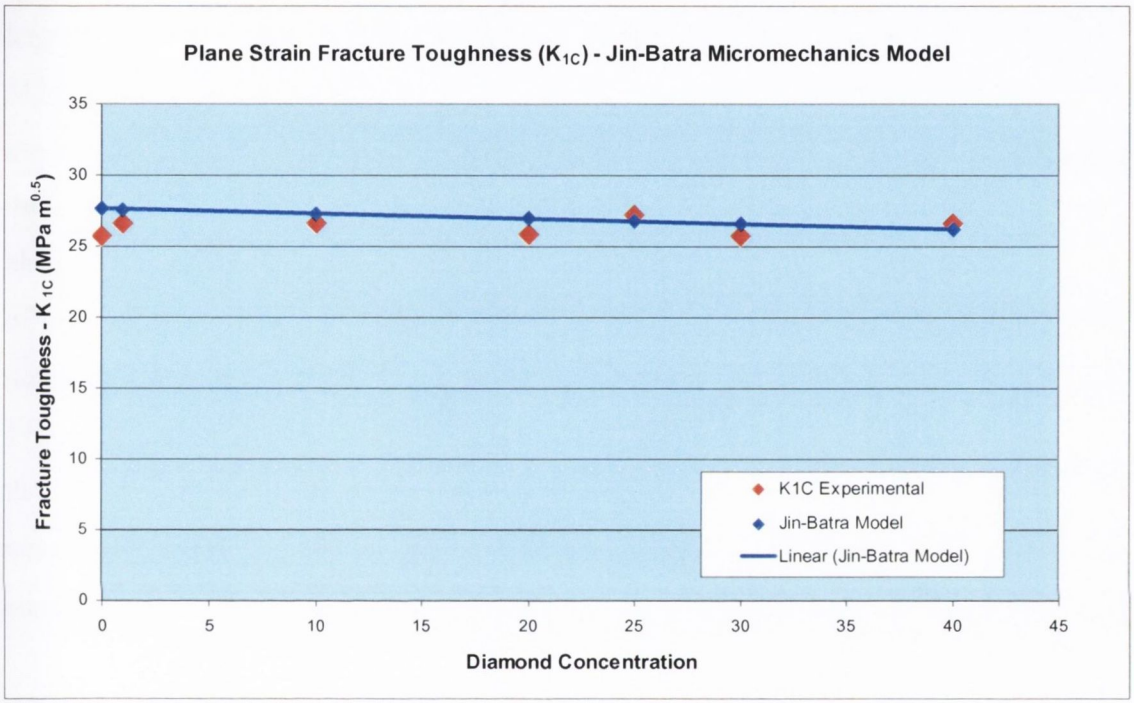

Figure 5.44. Fracture Toughness Specimen Results: Experimental and predicted results as determined using Jin-Batra Micromechanics model. The results for both experimental and model are average results for each diamond size.

5.7. Fracture Toughness & TRS Predictive Modelling

Attempting to model fracture toughness or TRS for DICoMM materials proved very difficult because of the variation and very non-descript experimental results having been found through this project work. However, analysing the fracture toughness results in concert with the TRS results using a methodology or modelling technique called The Theory of Critical Distances (TCD) will be shown to be very effective where a predictive model has been developed. Firstly, the basic methodology of TCD will be introduced and shown how it relates to the area of fracture mechanics. For the interested reader they are referred to the excellent book by Taylor [225].

5.7.1. Theory of Critical Distances & Fracture Toughness

The Theory of Critical Distance or Critical Distance Mechanics has been around for many years in various disguises. According to Taylor [225] the idea of TCD was first proposed in the 1930s and was the basis for the notch sensitivity rules devised by Neuber, Petersen and others. TCD is basically a predictive method for dealing with notches both sharp and blunt and also short cracks in components by predicting a value for a critical distance beyond the notch root which could be used to predict the fracture behaviour of the material under stress. This critical distance L is a characteristic material length parameter, and there are a number of methods of determining it. The Point Method (PM/TCD) is the simplest method of determining L, to the more complex methods: Line Method (LM), Area Method (AM) and the Volume Method (VM). For the Point Method, PM/TCD will be used to distinguish it from Powder Metallurgy (PM) already in use. Returning briefly to the scenario of plain specimens and the introduction of notches, the behaviour of the component changes depending on the behaviour of the notch, some notches behave like sharp cracks where others behave like blunt notches. Where the behaviour is similar to a blunt notch, upon loading failure does not occur until the notch root stress reaches the UTS, the plain specimen strength. Whereas other notches behave like sharp cracks of the same length and where the notch root radius ρ is small enough failure occurs when the stress intensity reaches K_C.

Returning to the simplest method of TCD, PM/TCD and linking L, the critical distance, to stress, the PM failure criterion states that failure will occur when the stress at a distance $L/2$ from the notch root becomes equal to σ_0.

$$\sigma\left(\frac{L}{2}\right) = \sigma_0 \tag{5.16}$$

So for predictions using TCD, one only needs two material parameters, the critical stress σ_0, and the critical distance, L.

Taylor [225] shows that a link can be made between Linear Elastic Fracture Mechanics (LEFM) and TCD.

In LEFM, K_C, the fracture toughness is related to fracture stress σ_f and the crack length, a, by:

$$\sigma_f = \frac{K_C}{\sqrt{\pi a}} \tag{5.17}$$

and by using a modified Westergaard stress/distance formula, which relates stress and distance from a crack tip, yielding a curve of stress versus distance,

$$\sigma(r) = \sigma\sqrt{\frac{a}{2r}} \tag{5.18}$$

However, equation 5.18 is only valid for $r << a$, which is satisfactory for TCD because of stresses close to the crack tip are the point of interest,

So Taylor [225] using the PM/TCD criterion shows that by combining Equations 5.17 and 5.18 one gets:

$$L = \frac{1}{\pi}\left(\frac{K_C}{\sigma_0}\right)^2 \tag{5.19}$$

where L = the critical distance,

K_C = fracture toughness,

σ_0 = failure stress.

So for this project the following statement linking TCD and its relationship to LEFM is as follows: for a plain specimen failure in a tensile test the stress is equal to the ultimate tensile strength, σ_{uts}, and so this must correspond to σ_0, and for the case of a long sharp crack, failure will occur when $K = K_C$, and rewriting Equation 5.19, $\sigma_{uts} = \sigma_0$ gives:

$$L = \frac{1}{\pi}\left(\frac{K_C}{\sigma_{uts}}\right)^2 \tag{5.20}$$

From this Equation 5.20, one can determine the critical distance L, which now will be used in this project to develop an upper and lower bound predictive model relating TRS and diamond size using PM cobalt fracture toughness and UTS.

For the 100% cobalt PM matrix hot pressed at 800°C, the average K_{IC} was found to be 25.6MPam$^{0.5}$, and the UTS value is taken as 890MPa. This gives a critical distance length, L = 264 μ, a material constant.

Taylor [225] introduced other fracture prediction models which use a material length constant in their formulation and are shown to be related to PM/TCD and LM methods of TCD. One such approach called the Imaginary Crack Method (ICM) which uses LEFM analysis. ICM was shown to be similar to PM/TCD and LM.

From LEFM, stress intensity, K, is defined as:

$$K = F\sigma_f\sqrt{\pi.a} \tag{5.21}$$

where σ_f = failure stress,

a = crack length and

F = a function crack shape, geometry and type of specimen loading.

Values of F can range from a numerical value to algebraic polynomials and trigonometric functions. The reader is referred to the Murakami [286] for a list of different combinations of crack type and loading configurations and the resultant F values.

Using ICM, a fixed amount, a_0, is added to the crack length, a, to give:

$$K = F\sigma_f\sqrt{\pi(a+a_0)} \tag{5.22}$$

Taylor shows that this imaginary crack, a_0, is the same as the critical distance L. So replacing a_0 and expressing Equation 5.22 in terms of σ_f, the failure stress, we get as:

$$\sigma_f = \frac{K}{F\sqrt{\pi(a+L)}} \tag{5.23}$$

Consider a diamond to be present on the tensile portion of a 3-point bend TRS specimen, in other words at the outer fibres of the TRS beam, but not proud of the surface, and modelled as a circle penny shaped crack in tension giving $F = 2/\pi$ [286]. Taking the diamond as being a flaw where the critical flaw size a is half it's diameter. Using

equation 5.23 the fracture stress σ_f is determined using different size flaws embedded in the cobalt matrix with L = 264μm and K_{IC} = 25.6MPam$^{0.5}$, which is the avegare K_{IC} for the 100% cobalt matrix. Figure 5.45 shows the fracture stress for cobalt with various flaw sizes plotted using a log-log scale. What is apparent from the graph is that the addition of diamond to the matrix would predict that it would have no effect, i.e. all specimens would fail at the UTS of the cobalt.

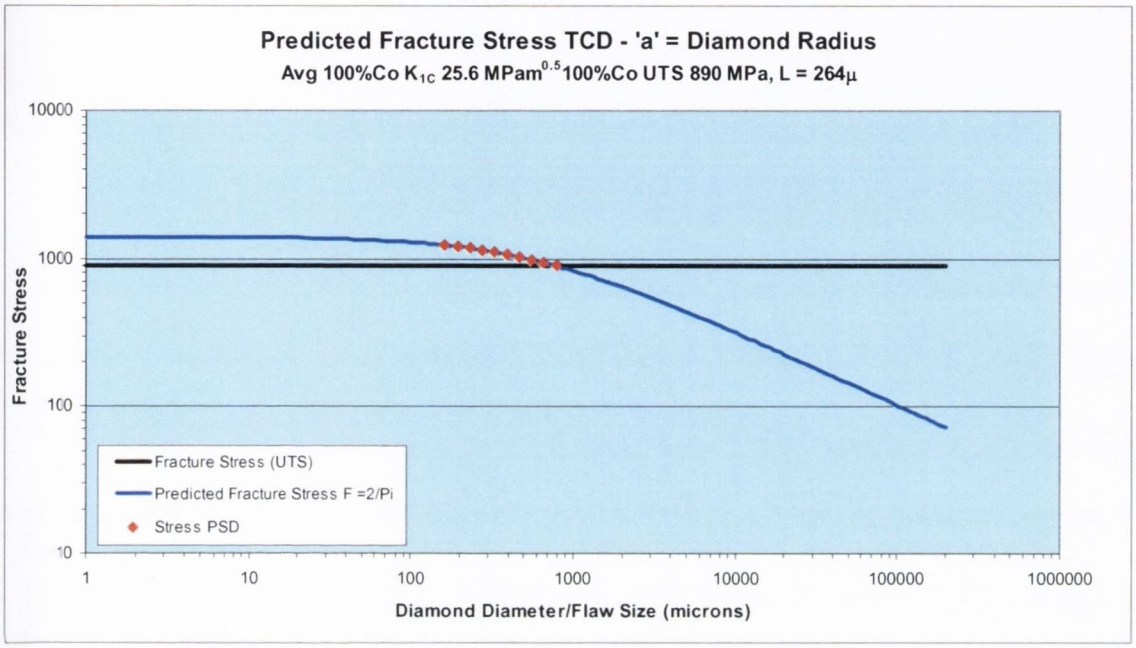

Figure 5.45. Fracture Toughness Specimen Results: Fracture stress σ_f as a function of defect size, i.e. diamond size, in 100%Cobalt PM matrix; hot pressed at 800°C. Red values indicate range of pertinent diamond sizes as used in this project.

At first Figure 5.45 looks disappointing but TCD should predict DC1 TRS results very well, because TRS data does show a drop in TRS in comparison to 100%Cobalt. So some effect must be influencing the experimental results. From a fracture mechanics/TCD point of view, a shifting of the 'Red' results which would be caused by a larger F value than that found for a penny shaped crack in tension, i.e. going from $F = 2/\pi$ to a value of F closer to 1. This would lower the values below the UTS of the 100%Cobalt. From an experimental point of view, residual stresses around the diamond would lower the TRS results however in this case the residual stresses around the diamond are compressive, so that would tend to move the points up, not down.

Another possibility is the clustering effect, which is found in many PMMC materials, and has also been found to occur without any difficulty with DICoMM materials. The effect of clustering increases with increasing diamond concentration, which increases F.

At very low diamond concentrations, one could typically get just a single diamond for very coarse diamond sizes but clustering would be present for the finer diamond sizes. At high diamond concentrations there would always be clusters. So considering clustering, if there were two or three diamonds close together or side by side, then the crack length would still be the same but F would be larger, approaching 1 as the number in the cluster increased. Figure 5.46 shows this, and indicates that clustering effect of the diamond does lower the points below the UTS line, which indicates that diamond clusters have the capacity to cause fast fracture to occur. How one defines a cluster whether as a circular or as an elliptically shaped flaw in tension does not matter because both will cause an increase in the F factor and so move the points downwards.

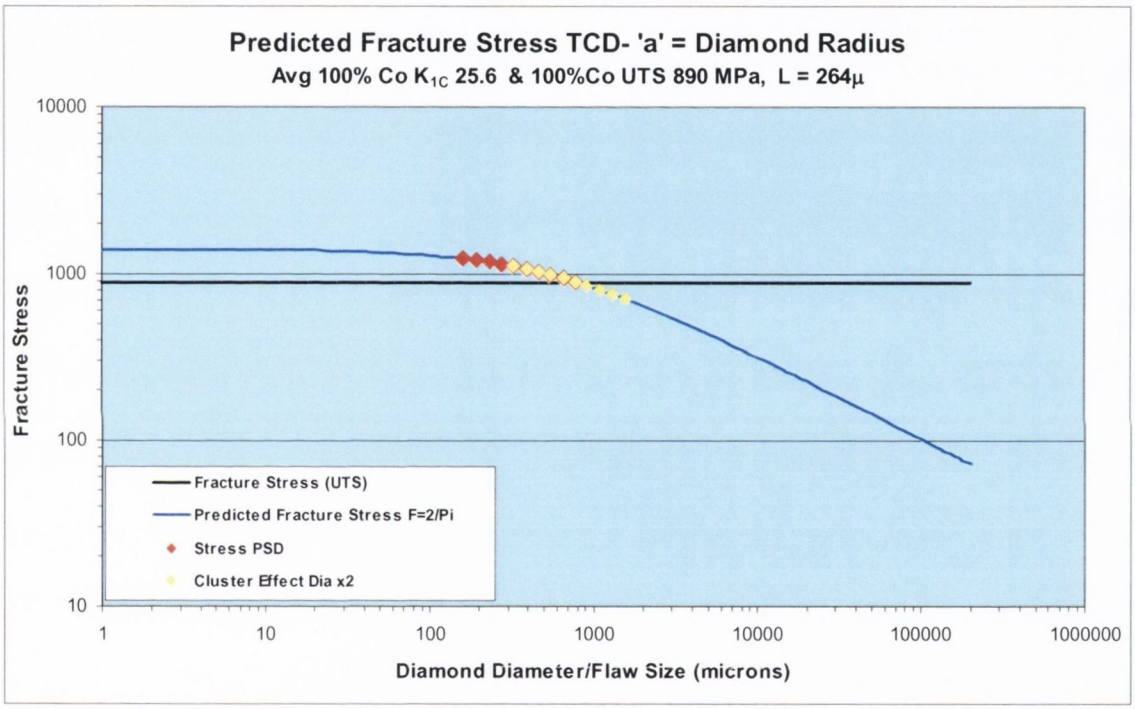

Figure 5.46. Fracture Toughness Specimen Results: Fracture stress σ_f as a function of defect size, i.e. diamond size, in 100%Cobalt PM matrix; hot pressed at 800°C. Yellow points indicate range of pertinent diamond sizes present as clusters.

The above Figure 5.46 shows the predicted fracture stress for flaws included in cobalt matrix. The yellow points represent the scenario where two diamonds are together as a cluster showing the shift downwards of the stress required to fracture the material. In Figure 5.47 shows the scenario where a cluster equals diamond size times 2 marked in red, and in yellow cluster equals diamond size times 3. As can be seen, the cluster effect has a strong effect on the fracture stress of DICoMM materials lowering it below the UTS of the cobalt matrix.

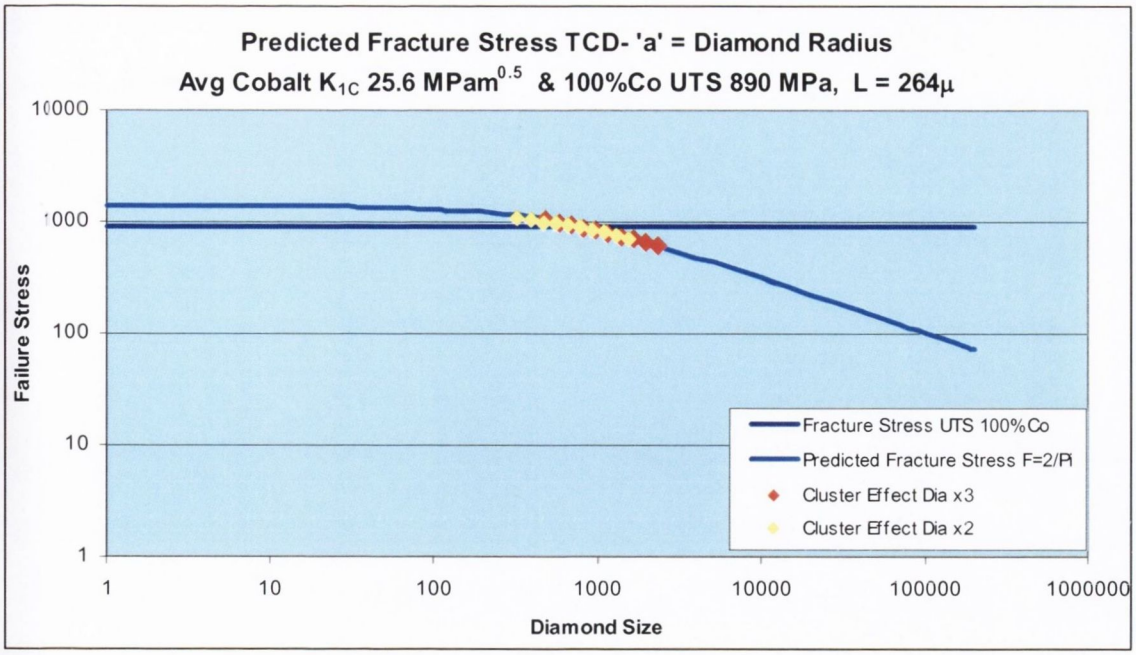

Figure 5.47. Fracture Toughness Specimen Results: Fracture stress σ_f as a function of defect size, i.e. diamond size, in 100% Cobalt PM matrix; hot pressed at 800°C. Red indicates cluster size i.e. diamond size x2 & yellow indicates cluster size i.e. diamond size times three (x3).

5.7.2. TCD & TRS Fracture Stress Analysis

Following the TCD analysis regarding the DICoMMs in the previous section, this section is going to examine prediction of the TRS fracture stress with the addition of diamonds in Couf cobalt matrix and compare to the experimental TRS results already reported. Having calculated the tensile fracture stress using the imaginary crack method (ICM) with two different values of F, i.e. $F = 2/\pi$ and $F = 1$, the predictive fracture stress (TRS_{Pred}) in bending is calculated taking into consideration the location of the diamond 'flaw', which is calculated using Equation 5.24

$$TRS_{Pred} = \sigma_f \frac{t/2}{\left(t/2 - d\right)} \tag{5.24}$$

where σ_f = failure stress calculated from Equation 5.23

F = a crack shape and geometry function,

t = beam height,

and d = distance from outer fibre to centre of diamond crystal.

Figure 5.48 shows the effect when by plotting TRS (40mm span) results versus diamond concentration with TRS predictions using the different F values. The TRS predictions

using $F = 2/\pi$ and $F = 1$, bracket the TRS experimental results for DC's 1 and 40 very nicely.

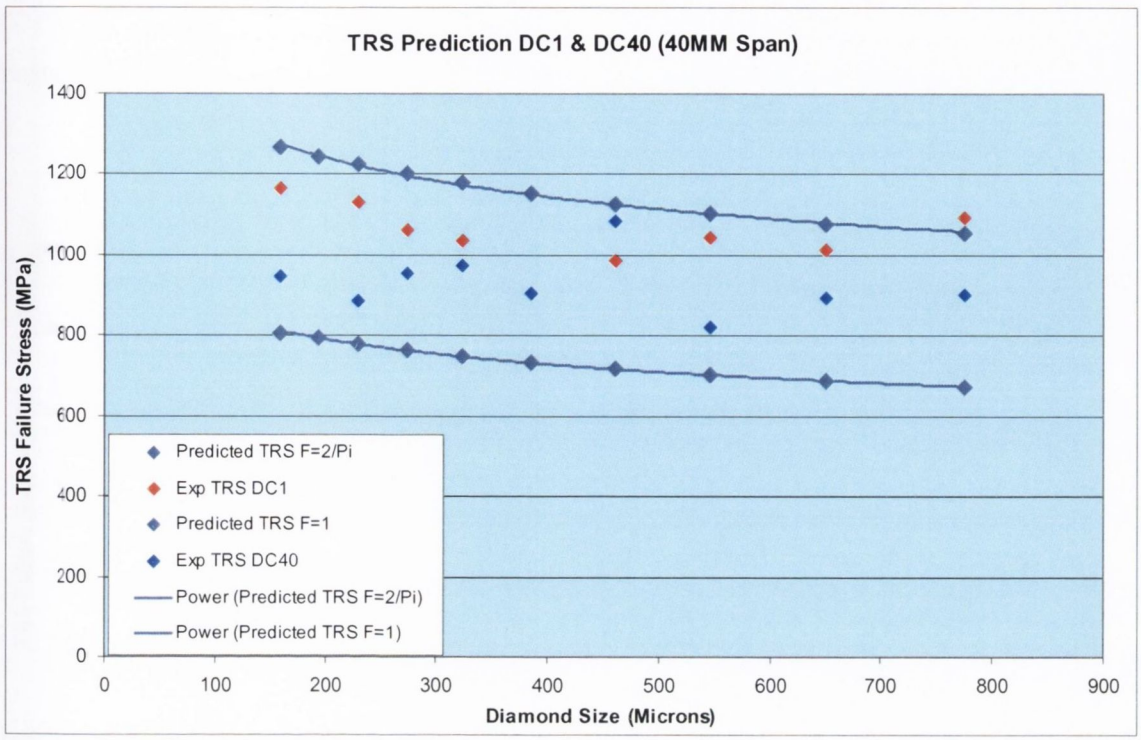

Figure 5.48. Predicted TRS fracture stress σ_f and experimental TRS failure stress plotted as a function of diamond size for DC1 & DC40 using 40mm span.

Figure 5.49 shows a similar plot where the TRS predictions are plotted against the experimental TRS results using 50mm span. Again the TRS predictions bracket the TRS experimental results for DC's 1 and 40.

Even though most of the values lie above the UTS for cobalt, this is to be expected because the TRS failure results are for bending which are always higher than tensile testing, this explains why the material doesn't fail at its UTS in these tests.

Regarding TCD predictions, the tensile UTS is the correct value to use even though, the TRS failures occur at a higher stress than the (tensile) UTS because even the pure cobalt will fail at a higher stress anyway, when loaded in bending. The TCD predictions are perfectly valid even though they are being applied to a bending application in addition to the effect of diamond particles.

Now the above predictions are for the situation of a penny shaped crack where $F = 2/\pi$, which is seen to be valid for low DC's, however when higher DC's are being analysed

the prediction line moves away from the data. So in accommodating these higher DC's, the problem of clustering becomes an issue, which is where a larger value of F is required in order to accommodate this effect. Figure 5.49 shows where plotting the results for $F = 1$ as well as $F = 2/\pi$, gives the range of possible predictions, which can be seen brackets all the data.

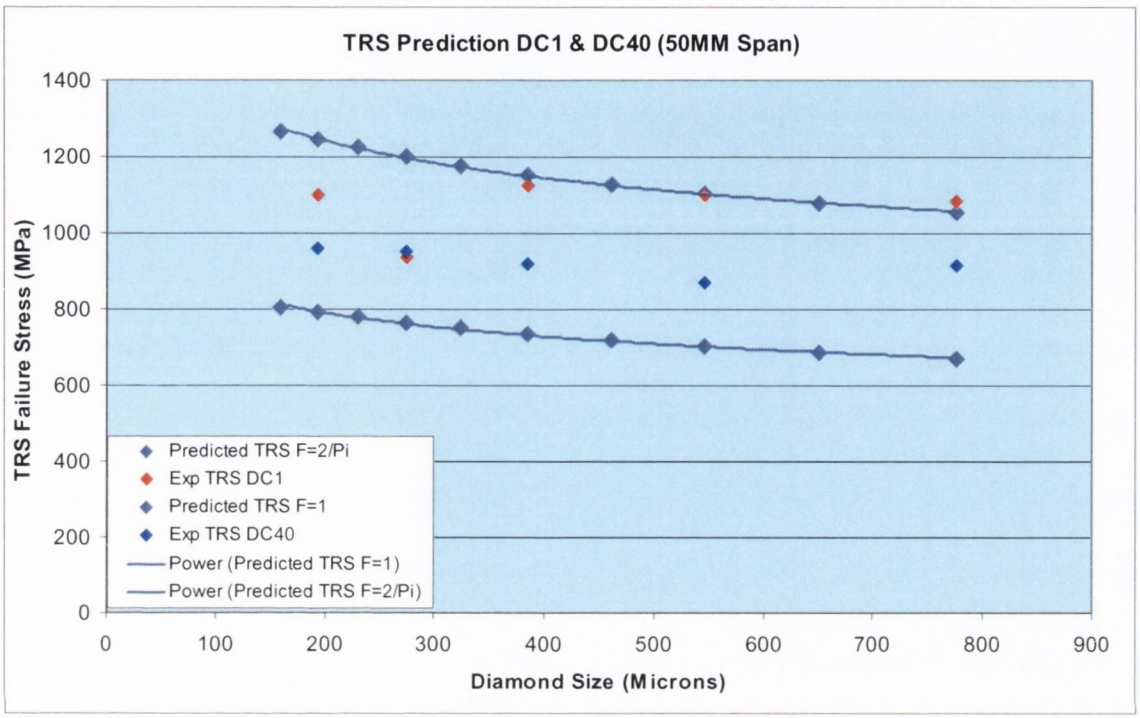

Figure 5.49. Predicted TRS fracture stress σ_f and experimental TRS failure stress plotted as a function of diamond size for DC1 & DC40 using 50mm span. The TRS prediction lines show upper & lower bound results for the two DCs.

Now when the experimental TRS failure stress for 100% cobalt specimens (max & min values) are plotted on the TRS prediction plots, Figure 5.50 one can see that the maximum TRS is higher than the TRS prediction lines and DICoMM results, and the minimum TRS results are in the middle of the experimental TRS results and between the two TRS prediction lines. This is indicating that pure Co fails at anything between about 1045MPa and 1623MPa, and so when diamond is added one of two possible failure outcomes are possible; (1) from a diamond crystal or (2) from the cobalt matrix. The TRS failure stress data are the combined TRS failure stress results for 40mm and 50mm spans.

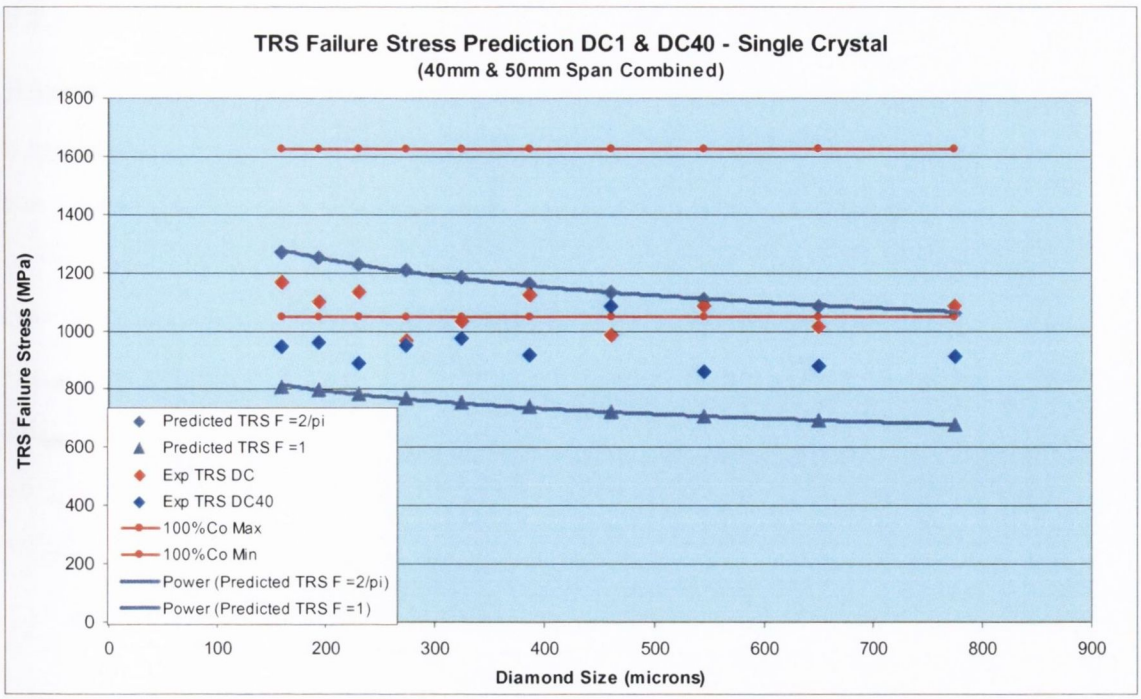

Figure 5.50. Predicted TRS fracture stress σ_f and experimental TRS failure stress plotted as a function of diamond size for DC1 & DC40 for 40mm & 50mm spans combined. The TRS prediction lines show upper & lower bound results for the two DCs.

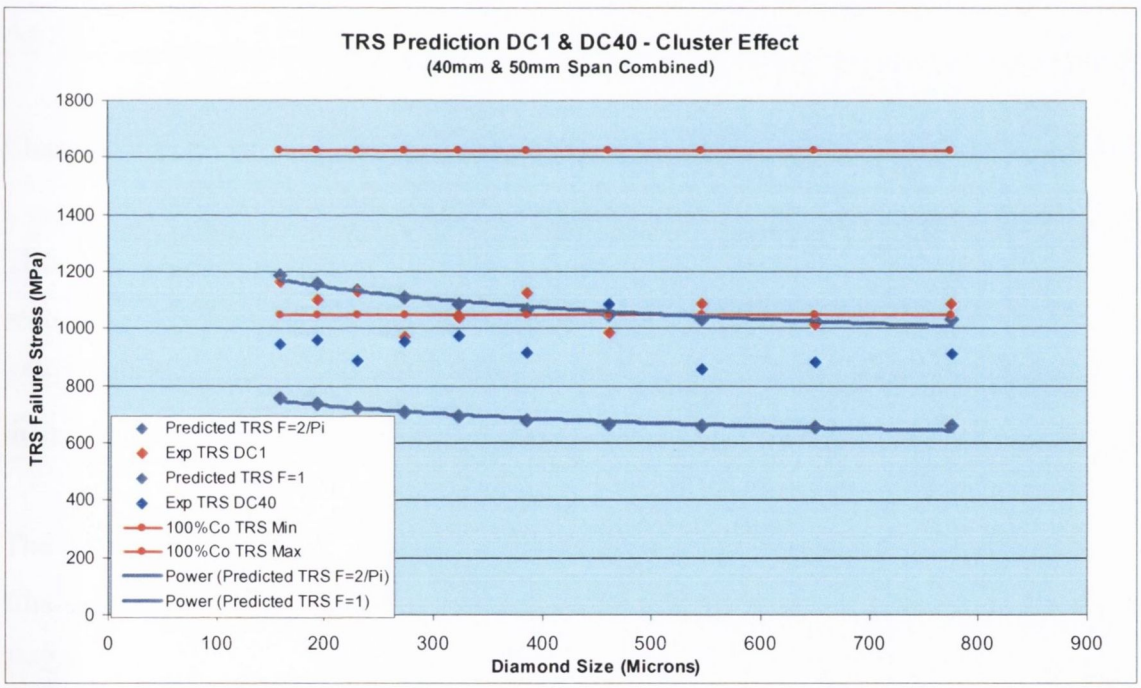

Figure 5.51. Predicted TRS fracture stress σ_f and experimental TRS failure stress plotted as a function of diamond size for DC1 and DC40 for 40mm & 50mm spans combined. The TRS prediction lines show upper & lower bound results for the two DCs.

When one examines the effect of clusters, where 'two' diamonds are viewed as touching, giving the effect of a larger flaw which initiates crack initiation the results can be seen in Figure 5.51 where the TRS prediction lines move downwards.

5.8. Charpy and TRS – Strain Energy Relationship

Analysis using strain energy is commonly used in stress analysis and fracture mechanics, e.g. strain energy release. Its application in this thesis allows the author to bring together the TRS strain energy and relate it to Charpy impact energy. The TCD TRS predictions in the previous section will be used to relate TRS and Charpy impact energy using strain energy. The energy stored in a beam when it is subjected to a force is called strain energy (or resilience), where the symbol U is used for strain energy. In TRS testing of DICoMM materials the fracture stress was found to occurr at the limit of proportionality, so the standard equation for strain energy can be used giving strain energy per unit volume:

$$U = \frac{\sigma^2}{2E}.per.unit.volume \qquad (5.25)$$

where E = Young's modulus of Elasticity for the material,

σ = stress, and in this project is the predicted TRS failure stress, σ_f.

Assuming that

$$\text{Charpy Impact Energy} \propto (TRS_{Pred})^2 = C(TRS_{Pred})^2. \qquad (5.26)$$

TRS_{Pred} is the predicted TRS failure stress using the ICM model as used in previous section, with $F = 2/\pi$ and $F = 1$. C is the limit of proportionality and is a fractional or effective volume factor for the Charpy specimens; a value of 5.0 cm^3 was used for all the diamond concentrations.

The Strain Energy prediction results using TCD can be seen in Figure 5.52 which shows Charpy impact energy for DC1, DC10 and DC40 with the predicted strain energy for $F=2/\pi$ and $F=1$ scenarios, where $F= 2/\pi$ representing a circular penny shaped flaw in tension and $F = 1$ representing a cluster again in tension in the TRS specimen.

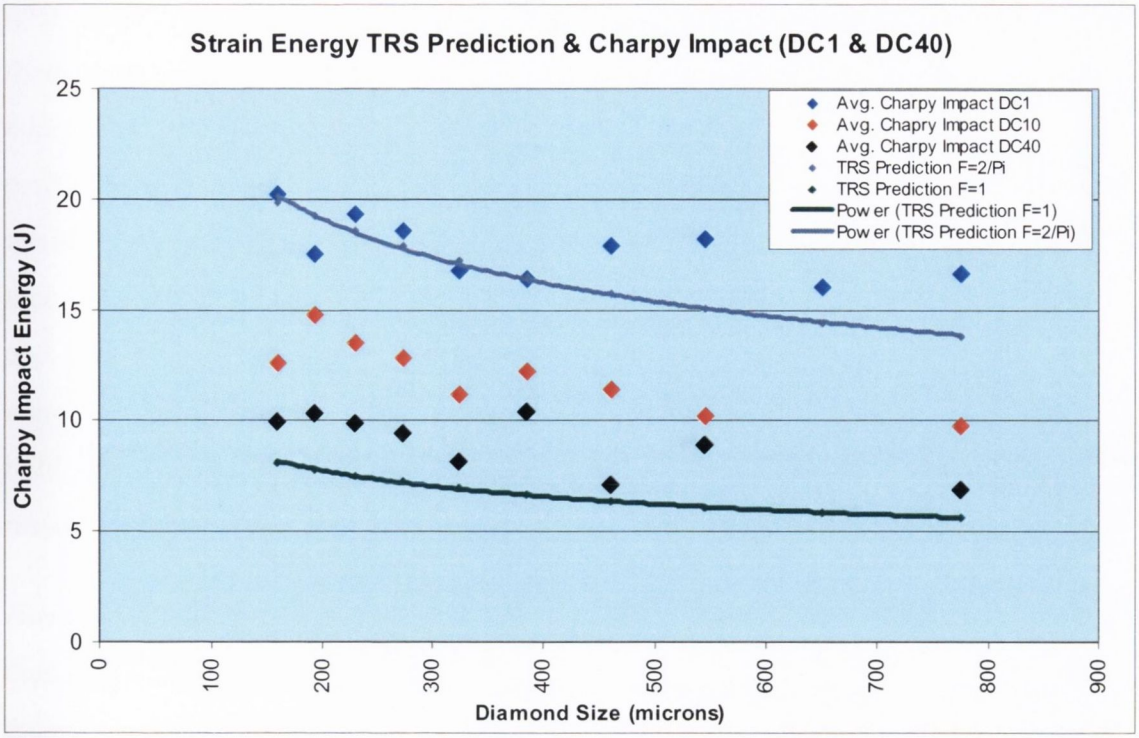

Figure 5.52. Predicted Strain Energy using Predicted TRS fracture stress σ_f and experimental Charpy impact energy plotted as a function of diamond size (microns) for DC1, DC10 & DC40. The Strain Energy TRS prediction lines show upper & lower bound results.

From the results in Figure 5.52 it is seen that for very low diamond concentration, DC1, the F=2/p scenario represents and can predict the Charpy impact energy very well, and as the diamond concentration increases, from DC10 to DC40, the Charpy impact energies are better represented and predicted by the F=1 scenario indicating a clustering effect due to the higher numbers of diamond crystals present. The other diamond concentrations show a gradual increasing drift towards the F=1 prediction line with increasing diamond concentration. The other graphs can be seen in Appendix 10.

5.9. Erosive Wear

In this section wear due to erosion will be examined and a wear model will be proposed. The results reported in Chapter Four, Results clearly show that diamond concentration and diamond size affect the erosion resistance of DICoMM materials. Results also show that pressure and angle of incidence have a significant effect on the erosion rates of these materials.

Regarding DICoMM materials and the role of IPS/MFP, the results presented in Figure 4.54 where a pressure of 3bar at an angle of 15 degrees, shows that increasing diamond

concentration from 10 to 30 causes an increases in wear resistance. Also for each diamond concentration, the finer diamond (60/70) shows less wear resistance than the coarser 40/45 size. This suggests that there is a compromise between IPS/MFP and particle size similar to that cited by [287] for PMMCs. Low diamond concentrations result in larger IPS/MFP distances which result in an increase in area of exposed metal than that for higher concentrations. Also, diamond size can influence the wear resistance and mass loss by a process of 'fall-out'. Finer diamond with their smaller radii, do not penetrate into the metal surface in comparison to coarser diamond so their bonding or hold is not as great as that for coarser diamond. This would explain the lower wear resistance for the finer diamond for both diamond concentrations in Figure 4.54.

However, when higher pressures (6bar) and steeper angles (45^{o}) are used, the coarser diamond 30/35 specimen shows the greatest erosive wear as seen in Figure 4.55. Coarser diamond has less number of crystals for a given diamond concentration than finer diamond. This gives a larger IPS/MFP distance for the coarser 30/35 diamond than the finer 60/70 diamond. The IPS/MFP for 30/35 is nominally 4.48mm where for 60/70 it is 1.89mm at DC30 [185]. So 30/35 specimen has larger areas of metal between the individual diamond crystals than the 60/70 specimen. This larger area of exposed matrix metal is very easily eroded.

The best erosion resistance of the 60/70 indicates that smaller MFP protects the diamond/metal sample from erosion at high angles and pressures. Also, even though the 60/70 diamond has less mechanical bonding because of a decreased level of 'embedded depth' in the cobalt metal, it has the lowest IPS/MFP than that for 30/35 or 40/45 diamond imparting the best erosive wear resistance to the diamond/cobalt material. With decreasing MPF, one gets an exponential increase in the number of diamonds for a given diamond concentration as seen in Figure 2.4 in Chapter Two, Literature Review e.g. at a DC of 30, 30/35 has 686 diamonds/cc, 40/45 has 1848 diamonds/cc with 60/70 having 8382 diamond/cc. The large increase in the availability of hard abrasion resistant particles on the surface gives a substantial increase in protection from erosion. The 'protection-effect' of the reinforcement in the soft metal matrix has been found to occur in PMMCs for low impingement angles [206]. Konstanty et al. [288] also state that for DIMMs the coarser diamond grits protect the metal matrix against wear abrasion.

5.9.1. Erosion Wear Model - Modified Finnie Erosion Model

In attempting to propose a predictive model of the erosion of diamond impregnated cobalt taking Finnie's formula for ductile wear [208] as a basis a number of factors must be determined i.e. gas stream velocity and particle velocity. Also, the author proposes that IPS/MFP must be incorporated into the predictive model to take into account the indications from the results obtained and elaborated in the previous paragraph.

Modelling the air blast apparatus must take into account that air is compressible and so the standard approach fluids mechanics cannot be applied, e.g. variations in density due to different pressures. So the erosion test apparatus was treated as the discharge of a compressible gas with a 'mass flow from a reservoir through an orifice' or 'convergent-divergent nozzle' application with compressible air flows as seen in Figure 5.53 [289].

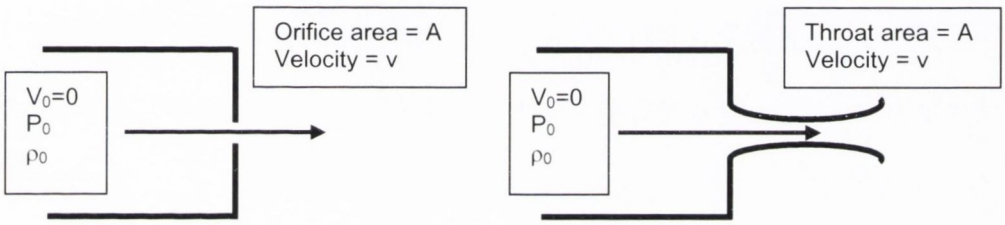

Figure 5.53. Flow Model – Convergent-Divergent Nozzle for Compressible Flows.

From this flow model analysis, the air velocity was calculated for each air pressure using Equation 5.27 [289].

$$V_g = \sqrt{\left[2\left(\frac{\gamma}{\gamma-1}\right)\frac{p_0}{\rho_0}\left(1-r^{(\gamma-1)/\gamma}\right)\right]} \qquad (5.27)$$

where V_g = velocity of the gas, air,

ρ_0 = density of air at a specified pressure in reservoir,

P_0 = pressure in reservoir,

r = ratio between pressure in reservoir to ambient pressure,

γ = specific heat for air, value of 1.401 at adiabatic conditions.

Important to point out that Equation 5.27 is for an ideal isentropic compressible flow which does not take into account frictional and discharge losses. The results assume that the coefficient of discharge C_d is unity which is reasonably approximate for this analysis. [289]. From the air velocity V_g, the particle velocity V_p can be determined using a one-dimensional numerical model where a particle is accelerated by a high speed gas. The particle velocity V_p can be calculated by a drag force on a single particle in a fluid flow [290]. Alkhimov et al. [291] obtained an empirical equation for calculating the velocity of a particle V_p in a nitrogen gas stream as follows:

$$v_p = \frac{v_g}{1 + 0.85\sqrt{\frac{D_p}{x}}\sqrt{\frac{\rho_p v_g^2}{P_o}}} \tag{5.28}$$

where V_p = particle velocity,

V_g = gas velocity,

D_p = particle diameter (abrasive particle diameter),

ρ_p = particle density,

P_o = gas pressure,

x = axial position, i.e. nozzle distance from sample.

Considering that air is 78% nitrogen, it was felt that use of the above empirical equation was a good approximation for calculating the particle velocities for this analysis, taking particle diameter in equation 5.28 as the abrasive particle diameter. A more correct method would be to measure the actual particle velocities, but this is very difficult to carry out in practise.

As already mentioned, for ductile materials erosion can be predicted using Equation 2.6 by Finnie [208]. However, Finnie's is the ratio of mass of erodent to mass of eroded material and is dimensionless. The equation proposed in this analysis is based on Finnie's equation for erosion. In this proposed erosion model, it takes into account the experimental results and the factors which are seen to influence erosion rate. Erosion rate in this model has units of mass/min. The variable k in Equation 2.6 is replaced by $tan\theta$, where θ is the angle of incidence of the stream of particles hitting the target specimen. Density of the DICoMM for each diamond concentration and combining the

IPS/MFP with particle velocity, a reasonable predictive erosion model is found as follows:

$$E_R = \tan\theta . \rho_{DC} . V_P \left(\frac{2}{3} \frac{D_P (1 - \nu_P)}{\nu_P} \right) \left(\frac{1}{1 - \nu_{por}} \right) \alpha \qquad (5.29)$$

where $tan\theta$ = tan of the angle of incidence of the stream of abrasive particles,

ρ_{DC} = density for each diamond concentration,

V_P = abrasive particle velocity,

ν_P = volume fraction, diamond concentration expressed as a volume fraction,

D_P = diameter of abrasive particle,

ν_{por} = porosity as a volume fraction, taken here as 0.05 porosity.

and α = constant.

Equation 5.29 is only applicable up to angles of 45°, the largest angle of incidence tested.

Equation 5.29 can be simplified by replacing the expression in brackets with IPS/MFP, λ_s as follows:

$$E_R = \tan\theta . \rho_{DC} . V_P \lambda_s \alpha \qquad (5.30)$$

where $tan\theta$ = tan of the angle of incidence of the stream of abrasive particles,

ρ_{DC} = density for each diamond concentration,

V_P = abrasive particle velocity,

λ_s = IPS/MFP

and α = constant.

Equation 5.30 is only applicable up to angles of 45°, the largest angle of incidence tested.

There are a number of limitations to the above model, including the different erosion wear mechanisms e.g. micro-ploughing/micro-cutting to spalling of the metal surface, which cannot be accounted for. Other factors influencing the model are the erosion efficiency, abrasive particulate surface roughness, angularity, density and also particle rotation as it impacts the metal matrix surface.

The predictive model with experimental results can be seen in Figure 5.54, with for 40/45 at two different diamond concentrations, DC10 and DC30 which shows experimental and theoretical results. The graph shows erosion rate plotted against a range of pressures and angles. The predictive model for DC10 and DC30 bracket the experimental results very well for 40/45 US Mesh size.

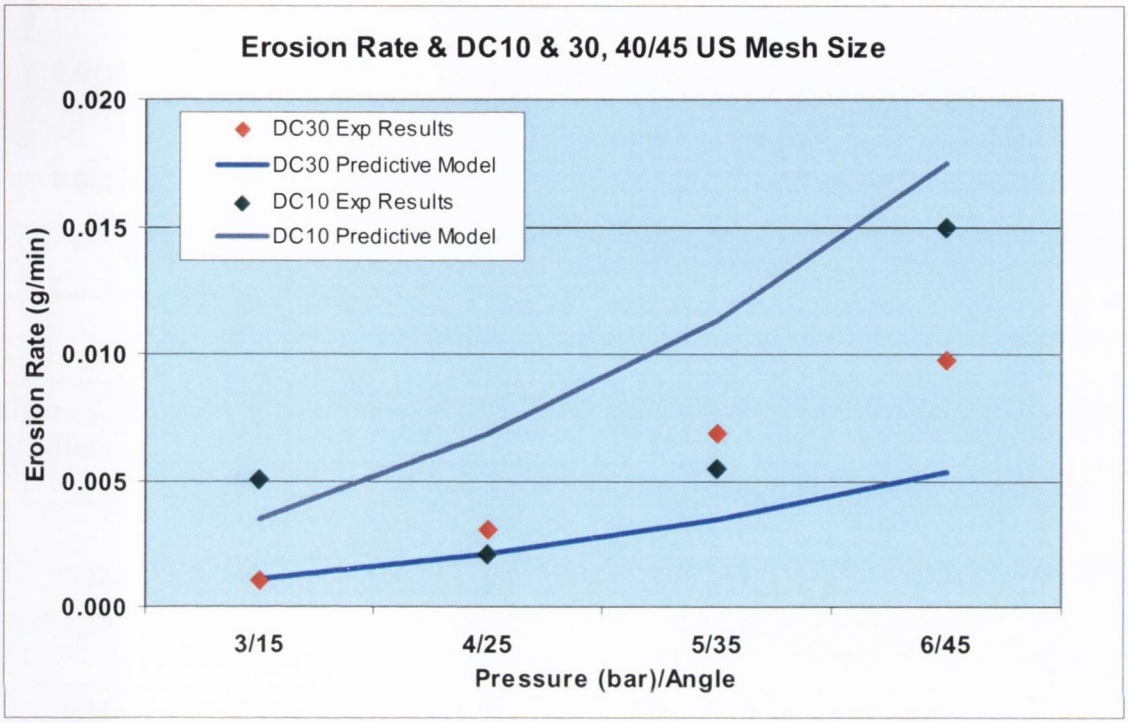

Figure 5.54. Wear Erosion Results: Experimental & Theoretical Results for 40/45, DC10 & DC30 @ different Pressures & Angles.

Regarding 30/35 US Mesh size, results for DC10 can be seen in Figure 5.55 with the prediction model line showing an increasing trend for erosion similar to the experimental results. However, results for 30/35 DC30 were not reliable because of an issue with the wear apparatus where the erodent got temporarily blocked during testing, one set of experimental results have been omitted. Only two results for DC30 30/35 are included to show that they are bracketed by the two prediction lines.

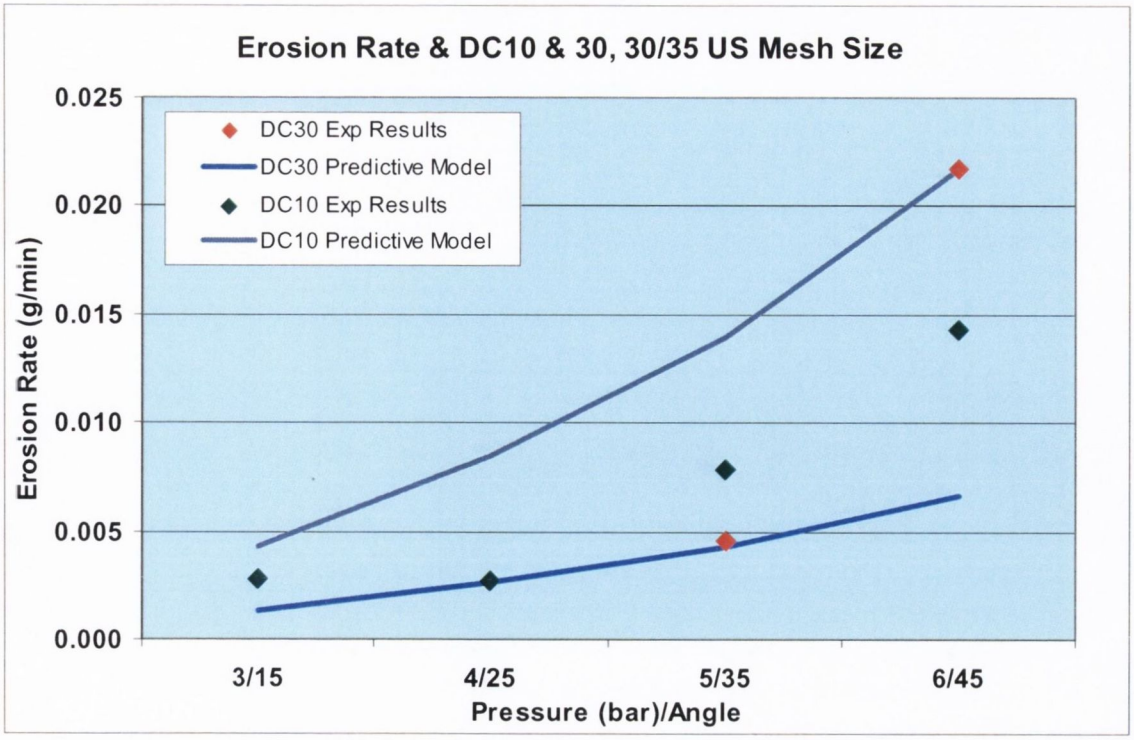

Figure 5.55. Wear Erosion Results: Experimental & Theoretical Results for DC10, 30/35 @ different Pressures & Angles.

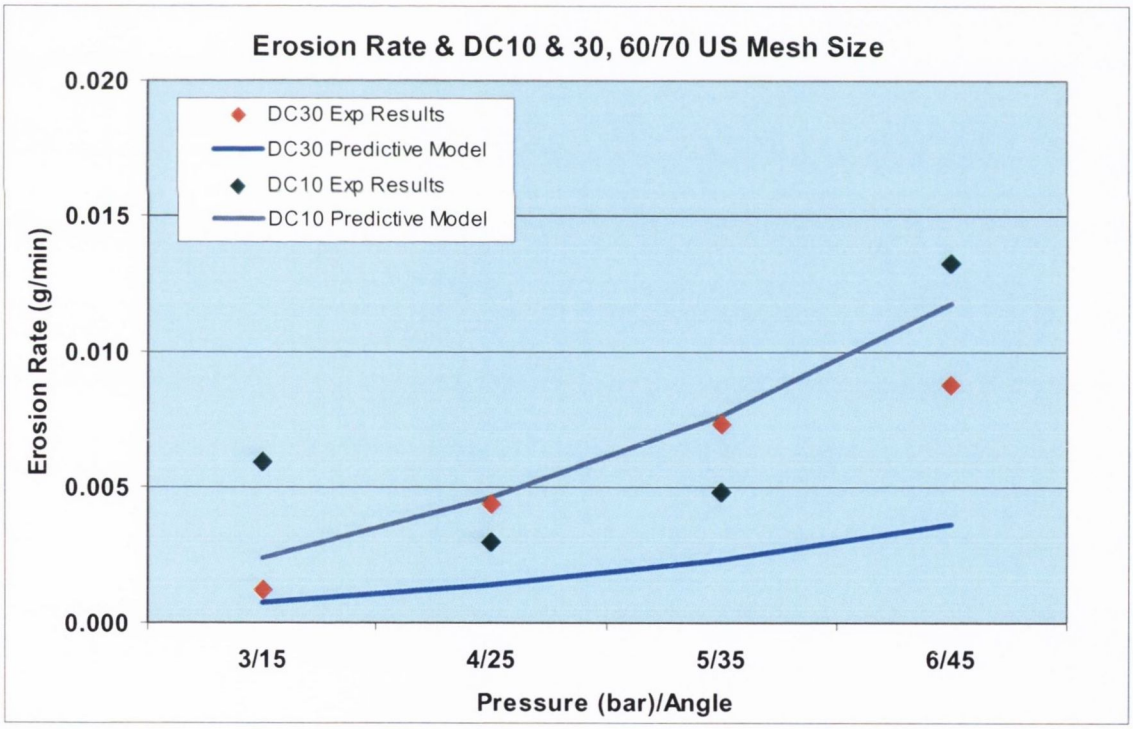

Figure 5.56. Wear Erosion Results: Experimental & Theoretical Results for DC10, 60/70 @ different Pressures & Angles.

The results for the finer diamond can be seen in Figure 5.56, with (a) for DC10 60/70, and (b) DC 30 60/70 which shows experimental and theoretical results. The graph shows erosion rate plotted against the different pressures and angles used. A close agreement is

found between experimental and theoretical predictions. However, more experimental work needs to be carried out to fully test the model's efficacy. It is important to be aware that investigative work into diamond impregnated metal matrices is difficult due to the large inherent variability resulting from the inhomogeneity of the mix caused by the large differences in the constituents e.g. densities, particle sizes, particle shapes and surface roughness. Also, in the field, different rock materials have different densities, angularity of rock fragments or detrius, the cutting speed as well as the m achine power will influence the impact velocity of rock detrius particles as the particles impact the metal matrix in the space between the rock surface and segment surface measured by the protrusion height.

5.9.2. Erosion Wear Patterns & Wear of Diamond Saw Blades

As already reported in Chapter Three, Experimental Procedures the erosive wear patterns found on the DICoMM materials specimens tested in this project are identical to those found by Liao et al [54]. The typical wear patterns found on the DICoMM test specimens show the characteristic comet tail formation behind the diamond crystals as the grit passes over the specimens as they are blasted. Comet tails are really only found for the shallow test angles. The author proposes that the formation of comet tails indicates that erosion is one of the wear mechanisms that operate during the cutting operation of a diamond saw blade as it cuts the rock workpiece.

Regarding the fractographic SEM images, the wear patterns found due to the different pressures and angles used show a variation in wear mechanisms which is supported by the literature. At low cutting angles the wear mechanism is different to that found for steeper angles e.g. 45°. This is especially for erosion at normal angles of incidence where Finnie's theoretical model is not valid. Formation of platelets lying parallel to the metal surface and their subsequent detachment are the major wear mechanism for steeper angles and especially at normal angles of incidence. The formation of platelets and break-off is the major mechanism for angular particles for steep angles.

For the DICoMM specimens, at shallow angles e.g. 15°, the erosive wear is by cutting and ploughing mechanisms which is the normal mechanism for ductile metals at shallow angles, which could be seen in Figure 4.59 in Chapter Four, Results. Regarding the steeper angles used, e.g. 45°, what could be called a mixed erosion wear pattern could be

seen where platelet type formation can be seen on the surface but also ploughing and cutting wear is also present, this could be seen in Figure 4.62 in Chapter Four, Results.

Interestingly, the erosive wear patterns found in this thesis are very similar to the wear patterns found by Ersoy et al. [198] who stated that they were caused by abrasive contact by the workpiece and metal matrix of the DIMM segment where the workpiece scratched it as seen in Figure 2.11 in the Chapter Two, Literature Review.

Also in Figure 4.66 where a 'pull-out' has occurred, rounding of the 'sharp' edges have occurred due to the erosive particles, which is similar to the wear patterns found for saw segments as seen in Chapter Two, Literature Review, Figure 2.13.

CHAPTER SIX: CONCLUSIONS & RECOMMENDATIONS

6.1. Introduction

This chapter will cover the main findings of the investigative work carried out into the mechanical properties of DICoMMs, with the main conclusions given. In addition to reporting the main conclusions of the experimental results and the effects of diamond size and diamond concentration, the results of predictive models used to model various properties will be outlined. Some of the predictive models combine different mechanical properties in a global sense so that fracture stress or impact energy could be modelled successfully.

From the outset, the addition of diamond to a PM cobalt metal matrix is detrimental to any mechanical property which is based on a fracture stress of some form, e.g. TRS or impact energy. Also, the addition of diamond causes a large level of scatter and variability in mechanical properties which is exacerbated with increasing diamond concentration and also strongly influenced by changes in diamond size. This made it very difficult to understand and make sense of the results found for the different DICoMM materials which also made it difficult to use predictive models.

6.2. Percent Theoretical Density (%TD)

Percent Theoretical Density (%TD) has been found to influence all mechanical properties investigated, i.e. hardness, impact energy, TRS and fracture toughness. The main conclusion being increasing percent theoretical density yields an increase in the mechanical property in question. However, the addition of diamond to the different specimen types, i.e. fracture toughness, TRS and Charpy impact, caused an increase in the variability in percent theoretical density which had a knock on affect on increasing the level of scatter in the mechanical property being reported.

6.3. Hardness

Hardness was found to decrease with increasing diamond concentration. Hardness was also found to increase as diamond size decreased or from a diamond tools perspective as the US Mesh size became finer; which was found within each diamond concentration. This general trend was found for TRS, Charpy impact and fracture toughness type

specimens. Regarding the modelling of hardness of DICoMM materials using the concept of fractional area, no predictive capability was found.

6.4. Fatigue Crack Propagation

Use of compliance coefficients from Jablonski [263] and ASTM have been proven to work poorly in the accurate determination of fatigue crack propagation and crack length measurement for small SENB type specimens. The newly determined compliance coefficients for small SENB specimens can accurately control the precracking stage of the fracture toughness determination of CoMM materials and with an acceptable error when used on DICoMMs. However, a sizeable percentage of DICoMM specimens still failed to grow a fatigue crack for various reasons of which the presence of diamond played a role.

6.5. Fracture Toughness

The determination of the plane strain fracture toughness of CoMM and DICoMM materials was successfully achieved using small SENB type specimens. For the correct determination of plane strain fracture toughness the requirement of an atomically sharp crack has been found to be unnecessary which is in agreement with [69]. Also the ASTM E399-90 dimensional $0.45<a/W<0.55$ requirement was also found to be unnecessary. In addition to this, the requirement for knife edges for CMOD gauge attachment was also unnecessary as found by [100]. The use of a fatigue precrack (FastTrack) or just an edm starter notch (SERIES-IX) both can be used to determine the plane strain fracture toughness of DICoMMs. The number of valid plane strain fracture toughness results was 42% for the standard ASTM E399-90 (FastTrack Method) and only 27% valid for the SERIES-IX method.

The average plane strain fracture toughness for PM Couf CoMM or 100% Couf cobalt was 25.60 $MPm^{0.5}$. The plane strain fracture toughness results for DICoMMs and CoMM ranged between 20 to $30MPam^{0.5}$. Interestingly for the DICoMM materials the plane strain fracture toughness of DICoMM materials tested, the average value was 26.09 $MPa.m^{0.5}$ for the SERIES-IX method of testing and for FastTrack K_{IC} result was $26.33MPa.m^{0.5}$. Overall, it has been found that the introduction of diamond into PM cobalt behaves as if it is present as a flaw. As diamond size is changed a variation in fracture toughness is seen to occur.

Regarding interparticle spacing (IPS) using either IPS/MFP or IPS/NND, for a constant diamond concentration a reasonable statistical significance was found for IPS/MFP and IPS/NND for plane strain fracture toughness (K_{IC}) for DICoMM materials. However, when the IPS/MFP or IPS/NND increases for a constant diamond concentration, increasing diamond size causes a decrease in plane strain fracture toughness. Overall, the results for both IPS/MFP and IPS/NND are contrary to that found by Bhat et al, [188] who found that increasing particle size for a given volume fraction increases the IPS/NND which increases toughness.

A number of models were examined regarding the prediction of the plane strain fracture toughness of DICoMMs and only some success was found ranging from very poor to reasonable. The different models were by Lin & Queeney [57], Kobayashi & Ohtani [223], Jin & Batra [224]. An interesting predictive model by Hahn & Rosenfield [221] (a Modified Rose-Johnson Model), whereby using pore size and volume fraction as the second phase constituent instead of the diamond size and concentration, proved a much better predictor of plane strain fracture toughness of DICoMMs. Indicating the flaw-like nature or role that diamond plays in PM cobalt metal matrix. A variant of Hahn-Rosenfield [221] model by Rabiei-Vendra-Kishi [220] used successfully for PMMCs was only marginally successful for DICoMMs where again porosity was used instead of diamond size and diamond concentration expressed as volume fraction.

6.6. Charpy Impact Energy

Overall the presence of diamond reduces the Charpy impact energy absorbed by the DICoMM materials and causes a large variability in results. A decrease in Charpy impact energy was found with increasing diamond concentration and with increasing diamond size. For each diamond concentration an increase in Charpy impact energy was found with increasing percent theoretical density.

Regarding interparticle spacing using either IPS/MFP or IPS/NND it was found that for a constant diamond concentration a statistical significance was found for Charpy impact energy of DICoMM materials. However, when IPS/MFP or IPS/NND was used for a range of diamond concentrations and diamond sizes combined no significance was found.

Regarding 'Available-Impact-Energy' of machine (50J & 300J), this was not found to influence or dependence on the Charpy impact energy for the range of DICoMM materials.

6.7. Transverse Rupture Strength (TRS)

With a constant diamond concentration, TRS increased with increasing percent theoretical density. The TRS of DICoMMs decreased with increasing diamond concentration. This was even evident with an increasing percent theoretical density. With increasing diamond concentration a shift downwards in TRS was found to occur.

A decrease in span (50mm to 40mm) for three-point bend was found to cause a reduction in the scatter in the TRS values for each diamond concentration. Also, the flexural strength (TRS) of the DICoMMs showed a dependence on tensile stressed volume (TSV), where as TSV increased the TRS decreased. It was also found that as diamond concentration increased TRS decreased for a given TSV, indicating that the diamonds present are behaving as flaws.

TRS and IPS/MFP, $\sqrt{}$IPS/NND and Log(IPS/NND) were found to be significantly correlated. As the diamond size became larger the IPSs increased resulting in lower TRS within each diamond concentration.

Using 'displacement-at-break' as a measure of ductility, for TRS DICoMMs it has been found that increasing diamond concentration causes a decrease in 'displacement-at-break' which is in agreement that found by Hosking et al. [192].

6.8. Fracture Stress Predictive Model

Using the Theory of Critical Distance and the average plane strain fracture toughness for CoMM & DICoMMs, the TRS fracture properties could be predicted with good accuracy for the range of diamond concentrations and diamond sizes used in this investigative work. The predictive models gave upper and lower bounds on the TRS fracture stresses by modelling the diamond as a flaw. It showed that with a constant diamond concentration, an increasing diamond size caused a decrease in TRS failure stress. Also that as diamond concentration increased a decrease in TRS fracture stress was found experimentally which was bounded by the fracture stress using TCD method.

TCD confirmed that the presence of diamond in COMM matrix is present as a flaw which initiating the fracture process.

In this thesis it has been found that TCD can also be used to successfully model the scenario of clustering which is commonly found in DIMMs, by treating the flaw size as two or more diamonds together.

Using strain energy concepts and the TCD predicted TRS fracture stresses a model was used to predict the experimentally determined Charpy impact energies for the different DICoMM successfully.

6. 9. Erosive Wear

The erosive wear of DICoMM materials was clearly shown to be related to diamond concentration and diamond size, with lower diamond concentrations showing increased erosion irrespective of diamond size.

The pressure and angle of incidence combination influences the results where at low pressures and angles, the coarser diamond shows better resistance than the finer diamond. However, where higher pressures and angles are used the finer diamond shows better resistance.

From the results it is clear that erosion of these types of materials is very complex with many interacting factors to consider, e.g. Mean Free Path (MFP), retention depth of diamond in metal matrix.

An empirical erosion model was proposed which reasonable predicts erosion of DICoMM materials incorporating MFP, erodent particle diameter and velocity, volume fraction of porosity, DICoMM material density and diamond concentration, however, more testing needs to be carried out to substantiate its robustness.

6.10. Recommendations for Future Work

The large volume of work carried out in this thesis shows the difficulty in understanding the class of materials called DIMMs and the difficulty in designing from first principles a diamond tool which can successfully cut the workpiece required. The predictive design

where matching mechanical properties of DIMM with the stone workpiece is a major obstacle to predictive design of these types of DI tools.

Regarding future work, and DICoMM materials, different hot pressing temperatures, different hot pressing profiles as well as the effects of coated diamonds are just a selection of the variables which need to be investigated. Certainly more work into wear of these materials is very much required if any major progress is to be achieved.

Regarding fracture toughness, the influence of yield strength in the validity criteria in the determination of plane strain fracture toughness needs to be investigated because yield strength increases with increasing percent theoretical density.

Finally, the results found for the cobalt based DIMM materials investigated in this thesis may not be found for other DIMM materials, as the presence of a good bonding between the diamond and metal matrix may influence the role that diamond plays in the overall material.

Regarding future work into the mechanical properties of DIMM materials in general much work has to be carried out to investigate other ranges of metal matrices which are used in the diamond tool industry. The effects of hot pressing temperatures, free-sintering, the role of diamond in each metal matrix used requires much investigative work.

Wear of DIMM materials is another area which is ripe for investigation and should aid the understanding of the role of the diamond in a 'soft' metal matrix as it cuts the stone workpiece and how other mechanical properties are inter-related.

Some of the recommended suggestions for future work above are only a selection of the many aspects which require investigation so that mechanical properties of DIMMs, the workpiece and cutting machine can be matched for optimum performance of the cutting operation.

References

[1]. Wapler H., 'New diamond forum – a Resume of the past or a challenge for the future of Diamond/CBN tools', Science and Technology of New Diamond, (1990) pp. 375-381.

[2]. Jennings M., Wright. D.,'Guidelines for sawing stone', Industrial Diamond Review 2/89.

[3]. Hughes, F.H., 'The Early History of Diamond Tools', Industrial Diamond Review, vol. 40 (1980).

[4]. Dan Fivehouse, 'The diamond drilling industry', London, 1976, p. 120.

[5]. Yu-Zan Hsieh , Jing-Fure Chen, Shun-Tian Lin, 'Pressureless sintering of metal bonded diamond particle composite blocks', J., Materials Science , Vol. 35 (2000), pp. 5383 – 5387.

[6]. S.R. Peacock, 'The future role of diamond in the construction industry', Finer Points, Issue Fall/Winter 2002. pp. 12-24.

[7]. M.A. Verspui, G. de With, P.G. Th. Van der Varst, M. Buijs, 'Bed thickness and particle size distribution in three-body abrasion', Wear 188 (1995) pp. 102-107.

[8]. A. Magnée, 'Modelization of damage by abrasion', Wear, 162-164 (1993) pp. 848-855.

[9]. M. Buijs, K. Korpel-van-Houten, 'A model for three-body abrasion of brittle materials', Wear 162-164 (1993) pp. 954-956.

[10]. A. Magnée, 'Generalized law of erosion: application of various alloys and intermetallics', Wear, 181-183 (1993) pp. 500-510.

[11]. J. Konstanty, 'Diamond retention characteristics of PM processed matrix materials', 3rd Intl. PM Conf., Ankara, September 4^{th} -8^{th}, 2002.

[12]. Konstanty & Busch , 'Hot Pressing of cobalt powders', Italian Diamond Journal, Diamante, Conf 1997, June 2^{nd} Switz.

[13]. Keun-Shyang Hwang, Tsung-Hsien Yang, 'Diamond cutting tools with a Ni_3Al + Copper Matrix', Intl. J. of Powder Metallurgy, Vol. 45, Iss. 6, 2009, pp. 37-43.

[14]. J. Konstanty, A. Romanski, H. Frydrych, 'Effect of mechanical properties of the matrix on its diamond retention capacity and wear characteristics during sawing hard stone by means of diamond impregnated tools', Proc. of 2000 Powder Metallurgy World Congress. Part 2. Edited by K. Kosuge, H. Nagai, Nov. 12-16, 2000, pp. 1629-1632.

[15]. M. Bonneau, 'A revolutionary binder for the diamond tool industry', Diamond Tools 99, Proc. EURO PM'99 International Workshop on Diamond Tool Production, Turin, Nov, 1999.

[16]. J.L. Ellis, 'Wear resistant alloy bonded carbides produced by PM', Powder Metallurgy International, Vol.16, No. 2, 1984.

[17]. P.A. Chalus, 'Metal powders for optimum grain retention', IDR 4/94, pp. 170-172.

[18]. Introduction to Powder Metallurgy', European Powder Metallurgy Association, 1998.

[19]. F. Thummler, R. Oberacker, 'An Introduction to Powder Metallurgy', Institute of Materials, 1993.

[20]. L. F. Pease, III, W. G. West, 'Fundamentals of Powder Metallurgy', MPIF Princeton, New Jersey, USA, 2002.

[21]. J. D. Dwan, 'Manufacture of diamond impregnated metal matrices', Materials Science and Technology, Sept- Oct 1998, Vol. 14, No.8, pp. 896-900, 1998.

[22]. Janusz Konstanty, 'Powder metallurgy Diamond Tools', The Metal Powders Technology Series, Elsevier, 2005.

[23]. J Konstanty, A. Bunsch, 'Hot pressing of cobalt powders', Powder Metallurgy Intl, 1991, Vol.34, No. 3 pp. 195-198.

[24]. Thakur, B.N. 'The Role of metal powders in manufacturing diamond tools', Superabrasives '85, April 22-25,1985, MR85-307, pp. 1-16.

[25]. Molinari, A. et al, 'Study of the Diamond –Matrix Interface in Hot-Presses Cobalt-based Tools', Materials Science and Engineering A130 (1990), pp. 257-262.

[26]. B. Kieback, Ch. Sauer, W. Tillmann, 'Optimisation of metallic binders used in diamond tool production', EURO PM '99, Nov 1999.

[27]. A.Romanski, J. Lachowski, J.Konstanty, 'Diamond retention capacity: evaluation of stress field generated in a matrix by a diamond crystal', IDR. 3/06, pp. 43-45.

[28]. Janusz Konstanty, 'Cobalt as a Matrix in Diamond Impregnated Tools for Stone Sawing Applications', Rozprawy Monografie 104, AGH Uczelniane Wydawnictwa Naukowo-Dydaktyczne, Krakow, 2002.

[29]. JOM, Vol. 50, Number 4, April, 1998, p. 41.

[30]. H. Hofmann D. Akyuz, 'Interface studies in cobalt –based diamond tools', Diamond Tools 99, pp. 89-96. Proc. EuroPM 99, Turin, Italy, Nov. 8-10, 1999.

[31]. A. Munier, J.E. Bidaux, R. Schaller, C. Esnouf,' Evolution of the microstructure of cobalt during diffusionless transformation cycles', J. Mater. Res., Vol.5 No. 4, Apr. 1990.

[32]. J. Konstanty, Bunsch, Cias, 'Factors affecting hardness and ductility of cobalt powders', Powder Met. Ind. Vol. 23, No. 6, p. 354. Dec. 1991.

[33]. J. Konstanty, 'Cobalt & diamond tooling', The Cobalt Conference, C8, 1997, April 23/24, 1997, Hong Kong.

[34]. Wu Liu, Manshan Lu, Shoji Goto, Setsuo Aso, ' Effect of thermomechanical circulation in short time on cobalt binder phase in WC-20wt. % Co', Intl. J. Refractory Metals & Hard Materials, Vol. 16, (1998), pp. 99-106.

[35]. J. Konstanty, 'Powder Metallurgy of Diamond Tools', Elsevier 2005, pp. 46.

[36]. D A Akyüz, S. Lauper, H Hofmann, 'Study of cobalt grain pinning by its oxides using image analysis', Intertech 99, Vancouver 1999.

[37]. D. A. Akyüz , P. Streit, H. Hofmann, J. Peersman, 'Hot pressing behaviour of fine cobalt powders', Second Intl Conf PM DIAMOND TOOLS '97, 2nd – 4th June,1997, Montreux, Switzerland.

[38]. M. Vedani, , H.G. Schmid, 'Influence of oxygen content on mechanical properties of cobalt bonds', Seminar Diabond '99, 1st -2nd – June, Nurnberg, Germany.

[39]. A. Romanski, 'Phase transformation in hot pressed cobalt and cobalt-diamond materials', Powder Metallurgy 2007, Vol. 50, No.2, pp. 115-119.

[40]. J. Dwan, 'HP/HT Manufacturing of Diamond', IMC -14, Proceedings of the Fourteenth Conf. of the Irish Manufacturing Committee, Editors: J. Monaghan, C.G. Lyons, pp. 471-480. Trinity College Dublin, 3rd -5th Sept. 1997.

[41]. Bailey, M.W., Hedges, L.K., 'Crystal Morphology Identification of Diamond', IDR 1/95.

[42]. Moore, M., 'Diamond Morphology', IDR 2/85.

[43]. http://www.abrasivesnet.com/en/product/mbs/diamond.b.htm.

[44]. American National Standards Institute (ANSI), Washinton DC, USA.

[45]. Fédération Europeene des Fabricants de Produits Abrasifs (FEPA), Paris, France.

[46]. R.M. German, 'The prediction of packing and sintering density for Bimodal Powder Mixtures', Volume 3, Sintering, Advances in Powder Metallurgy & Particulate Materials, 1992.

[47]. Konstanty, J., 'Materials Science of Stone Sawing', Industrial Diamond Review 1/91, pp. 27-31.

[48]. C.J. Santana, K.S. Jones, 'The effects of processing conditions on the density and microstructure of hot-pressed silicon powder', J. Mater. Sci. Vol. 31, (1996) pp. 4985 – 4990.

[49]. S.W. Webb, 'Diamond retention in sintered cobalt bonds for stone cutting and drilling', Diamond and Related Materials, Vol.8 (1999) pp. 2043-2052.

[50]. M.M Oliveira, J.D. Bolton, 'Mechanical properties of high speed steel base composites containing TiC and TiN ceramic additions', ICCM/9, Madrid, 12-16th July, 1993, pp. 149-156.

[51]. 'Standard test methods for metal powders and powder metallurgy products'. MPIF Standard (Issued 1980). MPIF Princeton, NJ, USA 1996.

[52]. Bullen, G.J., 'The Effect of Temperature & Matrix on the Strength of Synthetic Diamond', De Beers Project.

[53]. S. Evans, M R. Ney, 'Cobalt-catalyzed graphitization of diamond studied by X-ray photoelectron spectroscopy', J., Hard Materials, Vol. 1, No. 3, 1990, pp. 169-181.

[54]. Y.S. Liao, S.Y. Luo, 'Effects of matrix characteristics on diamond composites', Journal of Materials science Vol.28 (1993), pp. 1245-1251.

[55]. B. Kieback, Ch. Sauer, W. Tillmann, 'Optimisation of metallic binders used in diamond tool production', EURO PM '99, Nov 1999.

[56]. Anon., 'MBS diamond products for sawing and drilling applications', Brochure GES 91 – 966, GE Superabrasives, Worthington, OH, USA, 1991.

[57]. Lin, Z., Queeney, R.A., 'Fracture Resistance of Diamond Reinforced Hot Pressed Cu/Ni powders', Powder Metallurgy International Vol 18, #2, 1986.

[58]. A. L.Majstrenko, 'The strength and fracture of composite diamond-bearing tool materials', Advances in Fracture Research (Fracture 84), Proc. 6th Intl. Conf. Fracture (ICF6), New Delhi, India, 4th -10th Dec. 1984.

[59]. Haynes, R. 'Effects of porosity on the tensile strength of sintered irons', Int. J. Powder Met., Feb. 1991, pp. 49-51.

[60]. Danninger, H. , Janng, G., Weiss, B. , Stickler, R., 'The influence of porosity on static and dynamic properties of P/M iron', PM'90, World Conf. on Powder Metallurgy, London, July 1990, Vol. 1, pp. 433-439.

[61]. Melleanby, I. J., Phillips, R.A., Moon, J.R., 'Fracture and fatigue of powder metallurgy low alloy steels, ' Advances in PM Parts Production, Amsterdam, Nov. 1989, pp. 13.1 – 13.11.

[62]. Cadle, T.M., Langdgraf, C.J., Brewin, P. , Nurthen, P., 'Rolling contact fatigue resistance of P/M steel – Effects of sintering temperature and materials density', Advances in Powder Metallurgy, 1991, Vol. 1, pp. 175 – 181.

[63]. Haynes, R. , Egediege, J. T., 'Effects of porosity and sintering conditions on elastic constants of sintered irons,' Powder Metallurgy, 1989, Vol. 32, No.1, pp. 47 –52.

[64]. C. Verdu, C. Gatepin, R. Fougeres, 'Microcracks initiation and failure behaviour of sintered steels. Influence of phosphorus'. PM '94, Steels, pp. 871- 873.

[65]. Herve Chardin, Francois Grillon, Michel Jeandin, Michel Frainais, 'Superficial densification of P/M parts using ultrasonic shot-peening'. The International Journal of Powder Metallurgy, Vol. 32, No. 2, 1996, pp. 245-254.

[66]. Uwe Nutsch, Paul Beiss, Jans-Jürgen Jäger. 'Effects on density on mechanical properties, Thermal conductivity, and machinability of sintered stainless steels', EURO PM'97.

[67]. Standard 42, Metal Powder Industries Federation (MPIF), College Rd. East. Princeton, NJ.

[68]. Design Solutions, Brochure Information, Metal Powder Industries Federation (MPIF), College Rd. East. Princeton, NJ. 1993.

[69]. G. A. Gegel, P. Kurath, K. Boswell, 'Low cost fracture toughness testing of powder metal materials', Advances in Powder Metallurgy & Particulate Materials -1996', vol. 4, Part 13, pp.13-329-13-336. Compiled by T.M.Cadle, K.S.Narasimhan, Metal Powder Industries Federation. 105 College Rd., East Princeton, New Jersey, USA.

[70]. P. Ganesan, Ş. Domşa, P. Beiss, 'Fracture toughness of PM alloy steels', Powder Metallurgy, 2005, Vol.48, No.4, pp. 323-328.

[71]. L.Bertini, V. Fontanari, A. Molinari, G. Straffelini, 'Effect of notches on the fracture behaviour of sintered Steels', EURO PM'97.

[72]. R. A. Phillips, J.E.King, J.R.Moon, 'Fracture toughness of some high density PM steels', Powder Metallurgy , 2000, Vol. 43, No.1, pp. 43-48.

[73]. Peter Jones, Keith Buckley-Golder, Roger Lawcock, Rohith Shivanath, 'Densification Strategies for High Endurance P/M Components', The International Journal of Powder Metallurgy Vol. 33, No 3, 1997, pp. 37-44.

[74]. E.S. Palma, 'Influence of fatigue damage on ultimate tensile stress of sintered iron', Powder Metallurgy, 1997, Vol.40, pp. 211-213.

[75]. S. Peacock, J.R. Moon, 'Strengths and toughness of some PM steels consolidated by rotary forging and sintering', powder metallurgy, 2000, Vol. 43, No. 1, pp. 49-55.

[76]. J. Acedo, 'Study of sources of hardness variation in the manufacturing of shock absorber components', PM'94, Powder Metallurgy World Congress, Paris, 6-9 June, 1994, Vol. II, pp. 10491052.

[77]. James M. Dahl, Paul M. Novotny, 'Tech Spotlight, airframe and landing gear alloy', Advanced Materials & Processes, 3/99, pp. 23 – 25.

[78]. MPIF Standard 40, 'Determination of impact energy of unnotched powder metallurgy test specimens', Issued 1974, Revised in 1991, 1993, Metal Powder Industries Federation (MPIF), 105 College Rd., East Princeton, New Jersey, USA.

[79]. ASTM E23-88, 'Standard Test Methods for Notched Bar Impact Testing of Metallic Materials', 1989, American Society for Testing and Materials, Philadelphia, Pennsylvania, USA.

[80]. Kubel, E., 'Perfecting powder metallurgy', Advanced materials & Processes inc. Metal Progress,Vol.9,1987, pp. 52- 56.

[81]. G. Straffelini, V. Fontanari, A. Molinari, 'Strain Hardening behaviour of sintered steels under tensile and impact loading', Adv. Powder metallurgy & Particulate materials, Toronto, Canada, 1994, Vol.II pp. 51-60.

[82]. R. Shimansky, D. Slupe. 'An Instrumented Impact (Karbar) test procedure for sintered metal spur gears', pp. 185-201. Advances in Powder Metallurgy & Particulate Materials – 1994, Vol. 1. Metal Powder Industries Federation (MPIF), 105 College Rd., East Princeton, New Jersey, USA.

[83]. M. Svilar, E. Klar, 'Impact strength and fatigue properties of copper infiltrated P/M – steel', The Intl. J. Powder Metallurgy, Vol. 22, No. 2, pp. 105-112.

[84]. G. Straffelini, A. Molinari, D. Spoljaric, H. Danninger, 'Effects of notch geometry and microstructure on the impact behaviour of PM Fe-Mo steels', Advances in Powder Metallurgy & Particulate Materials – 1996, Vol. 4, Part 13, Editors, T. M. Cadle, K.S. Narasimhan, MPIF.

[85]. Shimansky, R.A., Collins, J., Orbison, J.G., 'Instrumented Charpy Impact Testing of Unnotched Powdered Metals', International Journal of Powdered Metals, Vol. 28, No. 4, October 1992.

[86]. B Augland, 'Fracture toughness and the Charpy V-notch test,' British Welding Journal, 1962, Vol.9, p. 434.

[87]. C.E. Turner, 'Measurement of fracture toughness by instrumented impact test,' Impact Testing of metals, Special technical publication 466, 1970, American Society for Testing and Materials, Philadelphia, Pa, USA, p.93.

[88]. Wang, K.C., Prucher, T., 'Fracture toughness measurements of P/M steels', Advances in Powder Metallurgy & Particulate Materials – 1994, Vol 1, Proc. Intl. Conf. & Exhibition on Powder Metallurgy & Particulate Materials, MPIF & APMI Intl., May 8-11, 1994, Toronto, Canada.

[89]. Mircea Terheci, 'Fracture toughness of commercially sintered low alloy steels – Part II. Results and Discussion', Eng. Frac. Mech., Vol. 56, No. 3, pp. 409 – 421, 1997.

[90]. Crane, L.W., Farrow, R.J., Powder Met. , 1980, #4, p. 198.

[91]. Fleck, N.A., Smith, R.A., Powder Met., 1981, Vol.24, #3, pp. 121-126.

[92]. D.L. Chen, B. Weiss, R. Stickler, D. Spoljaric, H. Danninger, 'Fracture toughness testing of PM materials', PM '94, pp. 843 –846.

[93]. Ingelstrom, N., Ustimenko,V., Powder Met. , 1975, 18 , (36) , p. 303.

[94]. Amador, J., Talacchia, S., Linaza, A., Jauregi, S., Rodriguez Ibabe, J.M., Urcola, J.J, 'Influence of the microstructure on the fatigue and fracture toughness of high speed steel powders sintered in a nitrogen atmosphere', PM'94, Powder Metallurgy World Congress. Paris, 6-9, June, 1994. Vol. II, pp. 1003 – 1006.

[95]. Y.T. Chen, 'Fracture Toughness Testing of PM materials', MPR June 1989, pp. 425-431.

[96]. Eva Dudrová, Radovan Bures, Margita Kabatova, Herbert Danninger, Marcela Selecka, 'Fracture Behaviour and Fracture Toughness of sintered steels, Euro PM'97, European Conf. Advances in Structural PM Component Production, Munich, Germany, Oct. 15-17, 1997, pp. 373-380.

[97]. R.A Phillips, J.E.King, J.R.Moon, 'Fracture toughness of some high density PM steels', Powder Metallurgy , 2000, Vol. 43, No.1 pp. 43-48.

[98]. Barnby, J.T., Ghosh, D.C., Dinsdale, K., Powder Met., 1973, 16, (31), p. 55.

[99]. ASTM E-399-90 'Standard Test Method for Measurement of Plane Strain Fracture Toughness'.

[100]. E.A. Steigerwald, 'Plane strain fracture toughness of high strength materials', Eng. Frac. Mechs. 1969, Vol. 1, pp. 473-494.

[101]. I.A. Ibrahim, F.A. Mohamed, E.J. Lavernia, 'Particulate reinforced metal matrix composites – a review', J. Mater Science Vol.26, (1991) pp. 1137-1156.

[102]. I. Sinclair, P.J. Gregson, 'Review, Structural performance of discontinuous metal matrix composites', Materials Science and Technology, 1997, pp. 709-726.

[103]. D. B. Miracle 'Metal matrix composites – From science to technological significance' Composites Science and Technology 65 (2005), pp. 2526-2540.

[104]. B. Terry, G. Jones, 'Metal Matrix Composites, Current Developments and Future trends in Industrial Research and Applications', Elsevier Advanced Technology, 1990.

[105]. Matthews, F.L., Rawlings, R.D., 'Composite materials: engineering and science', Chapman & Hall, 1st Edition, 1994.

[106]. C.K. Narula, P. Czubarow, D. Seyterth, 'Poly(borazinylamine): an excellent precursor for the preparation of low volume fraction metal-matrix composites containing metal borides and nitrides as ceramic phase', J. Mater. Sci. Vol. 33 (1998) pp. 1389-1397.

[107]. W. Frazier, 'Particulate Materials and Processes, a navy overview', Advanced Particulate Materials and Processes –1997, Proc. Fifth Intl Conf. On Advanced Particulate Materials and Processes (APMP). April 7-9, 1997, West Palm Beach .Florida.

[108]. K.I. Parashivamurthy, R.K. Kumar, S. Seetharamu, M.N. Chandrasekharaiah, 'Review on TiC reinforced steel composites', J. Mater. Sci. 36 (2001) pp. 4519-4530.

[109]. P. Yih, D.D. Chung, 'Titanium diboride copper-matrix composites', J. Mater Science, 32 (1997), pp. 1703-1709.

[110]. T.M. T. Hinder, A. Wisbey, P.S. Goodwin, 'Recent progress in developing particulate reinforced steel (BSS156) Matrix composites by mechanical alloying', pp. 211-218. Advanced Particulate Materials and Processes – 1997, Proc. Fifth Intl Conf. On Advance Particulate Materials and Processes (APMP) April 7-9, 1997, West Palm Beach, Florida.

[111]. Y.W. Know, J.H. Lee, C.T. Liu, 'Study of damage and crack in particulate composites', Composites Part B 29B (1998) pp. 443-450.

[112]. A.R. Kjar, J.L. Mihelich, T. Sritharan, C.J. Heatcock, 'Particle reinforced aluminium based composites', Light Weight Alloys for aerospace applications, Proc. Symp. TMS Nonferrous Metal Committee, TMS Annual Meeting, Las Vegas, Nevada, Feb. 28th – March 2nd , 1989. Editors: Eui W Lee, E. Henry Chia, Nack J. Kim. TMS Publications.

[113]. Don – Soo Shin, Jae-Chui Lee, Eui-Pak Yoon, Ho-In Lee, 'Effect of the processing methods on the formation of Al4C3 in Si/Cp /2024 Al Composites', materials Research Bulletin, Vol 32, No 9, pp. 1155-1163, 1997.

[114]. Hellier, A.K., Crosky, A., Park, B.G., 'Fracture and fatigue of Al_2O_3 based microsphere /6061-T6 Aluminium metal matrix composite', Proc. Ninth Intl. Conf. on Fracture. 1-5 April, 1997, Sydney, Australia, Editors, B.L. Karihaloo, Y-W Mai, M.I. Ripley, R.O. Ritchie. Advances in Fracture Research. PERGAMON, Vol.3. pp. 1685-1692.

[115]. Papakyriacou, M., Mayer, H.R., Tschegg-Stanzl, S.E., Groschl, M., 'Near-threshold crack growth in alumina particle reinforced 6061 aluminium alloy', Fatigue Fract. Engng. Mater. Struct. Vol 18, No. 4, 1995, pp. 477-487.

[116]. Leggoe, J.W., Hu, X.Z., Bush, M.B., 'Crack tip damage development and crack growth resistance in particulate reinforced metal matrix composites', Eng. Fracture Mechanics, Vol.53, No. 6, pp. 873-895,

[117]. Mingzhao Tan, Qibin Xin, Zhenghua Li, B.Y. Zong, 'Influence of SiC and Al_2O_3 particulate reinforcements and heat treatments on mechanical properties and damage evolution of Al-2618 Metal Matrix Composites', J. Mater Sci. 36 (2001) pp. 2045-2053.

[118]. U.T.S. Pillai, R.K. Pandey, P.K. Rohatgi, 'Effect of volume fraction and size of graphite particulates on fracture behaviour of Al-graphite composites', Eng. Frac. Mechs., Vol. 28, No.4, pp. 461-477.

[119]. Y.-F. Lee, S.-L. Lee, C.-L. Chuang, J.-C. Lin,' Effects of SiC_p reinforcement by electroless copper plating on properties of Cu/SiC_p composites', Powder Metallurgy, Vol. 42, No. 2, 1999, pp. 147-152.

[120]. Y.B. Liu, S.C. Lim, L. Lu, M.O. Lai, 'Fabrication of metal matrix particulate composites using powder metallurgy techniques', ICCM/9, Madrid, 12-16th July, 1993, pp. 770.

[121]. V.V. Bhanuprasad,, R.B.R. Bhat, A.K. Kuruvilla, K.S. Prasad, A.B. Pandey, Int. J. Powder Metall. 27 (1991) pp. 227-234.

[122]. M.K. Jain, V.V. Bhanuprasad,, S.V. Kamat, A. B. Pandey, V.K. Varma, B.V.R. Bhat, Y.R. Mahajan, Int. J. Powder Metall. 29 (1993) pp. 267-275.

[123]. A. M. Ritter, M. R. Jackson, R.N. Wright, 'Fracture of steel/carbide particulate composites', Advances in Fracture Research, Pergamon Press, Oxford, England, (1989).

[124]. Wu, Y., Lavernia, E.J., Scripta Metall. Mater. Vol. 27, pp. 173 (1992).

[125]. Nardone, V.C., Prewo, K.M., Scripta Metall. Vol. 20, pp. 43 (1986).

[126]. Arsenault, R.J., Scripta Metall. Mater. Vol. 25, pp. 2617, (1991).

[127]. Miller, W.S., Humpreys, Scripta. Metall. Mater. Vol. 25, pp. 33, (1991).

[128]. Taya, M., Lulay, K.E., Lloyd, D., Acta Metall. Mater., Vol. 39, pp. 73 (1991).

[129]. White, J., Palmer, I.G., Hughes, I.R., Court, S.A., in Proc. 'Aluminium-Lithium Alloys V', Williamsburg, Virginia, March 1989, Vol.3 edited by T.H. Sanders Jr. and E.A. Srarke Jr (Materials and Components Engineering Publications, Edgbaston, UK, (1989) pp. 1635.

[130]. Singer, A.R.E., Ozbek, S., Powder Metall. Vol. 28, pp. 72 (1985).

[131]. Ibrahim, I. A., Mohamed F.A., Lavernia, E.J., in 'Advanced Aluminium and Magnesium Alloys' edited by T. Khan and G. Effenberg (ASM International, Amsterdam, 1989), pp. 745.

[132]. Wu, Y., Lavernia, E.J., J. Metals Vol. 43, pp. 16 (1991).

[133]. Friend, C.M., J. Mater. Sci. Vol. 28, pp. 3005, (1987).

[134]. Qin, S., Gupta, M., 'The minimum volume fraction of SiC reinforcement required for strength improvement of an Al-Cu based composite', J. Mater. Sci., Vol 30. pp. 5223-5227, 1995.

[135]. S.A. Sushchenko, 'Photoelastic analysis of stress concentrations in a two-dimensional model of hard inclusions in a metal matrix', tribology Transactions, Vol. 40(1997), 2, pp. 386-390.

[136]. M.M. Oliveira, J. D. Bolton, 'Sintering of M3/2 high speed steel modified by additions of copper phosphide and titanium based ceramic compounds', Powder Metallurgy, 1995, Vol. 38, No. 2, pp. 131-140.

[137]. A. M. Ritter, M. R. Jackson, R. N. Wright, 'Plasma-sprayed stainless steel carbide', 'Processing & Properties for Powder Metallurgy Composites', Annual Meeting of the Metallurgical Soc., Denver, Colorado, February, 1987. pp. 59 – 77.

[138]. K.B. Lee, H.S. Sim, S.W. Heo, H.R. Yoo, S.Y. Cho, H. Kwon, 'Tensile properties & microstructures of Al composites reinforced with BN particles ', Composites : Part A 33 (2002) pp. 79 – 715.

[139]. Y. Sahin, M. Acilar, 'Production and properties of SiC_p-reinforced aluminium alloy composites', Composites: Part A 34 (2003) pp. 709-718.

[140]. M. Gupta, M.O. Lai, D. Saravanaranganathan, 'Synthesis, microstructure and properties characterization of disintegrated melt deposited Mg/SiC composites', J. Mater. Sci. 35. (2000) pp. 2155-2165.

[141]. Manuela Oliveira, John D. Bolton, 'Effect of ceramic particles on the mechanical properties of M3/2 high Speed Steel', The International Journal of Powder Metallurgy, Vol. 32, No.1, 1996. pp. 37-48.

[142]. H.W. Nam, Gamal A. Aggag, K. Takahashi, K.S. Han, 'The dynamic behaviour of metal matrix composites under low-velocity impact', Composites Science and Technology 60 (2000) pp. 817-823.

[143]. 'Metal Matrix Composites: Mechanisms & Properties', edited by Everett, R.K., Arsenault, R.J., Academic Press, 1991.

[144]. B. Roebuck, J. Lord: Mater. Sci. Technol., 1990, 6, pp. 1199 –1209.

[145]. B. Roebuck, J. Lord: in Proc. Meeting 'Test techniques for metal matrix composites', (ed. N.D.R. Goddard), pp. 110 – 128; 1991, Bristol, Institute of Physics.

[146]. A. Mortensen: in Proc. Conf. On 'Fabrication of particulates reinforced metal composites', (ed. J. Masouanave & F.G. Hamel), pp. 217 – 233; 1990, Materials Park, OH, ASM.

[147]. K.M Prewo: in Proc. Conf. 'Mechanical behaviour of metal matrix composites', (ed. J.E. Hack and M.F. Amateau), pp. 181 – 194; 1983, Warrendale, PA, AIME.

[148]. W.G. Patterson, M. Taya, in 'Metal Matrix Composites: Mechanisms & Properties', edited by Everett, R.K., Arsenault, R.J., pp. 183, Academic Press, 1991.

[149]. R. Giridhar, M.K. Surappa, 'Effect of ageing on impact fracture behaviour of 2024Al-Al_2O_3p composites made by casting route', ICCM/9 Proc. Ninth Intl. Conf. on Composite Materials, Madrid, 12-16 July, 1993, Vol. I, pp. 219-226.

[150]. H. Reshetnyak, J. Kübarsepp, 'Resistance of hardmetals to fracture', Powder Metallurgy, 1998, Vol. 41. No.3 pp. 211-216.

[151]. A. Chakraborty, S.B. Bhaduri, J.J. Reddy, Y.R. Mahajan, 'The effect of processing parameters on the mechanical properties of Al_2O_3 /SiC_w composites', PMI Vol. 23, No.3, 1991. pp. 169-173.

[152]. R. Vassen, M. Koldewitz, A. Ruder, 'Influence of binder content and particle size on green strength of WPP parts', Powder Metallurgy, 1995 Vol.38, No. 1, pp. 55-58.

[153]. A.H. Duwel, K.M. Mussert, M. Janssen, A. Bakker, S. Van Der Zwaag, 'A study on the fracture toughness of Al-based MMCs containing different volume fractions Al_2O_3', J. Matl. Sci Letts, Vol. 20, 2001, pp. 1147-1150.

[154]. Klimovicz, T.F., Veechio, K.S., 'The influence of ageing condition on the fracture toughness of aluminium-reinforced aluminium composites', Ed. By Liaw, P.K., Gungor, M.N., The Minerals, Metals and Materials Society, 1990, pp. 255.

[155]. Friend, C.M., 'Toughness in metal matrix composites', Mat. Sci. & Tech., Vol 5, 1988, pp. 17.

[156]. Mingzhao Tan, Qibin Xin, Zhenghua Li, B.Y. Zong, 'Influence of SiC and Al_2O_3 particulate reinforcements and heat treatments on mechanical properties and damage evolution of Al-2618 Metal Matrix Composites', J. Mater Sci. 36 (2001) pp. 2045-2053.

[157]. Kamat, S.V., Hirth, J.P. Mehrabian, R., ' Mechanical properties of particulate reinforced aluminium matrix composites', Acta Metall., Vol. 37, 1989, pp. 2395 – 402.

[158]. Flom, Y., Arsenault, R.J., 'Fracture of SiC/Al composites', in VI ICCM & II ECCM (Conf. Proc.) Vol. 2., ed. By Mathews, F.L., Bunsell, M., Hudgkinson, J. Mohton, J., Elsevier Applied Science, London, 1987, pp. 189 –198.

[159]. Flom, Y., Arsenault, R.J., 'Effects of particle size on fracture toughness of SiC/Al composite materials', Acta Metall., Vol. 37, 1989, pp.2413 – 2423.

[160]. McDonalds, D.C., Signorvelli, P.A., 'Evolution of low cost aluminium matrix composites for aircraft engine structured application', NASA Technical Memorandum 83357, 1983.

[161]. Davidson, D.L., 'Fatigue and fracture toughness of aluminium alloys reinforced with SiC and alumina particles', Composites, Vol. 24, No. 3, 1993, pp. 248-255.

[162]. J.D. Bolton, A.J. Grant, 'Fracture in ceramic reinforced metal matrix composites based on high-speed steel', J. Matl. Sci. 33, (1998) pp. 939-935.

[163]. J.B. Fogagnolo, M.H. Robert, E.M. Ruiz-Navas, J.M. Torralba, '6061 Al reinforced with zirconium diboride particles processed by conventional powder metallurgy and mechanical alloying' J. Mater. Sci. 39, (2004) pp. 127-132.

[164]. Dan Zhao, Floyd R. Tuller, 'Effect of particle size on fracture toughness in metal matrix composites', Technical Note, Eng. Frac. Mechs, Vol. 47, No.2, pp. 303-308, 1994.

[165]. F.F. Lange, J. Am. Ceram. Soc. 56, p. 445 (1973).

[166]. Akira Kobayashi, Nobuo Ohtani, 'On fracture characteristics of particle-dispersion composites', ICCMV 1985, San Diego, California, July 29,30, August 1,1985. pp. 363-371.

[167]. S.M. Barinov, V. Yu, Evdokimov, V. Ya. Shevchenko, 'Mechanical behaviour of nickel aluminide –zirconia transformation-toughened particulate composite', J. Mater Science 32 (1997) pp. 5053-5058.

[168]. D. Ray, B.K. Sarkar, N.R. Bose, 'Impact fatigue behaviour of vinylester resin matrix composites reinforced with alkali treated jute fibres', Composites: Part A 33 (2002) pp. 233-241.

[169]. J. Konstanty, 'Cobalt as a Metal Matrix in diamond impregnated tools for stone sawing applications', Rozrprawy Monografie 104, AGH Uczelniane Wydawnictwa Naukowo Dydaktyczne Krakow 2002, pp. 74-99.

[170]. J. Konstanty, 'Powder Metallurgy of Diamond Tools', Elsevier 2005, pp. 106-112.

[171]. M. Zeren, S. Karagöz, 'Defect characterization in the diamond cutting tools', Materials Characterization 57, (2006) pp. 111-114.

[172]. Fax Maxime Bonneau – Private Communication – August 1999.

[173]. R. Orban, S. Domsa, 'Metallic binder for diamond tool production using synthetic diamond', Diamond Tools 99, EURO PM 99, Italy, Nov. 8-10, 1999.

[174]. J. Konstanty, 'Developing a better understanding of the bonding and wear mechanisms involved in using diamond impregnated tools', Diamond Tools Turin 99.

[175]. S. Karagöz, M. Zeren, 'The property optimization of diamond-cutting tools with the help of micro-structural characterization', Intl. J. Refractory Metals & Hard Materials 19 (2001) pp. 23-26.

[176]. Yu-Zan Hsieh, Shun-Tian Lin, 'Diamond tool bits with iron alloys as the binding matrices', Materials Chemistry and Physics, vol.72, (2001) pp. 121-125.

[177]. T. Dobra, D. Bota, 'Hot pressed WC-W-Ni-Cu-Zn-Si composites for synthetic diamond drilling tools', EURO MAT, Padua/Venice, Italy, 25-28 September 1995, pp. 479-482.

[178]. Jean-Marc Borel, 'Non-cobalt metal powders for diamond tool bonds', Seminar Diabond '99, 1-2 June Nurnberg Germany 1999.

[179]. S. Karagöz, M. Zeren, 'The microstructural design of diamond-cutting tools', Materials Characterization 47 (2001) pp. 89-91.

[180]. Qin Eijie, Yin Sheng, Lai Heyi, 'Behaviour of carbide–forming elements in matrix materials of diamond tools', University of Science and Technology Beijing, Beijing 100083, China – No Journal or Conf ref.

[181]. Lan Sun, Jinsheng Pan, Changjian Lin, 'A new approach to improve the performance of diamond saw blades', Materials Letters 57 (2002) pp. 1010-1014.

[182]. J. Deng, X. Ai, 'Microstructure and mechanical properties of hot pressed TiB_2-SiC_w composites', Materials research Bulletin, Vol.33, No. 4., pp. 575-582, 1998.

[183]. Michal Besterci, Milan Slesar, Gerhard Jangg, 'Structure and Properties of dispersion hardened Al-Al_4C_3 Materials, PMI, Vol 24, No. 1, 1992, pp. 27 – 32.

[184]. B.I. Edelson , W.M. Baldwin, Jr. 'The effect of second phases on the mechanical properties of alloys', Transactions of the ASM, 1962, 55, pp. 230-250.

[185]. C. W. Corti, P. Cotterill, G. Fitzpatrick, Int. Met. Rev., Vol. 19, pp. 77-88, June 1974.

[186]. George E. Dieter, Mechanical Metallurgy, SI Metric Edition, McGraw Hill, 1988.

[187]. M. Gensamer, E.B. Pearsall, W.S. Pellini, J.R. Low, Jr., 'The tensile properties of pearlite, bainite and spheroidite', ASM Transactions, 23rd Annual Convention of Society, Oct. 20-24th, 1941, pp. 983-1019.

[188]. M. S. Bhat, & V. F. Zackay , 'Microstructure and Toughness in Ultra High Strength Steels', Fracture and Failure: Analyses, Mechanisms and Applications', Proceedings of the American Society for Metals Fracture and Failure Sessions, 1980 Western Metal and Tool Exposition and Conference (WESTEC), 17-20 March, 1980, Los Angeles, CA. Edited by : Paul. P. Tung, Suphal P. Agrawal, Arun Kumar, Michael Katcher. Materials/ Metalworking Technology Series, ASM, Metals Park, Ohio, USA.

[189]. Stephen M Copley, James C. Williams, 'Alloy and Microstructural Design', edited by John K. Tien, George S. Ansell, Materials Science Series, Academic Press, 1976, pp. 11-30.

[190]. T.S. Srivatsan, R. Annigeri, Amit Prakash, 'Tensile deformation and fracture behaviour of a tool steel based metal matrix composite', Composites Part A 28A (1997) pp. 377-385.

[191]. Dan Zhao, Floyd R. Tuller, 'Effect of particle size on fracture toughness in metal matrix composites', Technical Note, Eng. Frac. Mechs, Vol. 47, No.2, pp. 303-308, 1994.

[192]. F M Hosking, F. Folgar Portillo, R. Wunderlin, R. Mehrabian, 'Composition of aluminium alloys: fabrication and wear behaviour', J. Mater Sci. 17 91982) pp. 477-498.

[193]. Private communication, D Taylor, 2009.

[194]. M. Ritter, M. R. Jackson, R. N. Wright, 'Plasma-sprayed stainless steel carbide', 'Processing & Properties for Powder Metallurgy Composites', Annual Meeting of the Metallurgical Soc., Denver, Colorado, February, 1987. pp. 59 – 77.

[195]. Karl-Heinz Schwalbe, 'On the influence of microstructure on crack propagation mechanisms and fracture toughness of metallic materials', Eng. Frac. Mech. Vol.9. pp. 795-832. 1977.

[196]. J. D. Dwan, Powder Metallurgy, Vol. 41, No. 2, (1998), pp. 84-86.

[197]. S.W. Webb & W.E. Jackson, J. Manufac. Sci. Eng., Vol.120 (1998) pp. 84-92.

[198]. A. Ersoy, S. Buyuksagic, U. Atici, 'Wear characteristics of circular diamond saws in the cutting of different hard abrasive rocks', Wear 258 (2005) pp. 1422–1436.

[199]. A. DiIlio and A. Togna, International Journal of Machine tools and Manufacturing, Vol. 44, Issue 7-8 June (2004) pp. 839-846.

[200]. Y.S. Liao & S.Y. Luo, Wear, Vol.157 (1992) pp. 325-337,

[201]. S.Y.Luo, Int.J. Mach. Tools Manufac., Vol.36 (1996) pp. 661-672.

[202]. N.D. Wright & H. Wapler, Ann. CIRP, Vol. 35 (1986) pp. 239-244.

[203]. D.Miller & A. Ball, Wear, Vol.141 (1991) pp. 311-320.

[204]. J. Konsanty, Tai-Woung Kim, Sang-Beom Kim, 'Resistance to abrasive wear of materials used as metallic matrices in diamond impregnated tools'. Materials Science Forum, Vols. 534-536 (2007), pp. 1125-1128.

[205]. N. Axén, K.-H. Zum Gahr, 'Abrasive wear of TiC steel composite clad layers on tool steel', Wear 157 (1992) pp. 189-201.

[206]. S. Turenne, Y. Châtigny, D. Simard, S. Caron, J. Masounave, 'The effect of abrasive particle size on the slurry erosion resistance of particulate reinforced aluminium alloy', Wear, 141, (1990), pp. 147-158.

[207]. I.M Hitchings,' Abrasive and erosive wear of metal matrix composites', In: Proceedings of the 2nd European Conference on Advanced Materials and Processes, Euromat '91, 22-24 Jul 1991, Cambridge, UK.

[208]. I. Finnie, Proc. 3rd U.S. Natl. Congr. Appl. Mech., (1958).

[209]. I. Finnie, Wear, 3, (1960) pp. 87-103.

[210]. S. Ranganath, 'A review on particulate reinforced titanium matrix composites', J. Mats. Sci. 32 (1997) pp. 1-16.

[211]. D.H. Phar, S.M. Arnold, 'The applicability of the generalized method of cells for analyzing discontinuously reinforced composites', Composites: Part B 33 (2002) pp. 153-170.

[212]. C.F. Legzdins., I.V. Samarasekera, J.A. Mech, 'MMCX – an expert system for metal matrix composite selection and design', Canadian Metallurgical Quarterly, Vol. 36, No. 3, pp. 177-202, 1997.

[213]. Qiang Zhang, Gaohui Wu, Guoqin Chen, Longtao Jiang, Bofeng Luan, 'The thermal expansion and mechanical properties of high reinforcement content SiC_p/Al composites fabricated by squeeze casting technology', Composites: Part A 34 (2003) pp. 1023-1027.

[214]. L. Kowalski, J. Duszczyk, L. Katgerman, 'Thermal conductivity of metal powder polymer feedstock for powder injection moulding', J. Mats Sci. 34 (1991).pp. 1-5.

[215]. K.I. Parashivamurthy, R.K. Kumar, S. Seetharamu, M.N. Chandrasekharaiah, 'Review of TiC reinforced steel composites', J. Matls, Sci. 36 (2001) 4519-4530.

[216]. Nardone, V.C., Garosshen, T.J., 'Evaluation of the tensile and fatigue behaviour of a powder metallurgy beryllium/aluminium alloy', J. Materials Science, 32, (1997) pp. 2549-2557.

[217]. R. Biswas, J.L. Henshall, R.J. Wakeman, 'Fracture in a model brittle composite material: Quartz-Perspex', 9th 1-5/4/97, Paper 20, pp. 841-848.

[218]. J.R. Rice, M.A. Johnson, 'The role of large crack tip geometry changes in Plane Strain Fracture', Inelastic Behaviour of Solids, p. 641, 1970.

[219]. M. Manoharan & S.V. Kamat, (1991), 'On the fracture toughness of particulate reinforced Metal Matrix composites', Scripta Metall et Mat, 25 (9), 1991, pp. 2121-2125.

[220]. A. Rabiei, L. Vendra, T. Kishi, 'Fracture behaviour of particle reinforced metal matrix composites', Composites: Part A (2007), doi:10.1016/j.compositesa.2007.10.018.

[221]. G.T. Hahn, A.R. Rosenfield, 'Metallurgical Factors affecting fracture toughness of aluminium alloys', Metall. Trans. A 1975, 6A, pp. 653-668.

[222]. T.J. Downes, P.B. Prangnell, J. E. King. 'Mechanisms of fracture in discontinuous metal matrix composites', ICCM/9. Proc. Ninth Intl. Conf. on Composite Materials, Madrid, 12-16 July, 1993, pp. 665-671.

[223]. Akira Kobyashi & Nobuo Ohtani, 'On Fracture characteristics of particle-dispersion Composites', ICCMV '85, pp. 363-371.

[224]. Z-H. Jin, R.C. Batra, 'Thermal shock cracking in a metal-particle-reinforced ceramic matrix composite', Engineering Fracture Mechanics 62 (1999), pp. 339-350.

[225]. David Taylor, 'The theory of critical distance, a new perspective in fracture mechanics', Publishers: Elsevier, 1st Edition, 2007.

[226]. Eurotungstene Poudres, Cobalt News 04/1, pp. 3-6.

[227]. Turbula System Schatz, W. A. Bachofen AG, Maschinenfabrik, Basel, Switzerland.

[228]. Dr. Fritsch Sondermaschinen GmbH, Dieselstr, 8. D – 70736 Fellbach, Germany.

[229]. N.A. Pratten, 'Review, The precise measurement of the density of small samples', J. Mater Sci. Vol.16, (1981), pp. 1737-1747.

[230]. MPIF Standard 42, 'Determination of Density of Compacted or Sintered Metal Powder Products', Issued 1980, Revised in 1986, (formerly MPIF Standard 08, 13, 16 & 35), Metal Powders Industries Federation, 105 College Rd. East, Princeton, NJ, USA.

[231]. MPIF Standard 43, 'Determination of Hardness of Sintered Metal Powder Products', Issued 1974, Revised in 1991, (formerly included in MPIF Standards 08, 13), Metal Powders Industries Federation, 105 College Rd. East, Princeton, NJ, USA.

[232]. James M. Dahl, Paul M. Novotny, 'Tech Spotlight, airframe and landing gear alloy', Advanced Materials & Processes, 3/99, pp. 23 – 25.

[233]. D. K. Patrick, 'The history of impact testing', Industrial Heating, pp. 12 – 14, June 1999.

[234]. ASTM E23-88, 'Standard Test Methods for Notched Bar Impact Testing of Metallic Materials', American Society for Testing and Materials, Philadelphia, Pennsylvania, USA. 1989.

[235]. R.M Boothby , C.A. Hippsley, 'Impact and chevron notch fracture toughness testing of particulate metal matrix composites' Materials Science and Technology, June 1994, Vol. 10, pp. 565- 571.

[236]. T. Lorriot, 'Specimen loading determined by displacement measurement in instrumented Chary impact Test', Eng. Frac. Mechs. 65 (200), pp. 703-713.

[237]. Lin Wang, Jian-Lin Shi, Hang-Rong Chen, Zi-Le Hua, Tung-Sheng Yen. 'Effect of size of the starting powders on the thermal shock resistance of alumina ceramics', J. Materials Science Letters Vol. 20, pp. 341-342, 2001.

[238]. MPIF Standard 41, 'Determination of Transverse Rupture Strength of Powder Metallurgy Materials', Issued 1951, Revised in 1962 & 1973 & 1991, (formerly MPIF Standard 13), Metal Powders Industries Federation, 105 College Rd. East, Princeton, NJ, USA.

[239]. D. Sherman, I. Be'ery, 'Fracture mechanisms of sapphire under bending', J. Materials Science 35 (2000), pp. 1283-1293.

[240]. A. Zulfia, H.V. Atkinson, H. Jones, S. King, 'Effect of hot isostatic pressing on cast A357 aluminium alloy with and without SiC particle reinforcement', J. Mater. Sci. Vol. 34 (1999), pp. 4305-4310.

[241]. SERIES-IX Software, Instron Corp., High Wycombe, UK.

[242]. D. Broek, 'Elementary engineering fracture mechanics', Martinus Nijhoff, (1986), The Hague;

[243]. J.F. Knott, 'Fundamentals of fracture mechanics', Butterworths (1973), London.

[244]. Richard W. Hertzberg, 'Deformation and fracture mechanics of engineering materials', John Wiley and Sons, (1988) New York.

[245]. T.L. Anderson, 'Fracture Mechanics, Fundamentals and applications', CRC Press (1991) Boston.

[246]. P.C. Paris, 'Fracture Mechanics and fatigue: A Historical perspective', Fatigue & Fracture of engineering Materials & Structures, 1998; #21: pp. 535-540.

[247]. G.M. Boyd, 'From Griffith to COD and Beyond', Engineering Fracture Mechanics, 1972, Vol.4, pp. 459-482.

[248]. B. Cotterell, 'The Past, Present, and Future of Fracture Mechanics', Engineering Fracture Mechanics, Vol.69 (2002) pp. 533-553.

[249]. A.P.Parker, 'The mechanics of fracture and Fatigue, An introduction', Spoon, ed. 1, 1981.

[250]. G.R.Irwin, 'Analysis of stresses and strain near the end of a crack transversing a plate'. Trans. ASME, J. Appl. Mech, 24, p. 361 (1957).

[251]. Bahram Farahmand, G.E. Bockrath,'A theoretical approach for evaluating the plane strain fracture toughness of ductile metals', Eng. Frac. Mechs., Vol. 53, No.6, pp. 975-990, 1996.

[252]. ASTM E-399-90: 'Standard Test Method for Measurement of Plane Strain Fracture Toughness', American Society of Testing and Materials, Philadelphia, USA. 2003.

[253]. ASTM E-1290-02: 'Standard Test Method for Crack-Tip Opening Displacement (CTOD) Fracture Toughness Measurement', American Society of testing and Materials, Philadelphia, USA. 2003.

[254]. ASTM E-1820-01: 'Test Method for Measurement for Fracture Toughness', American Society of testing and Materials, Philadelphia, USA. 2001.

[255]. ASTM E-1823-96: 'Technology Relating to Fatigue and Fracture Testing', American Society of testing and Materials, Philadelphia, USA. 1996.

[256]. ESIS Recommendation for Determining the Fracture Resistance of Ductile Materials' European Structural Integrity Society, 1992.

[257]. ESIS Procedure for determining the Fracture Behaviour of Materials' European Structural Integrity Society, 1992.

[258]. BS7448: Fracture Mechanics Toughness Tests, Parts 1, 2, 3, & 4, British Standards Institute London.

[259]. Brown, W.F., Jr. Srawley, J.E., ASTM STP 410, 1966.

[260]. A. Bakker, 'Compatible compliance and stress intensity expressions for the standard three-point bend specimen', Fatigue Fract. Engng. Mater. Struct. Vol. 13, No. 2, pp. 145-154, 1990.

[261]. J.E. Srawley, B. Gross, 'Compendium of stress intensity factors for bend and compact specimens', Engng. Fract. Mech. Vol.4, pp. 587-589, (1976).

[262]. Srawley, J.E., 'Wide ranges stress intensity factor expressions for ASTM E399 standard fracture toughness specimens', International Journal of Fracture 1976; Vol. 12, pp. 475-476.

[263]. D. A. Jablonski, B. Journet, R.S. Vecchio, R. Hertzberg, 'Compliance functions for various fracture mechanics specimens', Engineering fracture mechanics, Vol. 22, No. 5 1985, pp. 819-827.

[264]. N. A. Fleck, 'Compliance methods for measurement of crack length', EMAS, 1991, pp. 69-93.

[265]. 'Measurement of crack length and load using strain gauges', Richards C E and Deans W F, EMAS 1980, pp. 28-68.

[266]. A. Saxena, S. Hudak, Int. J. Fracture, 14, pp. 453-468 (1978).

[267]. H. Tada, P. Paris, G. Irwin, ' The stress analysis of Cracks Handbook, Del Research Corp.., Hellertown, PA, pp. 2.16-2.18 (1973).

[268]. Ashok Saxena and S. J. Hudak, Jr., 'Review and extension of compliance information for common crack growth specimens', International Journal of Fracture, vol.14, pp. 453-468, 1978.

[269]. Saxena, A., Hudak, S.J., 'Review and extension of crack growth information for common crack growth specimens,' Scientific Paper 77 –9E7 – AFCGR-P1, Westinghouse R&D Center, Pittsburgh, PA, April 1977.

[270]. A. Saxena, S.J. Hudak, Jr., J.K. Donald, D.W. Schmidt, 'Computer controlled decreasing stress intensity technique for low rate fatigue crack growth testing', J. Testing and Evaluation, ASTM 6, pp. 167 (1978).

[271]. T.L. Anderson, 'Fracture Mechanics Fundamentals and Applications', 2nd edition CRC Press, 1995, pp. 607.

[272]. ASTM E399-90, 'Standard Test Method for Plane-Strain Fracture Toughness of Metallic Materials', A3. Special Requirements for the Testing of Bend Specimens, A3.5.6, pp. 506-536. American Society of testing and Materials, Philadelphia, USA.

[273]. ASTM E647-95a. 'Measurement of fatigue crack growth rates'. American Society of testing and Materials, Philadelphia, USA.

[274]. The Stress Analysis of cracks handbook 1973, H. Tada, P.C. Paris and G. R. Irwin.

[275]. FastTrack 2 Software Fatigue Crack Propagation da/dN, Catalogue Number 2490-906, Instron Corp., High Wycombe, UK.

[276]. FastTrack 2 Software K_{1C} Fracture Toughness Program 32-bit Version, Catalogue 2490-907B2, Instron Corp., High Wycombe, UK.

[277]. Scentis Image Analysis Software, Struers & MediaCybernetics Inchttp://www.struers.com/default.asp?top_id=3&main_id=67&sub_id=104&doc_id=525

[278]. U. Habel, J.H. Moll, F.J. Rizzo, J.J. Conway. 'Microstructure and properties of HIP P/M 706'. Advanced particulate Materials and Processes – 1997. Edited by F.H (Sam) Froes, John Hebeisen. pp. 447-456.

[279]. Ying Shi, Xiaoxian Huang, Dongsheng Yan, 'Mechanical properties and toughening behaviour of particulate reinforced zircon matrix composites', J. Mater. Sci. Letters Vol. 18 (1999) pp. 213-216.

[280]. Basic Distribution and Significance Tables, Table 10, The Correlation Coefficient. pp. 20.

[281]. James Reilly, 'Using Statistics', Gill & MacMillan, pp. 66-78, 2006.

[282]. Peter Jones, Keith Buckley-Golder, Roger Lawcock, Rohith Shivanath, 'Densification Strategies for High Endurance P/M Components', The International Journal of Powder Metallurgy Vol. 33, no 3, 1997, pp. 37-44.

[283]. R.M. Aikin, 'The Mechanical Properties of In-situ Composites', JOM, August, 1997, pp. 35-39.

[284]. T.J. Downes, J.E. King, 'The effect of microstructure on the fracture toughness of a metal-matrix composite'. Composites, Vol. 24. No. 3, 1993, pp. 276-281.

[285]. M D Dory, R.H. Dauskardt, A. Kant, R.O. Ritchie, 'Fracture of Synthetic diamond', J. Appl. Phys. 78 (5) 1st Sept. 1995.

[286]. Y. Murakami, 'Stress intensity factors handbook', Pergamon, Oxford, UK, 1987. p. 668.

[287]. N. Axén, K.-H. Zum Gahr, 'Abrasive wear of TiC steel composite clad layers on tool steel', Wear 157 (1992), pp. 189-201.

[288]. J. Konsanty, Tai-Woung Kim, Sang-Beom Kim, 'Resistance to abrasive wear of materials used as metallic matrices in diamond impregnated tools', Materials Science Forum, Vols. 534-536 (2007), pp. 1125-1128.

[289]. J.F. Douglas, J.M. Gasiorek, J.A. Swaffield, 'Fluid Mechanics', 3rd Ed. Longman Scientific & Technical, 1995, pp. 519-520.

[290]. Jingwei Wu, Hongyuan Fang, Sanghoon Yoon, Hyung Jun Kim, Changhee Lee, 'Measurement of particle velocity and characterization of deposition in aluminium alloy kinetic spraying process', Applied Surface Science 252 (2005), pp. 1368-1377.

[291]. A.P. Alkhimow, V.F. Kosarey, S.V. Klinkow. 'The features of cold spray nozzle design', J. Therm. Spray Technol. 10 (2001), pp. 375-381.

APPENDIX 1 - Cobalt Powder Couf

The following information is taken from Eurotungstene Poudres (ETP) [172].

Cobalt Powder - Type: COUF - (CO7106)

Properties

Physical Properties

Fisher grain size (FSSS) (microns)	0.8 - 1.05
Scott apparent density (g/cc)	0.5 - 0.85
Tap density (g/cc)	1.4 - 2.1
Specific area (m^2/g)	Typical: 2.3
Oxygen Content	Typical: 0.65%
Guaranteed	1.0% max.
Cobalt Content	
(excluding oxygen)	99.7% min.

Granules - Granulated powder had 1.3wt% binder; the binder is part of the polyacrylates family. The cobalt powder is available as granule of 63 - 350 microns, or 350 - 630 microns. This project used 63 - 350 microns.

Granulated powder gives good flow without any dust and a higher apparent density.

Recommended sintering cycle (HP)

Pressure (kg/cm^2)	300
Sintering Temperature	780 - 800 °C.
Typical Cycle	Increase for 4 to 6 minutes,
	Hold for 2 - 4 min.
	Then rapid cooling

Typical Hardness

H. Brinell	333
H. Rockwell B	110

APPENDIX 2 - Hot Press - Sintering Machine

The sintering press DSP 25 AT, is a hot press designed and built by Dr. Fritsch [184] as a R&D or a single-piece as well as series production press. It would not be a serious production type of hot press.

Their literature states, that only a few steps are sufficient to operate the press, and specially trained staff is not required. Apart from the graphite, the machines contain no parts subject to wear. The automatic programme and low energy costs guarantee an increase in efficiency. The sintering programmes can be pre-programmed and called up at any stage.

Technical Data

Temperature control and reading range - Thermocouple - 20 -1200°C, Type K is used on the machine.

Electrical Power - 25 kVA

Pressing power / force - DSP 25 AT 93kN.

Dimensions - DSP 25 AT 1500 x 1000 x 1500 mm.

Weight - DSP 25 AT 1000 kg.

APPENDIX 3 - Specimen Type Hot Pressing Materials Composition Spreadsheets – Charpy Impact, Tensile, TRS & Fracture Toughness Specimens

CHARPY Segment Calculations				BoartLongyear Samples		02/12/2003	
						Hot Pressing Test Temps	
Metal Matrix Composition				Metal Density g/cc	8.85	HP Temp 1	
Powder Name	Powder Size			App Density g/cc	2.30	HP Temp 2	800
COUF	1 micron			Binder Content	1.30%	HP Temp 3	
Granulated	63-350 microns (45-250 Mesh)					HP Temp 4	
Testing Repetions	4					HP Temp 5	
Hot Presing Temps	1			# Samples/Hot Pres	4	HP Temp 6	
Number of Grits Sizes	10			# Samples/Test	4	# HP Temps	1
Number of Dia Concs	5						
Total No. Pieces	200						

Sample Size	Length	Width(T)	Height	Vol cc
Total (I) mm	55	10	10	5.5
Impreg mm	55	10	10	5.5

Pressures	MPa	HP Forces	kN
Pressure 1	10	Force 1	22
Pressure 2	35	Force 2	77
Pressure 3	35	Force 3	77
Pressing Area sq. mm		2200	4 samples

Spreadsheet Legend		
Carats per Piece	cts	cts/P
Carats per HP Temp	cts	cts/T
Carats per HP Temp range	cts	Cts/HP
Matrix Vol (Dia & Co)	cc	Mxv
Matrix Mass (Dia & Co)	g	Mxm
Matrix (Dia & Co)		Mx
Metal Vol.	cc	Mv
Metal Mass	g	Mm
Diamond Conc		Dc
Diamond Vol.	cc	Dv
Diamond Mass	g	Dm

Grit Sizes ALL					Amount/Segmnt		Mixing Weight	Totals	Apparent	Mix. Bottle	Hot Pressing Weights		Segment
Impreg	Dc	Dv (cc)	Dm (g)	Mv (cc)	Dm (cts)	Mm (g)	Make-up Totals/ HP		Volume (cc)	50% Mixing	Mxm (g)	Mx Density	Density
	1	0.01375	0.0484	5.48625	0.242	48.5533	Matrix Mm (g)	194.21	84.44	168.88	48.60	8.84	Mx
							Grit (cts)	0.968					8.84

Grit Sizes ALL					Amount/Segmnt		Mixing Weight	Totals	Apparent	Mix. Bottle	Hot Pressing Weights		Segment
Impreg	Dc	Dv (cc)	Dm (g)	Mv (cc)	Dm (cts)	Mm (g)	Make-up Totals/ HP		ApprVol (cc)	50% Mixing	Mxm (g)	Mx density	Density
	10	0.1375	0.484	5.3625	2.42	47.4581	Matrix Mm (g)	189.83	82.54	165.07	47.94	8.72	Mx
							Grit (cts)	9.68					8.72

Grit Sizes ALL					Amount/Segmnt		Mixing Weight	Totals	Apparent	Mix. Bottle	Hot Pressing Weights		Segment
Impreg	Dc	Dv (cc)	Dm (g)	Mv (cc)	Dm (cts)	Mm (g)	Make-up Totals/ HP		ApprVol (cc)	50% Mixing	Mxm (g)	Mx density	Density
	20	0.275	0.968	5.225	4.84	46.2413	Matrix Mm (g)	184.97	80.42	160.84	47.21	8.58	Mx
							Grit (cts)	19.36					8.58

Grit Sizes ALL					Amount/Segmnt		Mixing Weight	Totals	Apparent	Mix. Bottle	Hot Pressing Weights		Segment
Impreg	Dc	Dv (cc)	Dm (g)	Mv (cc)	Dm (cts)	Mm (g)	Make-up Totals/ HP		ApprVol (cc)	50% Mixing	Mxm (g)	Mx density	Density
	30	0.4125	1.452	5.0875	7.26	45.0244	Matrix Mm (g)	180.10	78.30	156.61	46.48	8.45	Mx
							Grit (cts)	29.04					8.45

Grit Sizes ALL					Amount/Segmnt		Mixing Weight	Totals	Apparent	Mix. Bottle	Hot Pressing Weights		Segment
Impreg	Dc	Dv (cc)	Dm (g)	Mv (cc)	Dm (cts)	Mm (g)	Make-up Totals/ HP		ApprVol (cc)	50% Mixing	Mxm (g)	Mx density	Density
	40	0.55	1.936	4.95	9.68	43.8075	Matrix Mm (g)	175.23	76.19	152.37	45.74	8.32	Mx
							Grit (cts)	38.72					8.32

Dia Conc	Metal for ALL HP Temps			Grit for ALL HP Temps		TOTAL for ALL DC's & Temps	
1	Matrix Mm (g)		194.21	Diamond (cts)	0.97	METAL (I)	924.34
10	Matrix Mm (g)		189.83	Diamond (cts)	9.68	GRIT (cts)	97.77
20	Matrix Mm (g)		184.97	Diamond (cts)	19.36		
30	Matrix Mm (g)		180.10	Diamond (cts)	29.04		
40	Matrix Mm (g)		175.23	Diamond (cts)	38.72		

Total Grit / HP (cts)	97.768
Total Co / HP (g)	924.34
Total Grit /Test (cts)	97.768
Total Co / Test (g)	924.34

TENSILE Segment Calculations CERMEP MOULD SQUARE ENDS

Metal Matrix Composition

Powder Name	Powder Size	Density g/cc	8.85
COUF	1 micron	App Density g/cc	2.30
Granulated	63 - 350 microns (45 - 250 Mesh)		
Binder Content	1.30%		

HP Test Temps	
HP Temp 1	800
HP Temp 2	
HP Temp 3	
HP Temp 4	
HP Temp 5	
HP Temp 6	
# HP Temps	1

Sample Size	Length	Width (T)	CSA	Height	Vol cc
Total (I+B) mm	55	5	655	6	3.93
Impreg mm	55	5		6	3.93
Backing mm	0	0		0	0
Pressing Area sq. mm		655			

# Samples/ Run	1
# Samples/Temp	1
# Samples/Test	1

Impreg	Dc	Dv (cc)	Dm (g)	Mv (cc)	Amount/Segmnt Dm (cts)	Mm (g)	Mixing Weight Make-up Totals/ HP	Totals	Apparent Volume (cc)	Mix. Bottle 50% Mixing	Hot Pressing Weights Mxm (g)	Mx Density	Segment
	10	0.09825	0.34584	3.83175	1.7292	33.911	Matrix Mm (g)	33.91	14.74	29.49	34.2568275	8.72	Density
							Grit (cts)	1.7292		60% Mixing			Mx
										24.57			8.72

Impreg	Dc	Dv (cc)	Dm (g)	Mv (cc)	Dm (cts)	Mm (g)	Make-up Totals/ HP		ApprVol (cc)	50% Mixing	Mxm (g)	Mx density	Segment
	40	0.393	1.38336	3.537	6.9168	31.3025	Matrix Mm (g)	31.30	13.61	27.22	32.68581	8.32	Density
							Grit (cts)	6.9168		60% Mixing			Mx
										22.68			8.32

Dc	ALL HP Temps		Grit for ALL HP Temps	TOTAL for ALL Dc's & Temps			Total Grit / HP (cts)	8.65
10	Matrix Mm (g)		33.91	Diamond (cts)	1.73	METAL (I + B)	65.21	Total Co / HP (g)	65.21
40	Matrix Mm (g)		31.30	Diamond (cts)	6.92	GRIT (cts)	8.65	Total Grit /Test (cts)	8.646
								Total Co / Test (g)	65.21

HOT PRESSING Forces				Diamond Conc	Dc	Metal Vol. (cc)	Mv	Matrix Vol (cc)	Mxv
	MPa		kN	Diamond Vol. (cc)	Dv	Metal Mass (g)	Mm	Matrix Mass (g)	Mxm
Pressure 1	10	Force 1	6.55	Diamond Mass (g)	Dm				
Pressure 2	35	Force 2	22.93						
Pressure 3	35	Force 3	22.93						
Pressing Area sq. mm		655							

BEND (TRS) Segment Calculations				BoartLongyear Samples			02/12/2003		Spreadsheet Legend		
							Hot Pressing Test Temps		Carats per Piece	cts	cts/P
Metal Matrix Composition				Metal Density g/cc	8.85		HP Temp 1		Carats per HP Temp	cts	cts/T
Powder Name	Powder Size			App Density g/cc	2.30		HP Temp 2	800	Carats per HP Temp range	cts	Cts/HP
COUF	1 micron			Binder Content	1.30%		HP Temp 3		Matrix Vol (Dia & Co)	cc	Mxv
Granulated	63-350 microns (45-250 Mesh)						HP Temp 4		Matrix Mass (Dia & Co)	g	Mxm
Testing Repetions	4						HP Temp 5		Matrix (Dia & Co)		Mx
Hot Presing Temps	1			# Samples/Hot Pres	4		HP Temp 6		Metal Vol.	cc	Mv
Number of Grits Sizes	10			# Samples/Test	4		# HP Temps	1	Metal Mass	g	Mm
Number of Dia Concs	5								Diamond Conc		Dc
Total No. Pieces	200			Pressures	MPa		HP Forces	kN	Diamond Vol.	cc	Dv
				Pressure 1	10		Force 1	11	Diamond Mass	g	Dm
Sample Size	Length	Width(T)	Height	Vol cc			Force 2	38.5			
Total (I) mm	55	5	10	2.75			Force 3	38.5			
Impreg mm	55	5	10	2.75			Pressing Area sq. mm	1100	4 samples		

Grit Sizes ALL					Amount/Segmnt		Mixing Weight	Totals	Apparent	Mix. Bottle	Hot Pressing Weights		Segment
Impreg	Dc	Dv (cc)	Dm (g)	Mv (cc)	Dm (cts)	Mm (g)	Make-up Totals/ HP		Volume (cc)	50% Mixing	Mxm (g)	Mx Density	Density
	1	0.00688	0.0242	2.743125	0.121	24.2767	Matrix Mm (g)	97.11	42.22	84.44	24.30	8.84	Mx
							Grit (cts)	0.484					8.84

Grit Sizes ALL					Amount/Segmnt		Mixing Weight	Totals	Apparent	Mix. Bottle	Hot Pressing Weights		Segment
Impreg	Dc	Dv (cc)	Dm (g)	Mv (cc)	Dm (cts)	Mm (g)	Make-up Totals/ HP		ApprVol (cc)	50% Mixing	Mxm (g)	Mx density	Density
	10	0.06875	0.242	2.68125	1.21	23.7291	Matrix Mm (g)	94.92	41.27	82.54	23.97	8.72	Mx
							Grit (cts)	4.84					8.72

Grit Sizes ALL					Amount/Segmnt		Mixing Weight	Totals	Apparent	Mix. Bottle	Hot Pressing Weights		Segment
Impreg	Dc	Dv (cc)	Dm (g)	Mv (cc)	Dm (cts)	Mm (g)	Make-up Totals/ HP		ApprVol (cc)	50% Mixing	Mxm (g)	Mx density	Density
	20	0.1375	0.484	2.6125	2.42	23.1206	Matrix Mm (g)	92.48	40.21	80.42	23.60	8.58	Mx
							Grit (cts)	9.68					8.58

Grit Sizes ALL					Amount/Segmnt		Mixing Weight	Totals	Apparent	Mix. Bottle	Hot Pressing Weights		Segment
Impreg	Dc	Dv (cc)	Dm (g)	Mv (cc)	Dm (cts)	Mm (g)	Make-up Totals/ HP		ApprVol (cc)	50% Mixing	Mxm (g)	Mx density	Density
	30	0.20625	0.726	2.54375	3.63	22.5122	Matrix Mm (g)	90.05	39.15	78.30	23.24	8.45	Mx
							Grit (cts)	14.52					8.45

Grit Sizes ALL					Amount/Segmnt		Mixing Weight	Totals	Apparent	Mix. Bottle	Hot Pressing Weights		Segment
Impreg	Dc	Dv (cc)	Dm (g)	Mv (cc)	Dm (cts)	Mm (g)	Make-up Totals/ HP		ApprVol (cc)	50% Mixing	Mxm (g)	Mx density	Density
	40	0.275	0.968	2.475	4.84	21.9038	Matrix Mm (g)	87.62	38.09	76.19	22.87	8.32	Mx
							Grit (cts)	19.36					8.32

Dia Conc	Metal for ALL HP Temps			Grit for ALL HP Temps		TOTAL for ALL DC's & Temps		Total Grit / HP (cts)	48.884
1	Matrix Mm (g)		97.11	Diamond (cts)	0.48	METAL (I)	462.17	Total Co / HP (g)	462.17
10	Matrix Mm (g)		94.92	Diamond (cts)	4.84	GRIT (cts)	48.88		
20	Matrix Mm (g)		92.48	Diamond (cts)	9.68			Total Grit /Test (cts)	48.884
30	Matrix Mm (g)		90.05	Diamond (cts)	14.52			Total Co / Test (g)	462.17
40	Matrix Mm (g)		87.62	Diamond (cts)	19.36				

FRACTURE & FATIGUE Segment Calculations					BoartLongyear Samples			03/12/2003				
Metal Matrix Composition							**Hot Pressing Test Temps**		**Spreadsheet Legend**			
Powder Name		**Powder Size**		**Density g/cc**	8.85		HP Temp 1	800	Carats per Piece		cts	cts/P
COUF	1 micron			App Density g/cc	2.30		HP Temp 2		Carats per HP Temp		cts	cts/T
Granulated	63 - 350 microns (45 - 250 Mesh)			Binder Content	1.30%		HP Temp 3		Carats per HP Temp range		cts	Cts/HP
Testing Repetions		4					HP Temp 4		Matrix Vol (Dia & Co)		cc	Mxv
Hot Presing Temps		1		# Samples/Hot Pres	6		HP Temp 5		Matrix Mass (Dia & Co)		g	Mxm
Number of Grits Sizes		10		# Samples/Test	6		HP Temp 6		Matrix (Dia & Co)			Mx
Number of Dia Concs		5					# HP Temps	1	Metal Vol.		cc	Mv
Total No. Pieces		200							Metal Mass		g	Mm
					Pressures	**MPa**	**HP Forces**	**kN**	Diamond Conc			Dc
Sample Size	**Length**	**Width(T)**	**Height**	**Vol cc**	**Pressure 1**	10	**Force 1**	16.5	Diamond Vol.		cc	Dv
Total (I+B) mm	55	5	10	2.75	**Pressure 2**	35	**Force 2**	57.75	Diamond Mass		g	Dm
Impreg mm	55	5	8	2.2	**Pressure 3**	35	**Force 3**	57.75	Backing Vol		cc	Bv
Backing mm	55	5	2	0.55	**Pressing Area sq. mm**		1650	6 samples	Backing Mass		g	Bm

Grit Sizes ALL					**Amount/Segmnt**		**Mixing Weight**	**Totals**	**Apparent**	**Mix. Bottle**	**Hot Pressing Weights**		**Segment**
Impreg	**Dc**	Dv (cc)	Dm (g)	Mv (cc)	**Dm (cts)**	**Mm (g)**	**Make-up Totals/ HP**		**Volume (cc)**	**50% Mixing**	**Mxm (g)**	Mx Density	**Density**
	1	0.0055	0.01936	2.1945	**0.0968**	**19.4213**	**Matrix Mm (g)**	**116.53**	**50.66**	**101.33**	**19.44**	8.84	**Mx + B**
Backing					Bv cc	**Bm g**	**Grit (cts)**	**0.5808**		**60% Mixing**	**Bm g**		**8.84**
					0.55	**4.87**	**Backing Bm (g)**	29.21		**84.44**	**4.87**		

Grit Sizes ALL					**Amount/Segmnt**		**Mixing Weight**	**Totals**	**Apparent**	**Mix. Bottle**	**Hot Pressing Weights**		**Segment**
Impreg	**Dc**	Dv (cc)	Dm (g)	Mv (cc)	**Dm (cts)**	**Mm (g)**	**Make-up Totals/ HP**		**ApprVol (cc)**	**50% Mixing**	**Mxm (g)**	Mx density	**Density**
	10	0.055	0.1936	2.145	**0.968**	**18.9833**	**Matrix Mm (g)**	**113.90**	**49.52**	**99.04**	**19.18**	8.72	**Mx + B**
Backing					Bv cc	**Bm g**	**Grit (cts)**	**5.808**		**60% Mixing**	**Bm g**		**8.74**
					0.55	**4.87**	Backing Bm (g)	29.21		**82.54**	**4.87**		

Grit Sizes ALL					**Amount/Segmnt**		**Mixing Weight**	**Totals**	**Apparent**	**Mix. Bottle**	**Hot Pressing Weights**		**Segment**
Impreg	**Dc**	Dv (cc)	Dm (g)	Mv (cc)	**Dm (cts)**	**Mm (g)**	**Make-up Totals/ HP**		**ApprVol (cc)**	**50% Mixing**	**Mxm (g)**	Mx density	**Density**
	20	0.11	0.3872	2.09	**1.936**	**18.4965**	**Matrix Mm (g)**	**110.98**	**48.25**	**96.50**	**18.88**	8.58	**Mx + B**
Backing					Bv cc	**Bm g**	**Grit (cts)**	**11.616**		**60% Mixing**	**Bm g**		**8.64**
					0.55	**4.87**	Backing Bm (g)	29.21		**80.42**	**4.87**		

Grit Sizes ALL					**Amount/Segmnt**		**Mixing Weight**	**Totals**	**Apparent**	**Mix. Bottle**	**Hot Pressing Weights**		**Segment**
Impreg	**Dc**	Dv (cc)	Dm (g)	Mv (cc)	**Dm (cts)**	**Mm (g)**	**Make-up Totals/ HP**		**ApprVol (cc)**	**50% Mixing**	**Mxm (g)**	Mx density	**Density**
	25	0.1375	0.484	2.0625	**2.42**	**18.2531**	**Matrix Mm (g)**	**109.52**	**47.62**	**95.23**	**18.74**	8.52	**Mx + B**
Backing					Bv cc	**Bm g**	**Grit (cts)**	**14.52**		**60% Mixing**	**Bm g**		**8.58**
					0.55	**4.87**	Backing Bm (g)	29.21		**79.36**	**4.87**		

Grit Sizes ALL					**Amount/Segmnt**		**Mixing Weight**	**Totals**	**Apparent**	**Mix. Bottle**	**Hot Pressing Weights**		**Segment**
Impreg	**Dc**	Dv (cc)	Dm (g)	Mv (cc)	**Dm (cts)**	**Mm (g)**	**Make-up Totals/ HP**		**ApprVol (cc)**	**50% Mixing**	**Mxm (g)**	Mx density	**Density**
	30	0.165	0.5808	2.035	**2.904**	**18.0098**	**Matrix Mm (g)**	**108.06**	**46.98**	**93.96**	**18.59**	8.45	**Mx + B**
Backing					Bv cc	**Bm g**	**Grit (cts)**	**17.424**		**60% Mixing**	**Bm g**		**8.53**
					0.55	**4.87**	Backing Bm (g)	29.21		**78.30**	**4.87**		

Grit Sizes ALL					**Amount/Segmnt**		**Mixing Weight**	**Totals**	**Apparent**	**Mix. Bottle**	**Hot Pressing Weights**		**Segment**
Impreg	**Dc**	Dv (cc)	Dm (g)	Mv (cc)	**Dm (cts)**	**Mm (g)**	**Make-up Totals/ HP**		**ApprVol (cc)**	**50% Mixing**	**Mxm (g)**	Mx density	**Density**
	40	0.22	0.7744	1.98	**3.872**	**17.523**	**Matrix Mm (g)**	**105.14**	**45.71**	**91.42**	**18.30**	8.32	**Mx + B**
Backing					Bv cc	**Bm g**	**Grit (cts)**	**23.232**		**60% Mixing**	**Bm g**		**8.42**
					0.55	**4.87**	Backing Bm (g)	29.21		**76.19**	**4.87**		

Dia Conc	**Metal for ALL HP Temps**			**Grit for ALL HP Temps**		**TOTAL for ALL DC's & Temps**		**Total Grit / HP (cts)**	73.18
1	**Matrix Mm (g)**		**116.53**	**Diamond (cts)**	**0.58**	**METAL (I + B)**	**693.33**	**Total Co / HP (g)**	**839.35**
10	**Matrix Mm (g)**		**113.90**	**Diamond (cts)**	**5.81**	**GRIT (cts)**	**73.18**		
20	**Matrix Mm (g)**		**110.98**	**Diamond (cts)**	**11.62**			**Total Grit /Test (cts)**	**73.1808**
25	**Matrix Mm (g)**		**109.52**	**Diamond (cts)**	**14.52**			**Total Co / Test (g)**	**839.35**
30	**Matrix Mm (g)**		**108.06**	**Diamond (cts)**	**17.42**				
40	**Matrix Mm (g)**		**105.14**	**Diamond (cts)**	**23.23**				
	Backing Bm (g)		**29.21**						

APPENDIX 4 - Alignment of Three-Pt-Bend Fixture for Fracture Toughness Testing

Alignment Procedure is as follows:

1. To set up the 3-point bend fixture on an 8516 Instron servo-hydraulic test machine.
2. Move the lower rollers up so that the upper roller sits between the lower rollers.
3. Push the lower rollers together
4. Tighten the upper roller anvil using the appropriate Allen key.
5. Lower the actuator and piston to allow the lowers to now be adjusted.
6. Adjust the span of the lower rollers using the scale to 40mm. Check this measurement with a Vernier calliper.
7. Check the position of the rollers relative to the upper roller, ensuring that the upper roller is centred accurately.
8. Raise the lower rollers so that the upper roller is between the lower rollers again.
9. Two 7mm grade 2 gauge blocks are positioned on either side of the upper roller. See Figure C3.1 & Figure C3.2 below.
10. Push the lower rollers inwards against the gauge blocks.
11. Adjust and tighten the lower roller stops so as to prevent them from loosening and moving outwards when a load is applied to the test specimen.

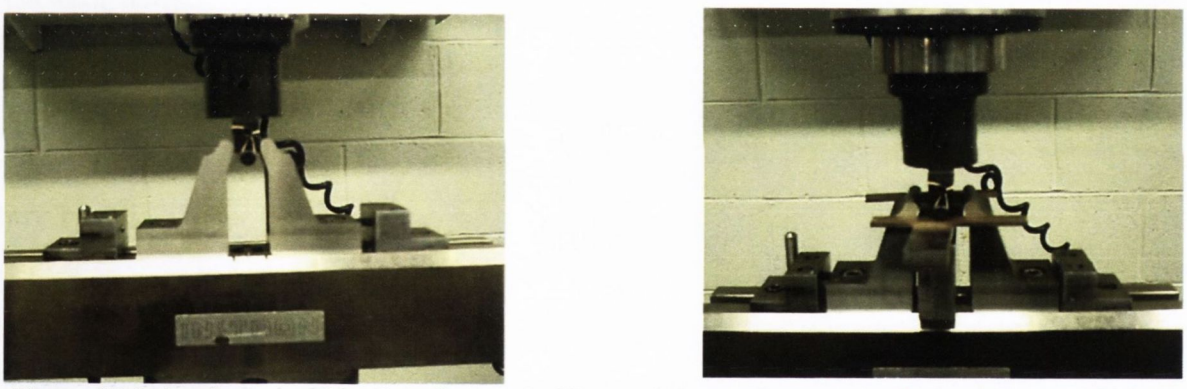

Figure C3.1 showing procedure for alignment of Upper & Lower Rollers of 3-Pt Bend Fixture Mk II.

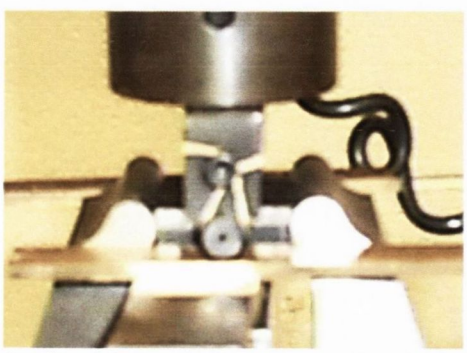

Figure C3.2 showing gauge blocks fitted between the upper roller & the lower rollers.

APPENDIX 5 - Fracture Toughness Test Procedure

(1) Set-up test, locate specimen correctly aligned on 3-pt bend fixture Mk II using simple alignment jig, attach CMOD gauge on knife edges for fatigue precracking. See Figure C.3.3 showing specimen on fixture with attached CMOD gauge ready for test.

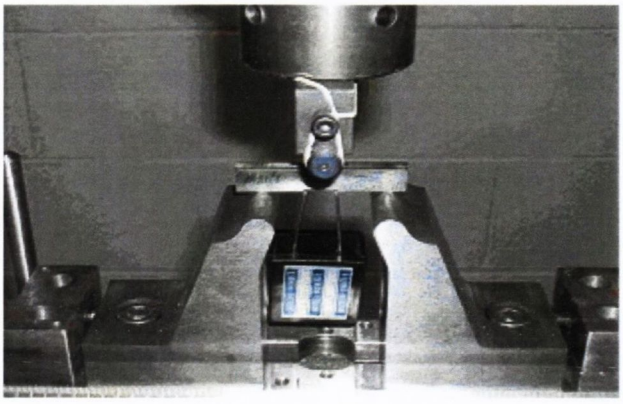

Figure C3.3. showing specimen on 3-pt-bend fixture Mark II with attached CMOD gauge.

(2) Input necessary specimen details into Fast Track da/dN software.

(3) Carry out Test. (where fatigue precracking was carried out using the Instron FastTrack, when the set crack length was reached, the machine would automatically change to Fracture Toughness software and carry out a K_{1C} test.)

(4) Measure initial crack length, Fatigue crack or EDM notch as per ASTM method, e.g. Surface 1, 25%, 50% 75% & Surface 2. Get average length and ensure that initial cracks are within the allowable percent.

Fracture Toughness Test Validity Check Criteria

The following are the main validity checks carried out to ensure that a valid Plane Strain Fracture Toughness (K_{1C}) is deemed to haven been determined.

(a) The purpose of notching and fatigue precracking the test specimen is to simulate an ideal plane crack with essentially zero tip radius – an atomically sharp crack - to agree with the assumptions made in stress intensity analyses. There are several requirements pertaining to fatigue loading. The most important is that the maximum stress intensity during the final stage of fatigue cycling shall not exceed 60 % of the subsequently determined K_Q if this is to qualify as a valid K_{1C} result.

(b) The loading rate should be such that the rate of increase of stress intensity is within the range 0.55 - 2.75 MPa $\sqrt{m}$ /s. This is arbitrarily defined as 'static' loading.

(c) The crack curvature and level of obliqueness is checked by measuring the initial crack length, Fatigue crack or EDM notch as per ASTM method, e.g. Surface 1, 25%, 50% 75% & Surface 2, which can be seen in Figure C.3.4. Get average length and ensure that initial cracks are within the allowable percent.

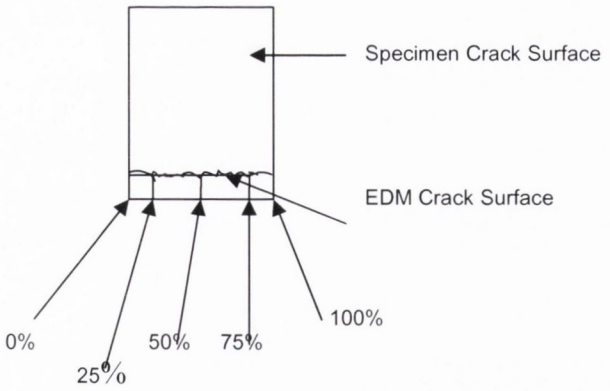

Figure C3.4. Shows in Schematic form the procedure for measuring initial crack notch.

(d) Then it must be determined whether this K_Q is consistent with the specimen size and material yield strength according to the following inequalities already mentioned, i.e.

$a \geq 2.5 (K_{1C} / \sigma_{ys})^2$

$B \geq 2.5 (K_{1C} / \sigma_{ys})^2$

$W \geq 5.0 (K_{1C} / \sigma_{ys})^2$

If K_Q meets these requirements then $K_Q = K_{1C}$. If not, the test is invalid and the result may be used only to estimate the fracture toughness: it is not an ASTM standard value.

APPENDIX – 6 - Hardness & %Theoretical Density

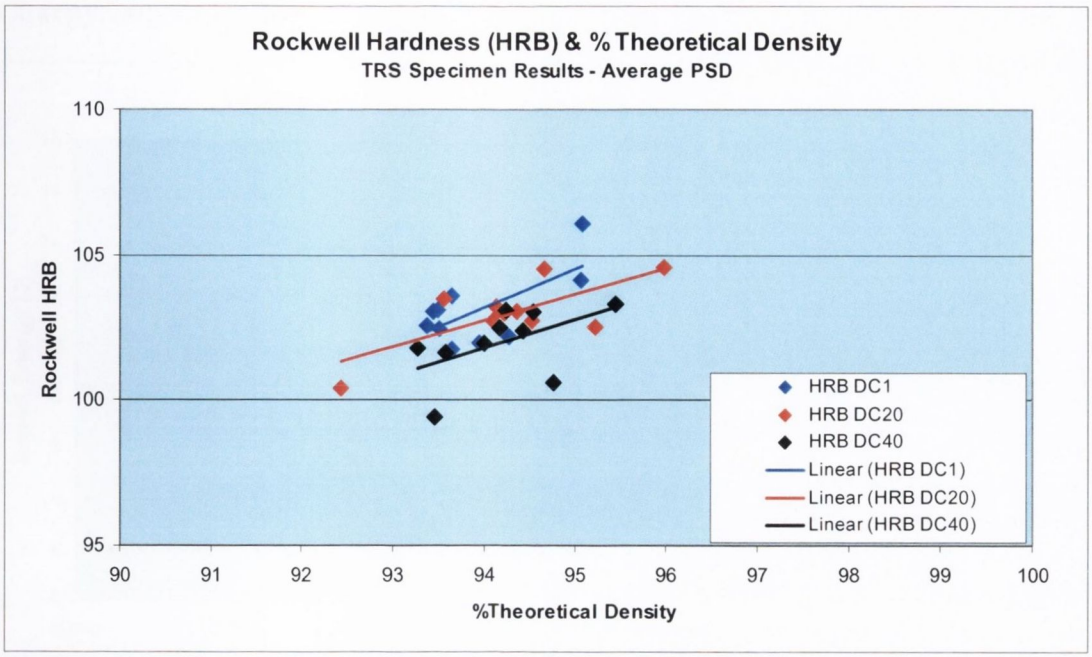

Figure C.5.1. TRS Specimen Results: Figure shows Rockwell hardness (HRB) plotted against percent theoretical density (%TD) for different diamond concentrations.

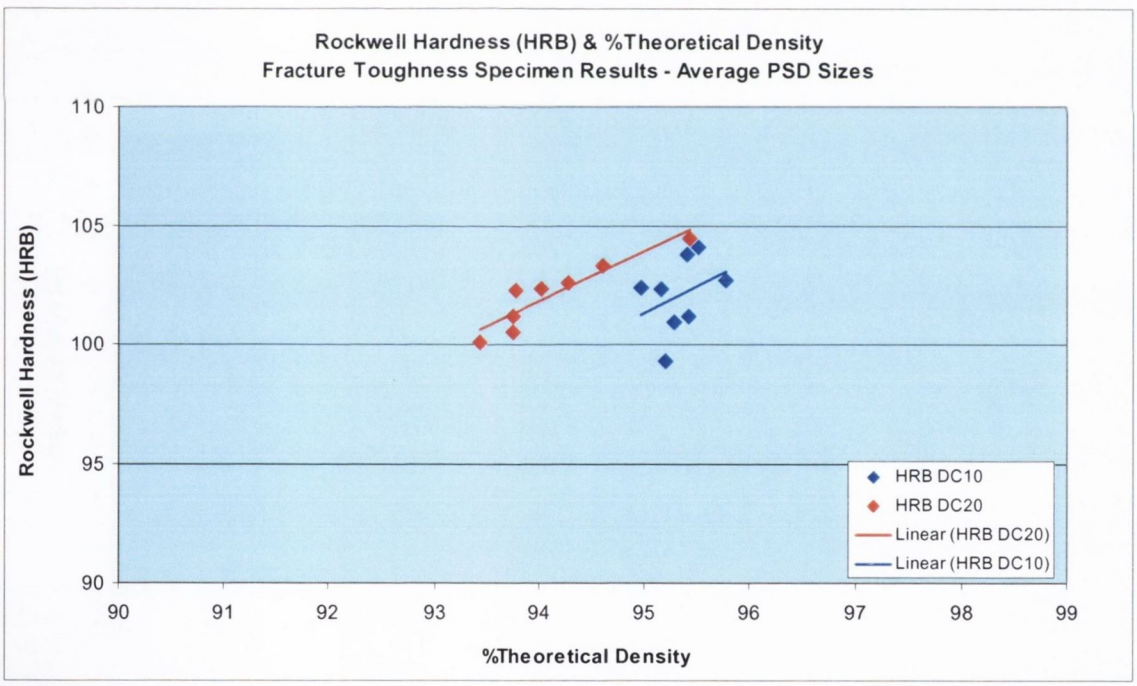

Figure C.5.2. Fracture Toughness Specimen Results: Figure shows Rockwell hardness (HRB) plotted against percent theoretical density (%TD) for different diamond concentrations.

APPENDIX 7 - Interparticle Spacing IPS/MFP & IPS/NND

Charpy Impact IPS/MFP & IPS/NND

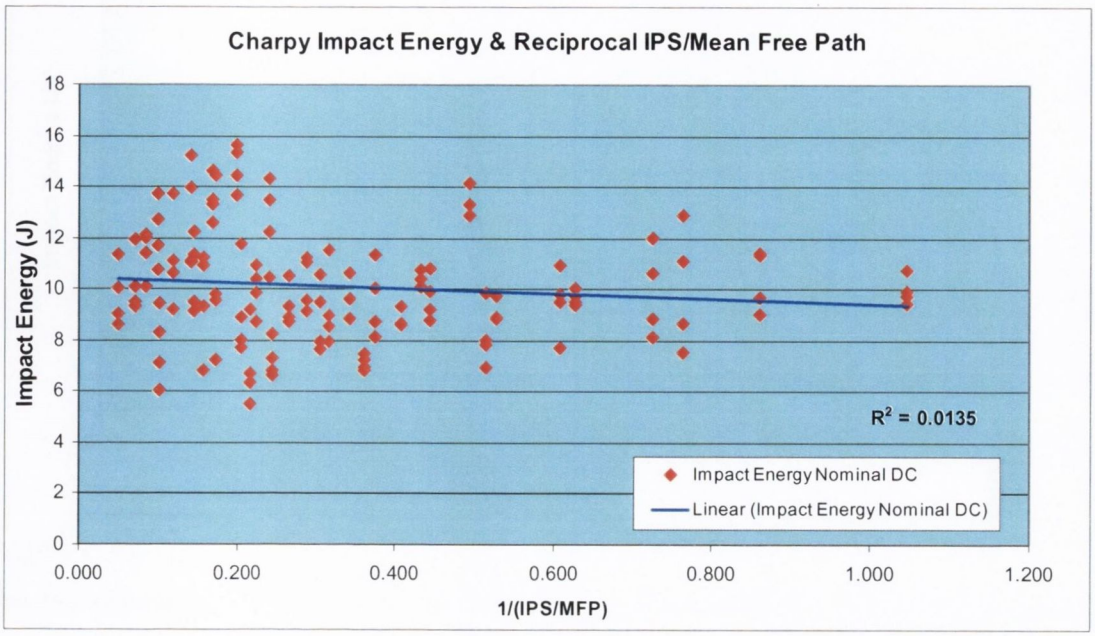

Figure C.5.3. Graph of Charpy Impact Energy plotted against Reciprocal of IPS/MFP. DC1 was not used because of its large IPS/MFP. R = 0.12.

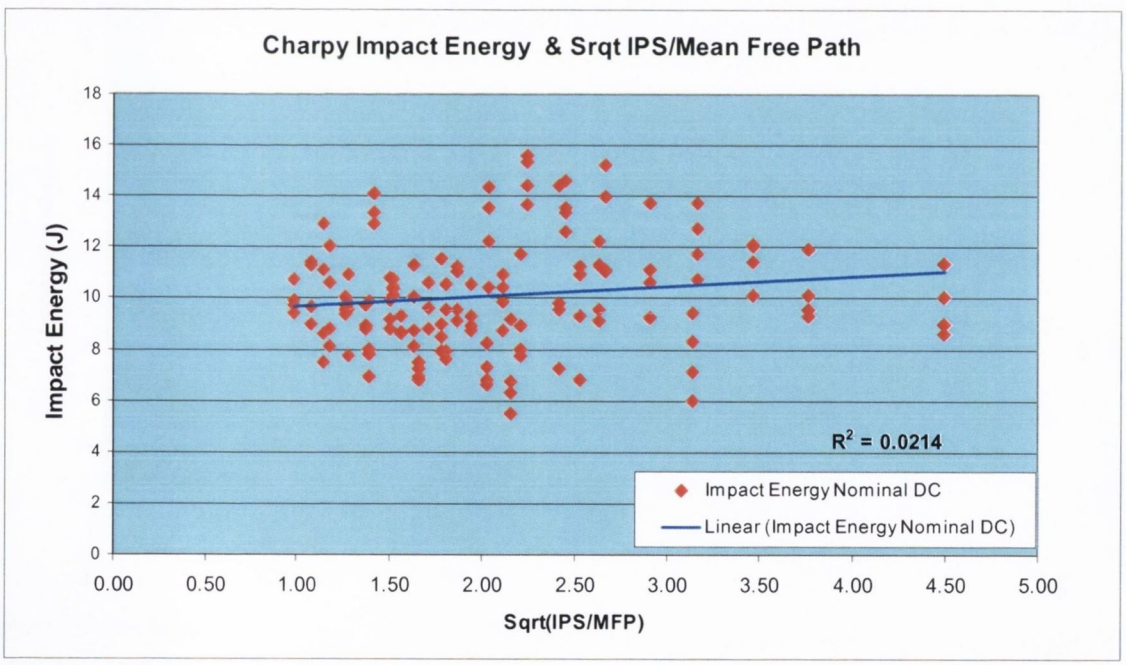

Figure C.5.4. Graph of Charpy Impact Energy plotted against SQRT of IPS/MFP. DC1 was not used because of its large IPS/MFP. R = 0.15.

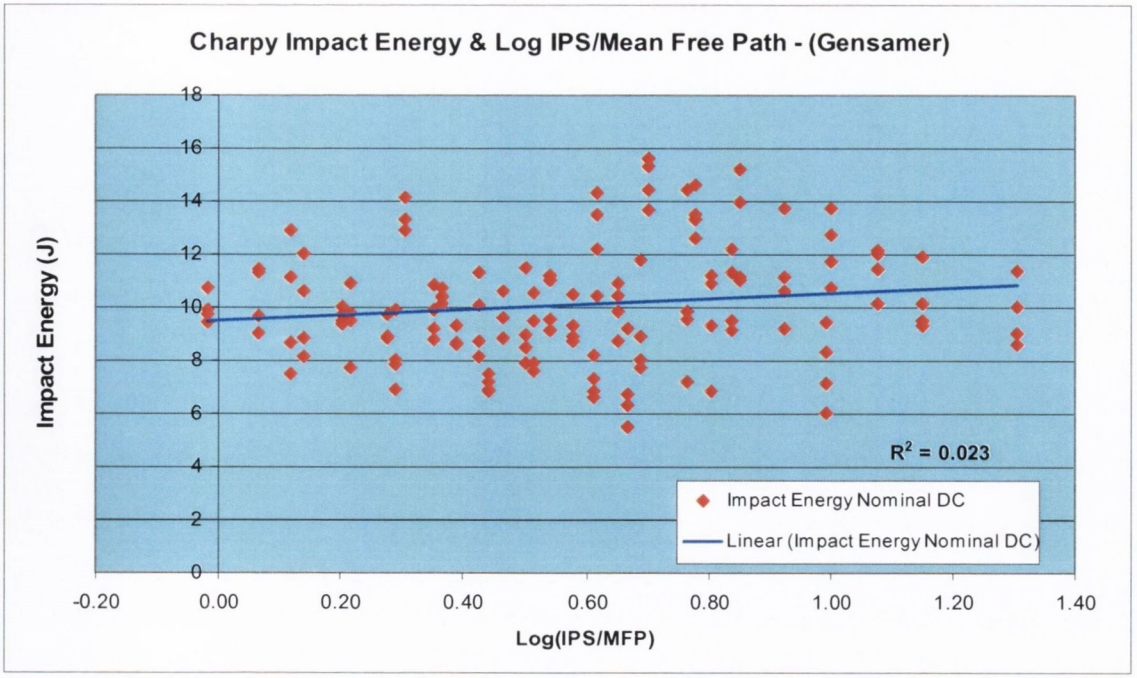

Figure C.5.5. Graph of Charpy Impact Energy plotted against Log of IPS/MFP. DC1 was not used because of its large IPS/MFP. R = 0.15.

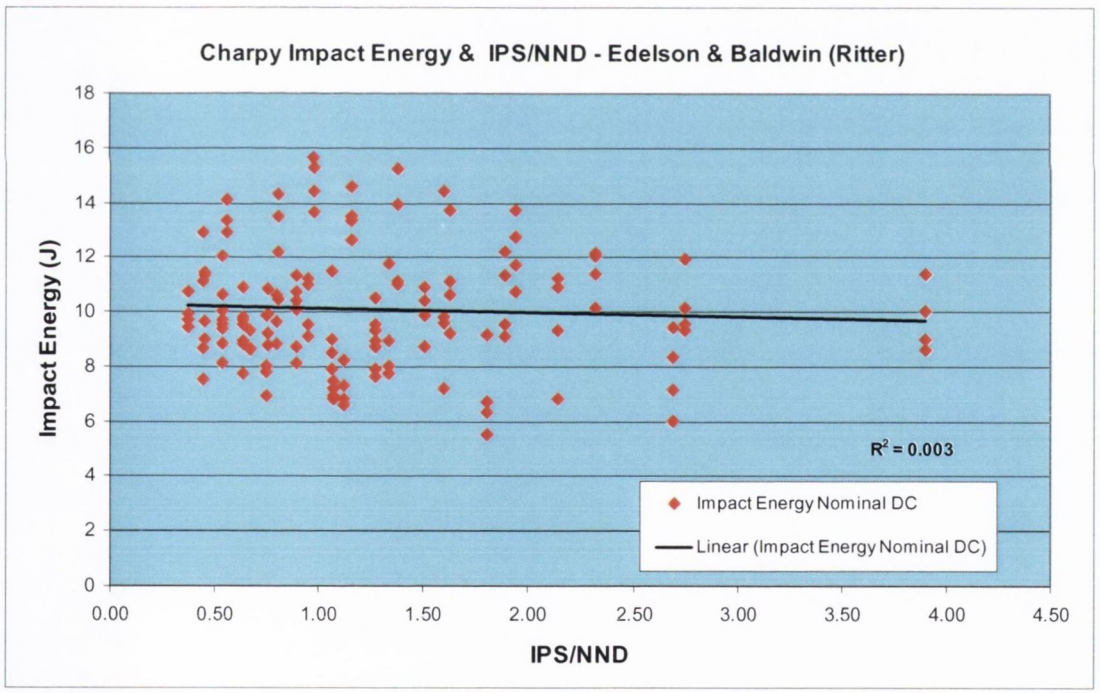

Figure C.5.6. Graph of Charpy Impact Energy plotted against IPS/NND. DC1 was not used because of its large IPS/ NND. R = 0.5.

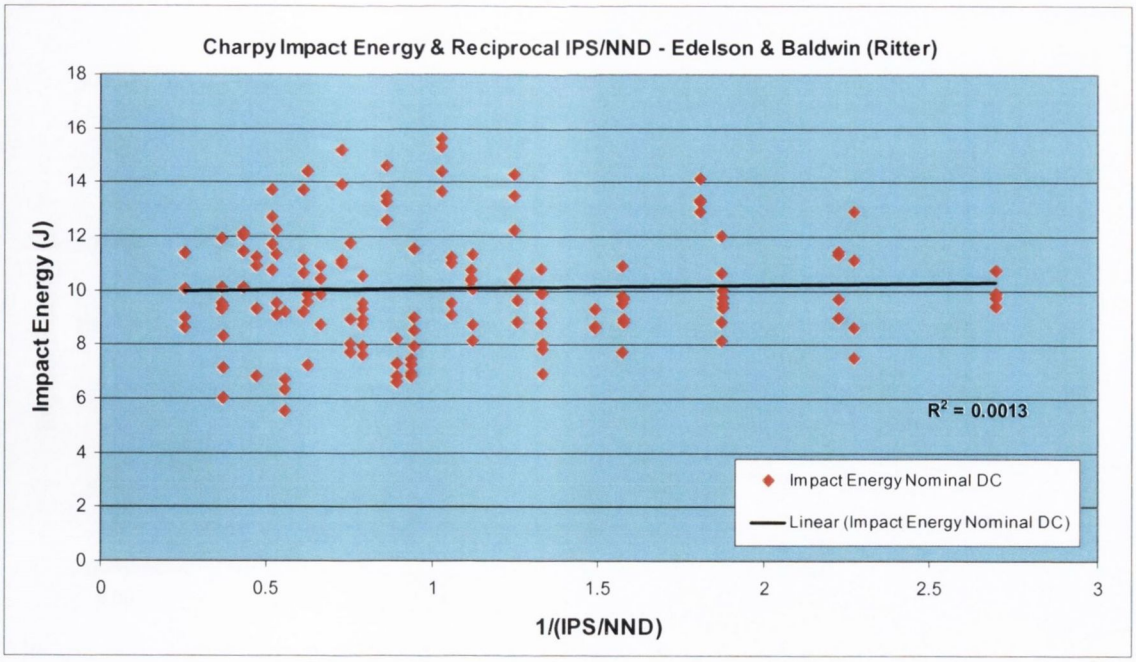

Figure C.5.7. Graph of Charpy Impact Energy plotted against Reciprocal of IPS/NND. DC1 was not used because of its large IPS/NND. R = 0.04.

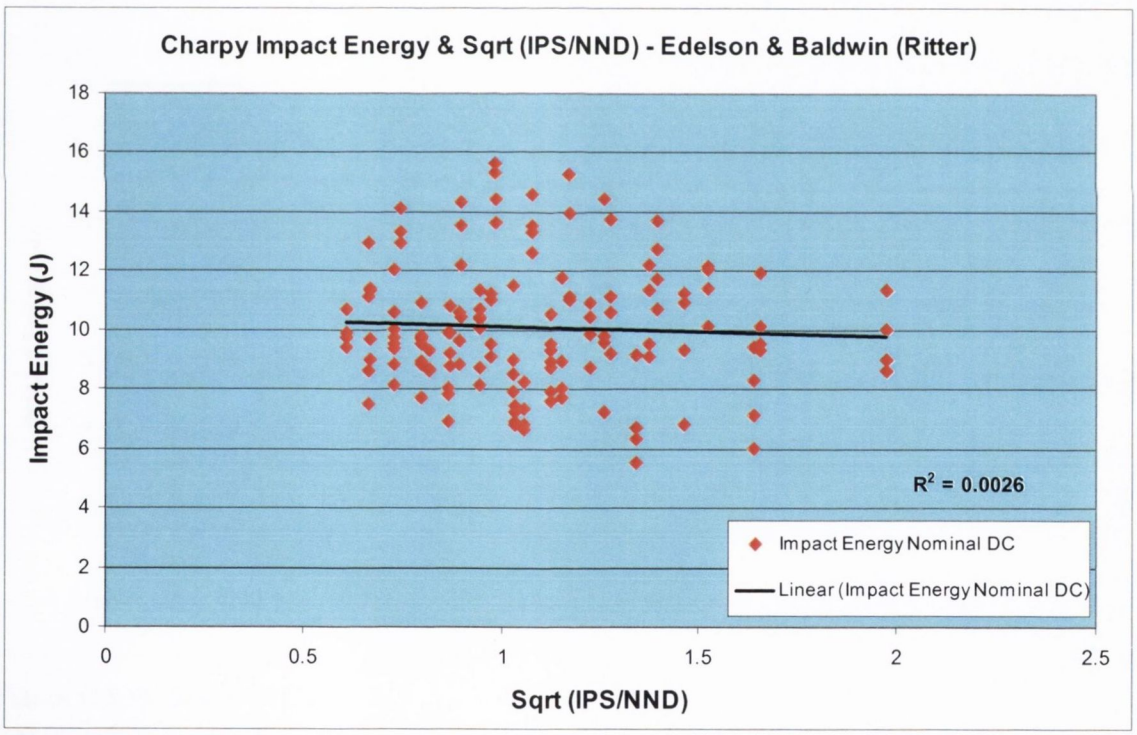

Figure C.5.8. Graph of Charpy Impact Energy plotted against SQRT of IPS/NND. DC1 was not used because of its large IPS/NND. R = 0.05.

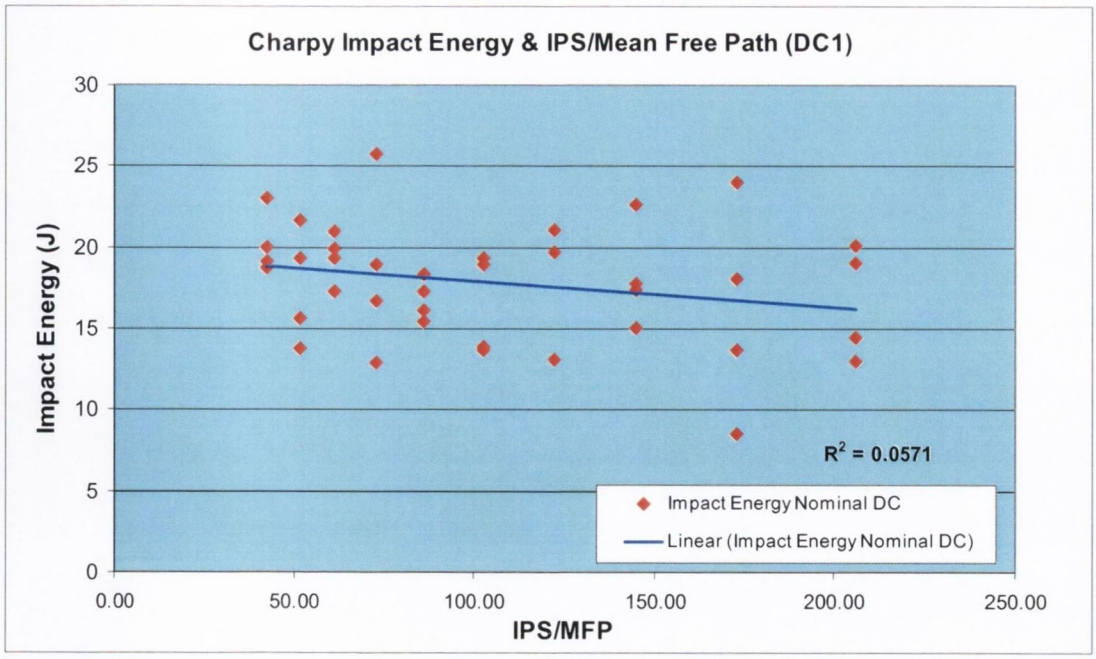

Figure C.5.9. Graph of Charpy Impact Energy plotted against Reciprocal of IPS/MFP. DC1 was not used because of its large IPS/MFP. R = 0.24.

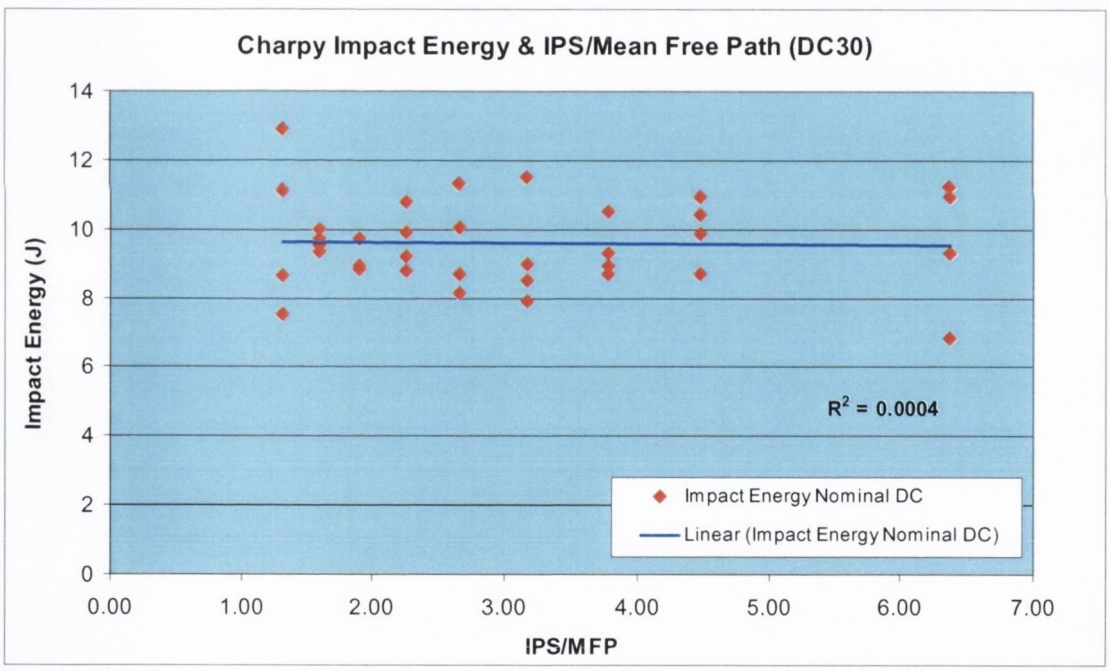

Figure C.5.10. Graph of Charpy Impact Energy plotted against Reciprocal of IPS/MFP. DC1 was not used because of its large IPS/MFP. R = 0.02.

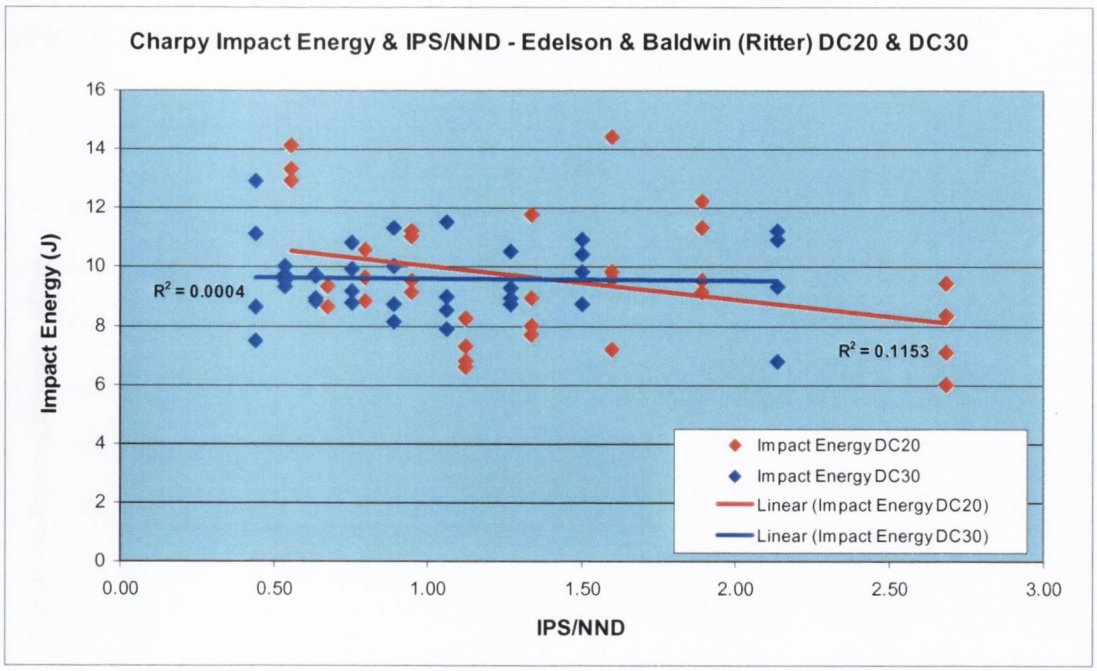

Figure C.5.11. Graph of Charpy Impact Energy plotted against IPS/NND for DC20 & DC30. R = 0.34 (DC20), R = 0.02.

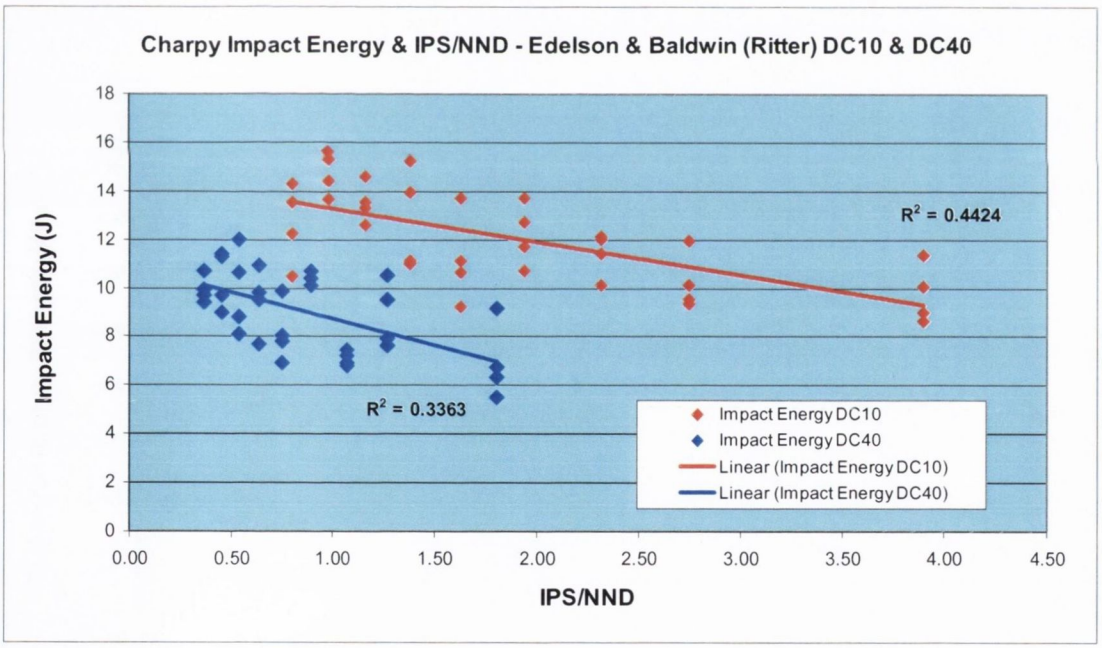

Figure C.5.12. Graph of Charpy plotted against IPS/MFP (mm) for DC10 & DC40. DC10, R = 0.67. DC40, R = 0.58.

APPENDIX 8 - Transverse Rupture Strength (TRS) IPS/MFP & IPS/NND

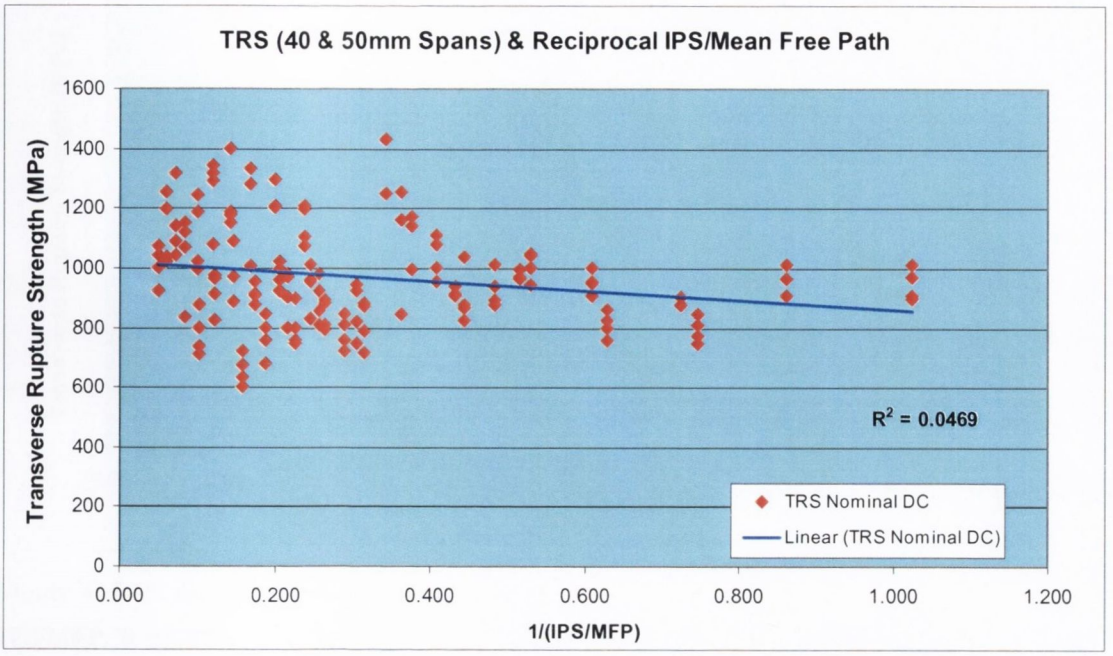

Figure C.5.13. Graph of TRS plotted against Reciprocal of IPS/MFP. DC1 was not used because of its large IPS/MFP. R = 0.22.

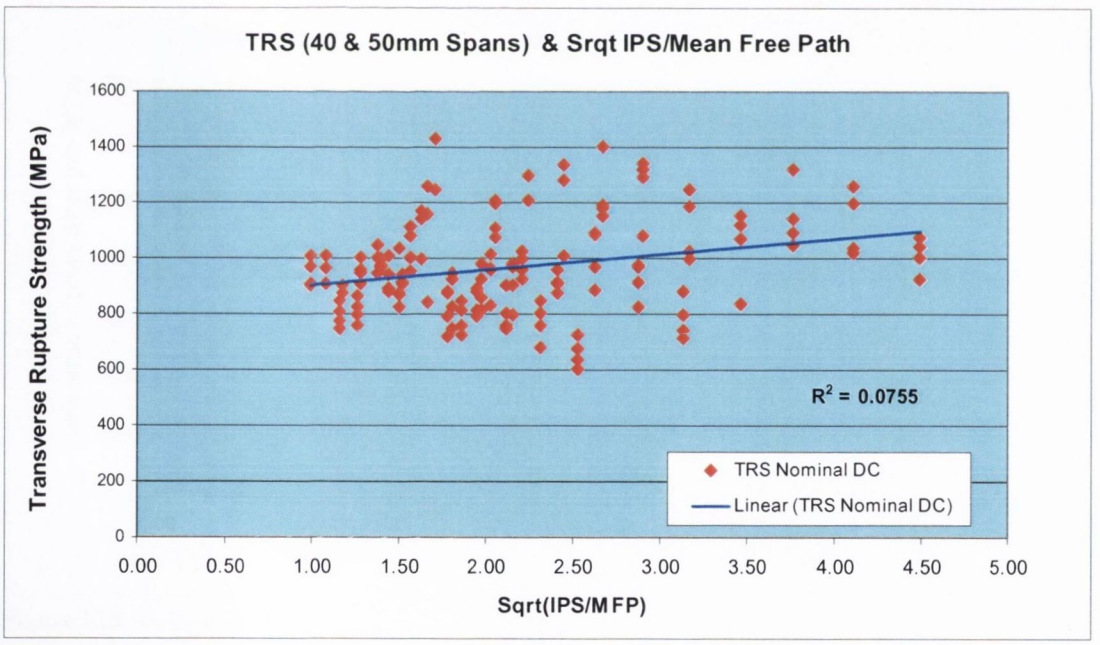

Figure C.5.14. Graph of TRS plotted against SQRT of IPS/MFP. DC1 was not used because of its large IPS/MFP. R = 0.27.

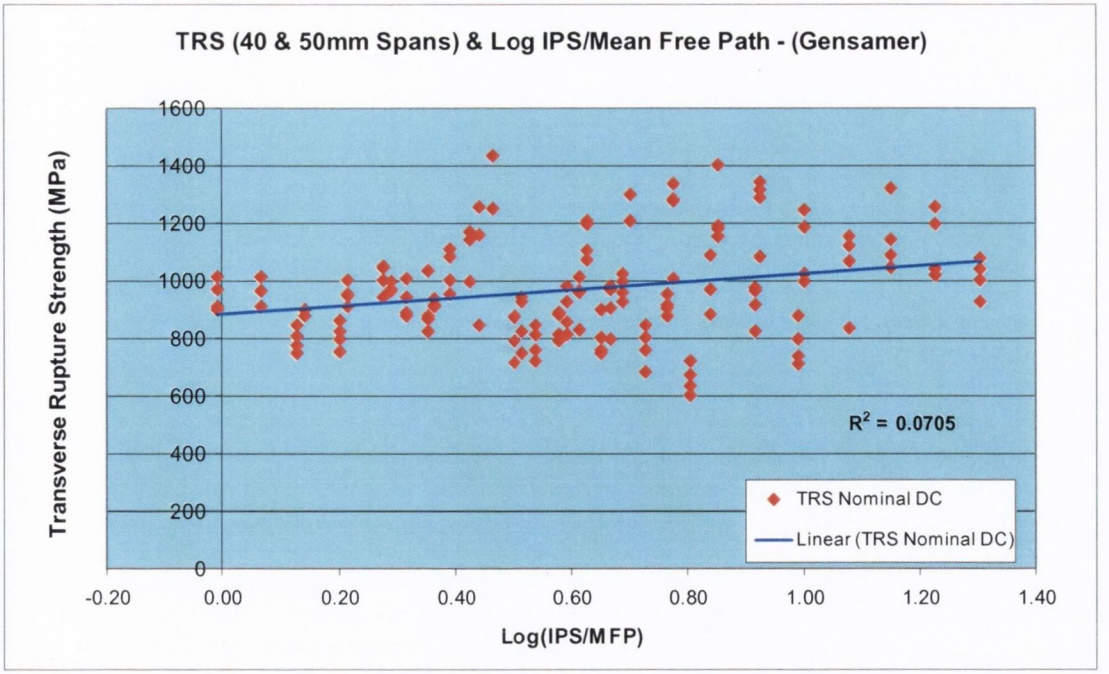

Figure C.5.15. Graph of TRS against Log of IPS/MFP. DC1 was not used because of its large IPS/MFP. R = 0.27.

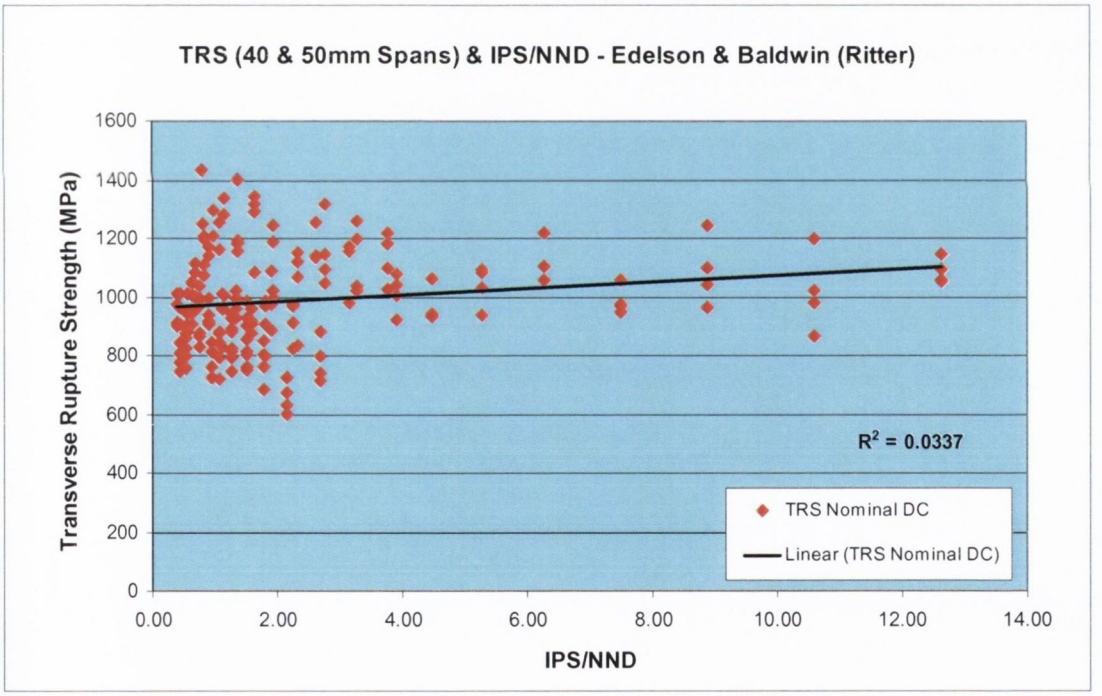

Figure C.5.16. Graph of TRS plotted against IPS/NND. DC1 is included in this plot. R = 0.18.

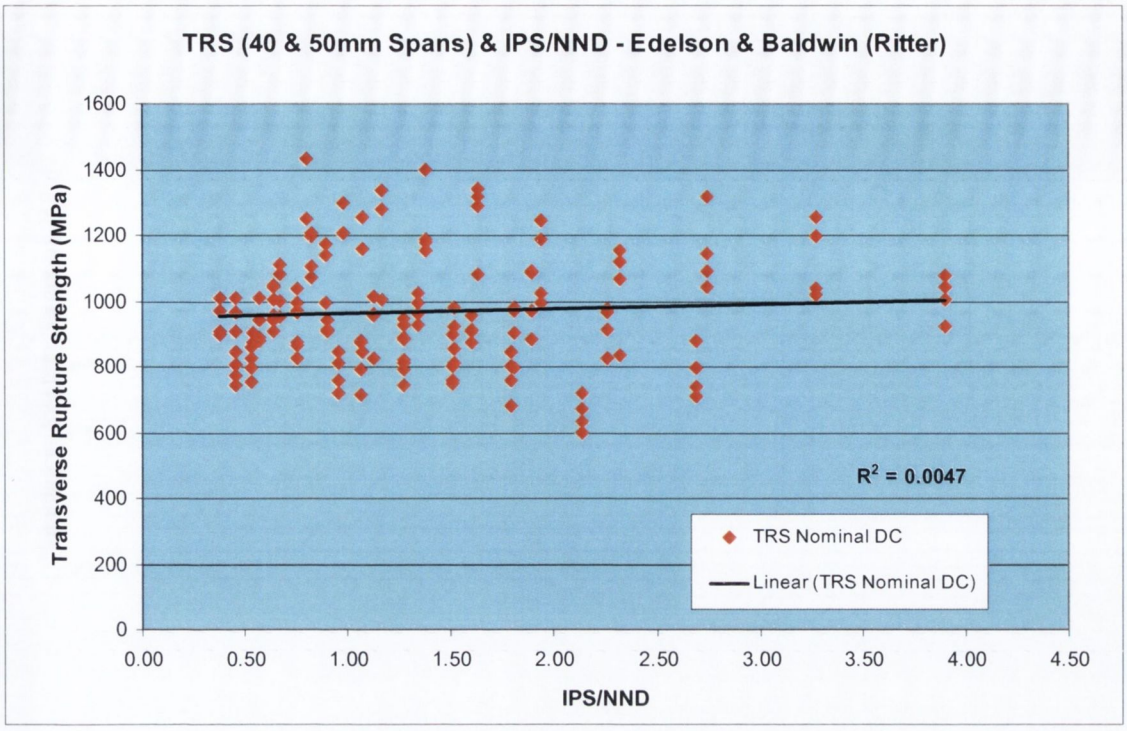

Figure C.5.17. Graph of TRS plotted against IPS/NND. DC1 was not used because of its large IPS/ NND. R = 0.07.

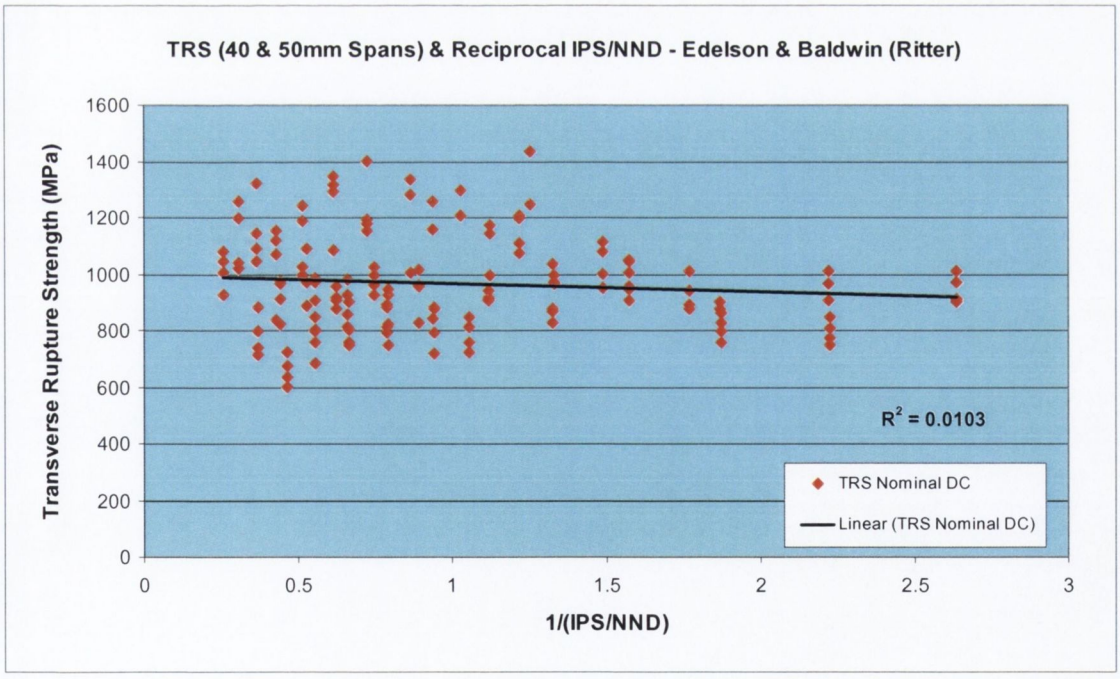

Figure C.5.18. Graph of TRS plotted against Reciprocal of IPS/NND. DC1 was not used because of its large IPS/ NND. R = 0.10.

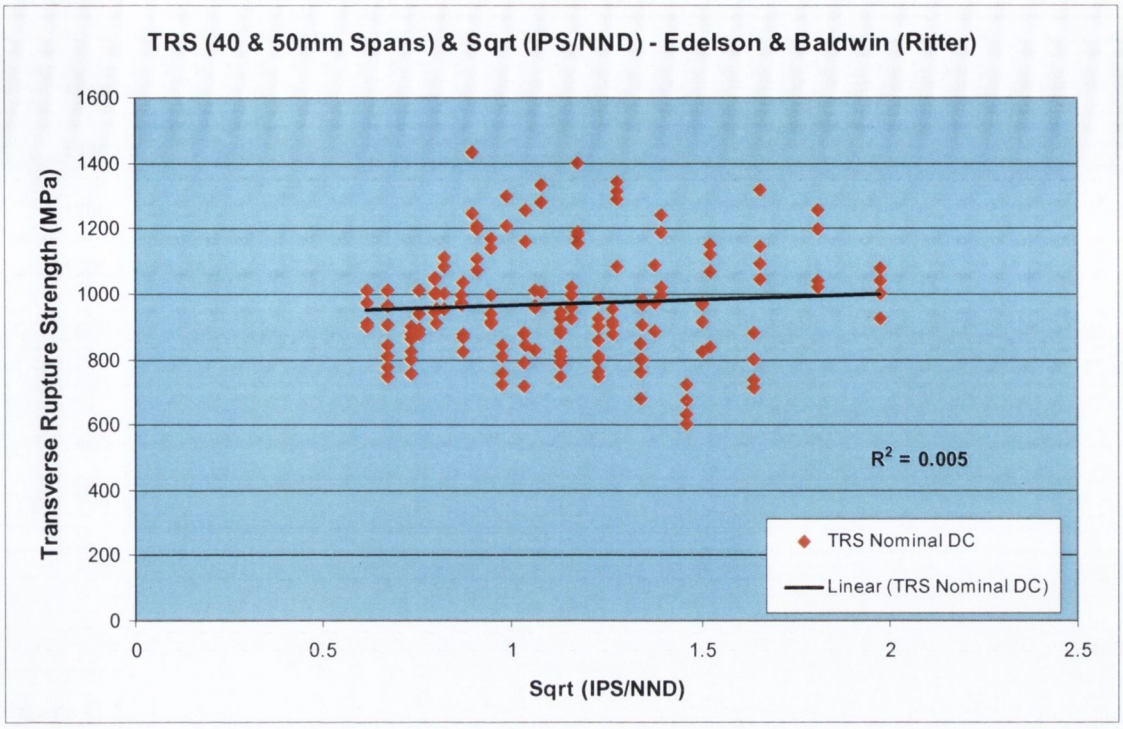

Figure C.5.19. Graph of TRS plotted against SQRT of IPS/NND. DC1 was not used because of its large IPS/NND. R = 0.07.

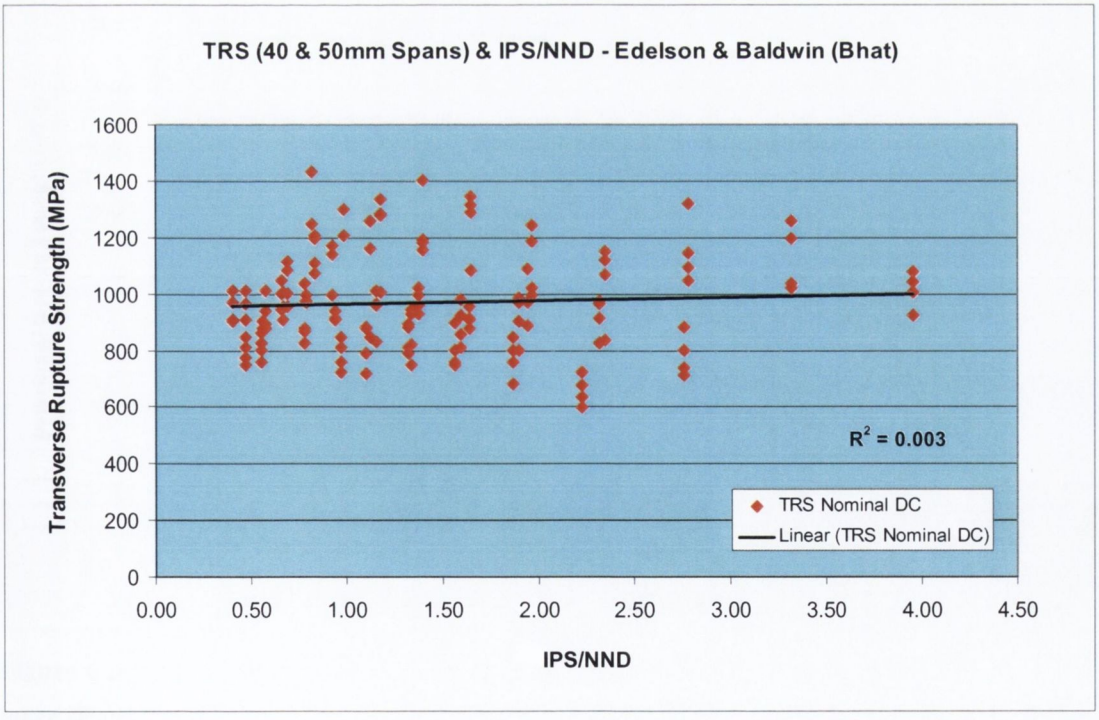

Figure C.5.20. Graph of TRS plotted against IPS/NND. DC1 was not used because of its large IPS/NND. R = 0.05.

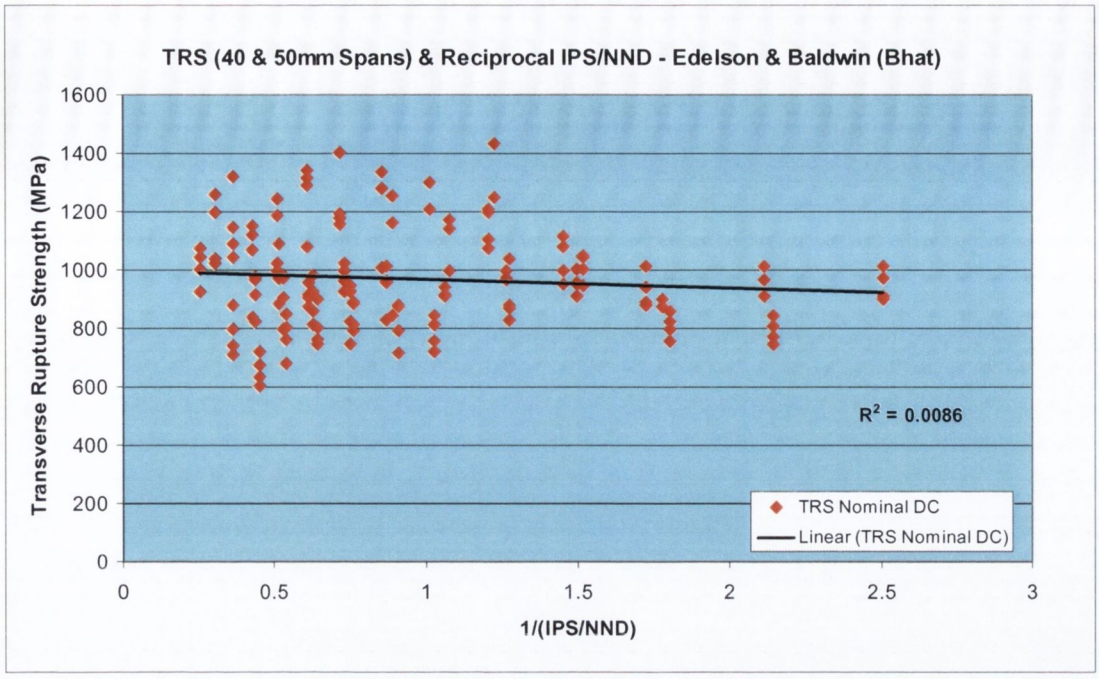

Figure C.5.21. Graph of TRS plotted against Reciprocal of IPS/NND. DC1 was not used because of its large IPS/ NND. R = 0.09.

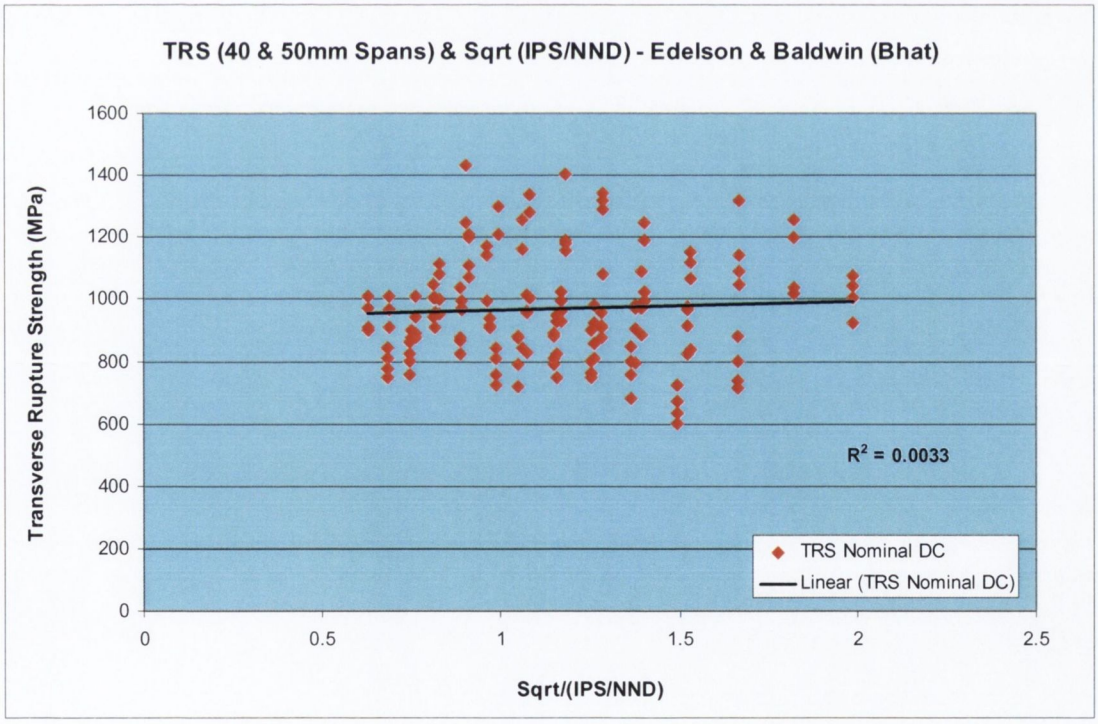

Figure C.5.22. Graph of TRS plotted against SQRT of IPS/NND. DC1 was not used because of its large IPS/NND. R = 0.06.

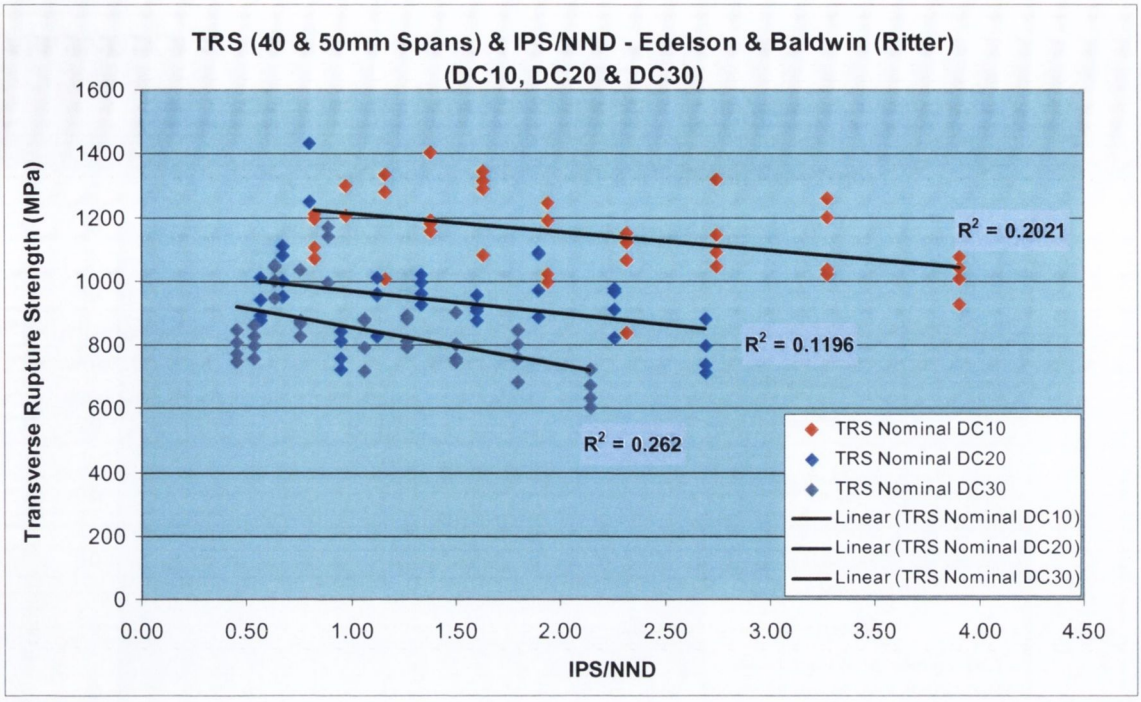

Figure C.5.23. Graph of TRS plotted against IPS/NND for diamond concentrations, DC10, DC20 and DC30. R values for DC10 = 0.45, DC20 = 0.35 & DC30 = 0.51.

APPENDIX 9 - Fracture Toughness IPS/MFP & IPS/NND

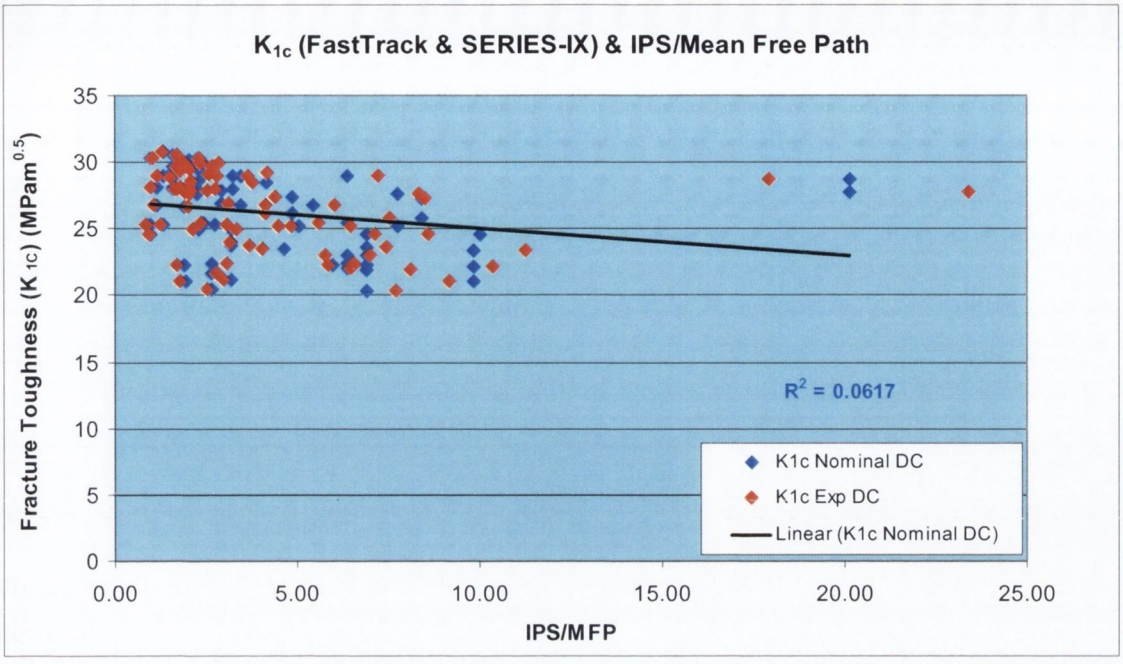

Figure C.5.24. Fracture Toughness Specimens; Graph of Plane Strain Fracture Toughness (K_{IC}) as determined using FastTrack & SERIES-IX plotted against of IPS/MFP. DC1 was not used because of its large IPS/MFP. R = 0.25.

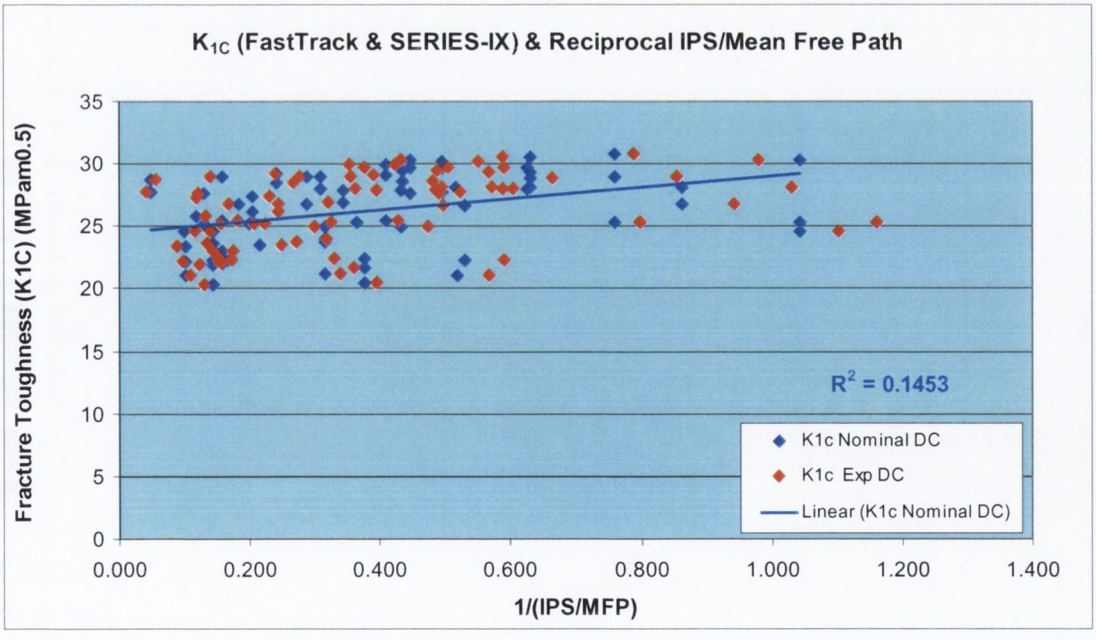

Figure C.5.25. Fracture Toughness Specimens; Graph of Plane Strain Fracture Toughness (K_{IC}) as determined using FastTrack & SERIES-IX plotted against Reciprocal of IPS/MFP. DC1 was not used because of its large IPS/MFP. R = 0.38.

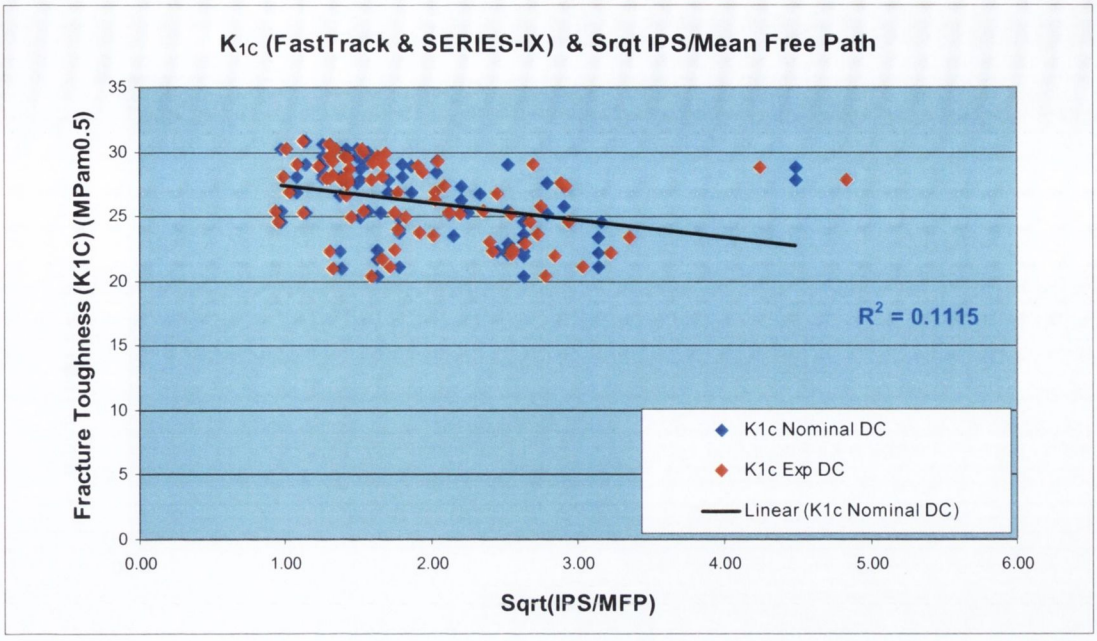

Figure C.5.26. Fracture Toughness Specimens; Graph of Plane Strain Fracture Toughness (K_{1C}) as determined using FastTrack plotted against SQRT of IPS/MFP. DC1 was not used because of its large IPS/MFP. R = 0.34.

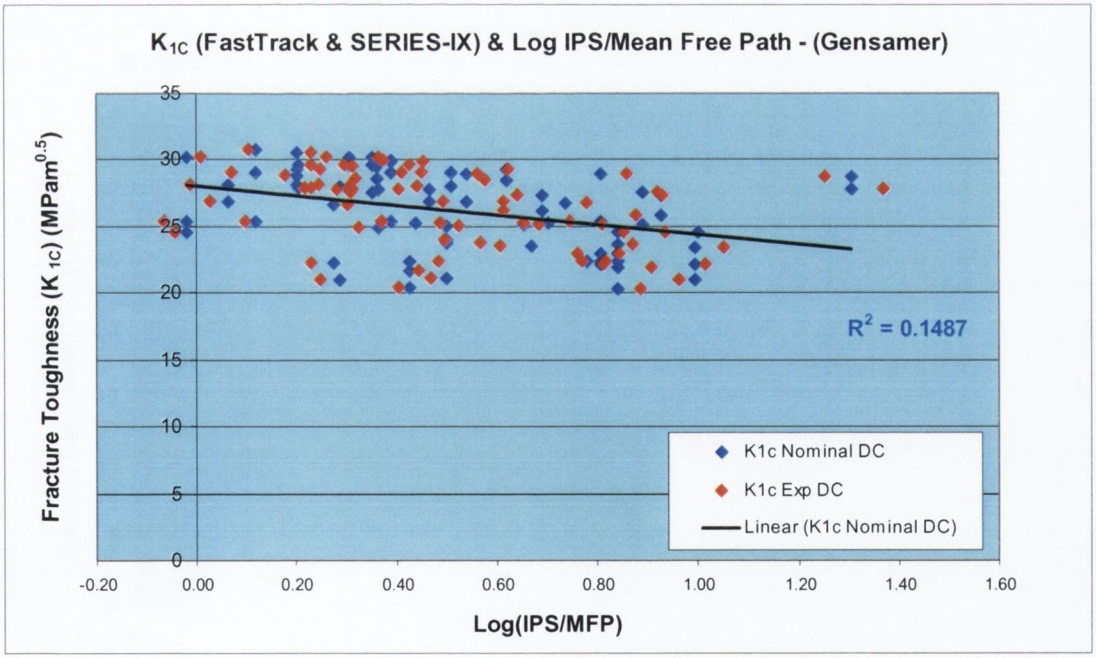

Figure C.5.27. Fracture Toughness Specimens; Graph of Plane Strain Fracture Toughness (K_{1C}) as determined using FastTrack plotted against Log of IPS/MFP. DC1 was not used because of its large IPS/MFP. R=0.39.

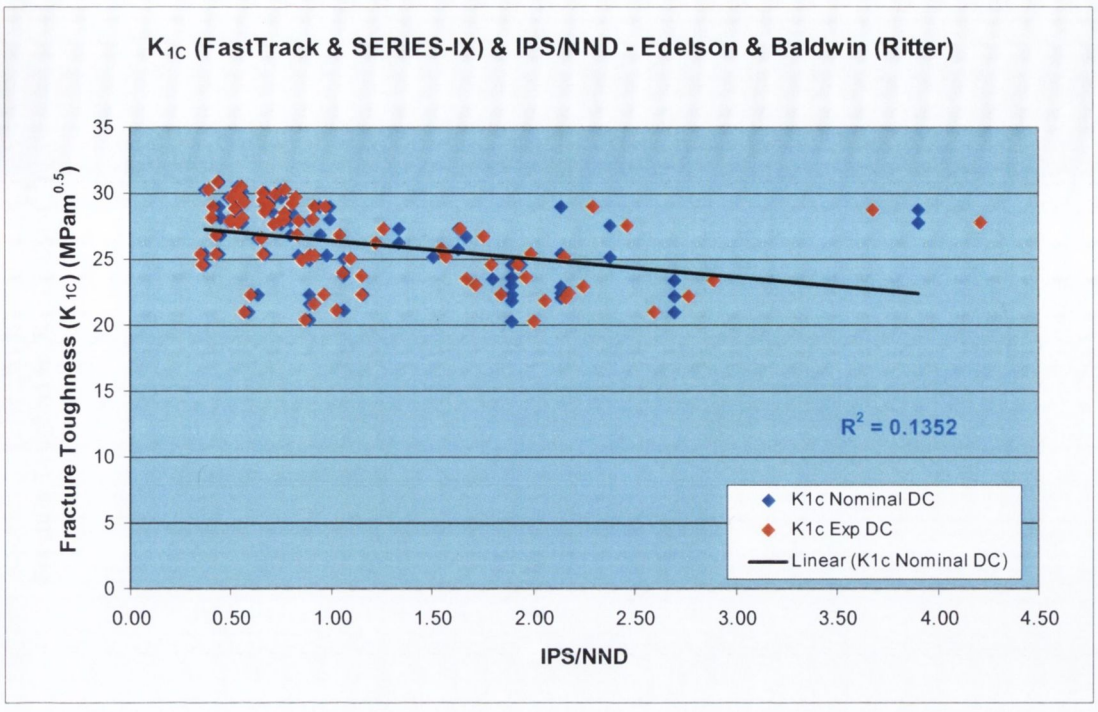

Figure C.5.28. Fracture Toughness Specimens; Graph of Plane Strain Fracture Toughness (K_{IC}) as determined using FastTrack plotted against IPS/NND. DC1 was not used because of its large IPS/MFP. R = 0.37.

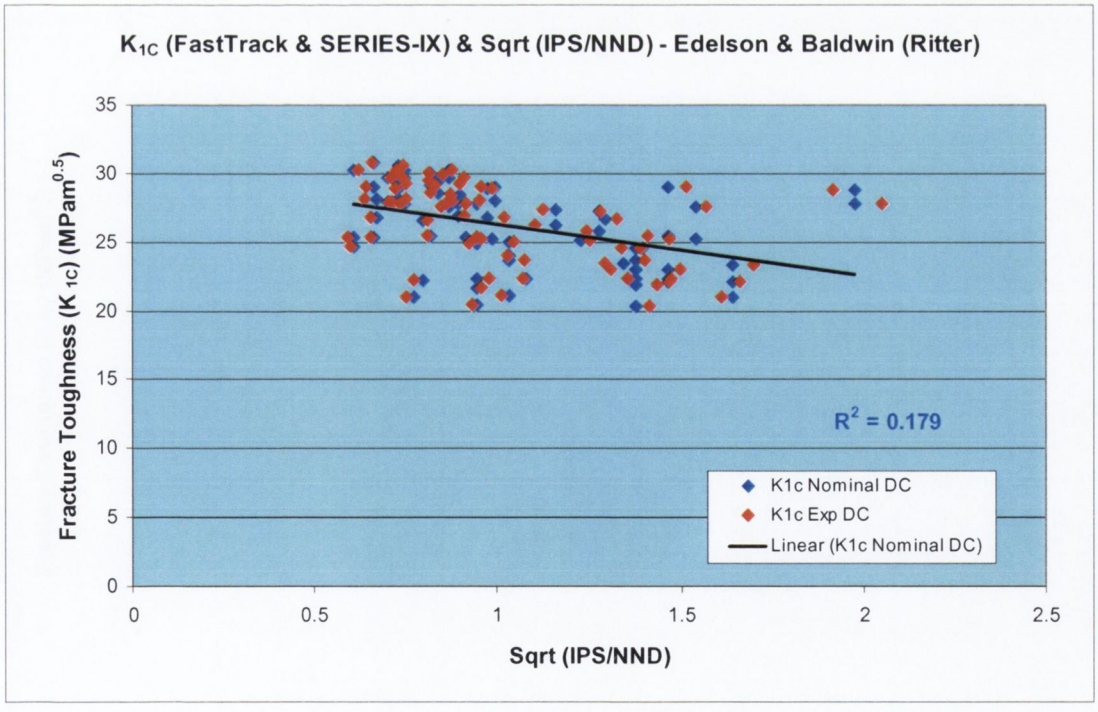

Figure C.5.29. Fracture Toughness Specimens; Graph of Plane Strain Fracture Toughness (K_{IC}) as determined using FastTrack plotted against SQRT of IPS/NND. DC1 was not used because of its large IPS/MFP. R = 0.42.

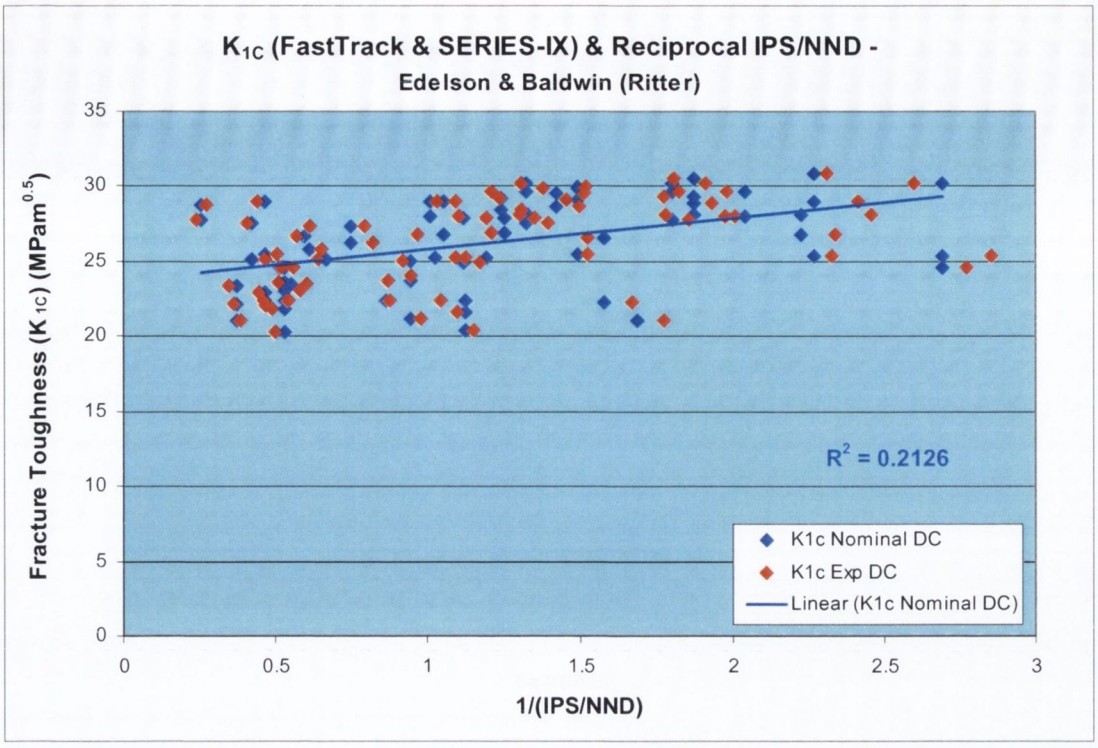

Figure C.5.30. Fracture Toughness Specimens; Graph of Plane Strain Fracture Toughness (K_{IC}) as determined using FastTrack plotted against Reciprocal of IPS/NND. DC1 was not used because of its large IPS/NND. R =0.46.

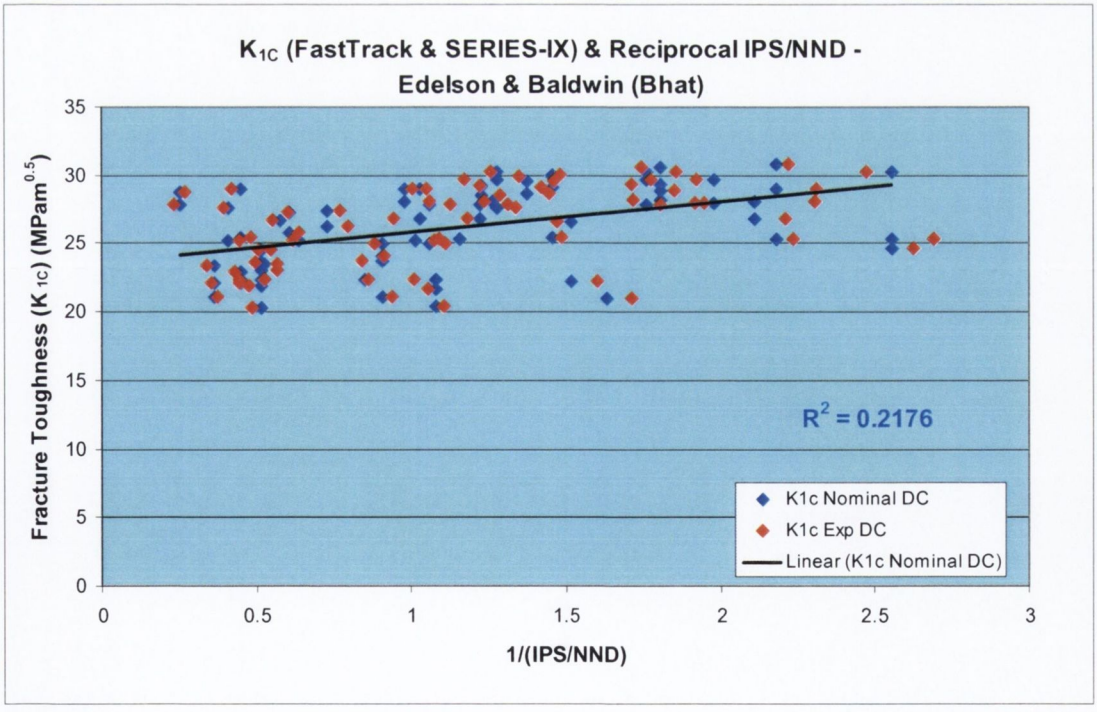

Figure C.5.31. Fracture Toughness Specimens; Graph of Plane Strain Fracture Toughness (K_{IC}) as determined using FastTrack & SERIES-IX plotted against Reciprocal of IPS/NND using Bhat version. DC1 was not used because of its large IPS/NND. R = 0.47.

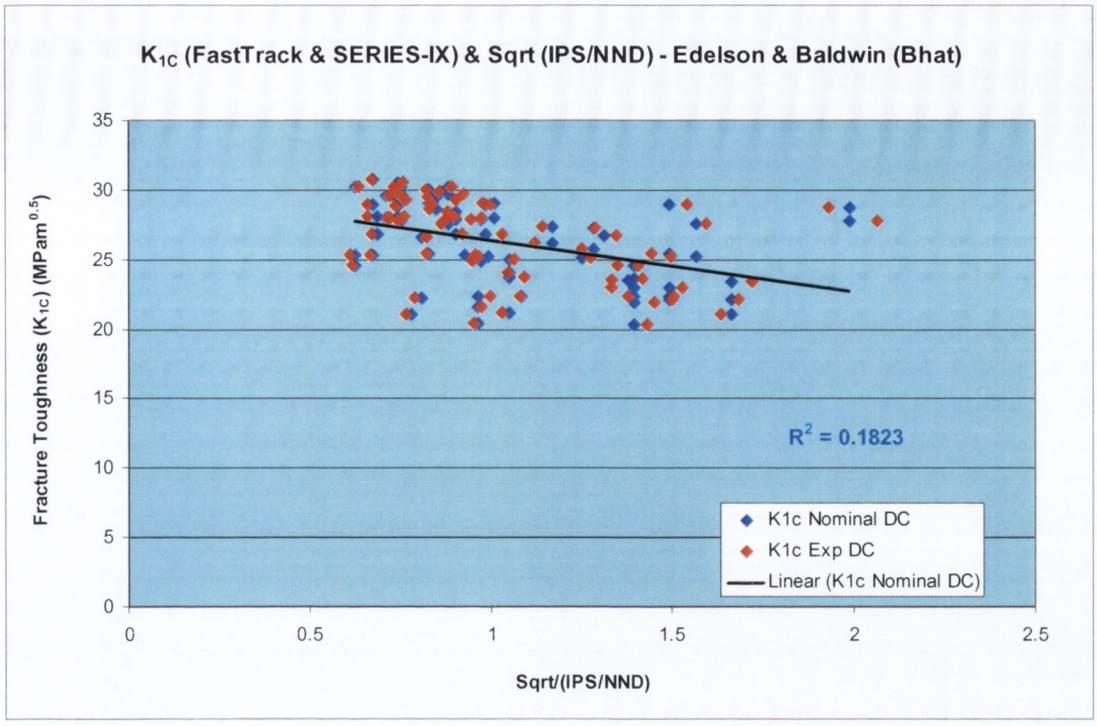

Figure C.5.32. Fracture Toughness Specimens; Graph of Plane Strain Fracture Toughness (K_{IC}) as determined using FastTrack & SERIES-IX plotted against Sqrt of IPS/NND using Bhat version. DC1 was not used because of its large IPS/NND. R = 0.43.

APPENDIX 10 - Strain Energy TRS Predictions & Charpy Impact Energies

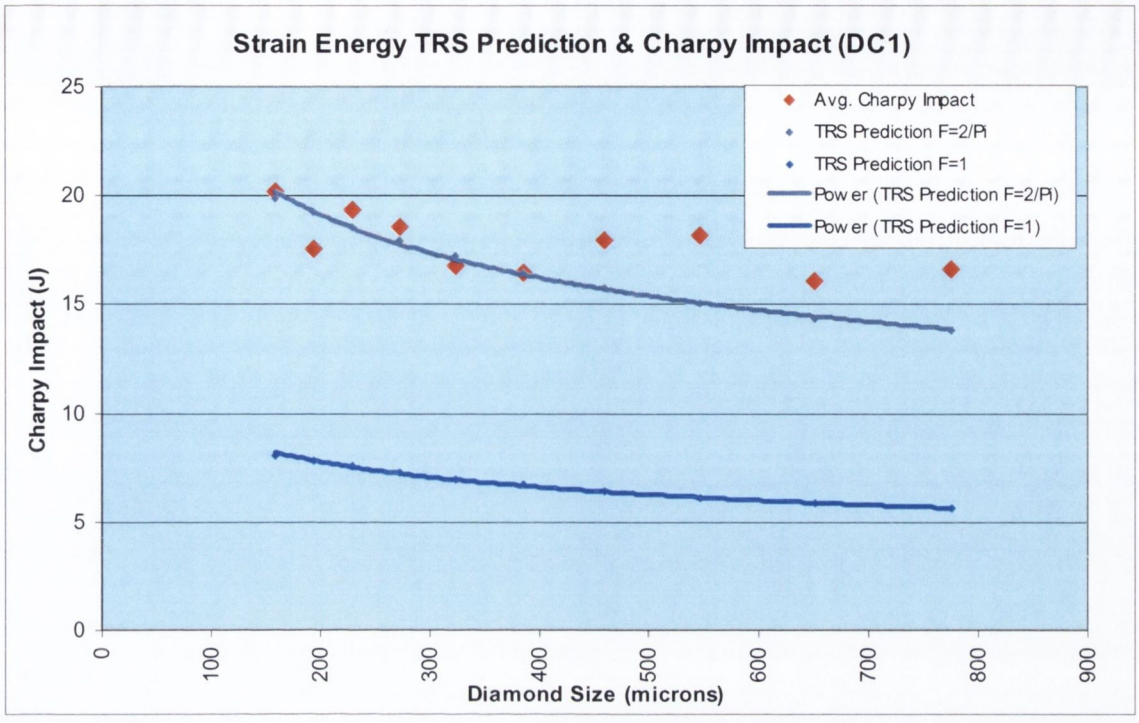

Figure C.5.33. Predicted Strain Energy using Predicted TRS fracture stress σ_f and experimental Charpy impact energy plotted as a function of diamond size (microns) for DC 1. The Strain Energy TRS prediction lines show an upper bound and a lower bound result.

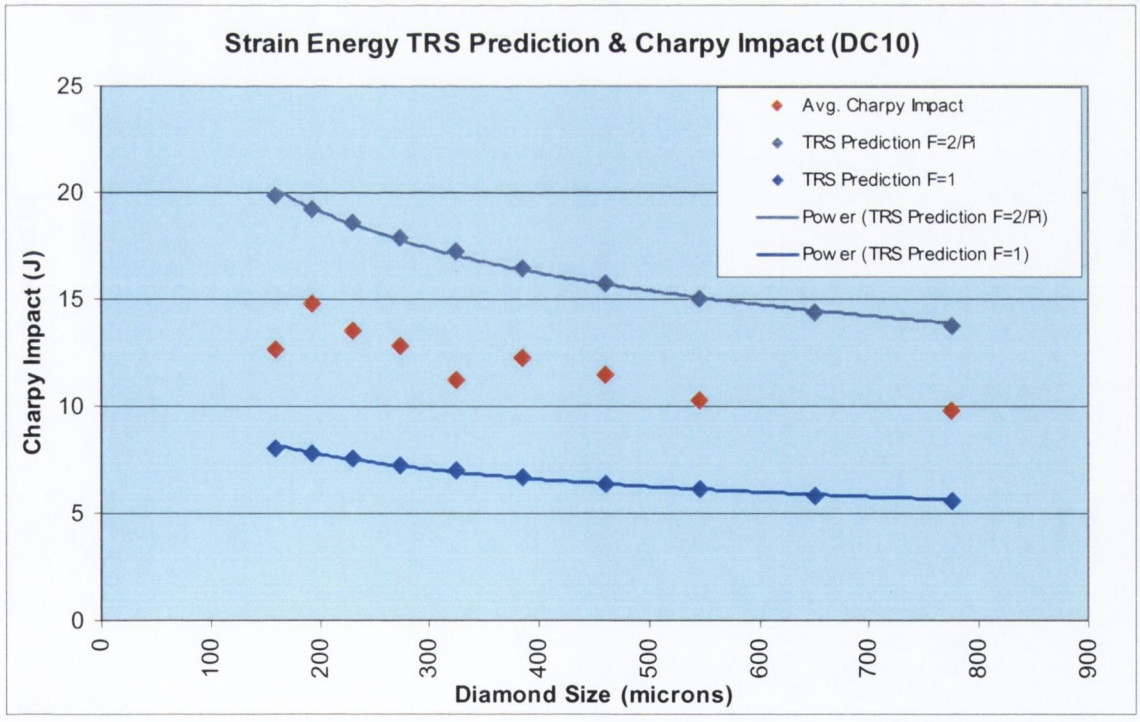

Figure C.5.34. Predicted Strain Energy using Predicted TRS fracture stress σ_f and experimental Charpy impact energy plotted as a function of diamond size (microns) for DC10. The Strain Energy TRS prediction lines show an upper bound and a lower bound result.

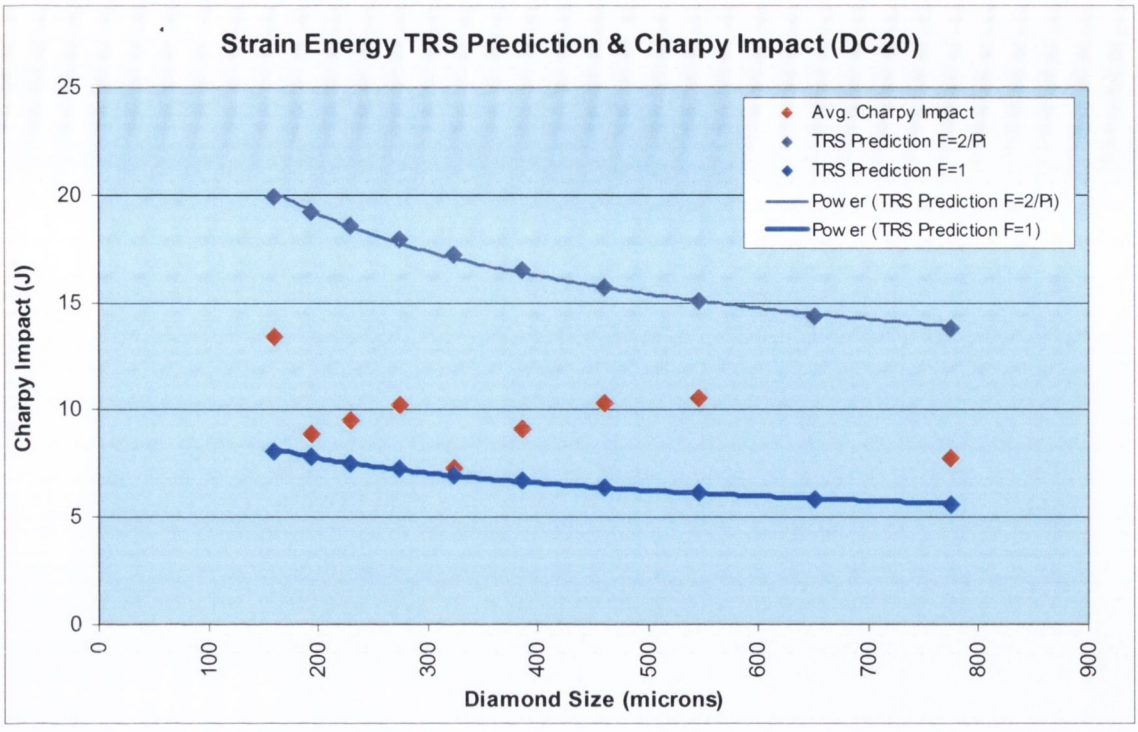

Figure C.5.35. Predicted Strain Energy using Predicted TRS fracture stress σ_f and experimental Charpy impact energy plotted as a function of diamond size (microns) for DC20. The Strain Energy TRS prediction lines show an upper bound and a lower bound result.

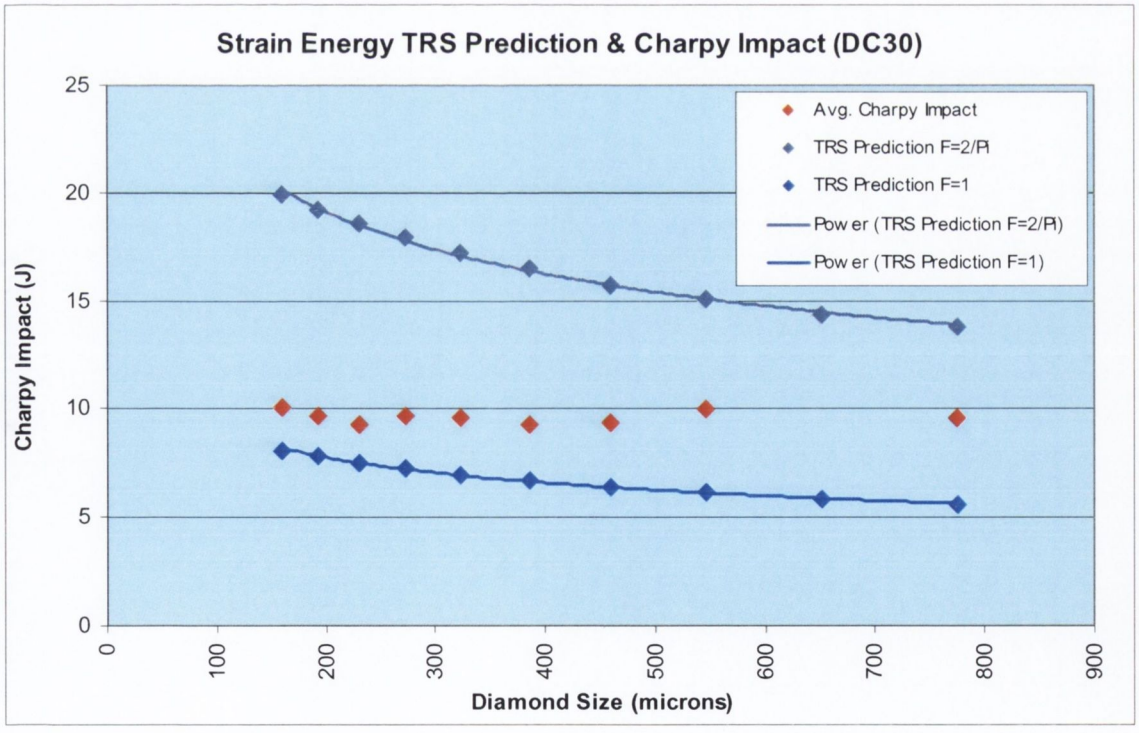

Figure C.5.36. Predicted Strain Energy using Predicted TRS fracture stress σ_f and experimental Charpy impact energy plotted as a function of diamond size (microns) for DC30. The Strain Energy TRS prediction lines show an upper bound and a lower bound result.

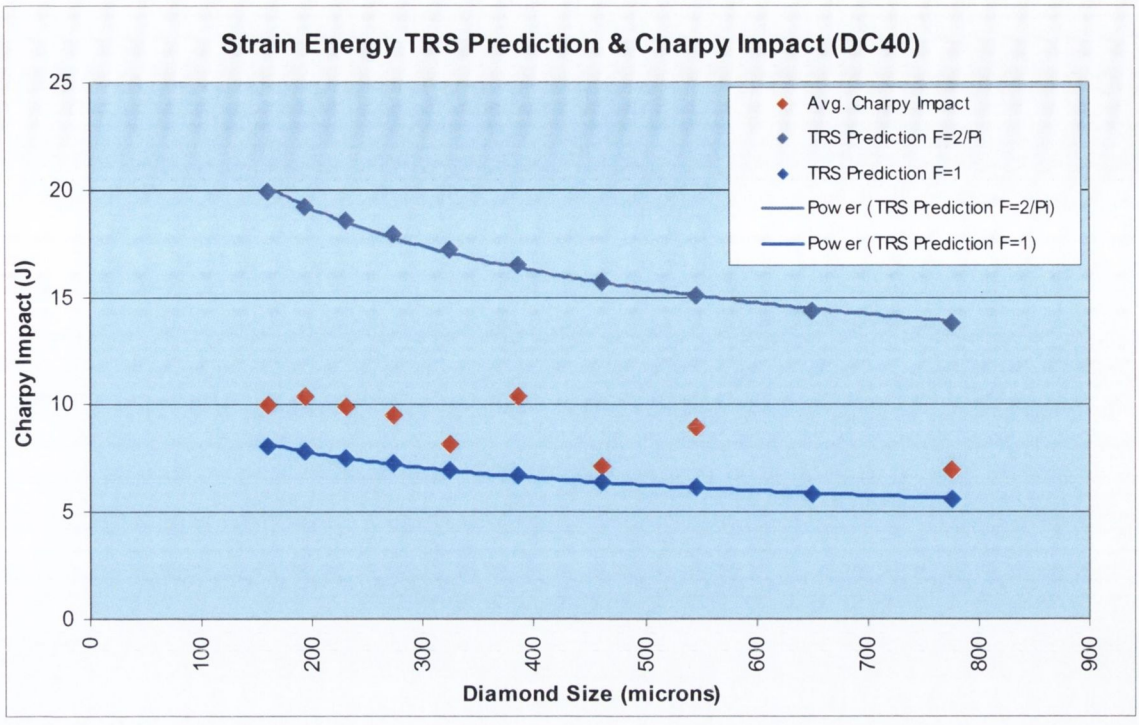

Figure C.5.37. Predicted Strain Energy using Predicted TRS fracture stress σ_f and experimental Charpy impact energy plotted as a function of diamond size (microns) for DC40. The Strain Energy TRS prediction lines show an upper bound and a lower bound result.